Department of Engineering Materials

University of Sheffield

RECYCLED COLOURLESS SODA-LIME-SILICA GLASS AS AN ALTERNATIVE FLUX IN WHITEWARES

by

Tarnkamol Tarvornpanich

A thesis submitted for the degree of Doctor of Philosophy

November 2006

To my parents Admiral Somchai and Nongnuch.

Abstract

The most common type of container glass which is landfilled in the UK is soda-lime-silica glass, comprising typically 71-75wt% silica, 12-16wt% soda and 10-15wt% lime. Considering its chemical similarity to that of the fluxing materials commonly used in whiteware bodies, it is sensible to investigate the use of SLS waste glass as replacement for these fluxes in whitewares. The present study aimed at the incorporation of colourless SLS waste glass into a standard whiteware formulation (i.e. 50wt% kaolinite clay, 25wt% quartz and 25wt% nepheline syenite) as a flux, and at the examination of the microstructural development on firing. Bulk samples with two (e.g. clay and quartz, SLS glass and clay, etc.), three (standard and fully SLS-fluxed whiteware) and four (mixed nepheline syenite SLS glass as flux system) components were studied in depth. After firing 3h at 1100°C, batches containing 6.25wt% SLS glass and 18.75wt% nepheline syenite attained open-pore closure and a bulk density of 2.45 g/cm^3, comparable to that of the standard body fired at 1200°C. SLS glass softens and melts, conferring early densification and overfiring on whitewares fired at commercially-applied firing temperatures. Severe bloating ruled out the use of higher amounts of SLS glass. The microstructural evolution examined using XRD, SEM/EDS, and TEM/EDS revealed the formation of a variable composition plagioclase, wollastonite, and cristobalite in batches containing SLS glass, in addition to primary and secondary mullites, partially dissolved quartz, and a glassy matrix as found in the standard whiteware. Na^+ and Ca^{2+} ions from SLS glass migrate towards clay mineral relicts to form plagioclase, limiting the extent of mullite crystallization in SLS containing batches. Wollastonite and cristobalite crystallize from the devitrification of SLS glass. The flexural strength of the body containing 6.25wt% SLS glass fired at 1100°C (~71 MPa) was higher, modulus of elasticity slightly lower, and fracture toughness comparable to those of the standard whiteware body fired at 1200°C. The Weibull modulus of the partially SLS-fluxed whiteware was lower due to the presence of crystals inhomogeneously distributed over a complex microstructure. From the physical and mechanical properties investigated in this study, SLS glass can be used as part of the fluxing system of some fully densified whitewares.

Acknowledgements

I would like to express my sincere gratitude and thanks to my supervisor Prof. William E. Lee for his advice and continuous encouragement throughout this study.

I would like to thank Dr. Michael Ojovan for helpful guidance and support.

I would also like to thank the technical and clerical staff of the Department of Engineering Materials for giving me every possible assistance. Special thanks to Mr. Ian Watts., Mr. Dean Haylock, Ms. Bev Lane, and Mr. Phil Staton for always being helpful and kind.

Thanks to all my friends for their friendship and encouragement, and thanks also to my colleagues in the Department of Engineering Materials for their friendship and help. Special thanks to Dr. Guilherme P Souza for his continuous support, help, useful discussion and encouragement.

I would like to thank Dr. Antonella Tucci, Dr. Leonardo Esposito and Dr. Elisa Rambaldi from the Italian Ceramic Center (Bologna, Italy) for their useful assistance on mechanical property measurements.

I gratefully acknowledge the financial support from The Government of Thailand for making the pursuit of this degree possible.

Last but most importantly, I would like to express my gratitude to my family especially my parents for their constant support and love, and for encouraging me and being my inspiration.

Publications and Presentations

The following presentations were made during the course of this thesis programme:

Tarvornpanich, T. and Lee, W. E., "Using Recycled Soda-Lime-Silica Glass in Porcelains", Poster Presented at the Annual Ceramic Convention, The Institute of Materials, Minerals and Mining, Keele, UK, 2003.

Tarvornpanich, T., Souza, G. P. and Lee, W. E., "Microstructure and Properties of Nepheline Syenite and SLS Glass Fluxed Whitewares", Oral Presentation on the 9th Conference and Exhibition of the European Ceramic Society, Portoroz, Slovenia, 2005.

The following paper was published, others are in preparation:

Tarvornpanich, T., Souza, G. P. and Lee, W. E., "Microstructural Evolution on Firing Soda-Lime-Silica Glass Fluxed Whitewares", *J. Am. Ceram. Soc.*, **88**[5], 1302-1308, 2005.

Contents

CHAPTER 1 - INTRODUCTION

1.1 - GENERAL BACKGROUND

The UK produces large volumes of waste container glass from bottle banks. It is estimated that around 2.4M tonnes of container glass are generated every year of which only 0.875M tonnes (~36.5%) are recycled (Enviros, 2004), so that large amounts are considered as waste and landfilled. Although the overall UK recycling rate has increased steadily in recent years, compared to Europe the UK is still lagging behind countries like Germany, Belgium and Switzerland, which have much higher recycling rates (over 80%). In 2003, Germany generated 4.147M tonnes of waste container glass and recycled 3.53M tonnes (~85%), Belgium generated 0.656M tonnes and recycled 0.57M tonnes (~87%), and Switzerland generated 0.308M tonnes and recycled 0.283M tonnes (~92%) (Butler and Hooper, 2005). Moreover, the recycling growth in the UK needed to meet the 60% glass recycling target for 2008 under the EU Packaging and Packaging Waste Directive (therefore the recent percent of recycled glass is still quite far from the goal of 60%). Besides the fact that glass is non-biodegradable and therefore a threat to the environment, dumping of this material is expensive. Some of the recycled container glass has been used as feedstock by UK glass container manufacturers to produce new bottles and jars. Because only a limited amount of glass can be re-melted to make new containers, new products utilizing recycled waste glass are needed to further promote glass recycling. Using recycled glass in traditional ceramic bodies is sensible for three main reasons. First, the wide compositional range of the raw materials used for traditional ceramics can tolerate high amounts of wastes. Second, the most common type of container glass is soda-lime-silica (SLS) glass which is, in essence, a vitreous silicate, as is the viscous liquid phase generated during the firing of traditional ceramic bodies. Third, SLS glass has similar chemical composition to nepheline syenite and feldspar fluxes used in traditional ceramic bodies.

Total UK pottery production (tile, tableware and sanitaryware) is 550,000 tonnes/year (Enviros, 2004), and their production consumes considerable amounts of raw materials and energy. The fluxing component of the body is essential to the

development of the glassy phase which accounts for the low porosity of the fired body. Without the flux, the firing temperature would have to be raised to dissolve more refractory components into the liquid that cools to glass. Most commercial whiteware fluxes used in the UK are imported and are the most expensive components in the body. The most common type used in the UK is nepheline syenite, the international supply of which is controlled by one company raising concerns over future supply prices (Hancock, 2005). Other types of fluxes such as feldspars are also expensive due to the cost of mining and processing. As container glass has a higher content of sodium and calcium than most of the mineral fluxes currently in use, it has the potential of being an effective promoter of vitrification (i.e. glass formation) of whiteware bodies. Soda-lime-silica (SLS) glass melts at lower temperature than mineral feldspars, thus it is likely to induce vitrification at substantially lower temperatures than typically required resulting in energy saving and prolonged furnace life. To produce whiteware parts, only transparent SLS glass is considered for use as an alternative flux. This is because the transparent SLS glass has its chemical composition mainly composed of silica, sodium and calcium and only small amounts of metal oxides such as iron so that, when mixed with other whiteware raw materials, a white final product will be achieved. Other glasses such as aluminosilicate glass, borosilicate glass or lead glass melt at higher temperatures than SLS glass (thus probably not as promising as SLS glass to be a fluxing agent), and they are also less available as a waste material. Coloured glass could also be investigated if glazing will be applied in the fired product. Some other glasses which are hazardous wastes (while SLS glass is non hazardous) are aimed to use in the cement industry instead. The recycled SLS glass in this work is intended to divert a waste material from normal landfill disposal into use as a valuable raw material, and therefore to reduce UK industries dependence on relatively expensive imported raw materials. This will also offer environmental benefits through lower energy consumption.

Previous studies (Brown and Mackenzie, 1982; Vangordon, 1983; Youssef *et al.*, 1998; Watanabe and Kato, 2001; Matteucci *et al.*, 2002; Braganca and Bergmann, 2004; Souza *et al.*, 2004; Tucci *et al.*, 2004) have revealed the potential of replacing natural fluxes by SLS waste glass. As the ceramic body is fired to a vitrified state, its triaxial components (clay, filler and flux) react to form a micro-composite of crystals

embedded in a glassy matrix. The vitrification temperature of ceramic bodies containing SLS waste glass has been found to be lower than that of their counterparts containing solely natural fluxes, suggesting that the whiteware production would require less energy, and be cheaper due to the use of a recycled waste as raw material. However, the literature on the microstructural investigation of SLS glass containing whitewares lacks a more fundamental study. A better understanding of the reactions on firing ceramic bodies with various wastes incorporated will lead to optimization of firing schedules and properties in the final products. Recently, Souza *et al.* (2004) showed that SLS waste glass added to a commercial porcelain stoneware formulation led to crystallization of an additional phase (plagioclase) as well as to those usually occurring in porcelains such as quartz, mullite and glass. The mineralogical transformations taking place at the early stages of densification still remain unclear.

1.2 - AIMS OF THE INVESTIGATION

The aim of this project is to determine the feasibility of using colourless SLS glass as a fluxing component in whitewares by partially and totally replacing nepheline syenite flux. This will be pursued by examining in detail the densification behaviour, phase development, microstructural evolution and physical and mechanical properties of SLS-based whiteware bodies upon firing, and comparing to those of nepheline syenite-based bodies. This project also aims at providing a better understanding of the basic science underpinning SLS-containing vitreous ceramic systems, and use this understanding to develop new triaxial formulations.

1.3 - THESIS PLAN

A review of the relevant literature is given in chapter 2, which emphasizes two main topics. One describes whitewares in general such as the definition and classification of whiteware products, raw materials and their functions, compositions of each type of whiteware, processing, reactions on firing and microstructure and properties. The other main topic is about the use of waste materials in ceramics with special attention given to SLS waste glass used in whitewares. The experimental methods employed in the present research are outlined in chapter 3. Results from the characterisation of

the four raw materials, as-received and fired, are presented and discussed in chapter 4. Results from the study of the interaction between raw materials on firing are presented in chapter 5. In chapter 6, the densification behaviour, phase development, microstructure and mechanical properties of the standard and SLS-containing whitewares are presented. A further discussion which draws together results from chapters 4, 5 and 6 is given in chapter 7 followed by conclusions and suggestions for further work.

CHAPTER 2 - LITERATURE REVIEW

2.1 - WHITEWARES

In this section, background on whitewares is given to provide a fundamental basis for the present study on the reformulation of whitewares using soda-lime-silica waste glass as a fluxing agent. This review focuses on types of whiteware, raw materials, processing, firing, microstructure and properties.

2.1.1 - Definition and classification

A whiteware is defined as a fired ware consisting of a glazed or unglazed ceramic body, which is commonly white, and of fine texture (Carty and Senapati, 1998). Whiteware products are often differentiated into three main classes: non-vitreous, semi-vitreous, and vitreous according to their degree of vitrification (and resulting porosity). Vitrification is the gradual formation of a high SiO_2 liquid that flows into and fills some of the pore volume, also bringing solid particles together. The degree of vitrification depends on firing temperature and time, as well as the composition of the ceramic body. Table 2.1 shows the definitions of each type of whiteware.

Table 2.1 - Types of whiteware and their characteristics.

Type	**ASTM definition** (ASTM, 1996)	**Firing temperature** (Rice, 1987)	**Porosity** (Rice, 1987)
Earthenware	A glazed or unglazed nonvitreous clay-based ceramic ware of medium porosity, such as bricks and wall tiles	900 - 1200°C	Usually 10%-25%
Stoneware	A glazed or unglazed vitreous or semi-vitreous ceramic ware, such as wall and floor tiles	1200-1350°C	0.5-2%
China	A glazed or unglazed vitreous ceramic ware used for non-technical purposes, such as dinnerware, sanitaryware, tableware, and artware	1100-1200°C	Usually less than 1%
Porcelain	A glazed or unglazed vitreous ceramic ware used for technical purposes, as the dental, electrical, chemical, structural, and thermal wares	1300-1450°C	Less than 1%

Earthenwares are porous, non-vitrified clay bodies fired at a wide range of temperatures from 800-900°C or up to 1100-1200°C depending on the type of clay used and its impurities. Its sintering is not complete therefore the porosity is quite high (10-20vol.%). It can be glazed or unglazed. Glazed bodies have surfaces which are impermeable to water, which would otherwise penetrate through the open pores of the ceramic ware. Examples of earthenwares are building bricks and roofing tiles. Stonewares are fired at temperatures roughly within the 1200-1350°C range, which is high enough to promote at least partial fusion or vitrification of the clay body, depending on its composition (Rice, 1987). Examples of stonewares are floor and wall tiles. Chinas are vitreous wares usually with less than 1vol.% total (open and closed) porosity. They are mostly used for non-technical purposes, such as art objects. Porcelains are fired at high temperatures compared to those of earthenwares, stonewares or chinas, until high amounts of liquid are formed on firing. They are used primarily for technical purposes. Whitewares can also be divided into two groups depending on whether they are opaque or translucent. Earthenwares and stonewares are opaque whereas porcelains and chinas are translucent.

2.1.2 - Traditional raw materials and their functions in whitewares

Whiteware bodies are usually prepared from raw materials which can be grouped by their function as clays, fluxes and fillers.

2.1.2.1 - Clays

In whitewares production, clay is the main raw material because it makes up about 50wt% of the overall constituents. It provides plasticity and green strength during the forming stages. In terms of processing aid for the forming operations, clays act as binders, with the advantage of being a cheap, natural binder. It contributes, however, substantially to the colour of the fired ware. The two types of clay commonly used in the whitewares industry are ball clay and china clay; which differ in purity and plasticity.

Ball clay is sedimentary or secondary clay of fine-grain size, having a particle size that ranges from 50-90% <2 μm (Echlin, 2002). Its fine particle size confers high

plasticity and green strength when mixed with water, and high shrinkage after firing. It is used mainly in the manufacture of whiteware. Nevertheless, it is impossible to use ball clay alone in whiteware formulations because of its excessive shrinkage, which may be as high as 20% when fired to maturity (Ryan and Radford, 1997). It is usually applied as an admixture to china clay to provide increased plasticity and workability. In order to achieve desirable levels of whiteness, not more than about 15% of ball clay can be added to a whiteware body (Rice, 1987), as adding more than this amount results in a grey, off-white, or buff colour. In porcelain, the presence of ball clay decreases its translucency, therefore only china clay is mostly used. In chemical composition, ball clay greatly resembles china clay in that kaolinite ($Al_2O_3 \cdot 2SiO_2 \cdot 2H_2O$) is the principal clay mineral present. Ball clay, however, contains more impurities than china clay, such as quartz, mica, iron and titanium oxides, and considerable amounts of organic matter. The type and amount of these impurities have a large effect on the physical properties of the clay and therefore on the whiteware body. The organic matter colours mostly the unfired product whereas the iron and titanium impurities colour the fired product, limiting the use of ball clays as raw materials for whiteware. In any case, the principal types of whiteware that contain ball clay are sanitary ware, wall and floor tiles, and tableware. Other characteristics of the fired body that are affected by the presence of impurities in the clay are its pore volume and homogeneity.

China clay or kaolin clay is primary clay. It has a larger particle size (~0.6-1 μm (Rice, 1987)) than ball clay, which results in lower plasticity and green strength. On the other hand, china clay is purer in composition and contains less impurity or organic matter, which gives a white body after firing. Because of the high percentage of kaolinite and low impurity level, china clay has long been used in the whiteware industry especially in china and porcelain.

Both ball clay and china clay contain kaolinite as the main clay mineral influencing the principal properties of the body, thus making kaolinite of interest. Kaolinite is a hydrous aluminosilicate originally formed by the decomposition of the mineral feldspar in granitic rocks under the influence of weathering and/or acidic water (Ryan and Radford, 1997). The decomposition process is regarded as a leaching of alkali and release of SiO_2 and is shown in Reaction 2.1:

$$K_2O{\cdot}Al_2O_3{\cdot}6SiO_2\ (s) \xrightarrow[+2H_2O]{-K_2O\ -4\ SiO_2} Al_2O_3{\cdot}2SiO_2{\cdot}2H_2O\ (s) \qquad (2.1)$$

Potash feldspar — kaolinite

Kaolinite consists of small hexagonal plate-like crystals (ranging from 0.3 μm to 1 μm diameter and approximately 0.05 μm thickness (Rice, 1987)), which often occur in stacks. It has a triclinic or monoclinic crystal structure, space group C1 or P1, made of tetrahedral-octahedral sheets (Figure 2.1).

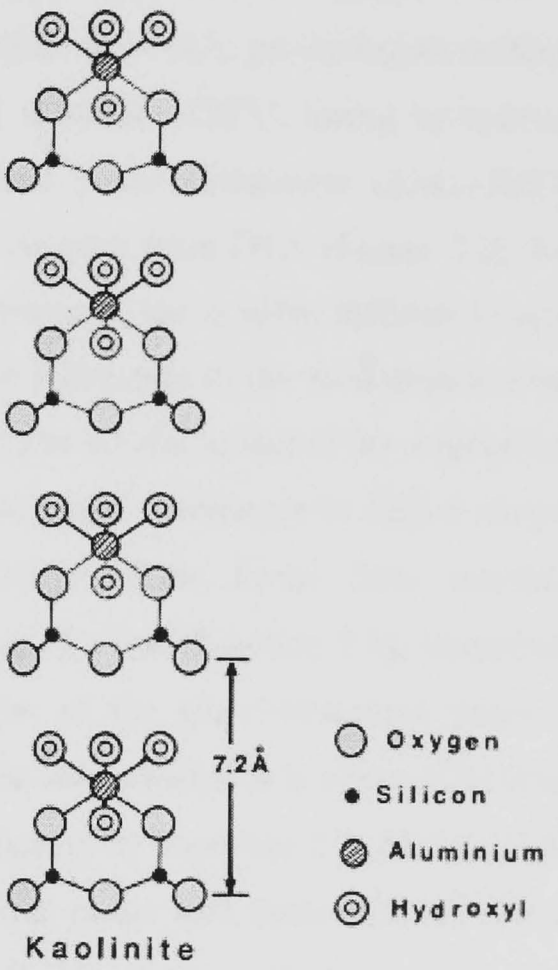

Figure 2.1 - a-b projection of the layer structure of kaolinite; the c axis spacing is 7.2 Å. (Rice, 1987)

The tetrahedral (silica) layers consist of silicon and oxygen ions in which each silicon ion is at the centre of a tetrahedron formed by oxygen ions. The octahedral (Gibbsite) layers consist of aluminium and hydroxyl ions, the hydroxyls forming the corners of an octahedron. When the two layers are combined a kaolinite sheet is formed. The link between the kaolinite sheets is achieved by Van der Waals' forces, supported by hydrogen bonds between the hydroxyl groups in the Gibbsite layer and

the oxygens in the silica layer of the neighbouring kaolinite sheet. A kaolinite sheet plus an interlayer forms a kaolinite unit structure, the distance from top to bottom being ~7.2 Å. A number of kaolinite unit structures are stacked together, forming hexagonal platelets.

On heating the kaolinite clay mineral from room temperature to 200°C, the mechanically combined water (pore water, or water absorbed onto the surfaces of clay particles) is released, disappearing as water vapour. A small endothermic peak in the temperature range 100-200°C (Figure 2.2) is usually due to this water release. Over the temperature range ~200-400°C, organic matter (if present in the clay) begins to oxidize and burns out as CO_2, producing an exothermic peak. The lattice of kaolinite starts to break down at ~550°C, losing its hydroxyl groups as water and leaving a semi-amorphous phase metakaolin ($Al_2O_3 \cdot 2SiO_2$) (Reaction 2.2). This reaction is endothermic as seen from DTA (Figure 2.2). Metakaolin has a slightly disordered crystalline structure that is often difficult to study by X-ray diffraction (XRD), but with electron diffraction in the transmission electron microscope (TEM) the particles show a structure similar to that of the original kaolinite (Rice, 1987). On further heating, metakaolin will decompose to higher temperature phases. At about 950°C, a cubic spinel-type phase forms from metakaolin by a process of recrystallisation with loss of silica (Reaction 2.3), immediately followed by mullite formation. The formation of the spinel-structured phase is the subject of some debate; it is difficult to be sure whether it is a transition alumina (e.g. θ, κ, γ, δ etc.) or contains silica as indicated by Reaction 2.3. Mullite ($3Al_2O_3 \cdot 2SiO_2$) forms from the transformation of spinel phase with further loss of silica, which recrystallises as cristobalite (Reaction 2.4). The sharp exothermic peak occurring at ~950-1000°C is also the subject of debate whether it actually corresponds to the formation of spinel-type phase (Brindley and Nakahira, 1959; Lawrence, 1972; Iqbal and Lee, 1999) or to the formation of mullite (Lee *et al.*, 1999; Chen *et al.*, 2004). According to Lawrence (1972), a small exothermic peak corresponding to the transformation of spinel phase to mullite is seen at ~1000-1100°C, however this peak has not been seen or clearly described in other work. A further small exothermic peak is often seen in kaolinite at 1200-1300°C resulting from continuing mullite formation and cristobalite development.

$$Al_2O_3 \cdot 2SiO_2 \cdot 2H_2O\ (s) \rightarrow Al_2O_3 \cdot 2SiO_2\ (s) + 2H_2O\ (g) \qquad (2.2)$$

kaolinite meta-kaolin

$$2(Al_2O_3 \cdot 2SiO_2)\ (s) \rightarrow 2Al_2O_3 \cdot 3SiO_2\ (s) + SiO_2\ (s) \qquad (2.3)$$

meta-kaolin spinel

$$2Al_2O_3 \cdot 3SiO_2\ (s) \rightarrow 3Al_2O_3 \cdot 2SiO_2\ (s) + SiO_2\ (s) \qquad (2.4)$$

spinel mullite

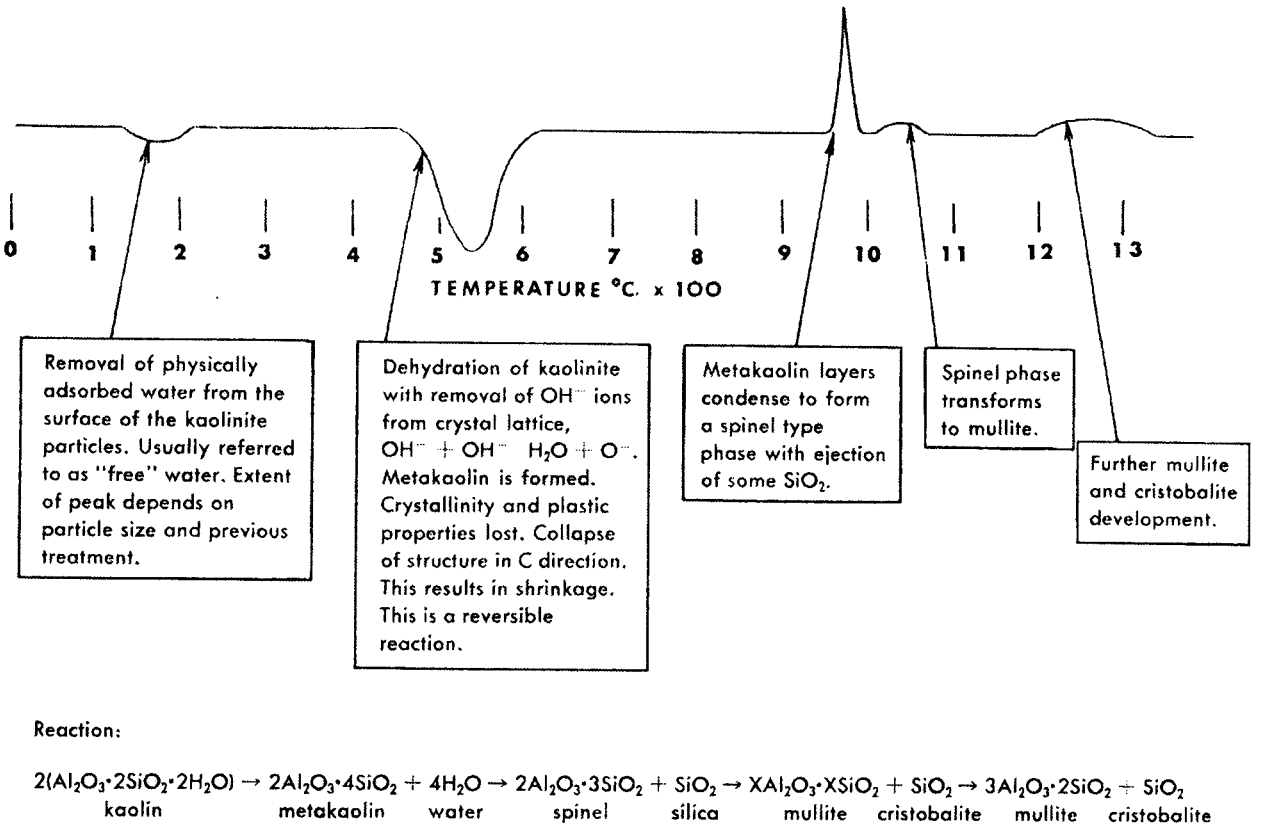

Figure 2.2 - Differential thermal analysis (DTA) curve of kaolinite. (Lawrence, 1972)

China clay and ball clay commonly contain other minor clay minerals and often mica usually in the form of muscovite ($K_2O \cdot 3Al_2O_3 \cdot 6SiO_2 \cdot 2H_2O$). Muscovite has pseudo-hexagonal plate-like crystals, which lose their combined water when heated to 800°C, decomposing at about 950°C, and forming liquid and mullite between 1100°C and 1200°C. Most muscovites show no thermal analysis peaks between room temperature and 1000°C. Muscovite has a layered structure of one octahedral and two tetrahedral sheets weakly bonded together by layers of potassium ions (Figure

2.3). Its unit structure is ~10 Å high. It has a monoclinic crystal structure, with space group C2/c.

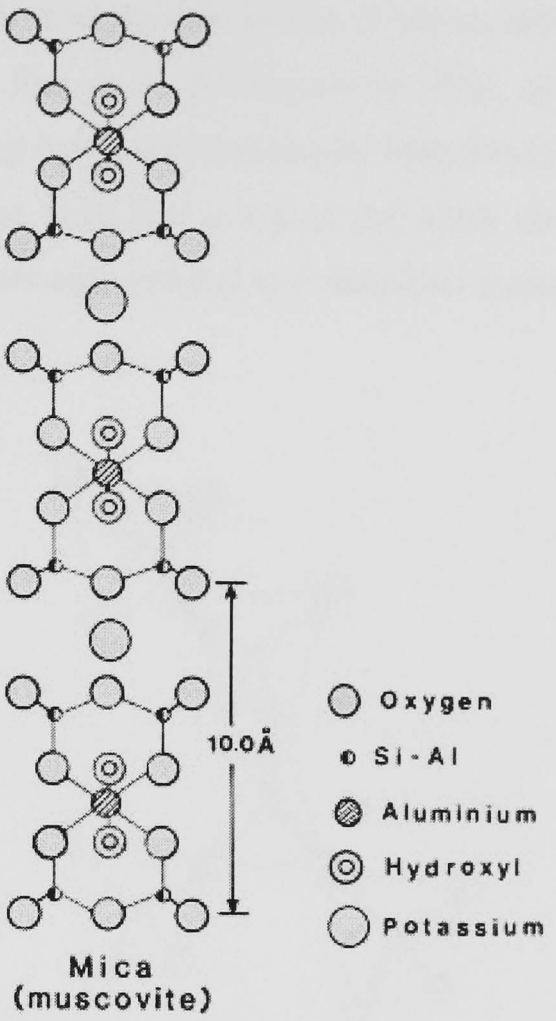

Figure 2.3 - a-b projection of the layer structure of muscovite; the c axis spacing is 10 Å. (Rice, 1987)

2.1.2.2 - Fillers

In their pure form clays exhibit high shrinkage when dried and fired, accompanied by deformation and cracking. Filler, a non-plastic and high melting point material, has to be added to whiteware bodies to reduce drying and firing shrinkage and also to reduce deformation (e.g. warping) when fired to temperatures which result in the relative large amount of glass in the bodies. Particles of the filler occupy part of the space left between clay and flux, and provide the skeletal structure, which restricts the shrinkage of the surrounding material. In addition, they open the structure of the body and allow gases evolved during drying and firing to escape. Fillers also play a very important role in the mechanical properties of the fired product. The most

common filler used in whitewares and many other ceramic bodies is silica (SiO_2), either in the form of quartz sand or flint.

Quartz sand is used in most whiteware bodies. It can be added as filler and/or as an impurity of clay and/or flux. It is an inexpensive filler, reducing the body drying shrinkage, and controlling its thermal expansion. Structurally, quartz is composed of SiO_4 tetrahedra, the same units that compose the silica sheets of clays. In quartz, however, the tetrahedra are arranged not in a sheet-like structure, but in spiral chains (Figure 2.4).

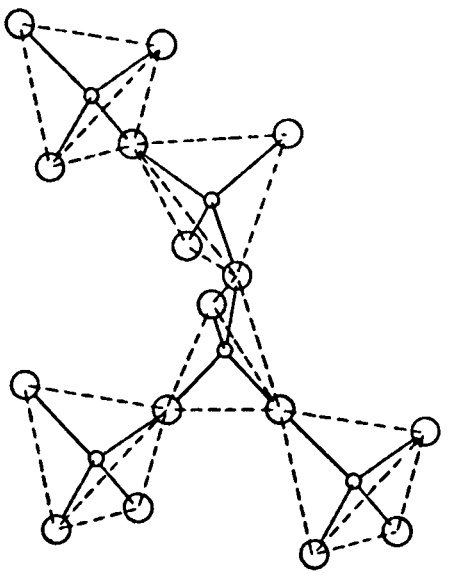

Figure 2.4 - Spiralled chains of SiO_4 in the structure of quartz. (Worrall, 1982)

Quartz undergoes a number of transformations with temperature, involving changes in crystal structure, density and thermal expansion behaviour. When heated, the room temperature form of quartz (α-quartz) will change to the high temperature form (β-quartz) at 573°C. This inversion involves only a slight change in the Si-O-Si bond angle, and therefore occurs rather rapidly, accompanied by a structural change resulting in a volumetric expansion of quartz grains on heating. The expansion accompanying this change results in a change in density from 2.65 g/cm^3 (α-quartz) to 2.53 g/cm^3 (β-quartz) as shown in Table 2.2. This inversion is reversible, as noticed by the sudden shrinkage of quartz particles on cooling when the fired ware reaches ~573°C.

Table 2.2 - Polymorphic forms of silica. (Hlavac, 1983)

Modification	Crystal structure	Density (g/cm^3)
α-quartz	Trigonal	2.65 (20°C)
β-quartz	Hexagonal	2.53 (600°C)
α-tridymite	Orthorhombic	2.26 (20°C)
β-tridymite	Hexagonal	-
γ-tridymite	Hexagonal	2.22 (200°C)
α-cristobalite	Tetragonal	2.32 (20°C)
β-cristobalite	Cubic	2.20 (500°C)
Silica glass	Amorphous	2.21 (20°C)

Note: temperatures in brackets indicate temperature upon measuring density.

If β-quartz is further heated, reconstructive transformations (conversions) take place. From the work of Fenner (1913), extensively quoted in literature, quartz is stable up to 870°C before it transforms to tridymite, and tridymite is stable from 870°C to 1470°C before it transforms to cristobalite:

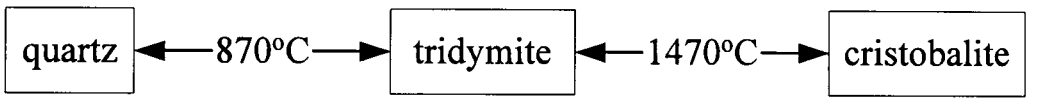

Figure 2.5 – Transformations of silica polymorphs.

However, many authors disagree that tridymite is a pure silica polymorph. Flörke (1955) (in the paper reviewed by Stevens *et al.* (1997)) suggested that tridymite is not a stable phase in the pure SiO_2 system and it only becomes stable in the presence of foreign ions such as Na^+, Ca^{2+} and Al^{3+}. Hlavac (1983) concluded that in a high purity system (impurities less than 0.01%), β-quartz is stable up to about 1025°C before converting to β-cristobalite which on cooling to 200-270°C, will undergo inversion to its low temperature form, α-cristobalite. If more impurities are present, β-quartz is then reconstructively transformed to γ-tridymite at ~870°C which, on cooling, will undergo inversion to its low temperature forms; β-tridymite at 163°C and α-tridymite at 117°C, or on further heating is transformed to β-cristobalite at

~1470°C. Above ~1726°C, β-cristobalite melts. The sequence of these polymorphic transformations of SiO_2 on firing as described by Hlavac (1983) is:

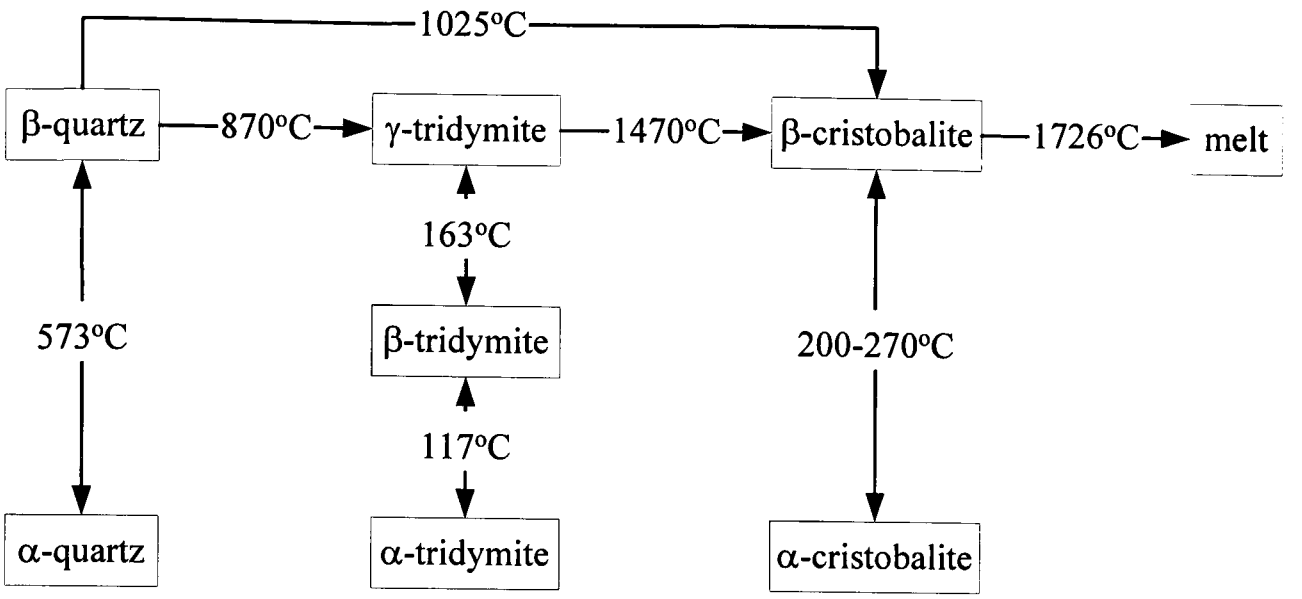

Figure 2.6 - Polymorphic transformations of silica. (Hlavac, 1983) **Horizontal arrows are reconstructive transformations (conversions), and vertical arrows are displacive transformations (inversions).**

Holmquist (1961) determined via heating mixtures of silica and alkali chlorides or alkali oxides at 860-1150°C that alkali oxides cause the conversion of quartz to tridymite with cristobalite as an intermediate transition product, in agreement with Stevens *et al.* (1997). Stevens *et al.* concluded in her work that in the pure silica system quartz converts to an amorphous transition phase after firing above 1300°C whereas when alkali ions (either Na or K ions) are present in the system, the conversion can start at temperatures as low as 1100°C and forming disordered cristobalite/tridymite before converting to cristobalite or tridymite depending on the temperature and alkali concentration. Tridymite is the main phase present at high alkali concentration. These conversions proposed by Stevens *et al.* (1997) are summarised in Figure 2.7. Tridymite and cristobalite structures are more open than those of quartz, which accounts for their lower density (Table 2.2). Stevens *et al.* (1997) also stated that because cristobalite and tridymite have more open structures than quartz there are voids in the structure which are large enough to accommodate atoms such as Na, K, Ca and these atoms may help to stabilise the structure.

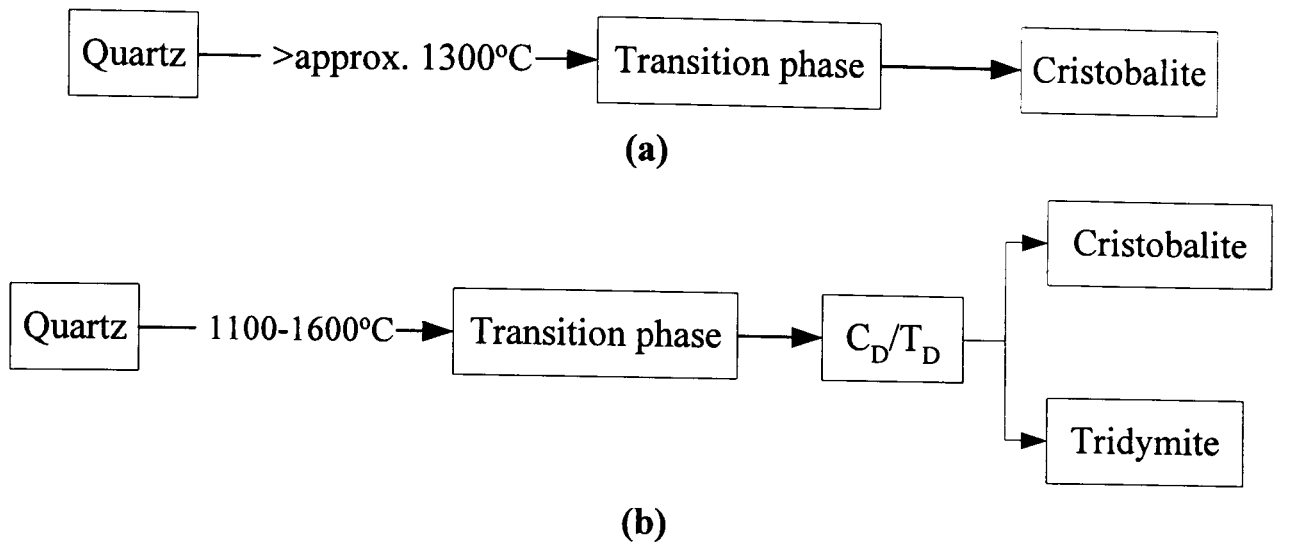

Figure 2.7 - Silica conversions in (a) pure silica system and (b) in the presence of alkali ions. (Stevens *et al.*, 1997)

The reconstructive transformations of silica are slow involving breakage and rearrangement of the strongly bound SiO_4 tetrahedra. Because these irreversible changes take considerable time, the degree to which they occur in whiteware bodies depends on how long the temperature is held at, or above, the transformation points and the amount of fluxes and mineralisers present. In fact, much of the cristobalite in fired whiteware bodies probably comes, not from the quartz changes, but from the free SiO_2, which is liberated when mullite forms from the spinel. However, it is possible to speed up the formation of tridymite and cristobalite by addition of small amount of fluxes or mineralisers (Lawrence, 1960; Holmquist, 1961; Ford, 1967; Stevens *et al.*, 1997; Hand *et al.*, 1998).

At high temperatures these conversions are hastened by the presence of fluxes. Fluxes also cause quartz particles to dissolve to form a silica-rich glass, with an increase in volume. The siliceous glass undergoes little thermal shrinkage on cooling (α ~$3x10^{-6}$ /K), but the partially dissolved quartz crystals have a large thermal expansion coefficient (α ~$23x10^{-6}$ /K) (Chaudhuri, 1982; Iqbal and Lee, 2000). On cooling, differential shrinkage causes stresses that may result in the cracking of large crystals (>30 μm), creating microcracks, which are commonly observed in and around large quartz grains in the whiteware body, and reducing the strength of the fired product. Improvements in the mechanical properties of stoneware have been observed by reducing the quartz particle size (Souza, 2005), as well as by substituting quartz with alumina (Al_2O_3) (Braganca and Bergmann, 2003; Amigo *et*

al., 2004). Alumina has no crystalline inversions within the firing temperature range of any whiteware, and has lower thermal expansion (α ~$8x10^{-6}$ /K) than quartz, consequently allowing the production of a ceramic body with a higher strength. The significantly higher cost of alumina compared to that of quartz is the major drawback for its use (Carty and Senapati, 1998). Another drawback is that alumina has a higher density (3.9 g/cm^3) than quartz, thus adding to the weight of the whiteware (Ryan and Radford, 1997).

Flint is another form of silica (SiO_2) which has traditionally been used in the UK and is still used in some whiteware formulations. It is usually produced from quartz sand (Newcomb, 1947) and consists of extremely small crystals of quartz bound together by molecules of water. It is less dense than quartz sand, due to the presence of water and micro pores. The density of flint is thus less than that of quartz, generally in the range 2.58 to 2.62 g/cm^3. Flint loses its combined water at ~400°C, causing the structure to loosen, and change to cristobalite at ~1100°C. The fine particles of flint make it more reactive than quartz, and in particular able to convert to cristobalite during firing more readily. Flint often contains lime as impurity and this promotes conversion. Traditionally, in the UK, flint has been the popular form of silica component of whiteware bodies, but it is nowadays replaced by quartz sand mainly for economic reasons (Ryan and Radford, 1997).

2.1.2.3 - Fluxes

Flux is a low melting mineral that is added to a whiteware body to enable it to vitrify more readily. The liquid phase, which forms on firing, acts as a bond for the other materials present, enhancing the fired properties of the body (Russell, 1991). Pure clay has to be fired to a very high temperature before even partial vitrification can take place. In the presence of flux, which contains alkali or alkali earth ions, the vitrification temperature can be reduced substantially. When heated to a sufficiently high temperature, flux melts and the alkali oxides diffuse out of the flux particles to react with the surrounding materials, particularly clay, and to some extent with filler to form a viscous liquid. This liquid draws together the crystalline particles, allowing densification to occur through a viscous composite sintering (VCS) process. When

cooled, the liquid forms a glass, which binds the crystalline phases in the body together. The main fluxing minerals used in the whiteware industry are feldspars and nepheline syenite.

Feldspars are the group of minerals consisting of alkali or alkali-earth alumino silicates. Three main types of feldspars are: potash feldspar (orthoclase or microcline), $K_2O \cdot Al_2O_3 \cdot 6SiO_2$, sodium feldspar (albite), $Na_2O \cdot Al_2O_3 \cdot 6SiO_2$, and calcium feldspar (anorthite), $CaO \cdot Al_2O_3 \cdot 2SiO_2$ (Dinsdale, 1986). Potash feldspar crystallises in the monoclinic form as orthoclase and in the triclinic form as microcline, while soda and lime feldspars crystallise in the triclinic form (Norton, 1969). The three main varieties of feldspar seldom occur purely and mixed crystals are usually found (Ryan and Radford, 1987). The solid solutions between potassium and sodium feldspar are known as alkali feldspars, whereas those between sodium and calcium feldspar are known as plagioclase feldspars (Figure 2.8). Solid solution in alkali feldspars occurs by a simple exchange of Na^+ and K^+, whereas plagioclase solid solution arises from the coupled substitution of $Na^{+1}$and Si^{+4} by Ca^{2+} and Al^{3+}.

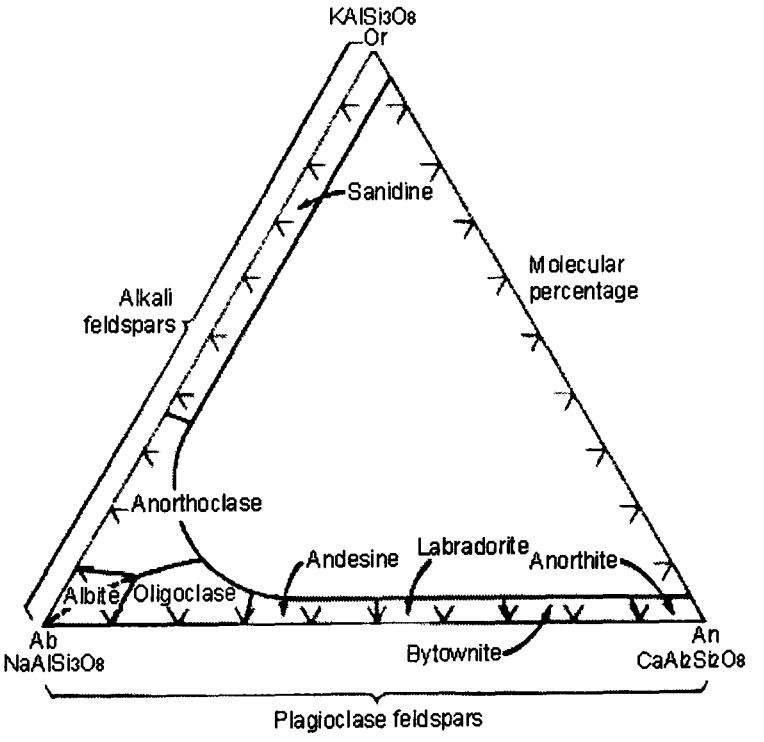

Figure 2.8 - Solid solutions of feldspars. (Deer *et al.*, 1992)

Feldspars are added to decrease the firing temperature and therefore to reduce costs. Feldspars do not have a defined melting point. When fired, they start to decompose and soften progressively until they become a viscous liquid. This softening and

melting is far more gradual in alkali aluminosilicates than in alkali-earth aluminosilicates (Table 2.3). Potash feldspar begins to melt at 1150°C, and soda feldspar melts at ≥1118°C. Lime feldspar, being high in alumina (36.7wt%) and low in silica, melts at a much higher temperature, 1550°C or above. If more than one alkali or alkali earth oxide is present, the reaction is greatly hastened and melting is completed at much lower temperatures. For example a mixture of potash and sodium feldspar can melt as low as 1070°C. Feldspar supplied to the whitewares industry is usually ground to fine particles (~40 μm), to increase reactivity of its fluxing components (Lawrence, 1972). Potash feldspar is preferred for the production of whitewares over sodium feldspar because of its higher viscosity when melted reducing the probability of deformation on firing, such as sagging in tableware (Baumgart *et al.*, 1984).

Table 2.3 - Theoretical composition, density and melting temperature of feldspars. (Hlavac, 1983)

Type of feldspar	Theoretical composition (wt%)					Density (g/cm^3)	Melting temperature (°C)
	SiO_2	Al_2O_3	CaO	Na_2O	K_2O		
$K_2O \cdot Al_2O_3 \cdot 6SiO_2$	64.75	18.32	-	-	16.93	2.54	≥ 1150
$Na_2O \cdot Al_2O_3 \cdot 6SiO_2$	68.73	19.44	-	11.83	-	2.62	≥ 1118
$CaO \cdot Al_2O_3 \cdot 2SiO_2$	43.79	36.65	20.16	-	-	2.75	≥ 1552

Nepheline syenite, as a substitute for feldspar, is being increasingly used in the whitewares industry, particularly in the manufacture of sanitaryware and porcelain. Nepheline syenite is a mixture of nepheline ($K_2O \cdot 3Na_2O \cdot 4Al_2O_3 \cdot 9SiO_2$), microcline ($K_2O \cdot Al_2O_3 \cdot 6SiO_2$) and albite ($Na_2O \cdot Al_2O_3 \cdot 6SiO_2$). It has higher alkali content and less free quartz than feldspars, hence it is a more powerful flux giving a more fluid liquid on firing and allowing faster firing schedules. Since nepheline syenite has lower silica and more alumina than most feldspars, substituting it into whiteware formulations means that, on one hand a lower melting temperature is achieved, while on the other hand a more viscous melt may result because of extra alumina. Nepheline syenite generally begins to sinter at 1060°C and has a density of $2.54 g/cm^3$. It melts within the 1150-1200°C range, depending on the alkali content. The replacement of feldspar by nepheline syenite in porcelain bodies has been

reported to increase the strength by the more efficient pore closure it promotes on melting (Sane and Cook, 1951; Holmstrom, 1981). Moreover, substitution of nepheline syenite for potash feldspar in wall tile bodies lowers water absorption, increases shrinkage and mechanical strength (Koenig, 1939; Koenig, 1964; Roy and Som, 1970). In electrical porcelain, substitution of nepheline syenite for potash feldspar increases firing range, strength, decreases water absorption and increases shrinkage at lower firing temperature (Oberschmidt, 1957).

2.1.3 - Whiteware body compositions

Most whiteware bodies, excluding bone china, are composed of clay (china and/or ball clay), quartz or flint, and feldspar or nepheline syenite flux. Typical whitewares are composed of 50wt% clay, 25wt% filler and 25wt% flux, referred to as triaxial bodies. The composition of the body depends on the availability of raw material and the type of whiteware. The proportions of constituents can be varied to meet process requirements and/or to alter the properties of the fired products to certain applications. Thus, the composition of whiteware bodies is still largely a matter of trial and error. Typical compositions for some well known products are shown in Table 2.4. The possible minor additions of further components are not specified.

Earthenware is a type of whiteware with a porous body. The firing temperature (900-1200°C) is somewhat below that required to produce a vitreous ceramic ware. The raw materials are selected clay, quartz and a flux consisting of some feldspar. The percentage of flux rarely exceeds 10wt%, and quartz ranges from 30-45wt%. The reactions occurring upon firing are similar to those in porcelains, even though there is less flux in the body. Stoneware can be made from either nonrefractory fireclay (clays rich in fluxing contaminants) or some combination of clays, fluxes and silica depends on the forming route and desired fired properties of the stoneware. China wares and porcelains are made of mixtures of various white-burning clays and fluxes of such a nature and proportions that will produce a dense, vitreous body. The temperatures of firing these bodies are usually higher than earthenware, being in the range 1100-1450°C (Table 2.1). Vitreous china consists of 50wt% clay (china and ball clay), some feldspar (10-20wt%) and quartz (35-45wt%). In general the composition of china is similar to that of porcelain, although these materials have

different final uses. Vitreous china is most often used in non-technical purposes such as for sanitary plumbing fixtures (Haber and Smith, 1991). Bone china differs from porcelains in containing bone ash (calcined animal bone) and Cornish stone. A typical composition of a commercial bone china is 25wt% china clay, 50wt% bone ash, and 25wt% Cornish stone. Cornish stone consists of sodium and potassium feldspars, mica and quartz. Bone ash consists predominantly of hydroxyapatite $Ca_{10}(PO_4)_6(OH)_2$ (Baumgart *et al.*, 1984; Dinsdale, 1986; Iqbal *et al.*, 2000). Thus the microstructure of fired bodies of bone china differs from other whiteware bodies as it contains two crystalline phases, β-tricalcium phosphate and anorthite, embedded in glass (Dinsdale, 1986). Porcelain is composed of china clay (kaolin), feldspar and quartz. Hard porcelain contains about two parts of kaolin, one part of feldspar and one part of quartz. It is fired at ~1400°C. Soft porcelain is fired at lower temperatures (~1250°C) and has higher amounts of feldspar (up to 30-40wt%). The term "soft" is related to the lower firing temperature than that of the "hard" (higher firing temperature) porcelain. The amount of kaolin in porcelain compositions is not less than 30wt% due to the need for plastic behaviour and dry strength for the unfired body. Occasionally, some of the kaolin clay can be substituted by plastic ball clays but this can cause some loss of translucency of the fired body.

Table 2.4 - Whiteware body compositions in wt%. (Rado, 1988)

Raw materials	Earthenware	Vitreous china	Bone china	Soft porcelain	Hard porcelain
Clay					
Ball clay	25	-	-	-	-
China clay	25	50	25	30-40	50
Flux					
Feldspars	5-20	10-20	-	30-40	15-25
Cornish stone	-	-	25	-	-
Filler					
Quartz/Flint	30-45	35-45	-	25-35	15-35
Bone ash	-	-	50	-	-

2.1.4 - Whiteware processing

Figure 2.9 shows a simplified processing route of a whiteware (Ryan and Radford, 1997).

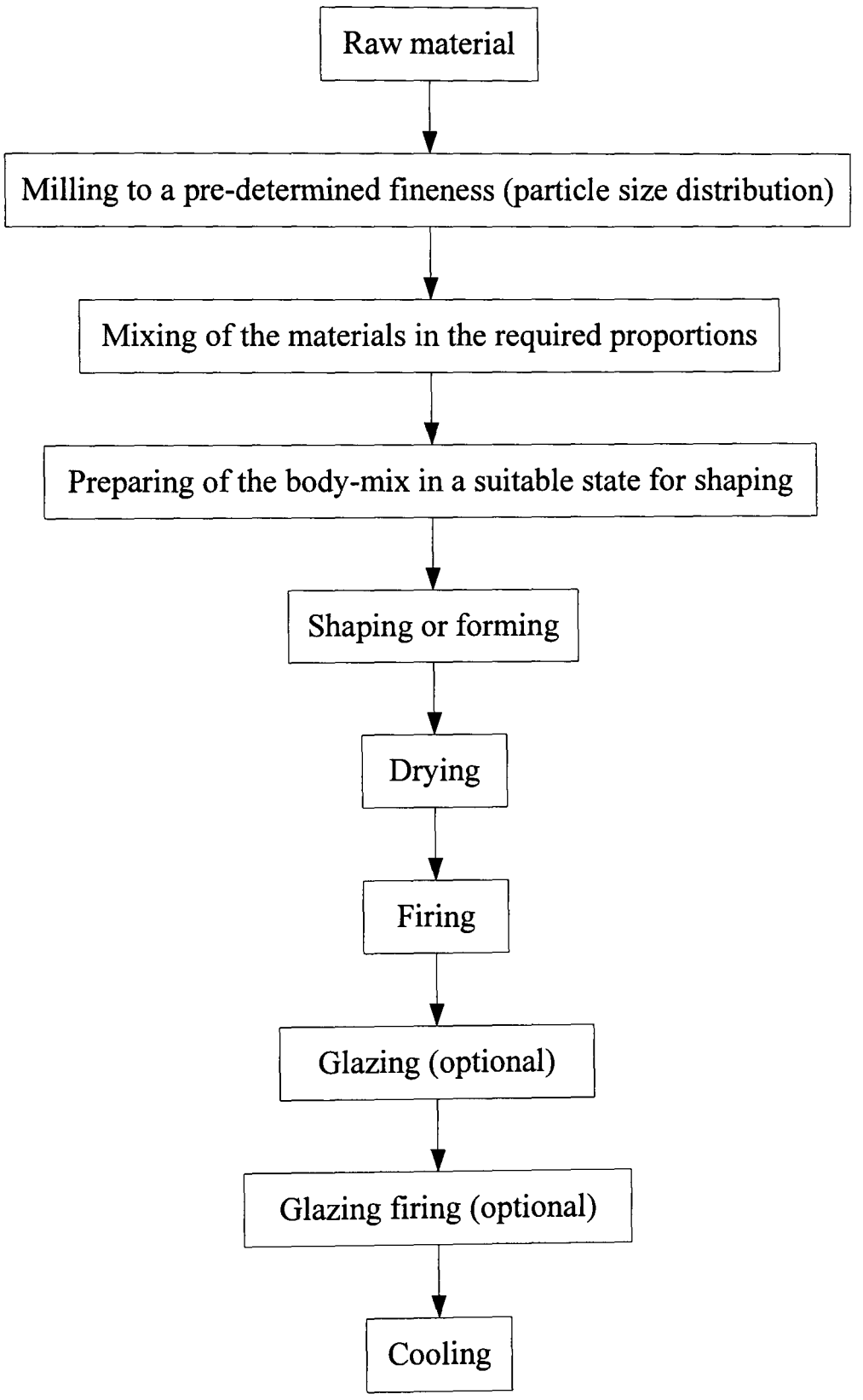

Figure 2.9 - Flowchart of whiteware processing. (Ryan and Radford, 1997)

The processing begins with the preparation of the raw materials to be used. Raw materials may be milled to a specific fineness. Flux and filler particles are usually coarser than those of clay. The specific ratios between raw materials vary depending on the type of product (see Table 2.4). This allows the body mixture to pack efficiently and so to keep the firing shrinkage low. Quartz and flux are commonly found in the market with a median particle size, which is about 10 μm (Baumgart, 1984). After preparation of the raw materials, the next step is processing the body. The body is processed by weighing the calculated portions of the different raw materials, mixing them thoroughly and crushing and grinding them to the desired fineness. In general for processing whitewares, a ball mill is used for mixing and grinding the raw materials. The body is then mixed with water to achieve the consistency needed for the chosen forming method. Typical forming methods for ceramic whiteware include dry pressing, plastic forming, and slip casting, each of which has a specific range of water contents associated with it (Norton, 1970; Ryan and Radford, 1997). Dry pressing requires the powder agglomerates or granules to have a low water content, commonly of about 5-15% (Haber and Smith, 1991). Bodies used for plastic forming usually have a water content of 20-30wt%. In slip casting, the slip may contain about 20-35wt% water to establish suitable rheology. After the whiteware body is formed, drying is carried out before firing to reduce the water content to a minimum before firing to prevent cracking. If water is removed from the body too rapidly, the surface of the ware will dry more extensively than the interior, thus subjecting the ware to tensile stresses, which result in cracking. The amount of water to be removed depends on the forming method employed. 18-20wt% water content has to be removed from unfired whiteware body formed by slip casting or plastic forming while 2-7wt% for dry pressing (Ryan and Radford, 1997). No shrinkage occurs in unfired, low water content whiteware body on drying due to the fact that the water is simply removed from voids between particles. Drying from high water content involves a linear shrinkage of 4-6% in most whiteware bodies (Ryan and Radford, 1997). After the whiteware is dried, it is fired at specific temperature to be densified and to develop the required properties. Some whitewares are glazed to provide smooth, shiny surfaces that seal their porosity. Glazing can be done before or after firing, followed by re-firing to set the glaze. However, in some products such as sanitaryware and tableware the glaze is applied to the dried ware and a single firing matures both the body and the glaze.

2.1.5 - Reactions in whiteware on firing and cooling

Reactions occurring on firing a whiteware body comprise transformations of mineral phases, formation of liquid phase (a melt), reactions between different crystal phases or with liquid phase, and formation of crystal phases from the melt as summarized in Figure 2.10. As the temperature is raised from room temperature to 200°C, the last traces of physically adsorbed water, which remain after the drying process, are completely removed. The degree of shrinkage during this period relates to the volume of water lost. Between 200-700°C, organic matter present in the clays is burnt off. The heating rate throughout this stage should not be too high to allow the gases to escape before the body vitrifies. Gases trapped in closed pores or liquid phases cause bloating in the fired product. Between 450-600°C, kaolinite crystals in the clay undergo the breakdown of their structure with the release of chemically-combined water to form meta-kaolinite. This reaction is accompanied by minor shrinkage due to the collapse of the kaolinite crystal structure with the loss of water and considerable increase in porosity. XRD traces show the absence of crystalline kaolinite above 600°C. At 573°C, quartz changes from a low to a high temperature form with accompanying volume expansion. This expansion of the quartz particles is not too apparent in whiteware bodies due to the compensating effect of shrinkage occurring between 450-600°C.

Between 700-1000°C, the potash feldspar is transformed into its high temperature form, leucite, while the mixed alkali feldspar is transformed into the homogeneous high temperature form, sanidine. At about 950°C, meta-kaolin transforms into spinel with the ejection of amorphous silica. Small (<0.5 μm) cuboidal crystals of primary mullite, believed to form from the spinel-structured phase, begin to develop in the clay relicts at 1000°C or above. The first interaction between the whiteware components occurs when feldspar starts to melt at about 1000-1100°C, depending on the alkali content. This also initiates the process of vitrification, the formation of liquid phase that bonds crystalline phases together. The surface tension of the liquid phase draws the crystal particles together. The spaces between the particles, which form the porosity in the body, decrease hence reducing the open porosity and increasing shrinkage of the body. The porosity is initially interconnected (open

pores), but the reduction in body volume results in the formation of isolated or closed pores. If sufficient liquid phase is present, all the open pores are removed and only the closed pores remain. With increasing temperature, the melting feldspar then dissolves some fine grains of quartz, which increases the viscosity of the melt (liquid phase).

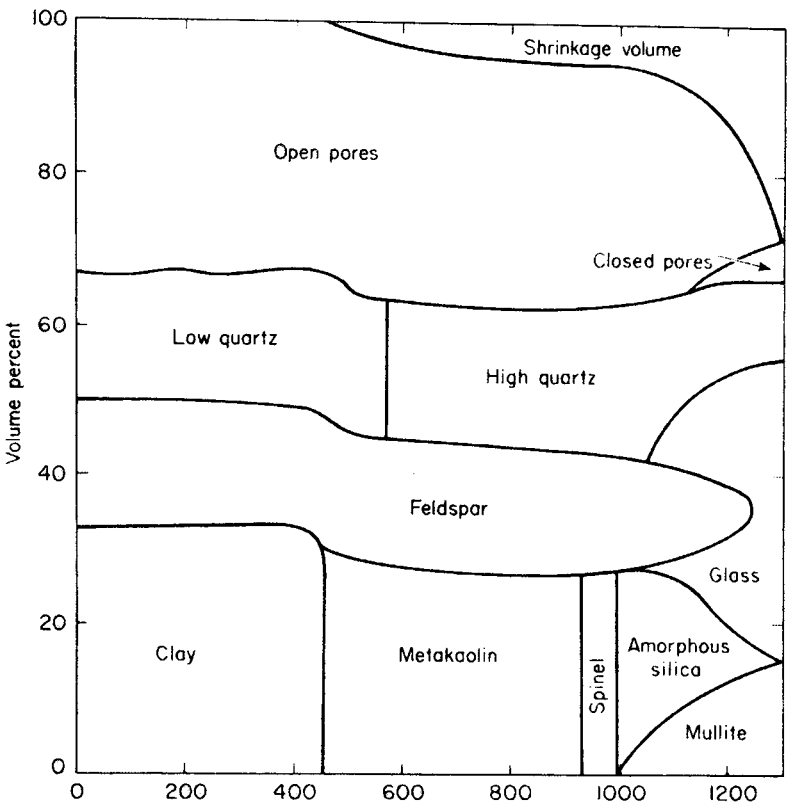

Figure 2.10 - Constituents in a triaxial body on firing. (Norton, 1970)

When the temperature is further increased long (>1 μm) needle-shaped crystals of secondary mullite, crystallising from the clay relicts permeated by feldspar melt are observed (Lundin, 1964; Schuller, 1964). Iqbal and Lee (1999) used electron microscopy and energy dispersive X-ray spectroscopy (EDS) on commercial porcelains and found that the Al_2O_3:SiO_2 ratio of cuboidal primary mullite was close to 2:1 (i.e., Al_2O_3-rich), while it was 3:2 for elongated secondary mullite and was related to the varying Al_2O_3 content in clay and feldspar relicts. The growth of these mullite crystals causes the liquid phase to become less viscous. This more reactive liquid phase then progressively dissolves the quartz crystals. No significant change is observed in the coarse quartz grains until a firing temperature of about 1200°C is reached. At this temperature, the dissolution of the quartz forms silica-rich amorphous solution rims around quartz grains and the feldspar is completely melted, and therefore no longer detectable by XRD. Above 1400°C little quartz remains, and

the whiteware body consists almost entirely of mullite and glass. If the liquid phase becomes completely saturated with silica, the remaining quartz is then transformed into cristobalite (Lundin, 1964).

After the appropriate densification has been achieved, the fired whiteware is cooled. As the ceramic body is cooled, the liquid phase changes to a glassy phase that bonds the mullite crystals and residual quartz particles. Usually, the cooling rate is faster than the heating rate. However, the cooling rate should be reduced when passing through the crystalline inversions involving volume changes. The inversions of quartz (at 573°C) and cristobalite (at 220-280°C) are crucial as these involve significant volume change and hence induce residual stresses. From the firing temperature down to 800°C, the liquid phase of alkali aluminosilicate is sufficiently fluid to relieve any stresses resulting from the thermal expansion mismatch between glass and crystalline phases. Below 800°C, the liquid phase begins to solidify and then shrinks more than the crystalline phases such as residual quartz grains causing stresses which can lead to cracking (Lundin, 1964). At 573°C, the β-quartz transforms to α-quartz, which has higher thermal expansion coefficient than the glassy phase. These stresses developed in the glass, which result from the thermal expansion mismatch between the glassy phase and α-quartz, are radial tensile and tangential compressive stresses (Newton, 1995), causing the circumferential cracks often observed around quartz grains. Davidge and Green (1968) have shown that the magnitude of these stresses increases with increasing the grain size. If cristobalite is present in the body similar cracking behaviour will be observed on its inversion (β-α cristobalite) between 220-280°C.

2.1.6 - Whiteware microstructure

Whitewares microstructures determine their properties. Whitewares always consist of more than one phase. Phases in whitewares include individual grains, glassy material, and pores. The microstructure in the final ware depends on the initial forming techniques, raw materials used, phase-equilibrium relations, kinetics of phase changes, grain growth, and sintering (Kingery, 1976). In low-fired whitewares, the primary determinants of microstructure are the raw materials and forming

methods including firing, and to some extent the phase changes involved in sintering, whereas in high-fired whitewares the equilibrium relations among different phases and the changes resulting from vitrification and high-temperature phase formation are much more important. In general, the microstructure of whitewares consists of a predominantly glassy phase (of varying composition) in which crystalline phases (which may have developed during the firing such as mullite and cristobalite or may have remained unreacted, or only partially reacted throughout, such as quartz) are more or less evenly distributed together with a pore phase (Figure 2.11). The pores may be open or closed depending on heat treatment (firing temperature, heating rate and soaking time). The open pores generated during forming a whiteware body can be eliminated or transformed to closed pores by vitrification on firing. If sufficient liquid is present all open pores are filled with liquid and a completely dense (vitreous) body is produced. Therefore earthenware, which is a non-vitreous product of whitewares, has a higher level of porosity than stoneware (vitreous or semi-vitreous), and china and porcelain (vitreous) as shown in Table 2.1. SEM images of porcelain show the so-called scaly primary mullite (Pm) formed in pure clay relict and the needle-like secondary mullite (Sm) crystals formed in the matrix containing mixed clay-feldspar grains (Figure 2.12(a)). Cracks, generally arising from thermal expansion mismatch between remnant quartz and glass, are observed within or around the quartz grains as shown in Figure 2.12(b).

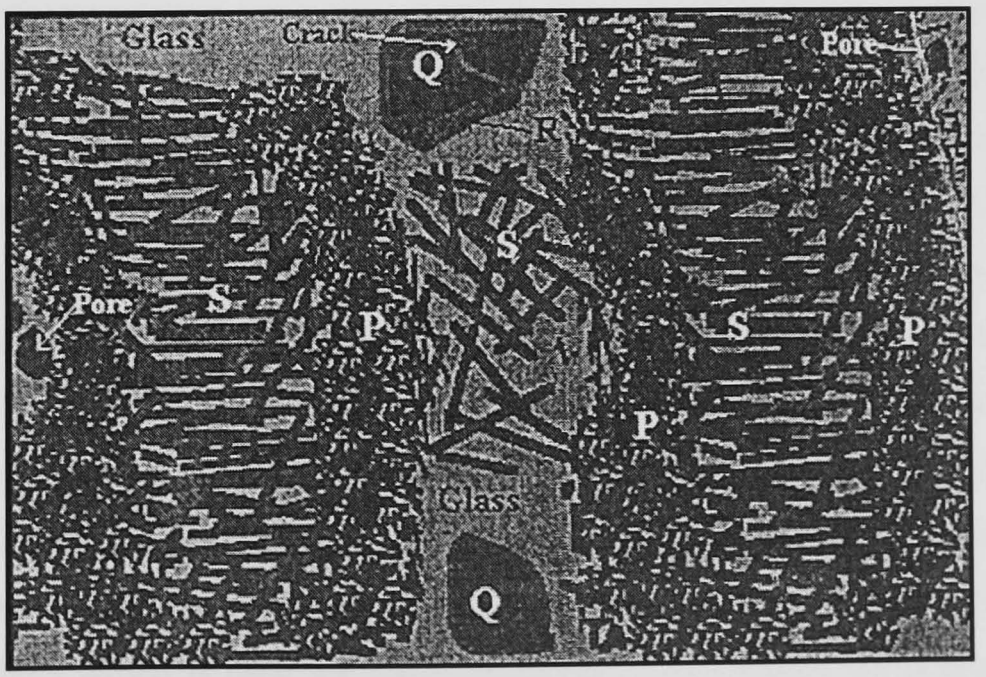

Figure 2.11 - Schematic of the general features observed in the microstructure of a whiteware body. (P = primary mullite, S = secondary mullite, Q = α-quartz, R = solution rim) (Iqbal and Lee, 1999)

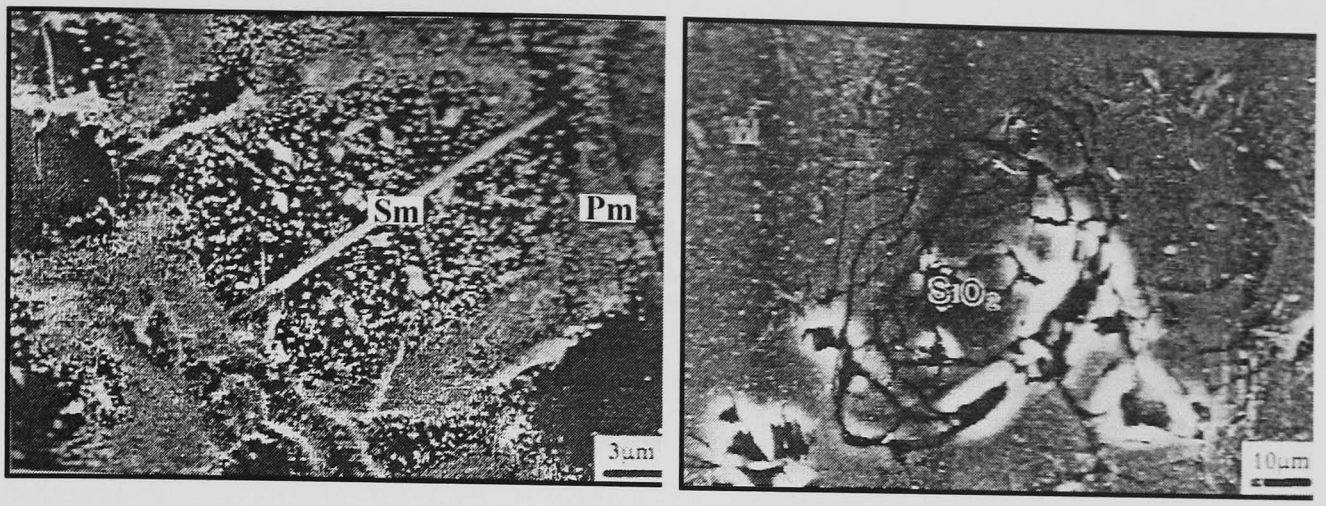

(a) (b)

Figure 2.12 – SEM/SE images showing (a) primary mullite (Pm), and secondary mullite (Sm) and (b) cracks within and around quartz (SiO_2) grain. (Iqbal and Lee, 2000)

2.1.7 - Whiteware properties

Unfired triaxial whiteware bodies consist of clay, flux and filler. The properties of unfired bodies depend on the characteristics of these constituents, and on their packing. The properties of fired bodies depend on the microstructure in the fired state i.e. the glassy phase, the crystals, cracks and pores. The inter-relationship of these features determines a wide range of fired properties. Selected properties of whitewares are listed in Table 2.5. Earthenware differs from porcelain in that it has lower firing temperature such that sintering does not yield complete densification. This is why earthenware is not translucent and shows a comparatively low strength. Water absorption varies over a wide range (6-8%). Earthenware has a low strength so that the ware can only find applications where high strength is not required. It is used in the manufacture of wall tiles, decorative ware and sometimes sanitaryware. In its mechanical strength earthenware is inferior to porcelain. The porous structure of the body implies little deformation during firing because of the small amount of melt produced at the firing temperature. Stoneware is a dense ceramic with 0.5-2vol% porosity. The water absorption varies between 0.2-2.5%. In general it has higher compressive strength but lower tensile strength comparing to hard porcelain. Hotel china (a china which is used for food containment) or vitreous china has less than 1vol% porosity and hence is much stronger than earthenware and stoneware. In vitreous china and bone china, unlike porcelain, the free silica crystals originally

introduced by the filler have not started to go into solution and remain unchanged. Therefore, high crystal/glass ratios are maintained, and probably because of this vitreous china and bone china are stronger than hard porcelain as seen from their Moduli of Rupture (MOR) given in Table 2.5. Hard porcelain is usually fired to high temperatures, which brings some of the silica from filler into solution to form more glass so enhancing the translucency of the fired ware. The decrease in crystal and increase in glass content results in a reduction in strength.

Table 2.5 - Properties of whiteware bodies (Rado, 1988)

Property	Earthenware	Stoneware	Hard porcelain	Bone china	Hotel china
Water absorption (%)	6-8	0.2-2.5	0-0.5	0-1	0.1-0.3
Specific gravity	2.6	2.5-2.65	-	2.75	2.6
Bulk density (kgm^{-3})	2200	2030-2480	2300-2500	2700	2600
Compressive strength					
Unglazed (MPa)	-	-	392-442	-	-
Glazed (MPa)	-	571	442-540	-	-
Tensile strength					
Unglazed (MPa)	-	-	23-34	-	-
Glazed (MPa)	-	11	29-49	-	-
Modulus of rupture					
Unglazed (MPa)	55-72	-	39-69	97-111	82-96
Glazed (MPa)	-	34	59-98	-	-
Modulus of elasticity					
Unglazed (GPa)	55	69	69-79	96	82
Impact strength					
Unglazed (Nm^{-1})	-	1766	1766-2158	-	-
Glazed (Nm^{-1})	-	-	1167	2188	-
Linear thermal expansion coefficient					
20-500°C ($\alpha \times 10^{-6}K^{-1}$)	7.3-8.3	-	-	8.4	7.3-8.3
20-700°C ($\alpha \times 10^{-6}K^{-1}$)	-	-	-	-	-
20-1000°C ($\alpha \times 10^{-6}K^{-1}$)	-	4.1	3.5-4.5	-	-
Thermal conductivity					
20-100°C ($Wm^{-1}K^{-1}$)	1.26	1.57	1.16-1.63	1.26	-

2.2 - USE OF WASTE MATERIALS IN TRADITIONAL CERAMICS

2.2.1 - Introduction

In recent decades, the growing consumption and consequent increase in industrial production has led to a rapid decrease of available natural resources, including both raw materials and energy sources. Traditional ceramic products have been created using raw materials that require high firing temperatures and energy intensive processing steps. The ceramic whiteware industry consumes large amounts of energy, especially during the firing process. Firing temperatures greater than 1200°C are required to sinter typical porcelain raw materials into dense products. Other manufacturing steps, such as the drying processes, are also energy intensive. Energy costs are a major portion of the total manufacturing costs, and thus new methods to reduce the amount of energy required will be a great benefit to the whitewares industry. Modifications to the raw material formulations, which lead to reduced firing temperatures, are of great commercial interest.

The volume of by-products and wastes with different natures and compositions increases annually. The disposal of large quantities of wastes is generating economical and environmental problems, resulting in increasing waste disposal costs. Therefore, alternative ways to reuse several types of waste materials have been attempted in recent years, including their incorporation in traditional ceramic products.

Traditional ceramic products such as porcelain or stoneware tiles are highly heterogeneous due to the wide range of raw materials used in their fabrication. Therefore there is a high tolerance for incorporating large amounts of suitable wastes as raw materials (Ferreira *et al.*, 2003). This fact attracts further interest since the traditional ceramics industry, which is classified as heavy industry, consumes huge amounts of diminishing mineral resources. Recycling of wastes as raw materials in the ceramics industry undoubtedly has both environmental and economical benefits (Boccaccini *et al.*, 2000).

2.2.2 - Waste glass

Many thousands of tonnes of glass are discarded daily throughout the world, much in the form of non-returnable bottles and containers. In the UK, it is estimated that ~3.4M tonnes of waste glass are generated every year and ~2.4M tonnes are container glasses (Enviros, 2004) and from this only 0.875M tonnes (or ~36.5%) of container glass is recycled so that large amounts are considered as waste and landfilled. Dumping of the glass is not only expensive and an assault on the environment but also a waste of useful raw material such as glass which can be 100% recyclable. Most waste container glass consists mainly of silicon, sodium, and calcium oxides, termed SLS glass. It is, by far, the most important glass economically and is the target of most recycling operations.

2.2.3 - Soda-lime-silica glass

SLS glass is primarily used for container glass such as bottles, jars and everyday drinking glasses. SLS glasses represent the largest group of commercially and technologically important silicate glasses (Shelby, 2005) comprising typically 71-75wt% silica, 12-16wt% soda and 10-15wt% lime. Alumina, magnesia, and several other oxides are also included as minor constituents for specific properties. The addition of MgO helps improve their resistance to devitrification and some Al_2O_3 improves their chemical durability. Due to the high alkali content the glass has a high thermal expansion coefficient (8.0-9.0 $x10^{-6}$ /K) and low viscosity due to the low Al_2O_3 content. SLS glass is made by melting a powder batch at high temperatures (~1500°C) and cooling to a rigid condition without crystallisation (melt-quenching process). The principal raw materials in SLS batches are silica sand (SiO_2), limestone ($CaCO_3$), and soda ash (Na_2CO_3). Silica sand is the main ingredient. The temperature needed to melt silica sand is high >1,700°C therefore sodium oxide (Na_2O) which is obtained from soda ash and acts as a flux is added to the silica sand to reduce the melting point. This mixture is unstable, because sodium ions are water-soluble and allow water to enter the glass structural network. Calcium oxide (CaO), derived from calcium carbonate (limestone, $CaCO_3$), is then added to the mix to adjust the viscosity and increase durability of the finished glass.

When an alkali or alkali earth oxide reacts with silica to form a glass, the Si-O network is broken up by the alkali or alkali earth ions. The structure of SLS glass is shown in Figure 2.13. The SLS glass network is formed by the silicon-oxygen tetrahedra and the large cations of Na^+ and Ca^{2+} fit into gaps in this network. The silicons and oxygens form a three-dimensional random network in which each silicon is surrounded by 4 oxygens, each approximately at the corner of a tetrahedron. Some of the oxygens are bonded to 2 silicons and some to 1 silicon. There are holes in this random network in which the sodium and calcium atoms lie surrounded by about 6 and 7 oxygens, respectively.

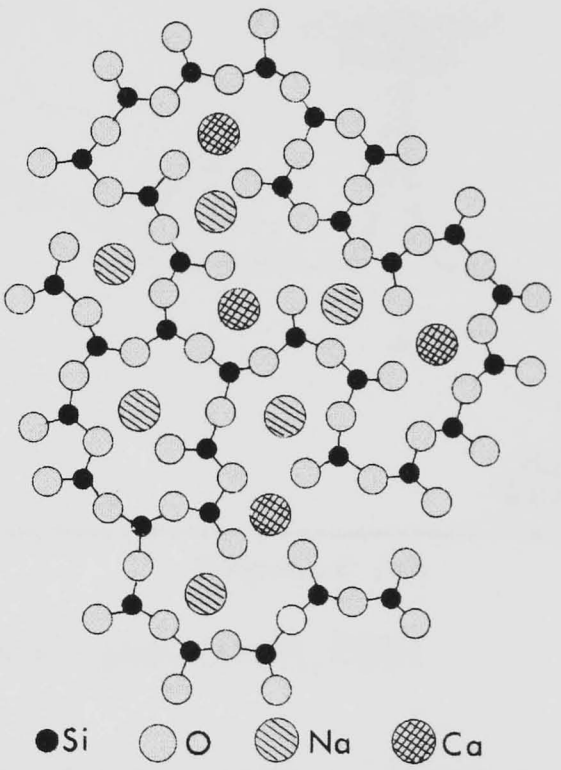

Figure 2.13 - Atomic structure of a soda-lime-silica glass. (Lawrence, 1972)

The addition of CaO into a silicate glass has a similar effect on the structures as Na_2O. But because of the greater charge of the Ca^{2+} ion, the Ca-O bond is much stronger than the Na-O bond. Therefore, the Ca^{2+} ions are held more firmly in the structure than the Na^+ ions.

2.2.4 - Crystallisation or devitrification of SLS glass

Glass is a metastable state of matter and under certain conditions, such as sufficiently long heating at suitable temperature, glass will devitrify or return to the crystalline,

more stable, state. On heating, the reduced glass viscosity allows the molecules enough mobility to develop crystal structures. SLS glass devitrifies easily. Slower temperature profiles and long soaks appear to promote devitrification. Devitrification is the tendency of glasses to crystallize, particularly when undergoing heating. The rate will depend on the composition and the thermal treatment. The type of crystal produced by devitrification will be ruled by the local glass composition.

A typical DSC curve for a glass where crystals form during heating and then melt at a higher temperature is shown in Figure 2.14.

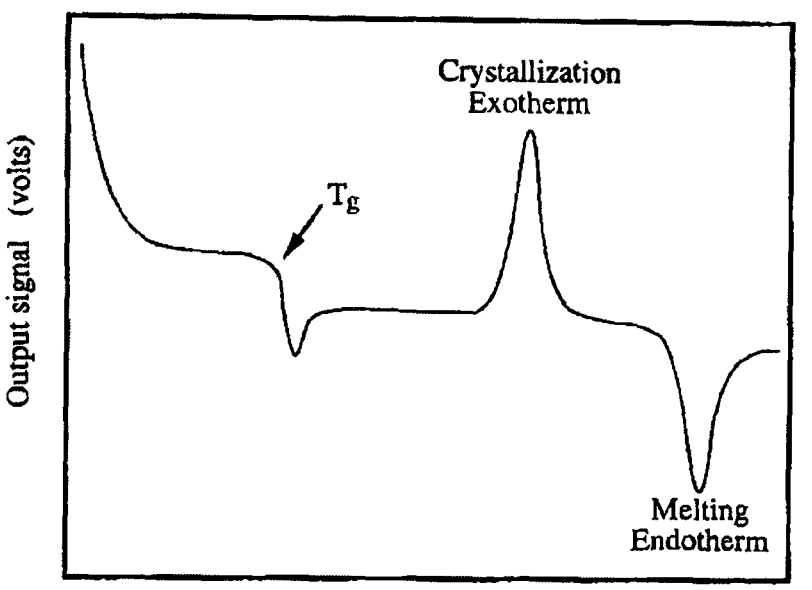

Figure 2.14 - DSC curve of a glass. (Shelby, 2005)

The first feature encountered during heating is the glass transformation temperature (T_g), which is the temperature at the onset of the glass transformation region during the heating. It is used as an indicator of the approximate temperature where the glass begins to convert from a solid to a liquid in the glass transition region. T_g of commercial SLS glass is in the range 550-580°C (Shelby, 2005). The next feature in this curve encountered during heating is an exothermic peak due to crystallisation of the glass. Crystallisation of glasses may range from the example shown here, where a single phase is formed, to complex curves, with multi peaks, which may or may not overlap, resulting from the formation of a number of crystalline phases. The endothermic peak at the highest temperature is due to melting of the crystals formed during heating. Endothermic peaks may also occur due to the presence of crystals which formed in the sample during cooling of the melt.

When SLS glass devitrifies the following crystals can form: cristobalite or tridymite (SiO_2), wollastonite ($CaSiO_3$) and devitrite ($Na_2Ca_3Si_6O_{16}$) (Boffe *et al.*, 1962). The first crystalline phase to form depends on the position of the glass in the phase diagram, but the composition of the vitreous phase can change during devitrification, so that a different crystal can subsequently appear. Figure 2.15 presents part of the ternary phase diagram of the Na_2O-CaO-SiO_2 system with information on crystalline compounds and weight percent compositions (Hlavac, 1983). It reveals that $Na_2O{\cdot}2SiO_2$ (sodium silicate) forms at high Na_2O contents at around 800°C, whereas $CaO{\cdot}SiO_2$ (wollastonite) forms at high CaO contents at around 1100°C. However, this phase diagram had been established for pure materials in equilibrium state whereas in real glasses the system is usually impure and far from equilibrium. Minor components may have an effect on the minerals precipitating and can have a great influence on the rate of crystallization, and hence this diagram can only be used as a first guide to devitrification products and their formation temperatures.

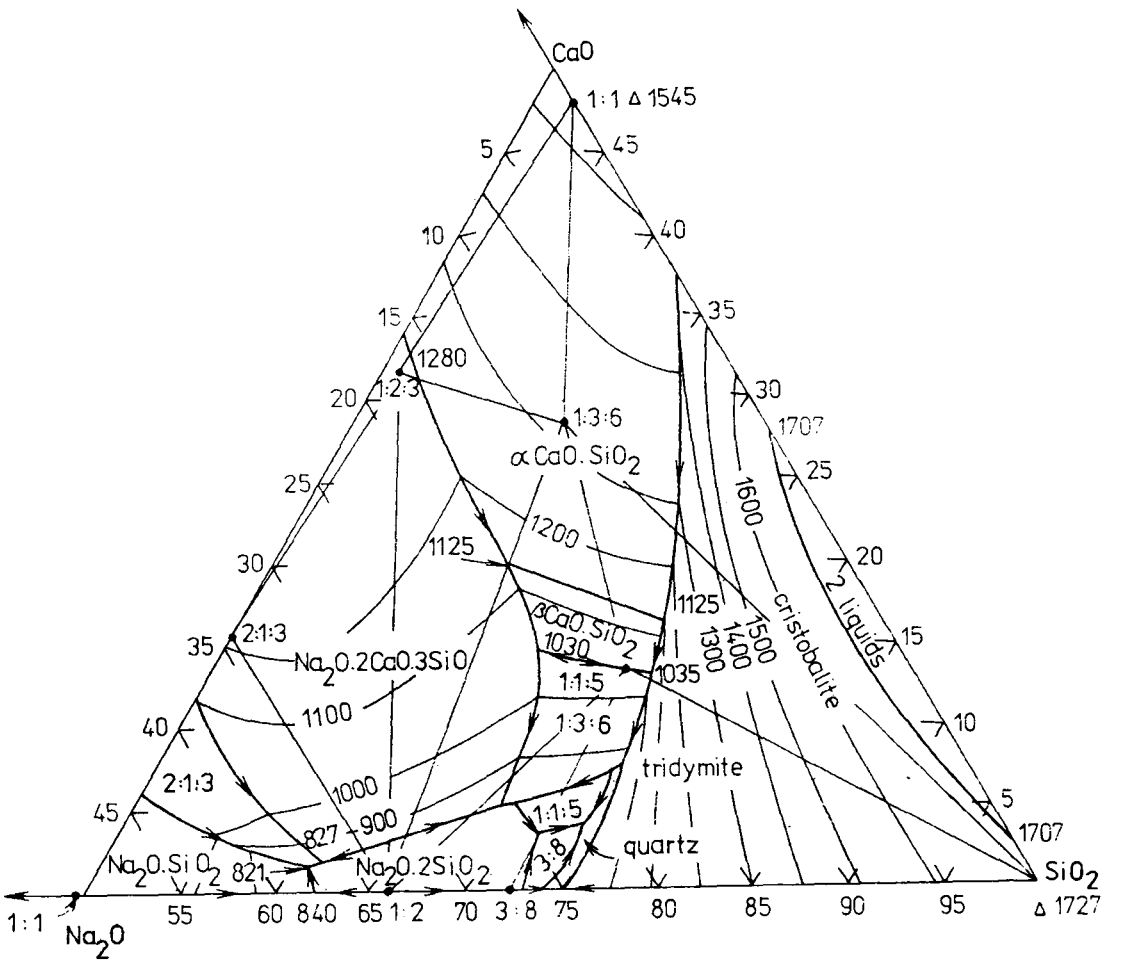

Figure 2.15 - Phase diagram of the system Na_2O-CaO-SiO_2. (Hlavac, 1983)

The morphology of crystals formed from devitrification of SLS glass is summarized in Table 2.6 and some of them are shown in Figure 2.16. Cristobalite occurring as a

devitrification product from SLS glass is usually in the dendritic form (Figure 2.16(a)) and is often found mixed with tridymite or β-wollastonite. Devitrite occurs either as radiating bunches or as fine needles (Figure 2.16(b)). It has similar morphology to β-wollastonite and is usually found mixed with β-wollastonite. Lath-like tridymite as shown in Figure 2.16(c) is often occurred in all silicate glasses and found together with cristobalite. Pseudo-wollastonite or α-wollastonite is the high temperature form of $CaSiO_3$ and is usually formed above 1120°C. It can occur in either lath-like, hexagonal plate or dendritic form. Its lath-like form is shown in Figure 2.16(d). β-wollastonite is formed below 1120°C. It is a common devitrification product of SLS glass and occurs in regions with a high local concentration of lime or as a product of the breakdown of devitrite above 1045°C.

Table 2.6 - The morphology of crystals produced by devitrification of soda-lime-silica glasses. (Clark-Monks and Parker, 1980)

Crystal	Composition	Comments
Cristobalite	SiO_2	Typically dendrites with 90° branching. Occasionally large hexagons.
Devitrite	$Na_2O{\cdot}3CaO{\cdot}6SiO_2$ $Na_2O{\cdot}2CaO{\cdot}3SiO_2$ $2Na_2O{\cdot}3CaO{\cdot}3SiO_2$	Radiating needles often as fans. Cubes, sometimes linked at the corners into rows. Simple or modified octahedra.
Sodium disilicate	$Na_2O{\cdot}2SiO_2$	Plates and needles
Sodium metasilicate	$Na_2O{\cdot}SiO_2$	Plates and needles
Tridymite	SiO_2	Dendrites with 60° branching, laths, hexagons
α-Wollastonite	$CaO{\cdot}SiO_2$	Hexagons, laths, dendrites. Hexagonal tablets can have a pronounced dendritic substructure
β-Wollastonite	$CaO{\cdot}SiO_2$	Laths, fibrous growths

Of these, $2Na_2O{\cdot}3CaO{\cdot}3SiO_2$, sodium disilicate, and sodium metasilicate are not normally found in commercial SLS glass compositions but the latter two may be found in sodium silicate glasses used for cheap glasswares or as water glass.

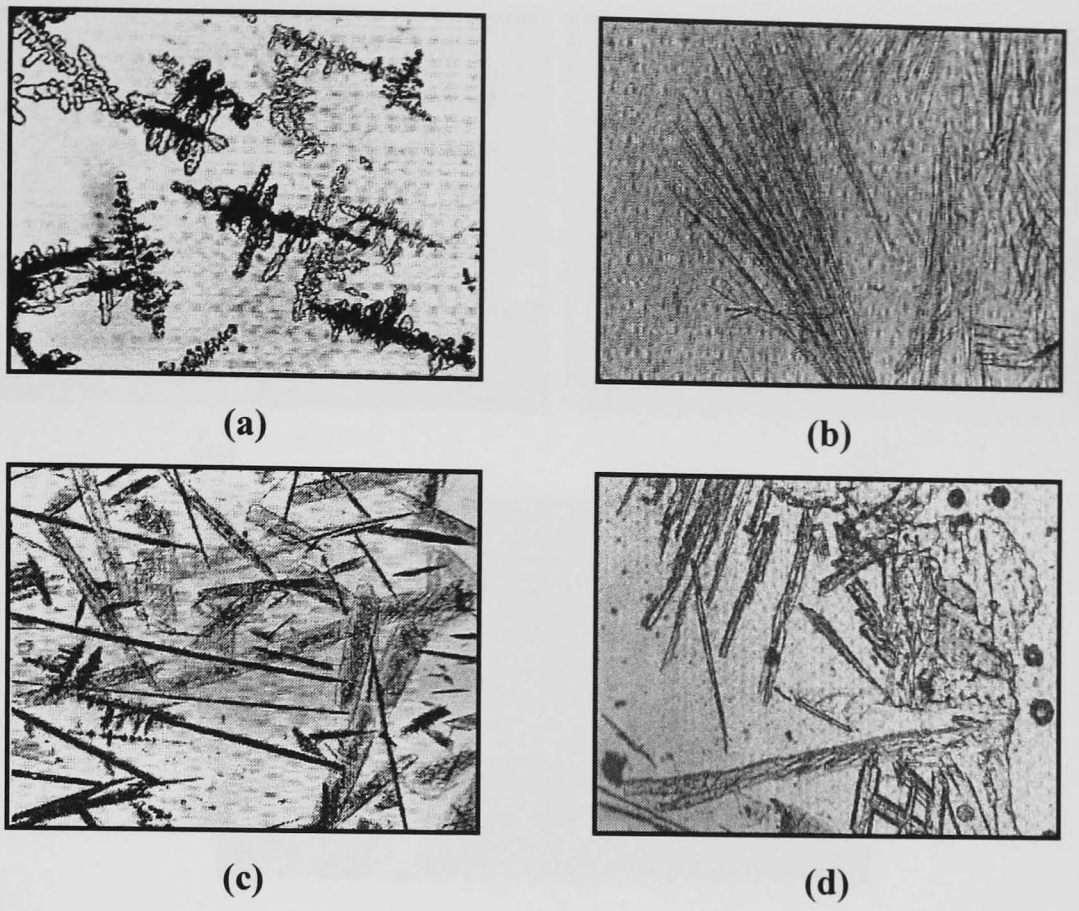

Figure 2.16 - Morphology of crystal phases formed from devitrification of SLS glass; (a) dendrite cristobalite (x50), (b) radiating needle-shaped devitrite (x50), (c) lath-like tridymite (x15), and (d) lath-like α-wollastonite (x48). ((a) and (c) from Taylor and Hill (1952), (b) and (d) from Clark-Monks and Parker (1980))

For clear sheet SLS glass, crystals formed by devitrification are usually composed of cristobalite and wollastonite (Willems, 1966) and occasionally composed of cristobalite and devitrite. Cristobalite first forms at the glass surface followed by devitrite as a result of volatilization, while at greater depths cristobalite forms followed by wollastonite. Usually the wollastonite is made up of long blades with a core of glass (Figure 2.17(a)). It is often accompanied by dendritic cristobalite as shown in Figure 2.17(b). If a small Na_2O loss occurs through volatilization at the glass surface, the devitrification products are initially cristobalite followed by devitrite. The morphology of devitrite formed together with cristobalite is shown in Figure 2.17(c).

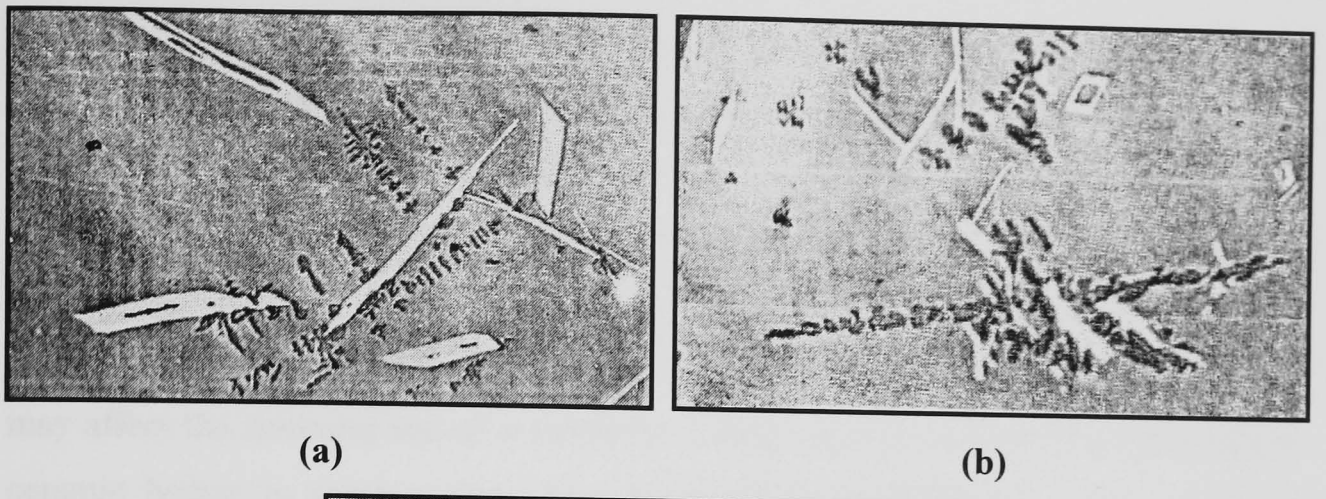

(a)

(b)

(c)

Figure 2.17 - Morphology of crystals formed from devitrification of clear SLS glass; (a) wollastonite blade with dendritic cristobalite (x100), (b) clusters of dendritic cristobalite with wollastonite (x100), and (c) cristobalite formed with devitrite (x100). (Willems, 1966)

2.2.5 - Sintering behaviour of glass powder and powder mixtures of glass and crystalline compounds

When heat is applied to powdered SLS glass, the glass goes through several stages until it melts into a viscous liquid. Glass does not melt at a particular temperature like a crystalline material. The variations in bond angles cause the glass to soften over a range of temperatures before it completely melts. SLS glass typically softens from ~550 to ~750°C. The viscosity of glass changes gradually over this range, allowing particles of glass to fuse and bond through a viscous flow sintering process. Sintering of glass particles can be used to create solid glass products by heating glass particles to above the sintering point and holding at that temperature until a dense body forms. A method of making tiles, bricks, and paving slabs by fusing recycled glass has been reported (Huan, 2002). The problems associated with the densification of pure SLS glass have been extensively studied in the last 10 years (Boccaccini *et*

al., 1996; Prado *et al.*, 2003; Prado *et al.*, 2004). Glass particles sinter by viscous flow thus reducing the surface area and hence total surface energy. The rate of densification depends on the initial green density of the glass powder compact. However, if concomitant crystallisation occurs on sintering, which is desirable in glass ceramics, the crystallised fraction of the body hinders the sintering path and therefore holds back densification. SLS glass readily crystallises on heating, which may affect the sintering and as a result the overall densification of SLS glass-based ceramic bodies to some extent when compared to other glasses which are more difficult to crystallise.

When powdered SLS glass is mixed with a crystalline phase (such as clay), the SLS glass is responsible for the sintering behaviour of the system. According to the basic theory of sintering (Reed, 1995) of a crystalline phase in the presence of a liquid phase (or so called vitrification), densification takes place by viscous flow caused by the surface tension of the liquid. The liquid phase in this system forms through melting of SLS glass. The viscosity of molten SLS glass has to decrease sufficiently for viscous flow to occur and serve as a bond for the crystalline phase. Figure 2.18 illustrates the sintering mechanism of such a mixture. It is worth mentioning that the viscosity for sintering glass particles is higher than that required for liquid-phase assisted vitrification, as that in conventional whiteware systems fluxed by feldspars.

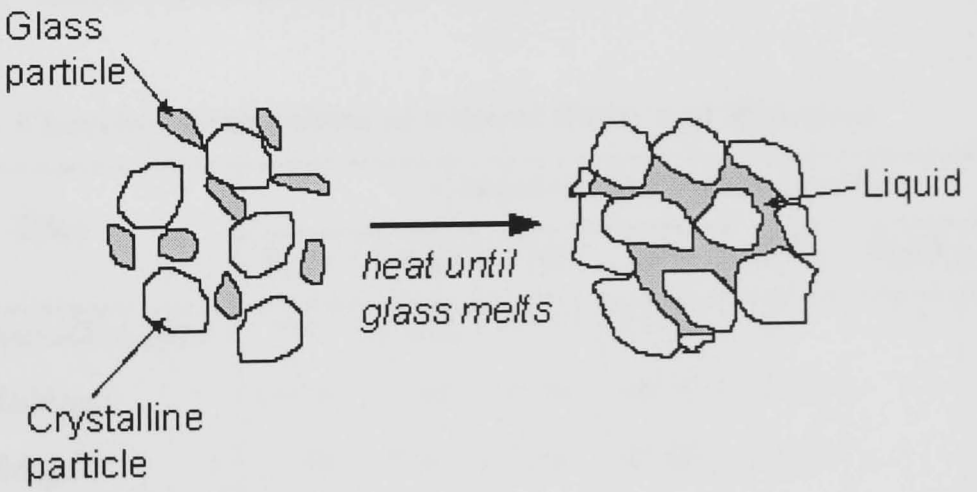

Figure 2.18 - The sintering mechanism of ceramic composites of glass and crystalline compounds

2.2.6 - SLS-based whitewares

Traditional ceramic industries currently use significant quantities of minerals such as nepheline syenite and feldspar, a natural flux used for producing whiteware products. These minerals typically account for ~25wt% of the composition of a whiteware body. Both minerals rely on high alkali contents for their fluxing action to produce liquid phase, which is an important constituent of, and significant for densification of, a whiteware body during the firing stage. The glassy phase generated on cooling is generally formed at temperatures above 1050°C. The high sintering temperatures of porcelain, and other whiteware, products lead to high energy consumption in the firing process. Considering the chemical similarity of the alkali content in natural fluxes (Hlavac, 1983) and SLS waste glass (Table 2.7), it is logical to utilise SLS waste glass as a replacement for natural fluxes in whitewares. Moreover, SLS glass is a viscous silicate, which has a softening point at ~720°C, for this reason SLS melts at lower temperature than natural fluxes. Therefore SLS–containing whitewares densify at reduced firing temperatures, which prolong furnace life and reduce energy costs.

Considerable attention has been given to the use of SLS glass as a fluxing agent in whiteware bodies. Due to similarities in manufacturing techniques for glass containers, the chemical compositions of container glass have relative uniformity and compatibility. All glass container manufacturers use the same basic SLS composition (Table 2.7), making the containers easy to recycle.

Table 2.7 - Chemical composition of natural fluxes and SLS glass

Flux	Chemical composition (wt%)						
	K_2O	Na_2O	CaO	SiO_2	Al_2O_3	MgO	Fe_2O_3
Soda-lime-silica glass	<1	12-16	10-15	71-75	1-3	1-3	<1
Potash feldspar	10.90	2.30	0.30	68.30	17.30	-	0.10
Soda feldspar	5.50	7.00	2.00	66.00	20.00	-	0.10
Nepheline syenite	4.50	10.50	-	24.00		-	0.10

Recycled glass can substitute for feldspar in porcelain bodies (Braganca and Bergmann, 2004), and in stoneware tile bodies (Arkhipov, 1979; Lincart, 1998;

Youssef *et al.*, 1998; Esposito *et al.*, 2001; Matteucci *et al.*, 2002; Tucci *et al.*, 2004; Souza *et al.*, 2004; Pontikes *et al.*, 2005). Some energy saving is associated with the use of recycled glass in these applications. An analysis of the literature (Table 2.8) reveals the growing trend for using glass waste in the technology of traditional ceramic production. The vitrification temperature of the SLS glass-containing porcelain stoneware decreased when comparing to conventional porcelain stoneware. This comes with the drawback of an increase in body firing shrinkage, and the benefit of lower water absorption (lower open porosity). The addition of SLS glass was reported to densify the ceramic bodies at temperatures lower than 1100°C (Youssef *et al.*, 1998), fostering the formation of closed porosity (lower bulk density) at higher firing temperatures. Gases from decomposition of clay, and volatilized from SLS melts become trapped in the densifying glass resulting in bloating (Matteuci *et al.*, 2002). With respect to mechanical properties, the flexural strength is generally improved, although Matteuci *et al.* (2002) reported a decrease in flexural strength in porcelain stoneware made with SLS additions. SLS glass promotes more effective melting of quartz leading to a more abundant and less viscous liquid phase (Matteuci *et al.*, 2002). However, this contradicts the result of Tucci *et al.* (2004) who found a high-viscosity liquid phase formed with SLS glass additions.

Table 2.8 - Selected properties of SLS glass-containing porcelain stoneware.

	Youssef *et al.* (1998)	Esposito *et al.* (2001)	Watanabe *et al.* (2001)	Artir *and Yilmaz* (2002)	Matteuci *et al.* (2002)	Tucci *et al.* (2004)	Pontikes *et al.* (2005)
Vitrification T.	↓	↓	↓	↓	↓	↓	↓
Firing shrinkage	↑	↑	↑	↑	↑	↑	↑
Water absorpion	↓	↓	↓	↓	↓	↓	↓
Bulk density	↑	-	-	-	↓	-	-
Flexural strength	-	↑	↑	-	↓	↑	↑
Compressive strength	↑	-	-	-	-	-	-
Viscosity of glassy phase	-	-	-	-	↓	↑	-

↑ = increase over traditional body ↓ = decrease over traditional body

The phase composition and microstructure of SLS-based porcelain stoneware reveal the formation of a variable composition plagioclase (albite and anorthite) in addition

to primary and secondary mullite, partially dissolved quartz and a glassy matrix as found in standard porcelain stoneware (Esposito *et al.*, 2001; Matteucci *et al.*, 2002; Tucci *et al.*, 2004). Ca^{2+} and Na^{+} ions from the SLS waste glass react with clay decomposition products to form calcium and sodium aluminosilicate crystal phases such as plagioclase. The formation of plagioclase inhibits the formation of mullite. Wollastonite is another new crystalline phase found in SLS-based porcelain stoneware (Souza *et al.*, 2004). Using >10wt% of SLS glass content in stoneware bodies revealed a deterioration in both physical and mechanical properties of fired bodies whereas bodies with 5-10wt% SLS content attain good properties (Matteuci *et al.*, 2002; Tucci *et al.*, 2004). For heavy clay products such as roofing tiles SLS glass addition up to 30wt% is feasible (Pontikes *et al.*, 2005). SEM images of SLS-containing roofing tiles after firing at 1000ºC show that glass grains are well adhered to the surrounding ceramic matrix (Figure 2.19(a)) along with formation of plate-like wollastonite crystals within the glass grains (Figure 2.19(b)).

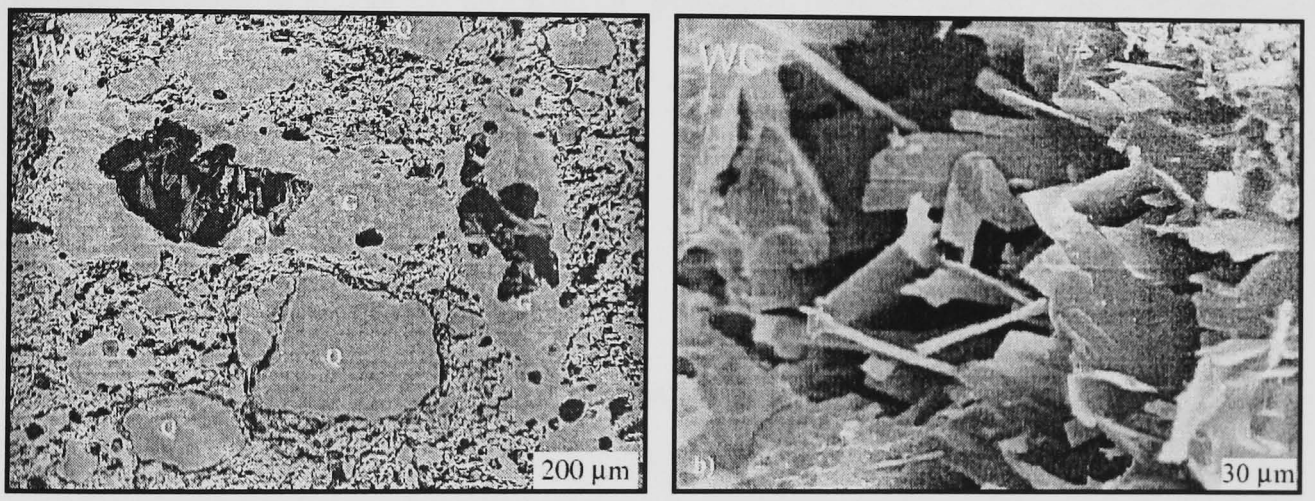

(a) **(b)**

Figure 2.19 - SEM/SE images of polished SLS-containing roofing tiles (WC) fired at 1000ºC showing softened glass grains adhering to surrounding matrix (a), quartz (Q) grains and glass (G) grains. (b) Plate-like wollastonite crystals in the glass grain centre. (Pontikes *et al.*, 2005)

Theoretically, there are numerous practical advantages to using SLS glass as a flux for whiteware. If the proper amount of SLS glass is added, it can accelerate vitrification at a relatively low firing temperature, and thus increase the strength and density of the body.

CHAPTER 3 - EXPERIMENTAL PROCEDURES

3.1 - INTRODUCTION

The aim of this research is to investigate the densification behaviour, physical and mechanical properties, including phase and microstructural changes in whitewares with total or partial replacement of nepheline syenite flux by colourless SLS glass. In this chapter the selection of raw materials and the procedures used to characterize them are outlined. To understand the many changes which take place during firing of whiteware batches (which comprise clay, flux and filler), the individual raw materials have been heated separately as well as the mixtures of two or more components in order to observe the interaction of these components on heating. The analytical techniques used to characterise the raw materials, two-component batches, and the final whiteware bodies are also described. In addition, this chapter covers the techniques used to assess the mechanical properties of the final whiteware bodies.

3.2 - RAW MATERIALS

3.2.1 - Clay

China clay (kaolin) was used as the main raw material. It was supplied by E.C.C. International Limited, Cornwall, UK. This clay was selected because of its high plasticity, high degree of fineness and white firing characteristic. The plasticity of the clay enhances the formability of the whiteware bodies and contributes to the green strength. The requirement of plasticity makes the clay an indispensable component in whitewares fabrication (Dinsdale, 1986). The use of a ball clay confers a high level of plasticity, while the china clay will provide the fired ceramic body with a desirable level of whiteness.

3.2.2 - Filler

A high grade quartz, Loch Aline sand, supplied by Tilcon (south) Limited, Stoke-on-Trent, UK, was used as filler.

3.2.3 - Flux

Nepheline syenite supplied by WBB Minerals, Staffordshire, UK, and recycled colourless SLS glass obtained from ground waste container bottles were used as fluxes in the whiteware compositions investigated. Powdered SLS glass was prepared by crushing cleaned colourless SLS waste glass bottles which were collected from domestic wastes, dry milling in a porcelain mill with zirconia media, and passing through a 75 μm sieve. Smaller particle size was not prepared to avoid the longer milling required, which is energy intensive. SLS glass was used to reduce the firing temperature of whitewares as it melts at lower temperature than natural flux such as nepheline syenite and feldspar (melting points of SLS glass, nepheline syenite and potash feldspar are ~800-900, 1150 and 1150°C respectively).

3.3 - CHARACTERIZATION OF RAW MATERIALS

To understand the influence of the incorporation of ground SLS glass as a raw material in whitewares, the first stage of this investigation was directed to the complete characterization of all raw materials used in the formulations. Raw materials were characterized in terms of chemical composition, particle size distribution, phase analysis (XRD), thermal analysis by differential thermal analysis (DTA) and thermogravimetric analysis (TGA), and microstructure by scanning electron microscopy (SEM). High temperature X-ray diffraction (HTXRD) was used to investigate the phase changes during heating and corroborate the results from thermal analysis.

The second step was to study the effect of heat on the raw materials. An unfired whiteware body is a mixture of minerals, and it is convenient to consider the effect of heat on each individual mineral and then to consider the effects of their interactions. Both physical and chemical changes which take place in the raw materials resulting in the disappearance of some minerals and/or the formation of new ones are studied. Each raw material was sprayed with 10wt% distilled water, hand granulated and pressed into 25 mm diameter pellets by uniaxially pressing at 40 MPa. Pressed pellets were dried in an electric oven at 110°C overnight and fired in an electric furnace at a heating rate of 10°C/min to selected temperatures (600-1200°C). Slowly

cooled and quenched samples were prepared. Quenched pellets were immediately dropped in cold water after firing to selected temperatures. XRD of samples quenched at either side of DTA peaks (i.e. immediately before and after a reaction was observed) were studied. Unquenched pellets were soaked at specific temperatures for 3h before cooling to room temperature at a cooling rate ~10°C/min. The fired pellets were analyzed by XRD and SEM to determine phase and microstructural changes on firing at different temperatures.

3.4 - INVESTIGATION OF INTERACTIONS BETWEEN RAW MATERIALS

To study the interactions between raw materials, six different binary mixtures as shown in Table 3.1 were prepared by mixing the two components in the same weight ratio as they figure in the conventional whiteware compositions (clay:flux:filler 50:25:25). After mixing, each mixture was characterized by DTA/TGA and high temperature XRD. 10wt% distilled water was added to the mixed powders, which were hand granulated and pressed at a pressure of 40 MPa. The resulting 25 mm diameter pellets were dried in an electric oven overnight at 110°C. The firing step was performed in an electric furnace following the same firing schedule used for firing raw materials as mentioned in section 3.3. The fired specimens were analyzed by XRD and SEM. Transformations and interactions upon heating of the binary mixtures were studied using complementary data from DTA/TGA, XRD and SEM.

Table 3.1 - Binary mixture compositions (wt%). "C" is kaolin clay, "Q" is quartz, "NS" is nepheline syenite, and "SLS" is SLS glass.

Raw materials	C-Q	C-NS	C-SLS	Q-NS	Q-SLS	NS-SLS
Kaolin clay	66.7	66.7	66.7	-	-	-
LA sand	33.3	-	-	50.0	50.0	-
Nepheline syenite	-	33.3	-	50.0	-	50.0
SLS waste glass	-	-	33.3	-	50.0	50.0

3.5 - DESIGNED WHITEWARE BATCH COMPOSITIONS

Five groups of batch compositions were investigated to study a new approach to whiteware body formulation when colourless SLS glass was used as an alternative flux. In all batches, the kaolin clay content was fixed at 50wt% and the quartz (LA sand) content was fixed at 25wt%. The nepheline syenite content was varied from 0-25wt%, and the sum of nepheline syenite and SLS glass contents was fixed at 25wt%, so that the flux content in the whiteware formulation remained fixed at 25wt%.

The first batch consisted of the three conventional whiteware raw materials: kaolin clay, quartz sand, and nepheline syenite; in the proportion of 50:25:25. The four other batches consisted of four raw materials: kaolin clay, quartz sand, and nepheline syenite partly replaced with ground SLS waste glass. The percent replacement of nepheline syenite with SLS waste glass was increased reaching full replacement in the last batch which consisted of kaolin clay, quartz sand, and SLS waste glass (no nepheline syenite). The composition of each batch is given in Table 3.2. Each batch is categorized by a number indicating the amount (in wt% based on 100wt% of nepheline syenite) of SLS waste glass substituting for nepheline syenite (i.e. S0 for 0wt% SLS glass and 100wt% nepheline syenite; S25 for 25wt% SLS glass and 75wt% nepheline syenite).

Table 3.2 - Whiteware batch compositions (wt%).

Raw materials	S0	S25	S50	S75	S100
Kaolin clay	50	50	50	50	50
LA sand	25	25	25	25	25
Nepheline syenite	25	18.75	12.5	6.25	-
SLS waste glass	-	6.25	12.5	18.75	25

3.6 - WHITEWARE BATCH PREPARATION

The batch compositions, shown in Table 3.2, were mixed and wet milled (50wt% solids) in a porcelain mill with zirconia grinding media for 6h at 80 rpm. To disperse clay agglomerates, the slurry was further milled for 30 min after adding 3 g of deflocculant (Dispex N40, Allied Colloids, Ltd., Bradford, UK). The slurries were then passed through a 212 μm sieve and oven-dried overnight at 100°C. The completely dried cakes were broken up in a porcelain mortar and pestle, and mildly ground until the agglomerates were finer and passed through a 212 μm sieve. The resulting powders were moistened by spraying with a fine mist of distilled water droplets (10wt%) and granulated by hand over a polyethylene sheet. The granulated powders were stored in closed plastic bags. A sample of each batch, before moistening, was collected and analyzed by XRD, HTXRD, DTA and TGA.

3.7 - SPECIMEN PREPARATION

The disc-shaped specimens were prepared by the uniaxially dry pressing method, as previously described. With this method, the powder granulates were placed in a steel die of 25 mm diameter and cylindrical shape. A pressure of 40 MPa was applied to the powder granulates to produce 25mm diameter disc specimens.

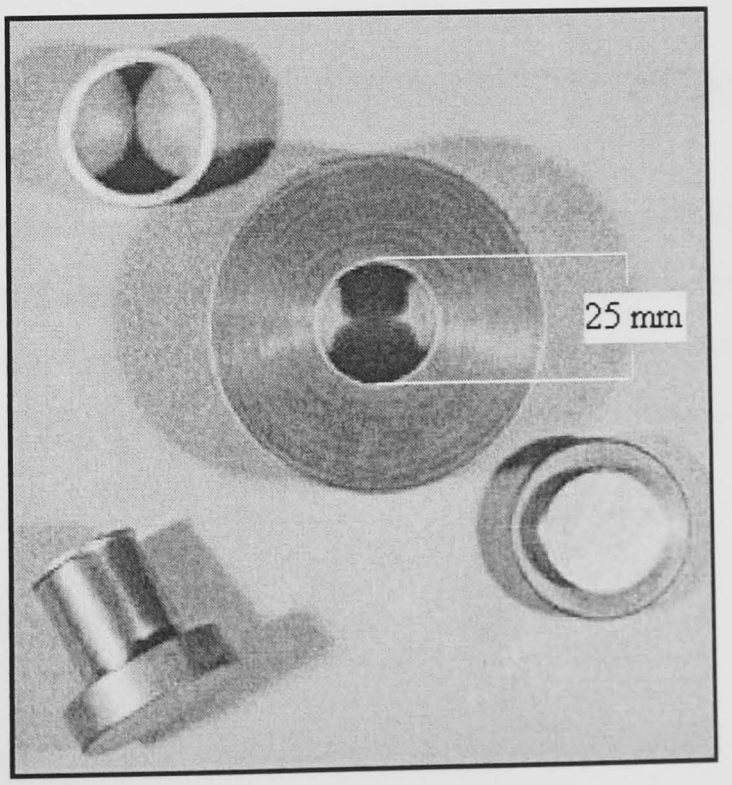

Figure 3.1 - Cylindrical steel die used in the pressing step.

3.8 - DRYING AND FIRING OF SPECIMENS

As-pressed specimens were oven-dried at 110°C for 24h. The dimensions and mass of specimens of each composition were measured prior to firing to enable the shrinkage and weight loss to be determined after firing. The specimens were arranged over a layer of alumina powder in an alumina crucible. The alumina powder was used to prevent samples from sticking to the crucible, and to allow the samples to be readily removed even if bloating or melting had occurred at high firing temperatures. The specimens were fired at 600, 800, 1000, 1050, 1100, 1150, 1200, 1250 and 1400°C, at a heating rate of 10°C/min with a soaking time of 3h. The heating rate and soaking time were selected following previous studies about standard porcelain, which were carried out in this department. All samples in this study were fired with the same heating rate and soaking time. After completion of the heating and soaking schedule, power to the furnace was automatically shut down and the cooling rate was then dictated by the cooling rate of the furnace which was calculated to be ~10°C/min on average. The specimens generally remained overnight in the furnace before they were removed. For quenched specimens, after the furnace was heated to the specific firing temperatures (600, 700, 800, 1000, 1100, 1200, 1300, 1400 and 1500°C), the specimens were taken out of the furnace and immediately dropped in cold water to stop any reactions which otherwise would occur on soaking and slow cooling.

3.9 - CHARACTERIZATION OF WHITEWARE SPECIMENS

The as-mixed batches were characterized by the following analytical methods: phase analysis by XRD and thermal analysis by DTA/TG. Fired specimens were analysed in terms of physical and mechanical properties, and phase and microstructural evolution by XRD, SEM/EDS, and TEM/EDS. These techniques and methods will be described in detail in the following section.

3.10 - ANALYTICAL TECHNIQUES

The analytical techniques used throughout this study are described in this section.

3.10.1 - Particle size analysis

The particle size distributions of the raw materials (as-received china clay, LA sand, nepheline syenite, and ground colourless SLS waste glass) were determined by laser particle size analyser (LS 130, Coulter Electronics Ltd., Luton, UK). The Coulter LS 130 Laser Sizing Unit uses Fraunhofer diffraction pattern analysis to determine the size of particles from 1-800 μm and a separate unit (PIDS, Polarisation Intensity Differential Scattering) to measure submicron particles (to 0.1 μm). Samples of each raw material were introduced into the instrument detection chamber together with a few drops of deflocculant (Dispex N40), to minimise agglomeration of the particles during the measurement. The number of drops for each type of material was chosen on the basis of trial experiments until the minimum particle size distribution (higher level of deflocculation) was achieved. The PSD's were plotted in terms of volume percent of particles.

3.10.2 - Chemical analysis

The chemical compositions of the waste glass and raw materials used were determined using inductively coupled plasma atomic emission spectroscopy (ICP-AES optical 3200 XL, Perkin-Elmer, USA), where samples in the form of aqueous solutions were introduced as aerosols into a plasma flame to produce characteristic emission from the elements (Boss and Fredeen, 1997). In this analysis, the sample is subjected to temperatures high enough to cause significant amounts of collisional excitation and ionization of the sample atoms to take place. Once the atoms or ions are in their excited state, they can decay to lower states through thermal or radiative (emission) energy transitions. The intensity of the light emitted, with specific wavelengths which are fingerprints of the sought elements, is measured and used to determine the concentrations of the elements of interest. The loss on ignition was measured by calculating the wt% difference between unfired samples and after firing 2h at 1000°C. The raw data were received in terms of the percentage of the chemical elements contained in each sample, and were converted into percent of their corresponding oxides.

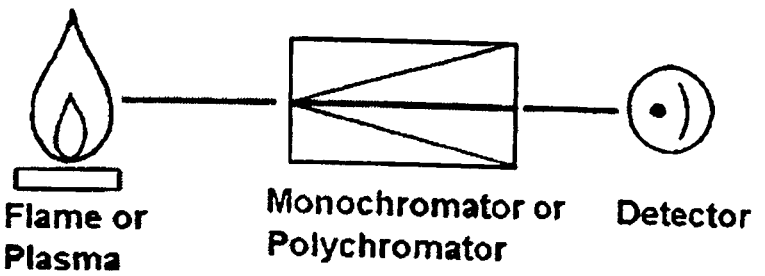

Figure 3.2 - Schematic of Atomic Emission Spectroscopy system. (Boss and Fredeen, 1997)

3.10.3 - Thermal analysis

Thermal analysis is a group of techniques used to measure a property change that occurs as a result of change of temperature (Haines, 1995). In each technique, the sample is subjected to a controlled temperature programme which involves heating and/or cooling, or holding the temperature constant. Thermal analysis techniques used in this work include TG and its derivative (DTG), DTA and dilatometry.

3.10.3.1 - Thermogravimetric analysis (TG) and derivative thermogravimetric analysis (DTG)

TG is a technique used to monitor weight changes in a material as a function of temperature under a controlled atmosphere (Haines, 1995). This test involves the measurement of weight changes in a sample while it is being continuously heated. The equipment is essentially a balance in which a small sample of material can be heated at controlled rate and temperature and weight of sample continuously recorded. Materials are recognized from the amount of weight loss and the temperature at which weight loss occurs. Changes in weight usually occur sharply at specific temperatures and correspond to the breaking of chemical or physical bonds. They are often associated with the loss of volatile substances such as water (H_2O), carbon dioxide (CO_2) or oxygen (O_2) from the molecules of the sample. The TG result is plotted as a graph of percent weight changes with temperature. The horizontal sections indicate no weight change and hence no decomposition, whereas slopes and curves show that a weight change has taken place due to some material loss. The curve also gives a quantitative result, by calculating the weight losses

between one plateau and another. In order to highlight the weight losses among the plateau, and make visual identification of reactions easier, a derivative thermogravimetric (DTG) trace is frequently drawn. The DTG trace represents the rate of mass change with time.

A Perkin Elmer Pyris TGA (Boston, Massachusetts, USA) was used for TG analysis in this work. Each sample was weighed into a sample holder, which was then placed on a thermobalance and the TG run was carried out under air atmosphere. A maximum temperature of 950°C was attained at a heating rate of 10°C/min, the same heating rate used for firing the whiteware specimens.

3.10.3.2 - Differential thermal analysis (DTA)

DTA is a technique used for measuring the temperature difference between a sample and an inert reference material as both are being heated under a controlled heating rate (Haines, 1995). A standard material (typically alumina) that undergoes no phase transitions in the temperature range of interest is used as the reference. As the heating progresses, any chemical or physical change in the sample results in the release or absorption of heat, and therefore a temperature difference occurs between the sample and the reference. This difference gives rise to a DTA curve, which is a plot of temperature difference between sample and reference against the heating or cooling temperature, consisting of a series of peaks (the exotherms) and troughs (the endotherms). If the reaction involves release of heat, the sample will be at higher temperature than the reference, and an exothermic peak is given. If the sample undergoes a reaction involving absorption of heat, its temperature will be less than that of the reference and an endotherm appears. Exotherms correspond mainly to chemical changes in compounds, such as crystallization, whereas endotherms indicate physical changes in the crystalline structure such as dehydroxylation or melting. The temperatures at which these exotherms and endotherms occur are used to identify (and characterise) the specimen. The method can be used to identify a wide variety of minerals, which undergo dehydration, oxidation or phase changes during heating. Furthermore, DTA results can be combined with the XRD traces of quenched samples at specific temperatures to obtain a more precise mineralogical analysis.

In this work, a Perkin Elmer Pyris DTA (Boston, Massachusetts, USA) was used to evaluate the thermal behaviour of raw materials, two-component mixtures, and whiteware batches. All samples were compared with an alumina standard, during heating and cooling in air at a constant rate of 10°C/min from 50°C to 1500°C. Platinum crucibles were used as sample holders.

3.10.3.3 - Dilatometry

Dilatometry is a technique used to measure the dimensional changes of a sample when it undergoes a controlled temperature programme such as heating or cooling. It gives a better understanding of thermal expansion and sintering behaviour of the material. A Netzsch DIL 402 C dilatometer (Selb, Bavaria, Germany) was used in this study. This equipment can measure dimensional changes as a function of temperature up to a maximum of 1500°C and the measurements can be carried out in air or other controlled atmospheres. The sample holder used is an alumina ceramic tube type holder. In this work, samples were pressed into 8mm diameter disks with 10 mm length before heating to a specific temperature in the dilatometer using a heating rate of 10°C/min and flowing air atmosphere. The dimensional changes (expansion/shrinkage) of each sample were plotted as a function of temperature.

3.10.4 - Phase analysis

The composition and structure of phases in a material and their evolution on firing are key to understanding the material's properties. The identity of crystalline phases can be easily determined in most cases by X-ray powder diffraction, except phases present in small (less than a few volume%) quantities whose peaks may not be easy to distinguish from the background noise. In this case, the use of microscopy techniques which will be mentioned in section 3.10.5 are needed. In the present work, XRD and HTXRD were used to study the phases present in the samples studied, as well as their changes occurring on firing.

3.10.4.1 - X-ray diffraction (XRD)

XRD analysis is a widely used method to detect crystalline phases. The method therefore is most appropriately used on crystalline materials, although non-crystalline or amorphous materials such as glass can also be studied. XRD diffractometers use a monochromatic X-ray beam to determine the phase composition by getting diffraction from the sample's atomic lattices (Cullity, 1978). Each mineral has a unique chemical composition and structure and thus a unique atomic lattice arrangement. When the X-ray beam is directed toward a sample, the atomic lattices of the sample diffract the beam at specific angles only, those which meet the Bragg condition. Bragg's law is shown in the following equation:

$$n\lambda = 2d\sin\theta \qquad (3.1)$$

where n is the diffraction order, λ is the wavelength of X-rays used (the value of λ varies according to the radiation used but typically is 1.5405Å for $Cu_{K\alpha}$ and 0.729Å for $Mo_{K\alpha}$ radiation), d is the lattice spacing (also known as d-spacing) and θ is the Bragg angle.

A diffraction pattern which contains peak positions (angles) and intensities of the diffracted beam is produced. Because every crystalline material will give a unique diffraction pattern, its peak positions and intensities can be checked against databases for identification.

In this study, the crystalline and glassy phases present in the raw materials (as-mixed and fired/quenched and unquenched), two-component batches (as-mixed and fired/quenched and unquenched) and whiteware batches (as-mixed and fired/quenched and unquenched) were identified using a Philips PW1730/10 diffractometer (Philips Electronic Instruments, Mahwah, NJ) operating at 50 kV and 30 mA. All samples were prepared by crushing into a fine powder (<75 μm) using a mortar and pestle. The powdered samples were then placed into the cavity of aluminium holders and their powder surfaces flattened using a glass slide. XRD analyses of powdered samples were carried out using monochromatic copper radiation ($Cu_{K\alpha}$= 1.5405 Å) and scanning over the selected angular range (2θ)

between 5 and 70° with a scanning speed of 0.5°/min and a step size of 0.02°. XRD data were analysed using WinXPow 2.10 (Darmstadt, Germany) software. Crystalline phases from XRD data were identified by comparing the peak positions and intensities from the diffraction patterns with those listed in the Joint Committee on Powder Diffraction Standards (JCPDS) files. The data obtained from a matched pattern usually includes the mineral name of the substance, chemical formula, and crystalline system. A list of the JCPDS card numbers used for phase identification in this study is shown in Table 3.3. The presence of glassy phase in some samples was identified by a characteristic hump in their diffraction patterns.

Table 3.3 - JCPDS cards number used for phase identification.

Phase	JCPDS files no.
albite	9-466
α-cristobalite	82-512, 39-1425
corundum	46-1212
devitrite	77-410
kaolinite	14-164
leucite	85-1419
microcline	19-932
mullite	15-776
muscovite	6-263
nepheline	9-338, 35-424
plagioclase (Na-rich anorthite)	9-465
α-quartz	46-1045
sanidine	19-1227
tridymite	18-1170
β-wollastonite	27-88

Quantitative XRD analysis of selected batches with selected firing temperatures, performed at the Italian Ceramic Center (Bologna, Italy), was determined by the Rietveld method. The Rietveld method is based on the normalization equation:

$$\Sigma_i X_i = 1 \tag{3.2}$$

where X_i is the weight fraction of a component (phase) i in the mixture.

When amorphous phase exists in the mixture, the Rietveld refinement procedure is performed using the General Structure and Analysis System (GSAS), which is a software package for the processing and analysis of both single crystal and powder diffraction data obtained with XRD. It can handle powder diffraction data from a mixture of phases and refine structural parameters for each phase (Larson and Von Dreele, 1999). A known amount (normally 10wt%) of an internal standard is added to the mixture and considered also as a component. The refined values of the Rietveld phase fractions are converted into weight fractions and rescaled into absolute values with respect to the amount of added spike. Therefore whenever glass phase exists in the system, the equation will change to:

$$\Sigma_i X_i + X_a = 1 \qquad (3.3)$$

The amount of amorphous phase (X_a) in the system can be calculated from equation 3.3 or directly from the weight of the internal standard as follow:

$$X_a = [100/(100\text{-}X_s)](1\text{-}X_s/X_{s,c}) \qquad (3.4)$$

where X_s is the actual weight of the internal standard and $X_{s,c}$ is refined weight of the internal standard.

For samples fired at selected firing temperatures, powder diluted with 10wt% corundum NIST 676 as internal standard was side-loaded into the sample holder to minimize preferred orientation. Data collection was performed using a Philips PW 1710 Diffractometer, with copper radiation ($Cu_{K\alpha}$= 1.5405 Å) and scanned over the angular range $10° \leq 2\theta \leq 70°$ with a scanning speed of 0.2°/min.

3.10.4.2 - High temperature X-ray Diffraction (HTXRD)

HTXRD was used in this study to help understand, *in situ*, the sequence of phase changes on firing. HTXRD was conducted using a STOE (STOE CIE & GmbH) STADI P XRD, coupled with a graphite furnace (STOE CIE & GmbH) element heating rotating 1 mm quartz glass capillaries, operating at 40 mA and 50 kV using molybdenum radiation ($Mo_{K\alpha}$ = 0.72906 Å). The fine powdered sample (<50 μm)

was contained in a capillary that was open to the atmosphere, so nominally runs in air. All powdered samples studied were heated from room temperature to 850°C at 50°C/min. Diffraction data were collected every 50°C increment.

3.10.5 - Microstructural analysis

Microstructural analysis is important for ceramic characterization as the ceramics properties are influenced significantly by their microstructures (ASM, 1991). In this study, the texture and microstructure, as well as the progress of mineralogical transformation and reactions upon firing, were examined by using SEM and TEM, with additional analytical techniques such as EDS.

3.10.5.1 - Scanning electron microscopy (SEM)

SEM is a method for high-resolution imaging of specimen surfaces. SEM uses electrons for imaging. The advantages of SEM over optical microscopy include greater magnification (up to 100,000X) and much greater depth of field. An incident beam is raster-scanned across the sample's surface, and the resulting electrons emitted from the sample are collected to form an image of the surface (Hren *et al.*, 1979). Imaging is typically obtained using secondary electrons for the best resolution of the fine surface topographical features. Alternatively, imaging with backscattered electrons gives contrast based on atomic number to resolve microscopic compositional variations, as well as topographical information. Qualitative and quantitative chemical analysis information is also obtained using an energy dispersive X-ray spectrometer with the scanning electron microscope. This chemical analysis is performed by measuring the energy and intensity distribution of the X-ray signal generated by a focused electron beam on the sample.

A JEOL 6400 scanning electron microscope (Model no. JEOL 6400, JEOL, Tokyo, Japan), equipped with Energy Dispersive Spectroscopy (EDS) (Model no. 6276, Link Analytical Systems, High Wycombe, Buckinghamshire, UK) was used to examine fine details of the microstructures of raw materials (fired and unfired), selected fired specimens of binary mixtures and of whiteware batches. SEM analysis of unfired raw materials was carried out to study their morphologies and particle sizes. To do this,

powders were dried overnight at 110°C, and a thin layer deposited onto double-sided sticky tape attached to an alumina stub. As an electric charge builds up on the surface of non-conductors and repels the electrons, a fine conductive coating of carbon or gold must be applied to glass or ceramics so that they can be examined in the scanning electron microscope. The selection of conductive material applied depends on the purpose of analysis. Carbon was applied when EDS analysis was anticipated because carbon has a low atomic number and therefore will not interfere with the chemical analysis of the specimen. When higher magnification and higher resolution are required, gold coating is used as it has a higher atomic number than carbon, thus enhancing the signal emitted from the sample and minimizing charging as it is a better electric conductor than carbon. The thickness of the coating layer should be just enough to create conductivity and maintain maximum surface morphology.

For SEM analysis of fired pellets, selected specimens were cut to smaller sizes with a diamond-impregnated saw and mounted in epoxy resin. This was carried out under vacuum to enable the resin to fill any open pores and so reduce pull out of surface material during grinding and polishing. After being left at room temperature for 24h, the mounted specimens were ground using silicon carbide (SiC) papers of 240, 400, 600, and 1200 grades respectively and subsequently polished with 6, 3 and 1 μm diamond pastes. After each stage of diamond polishing, the samples were cleaned with soap, petroleum ether, and water. After oven drying at 110°C overnight, silver paint was applied on the resin surface to provide a conducting path to the SEM's Al sample holder. After the silver paint dried, the specimens were coated with carbon or gold prior to analysis in the microscope.

Microstructures were examined by secondary electron imaging (SEI) and back-scattered electron imaging (BSI) to observe the shape, size, and distribution of the porosity and crystalline phases as well as densification and homogeneity of the sample. EDS was used to determine semi-quantitatively the elemental composition of glass and crystalline phases present. Samples for BS imaging and/or EDS analysis were carbon coated and high acceleration voltage (20 kV) was applied in order to maximize the signal coming from the samples. For SE imaging of samples with a light gold coating, low acceleration voltage (15 kV) was used in order to reduce the volume of interaction between the electron beam and the sample surface. Working

distances of 15 mm were used for SE imaging and BS imaging whereas an increased working distance (25 mm) was used for EDS analysis to maximize the angle of detection between the incident beam, the specimen and the EDS detector. Only the vitrified specimens were re-polished to remove the coating and etched by dipping for 3 min in a 5vol% hydrofluoric acid (HF) solution, followed by drying, silver painting, and re-coating with gold. These etched and gold-coated specimens were examined for the morphology of the crystalline phases present.

3.10.5.2 - Transmission electron microscopy (TEM)

Transmission electron microscope produces images by detecting electrons that are transmitted through the sample (Champness, 2001), while scanning electron microscope produces images by detecting signals which are emitted or backscattered from the surface due to interaction of the solid with the primary electron beam. Generally, the resolution of a transmission electron microscope is higher than that of a scanning electron microscope. TEM is primarily used for resolving submicron and nanometre particle sizes so that it gives finer microstructural details than the SEM. In addition, TEM gives local crystallographic information when operated in diffraction mode and is often used to characterise crystal defects such as dislocations and twins. However, SEM has compensating advantages, as it is able to image large areas of the specimen and also bulk samples which have a much greater depth of field compared to the thin and small areas imaged by the TEM.

TEM examines structure by passing electrons through a very thin ($\leq$ 100 nm) slice of the specimen. TEM equipment requires a high vacuum and a high voltage electron gun to enable the electrons to penetrate the sample. The image is formed as a shadow of the specimen on a phosphorescent screen. Sample preparation for TEM requires equipment, time and skill. In general, sample preparation for TEM involves samples being sectioned, polished, and ion milled to reach the submicron thickness necessary for the transmission of electrons through the sample.

In this work, a transmission electron microscope (Model 420, Philips) operating at 120 kV was used for bright-field (BF) imaging and selected area diffraction (SAD) analysis. The diffraction patterns arise in the back focal plane of the objective lens

and are effectively a cross section through reciprocal space. Examination of SAD patterns enables the crystallinity and crystal structures of many phases to be determined. The elemental compositions of crystals and glass were analyzed using the EDS system linked to this transmission electron microscope. Standard TEM specimen preparation techniques were used, involving grinding, polishing, Ar^+ ion beam thinning, and carbon coating.

For TEM analysis of powder samples such as the raw clay, the powder was dispersed in acetone. A copper grid (3 mm diameter) with a carbon film, being held by tweezers, was passed through the solution to collect some particles. The acetone then evaporates very quickly, leaving particles of the powder adhered to the carbon film on the grid. The sample is then kept in a plastic capsule. For TEM analysis of fired pellets, selected specimens were cut to thin pieces with a diamond-impregnated saw and glued to glass slides. The samples were then ground to very thin sections. Copper rings were adhered to thin areas of the samples. The samples were then cut with a scalpel to separate the 3 mm copper rings. The thin specimens glued to copper rings were ion beam milled (using Gatan Dual Ion Mill 600, Pleasanton, California, USA) for ~20 h until a hole in the centre was attained (its edges being <200 nm thick and so electron transparent). The milled specimens on the copper rings were carbon-coated, and kept in plastic capsules for TEM analysis.

3.11 - PROPERTY MEASUREMENTS AND EVALUATION

3.11.1 - Firing shrinkage and weight loss

Firing shrinkage is a key indicator of reactivity, in the form of densification through vitrification, during the firing process. The higher the firing shrinkage the denser the ceramic body becomes. To determine the linear shrinkage and weight loss in fired specimens, the dimensions and mass of specimens of each composition were measured before and after firing. The linear shrinkage expressed as a percentage of the original dimension of the dry specimen was calculated as (Ryan and Radford, 1997):

$$\% \text{ linear shrinkage} = (D_d - D_f)/D_d \cdot 100 \quad (3.5)$$

where D_d and D_f are the respective diameters of the specimen in the dry and fired conditions.

The weight loss was evaluated as a percentage of the dry weight as follows:

$$\% \text{ weight loss} = (W_d - W_f)/W_d \cdot 100 \quad (3.6)$$

where W_d and W_f are the weight of the dry and fired specimens respectively.

3.11.2 - Water absorption

Water absorption of fired specimens was measured by using the British Standard EN 99 (1991) method. Each specimen was dried in an oven at 110°C until constant mass was reached, and cooled in a dessicator over silica gel before being weighed and this weight recorded as m_1. The specimens were then placed vertically, with no contact between them in distilled water in the heating apparatus. The distilled water level was maintained 5 cm above the specimens throughout the test. After heating in boiling water for 2h, the heating apparatus was removed and the specimens allowed to cool for 4h in distilled water. Each specimen was then weighed and this weight recorded as m_2. Water absorption was calculated as a percentage of the dry mass using the expression:

$$\% \text{ water absorption} = (m_2 - m_1)/m_1 \cdot 100 \quad (3.7)$$

where m_1 and m_2 are the masses of the dry and wet specimens respectively.

The water absorption is attributed to the water being forced under pressure into the open (interconnected) pores. The addition of fluxing agents such as nepheline syenite or powdered glass, during the firing process, is thought to seal those pores, thus resulting in lower water absorption values by preventing water ingress via the open pores.

3.11.3 - Bulk density

Bulk density (ρ_s) of fired specimens was determined by using a mercury densitometer (Model P1210, Mettler-Toledo, Inc., Hightstown, NY) and calculated as:

$$\rho_s = \rho_{Hg} \cdot m_s / (m_2 - m_1) \tag{3.8}$$

where m_s is the mass of the sample, m_1 is the mass of mercury and its container, m_2 is the apparent mass of mercury and its container with the sample in it, (m_2-m_1) is the mass of mercury displaced, and ρ_{Hg} is the density of mercury.

3.11.4 - Mechanical properties

The samples for measuring mechanical properties of selected batches and firing temperatures were prepared and measured by an Italian research group in the Italian Ceramic Center (Bologna, Italy) using the following methods.

3.11.4.1 - Flexural strength

Samples from batch S0 fired at 1100 and 1200°C, and from batches S25, S50, S75 and S100 fired at 1100°C were selected for flexural strength measurement using a three-point bending test. The samples were prepared in the form of rectangular bars (70 mm × 10 mm × 6 mm). These rectangular bars were prepared by uniaxial pressing (32 MPa) a granulated powder (6wt% water) using a stainless steel mould. For the bending test the bars were used as fired, without any treatment such as grinding or polishing. At least 20 specimens were tested using a universal testing machine (10/M, MTS, USA), equipped with a three point bending fixture, 60 mm roller span, and a crosshead speed of 5 mm/min (Tucci *et al.*, 2005). Figure 3.3 illustrates the three-point bending method. The specimen with a rectangular shape was placed on two supporting rods, and the load was applied through one top rod at the centre of the span. Equation (3.9) was used to calculate flexural strength (Green, 1998):

$$\sigma = (3/2)(P \cdot L)/(b \cdot h^2) \tag{3.9}$$

where σ is the flexural strength, P is the applied load, L is roller span, b and h are the width and height of a tested rectangular bar respectively.

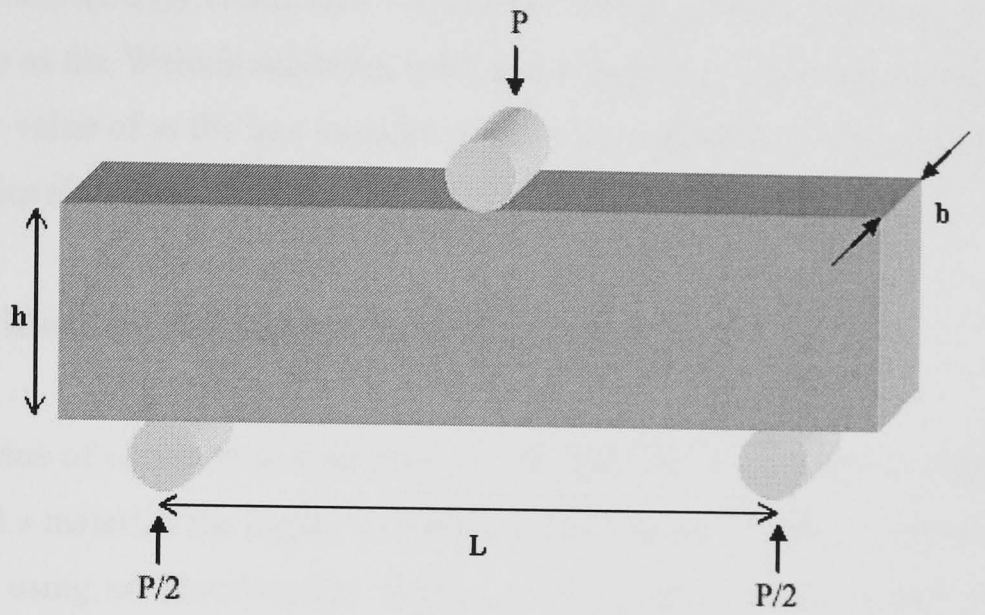

Figure 3.3 - Schematic illustration of three-point bending configuration.

The data obtained were used to calculate the average flexural strength values and Weibull's modulus (*m*) via the least squares method and linear regression analysis (Davidge, 1980), adopting a probability of failure (P_n) as:

$$P_n = (i-0.5)/N \tag{3.10}$$

where N is the number of strength measurements and i is the ranking number, where i = 1 for the weakest specimen and i = N for the strongest respectively.

The strength data were analyzed by means of the Weibull equation. This equation relates a specimen's failure probability to the stress undergone as follows:

$$P_n = 1 - \exp(-(\sigma-\sigma_u)/\sigma_0))^m \tag{3.11}$$

where σ_u is the stress below which fracture is assumed to have zero probability, implying an upper limit to the flaw size (in this case $\sigma_u = 0$), and σ_0 is a normalizing parameter or constant.

For plotting data it is convenient to take logarithms of equation (3.11) twice and rearrange as:

$$\ln\ln(1/(1-P_n)) = m\ln(\sigma - \sigma_0) - m\ln\sigma_0 \qquad (3.12)$$

Plotting $\ln\ln(1/(1-P_n))$ versus $\ln(\sigma - \sigma_0)$ yields a straight line of slope m. Constant m, referred to as the Weibull modulus, reflects the degree of variability in strength. The higher the value of m the less variable is strength. Values for m of 5-20 are common for ceramics (Davidge, 1980).

3.11.4.2 - Modulus of elasticity (Young's modulus, E)

The modulus of elasticity is a measure of the stiffness or rigidity of a material. The more rigid a material, the higher its modulus of elasticity. In the present work, it was evaluated using an extensometer applied to the middle of the surface of the test specimen subjected to the tensile stress. Three-point bending was used to cause the tensile stress to tested samples. This test were carried out on the samples from batch S0 fired at 1100 and 1200°C, and samples from batches S25, S50, S75 and S100 fired at 1100°C. Test specimens were prepared by the same method as previously mentioned for the flexural strength test. Young's modulus was determined from the curve load (P) versus the displacement at the load application point which in this case is at the centre (δ_c) (Green, 1998). Equation (3.11) was used to calculate the modulus of elasticity in the three-point bending test:

$$P = 4\, b \cdot h^3 \cdot E \cdot \delta_c / L^3 \qquad (3.11)$$

where P is the applied load, δ_c is the displacement at the load application point, E is the Young's modulus, L is roller span, b and h are the width and height of a tested rectangular bar respectively.

3.11.4.3 - Fracture toughness (K_{IC})

The fracture toughness (K_{IC}) was measured for samples from batch S0 fired at 1200°C and samples from batch S25 fired at 1100°C. A rectangular test beam with

single edge pre-crack notch was tested in a four-point bending fixture. K_{IC} was measured by subjecting notched bars to a four-point bending test (0.5 mm/min crosshead speed). The bars were cut to 45 mm x 7 mm x 4 mm, and notched using a 150 μm thick high-precision diamond saw. The notched bars, seven for each batch, were then placed in a four-point bending test fixture with the notch on the tensile side of the fixture (Figure 3.4). The outer rollers span (L) was 40 mm, whereas the inner roller span (l) was 20 mm. The measurement consists of loading the notched specimens by increasing the load until fracture occurs. K_{IC} was calculated from the breaking load, the depth of the notch, the dimension of the test beam and the span as in the following equations (Esposito *et al.*, 1995; Green, 1998):

$$K_{IC} = \sigma_0 \cdot Y \cdot \sqrt{a} \tag{3.12}$$

$$\sigma_0 = \frac{3 \cdot P \cdot (L - l)}{2 \cdot b \cdot h^2} \tag{3.13}$$

$$Y = f\left(\frac{a}{h}\right) = A_0 + A_1 \cdot \left(\frac{a}{h}\right) + A_2 \cdot \left(\frac{a}{h}\right)^2 + A_3 \cdot \left(\frac{a}{h}\right)^3 + A_4 \cdot \left(\frac{a}{h}\right)^4 \tag{3.14}$$

where a is the depth of the notch (1.75 mm), σ_0 is the mechanical strength, P is the applied load, h is the height of the bars, b is the thickness of the bars, Y is a dimensionless constant that depends on flaw size (a) or a function of the ratio a/h. The values of A_0, A_1, A_2, A_3 and A_4, for a/h = 0.25, are 1.99, -2.47, 12.97, -23.17 and 24.80, respectively.

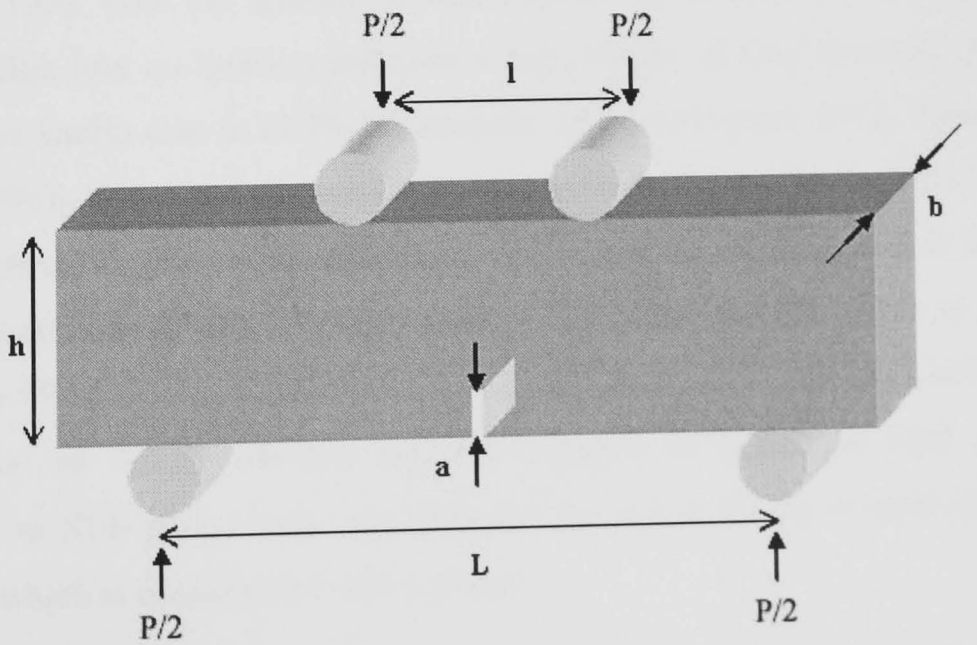

Figure 3.4 - Four-point bending fixture and notched specimen for fracture toughness (K_{IC}) measurements.

CHAPTER 4 - STUDY OF RAW MATERIALS

4.1 - INTRODUCTION

The raw materials used in this study were kaolin clay, quartz sand, nepheline syenite, and colourless SLS waste glass. As-received raw materials and powdered SLS glass were characterized by performing chemical analysis, particle size analysis, phase analysis, thermal analysis, and microstructural examination. Fired specimens of each raw material were also characterised by phase analysis and microstructural evolution to study the effect of heat on the individual raw material.

4.2 - CHEMICAL COMPOSITION

Table 4.1 shows the chemical composition of the raw materials (measured by ICPAES as discussed in section 3.10.2) in the form of oxides together with the loss on ignition, revealing that kaolin clay is high in SiO_2 and Al_2O_3 and has a small K_2O content as a result of the muscovite and microcline present (see XRD of as-received and fired kaolin clay in Figures 4.6 and 4.7, respectively). The loss on ignition is an important characteristic of clays due to its association with loss of hydroxyl ions in the clay mineral structure and also organic matter if present. Both are driven off on ignition of the clay to 1000°C, hydroxyl ions being driven off as vapour and organic matter as CO_2. Loss on ignition is also used as an estimate of the clay mineral content. High loss on ignition indicates a high degree of clay minerals (the weight loss of pure kaolin clay is 13.9% (Grimshaw, 1971; Lawrence, 1972; Papargyris and Cooke, 1996)), which are responsible for the high plasticity. The kaolin clay used as a raw material in this work undergoes ~12% loss on ignition which indicates it contains more than 86wt% of clay minerals. The quartz is highly pure as it contains more than 99wt% SiO_2. Colourless SLS glass is high in Na_2O, CaO and SiO_2, but almost free of Al_2O_3, whereas nepheline syenite is higher in K_2O and Al_2O_3 compared to SLS glass. Each raw material has a low Fe_2O_3 content (between 0-0.3wt%), which is essential for white bodies.

Table 4.1 - Chemical composition (wt%) of raw materials.

Oxides	Raw materials			
	Kaolin clay	Quartz	Nepheline syenite	SLS waste glass
SiO_2	49.34±0.20	99.80±0.40	58.30±0.30	73.96±0.30
Al_2O_3	34.72±0.20	<0.10	24.40±0.20	0.96±0.02
Fe_2O_3	0.26±0.02	<0.10	<0.10	<0.10
CaO	0.10±0.02	0.10±0.02	0.70±0.02	11.95±0.07
Na_2O	0.27±0.02	0.20±0.02	7.00±0.08	11.72±0.07
K_2O	2.98±0.02	0.60±0.02	8.40±0.08	1.22±0.02
MgO	0.28±0.02	<0.10	<0.10	0.75±0.02
TiO_2	<0.10	<0.10	<0.10	<0.10
LOI[+]	12.02±0.20	0.20±0.20	1.10±0.20	-

[+]LOI - Loss on ignition

4.3 - PARTICLE SIZE ANALYSIS

The PSD's of as-received china clay (kaolin), quartz, nepheline syenite, and of the ground colourless SLS waste glass as determined by laser particle size analysis (described in section 3.10.1), are shown in Table 4.2.

Table 4.2 - Particle size distributions of raw materials.

Volume (%) less than	Particle diameter (μm)			
	Kaolin clay	Quartz	Nepheline syenite	SLS waste glass
10	1.46	190.50	1.54	11.27
25	3.47	223.20	3.79	24.41
50	7.87	260.50	10.49	52.48
75	16.38	307.40	21.39	116.60
90	119.50	359.00	35.57	186.30

90vol% of clay particles are <120 μm in size, with 50vol% less than 8 μm. It is expected that the clay ultimate particle size is well below 8 μm, as the clay particles are usually agglomerated. Quartz has the largest particle size compared to the other

raw materials used, ranging from 190 to 360 μm. Nepheline syenite has finer size with 90vol% particles <40 μm. SLS glass has 50vol% of particles <55 μm. Fine silica particles also tend to flocculate due to weak interactions between Si-O (Srinivara *et al.*, 2000), therefore their particle size shown in Table 4.2 may be an overestimate, measuring agglomerates rather than ultimate particles. SEM micrographs (section 4.6) confirm these comments about the particle sizes given in Table 4.2.

4.4 - THERMAL BEHAVIOUR

DTA and TG/DTG traces of raw materials are given in this section. The thermal events are studied and explained with reference to other complementary techniques such as XRD of fired samples quenched on either side of DTA peaks (see section 4.5), and published data.

4.4.1 - Kaolin clay

Figure 4.1(a) shows the DTA curve recorded on heating and cooling the kaolin clay between 50 and 1500°C at heating and cooling rates of 10°C/min in air. The kaolin clay exhibits two characteristic endothermic peaks, one which has its minimum at ~179°C and another between ~450°C and 650°C which has its minimum at ~545°C. These events, as observed by other authors (Papargyris and Cooke, 1996; Lee *et al.*, 1999; Chen *et al.*, 2004), are associated with the evaporation of adsorbed physical water and the dehydroxylation of kaolinite (loss of structural water) leading to the formation of metakaolin, respectively. The exothermic reaction at ~212°C is probably due to organic matter burn out. The exothermic peak at ~982°C is likely due to formation of new crystalline phases such as a Si-containing γ-Al_2O_3 with spinel structure (Brindley and Nakahira, 1959; Iqbal and Lee, 1999) or a primary mullite (Al_2O_3:SiO_2 = 2:1) (Lee *et al.*, 1999; Chen *et al.*, 2004). There is still considerable disagreement regarding the cause of the exothermic peak at ~980°C. According to the XRD study on quenched clay pellets (Figure 4.5), small mullite peaks are present in the sample quenched from 950°C, and its distinctive peaks are present in the sample quenched from 1150°C. This would suggest that the

crystallisation of mullite actually began before the peak at ~982°C. However, the actual temperature at which the sample was taken from the furnace is likely to be higher than 950°C due to the 10°C/min heating rate used in the experiment for quenching. The time elapsed until the sample was effectively taken out of the furnace and quenched has certainly allowed the sample to reach higher temperatures. Moreover, the temperature measurement in the DTA system is more accurate than that in the furnace used to heat the sample for quenching due to the thermocouple placed very near the sample in the DTA crucible. Therefore, the peak at 982°C in the DTA of kaolin clay, with onset at ~15°C lower than 982°C, can actually be associated with the crystallisation of mullite. Spinel XRD peaks were detected after clay pellets were quenched from 800°C. These peaks are present up to 950°C (Figure 4.5). As a result, the broad and small exothermic peak observed between 800-950°C could be related to the spinel formation. McConville *et al.* (2005) observed spinel peaks at higher temperatures for pure kaolinite. The discrepancy between crystallisation temperatures for these phases may be explained by the presence of impurities in the kaolin clay used in the present study (e.g. potassium). The small exothermic peak at ~1202°C is possibly due to the formation of Al_2O_3:SiO_2 = 3:2 mullite. In summary, although there is debate in the literature about the actual meaning of the DTA exotherm at ~980°C, the sequence of reactions on heating kaolin clay is well established i.e. kaolin - metakaolin - spinel - mullite, and is consistent with the experimental data shown in the present study.

In the TG/DTG traces of kaolin clay (Figure 4.1(b)), recorded by heating from 50 to 950°C at the same heating rate as that used in the DTA, a one-step weight loss is observed. A weight loss of ~10.6% occurs over the range 400-750°C, correlating with the second endothermic effect on the DTA curve centred at ~545°C, which is due to the loss of structural water from kaolinite. The weight loss due to removal of adsorbed water is less than 1% and is detected at the beginning of the TG/DTG traces. The weight loss does not change significantly on heating above 750°C. The total weight loss from the TG curve (~12%) was close to the 12.02wt% observed on the loss on ignition for the clay (Table 4.1). The theoretical value of loss on ignition for pure kaolin clay is 13.9% due to the loss of structural water.

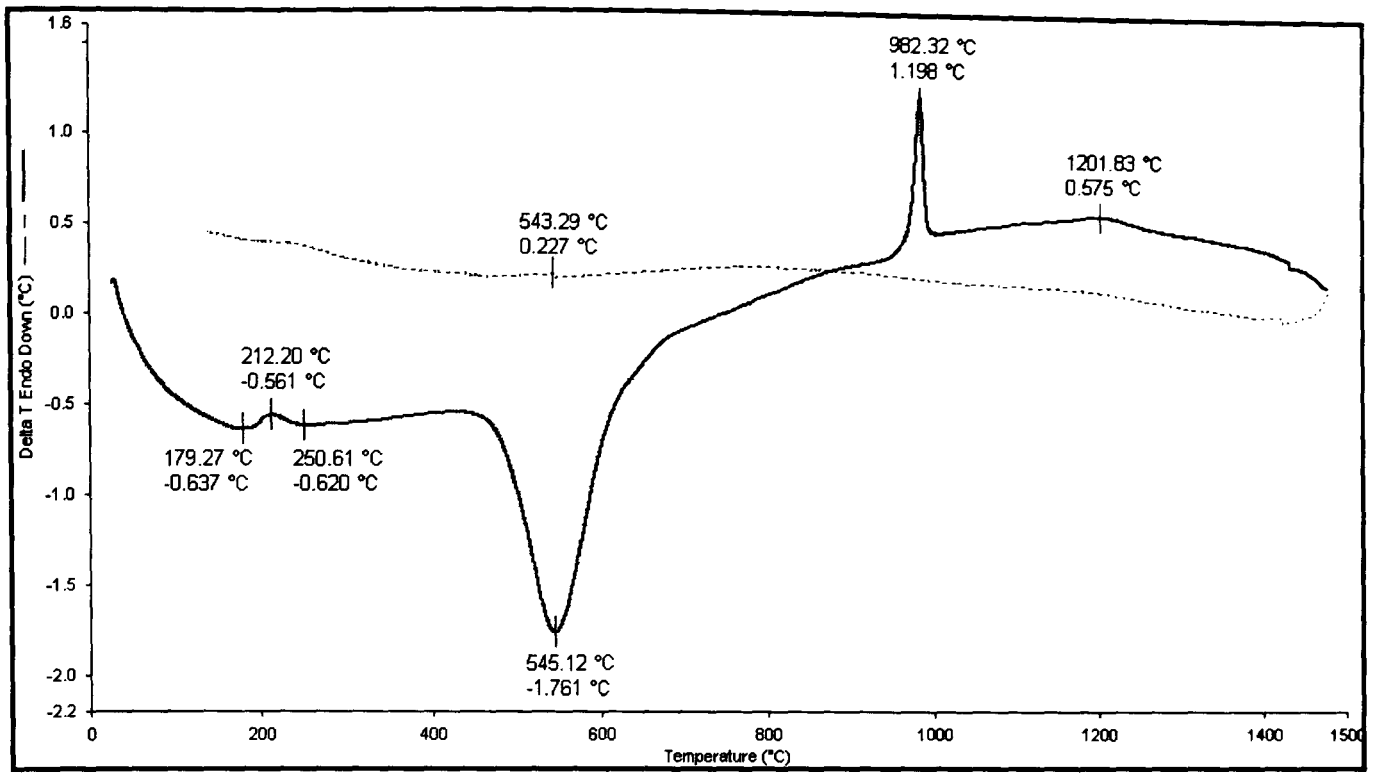

(a)

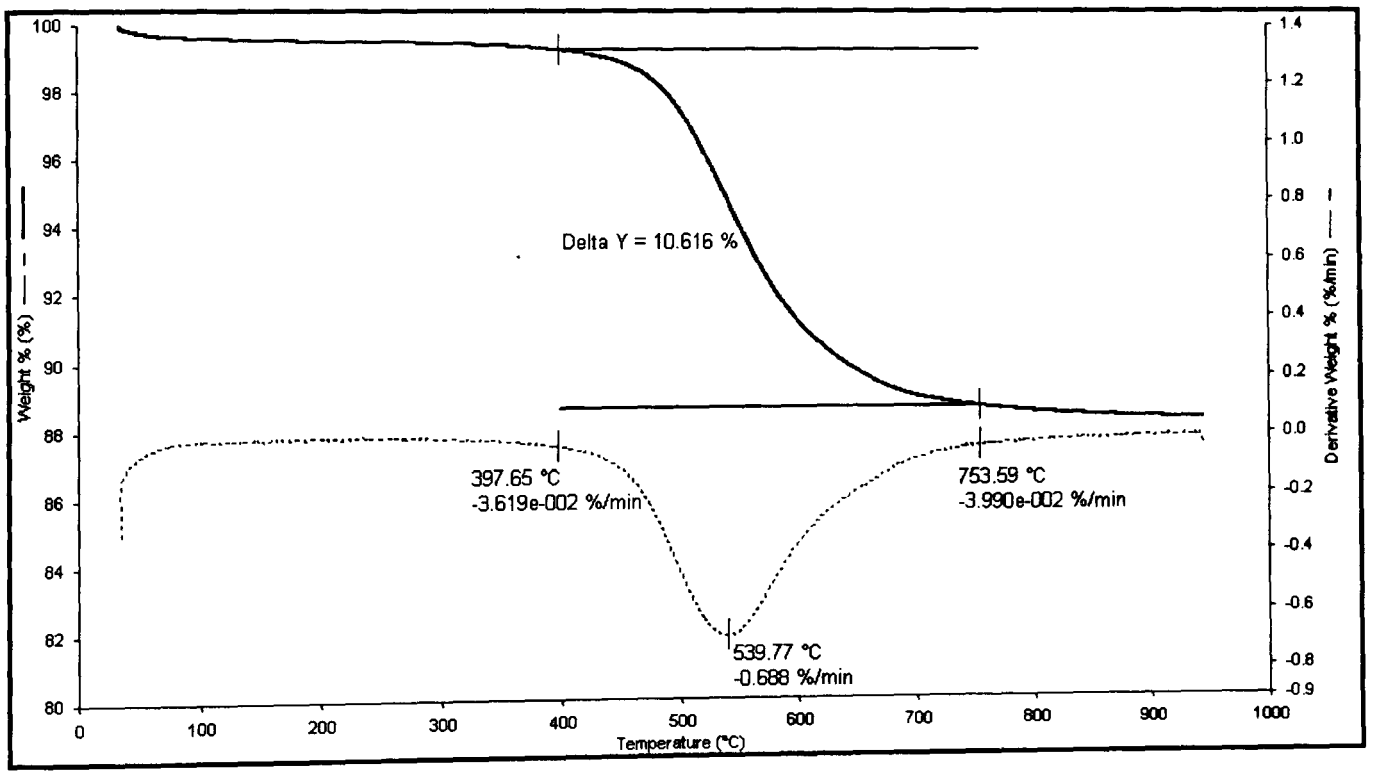

(b)

Figure 4.1 - DTA (a; — heating curve, --- cooling curve) and TG/DTG (b; — TG, --- DTG) of kaolin clay.

4.4.2 - Quartz sand

On heating quartz from 50°C to 1500°C, the DTA curve (Figure 4.2) shows one displacive transition (involving only minor structure change without any bond

breakage) of the low temperature form of quartz (α-quartz) to its high temperature form (β-quartz) confirmed by the presence of an endothermic peak at 568.91°C. The reconstructive transformation (involving bond breakage and rearrangement) of β-quartz to tridymite was not observed. Many researchers (Lawrence, 1960; Holmquist, 1961) stated that in the presence of fluxes or other impurities, quartz converts sluggishly to tridymite at 870°C, and in the absence of fluxes and impurities, it converts sluggishly to cristobalite at 1470°C. Hlavac (1983) suggested that high purity (impurity content <0.01%) β-quartz is stable up to ~1025°C and is then reconstructively transformed into cristobalite (β-cristobalite), but if it contains more than 0.01% impurities then it converts into tridymite (γ-tridymite) at 870°C which later transforms into β-cristobalite above 1470°C. Hand *et al.* (1998) studied silica polymorphs by firing pure quartz with and without mineral additives. Tridymite was not found to be a stable form in the pure silica system and, without mineral additives, no tridymite conversion was observed and cristobalite only crystallised when the firing temperature was 1300°C and above. This conversion also occurred when heating above 1300°C and/or soaking at high temperature for many hours.

In the present work, the transformation of β-quartz to β-cristobalite was not detected in the DTA curve which revealed only displacive inversions (Figure 4.2). However, cristobalite was detected on cooling by the presence of an exothermic peak arising from the inversion of β-cristobalite to α-cristobalite, the low temperature form of cristobalite at ~219°C. The temperature of the α-β cristobalite inversion is 267°C for the ordered form (Hlavac, 1983). The values in the 200-270°C range are indicative of a defective structure (disordered), formed for instance by heating silica gels or fused quartz glass to various temperatures. Therefore it is expected that the cristobalite formed in the present study would be disordered. No weight loss was detected from the TG/DTG curve of quartz due to its small amount. The small loss on ignition ~0.2% from Table 4.1 may be due to moisture which silica adsorbed from the environment (Yang and Wang, 2006).

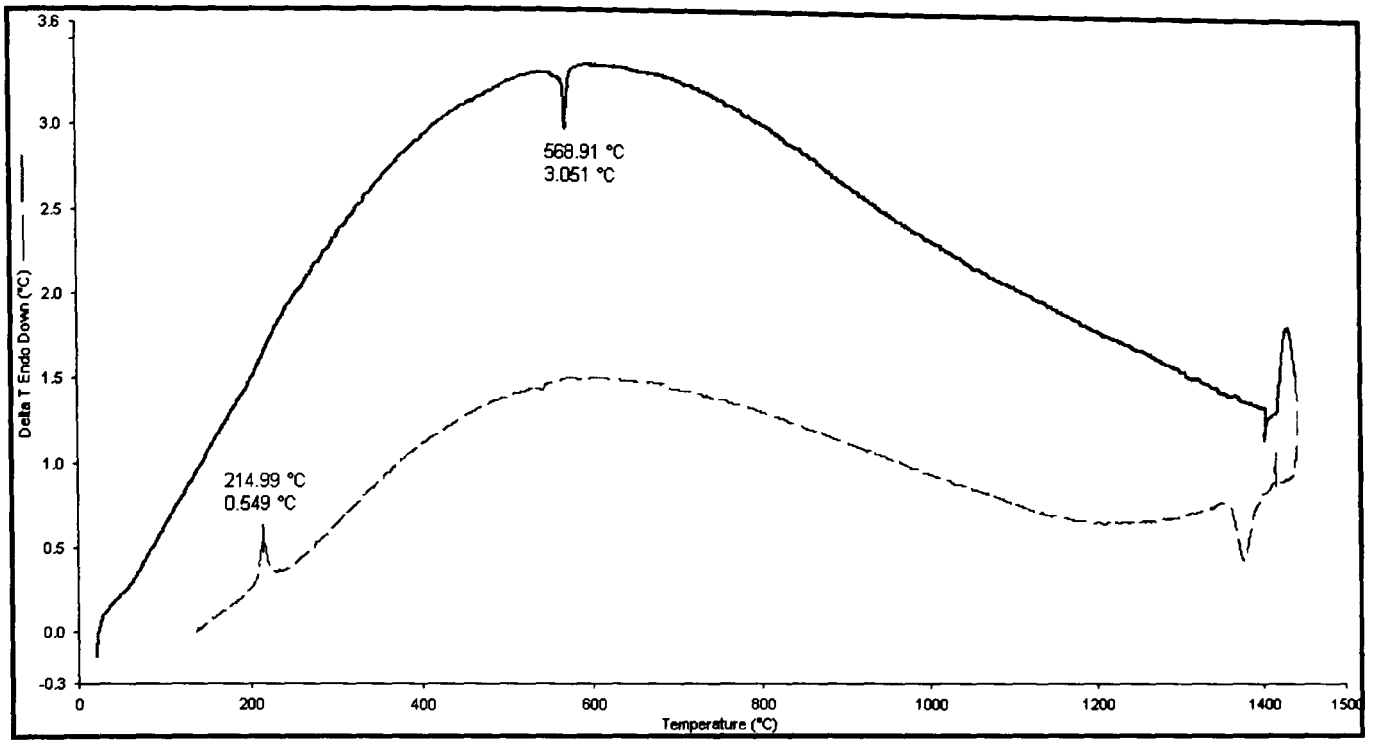

Figure 4.2 - DTA of quartz. (— heating curve, --- cooling curve)

4.4.3 - Nepheline syenite

DTA of nepheline syenite (Figure 4.3(a)), recorded on heating and cooling nepheline syenite between 50°C and 1500°C, reveals no clearly defined peaks apart from a broad endothermic drift between 900-1200°C, as a result of its gradual melting. No crystallization was observed. According to the literature (Hlavac, 1983; Esposito *et al.*, 2005), minerals in nepheline syenite such as microcline, nepheline and albite start to melt at temperatures above 1100°C. Potash feldspar is known to dissociate into liquid and leucite (this phase transformation will be explained by XRD discussed in section 4.5). The TG/DTG curves (Figure 4.3(b)) reveal two weight loss steps over the 185-285°C and 590-730°C temperature ranges. These weight losses are, however, minor, and may be related to organic matter burn out and CO_2 released from contaminant carbonate breakdown, respectively.

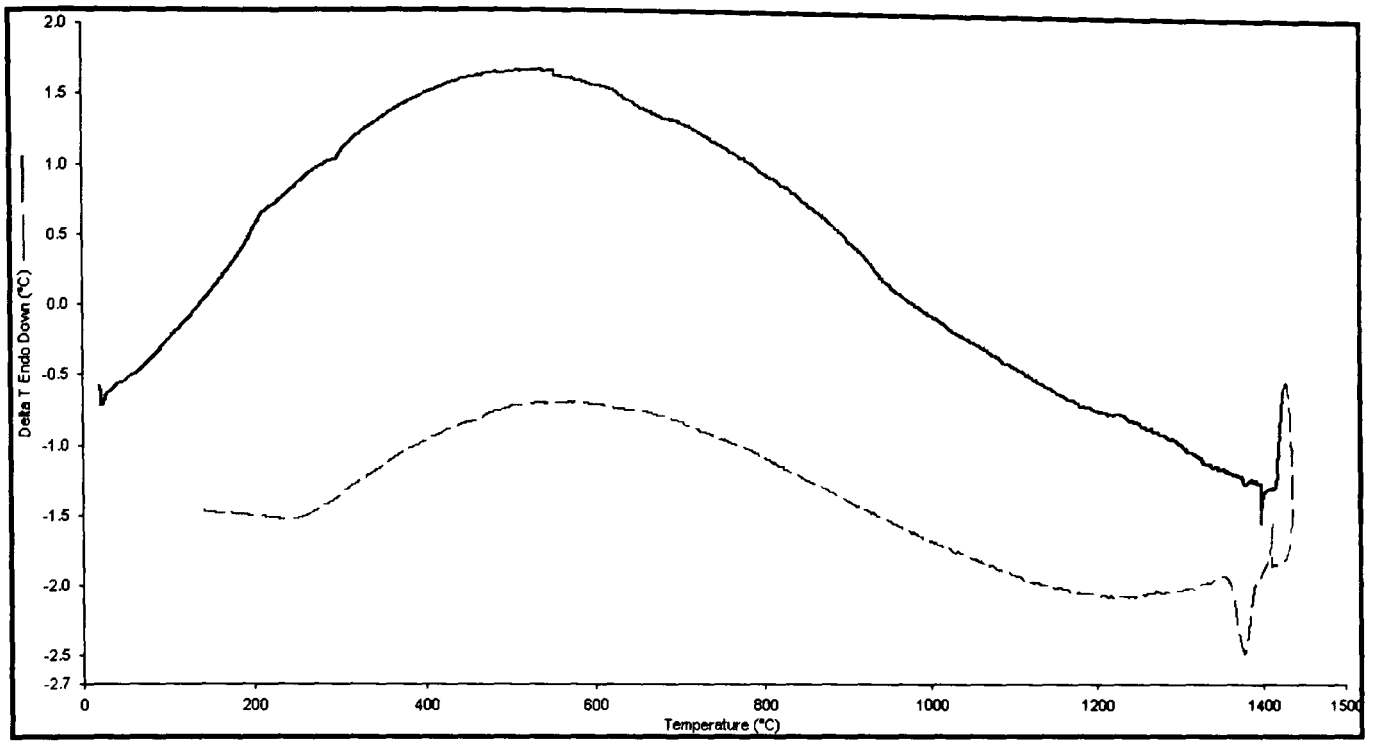

(a)

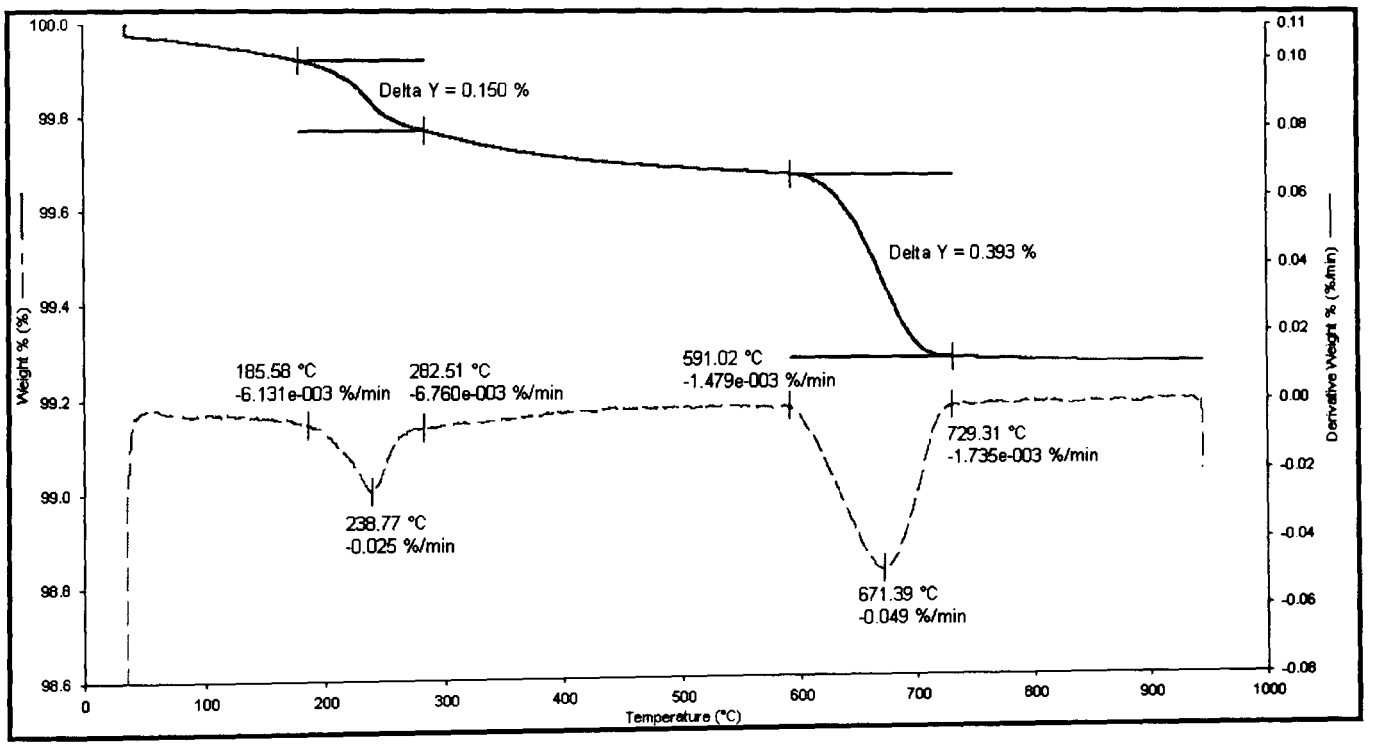

(b)

Figure 4.3 - DTA (a; — heating curve, --- cooling curve) and TG/DTG (b; — TG, --- DTG) of nepheline syenite.

4.4.4 - Soda lime silica glass

Figure 4.4(a) shows DTA of ground SLS glass recorded on heating and cooling between 50°C and 1500°C at 10°C/min. Two endothermic peaks were observed at ~100°C and ~128°C, which are probably due to the evaporation of moisture and

removal of organic matter (such as paper and resin/glue attached to the recycled bottle used), respectively. An endothermic peak which begins at ~563°C was attributed to the glass transition temperature (T_g) of the SLS glass mix used. The low transition temperature can be explained by the high level of alkalis. An exothermic hump centred approximately at 760°C is due to crystallization. This broad exothermic peak is likely to be associated with the formation of crystalline phases. The peak has a large and asymmetric shape probably referring to the crystallisation of more than one phase at temperatures close to the peak temperature. To clarify this phenomenon, XRD analysis of SLS pellets fired to various temperatures (below and above the observed peak) and quenched in water was carried out. XRD (Figure 4.14) reveals cristobalite, quartz, devitrite ($Na_2Ca_3Si_6O_{16}$) and wollastonite ($CaSiO_3$) crystalline phases in SLS pellets quenched from temperatures between 600-800°C. These phases were formed from devitrification of the SLS glass.

As the crystallisation event proceeds in a glass, the heat of crystallisation is evolved and an exothermic peak appears on the DTA curve. The DTA peak shape is affected by the crystallisation mechanism taking place. According to the studies about $Li_2O{\cdot}SiO_2$ glass conducted by Marotta *et al.* (1980) and borosilicate glass conducted by Lima and Monteiro (2001), it was concluded that sharp and broad peaks have been attributed to bulk and surface nucleation, respectively. Many papers report surface crystallisation of SLS glass (Swift, 1947; Neely and Ernsberger, 1966; Prado and Zanotto, 2002). Most commercial glass compositions tend to crystallize mainly on the surface because of heterogeneities present. Even dust has been shown to greatly enhance surface crystallization of SLS glass (Swift, 1947; Neely and Ernsberger, 1966). Moreover, crushing and milling SLS glass leaves broken chemical bonds on its surface, which render it highly reactive. The endothermic peak at ~990°C appeared to be associated with melting of crystalline compounds. XRD of SLS pellets quenched from 900°C (Figure 4.15) with no peaks (only an amorphous hump) confirmed the melting of crystalline phases. The DTA curve fell drastically at higher temperatures indicating the presence of a large amount of liquid formed.

TG/DTG (Figure 4.4(b)), reveal three weight loss steps. The weight loss at between 50-100°C is ~0.08wt%, corresponding entirely to the first DTA endothermic peak. The weight loss at 100-150°C is around 0.12wt%, which correlates with the second

DTA endothermic event at ~128°C. The third weight loss from 460-650°C is probably due to organic matter burn off (Kirby, 2001).

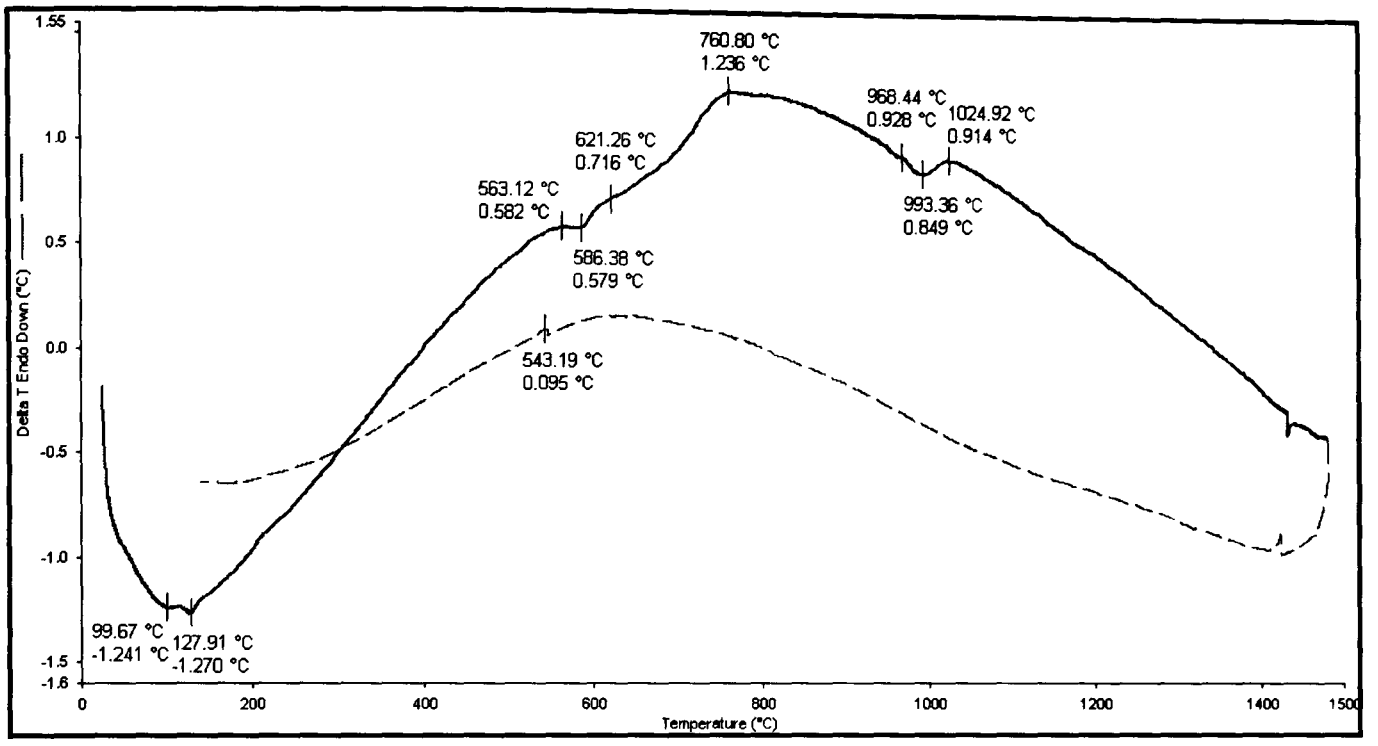

(a)

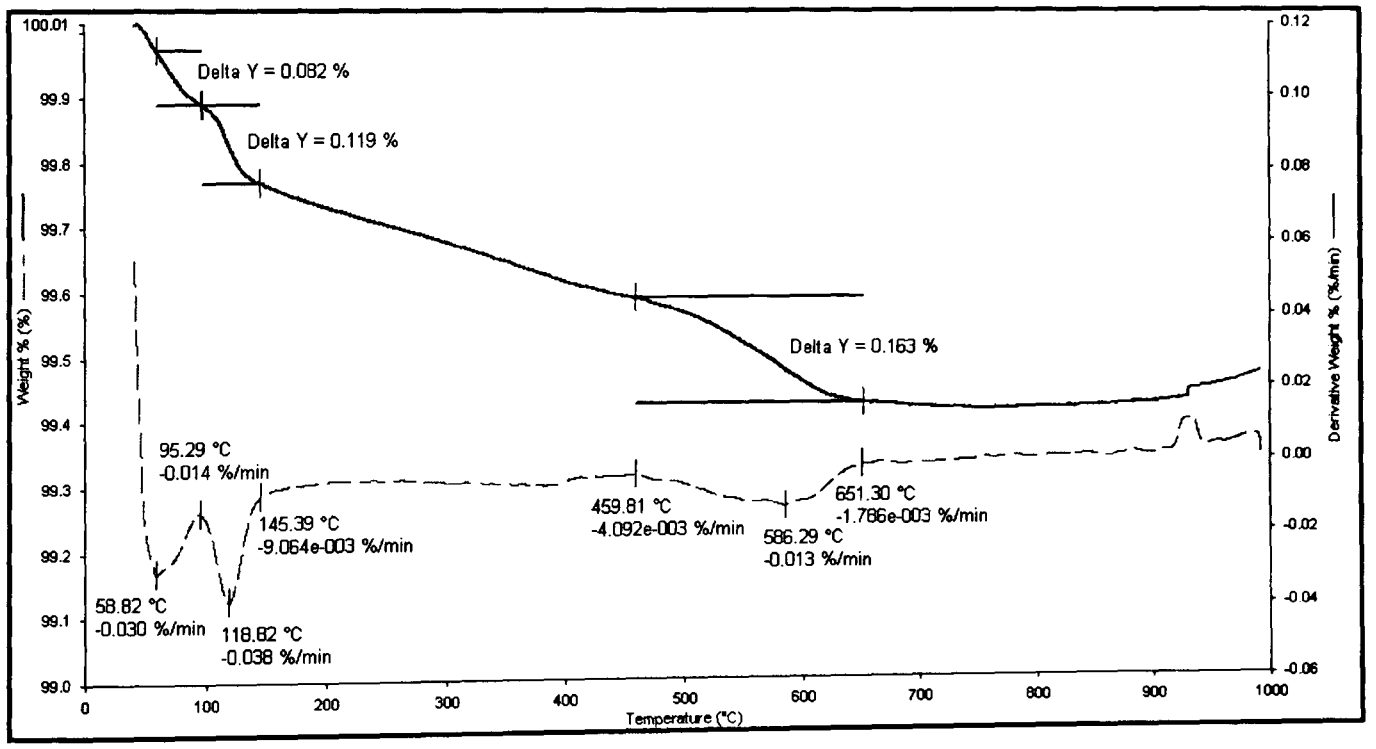

(b)

Figure 4.4 - DTA (a; — heating curve, --- cooling curve) and TG/DTG (b; — TG, --- DTG) of SLS glass mix.

4.5 - PHASE EVOLUTION

The mineralogy of the raw materials as well as the mineralogical changes taking place upon firing were studied using standard powder XRD and *in situ* high-temperature XRD. This section starts with XRD of raw materials quenched from specific temperatures, below and above each heat effect (peak) found in their DTA traces to assist in determining the reactions or phase changes which were taking place during heating. *In situ* HTXRD (with $Mo_{K\alpha}$ radiation source) traces of each raw material follow the quenching studies. *In situ* diffraction measurements of raw materials were made using a heating rate of 50°C/min, and measurements were performed at 50°C intervals from room temperature to 850°C. The *in situ* HTXRD sequence gives some details which are impossible to achieve from standard powder XRD about phase changes on heating. From i*n situ* HTXRD, the progress of reactions as they take place could be observed and the phases present in a sample could be identified without prior cooling. Finally, XRD of raw materials fired to specific temperatures and soaked for 3h were observed and used to explain the phase evolution on heating each raw material.

4.5.1 - Kaolin clay

Figure 4.5 shows XRD of as-received and fired kaolin clay pellets quenched after firing to particular temperatures. XRD of the as-received kaolin clay showed predominantly a well-crystallised kaolinite ($Al_2Si_2O_5(OH)_4$, JCPDS no.14-164) with minor α-quartz (SiO_2, JCPDS no.46-1045), muscovite ($KAl_2(Si_3Al)O_{10}(OH)_2$, JCPDS no.6-263) and microcline ($KAlSi_3O_8$, JCPDS no.19-932) impurities. Kaolinite was identified by its 7.17 and 3.58 Å peaks (2θ = 12.34° and 24.86° respectively), which disappeared after heating to 500°C where kaolinite undergoes a phase transformation from 450-550°C to form the semi-amorphous phase metakaolinite (Brindley and Nakahira, 1959). Metakaolinite had no distinct diffraction peaks, indicating its predominantly amorphous nature, and therefore the XRD patterns show the absence of kaolinite peaks above this temperature range. This reaction occurred at lower temperature when compared with the *in-situ* high temperature XRD (Figure 4.6) where kaolinite peaks were still present at 500°C and did not disappear until 550°C. Heating rate may be a factor in this difference. The

slower heating rate (10°C/min) used on firing samples before quenching may have given more time for kaolinite/metakaolinite reaction to occur when compared with the faster heating rate (50°C/min) used in the graphite furnace of the *in-situ* HTXRD equipment. Also, kaolinite may have had longer time for dehydroxylation during the few minutes effectively taken to quench the bulk specimen, compared to the powder analysed on the HTXRD machine.

α-quartz was identified by its characteristic 3.34, 4.26 and 1.82 Å peaks (2θ = 26.64°, 20.86°, 50.14°, respectively). Muscovite which is commonly present in kaolin clay as an accessory mineral was identified by its 9.95, 4.97 and 3.32 Å peaks (2θ = 8.88°, 17.83° and 26.83° respectively). From JCPDS card no. 6-263, the muscovite present in this clay is the $2M_1$ polytype, which is the most stable (Brown, 1984; Barlow and Manning, 1999). However, many of its small peaks overlap with those of kaolinite, making it difficult to identify. Muscovite peaks are very weak in the samples fired at 950°C and cannot be distinguished in the samples fired at 1150°C. Complete muscovite breakdown must have occurred on firing between 950°C and 1000°C, which is consistent with previous work (e.g. Norton, 1962; Grimshaw, 1971). Microcline which was identified by its 3.24 Å peak (2θ = 27.51°) is present in very small quantities. This potassium feldspar melted and disappeared at 1150°C, consistent with Hlavac's work (1983).

Broad spinel peaks of γ-alumina (Al_2O_3, JCPDS no. 10-425), which is normally identified by its main diffraction peaks of 1.98 and 1.39Å (2θ = 45.86° and 67.03°), arose by 800°C and were no longer detected at 1150°C. Mullite ($Al_2Si_2O_5$, JCPDS no.15-776) began to develop in small quantities at 850°C. It was unambiguously detected above 950°C and continued up to 1150°C showing sharp and distinct peaks. Its main peaks are 3.39, 3.85 and 2.21Å (2θ = 26.21°, 25.83° and 40.79° respectively). Formation of mullite from kaolin at temperatures lower than those predicted from the SiO_2-Al_2O_3 phase diagram (1547-1587°C) can be attributed to the presence of fluxing oxides especially K_2O (~3wt%), which are derived from microcline and/or muscovite present in the raw kaolin clay. These impurities foster the formation of a viscous liquid, which enhances diffusion leading to mullite crystallisation at lower firing temperatures.

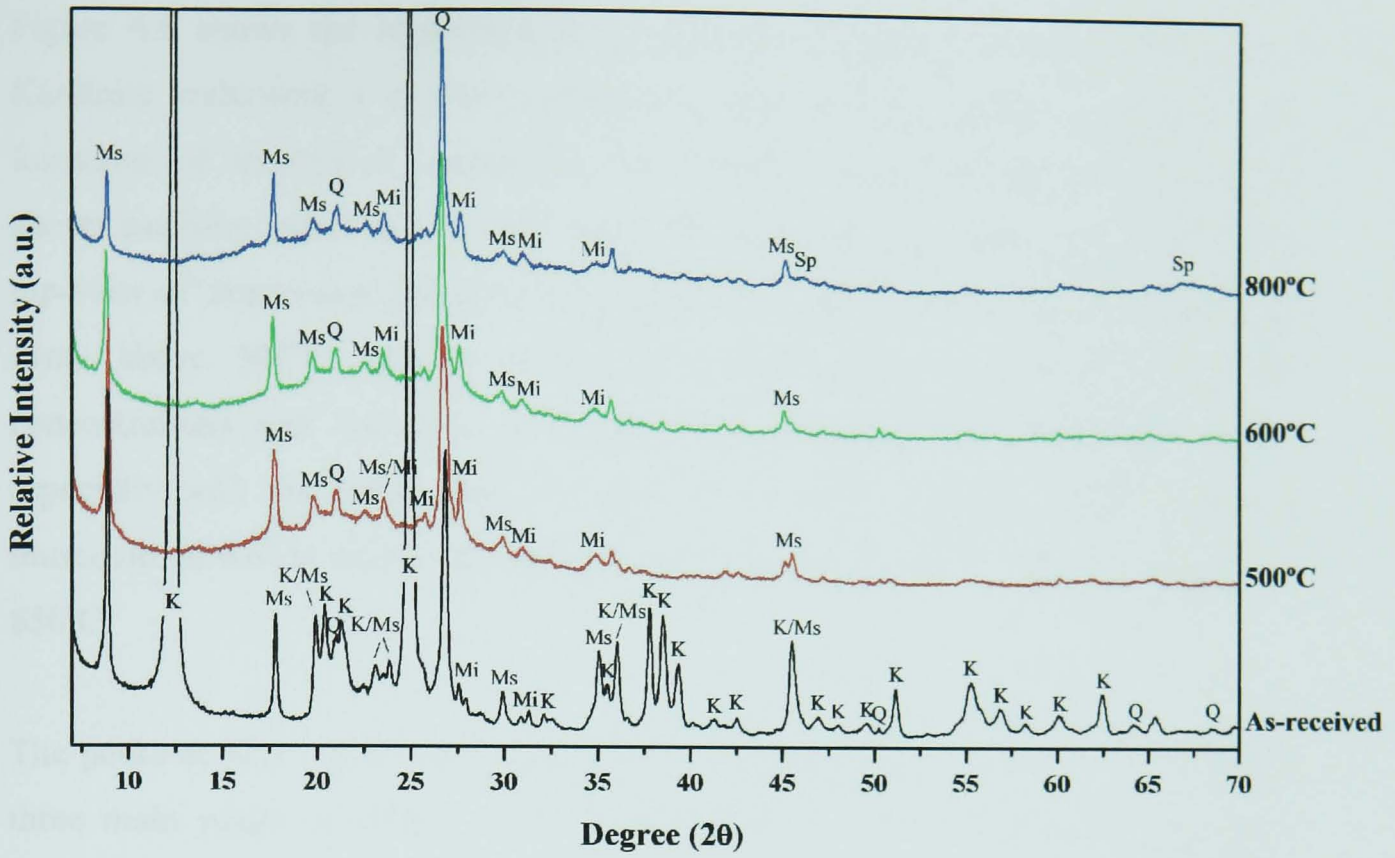

(a)

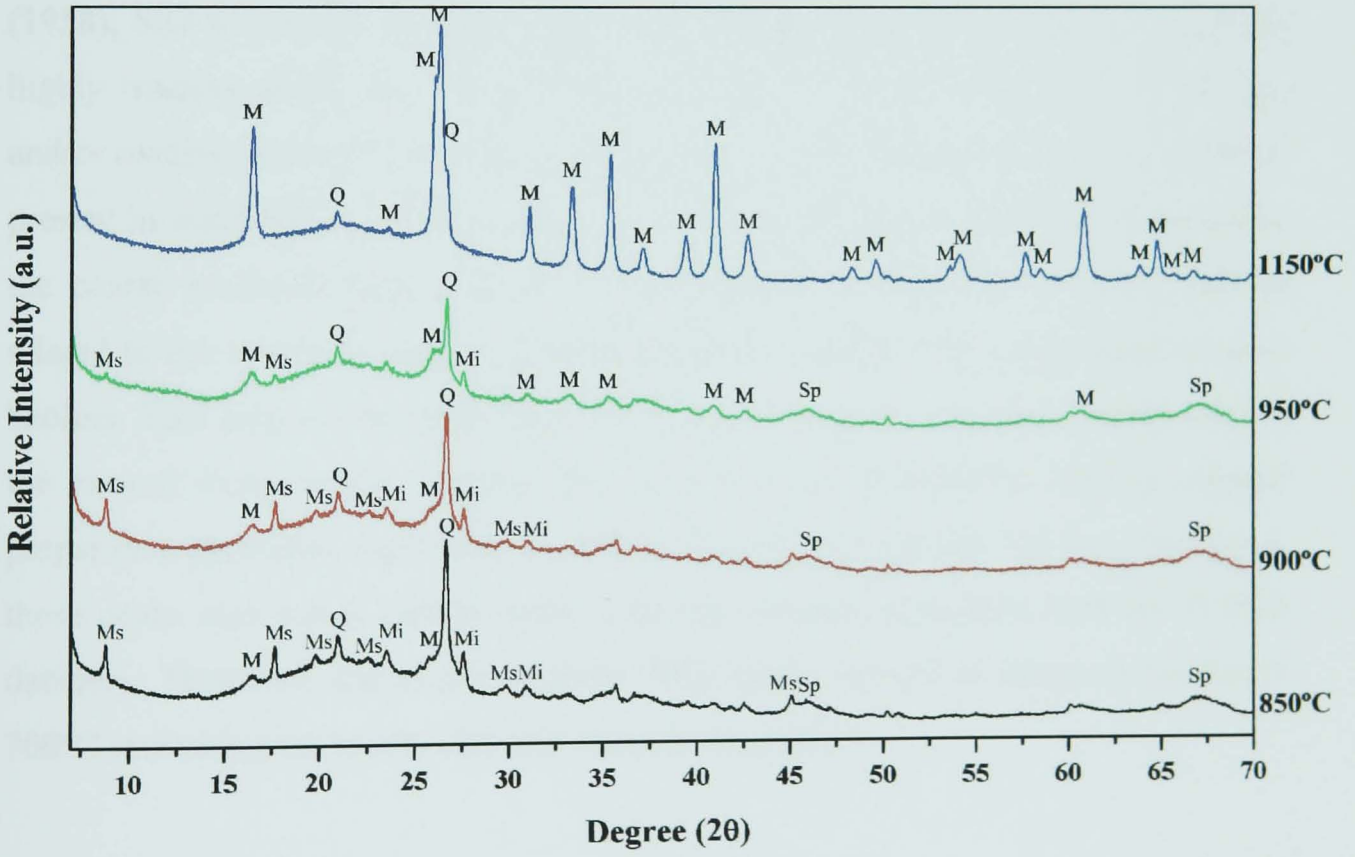

(b)

Figure 4.5 - XRD of as-received kaolin clay and of fired pellets quenched from 500, 600, 800 (a) and from 850, 900, 950 and 1150°C (b). (**K** – Kaolinite-1A, 14-164, **Q** – α-quartz, 46-1045, **M** – Mullite, 15-776, **Mi** – Microcline, 19-932, **Ms** – Muscovite-2M#1, 6-263, **Sp** – γ-alumina spinel, 10-425).

Figure 4.6 shows the high-temperature diffraction sequence for the kaolin clay. Kaolinite underwent a dehydroxylation step from 450 to 550°C, resulting in the formation of amorphous metakaolin. The HTXRD traces in Figure 4.6(a) clearly shows kaolinite peaks at 5.5°, 9.2° and 11.3° disappear after heating to 550°C. The top-view of these traces (Figure 4.6(b)) shows intensities of these peaks, which fade away above 500°C. Quartz, microcline and muscovite are present in small concentrations and therefore their low intensity peaks are difficult to detect, especially with the rather noisy background. However a poorly defined peak of muscovite at 4.6° is visible and seems to be stable as the clay sample was heated to 850°C.

The peaks at 12.1°, 21.0° and 25.0° formed at temperatures above 700°C match the three main peaks of silicon oxide (SiO, JCPDS no. 30-1127). SiO, an oxygen-deficient form of SiO_2, has been reported in the literature as reaction product of the kaolinite lattice's breakdown (West, 1958; Lawrence, 1972). According to West (1958), SiO is a stable compound below its melting point at 1390°C but becomes highly reactive above this temperature and may volatilise in the form of SiO gas and/or oxidize to form cristobalite or amorphous silica. He also found out that SiO is present in much higher amounts after firing fine kaolinite powder when compared to the coarse kaolinite, indicating that SiO formation in kaolinite on firing may be related to the structural imperfection of the lattice such as that encountered in finer kaolins. This supports the possibility of SiO being present in the fired kaolin used in the present study, which contains very fine particles of kaolinite after the sample preparation procedure (grinding) for HTXRD (section 3.10.4.2). On the other hand, those peaks also match certain types of poorly crystallised mullite from the JCPDS database. Therefore, the nature of those XRD peaks formed at temperatures above 700°C on heating the kaolin clay still remains uncertain.

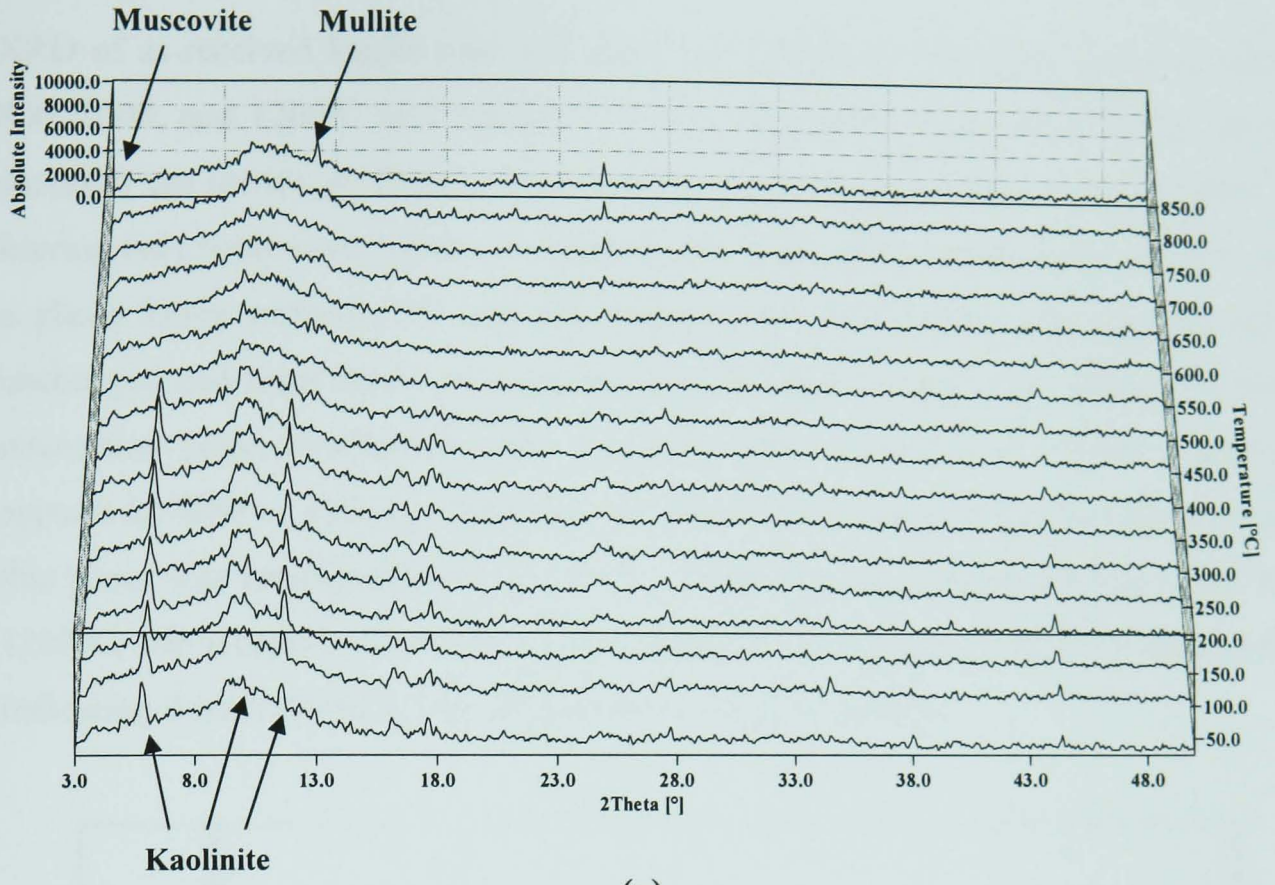

Figure 4.6 - *In situ* HTXRD of as-received kaolin clay as a function of temperature (a). (b) is a top view perspective of the traces in (a), showing higher peak intensities with darker shades.

XRD of as-received kaolin clay and fired clay pellets after holding for 3h at 600, 800, 1000, and 1200°C and cooling to room temperature (and powdered for XRD analysis) are shown in Figure 4.7. Kaolinite peaks disappear after firing to 600°C, leaving only muscovite, quartz, microcline and an amorphous material, indicated by a glassy hump between 15° and 30° degrees (2θ). Most phases remain relatively unchanged and some have lower intensities with higher temperature. Muscovite and microcline peaks disappeared after the kaolin clay was fired at 1000°C. Mullite appears at 1000°C, although DTA and quenched XRD experiments have shown that this phase was initially formed at ~970°C. When the firing temperature is raised to 1200°C, the intensity of mullite peaks increases and sharper peaks are observed, indicating further development and growth of mullite crystals.

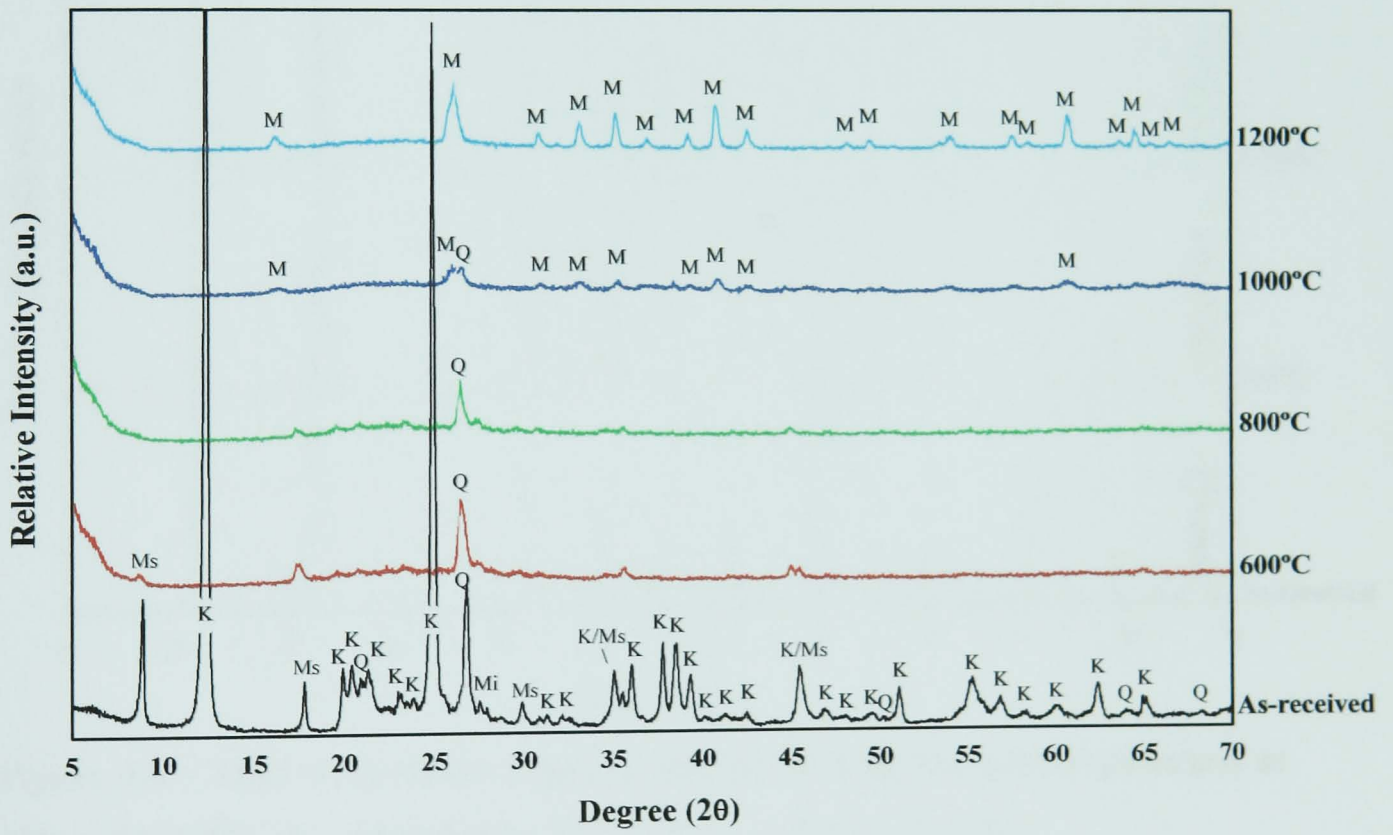

Figure 4.7 - XRD of as-received kaolin clay and of fired pellets holding 3h at the indicated temperatures. (**K** – Kaolinite-1A, 14-164, **Q** – α-quartz, 46-1045, **M** – Mullite, 15-776, **Mi** – Microcline, 19-932, **Ms** – Muscovite-2M#1, 6-263)

4.5.2 - Quartz sand

XRD of unfired quartz shows clear α-quartz (SiO_2, JCPDS no. 46-1045) peaks, the strongest among them appearing at $2\theta = 26.64°$. The phase changes of quartz on firing have been studied extensively elsewhere (Worrall, 1982; Stevens *et al.*, 1997;

Hand *et al.*, 1998; Altamirano-Juarez *et al.*, 2001). From DTA (Figure 4.2), α-quartz transforms to its high temperature form, β-quartz, at ~570°C. However, β-quartz was not detected in XRD of quartz quenched from 600°C. This is because the displacive change between the two forms occurs rapidly (Ford, 1967; Grimshaw, 1971; Hlavac, 1983), and quenching in water was not rapid enough to inhibit the β to α-quartz inversion. After quenching from 1300°C, XRD shows residual quartz peaks and a single peak at 21.98° (4.04 Å) of cristobalite (SiO_2, JCPDS no. 39-1425). This result is consistent with Cole (1935), who established 1250°C as the lowest temperature of the conversion of quartz to cristobalite in the absence of any flux.

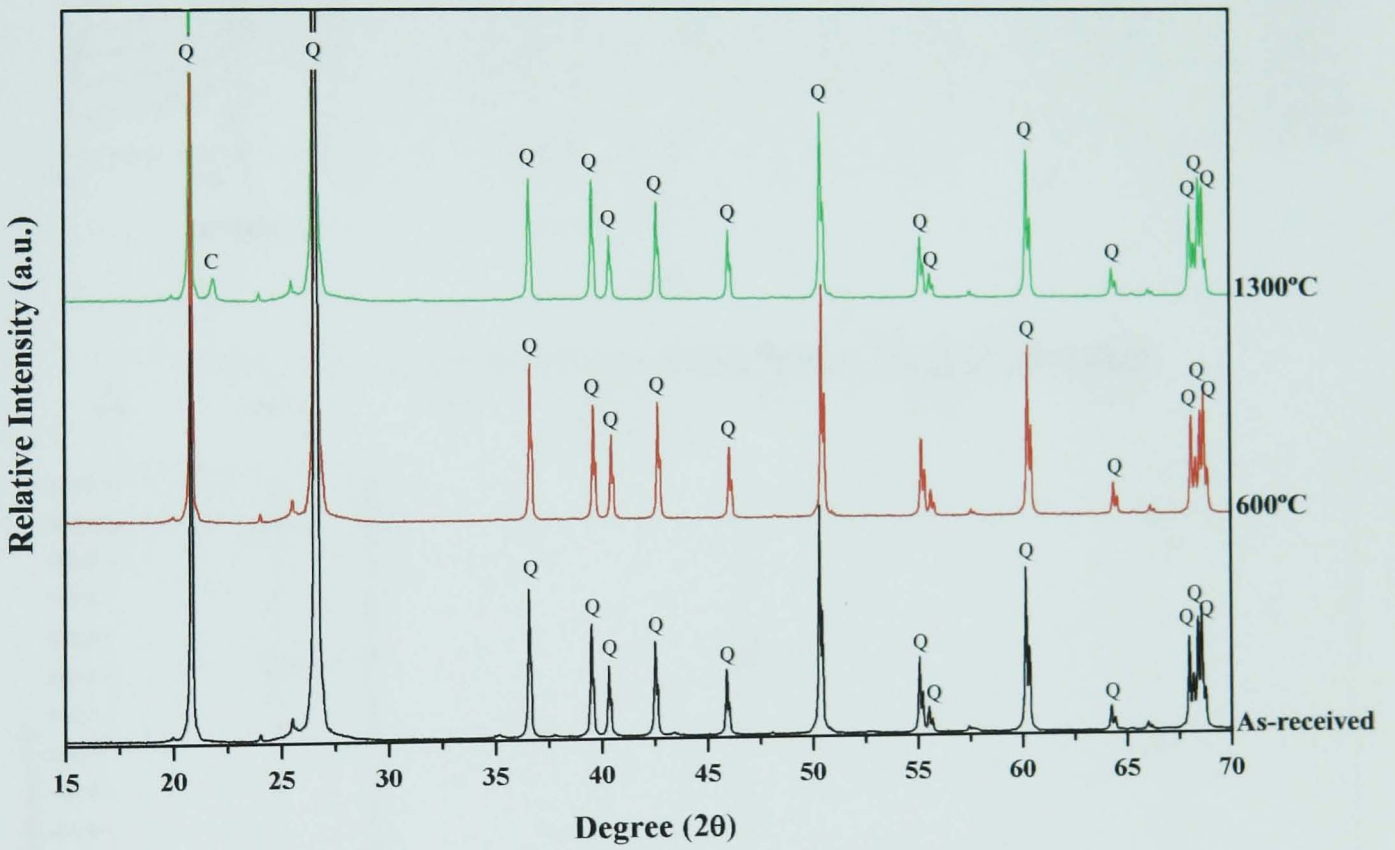

Figure 4.8 - XRD of as-received quartz and of fired quartz pellets quenched at 600 and 1300°C. (**C** – Cristobalite, 39-1425, **Q** – α-quartz, 46-1045)

The *in-situ* HTXRD showed the 573°C α-β quartz inversion, which can be observed by the shift of the diffraction peaks toward lower angles (or higher d-spacings), as shown in Figure 4.9(a). This phase change is clearly seen from the top-view perspective of the traces (Figure 4.9(b)), which also shows the disappearance of the peak at ~18.4°, and the slight shift of all other peaks at 500-600°C. This temperature range corresponds, however, to the time required for the quartz sample to reach

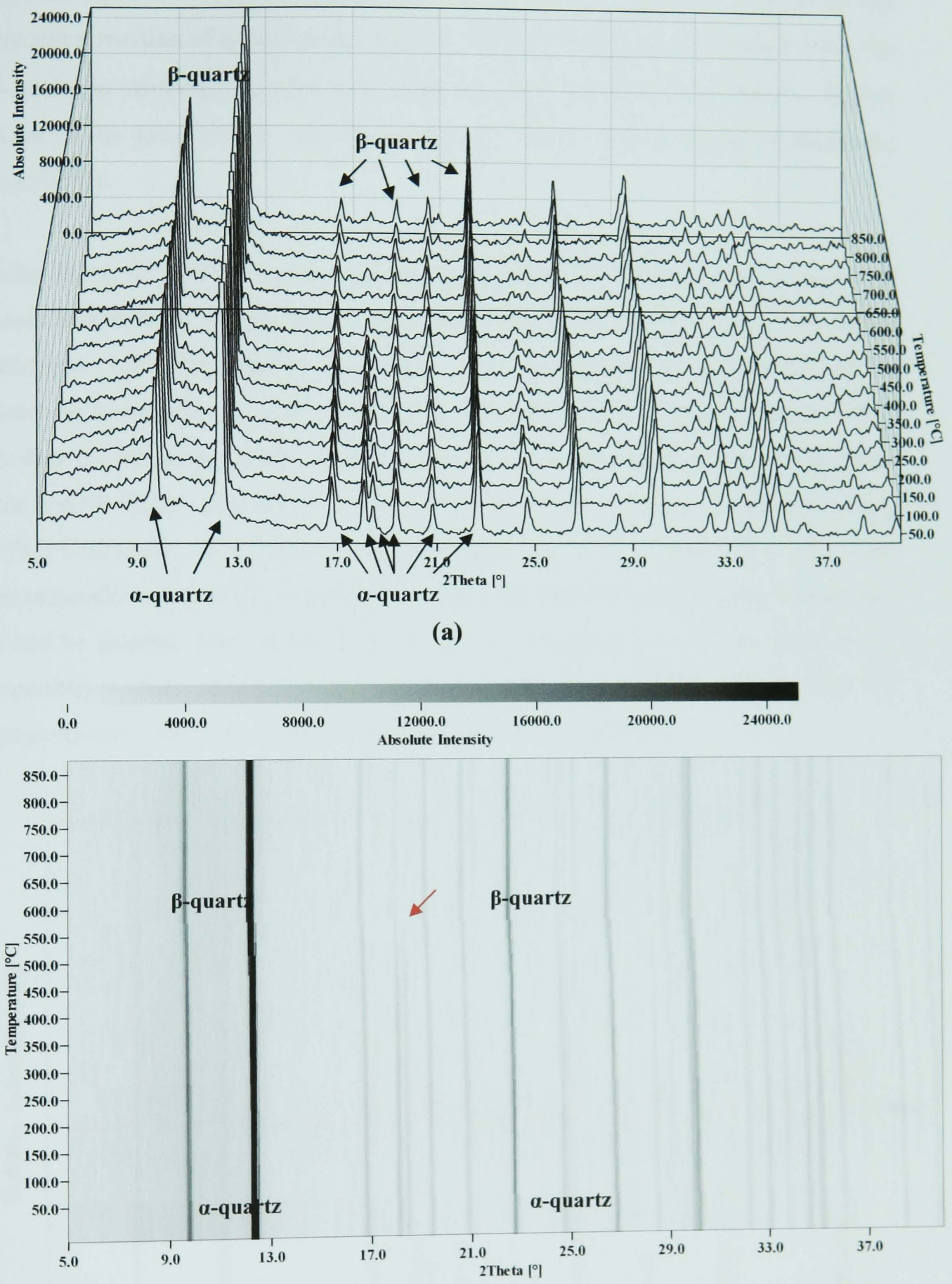

Figure 4.9 - *In situ* HTXRD of as-received quartz as a function of temperature (a). (b) is a top view perspective of the traces in (a), showing higher peak intensities with darker shades. (Red arrow shows the disappearance of 18.4° α-quartz peak).

thermal equilibrium with the heating chamber and the capillary glass, since the inversion reaction of quartz occurs quickly. Neither the β-quartz to tridymite nor the β-quartz to cristobalite conversions were observed, due to the fact that the former requires the presence of mineralisers and the latter requires higher temperatures (~1300ºC).

After firing to 1300ºC, holding at that temperature for 3h, and cooling slowly to room temperature, cristobalite is clearly distinguishable (Figure 4.10) with higher intensity peaks compared to the results from quenched samples (Figure 4.8). A decrease in intensity of quartz peaks after firing to 1300ºC is also observed. Many studies on the polymorphic forms of silica suggest that higher firing temperatures and longer firing times result in greater conversion of quartz to cristobalite (Cole, 1935; Grimshaw, 1971; Hlavac, 1983; Stevens *et al.*, 1997; Hand *et al.*, 1998). This corresponds well with the present work, where the amount of cristobalite formed was found to increase with increasing soaking time (Figure 4.8 and 4.10). These semi-quantitative observations are based on the fact that peak intensities in XRD traces are proportional to the volume fractions of the phase being analysed.

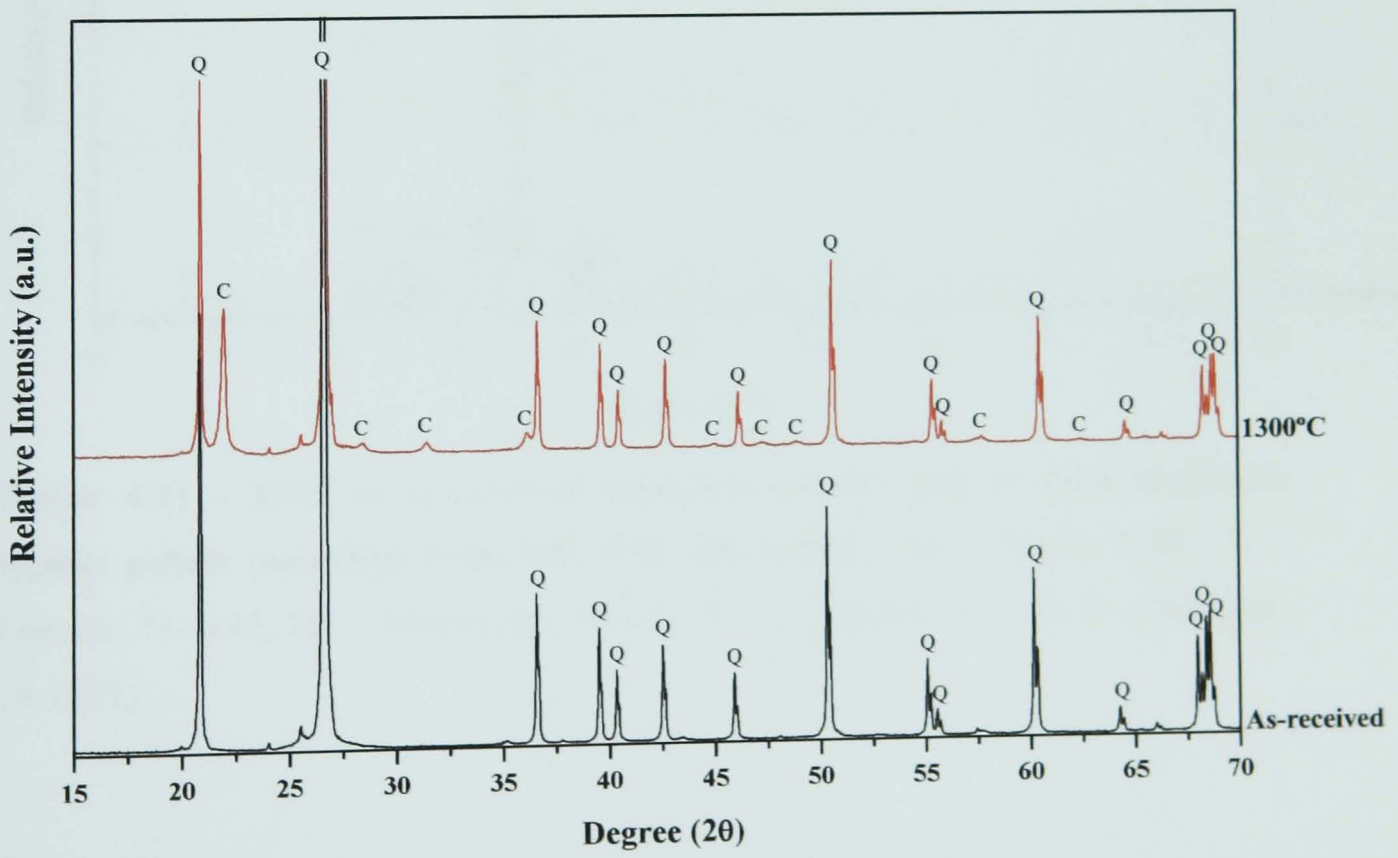

Figure 4.10 - XRD of as-received quartz and of fired quartz pellets held 3h at 1300ºC and slowly cooled. (**C** – Cristobalite, 39-1425, **Q** – α-quartz, 46-1045)

4.5.3 - Nepheline syenite

XRD of as-received nepheline syenite and fired pellets quenched from 800, 950 and 1100°C are shown in Figure 4.11. As-received nepheline syenite revealed microcline ($KAlSi_3O_8$, JCPDS no. 19-932) along with a small proportion of nepheline ($NaAlSiO_4$, JCPDS no. 35-424) and albite ($NaAlSi_3O_8$, JCPDS no. 9-466). Microcline is identified by its main diffraction peaks of 3.27 and 3.22 Å (2θ = 27.3° and 27.68°, respectively), nepheline is identified by its 3.83 and 3.00 Å peaks (2θ = 23.20° and 29.70°) and albite is identified by its 3.77 and 3.21 Å peaks (2θ = 23.50° and 27.70°).

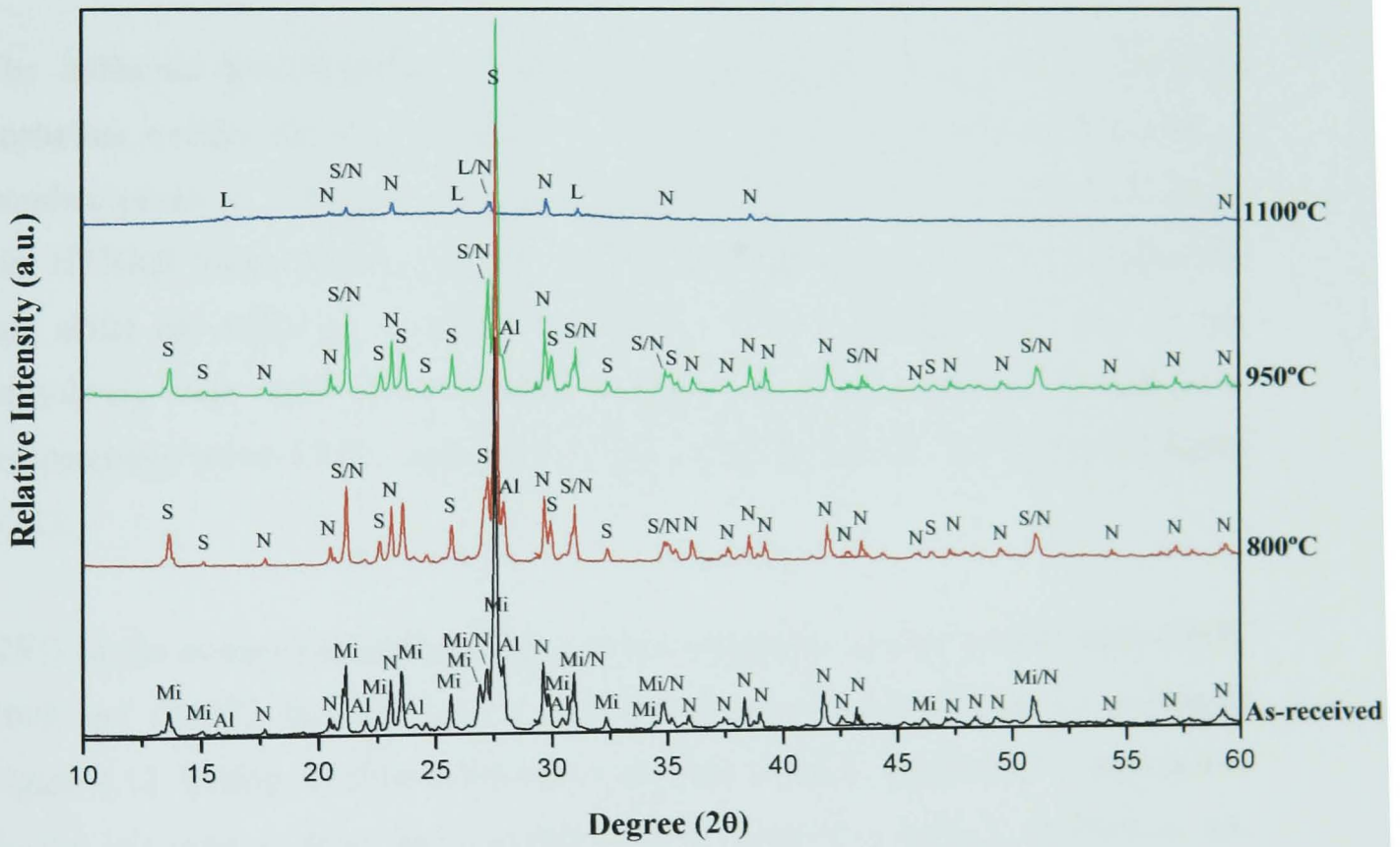

Figure 4.11 - XRD of as-received nepheline syenite and of fired nepheline syenite pellets quenched from 800, 950 and 1100°C. (**Al** – Albite, 9-466, **L** – Leucite, 71-1147, **Mi** – Microcline, 19-932, **N** – Nepheline, 35-424, **S** – Sanidine, 19-1227)

After firing at 800°C, the Si and Al in microcline become disordered, and sanidine ($(K,Na)AlSi_3O_8$, JCPDS no. 19-1227) forms. The interpretation of these XRD traces was difficult because of the extensive peak overlap. However, the polymorphic transformations of feldspar are of less interest because alkali feldspars usually melt during the fabrication of whitewares. Microcline melts incongruently to leucite and liquid (Barth, 1969; Hlavac, 1983). In this work, after quenching nepheline syenite from 1100°C, small peaks of leucite ($KAlSi_2O_6$, JCPDS no. 71-1147) were detected at 16.44°, 25.89° and 27.23° together with an amorphous hump and decreasing peaks of nepheline and sanidine. These observations indicate partial melting of nepheline syenite at 1100°C. The complete melting of nepheline syenite occurs at higher firing temperatures (~1200°).

The indistinct transformation of microcline to sanidine from normal XRD of nepheline syenite, shown in Figure 4.11, is clarified by the increase of intensity of sanidine peaks at 9.76° and 10.8° at temperatures above 600°C, as shown in the *in situ* HTXRD traces (Figure 4.12(a)) and their top-view (Figure 4.12(b)). Nepheline and albite are stable up to 850°C consistent with normal XRD and they do not completely melt until above 1100°C. There is no sign of leucite formation at temperatures below 850°C, consistent with the standard powder XRD results (Figure 4.11).

XRD of the as-received nepheline syenite and nepheline syenite pellets fired at 800, 1000 and 1200°C, held for 3h and then cooled to room temperature are shown in Figure 4.13. Similar to observations for quenched samples; microcline dissociated to leucite and glass on firing between 800-1000°C. Leucite ($KAlSi_3O_6$, JCPDS no. 85-1419) was detected from its main peaks of 3.28, 3.39 and 5.36 Å (2θ = 27.17°, 26.28° and 16.52°) after firing at 1000°C.

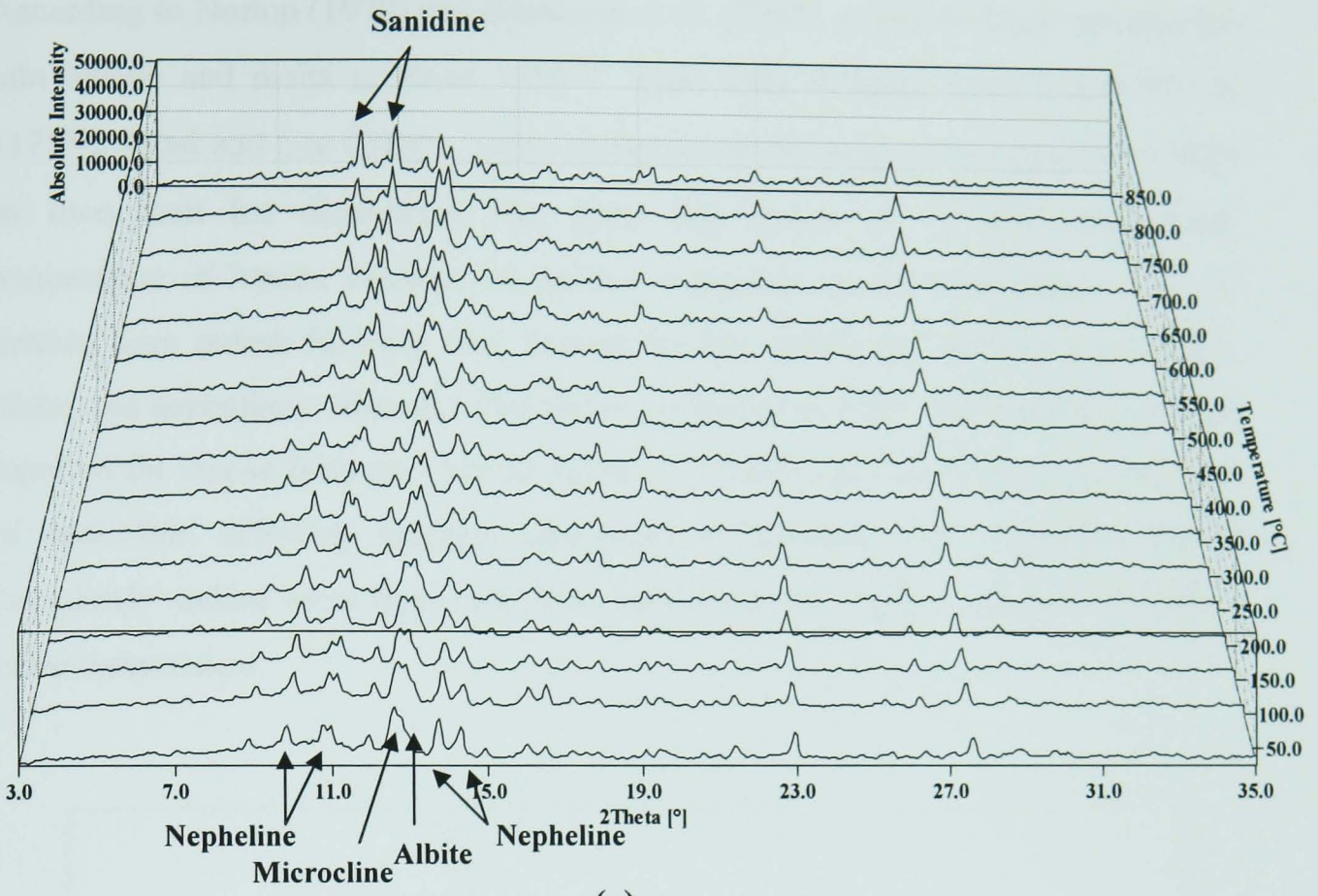

(a)

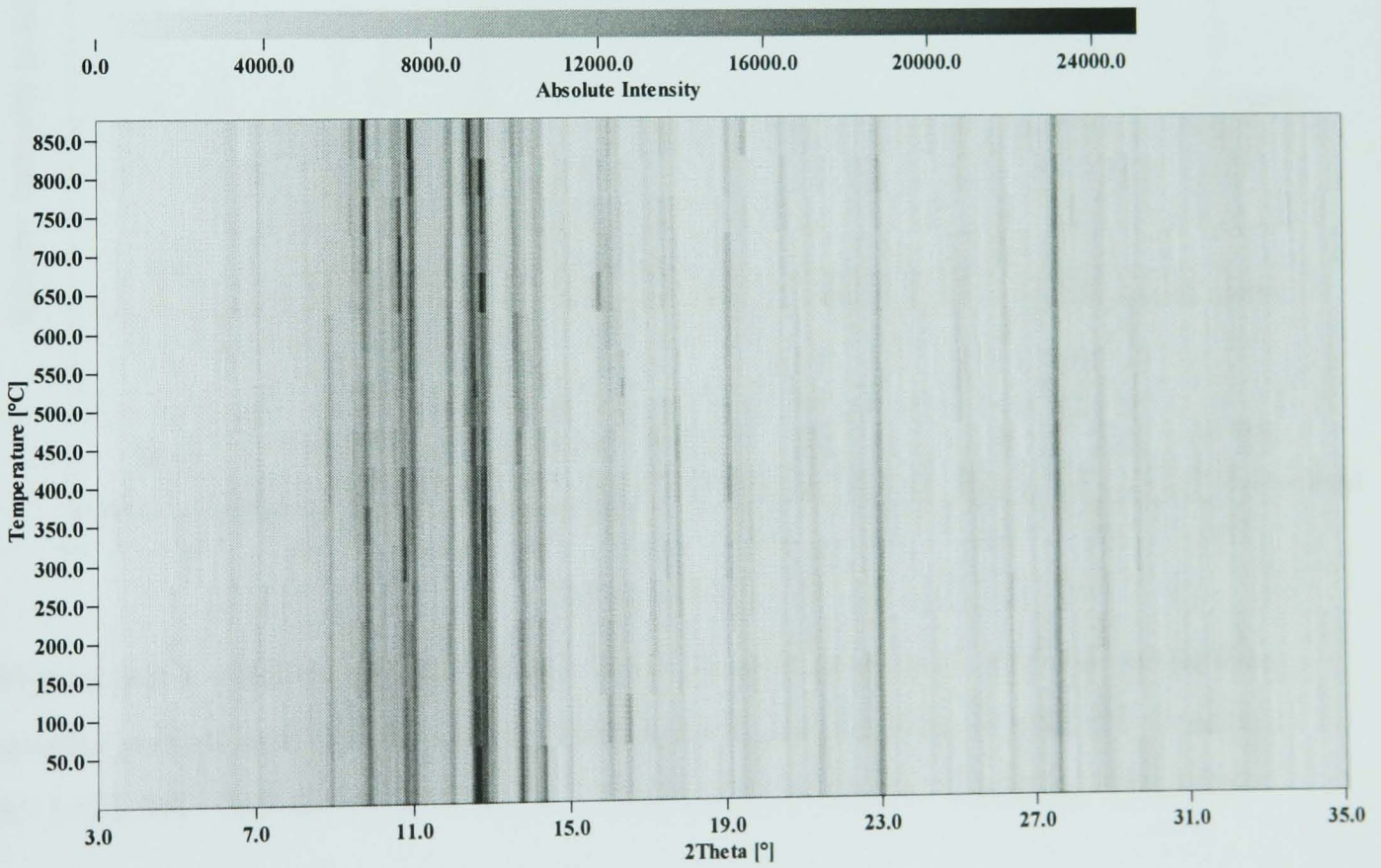

(b)

Figure 4.12 - *In situ* HTXRD of as-received nepheline syenite as a function of temperature (a). (b) is a top view perspective of the traces in (a), showing higher peak intensities with darker shades.

According to Norton (1970) and Baumgart *et al.* (1984), potash feldspar decomposes into leucite and melts at about 1150°C while soda feldspar melts completely at 1175°C. Iqbal and Lee (2000) observed that potash feldspar never crystallized from its own melt but dissociated into glass and leucite at ~1170°C. The lower temperature of leucite detected on heating nepheline syenite compared to that on heating pure potash feldspar may account for the additional feldspars present (i.e. albite and nepheline). Also, the dissolution of leucite at lower temperature than that reported for leucite from pure potash feldspar (1530°C) may result from the presence of nepheline, affecting leucite's dissolution temperature. All crystalline phases completely melted when fired to 1200°C, leaving an amorphous hump on cooling to room temperature.

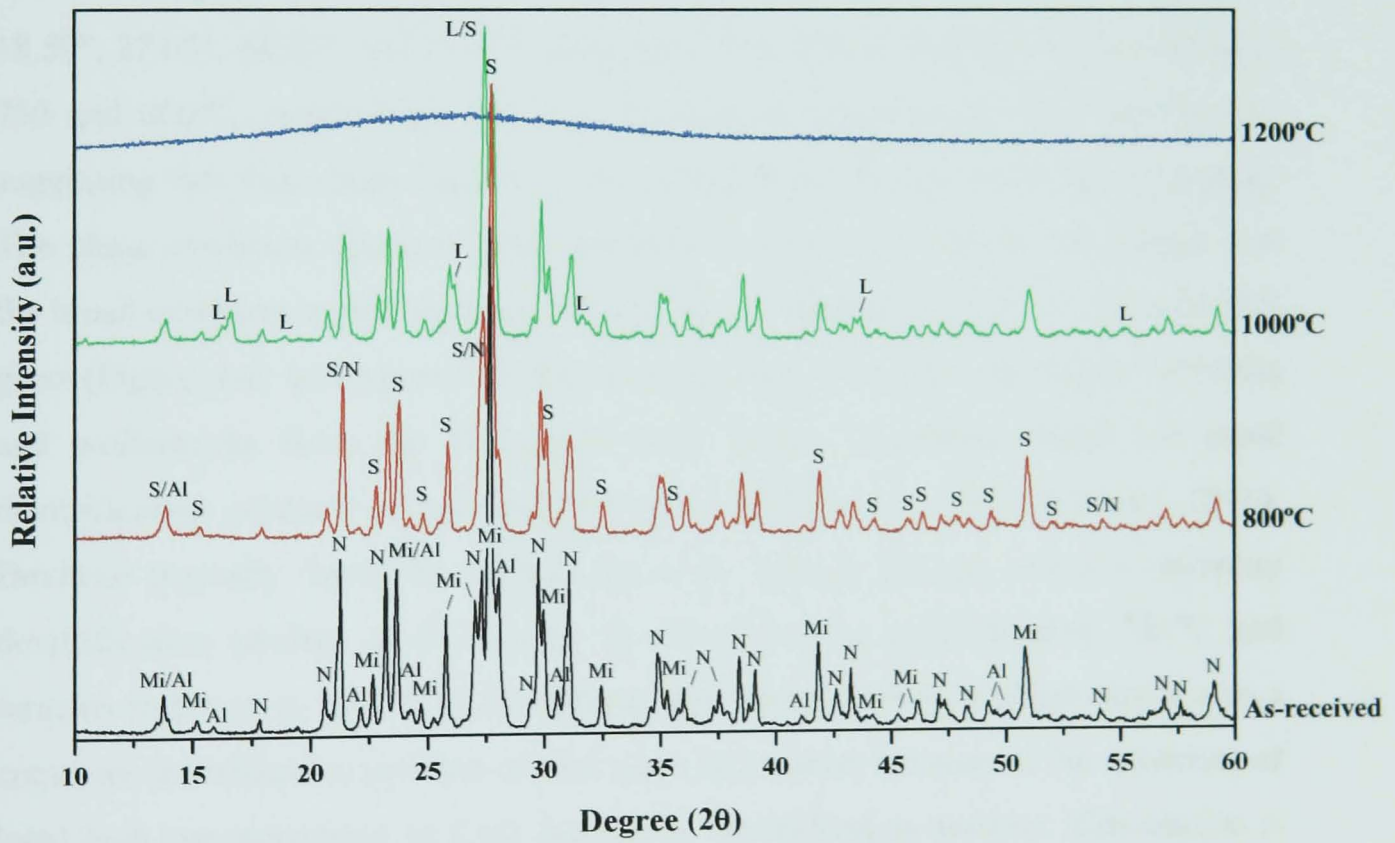

Figure 4.13 - XRD of as-received nepheline syenite and of fired nepheline syenite pellets held for 3h at 800, 1000, 1200°C. (**Al** – Albite, 9-466, **L** – Leucite, 85-1419, **Mi** – Microcline, 19-932, **N** – Nepheline, 35-424, **S** – Sanidine, 19-1227).

4.5.4 - Soda-lime-silica glass

XRD of as-received (powdered) SLS glass and of fired pellets quenched from 600-900°C is shown in Figure 4.14. XRD of powdered SLS glass shows no crystalline peaks, but the characteristic amorphous hump expected for glass. The first diffraction peaks appear when quenching a SLS sample from 600°C. They were identified as cristobalite (SiO_2, JCPDS no. 82-512) and α-quartz (SiO_2, JCPDS no. 46-1045). Cristobalite is recognized by its main peaks at 21.76°, 30.96° and 35.91°, while quartz is identified by its main peak at 26.6°. A small peak of wollastonite ($CaSiO_3$, JCPDS no. 27-88) at 29.91° was detected when SLS pellets were quenched from 650°C. Wollastonite peaks are prominent and increase in intensity with increasing firing temperature. Devitrite ($Na_2Ca_3Si_6O_{16}$, JCPDS no. 77-410) appears from 700-800°C. The presence of this crystalline phase is identified by its main peaks at 18.59°, 27.03°, 28.83°, and 29.91°. Quartz and cristobalite disappeared after firing at 750 and 800°C, respectively. No crystalline peaks remained at 900°C and above, suggesting that they melted and were incorporated into the glass formed on cooling. The phase evolution observed from quenched samples leads to the conclusion that the broad exothermic peak between 600 and 900°C present on the DTA curve of SLS glass (Figure 4.4) corresponds to the crystallization of cristobalite, quartz, devitrite and wollastonite from the SLS glass melt. These crystalline phases are usual devitrification products of reheated SLS glass (Boffe *et al.*, 1962; Willems, 1966). Devitrite typically forms by crystallization in Na-rich glasses and is a common devitrification product in SLS glass. It crystallizes at approximately 725°C and remains stable up to 1045°C (Clark-Monks and Parker, 1980). Wollastonite is also a common devitrification product of SLS glass and occurs because of the existence of local high concentrations of CaO during the devitrification process. Cristobalite is another phase crystallising during the devitrification process.

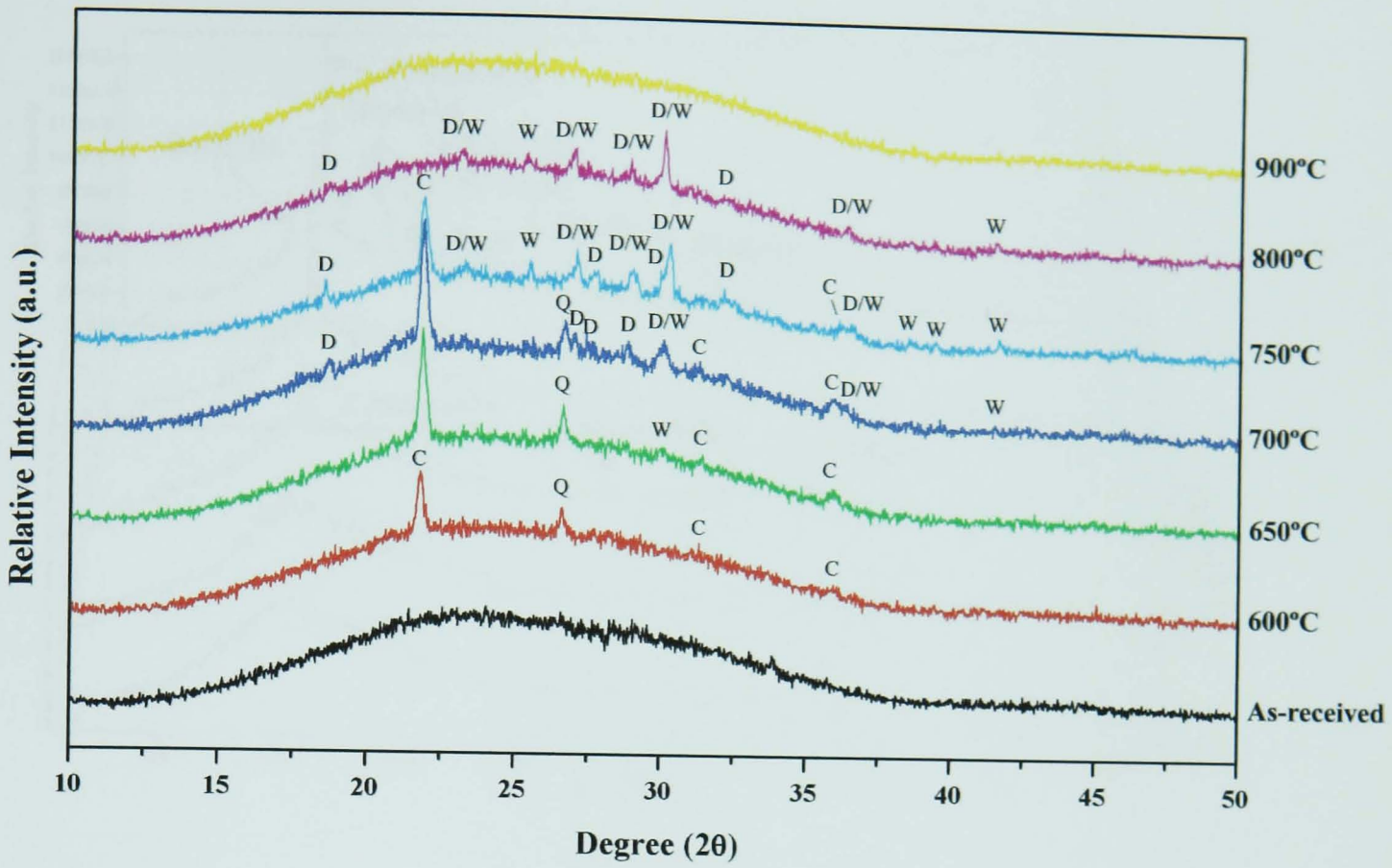

Figure 4.14 - XRD of as-received/powdered SLS glass and of fired SLS pellets quenched from 600, 650, 700, 750, 800 and 900°C. (**C** – Cristobalite, 82-512, **D** – Devitrite, 77-410, **W** – Wollastonite-2M, 27-88)

In-situ HTXRD traces of powdered SLS glass (Figure 4.15(a)) reveals that β-cristobalite (high temperature form of cristobalite, JCPDS no. 27-605) crystallized when heating the glass above 700°C as confirmed by the presence of its main peaks at 10.0° and 25.0°. The peak at 20.96° matched the main peak of sodium oxide (Na_2O, JCPDS no. 3-1074). From XRD of quenched SLS samples, cristobalite could be distinguished at lower temperature (600°C). This might be due to the slower heating rate (10°C/min) used for firing samples in the quenching experiments compared to that used with the graphite furnace for *in-situ* high temperature XRD (50°C/min). The slower firing rate may have given more time for this phase to develop. Devitrite begins to form on heating at 800°C, identified by its main peaks at 8.5°, 12.3° and 13.5°. The main peak of wollastonite at 13.6° was detected on heating to 850°C. The formation of these crystalline phases is clearly seen by the darker lines associated with their peaks appearing in the top-view diagram of the HTXRD traces (Figure 4.15(b)) at temperatures between 700-850°C.

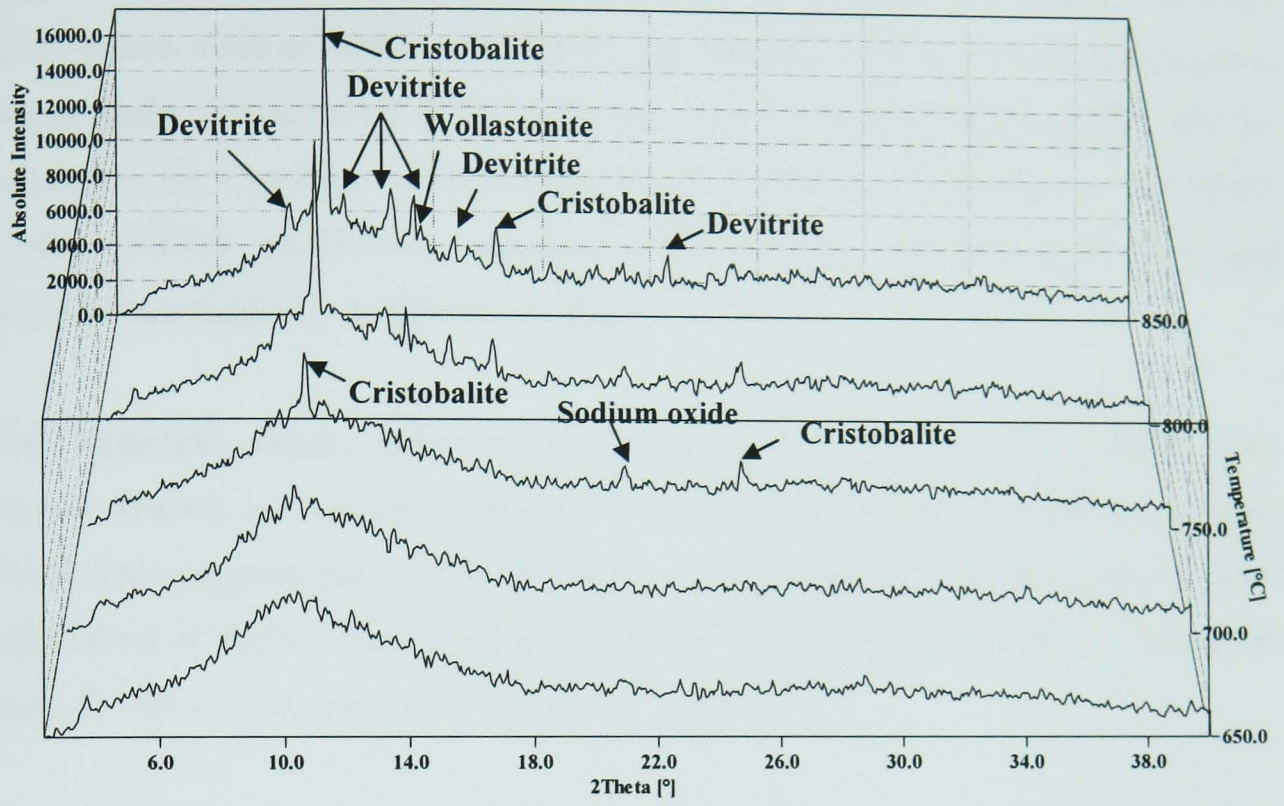

(a)

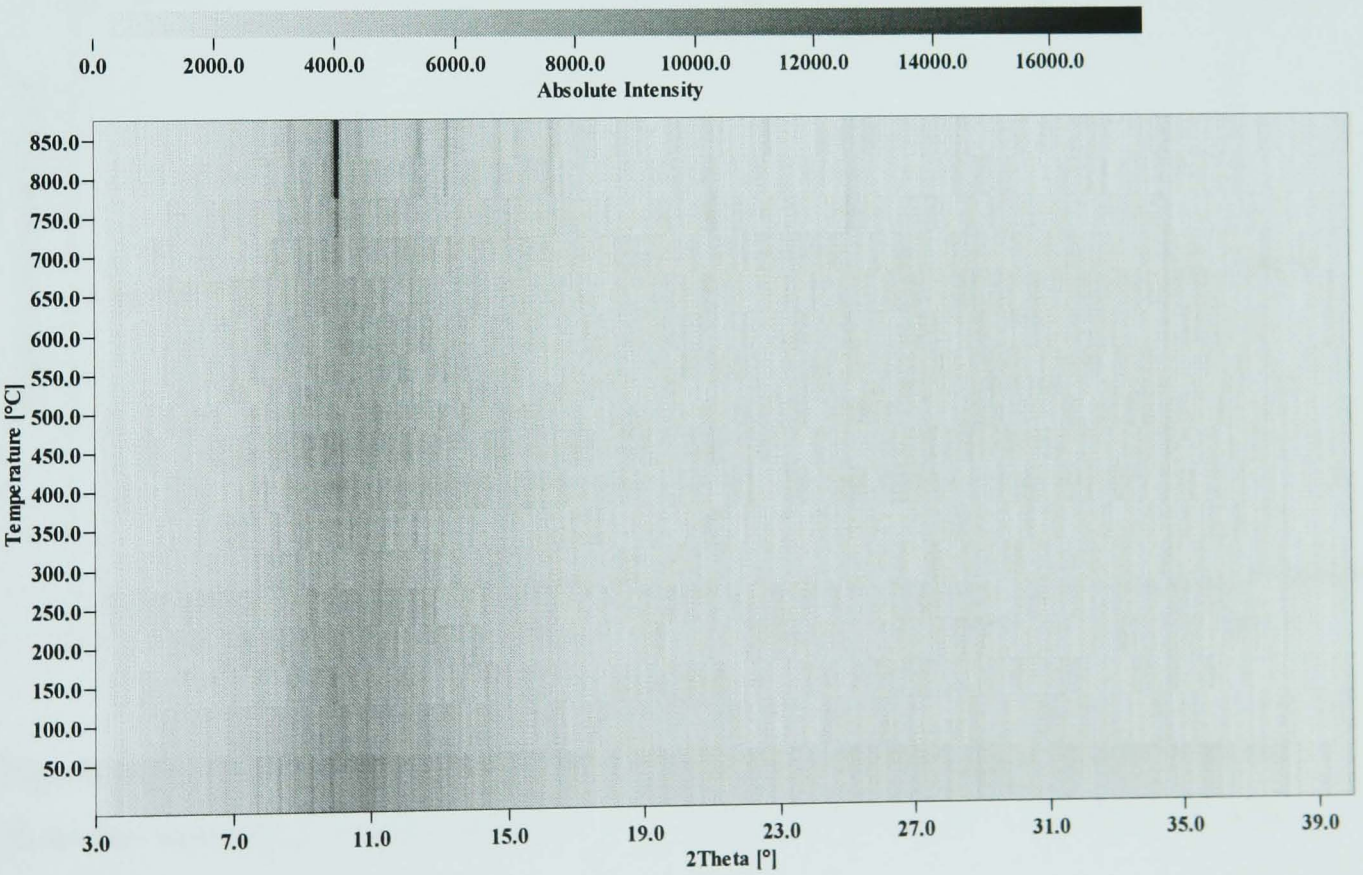

(b)

Figure 4.15 - *In situ* HTXRD of ground SLS waste glass as a function of temperature (a). (b) is a top view perspective of the traces in (a), showing higher peak intensities with darker shades.

Figure 4.16 shows XRD spectra corresponding to as-received SLS ground glass, and glass pellets fired at 800°C and 1000°C and naturally cooled to room temperature. Many peaks are observed in the XRD trace of SLS pellets fired at 800°C for 3h, indicating the formation of crystalline phases which were identified as cristobalite (SiO_2, JCPDS no.82-512), devitrite ($Na_2Ca_3Si_6O_{16}$, JCPDS no.77-410) and wollastonite ($CaSiO_3$, JCPDS no. 27-88).

The crystalline phases observed after firing the SLS glass for 3h at 800°C were clearly distinct and intense compared to those in the quenched specimens (Figure 4.14). This suggests that crystal growth occurred during the 3h soaking time for SLS glass fired at 800°C. After heating to 1000°C, no crystalline phases are present as they all melt at temperatures between 900-1000°C.

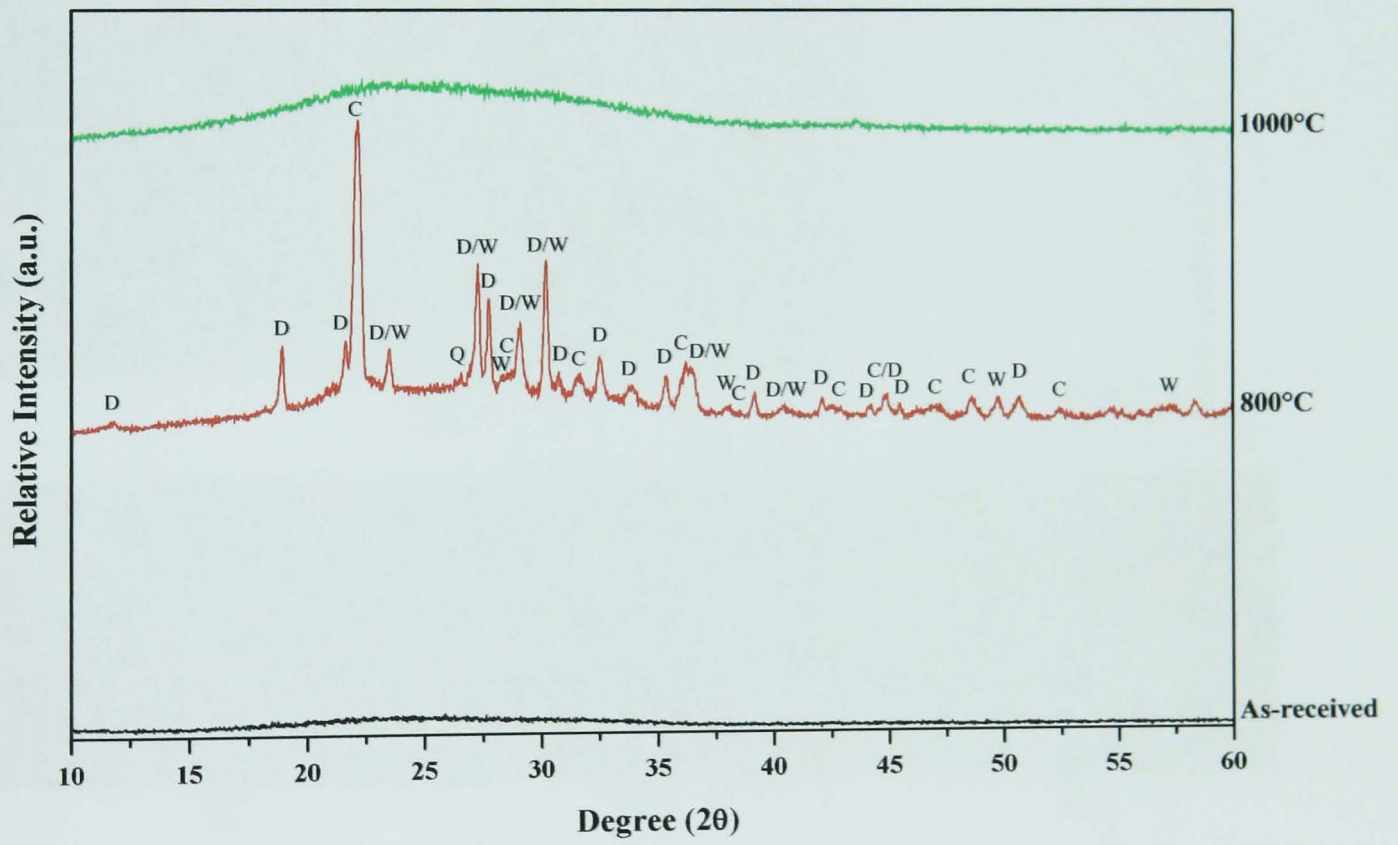

Figure 4.16 - XRD of as-received SLS glass and fired SLS glass pellets held for 3h at the indicated temperatures (**C** – Cristobalite, 82-512, **D** – Devitrite, 77-410, **W** – Wollastonite-2M, 27-88).

4.6 - MICROSTRUCTURAL EVOLUTION

The microstructures of raw materials fired at different temperatures are examined in order to understand their development and changes occurring on firing. These data will then be compared to observations of phase and microstructural evolution on firing binary (chapter 5) and ternary and quaternary (chapter 6) mixtures.

4.6.1 - Kaolin clay

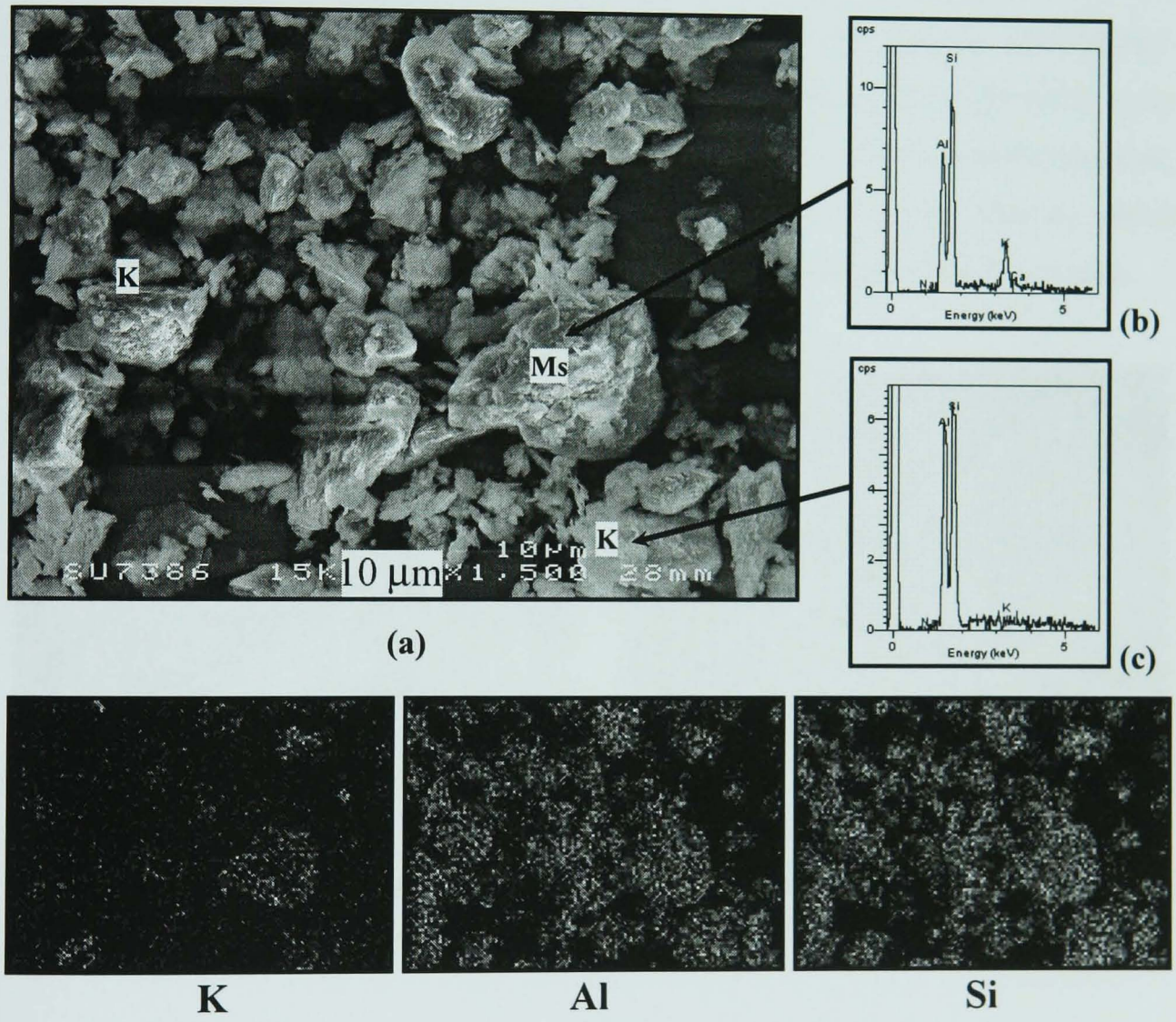

Figure 4.17 - SEM/SE image of the as-received kaolin clay (a). EDS traces of kaolinite (K) and muscovite (Ms) are shown in (b) and (c) respectively. X-ray dot mapping is shown in (d), where the brighter regions are higher in the corresponding element.

SEM/SE image of as-received kaolin clay (Figure 4.17(a)) shows clay particle and muscovite agglomerates. The length of the text box, given by the value indicated inside it, is the actual scale bar of the micrograph. This is applied for all the micrographs throughout this thesis. EDS of kaolinite is high in Al and Si with the ratio ~1:1. Muscovite agglomerates (~10-20 μm) are identified by EDS which shows the K:Al:Si ratio ~1:2:3, which is close to $KAl_2(Si_3,Al)O_{10}(OH)_2$. EDS and X-ray dot maps show that this agglomerate is high in potassium compared to its surroundings.

The morphology of the kaolin particles is shown in SEM/SE images (Figure 4.18 (a)-(b)). The kaolin particles are typically submicron-sized and platy in morphology. Plates of hexagonal shape are often identified as kaolinite, although other layer structured minerals may have the same shape. Kaolin plates are stacked together, forming agglomerates. The stacks are composed of small hexagonal platelets which can be seen separated in some areas. Most of the platelets are less than 1 μm wide.

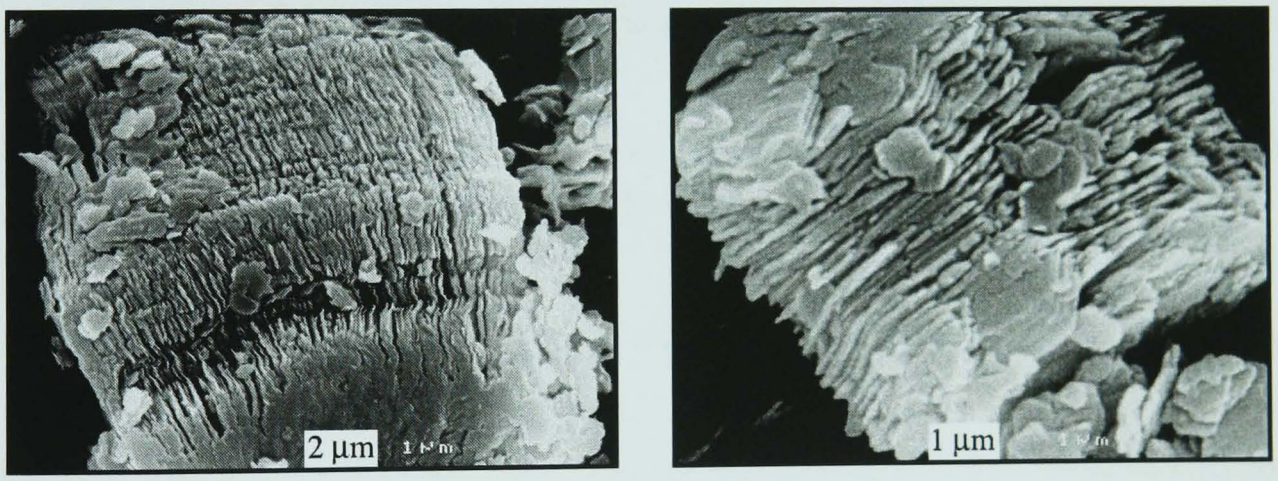

(a) (b)

Figure 4.18 - SEM/SE images of as-received kaolin clay show well crystallized stacks of pseudo-hexagonal kaolinite platelets.

TEM/bright-field image of as-received kaolin clay (Figure 4.19) reveals pseudo-hexagonal kaolinite particles. The particle diameters range from 200-500 nm. The brighter and small texturing visible on the particles results from the loss of water due to the high vacuum in the TEM. This texture was also mentioned by McConville (1998) on studying thermal transformations in kaolinite clay materials using TEM analysis. The diffraction pattern (inset, Figure 4.19(a)) is that of the [112] zone axis of kaolinite. The EDS trace (Figure 4.19(b)) shows the presence of Al and Si in the

crystal in approximately 1:1 ratio consistent with the chemical composition of kaolinite ($Al_2Si_2O_5(OH)_4$).

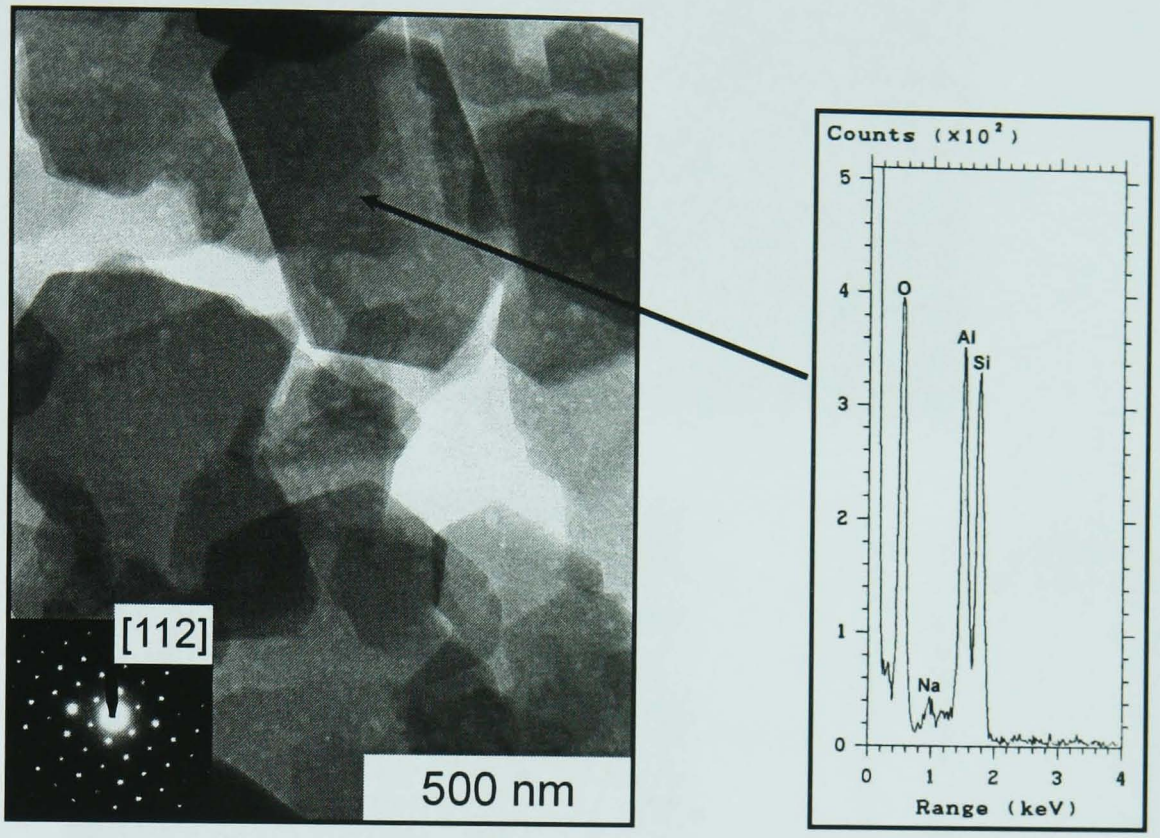

(a) (b)

Figure 4.19 - TEM/BF image of kaolinite crystals in the clay (a). Inset in (a) is a [112] zone axis diffraction pattern of a kaolinite crystal. (b) is EDS of kaolinite.

SEM/SE images of cross-sectioned, polished and etched pressed pellets fired 3h at 800°C show metakaolin platelets which retain their original pseudo-hexagonal kaolinite particle morphology; some remnant stacks are shown in Figure 4.20(b). Although dehydroxylation has already taken place at this temperature, the platelets of metakaolin have maintained the size and morphology of the original raw material. On firing at higher temperatures, such as 1000°C, the stacks collapse so the individual platelets in the crystals are no longer separated (Figure 4.21). The pseudo-hexagonal crystallite shapes have gone and significant coalescence and rounding of particles occurred; the particles becoming irregular in shape. The clay particles have begun to be fused together by the amorphous, silica-rich phase from the breakdown of the clay mineral, although the structure was still porous.

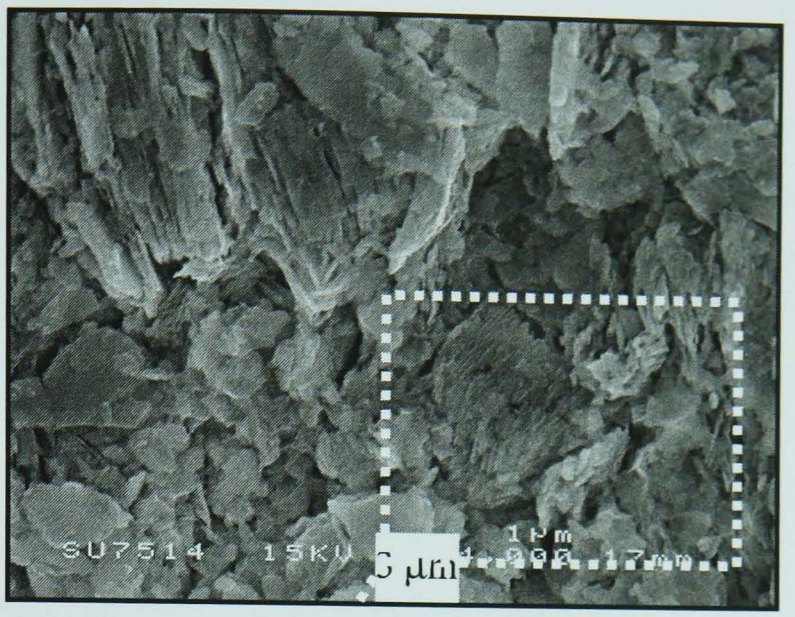

(a)

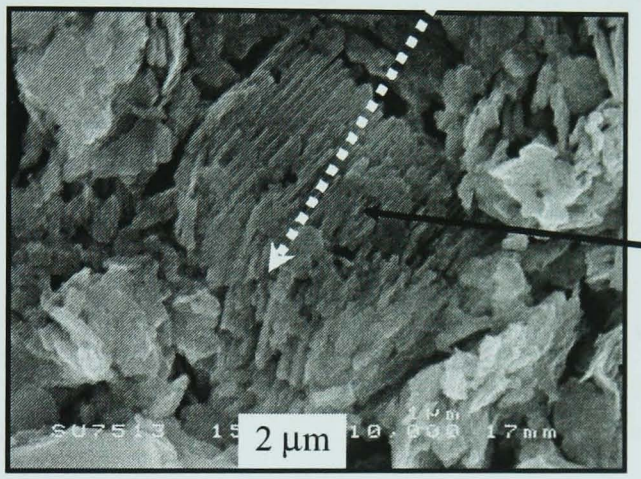

(b)

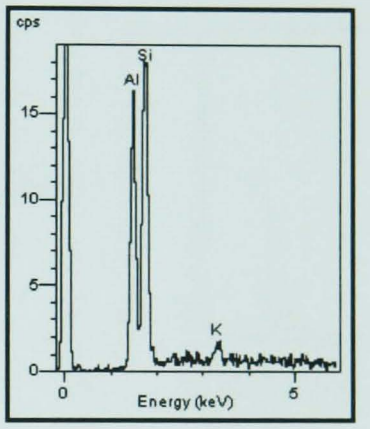

(c)

Figure 4.20 - SEM/SE images of cross-sectioned and etched samples made from kaolin clay pellets fired 3h at 800°C (a) and of a selected area at high magnification (b). (c) is EDS of metakaolin platelets shown in (b).

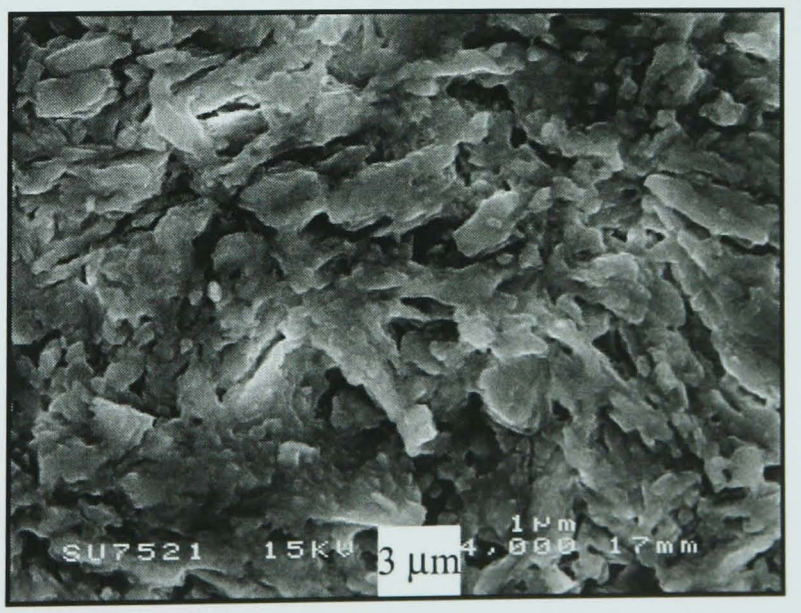

Figure 4.21 - SEM/SE images of cross-sectioned and etched kaolin clay pellets fired 3h at 1000°C.

Evidence of K-feldspar impurity in kaolin clay is shown in the SEM/SE image of kaolin clay pellets fired at 1000°C (Figure 4.22 (a)). EDS (Figure 4.22 (b)) reveals peaks of Al, Si, and traces of K with K:Al:Si ratio ~ 1:1:3, indicating that the particle in the centre of the SEM/SE image (Figure 4.22 (a)) may be a K-feldspar (KF). K-feldspar could not be detected from the XRD of samples fired at 1000°C, perhaps due to the small amount of this type of impurity present.

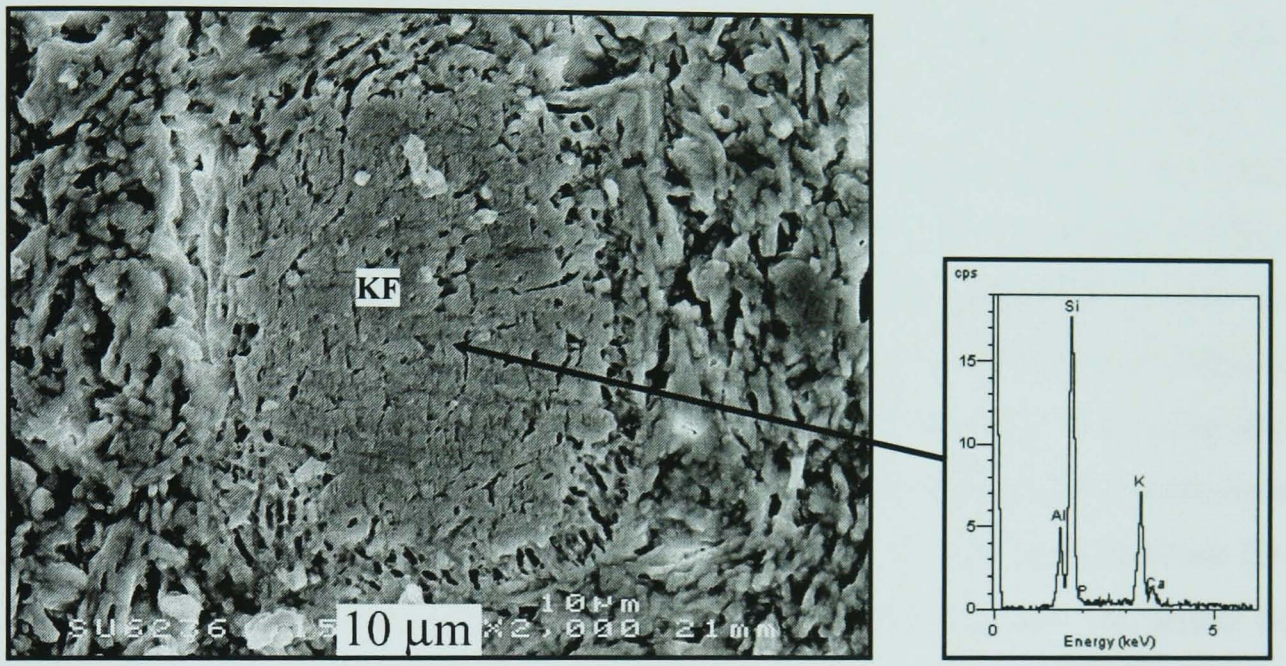

Figure 4.22 - (a) SEM/SE image of cross-sectioned, etched kaolin clay pellet fired at 1000°C showing a K-feldspar particle denoted 'KF' and its EDS (b). EDS element maps are shown in (c), where the brighter regions are high in the corresponding elements.

A spinel-type phase is formed from the aluminous sheet of metakaolin. The presence of spinel phase was detected by XRD of kaolin clay pellets quenched from 800, 850, 900 and 950°C but not detected in SEM images. As heating continues, mullite is formed. XRD of kaolin clay pellets fired for 3h at 1000°C contains broadened, weak

peaks attributable to poorly crystallized mullite, which is difficult to see in the SEM. XRD of 1200°C samples reveals mullite peaks indicating mullite development. The SEM/SE image in Figure 4.23 of a cross-sectioned, polished and etched kaolinite pellet fired 3h at 1200°C shows a dense sample due to the formation of liquid phase. This is more pronounced at this temperature as seen by the relicts of clay particles fused together. Partially dissolved quartz particles are visible as impurity of the raw kaolin clay. Some quartz particles have a ragged rim, indicating the first stages of cristobalite formation. Some interconnected but mostly isolated pores are also observed. A higher magnification image (Figure 4.24(a)) shows that the sample is largely composed of a mass of mullite crystals, scale-like and small (~1-2 μm long) rod-like in morphology. The chemical composition (EDS traces in Figure 4.24(b)-(c)) is fairly different between these two mullite types. The scale-like crystals are higher in Al but lower in K compared to the rod-like ones. This difference in shape is then explained by the formation of scale-like mullite in the area once rich in clay and the formation of rod-like mullite in the area containing impurities such as muscovite and K-feldspar, which is the source of potassium and can act as flux to facilitate the liquid formation on firing, allowing crystallisation of longer crystals. The higher Si content in the chemical composition of mullite crystals is likely a result of the glassy phase covering the crystals and in the background. Iqbal and Lee (2000) suggested a new notation: Type I for the cuboidal or scale-like low aspect ratio (1-3:1) primary mullite derived from pure clay; Type II for the 3-10:1 aspect ratio secondary mullite detected in feldspar-penetrated clay relicts; and Type III for the very high aspect ratio (30-40:1) secondary mullite needles. From the microstructure of kaolin clay fired at 1200°C in the present study, only Type I and II were present.

The observation of primary mullite (Pm) and secondary mullite (Sm) in Figure 4.24 is interesting. Conventionally, clays only decompose to form primary mullite and feldspar flux/clay mixtures form secondary mullite (Iqbal and Lee, 2000). However, in this case the alkali impurities in the clay have led to secondary mullite formation in, ostensibly, pure clay.

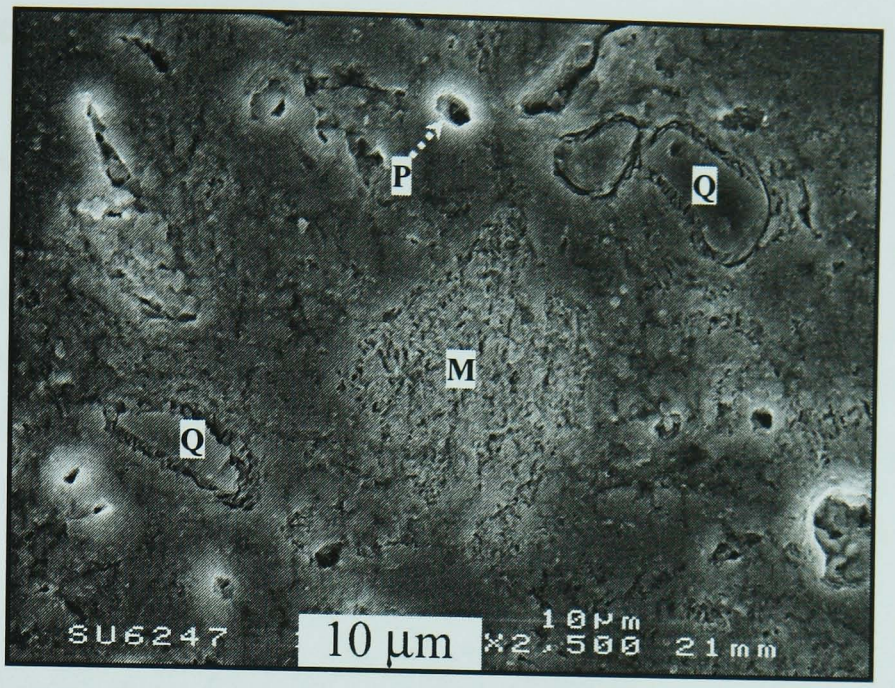

Figure 4.23 - SEM/SE image of a cross-sectioned, polished and etched kaolin clay pellet fired 3h at 1200°C. (M = mullite, P = pore, Q = quartz)

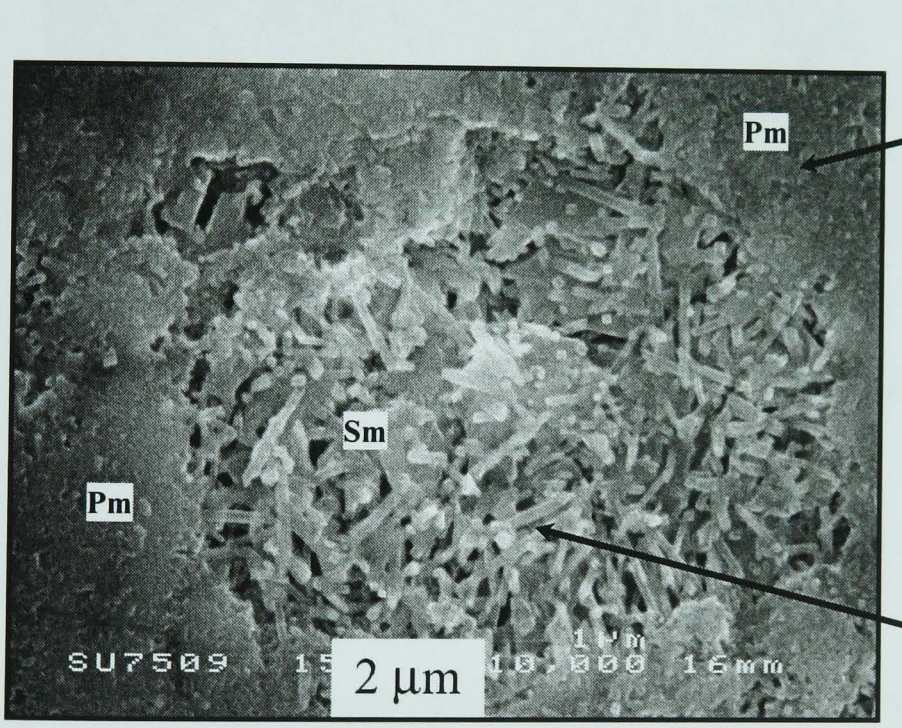

(a)

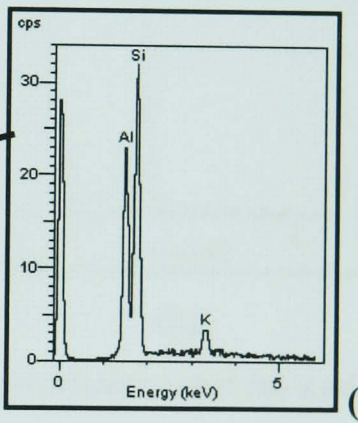

(b)

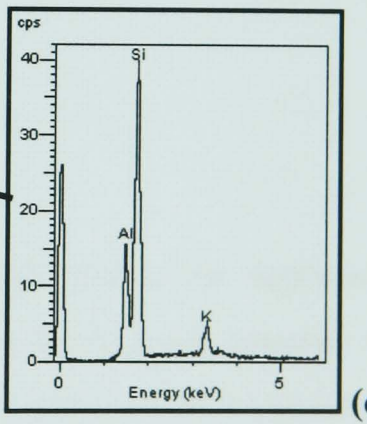

(c)

Figure 4.24 - SEM/SE image of cross-sectioned, etched kaolin clay pellets fired 3h at 1200°C. (a) shows mullite particles. (b) is EDS of scale-like crystals, and (c) is EDS of rod-like crystals shown in (a). (Pm = primary mullite, Sm = secondary mullite)

4.6.2 - Quartz sand

SEM/SE of as-received quartz particles (Figure 4.25 (a)) shows that all particles are irregular in shape and range in particle size from a few microns to less than 200 μm. The particle size ranging from 190 to 360 μm as determined by laser size analysis (Table 4.2) is therefore an overestimate of the ultimate quartz particles, being a measure of agglomerates instead. The EDS trace (Figure 4.25(b)) is high in Si with no trace of other elements.

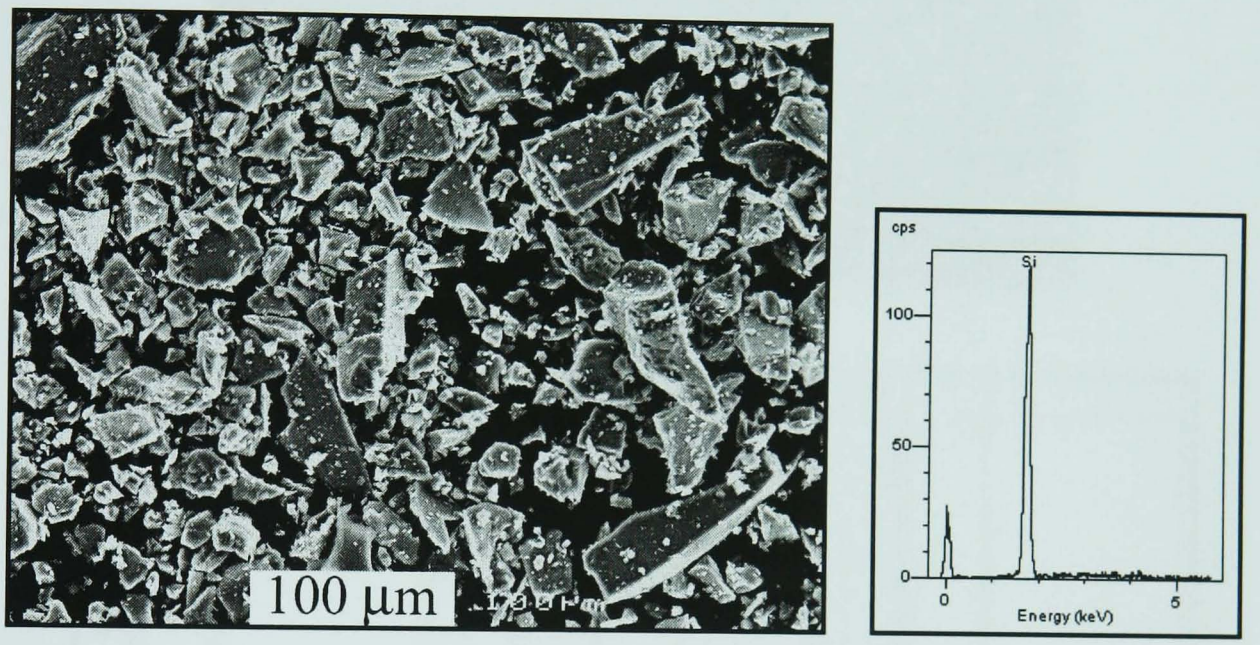

(a) (b)

Figure 4.25 - SEM/SE image of the as-received Loch Aline quartz sand (a) and EDS of quartz (b).

4.6.3 - Nepheline syenite

SEM/SE of as-received nepheline syenite (Figure 4.26(a)) reveals the nepheline syenite used in this work is composed of microcline, nepheline and small amounts of albite as shown by its XRD trace (Figure 4.11 - 4.13). Most particles are irregular in shape and have sizes ranging from a few microns to tens of microns. EDS taken from different particles reveal various chemical compositions. Some are high in K and have the K:Al:Si ratio ~1:1:3 which is characteristic of K-feldspar such as microcline (Figure 4.26(c)). Others have a similar Al:Si ratio, but are depleted in K. Na is a light element and is not easy to detect in the SEM EDS detector, since a beryllium

window was always used to protect the EDS detector. Therefore, the EDS traces of nepheline and albite show only a small trace of Na.

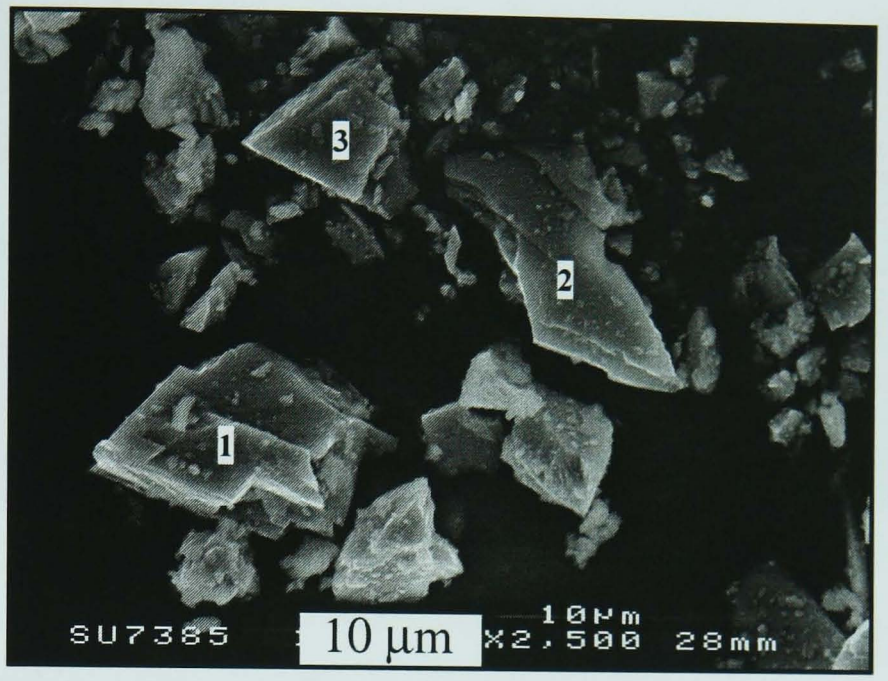

(a)

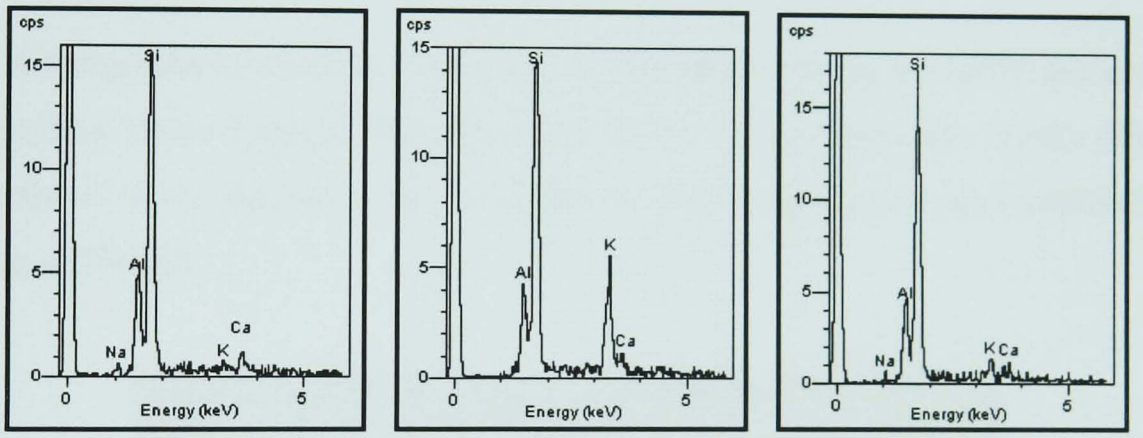

(b) **(c)** **(d)**

Figure 4.26 - SEM/SE image of as-received nepheline syenite (a). EDS of selected nepheline syenite particles labelled "1", "2" and "3" are shown in (b) - (d), respectively.

SEM/SE images of the surface nepheline syenite pellets fired 3h at 1000°C and 1200°C are shown in Figure 4.27 (a)-(b). The roughness of the surface with interconnected pores and crystalline matrix is evident in the sample fired to 1000°C (Figure 4.27 (a)), while a smooth surface is apparent in the sample fired to 1200°C (Figure 4.27(b)). This smooth glassy phase seems to be homogeneous and contained large (10-80 µm diameter) and (rounded) isolated pores. The presence of glassy phase all over the sample corresponds well with the XRD (Figure 4.13) which shows no trace of crystalline phases present at this high temperature as all crystalline phases

from nepheline syenite were completely melted at 1200°C. Glassy phase formation seems to start above 1000°C.

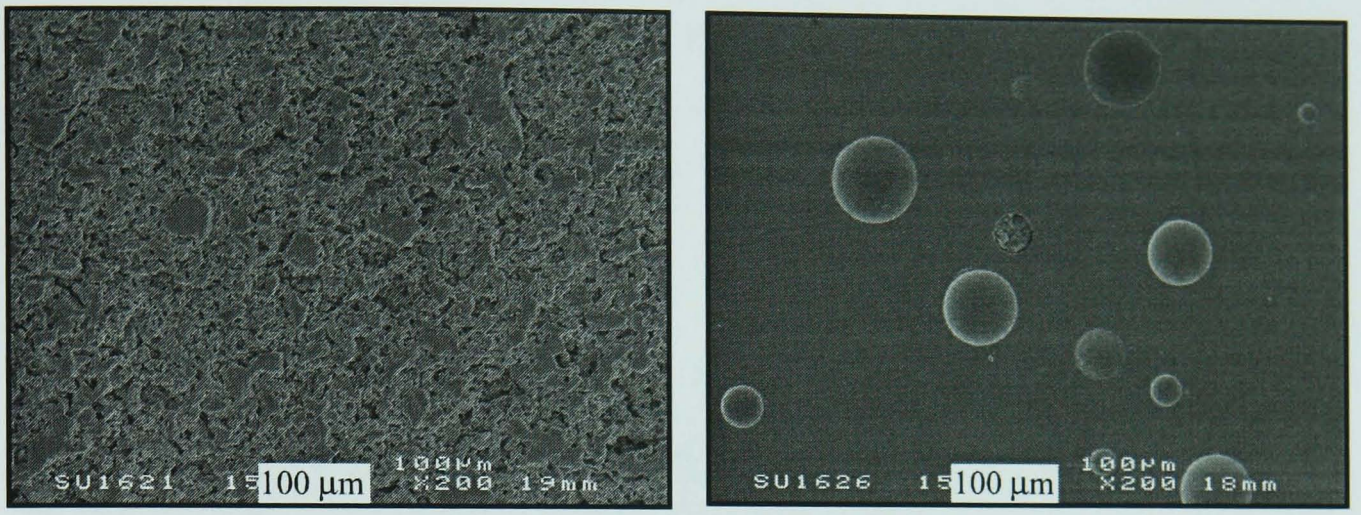

(a) 1000°C **(b) 1200°C**

Figure 4.27 - SEM/SE images of cross-sectioned nepheline syenite pellets fired at (a) 1000°C, and (b) 1200°C for 3h.

SEM micrographs of un-etched and etched samples after firing at 1000°C are similar, as no glassy phase formed. SEM/SE image of the etched nepheline syenite (Figure 4.28) shows some distinct features, visible in their magnified images explained in Figures 4.29-4.30.

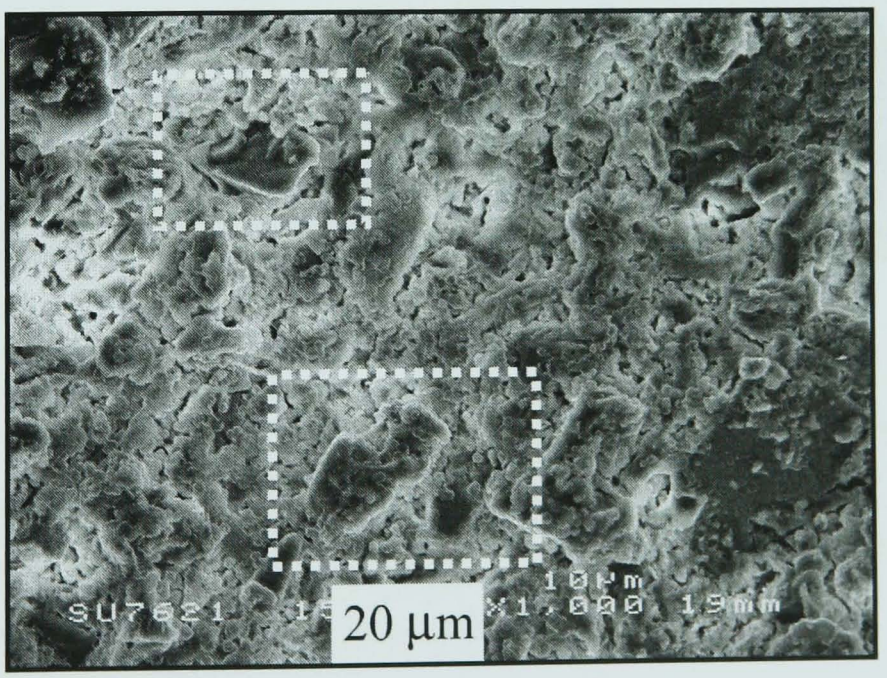

Figure 4.28 - SEM/SE image of a cross-sectioned, etched nepheline syenite pellet fired at 1000°C for 3h.

Figure 4.29(a) shows an irregular-shaped particle (~15-20 μm) with smooth surface surrounded by agglomerates of smaller and rougher particles. EDS (Figure 4.29(b)) shows K, Al and Si content is in a K:Al:Si ratio ~ 1:3:5, revealing that the K content is too low for the chemical composition of K-feldspar. In contrast, EDS of the small particle nearby (Figure 4.29(c)) is high in K. The bigger particle in the middle is believed to come from a K-feldspar which later gave off potassium ions to the liquid that cooled to glass.

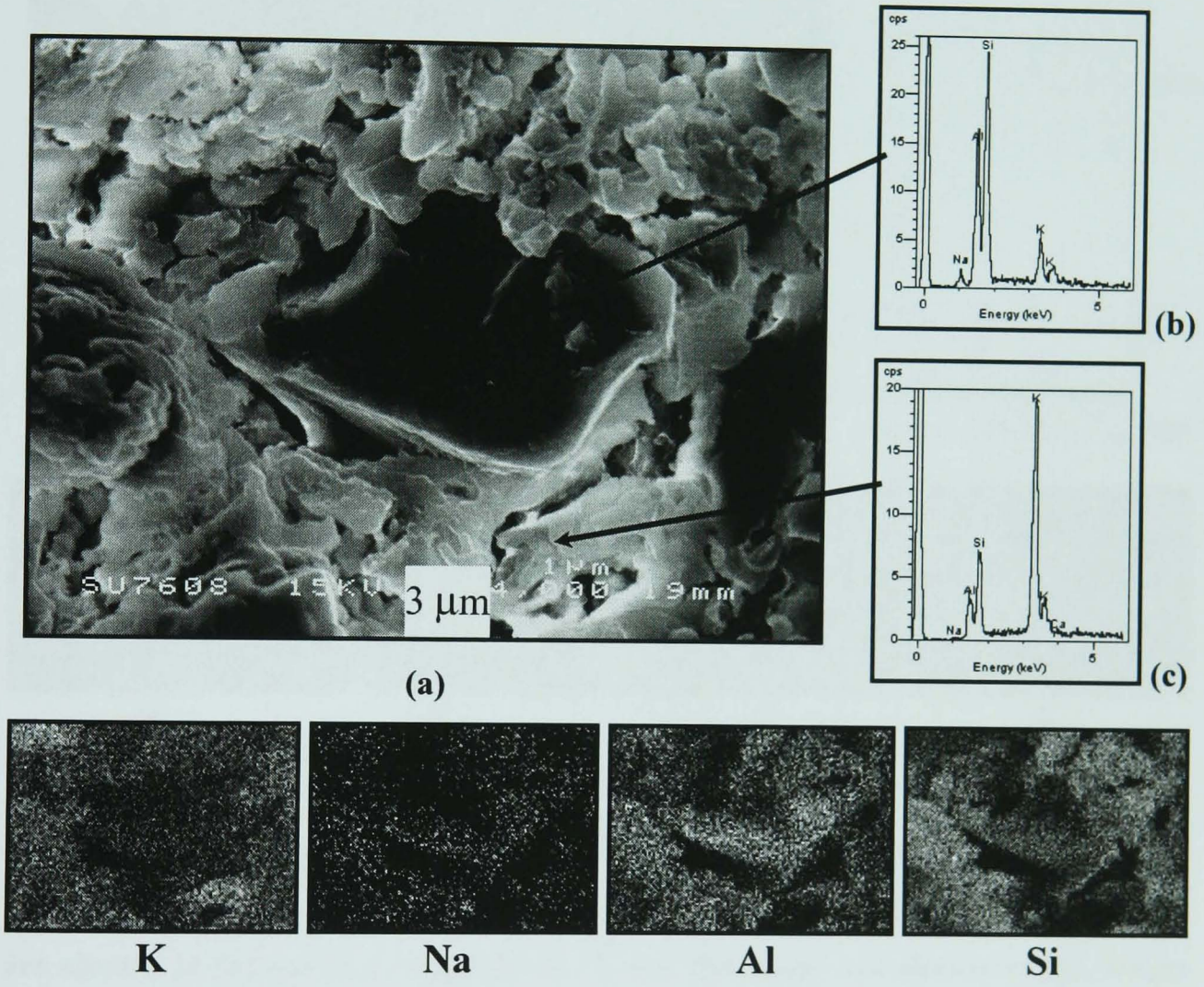

Figure 4.29 - SEM/SE image of cross-sectioned, etched nepheline syenite fired at 1000°C (a). (b) and (c) are EDS of particles in the middle and in the right bottom corner of (a), respectively. X-ray dot maps are shown in (d), where the brighter regions are higher in the corresponding elements.

Another feature commonly seen in samples fired at 1000°C is shown in Figure 4.30(a). It shows a large particle with rough surface that partially formed rounded, nodular particles. EDS of this large particle (Figure 4.30(b)) indicates K and Al in an

almost equal intensity while Si intensity is approximately three times those of K and Al, indicative of K-feldspar. EDS of the rounded particles formed on top of K-feldspar is shown in Figure 4.30(c), revealing higher levels of K.

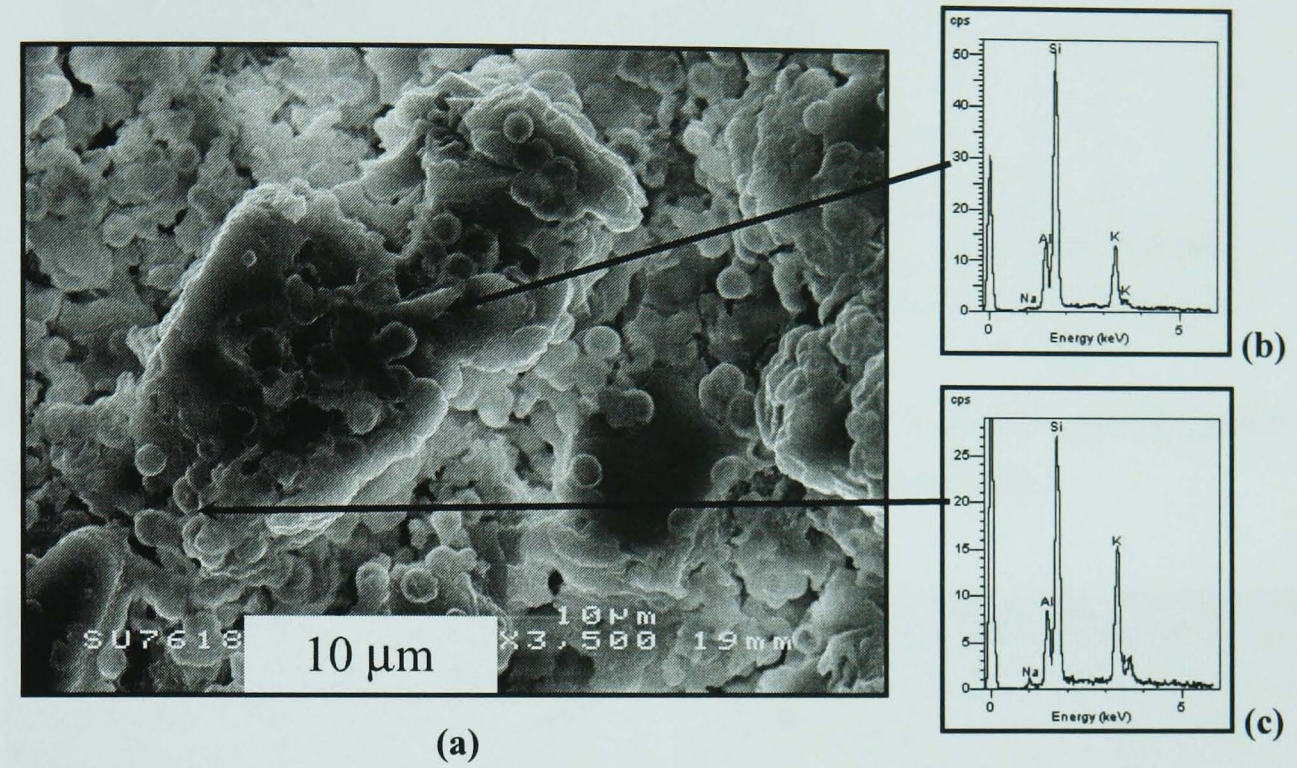

Figure 4.30 - SEM/SE image of cross-sectioned, etched nepheline syenite fired at 1000°C. EDS of a large particle in the centre and rounded particles on top of it are shown in (b) and (c), respectively. X-ray dot maps are shown in (d), where the brighter regions are higher in the corresponding elements.

The agglomerates of rounded (~1-2 µm) crystals are shown in the SEM/SE image (Figure 4.31(a)) at higher magnification. The chemical composition of the rounded crystal agglomerates (Figure 4.31(b)) is higher in K than Si and Al, whereas that of the rounded crystals on the surface of K-feldspar (Figure 4.30(c)) is higher in Si than K and Al. The higher Si content in the EDS trace from Figure 4.30(c) is likely due to the detection of not only rounded particles but also the K-feldspar underneath. Therefore the higher Si intensity came from the K-feldspar.

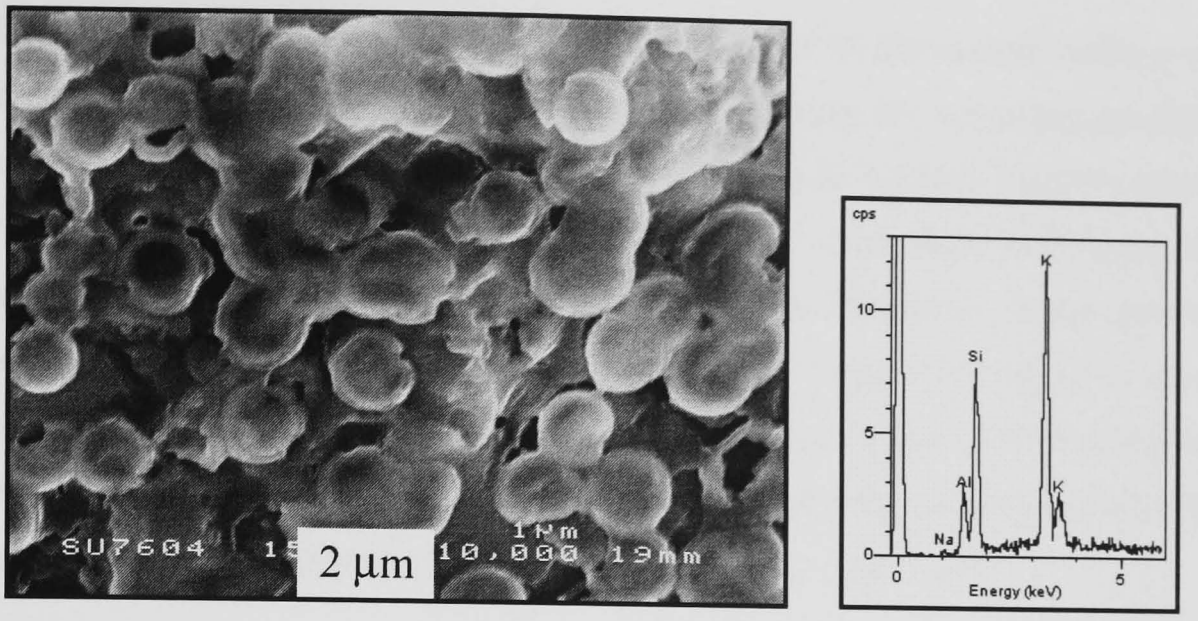

(a) (b)

Figure 4.31 - SEM/SE image of cross-sectioned, etched nepheline syenite pellets fired at 1000°C, showing rounded particles (a) and their EDS (b).

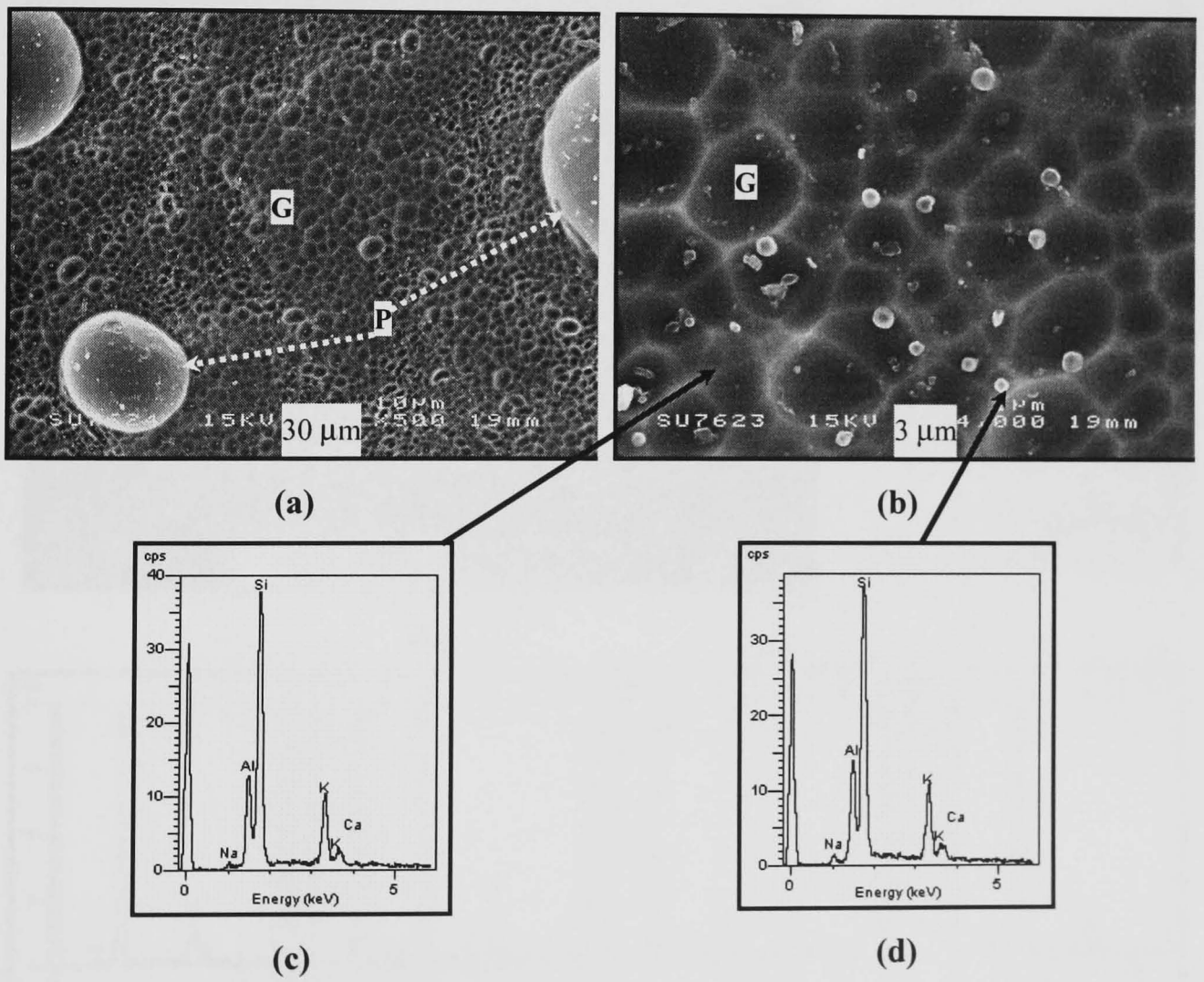

(a) (b)

(c) (d)

Figure 4.32 - SEM/SE image of cross-sectioned, etched nepheline syenite pellets fired 3h at 1200°C (a), and area at high magnification (b). (c) is EDS from glassy phase, and (d) is EDS of rounded crystals shown in (b). (G = glassy phase, P = pore)

After etching samples fired at 1200°C, the glassy phase on the sample surfaces was removed, showing a rough glassy phase and also revealing the remaining un-melted feldspar particles with a rounded shape as shown in Figure 4.32(b). These remaining particles are less than 1 μm in diameter. Their chemical composition is similar to that of the glassy phase. This could be due to the size of the EDS probe, larger than that of the particle so the EDS trace is therefore detecting signal from selected crystals together with glassy phase in the background. These remaining un-melted feldspar particles were not detected by XRD probably due to the small amount present. XRD cannot detect crystalline phases with concentration lower than 1vol%.

4.6.4 - Soda lime silica glass

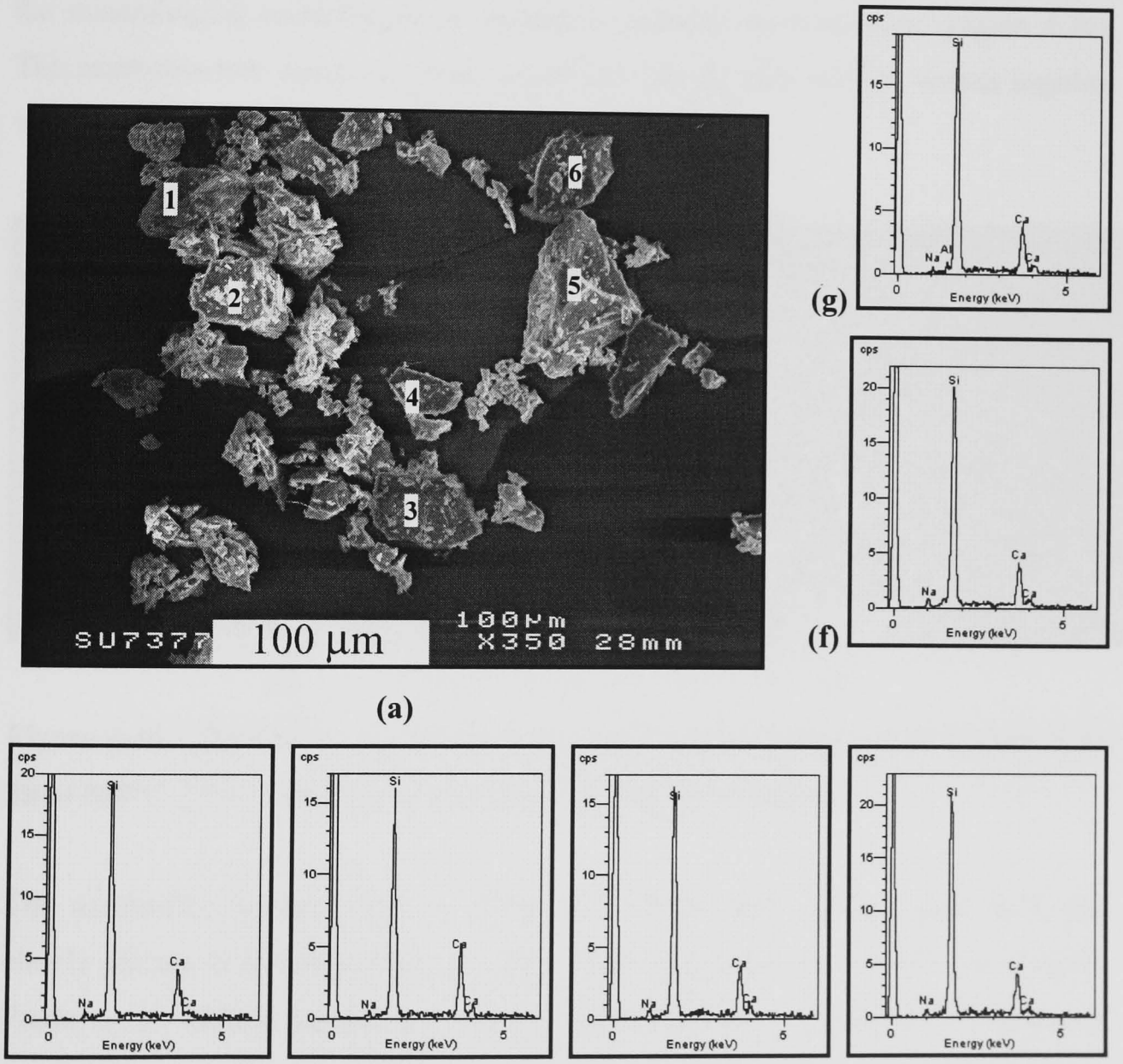

Figure 4.33 - SEM/SE image of the powdered, as-ground SLS glass (a). EDS of randomly selected SLS particles labelled "1", "2", "3", "4", "5" and "6" are shown in (b) - (g) respectively.

SEM/SE image of powdered SLS glass and EDS traces from selected particles are shown in Figure 4.33. SLS glass particles have irregular shape, ranging from 10-100 μm in size. Their chemical composition is slightly different (Na is hardly detected by the EDS detector as mentioned earlier), as various types of colourless container glass were used (described in section 3.2.3).

The glass powder was pressed into pellets and fired at various temperatures. XRD of (pelletised) SLS glass fired 3h at 800°C (Figure 4.16), reveals three main crystalline phases from devitrification of SLS glass after reheating at this temperature: cristobalite, devitrite and wollastonite. SEM images of SLS pellets fired at 800°C were covered with glassy phase. After chemically etching with 5% HF for 3 mins, the mineralogical assemblages of crystalline particles were revealed (Figure 4.34). The microstructure comprises many crystalline phases with specific shapes together with isolated and rounded pores (≤20 μm).

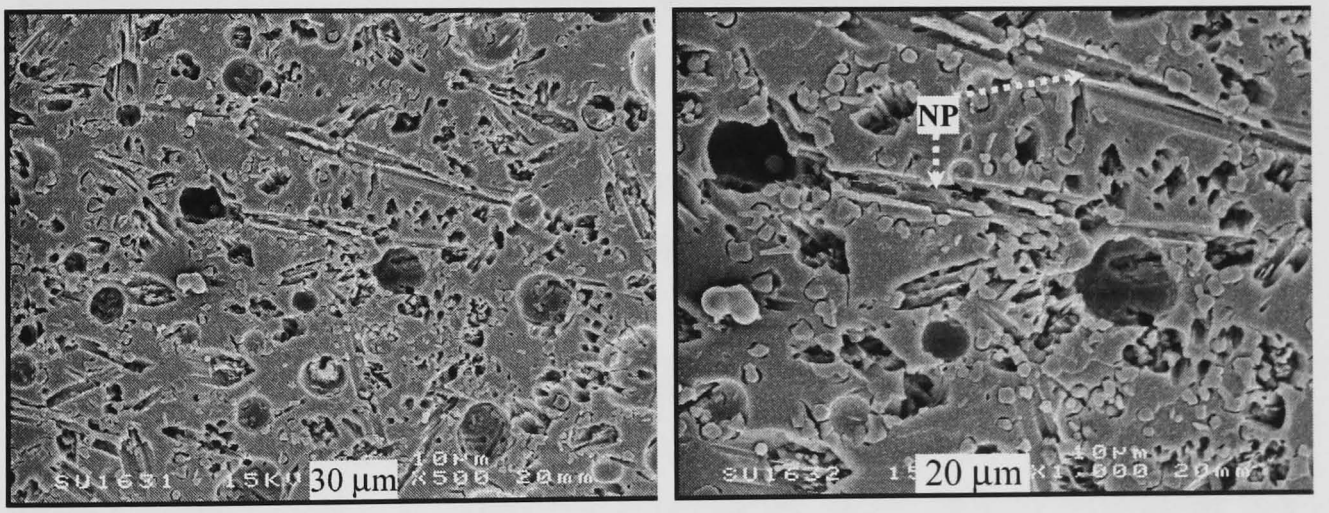

(a) (b)

Figure 4.34 - SEM/SE image of cross-sectioned, etched pelletised SLS glass fired 3h at 800°C. (NP = needle-like features with equiaxial pores)

The needle-like features with equiaxial pores (NP) observed in Figure 4.34 and clearly shown in Figure 4.35(a) are remnants of wollastonite or devitrite crystals. Prado *et al.* (2003) studied the crystallization of SLS glass beads and observed needle-like crystals which were identified as devitrite. Clark-Monks and Parker (1980) defined the morphology of devitrite as radiating bunches of needles, and fan-shaped while wollastonite was fibrous, needle-like growths or laths. However, according to Morey (1938), studies on the chemical durability of glass indicated that

wollastonite glass can be decomposed easily in acids. Therefore, these needle-like pores were probably generated by selective leaching of the wollastonite crystals which are more soluble in HF acid than the glassy phase. EDS of the glassy phase in the background of the needle-like pores is shown in Figure 4.35(b).

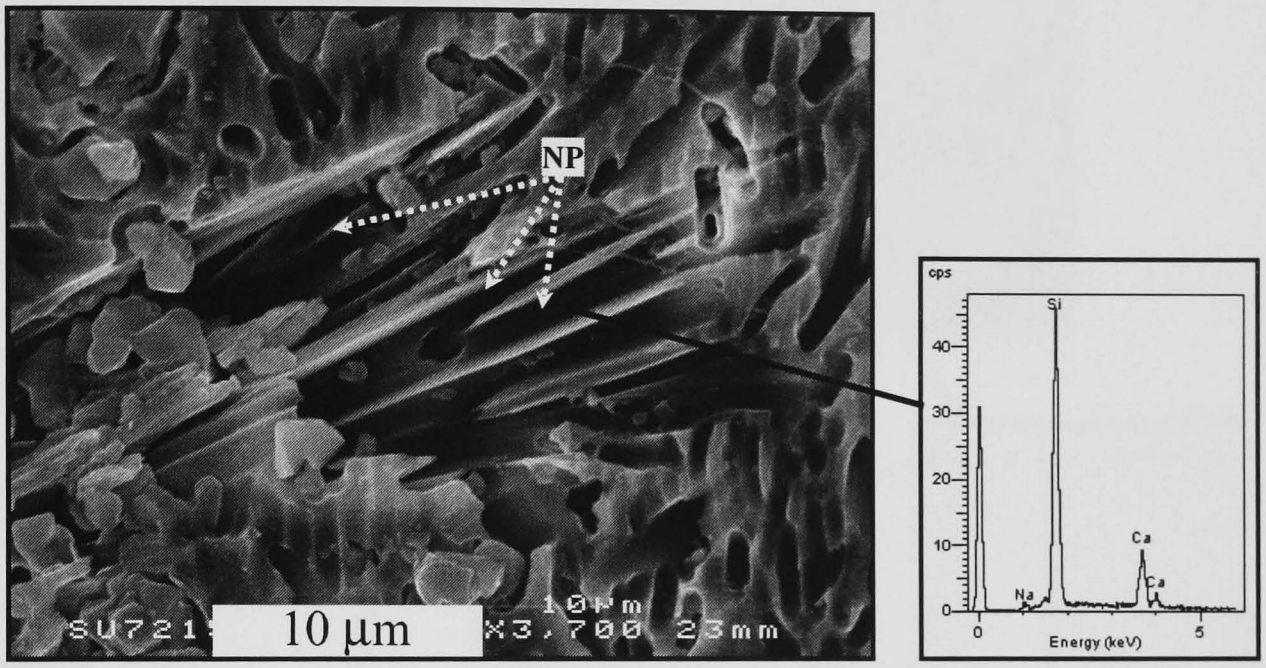

(a) (b)

Figure 4.35 - SEM/SE image of cross-sectioned, etched SLS pellets fired 3h at 800°C showing traces of whisker-like wollastonite crystals (a) with their EDS (b). (NP = needle-like features with equiaxial pores)

The fine rounded grains observed covering the surface of the etched SLS pellets are shown in detail in Figure 4.36(a). EDS (Figure 4.36(b)) shows that the rounded crystals contain mostly Si, indicating a crystalline phase such as cristobalite (C). EDS of the glassy phase (G) is shown in Figure 4.36(a), revealing high Si and some Ca, and traces of Na. The Ca in the cristobalite particle adjacent to the glassy phase (Figure 4.36(b)) may arise from the background glass. The overall view of Figure 4.36(a) shows fine cristobalite particles (~2 µm diameter) merged with glassy phase and a Ca-bearing phase (Ca).

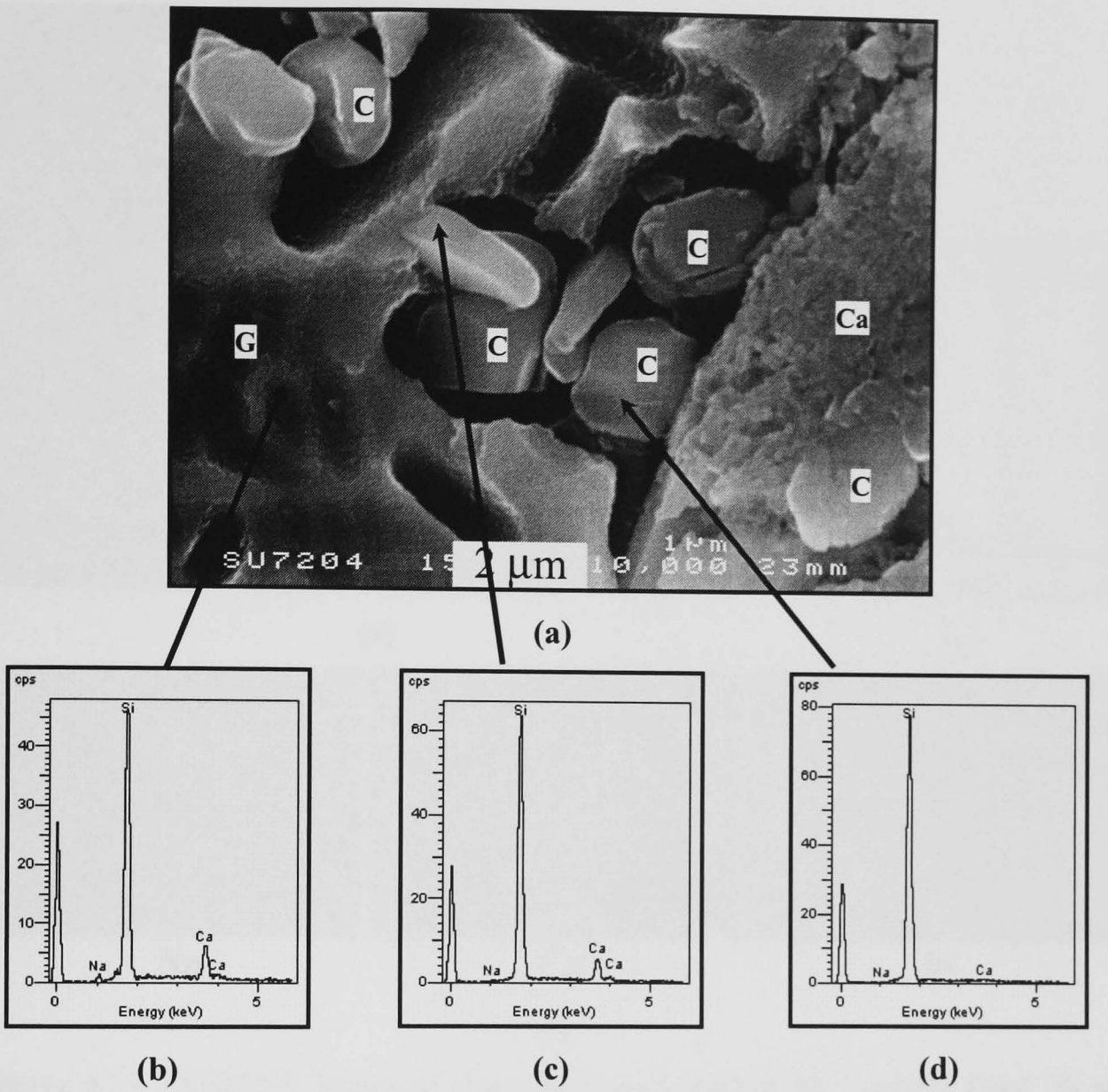

Figure 4.36 - SEM/SE image of cross-sectioned, etched SLS glass pellets fired 3h at 800°C (a). EDS of glassy phase, cristobalite particle near glassy phase and the cristobalite particle are shown in (b), (c) and (d), respectively. (C = cristobalite, Ca = calcium-bearing phase, G = glassy phase)

The Ca-bearing phase is shown in Figure 4.37 together with its EDS trace and X-ray dot maps. Areas with high Si concentration correspond to cristobalite particles. Areas with some Na, Ca and high Si correspond to glassy phase coming from SLS glass. The Ca-bearing phase could not be identified.

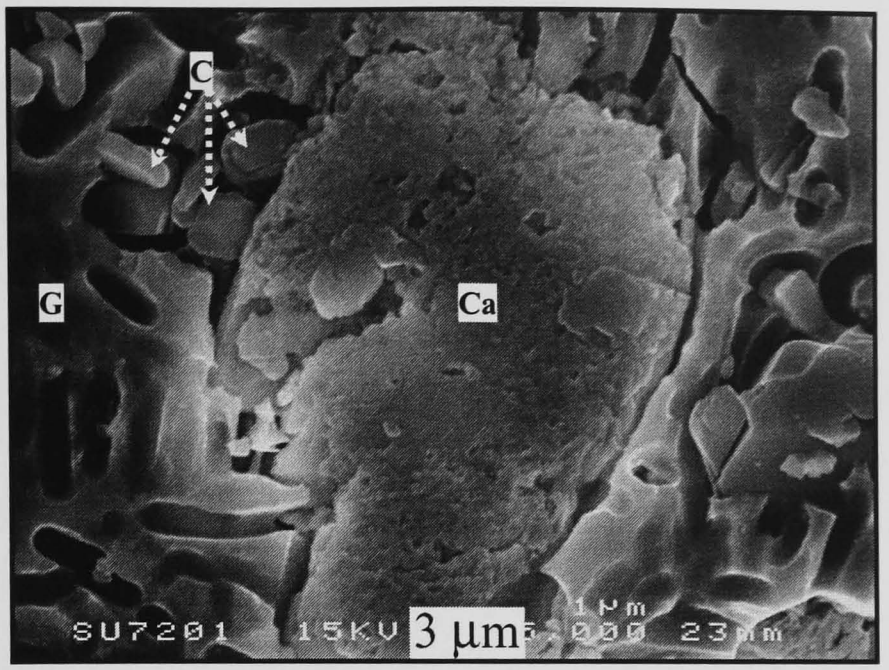

(a)

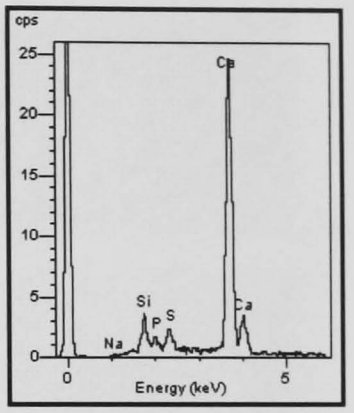

(b)

Na Ca Si

(c)

Figure 4.37 - SEM/SE image of cross-sectioned, etched SLS pellets fired 3h at 800°C showing a high Ca-bearing phase (a). EDS from this Ca-bearing phase is shown in (b) and X-ray dot maps are shown in (c), where the brighter regions are higher in the corresponding element. (C = cristobalite, Ca = calcium-bearing phase, G = glassy phase)

Cristobalite (C), Ca-bearing phase (Ca), needle-like pores (NP) and glassy phase (G) are all shown in Figure 4.38(a). Crystals of cristobalite are scattered all over the sample surface, and are clearly identified by the X-ray dot maps (Figure 4.38(b)) showing high Si concentration with many rounded and fine contours. Areas with high Ca concentration but depleted in Si and Na correspond to the Ca-bearing phase. Areas with Si, Na and Ca correspond to glassy phase which came from molten SLS particles. The EDS traces of these three specific phases (glassy phase, Ca-bearing phase and cristobalite) are shown in Figure 4.38(c)-(e).

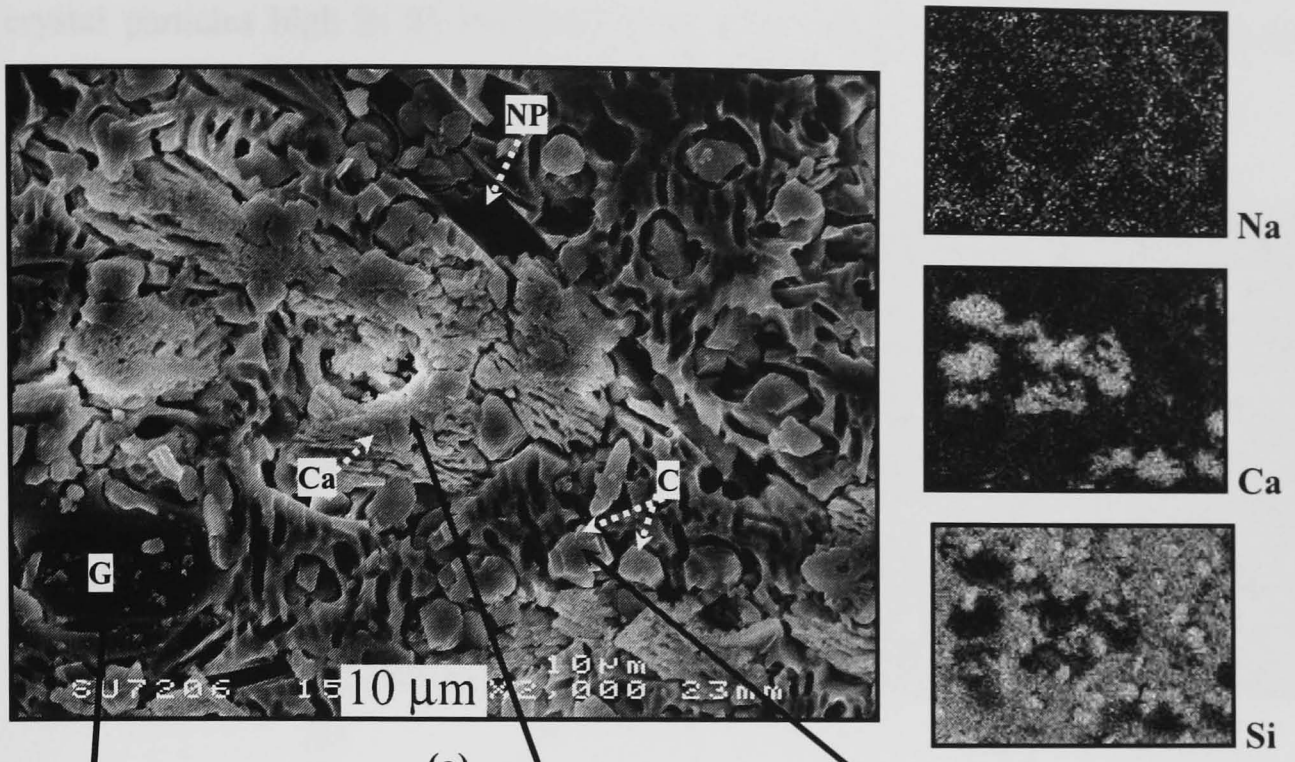

Figure 4.38 - SEM/SE image of cross-sectioned, etched SLS pellets fired 3h at 800°C showing high a Ca-bearing phase surrounded by cristobalite and glassy phase (a). X-ray dot maps are shown in (b), where the brighter regions are higher in the corresponding element. EDS from corresponding areas are shown in (c)-(e). (C = cristobalite, Ca = calcium-bearing phase, G = glassy phase, NP = needle-like pore)

SEM/SE images of etched samples prepared from SLS pellets fired 3h at 1000°C are shown in Figure 4.39(a)-(b). The overall microstructure (Figure 4.39(a)) revealed mainly glassy phase (G) and pores (P). The rough surface was caused by chemical etching which removed part of the glassy phase. XRD of SLS pellets fired 3h at 1000°C (Figure 4.16) revealed no crystal peaks and only an amorphous hump which is indicative that all crystalline phases have been dissolved and became liquid. Small

crystal particles high in Si (believed to be cristobalite, C) remain and were not detected by XRD (Figure 4.39(b)).

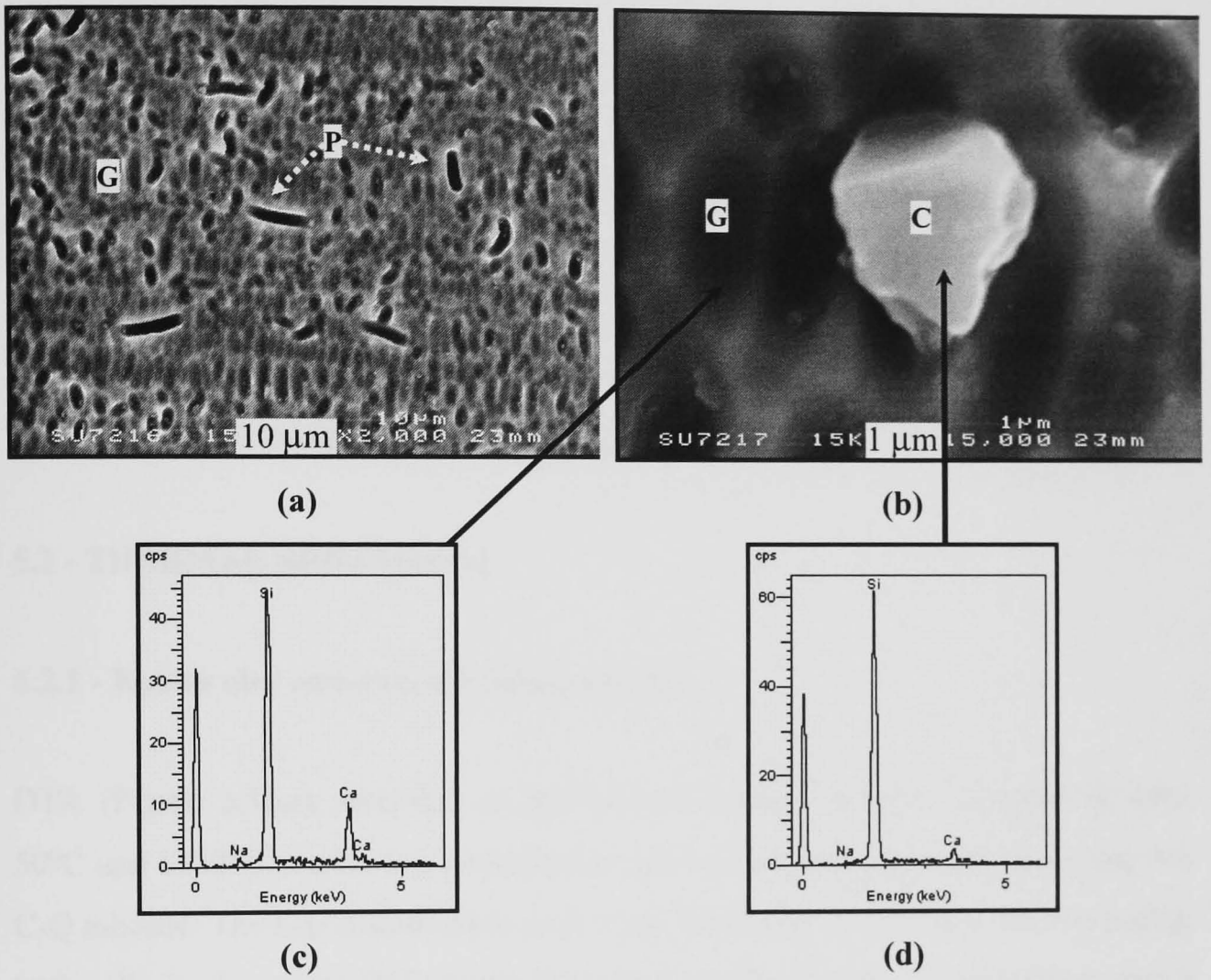

Figure 4.39 - SEM/SE image of cross-sectioned, etched SLS pellets fired 3h at 1000°C (a) and (c). EDS of glassy phase and an isolated and irregular particle, near glassy phase are shown in (b) and (d), respectively. (C = cristobalite, G = glassy phase, P = pore)

CHAPTER 5 - INTERACTIONS BETWEEN BINARY MIXTURES OF RAW MATERIALS

5.1 - INTRODUCTION

To understand the interaction between raw materials upon firing, binary mixtures of raw materials (clay-quartz, clay-nepheline syenite, clay-SLS glass, quartz-nepheline syenite, quartz-SLS glass and nepheline syenite-SLS glass) in the relative proportion as shown in Table 3.1 were also prepared, characterised by DTA, fired at 600-1200°C and characterised by XRD and SEM.

5.2 - THERMAL BEHAVIOUR

5.2.1 - Kaolin clay and quartz mixtures (C-Q)

DTA (Figure 5.1(a)), recorded on heating and cooling the C-Q mixture between 50°C and 1250°C, shows two endothermic and two exothermic peaks on heating the C-Q mixture. The first endothermic peak arises from dehydroxylation (corresponding to the elimination of the OH^- groups from the crystalline lattice of kaolinite) having a minimum at ~520°C and the second one, at ~571°C, is due to the $\alpha \rightarrow \beta$ quartz inversion. The first intense exotherm at ~990°C is probably the most widely disputed DTA peak known (as discussed in section 4.4 for DTA of fired kaolin clay). The exact phase that appears, which was not altered by the presence of quartz on heating, is still a point of controversy. However, experimental data have shown that this peak is due to crystallisation of mullite as discussed in section 4.1.1. The other broad and indistinct peak beginning at ~1220°C is probably due to the formation of secondary mullite. Lundin (1954), Schuller (1964) and Iqbal and Lee (2000) stated that secondary mullite forms in the presence of feldspar. Even though there is no addition of flux in this mixture, secondary mullite formation may arise from the presence of alkali impurities such as microcline and muscovite in the clay. The chemical composition of kaolin clay (Table 4.1) reveals almost 3wt% of K_2O. The dotted cooling curve shows only the exothermic peak resulting from the inversion of β to α-quartz at ~566°C. No peak was detected between 200-270°C which implied that

cristobalite was absent. Even though the C-Q mixture quenched from 1250°C (Figure 5.7 in section 5.3.1) reveals a small cristobalite peak, the amount may be too small to be detected by DTA.

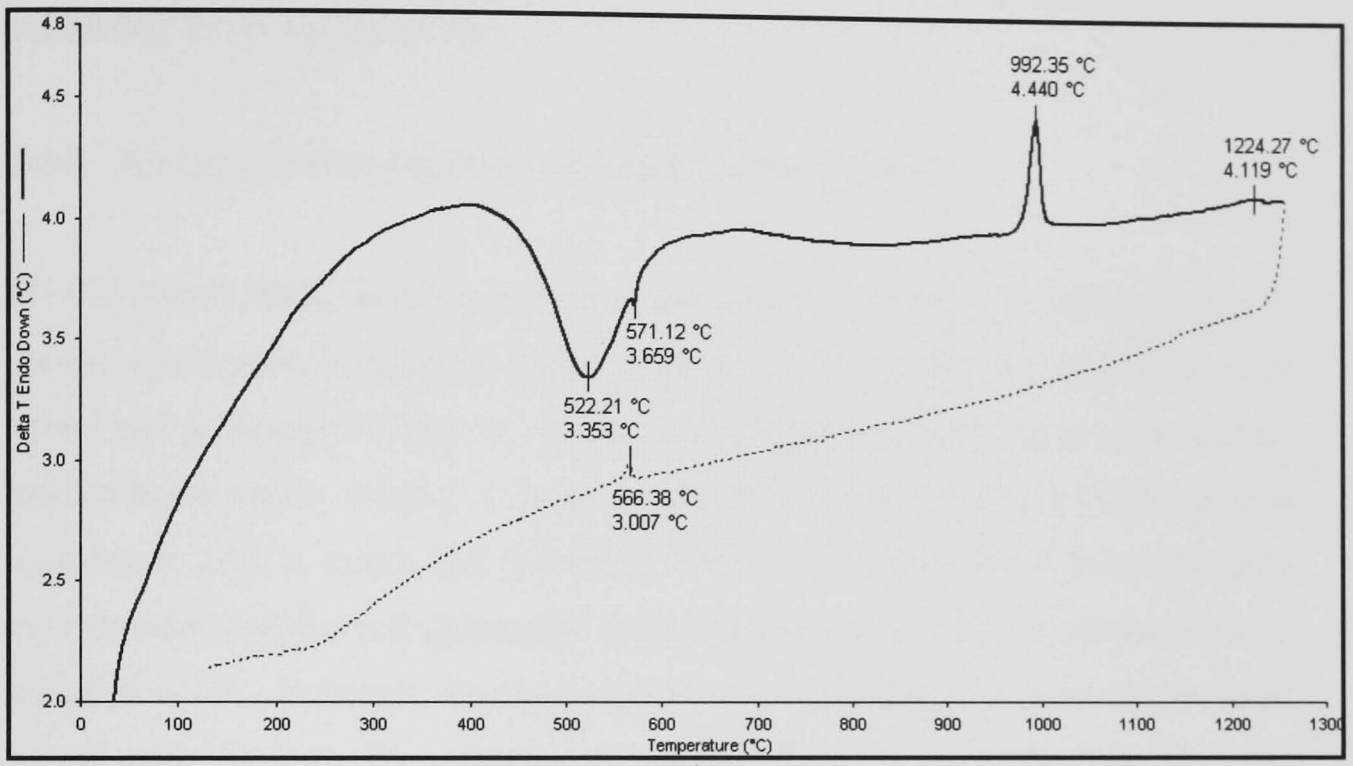

(a)

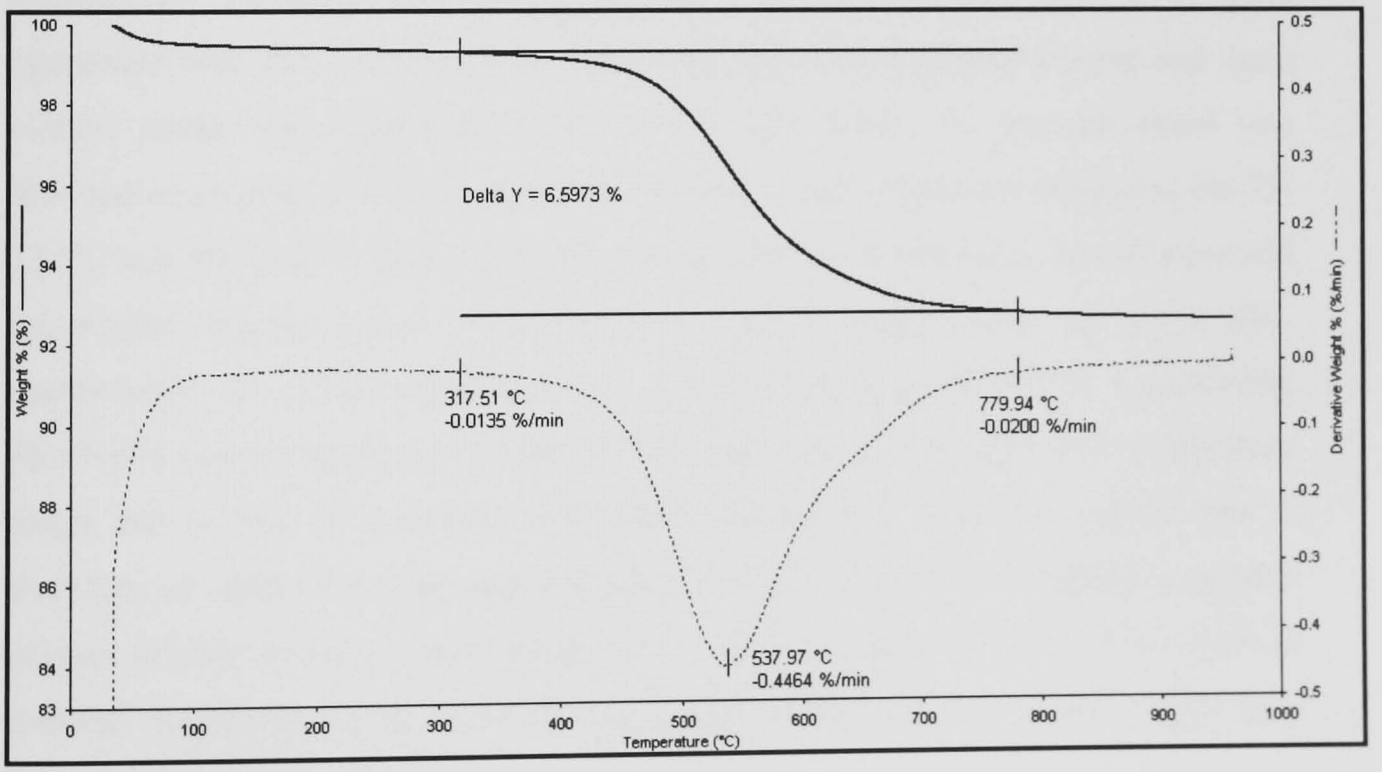

(b)

Figure 5.1 - DTA (a; — heating curve, --- cooling curve) and TG/DTG (b; — TG, --- DTG) of kaolin-quartz mixture.

TG/DTG of C-Q (Figure 5.1(b)) showed a weight loss of ~6.6% between 300-800°C. Since no weight loss was detected in TG/DTG of pure quartz (Figure 4.2(b)), the weight loss from C-Q corresponds to the loss of structural water from kaolinite (the weight loss of kaolin clay alone is ~10.2%, thus 6.6% loss corresponds to the mixture containing 2/3 its weight of clay).

5.2.2 - Kaolin clay and nepheline syenite mixtures (C-NS)

DTA (Figure 5.2(a)), recorded on heating the mixture of C-NS from 50°C to 1250°C, shows an endothermic dehydroxylation peak at ~520°C, a sharp exothermic peak of spinel and/or primary mullite at ~990°C and a large, broad exotherm of secondary mullite beginning at ~1140°C. Comparing the DTA traces of C-Q and C-NS, the first exothermic peak is narrow and remains at ~990°C in both mixtures. It can probably be concluded that the first exothermic event is independent of the raw material that is mixed with clay. However, the second exothermic event depends on the raw material mixed with the clay. The presence of nepheline syenite shifts the peak to lower temperatures, from 1220 to 1140°C. Nepheline syenite reduced the liquid formation temperature, therefore accelerating secondary mullite growth. This is in good agreement with XRD of quenched C-NS which shows an amorphous hump and sharp mullite peaks when quenched from 1050°C and above. No thermal event was detected on cooling. TG/DTG traces showed two small weight loss steps over the 75-125°C and 200-285°C temperature ranges, which may be related to loss of adsorbed (physically bound) water (~0.3wt%) and organic matter burn out (~0.2wt%), respectively. A ~7.5% weight loss was detected between 370-770°C. Considering 66.67wt% clay in the mixture causes ~7% weight loss on heating to this temperature range due to loss of structural water from kaolin clay, the extra weight loss is therefore an effect from heating nepheline syenite. TG/DTG of nepheline syenite (Figure 4.3(b)) reveals a small weight loss (~0.4wt%) between 590-730°C which is difficult to observe in the C-NS mixtures due to superposition of this weight loss with the bigger loss of structural water from the clay.

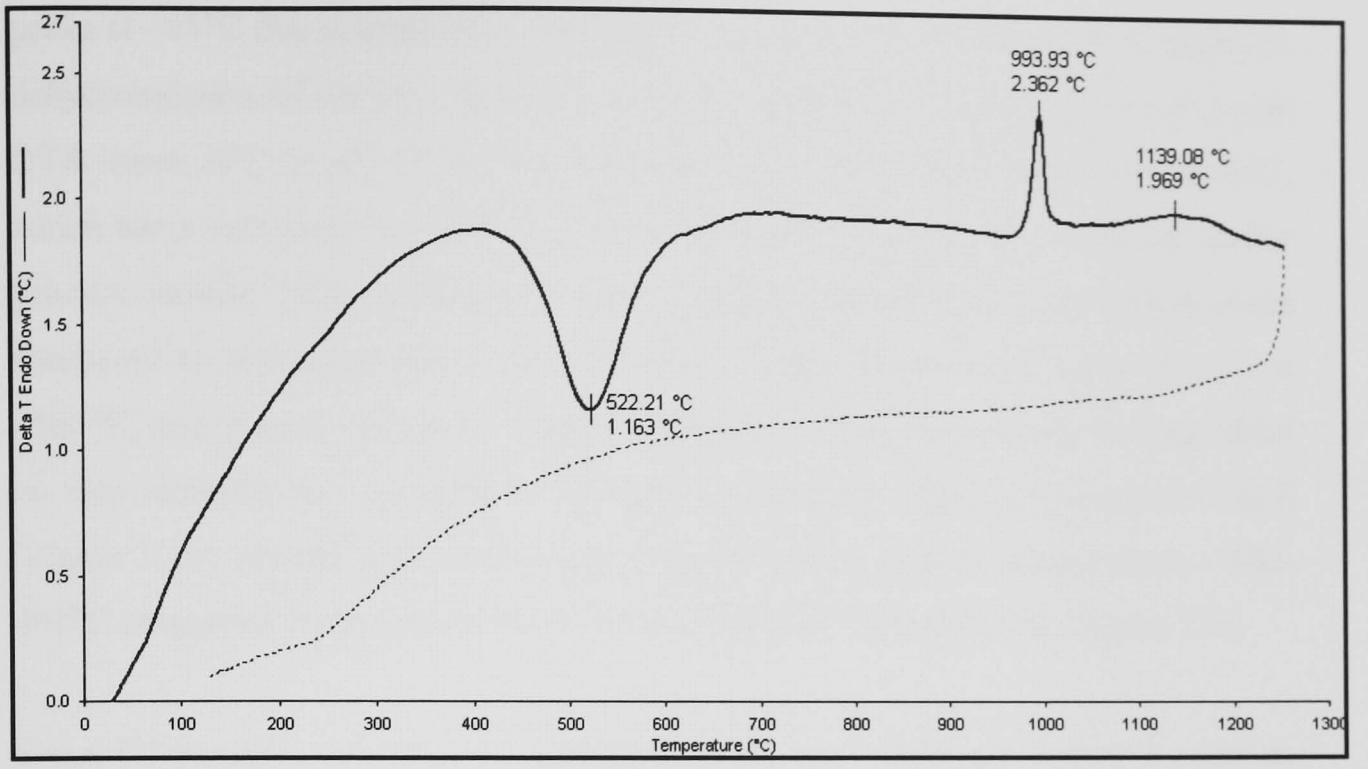

(a)

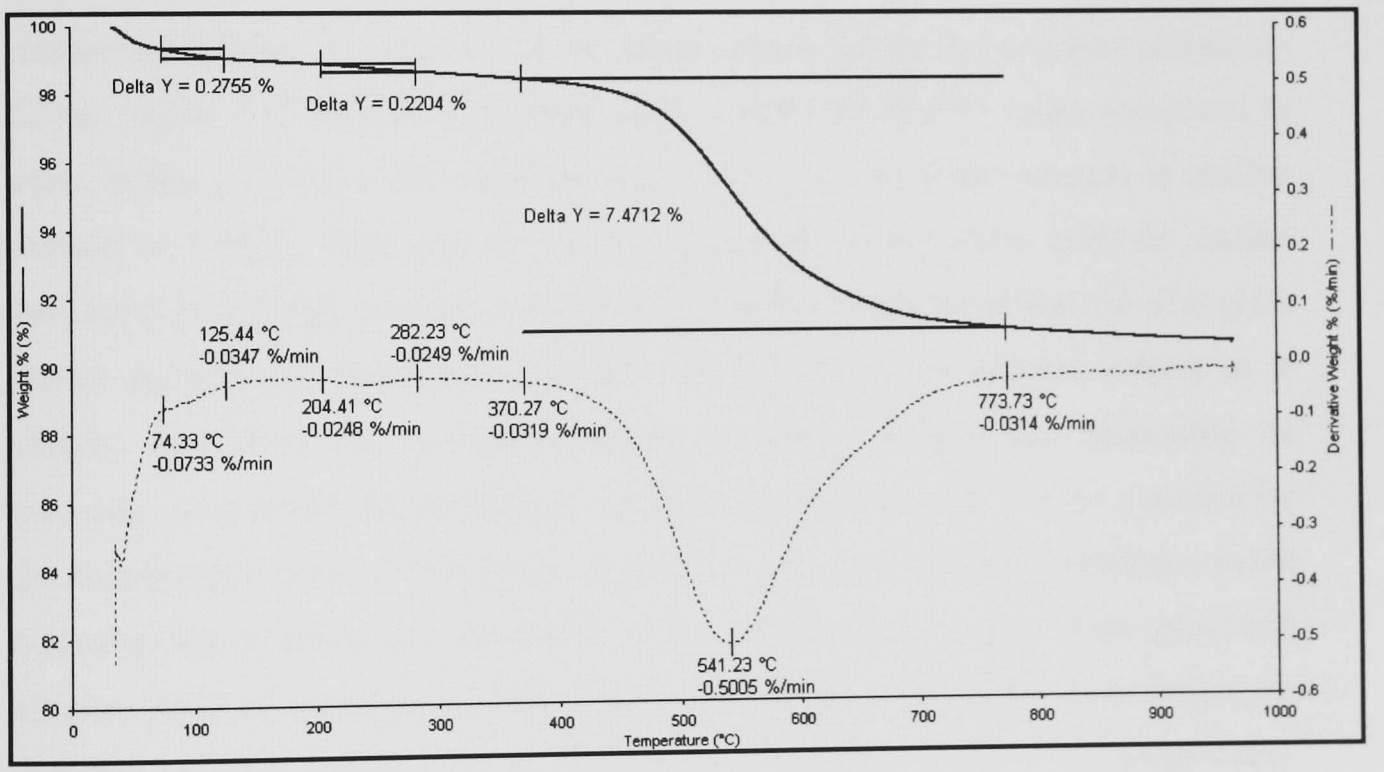

(b)

Figure 5.2 - DTA (a; — heating curve, --- cooling curve) and TG/DTG (b; — TG, --- DTG) of the kaolin-nepheline syenite mixture.

5.2.3 - Kaolin clay and SLS glass mixtures (C-SLS)

DTA recorded on heating and cooling the C-SLS mixture over the 50-1250°C temperature range is shown in Figure 5.3(a). The heating curve reveals endothermic

peaks at ~65°C due to removal of moisture or physically absorbed water followed by dehydroxylation of kaolinite at similar temperatures (~520°C) to those present in the DTA traces of C-Q and C-NS. The broad and small exotherm between 900-1000°C, which has a maximum at ~970°C, is probably due to the formation of spinel and/or primary mullite. This exothermic peak is smaller and shifts to lower temperatures compared to that observed in the C-Q and C-NS mixtures. SLS glass has T_g at ~563°C, and starts to soften at ~720°C. Molten SLS then has a strong fluxing effect on clay sintering and accelerates the mullite formation. XRD of quenched C-SLS (Figure 5.11) reveals the presence of a small mullite peak at temperatures ~800-900°C compared to that above 950°C for C-Q (Figure 5.7) and C-NS (Figure 5.9).

Since DTA peaks are directly connected to the heat exchange during a reaction which corresponds to the energy of that reaction, it can be predicted that the area under a characteristic peak is proportional to the energy exchanged during the reaction and hence the amount of the phase which causes the reaction (Smykatz-Kloss, 1974). The smaller exothermic peak at the 900-1000°C range compared to those in the C-Q and C-NS mixtures may result from the lower amount of mullite formed in C-SLS. This will be further explained in the phase analysis section (section 5.3). Another possible reason for the smaller exotherm is that the SLS glass shows endothermic behaviour over this temperature range (Figure 4.4(a)) as it absorbs heat from the system increasing molecular motion and decreasing its viscosity. As a result, the exothermic contribution from the clay will be hindered by the endothermic trend of SLS glass. A possible reason for the broad exotherm is the crystallization of more than one phase. In the C-SLS mixture, apart from spinel and mullite, XRD of quenched C-SLS (Figure 5.11) from 650-1100°C also shows the presence of other phases such as cristobalite, wollastonite, albite and plagioclase. The formation of cristobalite occurred from 650-1050°C, albite from 700-900°C, wollastonite from 800-1000°C and plagioclase from 1000-1100°C. However, no clear crystallization (exothermic peaks) of these phases was observed by DTA (Figure 5.3), only a combination of two broad exotherms on the DTA curve from ~650-850°C and ~1000-1150°C. The first is probably due to the crystallization of cristobalite, albite and wollastonite. The latter could arise from plagioclase or secondary mullite formation. Notwithstanding, if the broad exotherm between 900-1000°C in Figure 5.3(a) corresponds to crystallization of plagioclase in addition to

spinel and primary mullite, the broad and low intensity exotherm between 1000-1150°C will be associated with the crystallization of low amounts of another phase such as secondary mullite. XRD cannot distinguish between primary and secondary mullite, therefore it is left to SEM investigation to prove if secondary mullite has ever formed in this mixture. TG/DTG of C-SLS mixture (Figure 5.3(b)) shows only the ~7wt% weight loss mainly from the loss of structural water in kaolin clay.

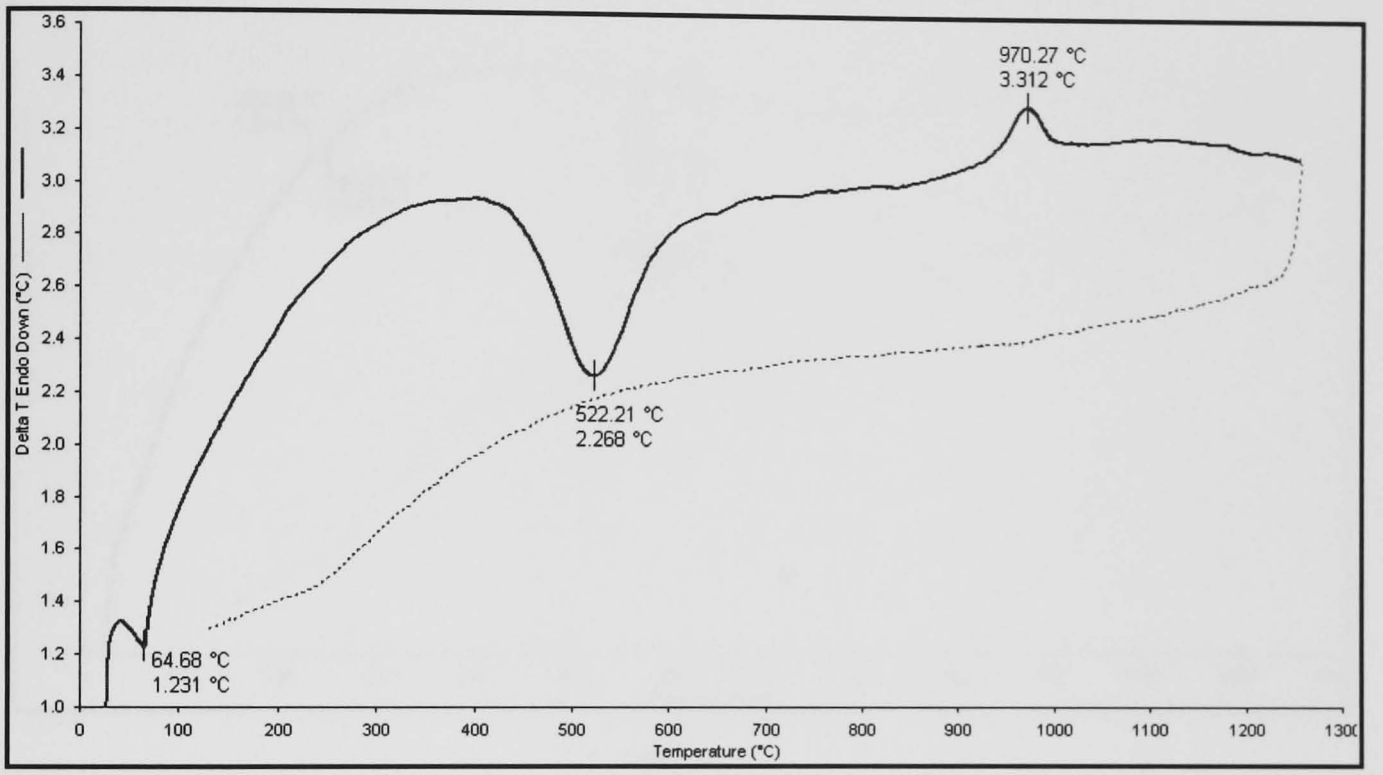

(a)

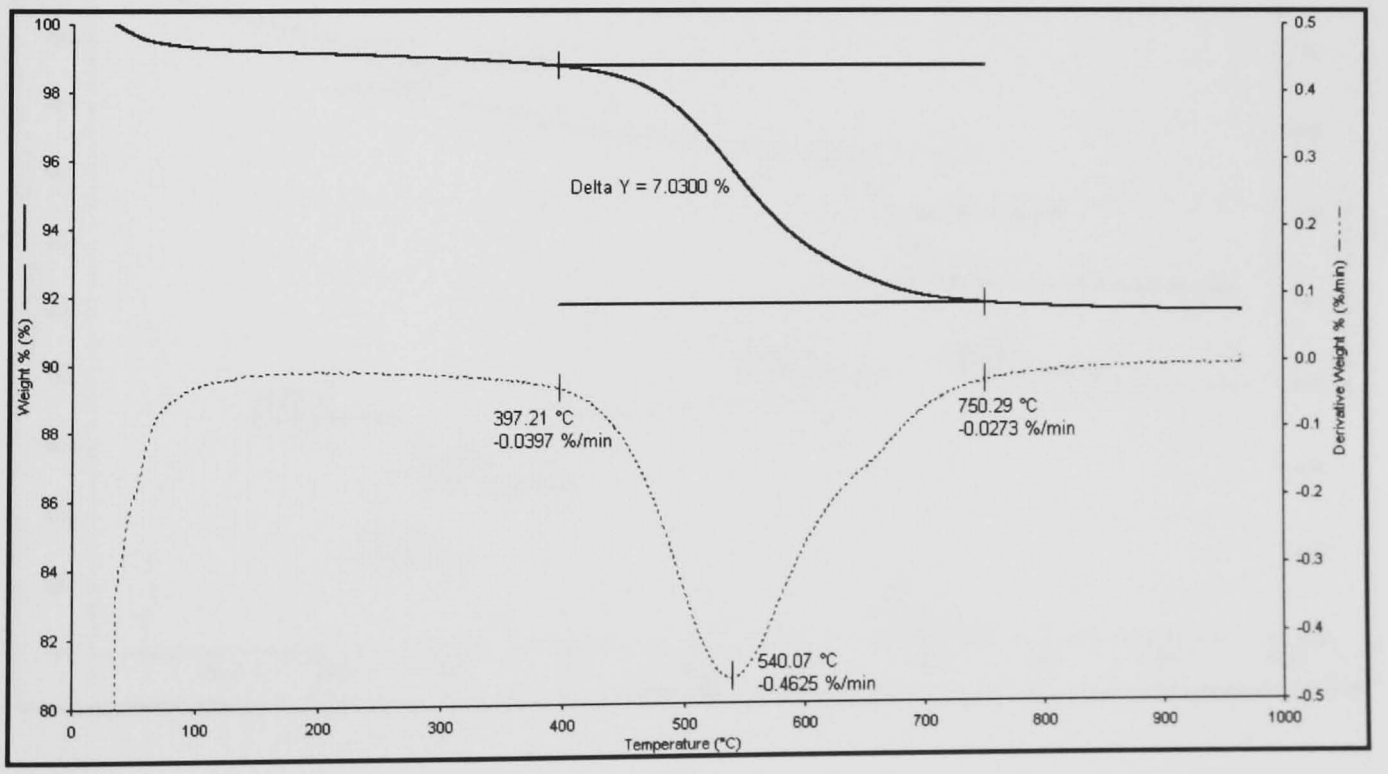

(b)

Figure 5.3 - DTA (a; — heating curve, --- cooling curve) and TG/DTG (b; — TG, --- DTG) of the kaolin-SLS glass mixture.

5.2.4 - Quartz and nepheline syenite mixtures (Q-NS)

DTA recorded on heating and cooling the Q-NS mixture over the 50-1250°C temperature range is shown in Figure 5.4(a) and TG/DTG recorded on heating from 50°C to 950°C is shown in Figure 5.4(b).

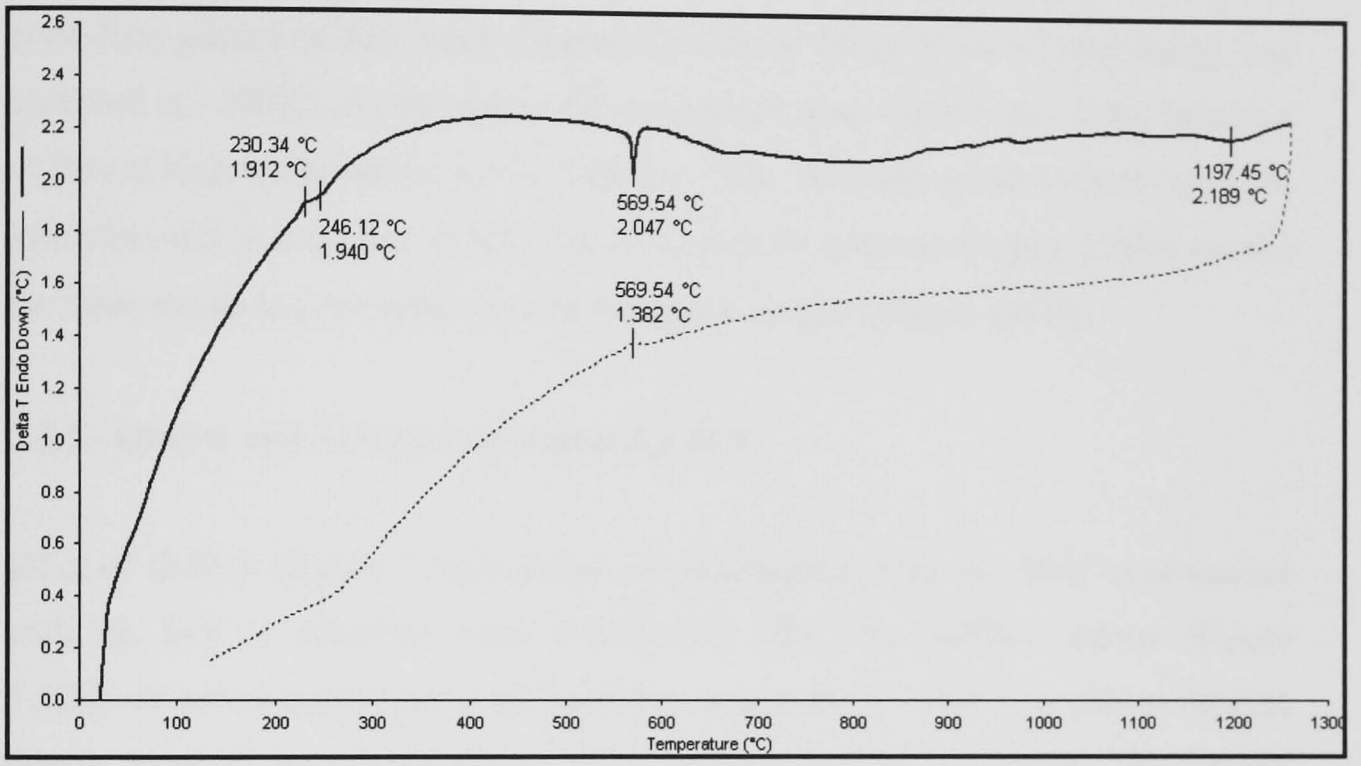

(a)

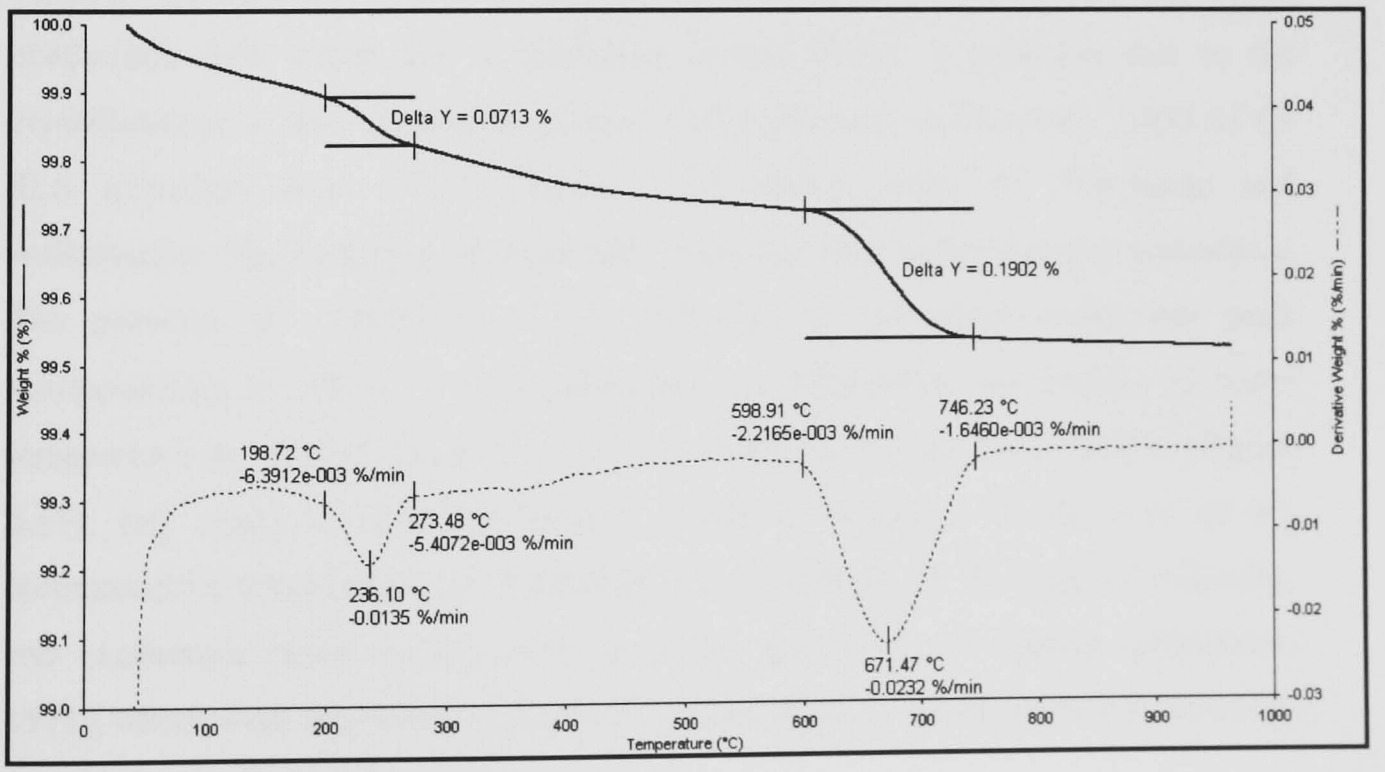

(b)

Figure 5.4 - DTA (a; — heating curve, --- cooling curve) and TG/DTG (b; — TG, --- DTG) of quartz-nepheline syenite mixture.

DTA of quartz and nepheline syenite (Figure 5.4(a)) does not show any change other than the removal of organic matter from nepheline syenite at ~230°C and the α-β quartz structural inversion at ~570°C. The continuous endothermic drift at >600°C results from gradual sintering or melting of nepheline syenite. The broad endothermic peak with a minimum around 1200°C is probably due to liquid formation. XRD of Q-NS after heating to 1100°C (Figure 4.13) shows no sign of crystalline phases as they were completely melted. No inversion of cristobalite was observed at ~200°C, as cristobalite did not convert from quartz even in the presence of flux at high temperatures (up to 1250°C). Thus, the cooling curve shows only the inversion of β to α-quartz. TG/DTG curves of Q-NS mixtures (Figure 5.4(b)) exhibit the same trends as previously seen for nepheline syenite (Figure 4.3(b)).

5.2.5 - Quartz and SLS glass mixtures (Q-SLS)

DTA of Q-SLS (Figure 5.5(a)) shows an endothermic peak at ~90°C concomitant with the loss of adsorbed water (~0.13wt%) found in TG/DTG curves (Figure 5.5(b)). A broad exothermic peak having a maximum at ~325°C is due to organic matter burn-off and corresponds to a weight loss of ~0.2wt%. The second endothermic peak at ~570°C is due to the α → β quartz inversion. The broad exothermic drift which has a maximum around 810°C is probably due to the crystallization of two crystalline phases: cristobalite and wollastonite. XRD of Q-SLS quenched from 750°C (Figure 5.15) shows peaks of cristobalite and wollastonite. The formation of cristobalite increases with higher firing temperatures. The presence of cristobalite is also indicated by the sharp exothermic peak corresponding to the β → α transformation of cristobalite on cooling to room temperature at ~210°C. From the XRD of Q-SLS quenched from 1250°C (Figure 5.15), tiny peaks of tridymite appear, which is indicative of the start of the reconstructive transformation of cristobalite to tridymite. In the case of tridymite, two exothermic peaks usually occur at 117°C and 163°C on cooling (Grimshaw, 1971), which were not observed in this DTA trace (Figure 5.5(a)) probably due to the small amount of tridymite present.

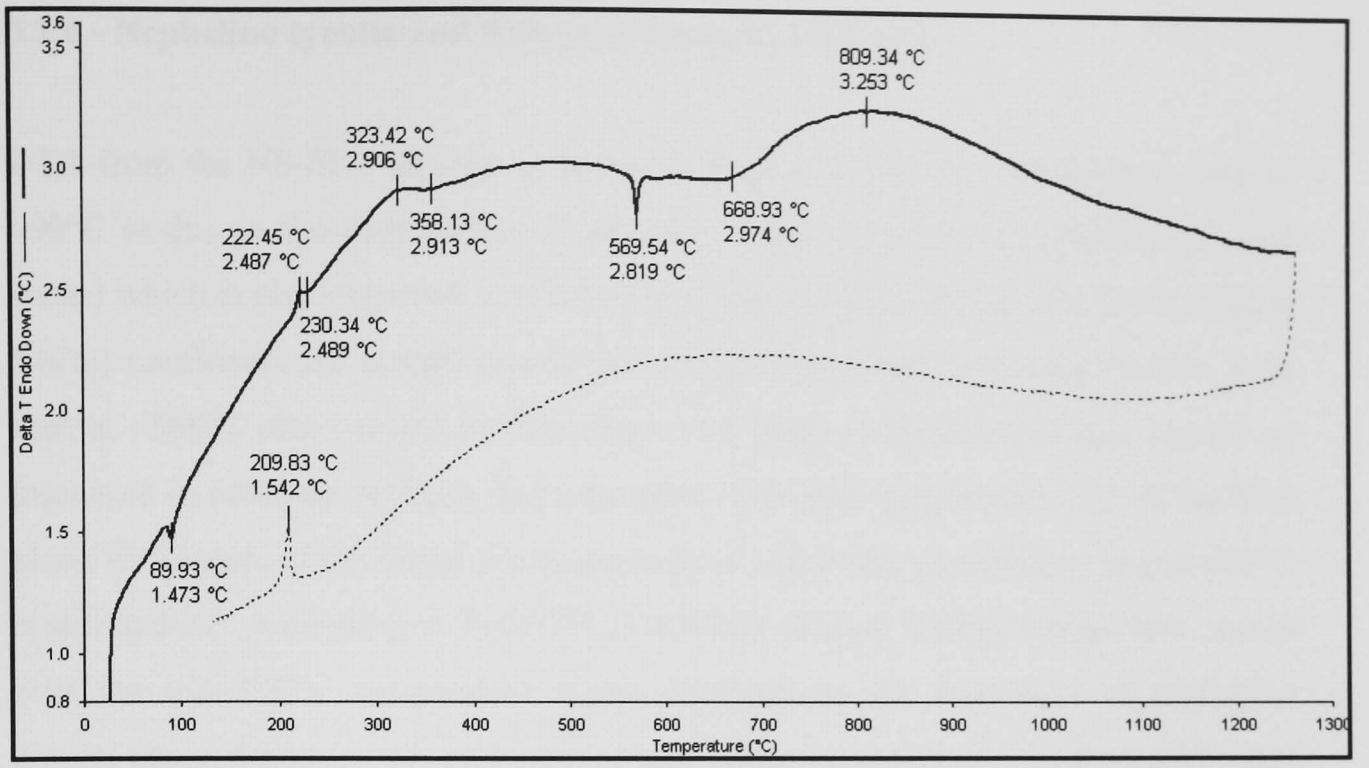

(a)

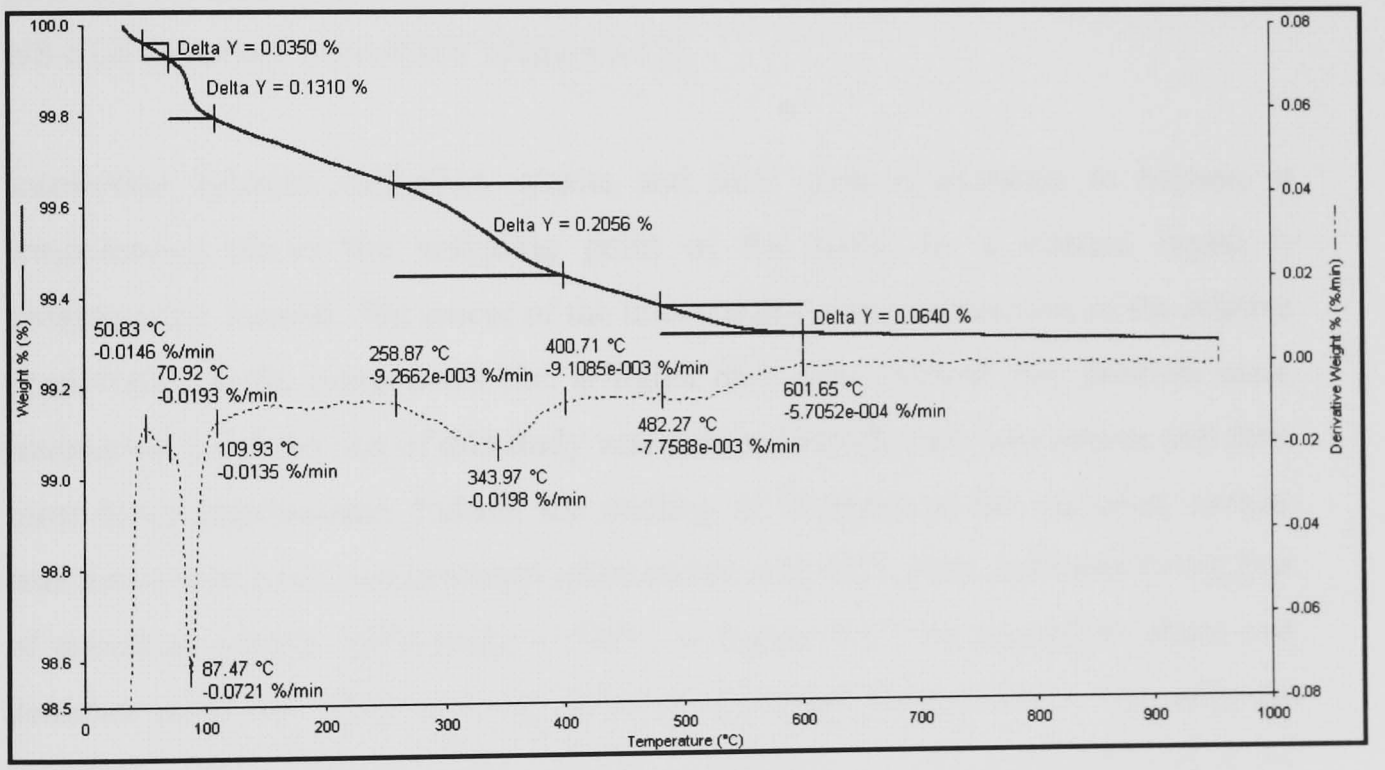

(b)

Figure 5.5 - DTA (a; — heating curve, --- cooling curve) and TG/DTG (b; — TG, --- DTG) of the quartz-SLS glass mixture.

5.2.6 - Nepheline syenite and SLS glass mixtures (NS-SLS)

DTA from the NS-SLS mixture is shown in Figure 5.6(a). An endothermic peak at ~90°C is due to the evaporation of adsorbed water (moisture or physically bound water) which is also observed in DTA of SLS glass (Figure 4.4(a)). TG/DTG (Figure 5.6(b)) confirmed the weight loss at this temperature. The broad endothermic peak start at ~560°C also present in DTA from SLS glass (4.4(a)) most likely comes, as discussed in previous sections, from the glass transition temperature (T_g) of the SLS glass. The nature of the broad endothermic peak which has a minimum around 660°C is still unclear. According to TG/DTG of NS-SLS (Figure 5.6(b)), weight loss occurs over the 600-700°C temperature range, similarly to the behaviour of nepheline syenite alone, therefore this endotherm corresponds to release of CO_2 from carbonate contamination. The broad exothermic peak with maximum at ~802°C comes probably from the formation of cristobalite and wollastonite, as suggested by XRD of NS-SLS quenched from 800°C (Figure 5.17).

Interaction between nepheline syenite and SLS glass is expected to happen at temperatures above the softening point of the latter, as a viscous liquid is progressively formed. The extent of the interactions may be a function of the relative proportions of the components (i.e. a higher SLS glass content may promote more interactions), but the aim of this study was only to identify such interactions and their most likely mechanisms. Indeed, the melting of feldspars in the nepheline syenite was detected at lower temperatures when mixed with SLS glass, indicated by the loss of nepheline syenite XRD peaks at 950°C in Figure 5.17. No crystalline phase was detected from the XRD trace of NS-SLS quenched from 1100°C, but only the amorphous hump of glassy phase, thus the endotherm ~1150°C is possibly due to the complete melting of any remaining crystalline phases in the NS-SLS mix. The minor weight loss steps over the 200-260°C and 600-700°C temperature ranges in Figure 5.6(b) were similar to what happened to nepheline syenite alone, thus attributed to organic burn off and carbonate contamination from nepheline syenite.

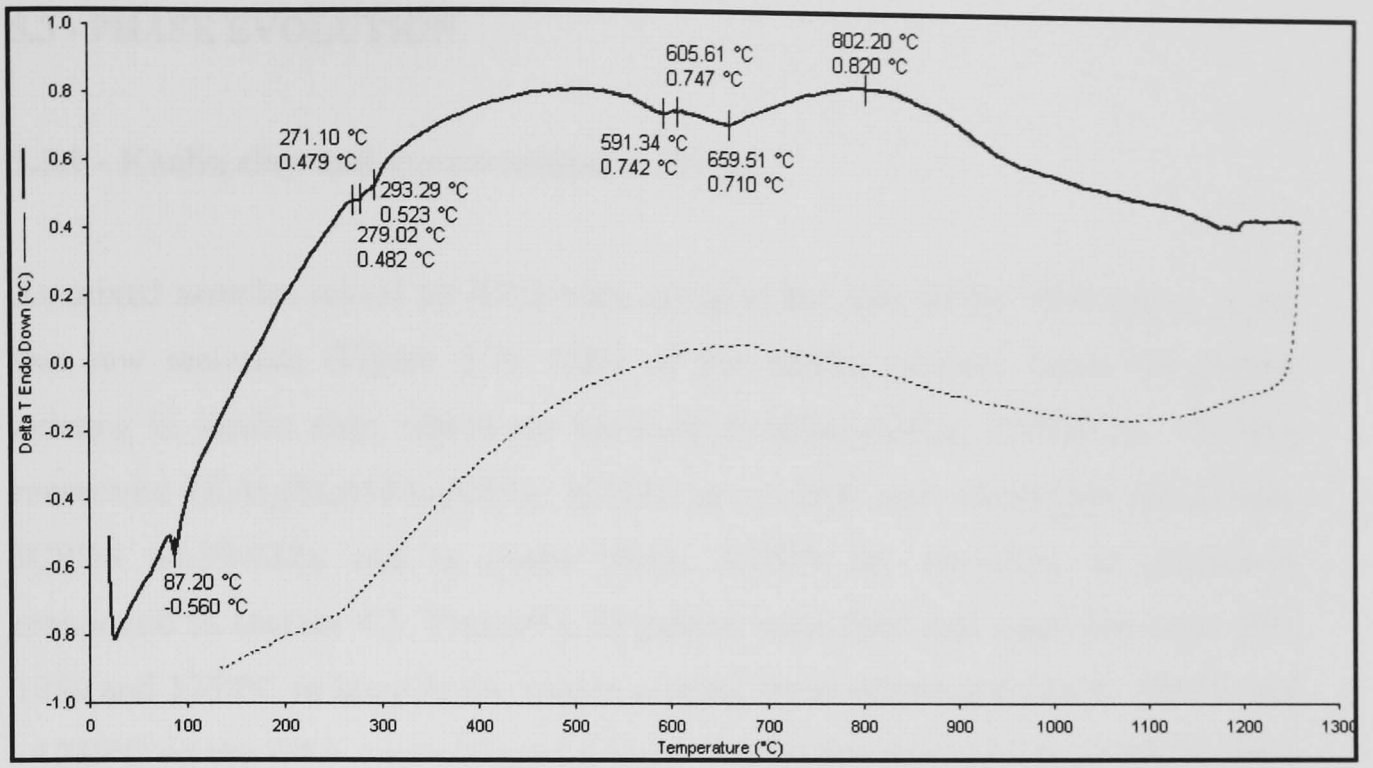

(a)

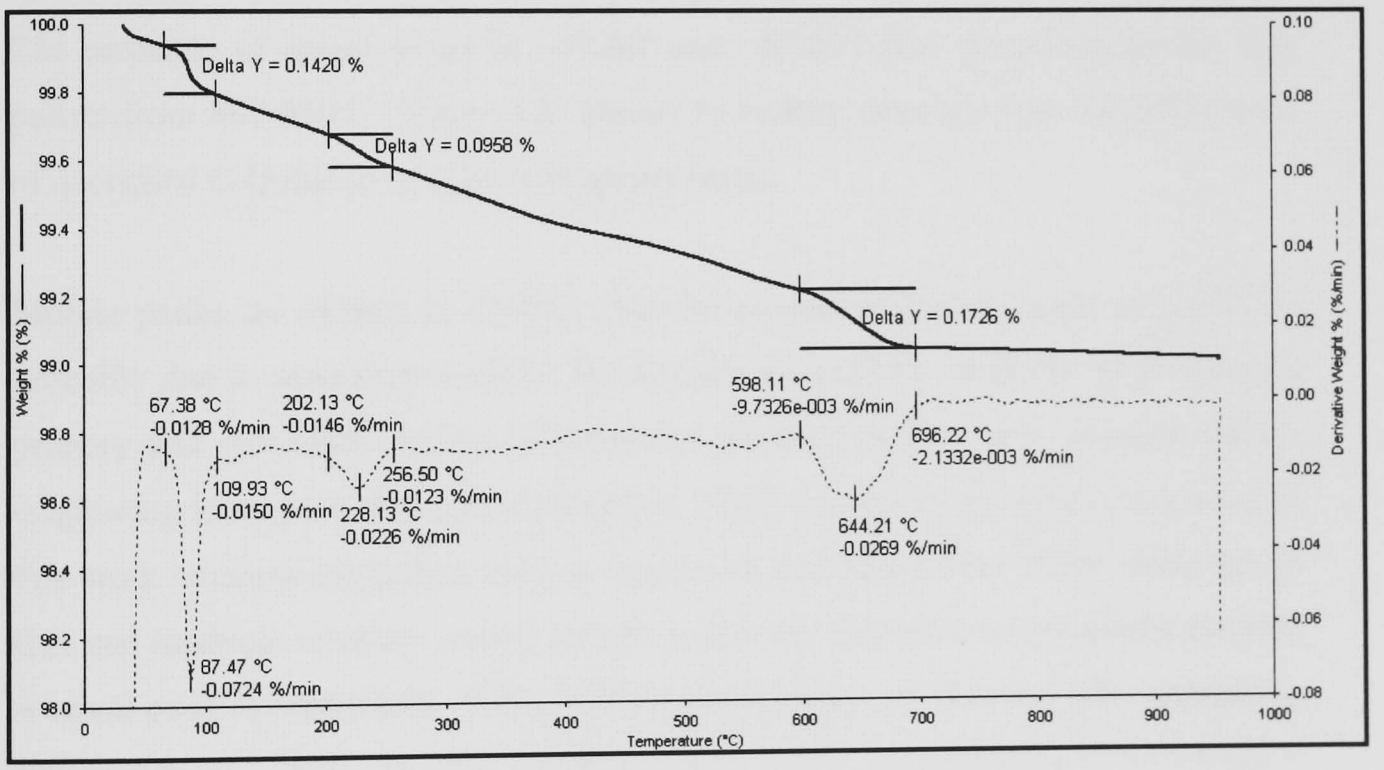

(b)

Figure 5.6 - DTA (a; — heating curve, --- cooling curve) and TG/DTG (b; — TG, --- DTG) of the nepheline syenite-SLS glass mixture.

5.3 - PHASE EVOLUTION

5.3.1 - Kaolin clay and quartz mixtures (C-Q)

As-mixed samples reveal an XRD trace equal to the sum of the XRD traces of the two raw materials (Figure 5.7). XRD of the unfired mixture shows the phases existing in kaolin clay, which are kaolinite ($Al_2Si_2O_5(OH)_4$, JCPDS no. 14-164), muscovite ($KAl_2(Si_3Al)O_{10}(OH)_2$, JCPDS no. 6-263) and microcline ($KAlSi_3O_8$, JCPDS no.19-932); and in quartz (SiO_2, JCPDS no. 46-1045), as previously mentioned in section 4.5. Pressed C-Q pellets were fired and quenched from 950, 1050 and 1250°C to identify the phases causing the exothermal peaks at ~990°C and ~1220°C on the DTA curve (Figure 5.1(a)). C-Q pellets quenched from 950°C show small mullite peaks ($Al_2Si_2O_5$, JCPDS no. 15-776) therefore the exothermic peak at 990°C results from the formation of primary mullite as discussed in chapter 4.1.1. The presence of spinel peaks at ~45.86° and ~67.03° after quenching kaolin clay pellets from 800-950°C (Figure 4.5) cannot be readily detected from the XRD trace of quenched C-Q due to overlap with quartz peaks.

Mullite peaks are evident at 1250°C, thus the second exothermic peak at 1220°C is probably due to secondary mullite. No distinction could be made by XRD between primary and secondary mullite. Without the presence of flux, only primary mullite originating from pure clay forms (Schuller, 1964). However, the kaolin clay used in this work contains impurities such as muscovite and microcline which could act as flux and facilitate mullite's crystal growth and/or the formation of secondary mullite. A small peak of cristobalite (SiO_2, JCPDS no. 82-512) was detected after quenching a sample from 1250°C. Its main diffraction peak is at a lattice spacing of 4.09Å (2θ = 21.69°), which according to Brindley and Ougland (1962) is indicative of a disordered lattice structure. This cristobalite is believed to crystallise from a highly-reactive viscous silica matrix forming concurrent with formation of the spinel-type phase and mullite (Carty and Senapati, 1998; McConville *et al.*, 1998). The low intensity of the cristobalite main XRD peak indicates its presence in small quantities, thus no thermal effect was observed from cristobalite in the DTA trace of C-Q. Quartz is relatively stable and remains unchanged until 1250°C. The displacive transition β to α-quartz (DTA trace, Figure 5.1(a)) confirmed its presence.

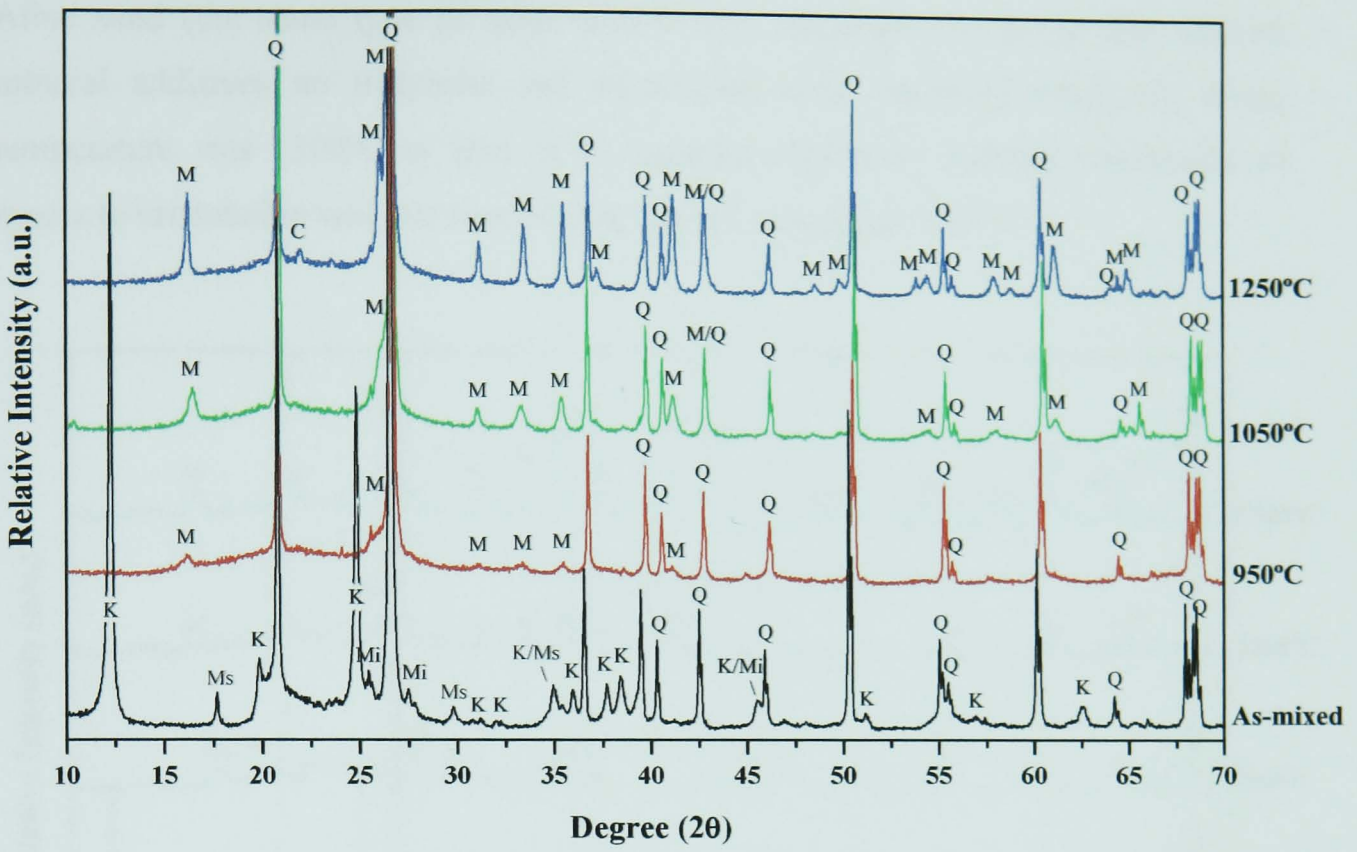

Figure 5.7 - XRD of mixtures of kaolin clay and quartz; as-mixed and fired pellets quenched from 950, 1050, and 1250°C (**C** – Cristobalite, 82-512, **K** – Kaolinite-1A, 14-164, **M** – Mullite, 15-776, **Mi** – Microcline, 19-926, **Ms** – Muscovite-2M#1, 6-263, **Q** – α-quartz, 46-1045).

Phase evolution of the C-Q mixture after firing and holding 3h at various firing temperatures, followed by natural cooling to room temperature, is shown in Figure 5.8. After soaking at 600°C for 3h, kaolinite disappears, semi-amorphous metakaolin forms while other phases remain unchanged. After heating to 1000°C, muscovite and microcline disappear.

Mullite was detected at 1000°C, with increasing peak intensity at higher temperatures. The cristobalite main peak was noticed in low intensity after heating for 3h at 1200°C. It is believed to form from the transformation of kaolin clay, and not from reconstructive transformation of quartz. After 3h soaking at 1200°C, quartz is still present in the as-mixed batch and remains unchanged. Quartz present in the C-Q mixture maintains the same relative intensity, indicating a low dissolution rate. The conversion of quartz takes considerable time and the rate of conversion depends on temperature, soaking time, particle size and the alkalis present (Ford, 1967). Hand *et al.* (1998) studied the transformation of quartz using both Iota quartz and Loch

Aline sand (the same type of sand used in this research) and found that without mineral additives no tridymite and cristobalite were produced when the firing temperature was 1300°C or less. It is expected, therefore, that the conversion of quartz to cristobalite will not occur during the 3h soaking at 1200°C.

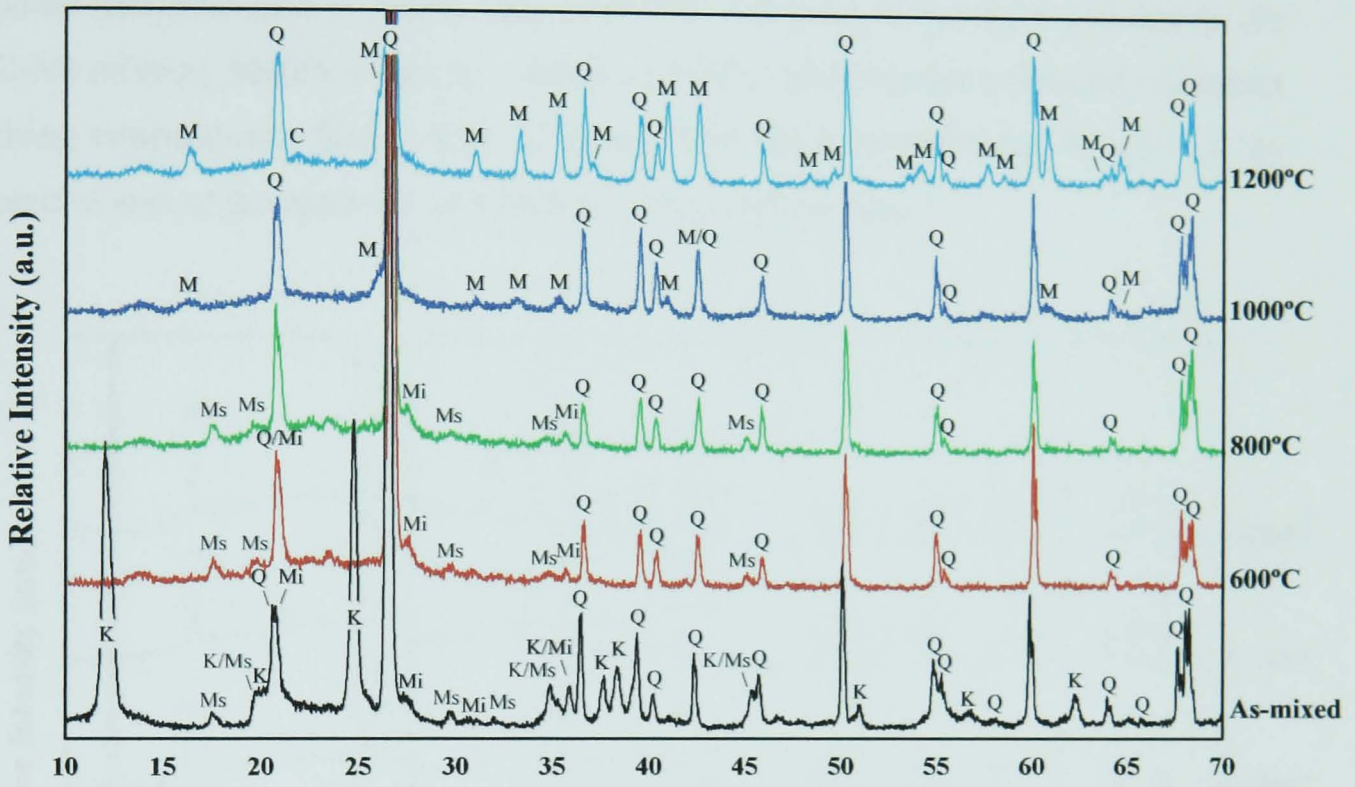

Figure 5.8 - XRD of mixtures of kaolin clay and quartz; as-mixed, fired 3h at 600, 800, 1000, and 1200°C and normally cooled (**C** – Cristobalite, 82-512, **K** – Kaolinite-1A, 14-164, **M** – Mullite, 15-776, **Mi** – Microcline, 19-926, **Ms** – Muscovite-2M#1, 6-263, **Q** – α-quartz, 46-1045).

5.3.2 - Kaolin clay and nepheline syenite mixtures (C-NS)

XRD of the as-mixed sample in the unfired state shows the mixture of constituents from kaolin clay and nepheline syenite. The composition of these two raw materials was discussed earlier in sections 4.5.1 and 4.5.3. Nepheline syenite usually contains small amounts of albite revealed by low intensity peaks in XRD (Figures 4.11 and 4.13). Because the 33.4wt% nepheline syenite content in the C-NS mixture leads to low albite content in this mixture, the albite peaks are difficult to detect. Powder from the C-NS mixture was pressed, fired and quenched from 950, 1050, 1150 and 1250°C to study its phase evolution and to assist in solving its DTA trace (Figure

5.2(a)). Samples quenched from 950°C show remaining microcline, nepheline and quartz from raw materials, as well as sanidine and low intensities of mullite and spinel peaks. Microcline, nepheline and sanidine disappear in the sample quenched from 1050°C, showing that all nepheline syenite components are completely melted by this temperature. The amorphous hump between 20-30° is evidence of liquid phase formation and is clearly seen at 1050°C. No trace of leucite was found in the C-NS mixture. Mullite peaks are evident at 1050°C and increase in intensity at higher firing temperatures. Slight shifts in these XRD traces occurred due to error in the precise zero of the machine, and such error was not corrected.

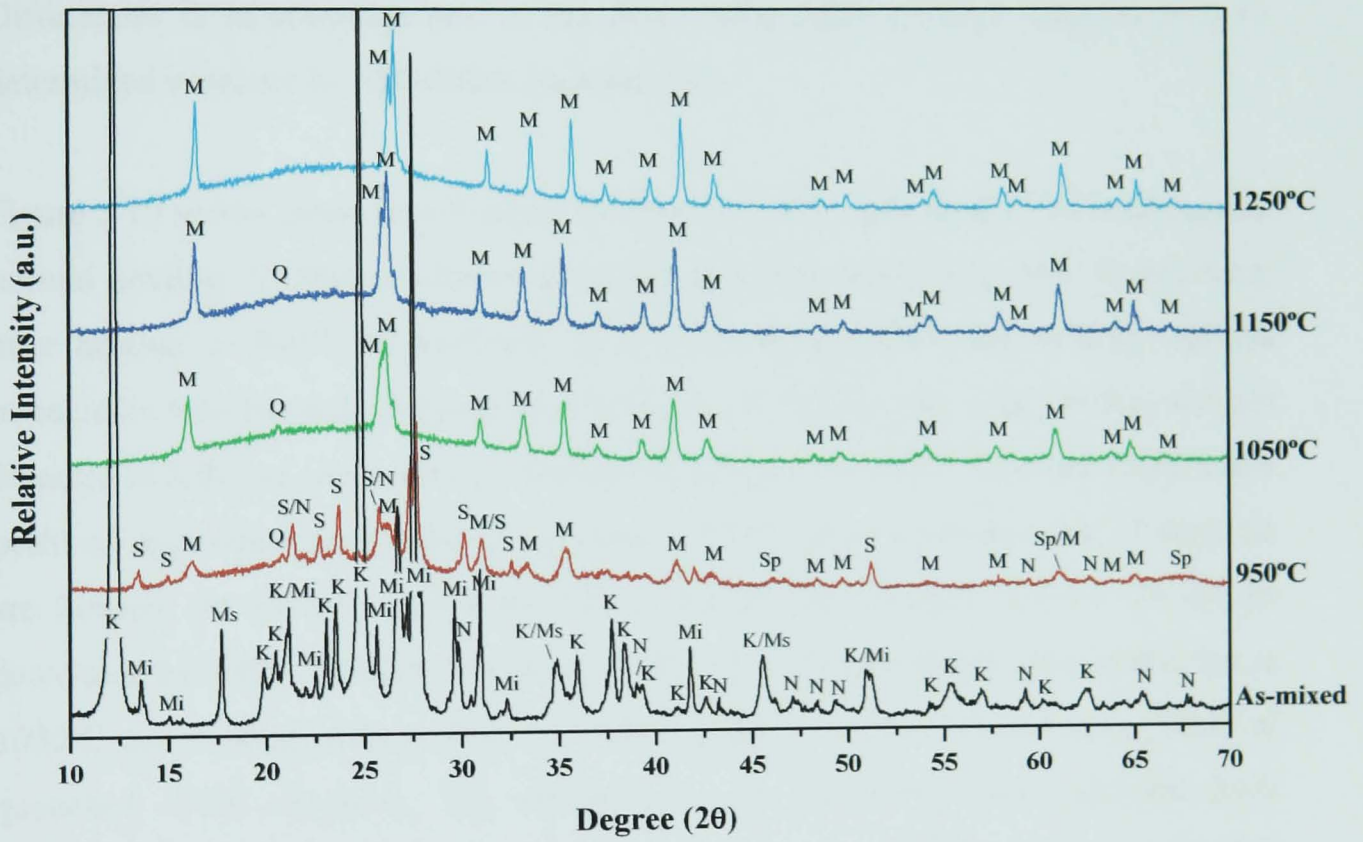

Figure 5.9 - XRD of mixtures of kaolin clay and nepheline syenite. As-mixed and fired pellets quenched from 950, 1050, 1150, and 1250°C are shown (**K** – Kaolinite-1A, 14-164, **M** – Mullite, 15-776, **Mi** – Microcline, 19-926, **Ms** - Muscovite-2M#1, 6-263, **N** – Nepheline, 35-424, **Q** – α-quartz, 46-1045, **S** – Sanidine, 19-1227, **Sp** – γ-alumina spinel, 10-425).

Comparing intensities of mullite peaks in the C-NS mixture with those from the C-Q mixture suggests that mullite is more abundant in the former case when fired to the same firing temperatures (≥950°C). This is thought to be due to the fluxing action of nepheline syenite which dissolves clay and accelerates the formation of liquid at

lower firing temperatures, thus advancing the mullite growth. According to Lundin (1954), Schuller (1964) and Iqbal and Lee (2000), secondary mullite originates from reaction of clay and feldspars at a reaction inter-layer between the feldspar and clay relicts. Therefore not only primary mullite but also secondary mullite should be found in this mixture after firing until liquid phase is formed. The formation of secondary mullite in the C-NS mixture should then occur at lower temperatures than in C-Q which has only small amounts of alkali impurities to facilitate formation of this type of mullite. This is associated with the presence of a second exotherm at ~1140°C for C-NS (Figure 5.2(a)) and ~1225°C for C-Q (Figure 5.1(a)). The two types of mullite (primary and secondary) cannot be distinguished by XRD. Differences in morphology and in the Al_2O_3:SiO_2 ratio of these mullites may be determined however by SEM/EDS (section 5.4).

Figure 5.10 shows phase development on firing a C-NS mixture after 3h soaking and normal cooling. Similar to observations in individual kaolin clay or C-Q mixtures, after heating to 600°C all kaolinite XRD peaks disappeared and semi-amorphous metakaolin was formed. Metakaolin reflections are diffuse and weak, so they are not detected in XRD of any heated kaolin clay (Santos *et al.*, 2005). The main diffraction peaks of microcline have reduced intensity at 800°C when trace amounts of sanidine are formed. At 1000°C, nepheline and muscovite have melted and are no longer detectable by XRD. Sanidine begins to melt as shown by reduced peak intensities at 1000°C and is completely melted by 1200°C (actually 1050°C as shown by XRD of quenched C-NS samples). The existence of an amorphous phase derived from viscous liquid is evidenced by the increased hump ~25° in XRD of mixtures fired at ≥1000°C. Leucite does not form even though samples were left 3h soaking at 1000°C, the same firing temperature at which leucite was found when firing nepheline syenite pellets alone (see Figure 4.14). It seems that microcline prefers to melt and form liquid phase which later interacts with the surrounding decomposed clay, to transforming to leucite. This is possible due to the concentration gradient of alkali that controls this phenomenon.

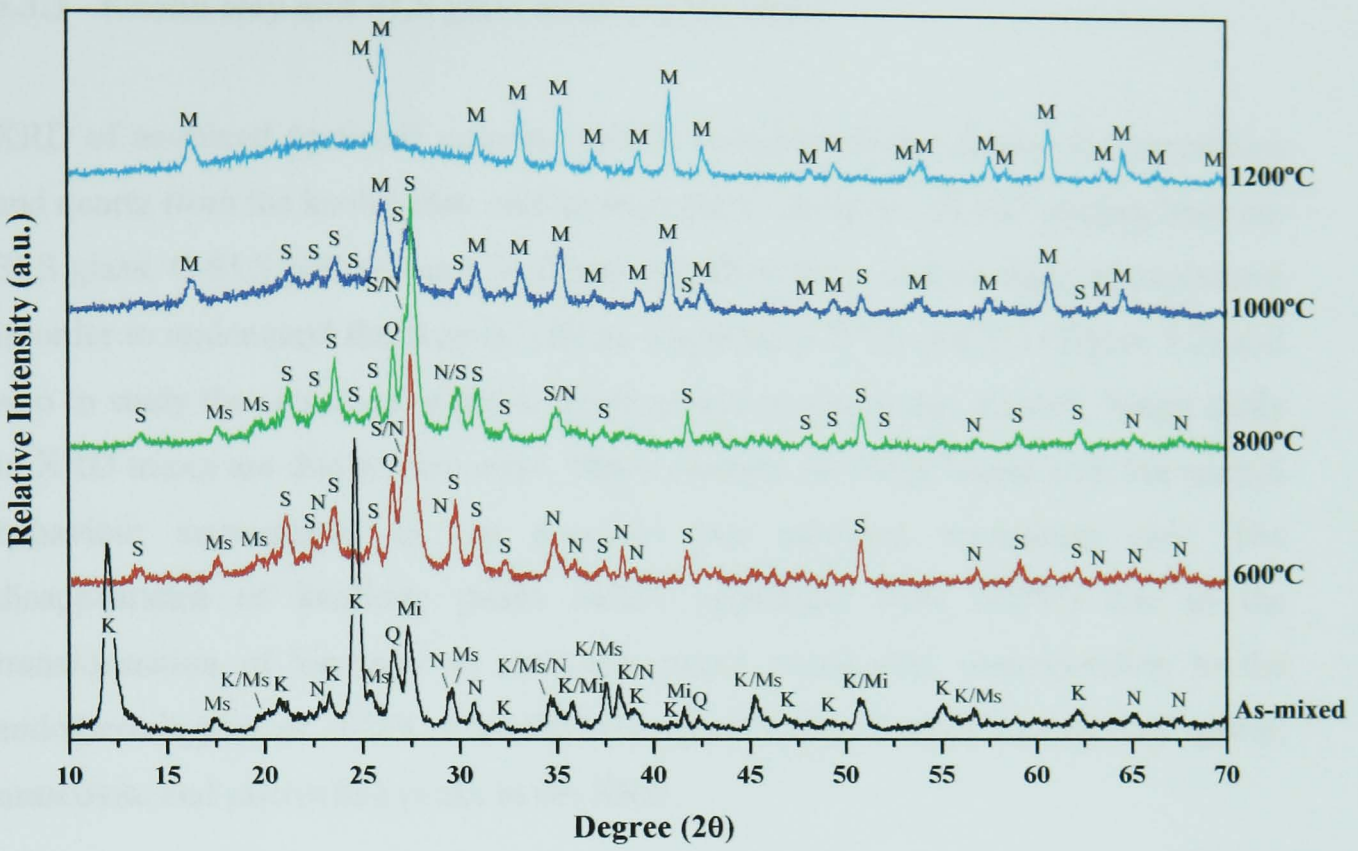

Figure 5.10 - XRD of mixtures of kaolin clay and nepheline syenite; as-mixed and fired 3h at 600, 800, 1000, and 1200°C and normally cooled are shown (K – Kaolinite-1A, 14-164, **M** – Mullite, 15-776, **Mi** – Microcline, 19-926, **Ms** - Muscovite-2M#1, 6-263, **N** – Nepheline, 35-424, **Q** – α-quartz, 46-1045, **S** – Sanidine, 19-1227).

The first interaction detected by XRD between these two constituents occurs when liquid from nepheline syenite melting dissolves quartz impurity from the clay. The diffraction peaks of quartz reduce and disappear with increasing firing temperature from 800-1200°C (Figure 5.10). Since no cristobalite peaks were present in these XRD traces, all dissolved quartz went to the liquid phase. Molten nepheline syenite is also expected to dissolve any cristobalite developed from the highly reactive amorphous silica given off by the break up of the kaolinite lattice. Another interaction which is thought to occur before those mentioned above but cannot be detected by XRD is the interaction between the liquid from melting nepheline syenite and metakaolin. Mullite was detected at 1000°C, and the intensity of its diffraction peaks increased at higher temperatures.

5.3.3 - Kaolin clay and SLS glass mixtures (C-SLS)

XRD of as-mixed (unfired) samples reveals kaolinite, minor muscovite, microcline and quartz from the kaolin clay, and an amorphous hump at ~20-30° coming from the SLS glass. C-SLS pellets were fired and quenched from various firing temperatures in order to understand the thermal effects observed in DTA and TG (Figure 5.3) and also to study the sequence of phase development on firing this mixture. Slight shifts in XRD traces are due to zero error. Phase changes on firing began with the normal behaviour encountered in the previous two mixtures containing clay. The disappearance of kaolinite peaks (when quenching from 600°C) due to the transformation of kaolinite to semi-amorphous metakaolin corresponding to the endothermic peak at ~522°C from the DTA trace (Figure 5.3(a)), leaving only quartz, muscovite and microcline peaks in the XRD.

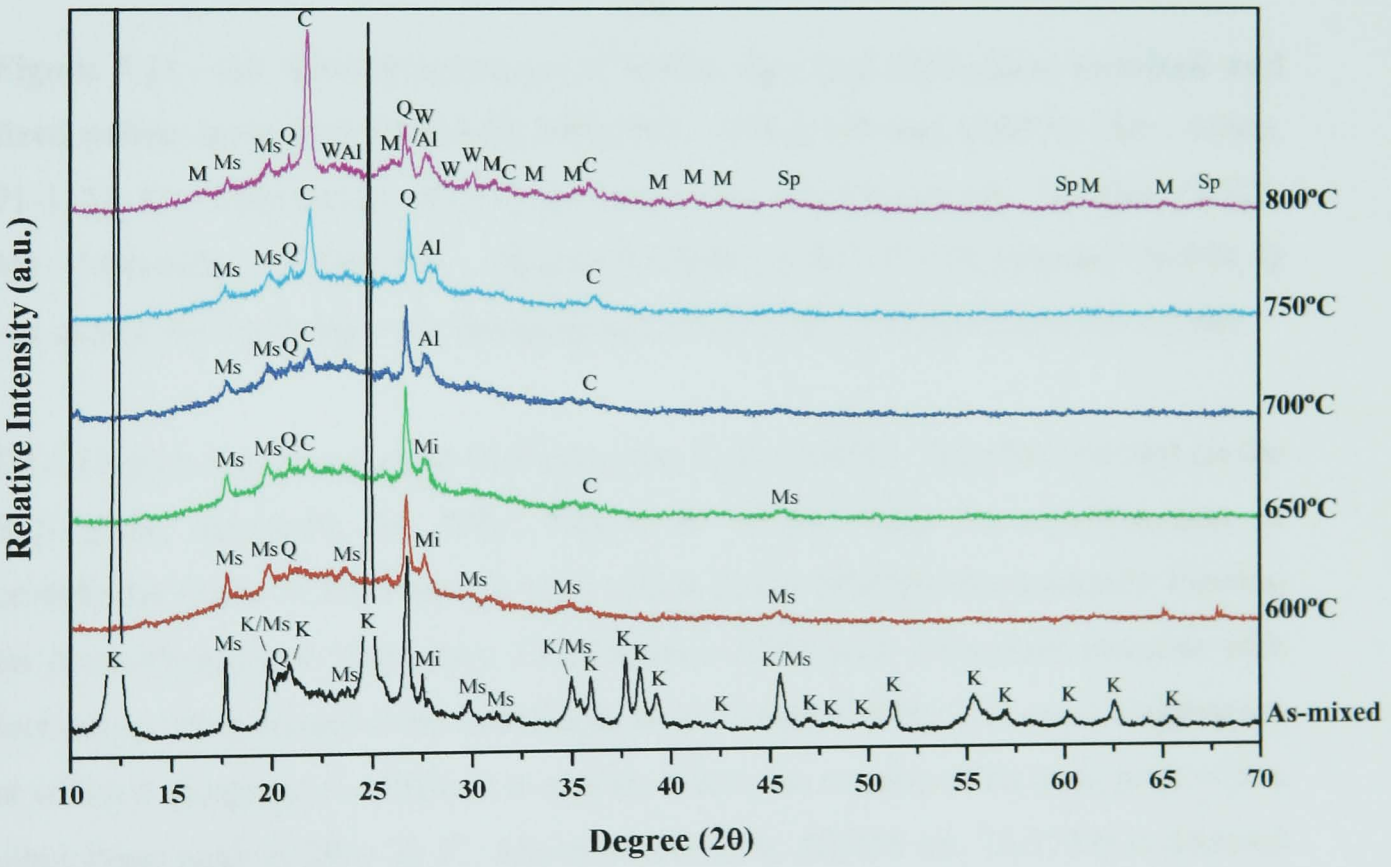

(a)

Figure 5.11 - (a) XRD of mixtures of kaolin clay and SLS glass; as-mixed and fired pellets quenched from 600, 650, 700, 750 and 800°C. (**Al** – Albite, 71-1153, **C** – Cristobalite, 82-512, **K** – Kaolinite-1A, 14-164, **M** – Mullite, 15-776, **Mi** – Microcline, 19-926, **Ms** – Muscovite-2M#1, 6-263, **P** – Plagioclase, 20-528, **Q** – α-quartz, 46-1045, **Sp** – γ-alumina spinel, 10-425, **W** – Wollastonite-2M, 27-88).

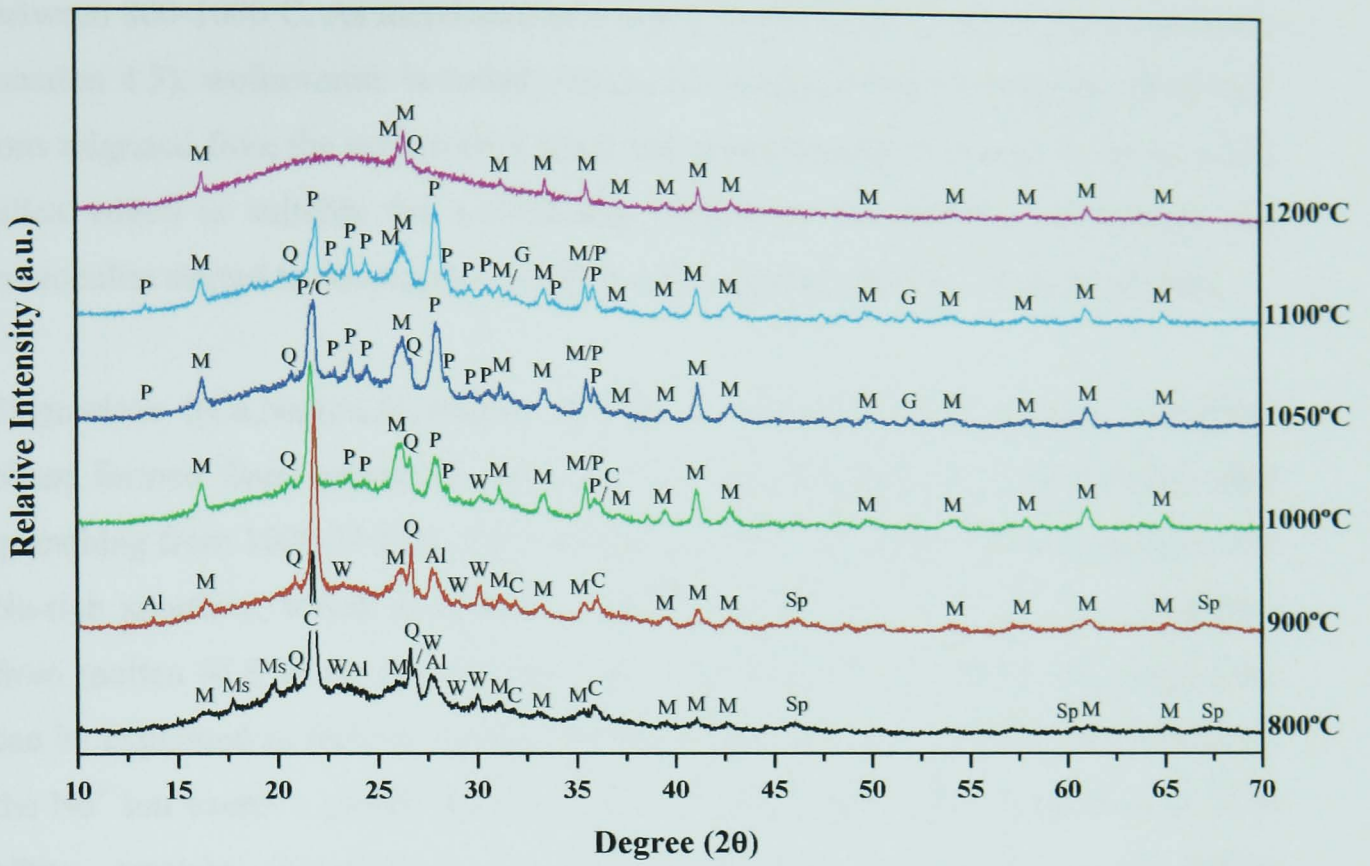

(b)

Figure 5.11 - (b) XRD of mixtures of kaolin clay and SLS glass; as-mixed and fired pellets quenched from 800, 900, 1000, 1050, 1100 and 1200°C. (**Al** – Albite, 71-1153, **C** – Cristobalite, 82-512, **K** – Kaolinite-1A, 14-164, **M** – Mullite, 15-776, **Mi** – Microcline, 19-926, **Ms** – Muscovite-2M#1, 6-263, **P** – Plagioclase, 20-528, **Q** – α-quartz, 46-1045, **Sp** – γ-alumina spinel, 10-425, **W** – Wollastonite-2M, 27-88).

DTA (Figure 4.4) reveals that SLS glass has T_g at ~563°C. The effect of heat on the SLS glass, detectable by XRD, begins at ~650°C with the crystallization of cristobalite (SiO_2, JCPDS no. 82-512), which is a crystalline phase usually forming on devitrification of SLS glass. Cristobalite's XRD peak intensities increase with increasing firing temperature, and disappear at ~1100-1200°C. The exact temperature at which it disappears is difficult to specify due to the overlap of its main peak with a plagioclase peak at $2\theta = 21.7°$. Albite ($NaAlSi_3O_8$, JCPDS no. 71-1153) is detected in the C-SLS mixture quenched from 700-900°C, and because this phase contains Al_2O_3 it is therefore believed to be the first phase developed from the interaction between both components from the C-SLS mixture. It was probably formed from the Na^+ ions migrating from molten SLS glass which react with Al_2O_3 and SiO_2 supplied from the surrounding metakaolinite. Wollastonite ($CaSiO_3$, JCPDS no 27-88), another common crystalline phase from the devitrification of SLS glass, is evident

between 800-1000°C. As mentioned previously in the XRD results of fired SLS glass (section 4.5), wollastonite is usually formed in a region high in calcium. After Na^+ ions migrated from the molten SLS glass, this glass became very high in calcium and silica which is suitable for wollastonite formation. At 1000°C, wollasonite and cristobalite started to decompose, as detected by decreasing XRD peak intensities.

Plagioclase ($(Ca,Na)(Al,Si)_2Si_2O_8$, JCPDS no. 20-528) is the second crystalline phase formed from interaction between clay and SLS glass and is detected after quenching from 1000-1100°C. XRD (Figure 5.11) reveals the plagioclase present is a Na-rich anorthite, which is a reaction product of the Na^+ and Ca^{2+} ions migrating from molten SLS to the decomposed clay. The formation of albite and plagioclase can be explained as follows. During the heating of SLS glass in this C-SLS mixture, the Na^+ ion exerts a greater affinity than Ca^{2+} to combine with metakaolin to form albite crystals ($NaAlSi_3O_8$) instead of anorthite ($CaAl_2Si_3O_8$). At higher temperatures, Ca^{2+} ions possibly migrating from molten SLS glass and from dissolved wollastonite displace some Na^+ ions from albite molecules, which go into solid solution with the remaining $NaAlSi_3O_8$ crystals during crystallisation giving rise to plagioclase. Plagioclase can be identified by its main peaks at 3.19 Å, 3.21 Å, 3.18 Å, 4.04 Å and 3.77 Å (2θ = 27.89°, 27.75°, 28.03°, 21.98° and 3.77° respectively). It disappears in samples quenched from 1200°C.

Mullite appears at ≥800°C. Its XRD peaks have low intensities compared to those detected in the C-Q and C-NS mixtures at the same firing temperatures. The lower relative intensity of mullite peaks in the C-SLS mixture is probably due to the lower alumina content in the mixture, and also to the formation of albite and later plagioclase at the expense of the alumina from clay, decreasing the alumina content available for mullite formation. After quenching from 1200°C, only mullite, remnant quartz and glassy phase are present.

XRD analysis of the mixture of clay and SLS glass before and after firing for 3h at 600, 800, 1000, and 1200°C is shown in Figure 5.12. After firing to 600°C, holding for 3h and normally cooling to room temperature, the remaining crystalline phases are muscovite, microcline and quartz. In addition to muscovite, microcline and quartz, four new crystalline phases: cristobalite, wollastonite, albite and mullite were

identified in the C-SLS mixture fired at 800°C, similarly to those found in quenched samples from the same temperature. Formation of devitrite was observed in the XRD trace of SLS fired 3h at 800°C (Figure 4.16), and of SLS quenched from 700-800°C (Figure 4.14). Nonetheless, devitrite was not observed in the mixture of C-SLS fired at the same temperature. The concentration gradient of sodium in the C-SLS mixture, forcing Na^+ ions from SLS glass to migrate to the clay surrounding, may have suppressed the formation of devitrite in SLS glass particles. Such a chemical concentration gradient is not expected to be present in the pure SLS sample.

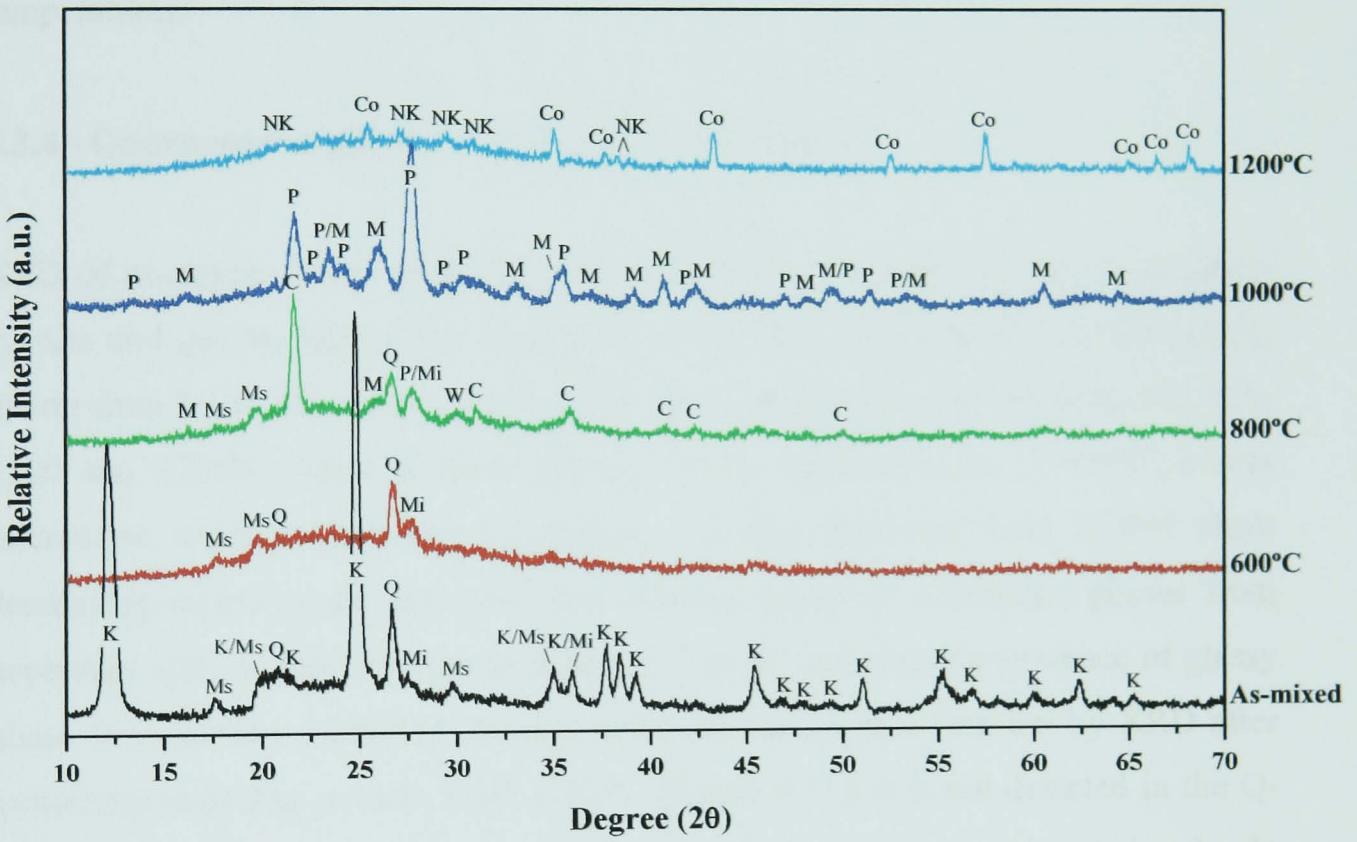

Figure 5.12 - XRD of mixtures of kaolin clay and SLS glass; as-mixed and pellets fired 3h at 600, 800, 1000, and 1200°C and normally cooled are shown (**Al** – Albite, 71-1153, **C** – Cristobalite, 82-512, **Co** – Corundum, 46-1212, **K** – Kaolinite-1A, 14-164, **M** – Mullite, 15-776, **Mi** – Microcline, 19-926, **Ms** – Muscovite-2M#1, 6-263, **NK** – Nepheline, 9-338, **P** – Plagioclase, 20-528, **Q** – α-quartz, 46-1045, **W** – Wollastonite-2M, 27-88).

Muscovite, microcline and quartz were originally present in the clay. The Na_2O-CaO-SiO_2 phase diagram (Figure 2.9) suggests that cristobalite and wollastonite should crystallise from SLS glass. When the firing temperature reaches 1000°C, the amount of cristobalite decreases and wollastonite, muscovite, microcline, quartz and

albite disappear, being replaced by mullite and plagioclase. Higher plagioclase peak intensities compared to those of quenched samples is due to the holding time of 3h, indicating its formation is soaking time (kinetics) dependent. On further increasing the firing temperature to 1200°C, mullite and plagioclase disappear. A K-rich nepheline (potassium-sodium aluminosilicate) which normally crystallises from glass that is high in potassium and sodium forms. Potassium present in the glass derives from muscovite and microcline being dissolved when heated above 1000°C. The corundum peaks present in the mixture fired at 1200°C arise from the alumina powder used to prevent samples from sticking to the crucible when firing at high temperatures.

5.3.4 - Quartz and nepheline syenite mixtures (Q-NS)

XRD of as-mixed Q-NS samples shows the mixture of phases present in nepheline syenite and quartz. Microcline, nepheline and albite from nepheline syenite and α-quartz from Loch Aline sand. Q-NS pellets were fired and quenched from 800, 900, 1100 and 1200°C. Most of these phases remain unchanged up to 900°C, except microcline which transformed to sanidine. Samples quenched from 1100°C show decreasing quartz peaks and only tiny remnant peaks of crystalline phases from nepheline syenite. The amorphous hump at ~20-30° indicates the presence of glassy phase from molten nepheline syenite. Although leucite was detected by XRD after quenching nepheline syenite from 1100°C (Figure 4.11), it is not detected in the Q-NS mix. Crystalline phases from nepheline syenite were no longer detected and only remnant quartz and glass are present in the XRD of samples quenched from 1200°C.

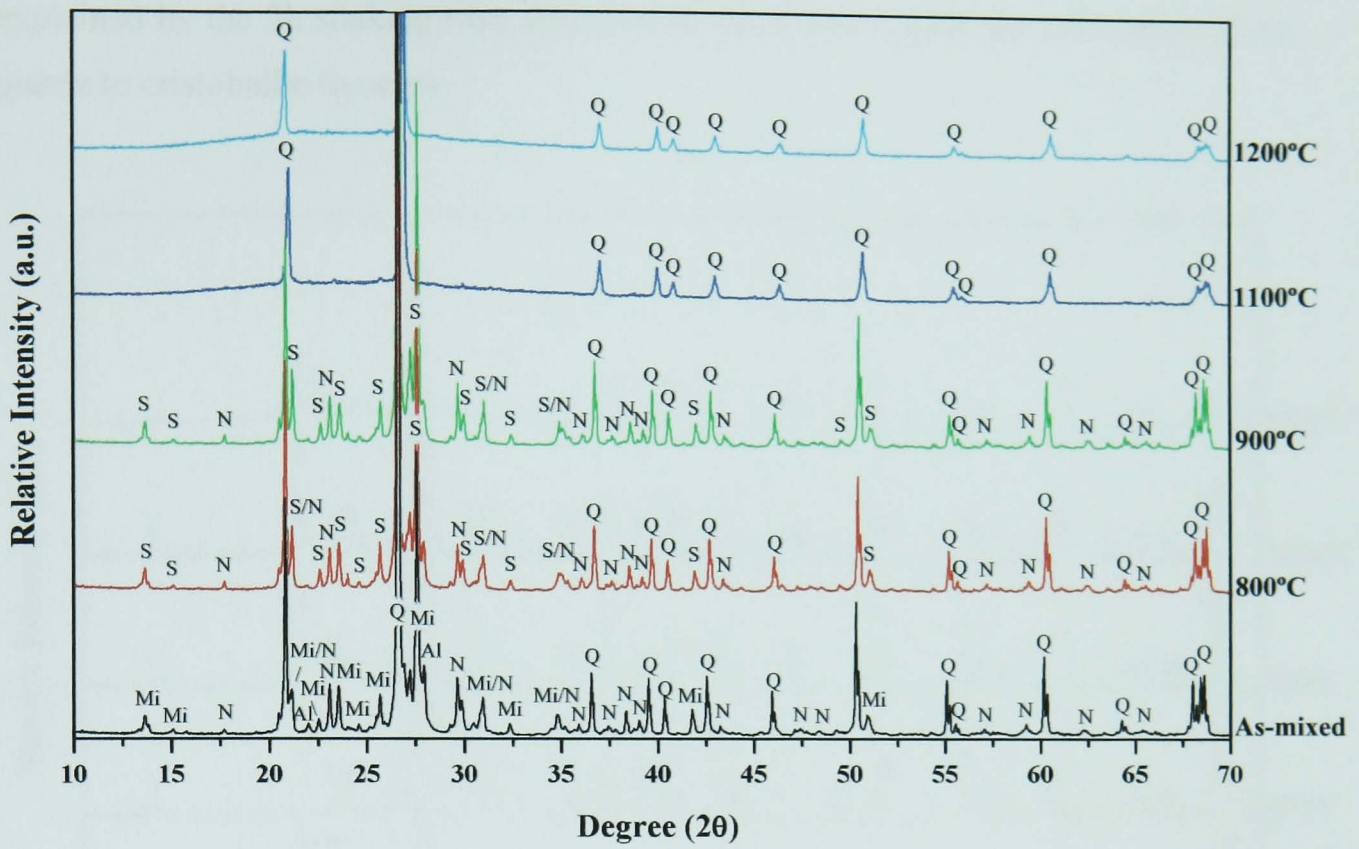

Figure 5.13 - XRD of mixtures of quartz and nepheline syenite; as-mixed and fired pellets quenched from 800, 900, 1100, and 1200°C are shown (**Al** – Albite, 9-466, **C** – Cristobalite, 39-1425, **Mi** – Microcline, 19-932, **N** – Nepheline, 35-424, **S** – Sanidine, 19-1227, **Q** – α-quartz, 46-1045).

The phase transformation sequence observed when Q-NS was fired and held for 3h before cooling (at 10°C/min) to room temperature is shown in Figure 5.14. No interaction between quartz and nepheline syenite was observed by XRD at low firing temperatures. Interactions were detected when nepheline syenite melted at temperatures above 1000°C and molten nepheline syenite in contact with quartz particles led to their dissolution. Decreasing intensity of the quartz diffraction peaks at firing temperatures between 1000-1200°C was observed. Lundin (1954) reported that if enough quartz is present to saturate the melt with silica, its dissolution stops and the remaining quartz transforms partially into cristobalite (some SiO_2 remains in the glass). Cristobalite (SiO_2, JCPDS no. 39-1425) was formed in the Q-NS mixture when heated to 1200°C and soaked for 3h. Remnant quartz and cristobalite are the only crystalline phases present after firing 3h at 1200°C. No cristobalite peak was detected from Q-NS quenched from 1200°C due to the lack of time for conversion of quartz to cristobalite. The fact that cristobalite was identified in Q-NS pellets fired 3h at 1200°C and slowly cooled (Figure 5.14) (and not in the quenched samples) can be

explained by the 3h soaking time and slow cooling allowed for the conversion from quartz to cristobalite to occur.

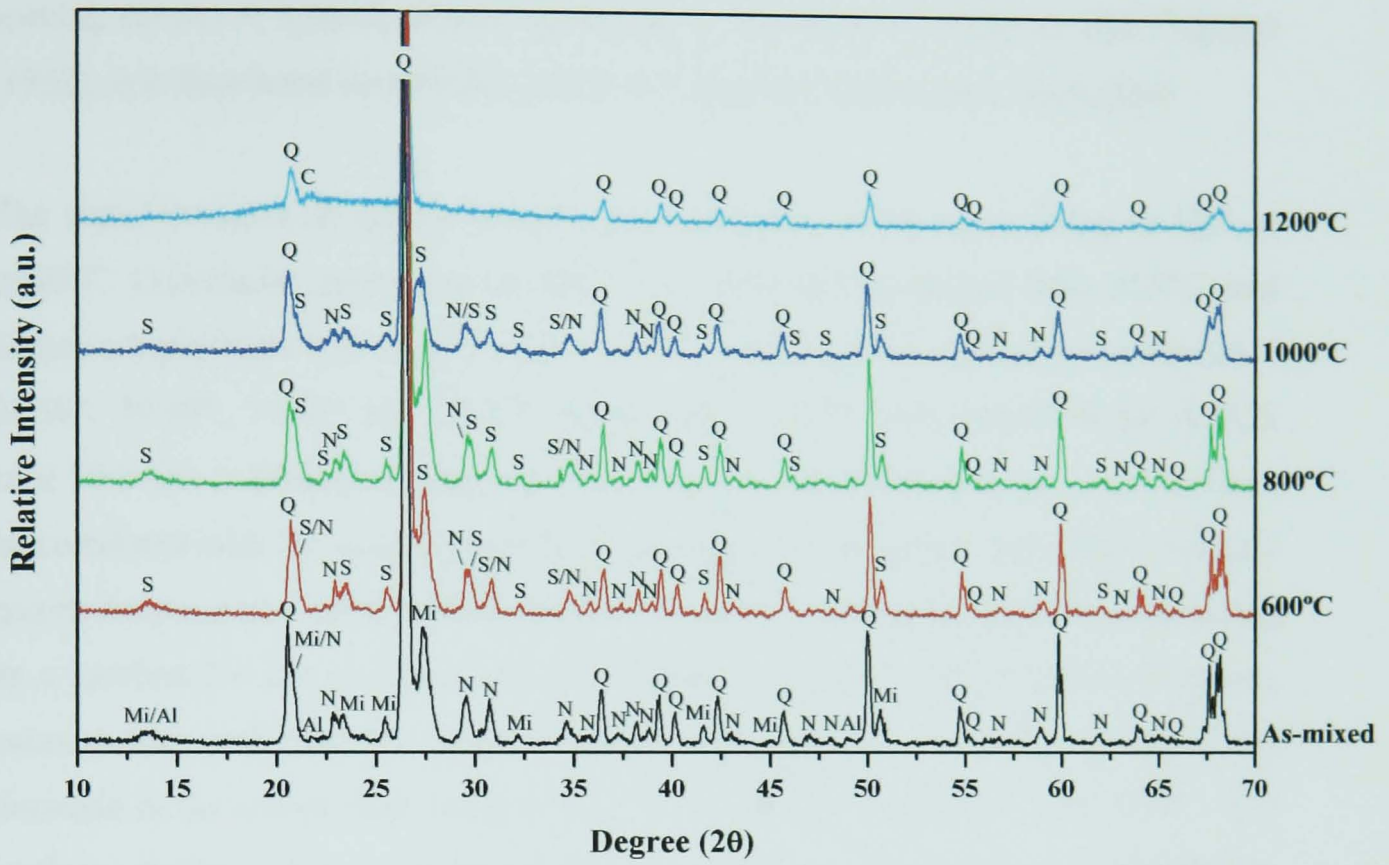

Figure 5.14 - XRD of mixtures of quartz and nepheline syenite; as-mixed, fired 3h at 600, 800, 1000, and 1200°C and normally cooled are shown (**Al** – Albite, 9-466, **C** – Cristobalite, 39-1425, **Mi** – Microcline, 19-932, **N** – Nepheline, 35-424, **S** – Sanidine, 19-1227, **Q** – α-quartz, 46-1045).

5.3.5 - Quartz and SLS glass mixtures (Q-SLS)

The mineralogical changes of Q-SLS mixtures as a function of temperature are summarized using XRD traces of samples quenched from specific firing temperatures as shown in Figure 5.15. The as-mixed powder shows the quartz peaks and the amorphous hump of SLS glass at 2θ ~20-30°. The XRD traces remain relatively unchanged up to 700°C. After heating to 750°C, SLS glass devitrified to cristobalite (SiO_2, JCPDS no. 82-512) and wollastonite ($CaSiO_3$, JCPDS no. 27-88). The cristobalite formed at 750°C must result from devitrification of SLS glass and not from quartz transformation because this firing temperature is too low for conversion of quartz to cristobalite. Moreover, analysis of quenched SLS (Figure 4.14) and quenched C-SLS (Figure 5.11), cristobalite and wollastonite are always the

main crystalline phases formed from molten SLS glass. A main cristobalite peak at 4.08 Å (2θ = 21.8°) confirms its presence. Cristobalite has a lattice spacing d(101) = 4.04 Å in the well crystallized form. Cristobalite formed below 900°C has a lattice spacing d(101) = 4.08 Å which, according to the work of Brindley and Ougland (1962), is a disordered cristobalite which normally devitrifies from silica glass.

The transformation of quartz to cristobalite possibly starts when firing Q-SLS at ≥900°C. Cristobalite present in the XRD trace of Q-SLS quenched from 900°C and higher temperatures has 4.04 Å, 2.48 Å, 2.84 Å, and 3.14 Å diffraction peaks (2θ = 21.98°, 36.08°, 31.46° and 28.44° respectively) which were identified by JCPDS card 39-1425. It formed through the reconstructive transformation of quartz and can be correlated with the concomitant decrease of the quartz peaks' intensities. As pure quartz does not convert to cristobalite below 1300°C, SLS glass appears to be acting as a catalyst for this process. The cristobalite is formed at the expense of quartz, consequently reducing the quartz content of the mixture on firing. A significant decrease in the quartz peak intensity was observed after quenched from 900°C. It is unclear whether quartz is dissolving into the melt then recrystallizing as cristobalite, or transforming directly to cristobalite from the solid state. The conversion of quartz to cristobalite was, however, suggested by Sosman (1965) and Stevens *et al* (1997) to occur via an amorphous phase.

Comparing Q-SLS mixtures to Q-NS mixtures, the conversion of quartz to cristobalite is not present in Q-NS quenched from 1200°C or below. Even though Q-NS samples were held 3h at 1200°C, only tiny cristobalite peaks are present. The explanation for this may be related to the higher melting point of nepheline syenite. Nepheline syenite usually melts above 1000°C, thus the Q-NS sample has to be fired above 1000°C before alkalis from the molten nepheline syenite will react with the surrounding quartz. The conversion of quartz to cristobalite in Q-SLS mixtures can occur at lower temperature due to the fact that the SLS glass used in this study softens at low temperature (>563°C), and alkalis from molten SLS glass hasten (or mineralize) the conversion of quartz.

After heating to 1250°C, little quartz remains and tridymite (SiO_2, JCPDS no. 18-1170) is starting to be detected (Figure 5.15). It transforms from cristobalite and is

observed by the development of the 4.33 Å (2θ = 20.5°) and 3.82 Å (2θ = 23.3°) diffraction peaks.

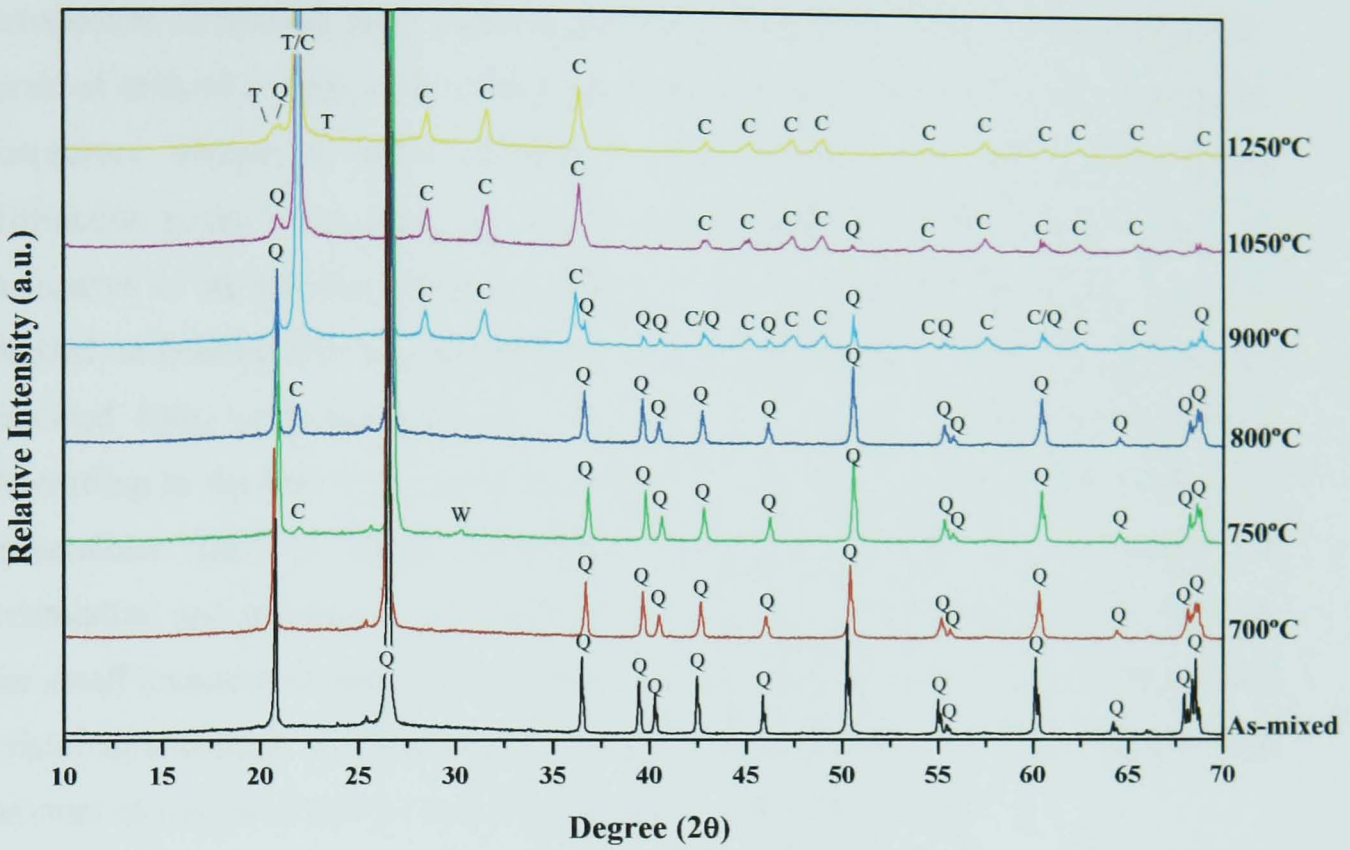

Figure 5.15 - XRD of mixtures of quartz and SLS glass; as-mixed and fired pellets quenched from 700, 750, 800, 900, 1050, and 1250°C are shown (C – Cristobalite, 82-512/39-1425, **Q** – α-quartz, 46-1045, **T** – Tridymite, 18-1170, **W** – β-wollastonite, 27-88).

When Q-SLS pellets were fired and left soaking for 3h before cooling to room temperature, the phase transformation sequence is more clearly detected (Figure 5.16). After heating Q-SLS mixtures 3h at 800°C, SLS glass devitrified to cristobalite, wollastonite and devitrite ($Na_2Ca_3Si_6O_{16}$, JCPDS no. 77-410). Devitrite is not detected in quenched samples probably due to insufficient time for crystallization to occur. At higher firing temperature, quartz changes to cristobalite resulting in decreased intensity of the quartz peaks. Quartz is present until 1000°C and can be easily identified by the 3.34 Å (2θ = 26.64°) and 1.81 Å (2θ = 50.14°) diffraction peaks. After firing 3h at 1200°C no quartz peaks remain.

With 3h holding time XRD (Figure 5.16) clearly shows formation of tridymite after cristobalite. XRD of samples fired at 1000°C shows three characteristic peaks of

tridymite at 20.5, 21.6 and 23.3° in addition to the 21.8° peak of cristobalite. The polymorph of tridymite was identified as a monoclinic form by comparing the peaks at 20-40° with those of the JCPDS data of tridymite-M. The original 4.04 Å cristobalite diffraction peak shifts toward 4.11 Å at $2\theta = 21.6°$, which is the main peak of tridymite. When the firing temperature was raised to 1200°C, cristobalite intensities decreased while tridymite intensities increased and much sharper diffraction peaks were observed. The decreased peak intensities of cristobalite are indicative of its transformation to tridymite. The formation of tridymite seems to depend on holding time and temperature as indicated by the low amount of tridymite detected from quenched samples even after high firing temperatures (1250°C). According to Stevens *et al.* (1997), soaking time, firing temperature and amount of mineralizer (such as alkali carbonates) were important factors in formation of cristobalite and tridymite. Cristobalite was found to be the dominant phase formed for small amounts of mineralizer, and when the amount of mineralizer increased, the cristobalite content decreased and a large amount of tridymite was formed. The amount of tridymite also increased with increasing soaking time.

The conversion of quartz into tridymite under the effect of various mineralizers has been extensively studied. Holmquist (1961) found that alkali oxides lead to the formation of tridymite with cristobalite as a possible intermediate transition product. The Si-O distances in quartz and cristobalite are nearly identical, being 1.62 and 1.63 Å, respectively. The Si-O distance in tridymite is 1.54 Å, so that a greater amount of energy would be required to bring about formation of tridymite than cristobalite from quartz. The necessary structural changes to the crystal lattices in going from quartz to cristobalite appear to be less than those required in the change from quartz to trydimite. Stevens *et al.* (1997) stated that tridymite is not a stable phase of pure silica. It never forms from pure quartz and the conversion of quartz to tridymite only occurs when alkalis are present. Cristobalite and tridymite have lower densities than quartz (see Table 2.2) and hence a more open structure. The voids in their structure are large enough to accommodate atoms such as sodium, potassium and calcium which also help stabilize the structure. Tridymite especially requires alkalis to stabilise its structure and cannot exist without them. Stevens *et al.*(1997) also stated that cristobalite formed in the presence of alkalis was disordered and contained stacks of tridymite in regions of high alkali concentration and this disordered

cristobalite then converted to tridymite in the presence of high alkalis with enough soaking time. The transformation will occur as follows:

Quartz→ Disordered Cristobalite → Tridymite

Hrma *et al*. (2002) stated that tridymite is a phase which crystallizes from all glasses in which the SiO_2 content >75.3wt%. The SLS glass used in this research has a SiO_2 content of 73.96wt%, possibly ruling out tridymite as a devitrification product from this SLS glass. This is consistent with XRD of fired SLS glass (Figure 4.14 and 4.16) which show no trace of tridymite. Q-SLS mixtures have a total SiO_2 content of ~86.88wt%, therefore when quartz dissolved, the silica content in the liquid phase increased beyond the limit for tridymite formation.

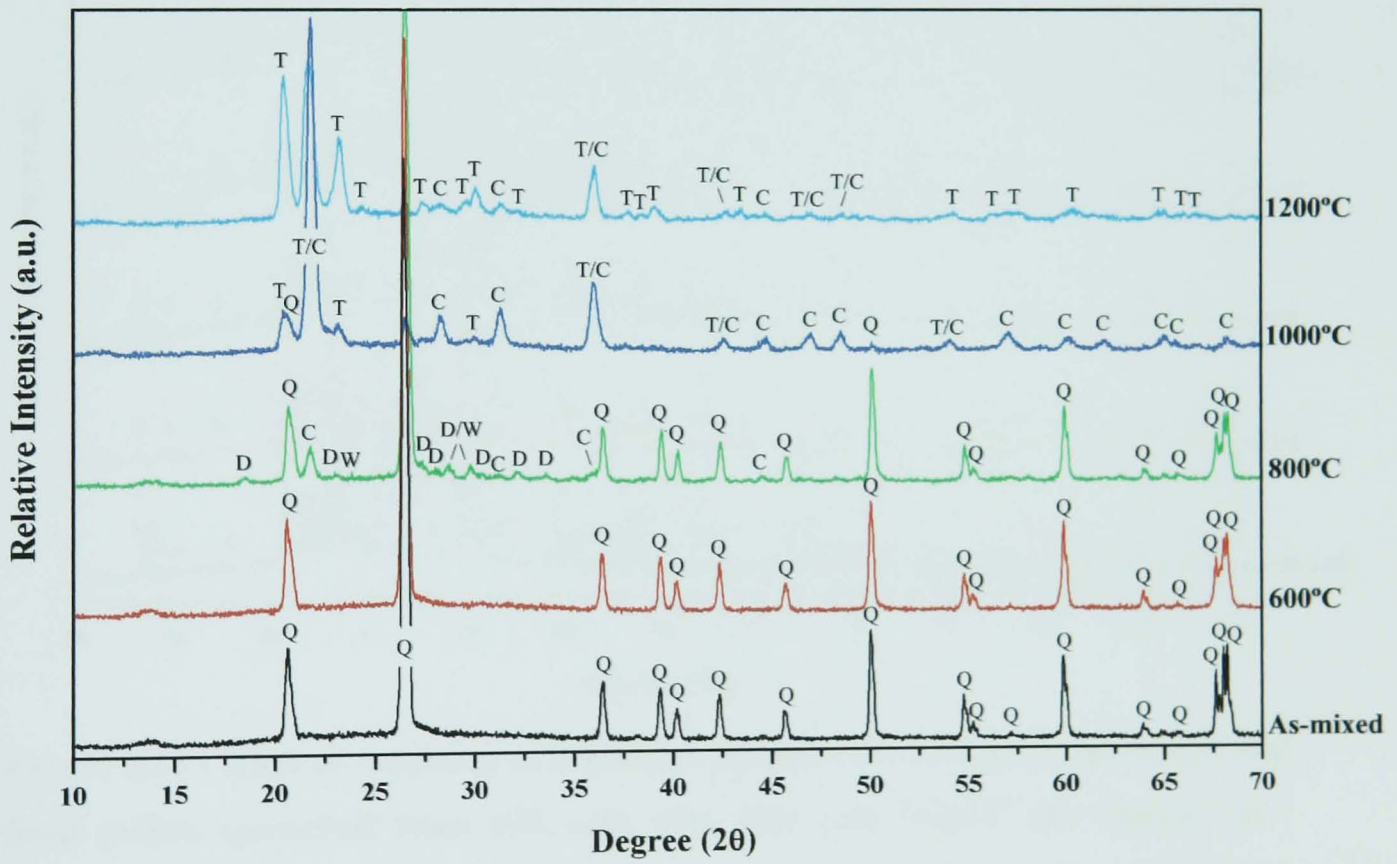

Figure 5.16 - XRD of mixtures of quartz and SLS glass; as-mixed and pellets fired 3h at 600, 800, 1000, and 1200°C and slow cooled are shown (**C** – Cristobalite, 82-512/39-1425, **D** – Devitrite, 77-410, **Q** – α-quartz, 46-1045, **T** – Tridymite, 18-1170, **W** – β-wollastonite, 27-88).

5.3.6 - Nepheline syenite and SLS glass mixtures (NS-SLS)

Figure 5.17 shows XRD of as-mixed NS-SLS and of quenched from specific firing temperatures. The as-mixed sample contains phases from nepheline syenite i.e. microcline, nepheline and albite; and SLS glass is detected by the amorphous hump between 2θ = 20°-35°. No crystalline phase was formed from the interaction of nepheline syenite and SLS glass. Nepheline syenite in this mixture undergoes similar phase transformations to those occurring when it is heated alone. Sanidine formed from mixed feldspars (e.g. microcline, albite) at ≥600°C, and later melts along with all phases present in nepheline syenite at high firing temperature.

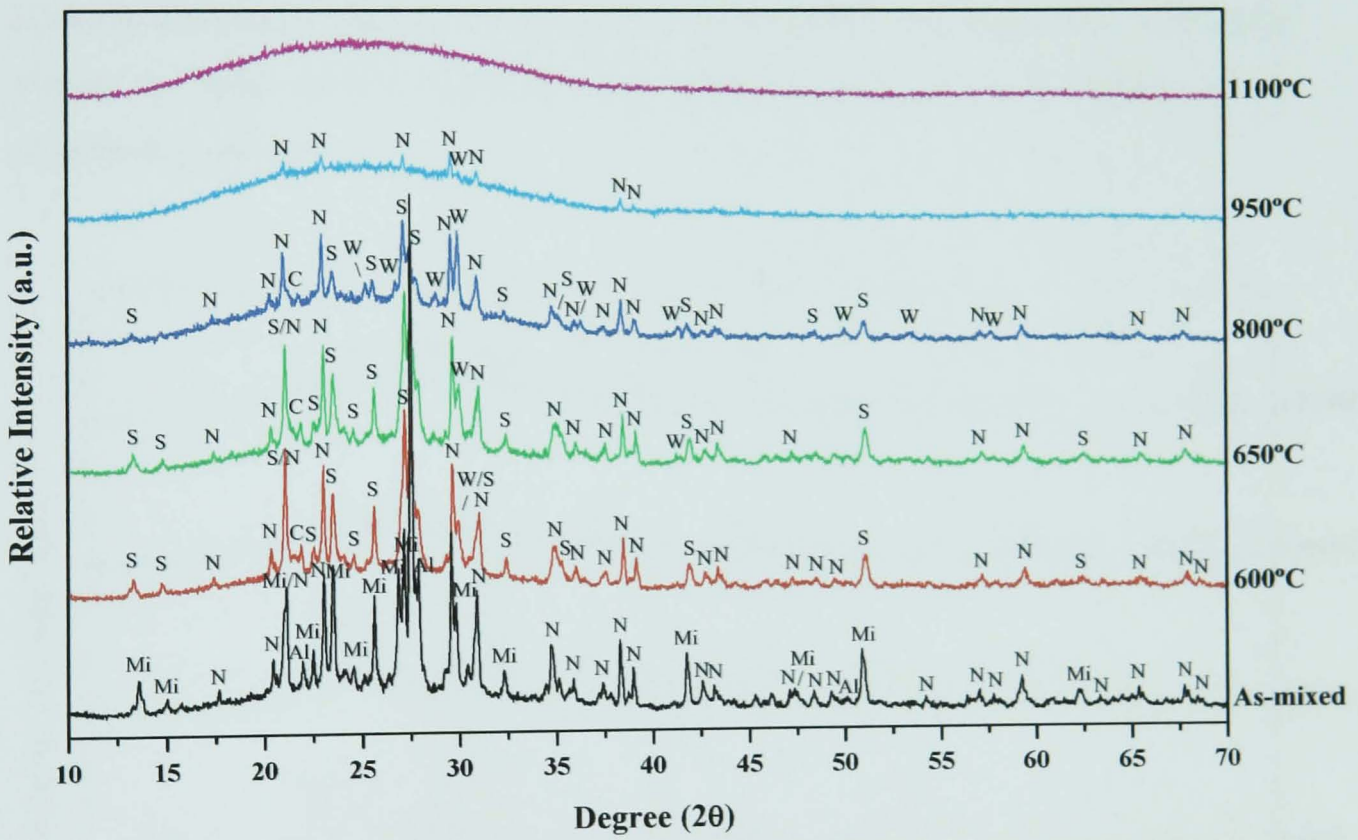

Figure 5.17 - XRD of mixtures of nepheline syenite and SLS glass; as-mixed and fired pellets quenched from 600, 650, 800, 950, and 1100°C are shown (**Al** - Albite, 9-466, **C** – Cristobalite, 82-512, **Mi** – Microcline, 19-932, **N** – Nepheline, 35-424, **S** – Sanidine, 19-1227, **W** – β-wollastonite, 27-88).

The differences between firing nepheline syenite alone and NS-SLS are decreased peak intensities for sanidine, nepheline and albite occurring at lower firing temperatures, and also the absence of leucite peaks. When SLS glass in this mixture was heated, it devitrified to cristobalite at ~600°C and wollastonite at ~650°C.

Crystalline phases from nepheline syenite and those devitrified from SLS glass were mostly melted at 950°C and completely melted by 1100°C.

XRD (Figure 5.18) shows the phase transformation sequence of the mixture of nepheline syenite and SLS glass on firing with 3h soaking. Starting with the formation of sanidine at 600°C, cristobalite and wollastonite crystallized from the devitrification of SLS glass and are present after firing between 600-800 and 800-1000°C, respectively. SLS glass apparently hastens the dissolution of nepheline syenite. Nepheline syenite starts to melt at low temperatures when mixed with SLS glass and no trace of nepheline remained when this mixture was fired to 1000°C. Potassium-enriched nepheline crystallized from the liquid phase at 1200°C. Corundum present in samples fired between 1000-1200°C was added due to the large amount of liquid phase expected to form, preventing samples from sticking to the crucible on cooling.

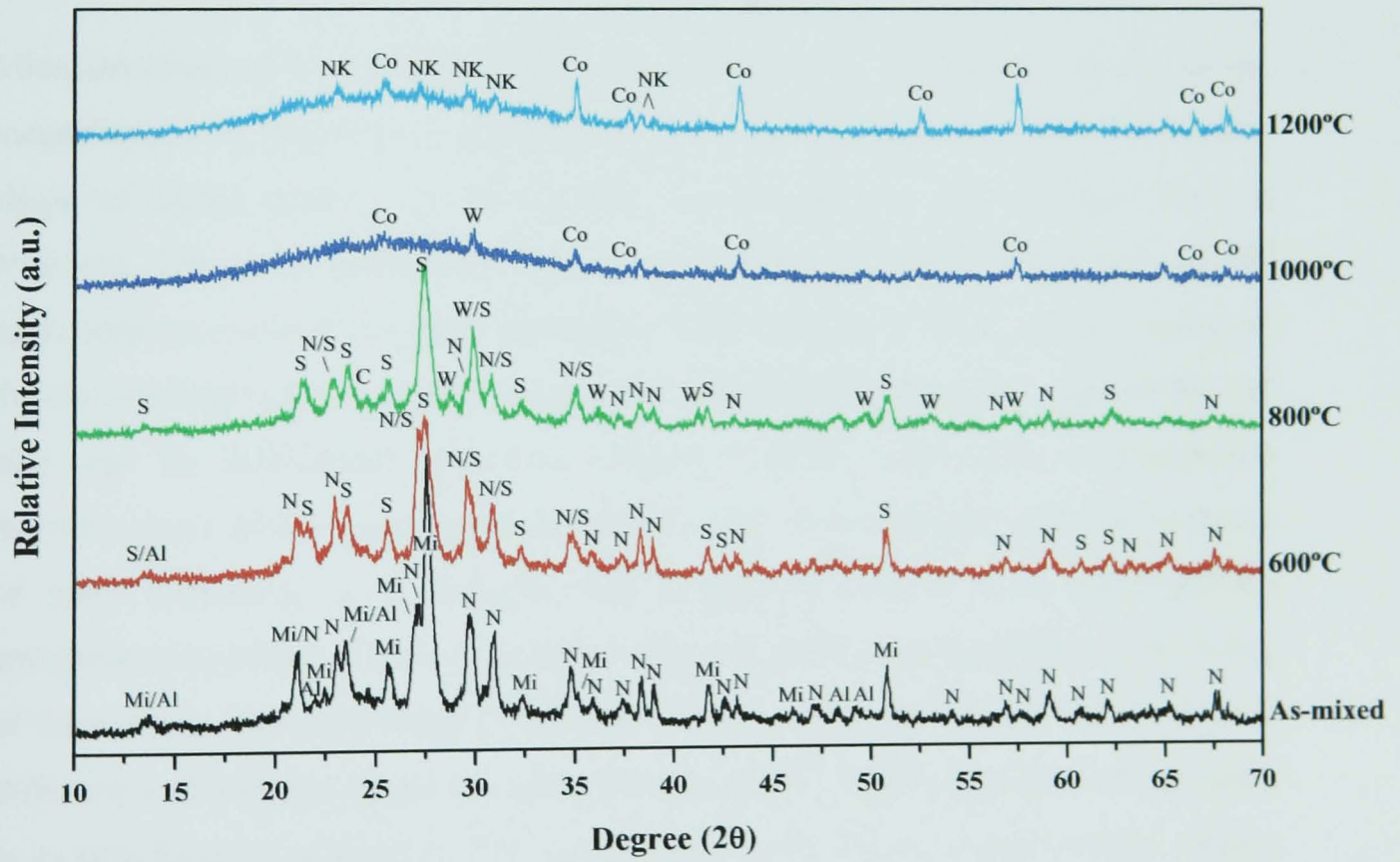

Figure 5.18 - XRD of mixtures of nepheline syenite and SLS glass; as-mixed, and pellets fired 3h at 600, 800, 1000, and 1200°C and slow cooled are shown (**Al** – Albite, 9-466, **C** – Cristobalite, 82-512, **Co** – Corundum, 46-1212, **Mi** – Microcline, 19-932, **N** – Nepheline, 35-424, **NK** – Nepheline, 9-338, S – Sanidine, 19-1227, W – β-wollastonite, 27-88).

5.4 - MICROSTRUCTURAL EVOLUTION

5.4.1 - Kaolin clay and quartz mixtures (C-Q)

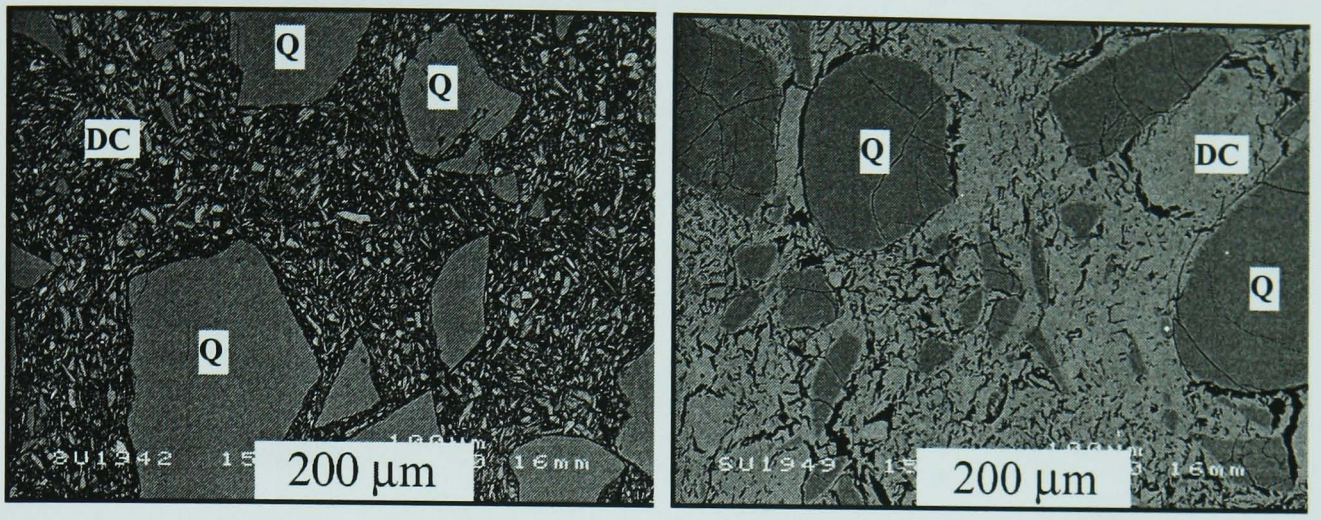

(a) 1000°C **(b) 1200°C**

Figure 5.19 - SEM/BS images of cross-sectioned, polished C-Q pellets fired 3h at 1000°C (a) and 1200°C (b). (DC = decomposed clay, Q = quartz)

Microstructures of C-Q mixtures fired 3h at 1000°C and 1200°C are shown at low magnification in Figure 5.19. After firing 3h at 1000°C (Figure 5.19(a)) the angular shape of quartz grains (Q) surrounded by decomposed clay particles (DC) is observed. The quartz grains show no sign of dissolution. The microstructure is still open with no evidence of glass formation. After firing at 1200°C, partial fusing of the decomposed clay resulted in progressive densification, where no agglomerates of clay can be individually observed (Figure 5.19(b)). The more homogeneous microstructure of the decomposed clay (DC) under back-scattered signal is evidence of glass formation, as it suggests that a material with a more homogeneous composition appeared. Partial dissolution of quartz grains was suggested by rounding of their edges, providing silica to the liquid formed on firing. Quartz and glass have different coefficients of thermal expansion, and quartz inverts abruptly from its alpha to its beta form on cooling at ~573°C producing cracks. Some of these cracks, clearly visible in Figure 5.19(b), may have also resulted from grinding of samples prior to microscopic examination.

The presence of K-feldspar (KF) as an impurity in the kaolin clay used, revealed by XRD (Figure 5.7 and 5.8), is confirmed in the SEM (Figure 5.20) showing a bright

grey particle in the top left corner. EDS and X-ray dot mapping show that this type of particle is probably microcline as it is high in K, Al and Si.

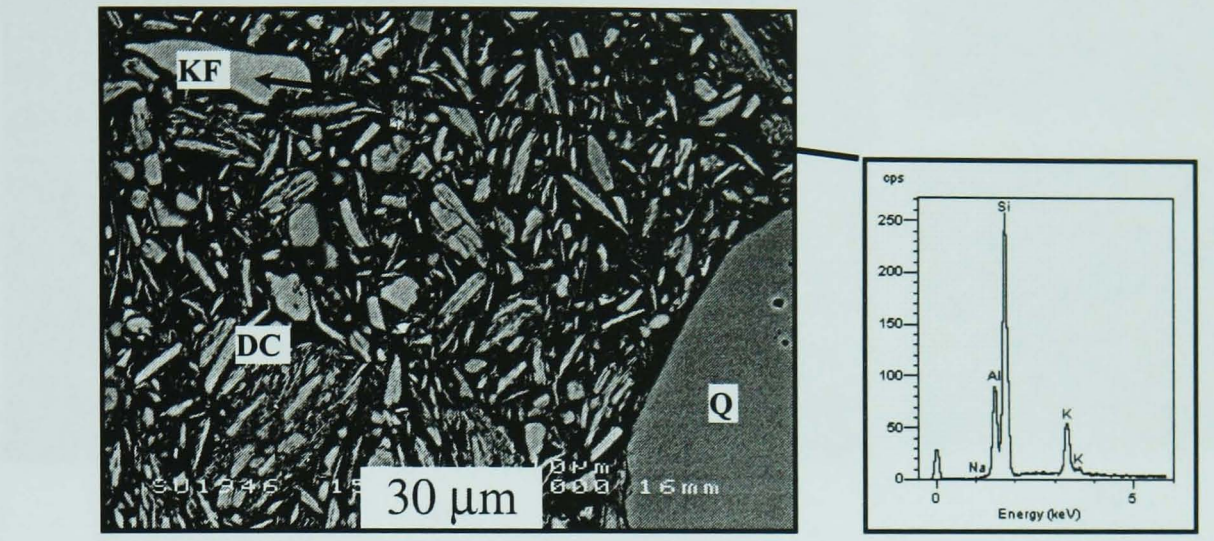

Figure 5.20 - SEM/BS image of a cross-sectioned, polished pellet made from C-Q fired 3h at 1000°C (a). (b) is an EDS trace for the irregular K-feldspar crystal shown in the top left corner of (a). X-ray dot mapping is shown in (c), where the brighter regions are higher in the corresponding element. (DC = decomposed clay, KF = K-feldspar, Q = quartz)

Etched samples of C-Q fired for 3h at 1000°C are shown in Figure 5.21. A newly-formed rod-like crystalline phase formed in the bulk of some crystals in the clay relicts (which X-ray dot mapping indicated was high in K in Figure 5.22(b)) in addition to agglomerates of decomposed clay and irregular α-quartz grains. Details of the rod-like crystals are revealed at higher magnification (Figure 5.21(b)) and explained in detail later in Figures 5.22-5.23. EDS of the quartz and decomposed clay relicts are presented in Figure 5.21(c) and (d). EDS of decomposed clay reveals Al, Si and a trace of K. The K detected probably came from either dissolved muscovite or molten K-feldspar, both of which were impurities in kaolin clay.

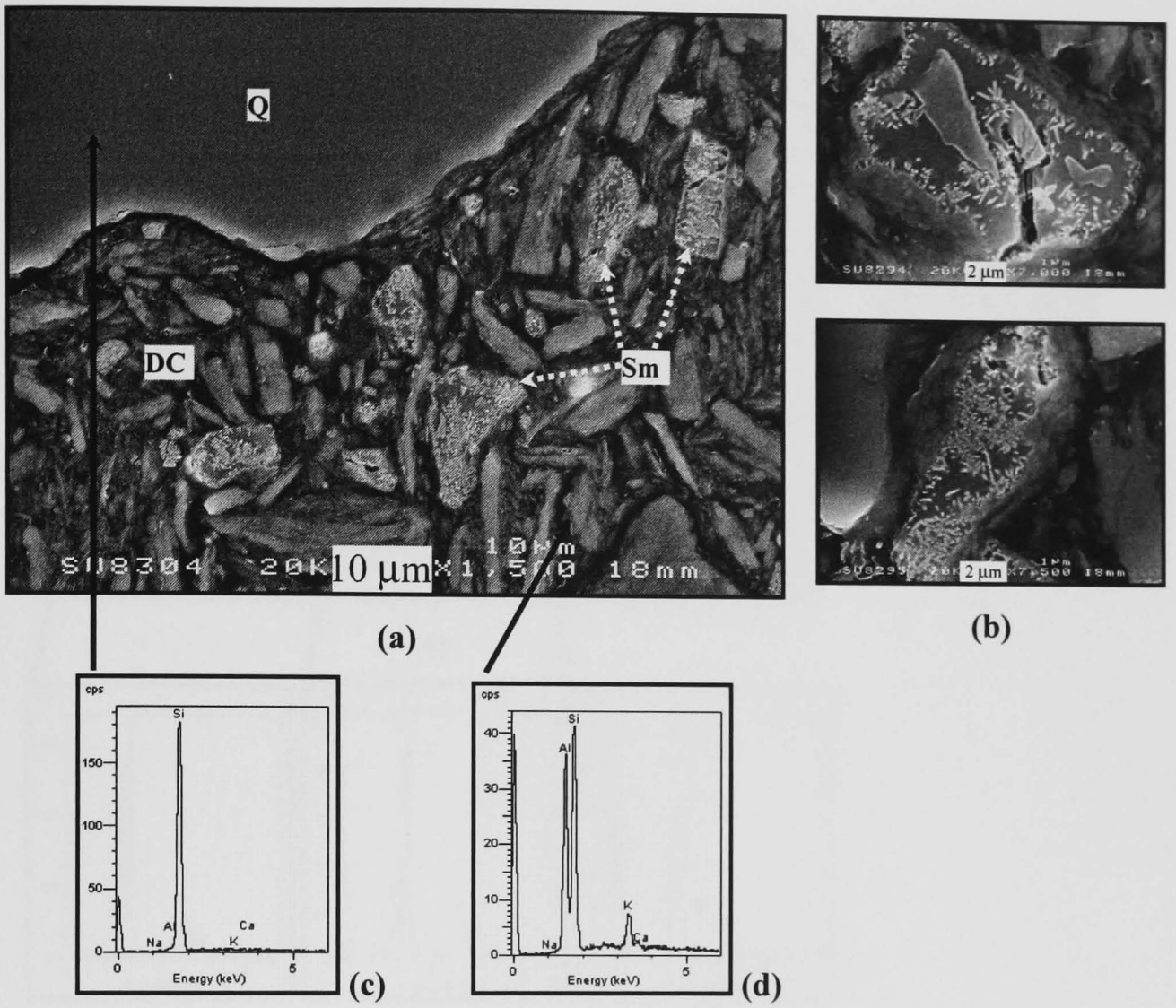

Figure 5.21 - SEM/BS images of a cross-sectioned, etched sample made from C-Q fired 3h at 1000°C (a) and of primary mullite present in this sample (b). EDS traces for quartz and decomposed clay relicts are shown in (c) and (d) respectively. (DC = decomposed clay, Sm = Secondary mullite, Q = quartz)

SEM/SE image (Figure 5.22(a)) shows the rod-like crystals (≥1µm long and ≤0.3µm wide) clearly formed in an area of feldspar particle surrounded by decomposed clay agglomerates. These rod-like crystals are secondary mullite (Sm), type II for 3-10:1 aspect ratio, which appear to have crystallised from decomposed clay (DC) relicts and molten K-feldspar impurity. They seem to grow in the liquid towards the centre of the feldspar particles. X-ray dot mapping in Figure 5.22(b) confirms the area occupied by the rod-like mullite is high in K, Si and Al, indicating that this area originally was K-feldspar. EDS of the rod-like mullite (Figure 5.22(e)) is high in Si and similar to that of the glassy phase (G) (Figure 5.22(d)), probably because the EDS probe is not small enough to analyse only mullite particles, glassy phase inevitably contributing X-rays to the signal defected.

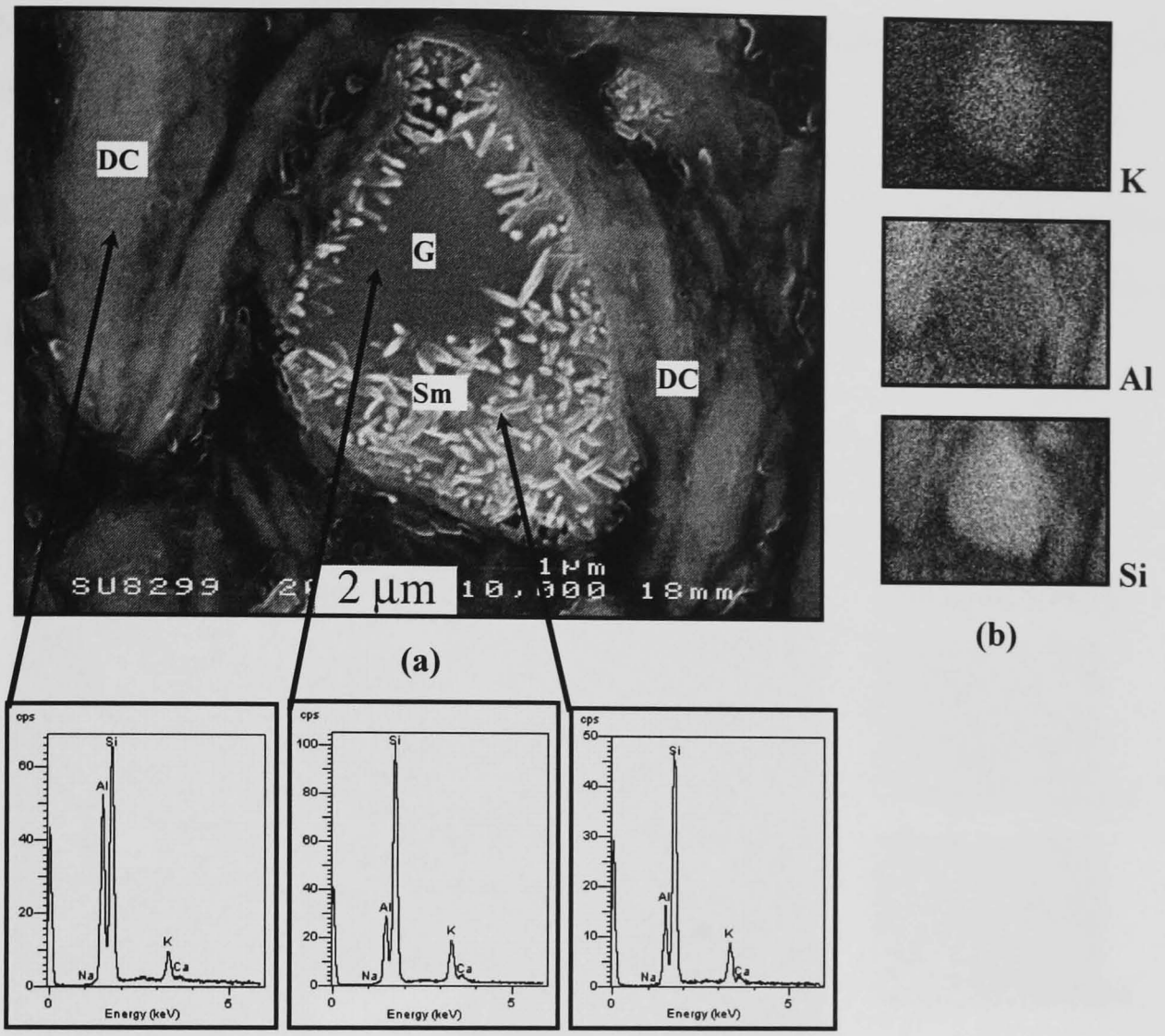

Figure 5.22 - SEM/SE image of cross-sectioned, etched sample made from C-Q pellets fired 3h at 1000°C showing mullite crystals surrounded by decomposed clay (a). X-ray dot mapping is shown in (b), where the brighter regions are higher in the corresponding element. EDS traces from decomposed clay, glassy phase and mullite particles from corresponding areas are shown in (c)-(e). (DC = decomposed clay, G = glassy phase, Sm = secondary mullite)

The same type of mullite is also shown at high magnification in Figure 5.23(a), revealing remnant K-feldspar (KF). The molten-like areas were etched away by HF acid, revealing the remaining undissolved part surrounded by glassy phase and rod-like mullite particles which cannot be seen in unetched samples. EDS of K-feldspar reveals a high K peak. EDS in Figure 5.23(c)-(f) clearly shows the decrease in K content from K-feldspar, glassy phase, rod-like mullite in glassy phase and finally decomposed clay, suggesting the diffusion of K^+ from the molten (liquid) feldspar to its surroundings. Furthermore, the increase in mullite crystal size from the clay-feldspar relict interface to the feldspar relict centre (Figure 5.22(a) and Figure

5.23(a)) is related to lower matrix viscosity arising from increasing K content (Lee and Iqbal, 2001).

The fact that mullite found in fired C-Q samples grew as elongated (rod-like) particles at low firing temperature (1000°C) may arise from the presence of liquid derived from alkali impurities (such as K-feldspar and muscovite) in the clay.

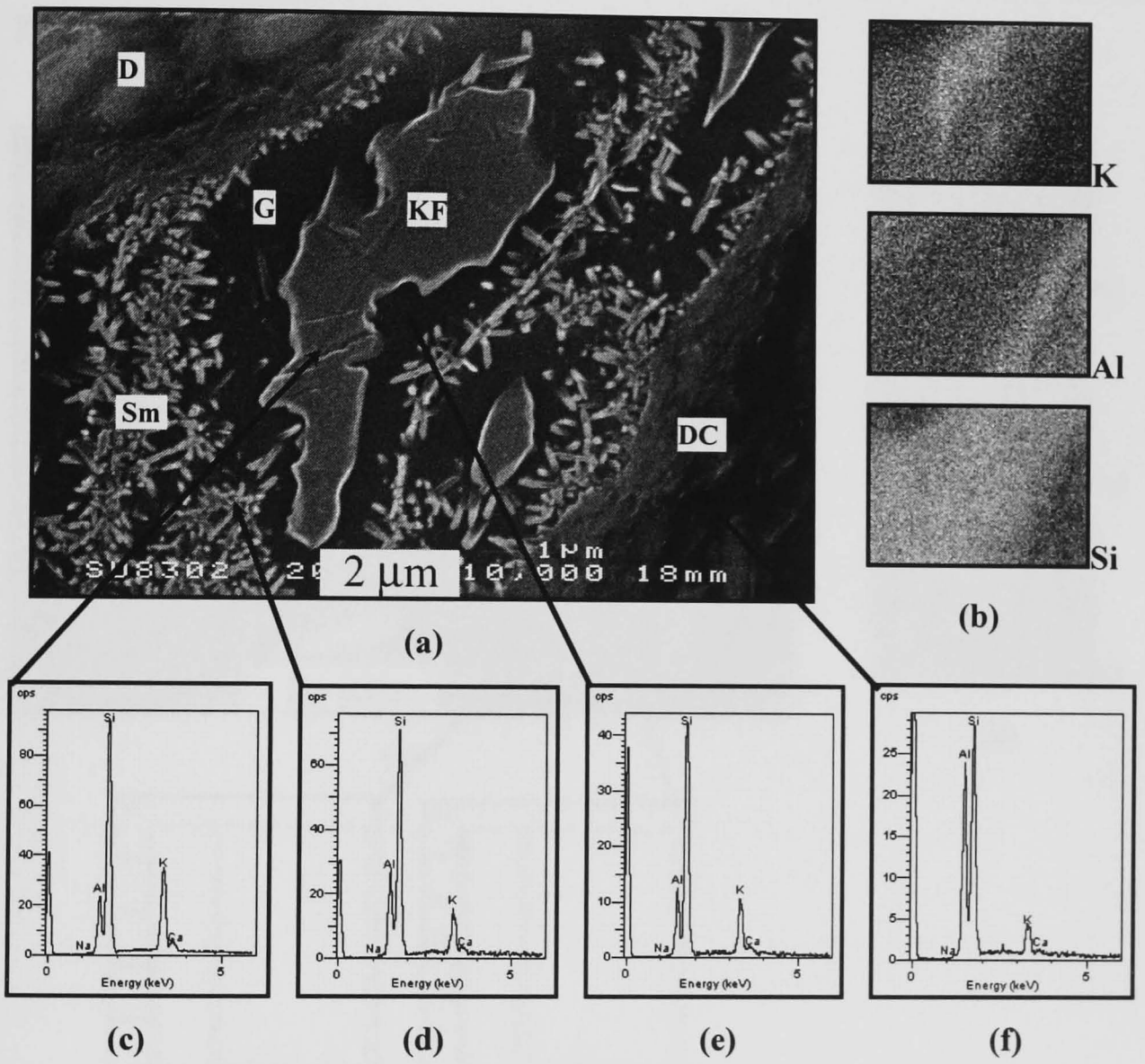

Figure 5.23 - SEM/SE image of cross-sectioned, etched sample made from C-Q pellets fired 3h at 1000°C showing mullite crystals in the area of glassy phase surrounded by molten K-feldspar (a). X-ray dot mapping is shown in (b), where the brighter regions are higher in the corresponding element. EDS traces from remaining K-feldspar, mullite particles, glassy phase and decomposed clay from corresponding areas are shown in (c)-(f). (DC = decomposed clay, G = glassy phase, KF = K-feldspar, Sm = secondary mullite)

After firing to 1200°C, mullite is more evident in the microstructure as revealed by SEM (Figure 5.24(a)). Primary mullite (type I) from clay relicts is easily detected. Small elongated type II secondary mullite particles (≤2 μm) are shown in the area of glassy phase high in K from dissolved feldspar and muscovite. X-ray dot mapping for K (Figure 5.24(b)) shows its distribution in areas where secondary mullite (Sm) is present. Partially dissolved quartz particles are also evident surrounded by their solution rim. EDS of partially dissolved quartz and its solution rim are shown in Figure 5.24(c) and (d).

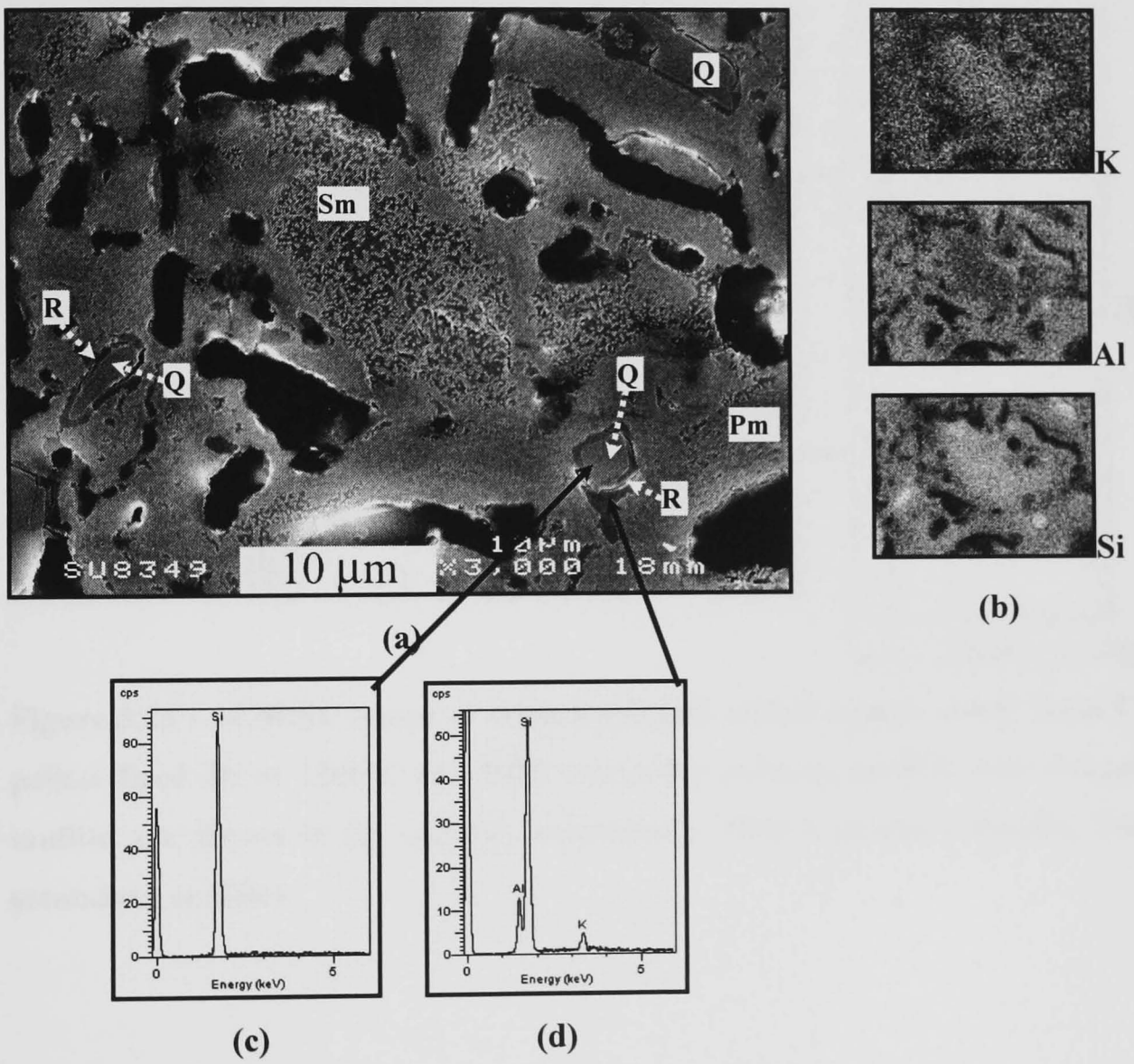

Figure 5.24 - SEM/SE image of cross-sectioned, etched sample made from C-Q pellets fired 3h at 1200°C (a). X-ray dot mapping is shown in (b), where the brighter regions are higher in the corresponding element. EDS traces from quartz particles and glassy phase surrounding quartz from corresponding areas are shown in (c) and (e) respectively. (Pm = primary mullite, Sm =secondary mullite, Q = quartz, R = solution rim)

More detailed microscopy of primary and secondary mullite in C-Q fired at 1200°C is shown in Figure 5.25. Primary mullite (type I) has a scale-like morphology and is ≤0.5 μm in size. Secondary mullite (type II) has an elongated shape and is ≤2 μm long and ≤0.5 μm wide. Secondary mullite is expected to develop more in the mixture containing higher flux contents such as C-NS (section 5.4.2). The chemical composition of primary mullite crystals was Al-rich whereas secondary mullite crystals had lower Al contents. High Si peaks in EDS from both mullites, comes from the surrounding glassy phase, as explained earlier in section 5.4.1.

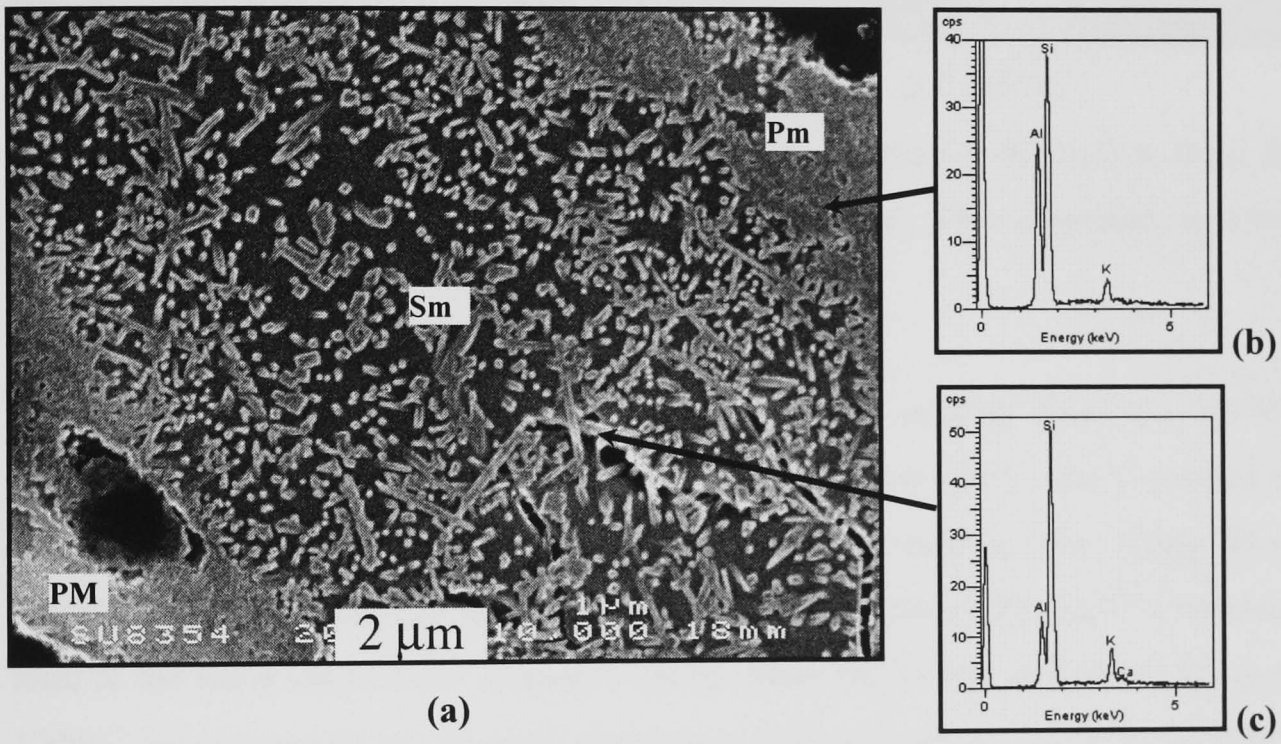

Figure 5.25 - SEM/SE image of cross-sectioned, etched sample made from C-Q pellets fired 3h at 1200°C (a). EDS traces for primary mullite and elongated mullite are shown in (b) and (c), respectively. (Pm = primary mullite, Sm = secondary mullite)

5.4.2 Kaolin clay and nepheline syenite mixtures (C-NS)

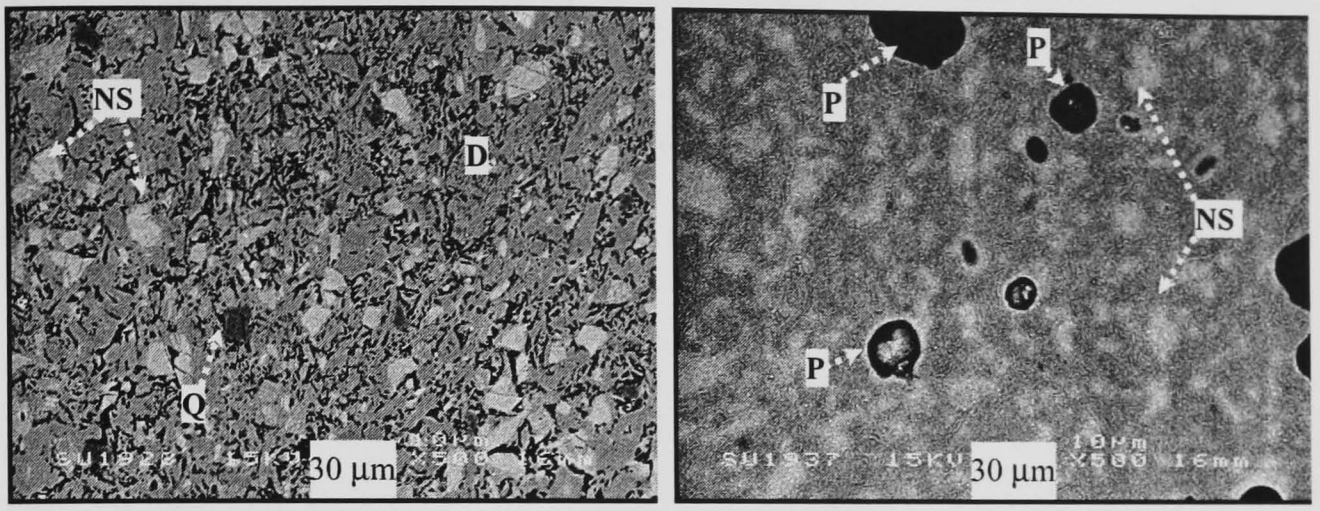

(a) 1000°C **(b)** 1200°C

Figure 5.26 - SEM/BS images of cross-sectioned, polished C-NS pellets fired 3h at 1000°C (a), and 1200°C (b). (DC = decomposed clay, NS = nepheline syenite, P = pore, Q = quartz)

Figure 5.26(a) shows the microstructure of a C-NS mixture fired at 1000°C, revealing the welded (partially fused) and decomposed clay (DC). This is a result of the presence of flux (nepheline syenite) which started melting after firing 3h at 1000°C. The microstructure is clearly denser than that shown for the C-Q mixture fired at the same temperature (Figure 5.19(a)). More liquid was formed on firing at 1200°C, as revealed by its "smooth" appearance with isolated and rounded pores (P). Contours of some partially unmelted feldspar particles are still visible in Figure 5.26(b).

The brighter particles in Figure 5.27(a) are feldspar derived, as revealed by EDS (Figure 5.27(c)). In this EDS trace, the ratio between the elements approaches that of K-feldspar ($KAlSi_3O_8$). The darker particles in Figure 5.27(a) are decomposed clay material, having the average chemical composition shown in the EDS trace in Figure 5.27(b). The potassium can come both from impurities in the original clay and from the nepheline syenite forming the glass partially covering the microstructure.

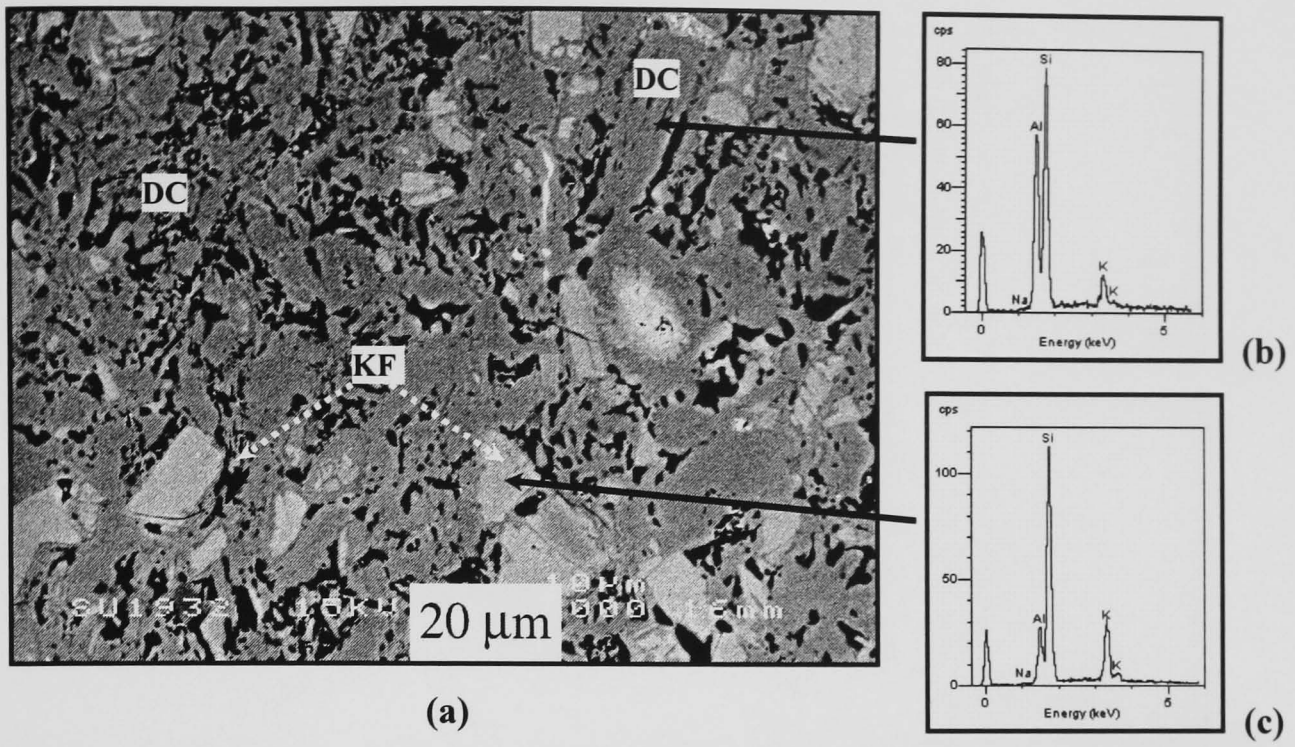

Figure 5.27 - SEM/BS image of a cross-sectioned, polished pellet made from C-NS fired at 1000°C. (b) and (c) are EDS traces of decomposed clay relicts (dark grey) and of the irregular K-feldspar crystals (brighter grey particles) shown in (a), respectively. X-ray dot mapping is shown in (d), where the brighter regions are higher in the corresponding element. (DC = decomposed clay, KF = K-feldspar)

After etching, the elongated mullite particles formed at the interface between decomposed clay and nepheline syenite particles are evident in an SEM/SE image of C-NS fired at 1000°C for 3h (Figure 5.28(a)). Due to the presence of nepheline syenite flux in this mixture, secondary mullite crystals crystallised from molten feldspar particles, as seen in SEM/SE image (Figure 5.29(a)), are much more developed and longer in size (~2-5 µm long and ≤0.5 µm wide) than those found in the C-Q mixture (≤2 µm long and ≤0.5 µm wide) given the same firing treatment. The same type of secondary mullite, as observed in Figure 5.29(a), is shown in Figure 5.29(b) at higher magnification.

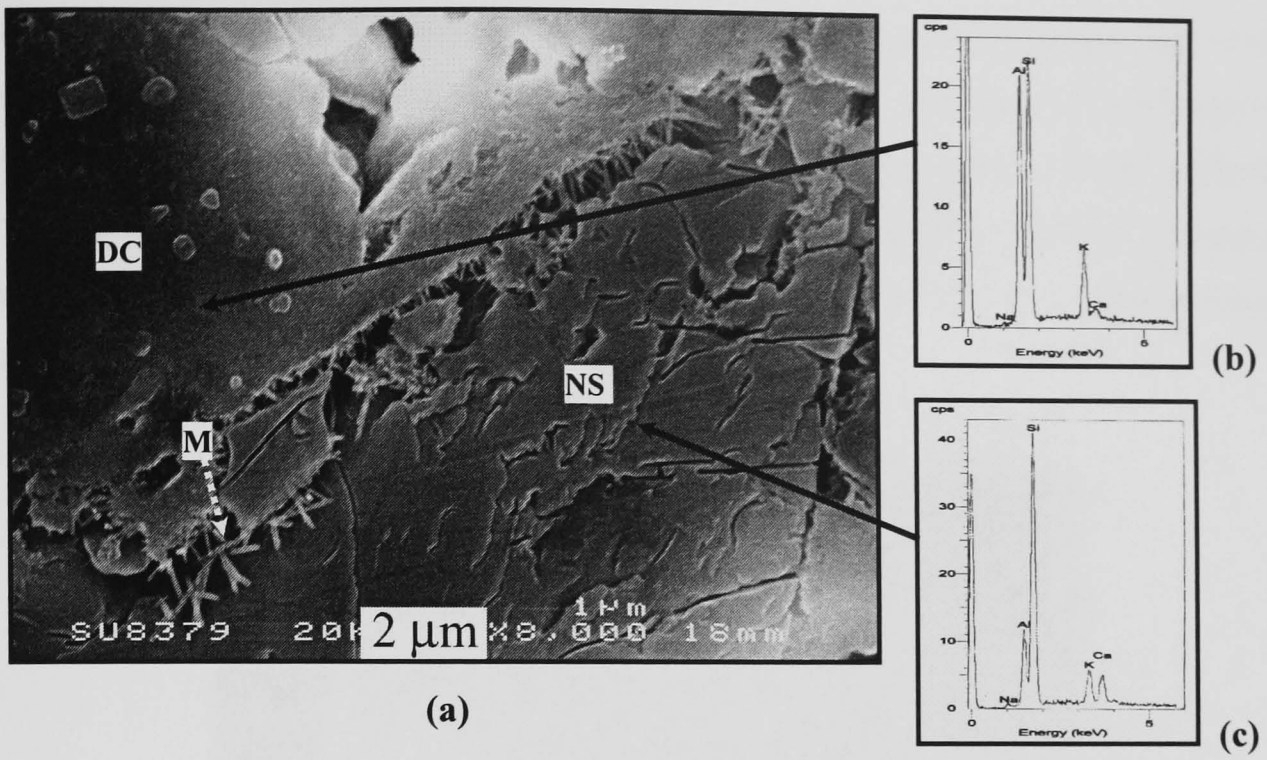

Figure 5.28 - SEM/SE image of a cross-sectioned, etched sample made from C-NS pellets fired 3h at 1000°C (a). EDS traces from decomposed clay and nepheline syenite particles are shown in (b) and (c), respectively. (DC = decomposed clay, M = mullite, NS = nepheline syenite)

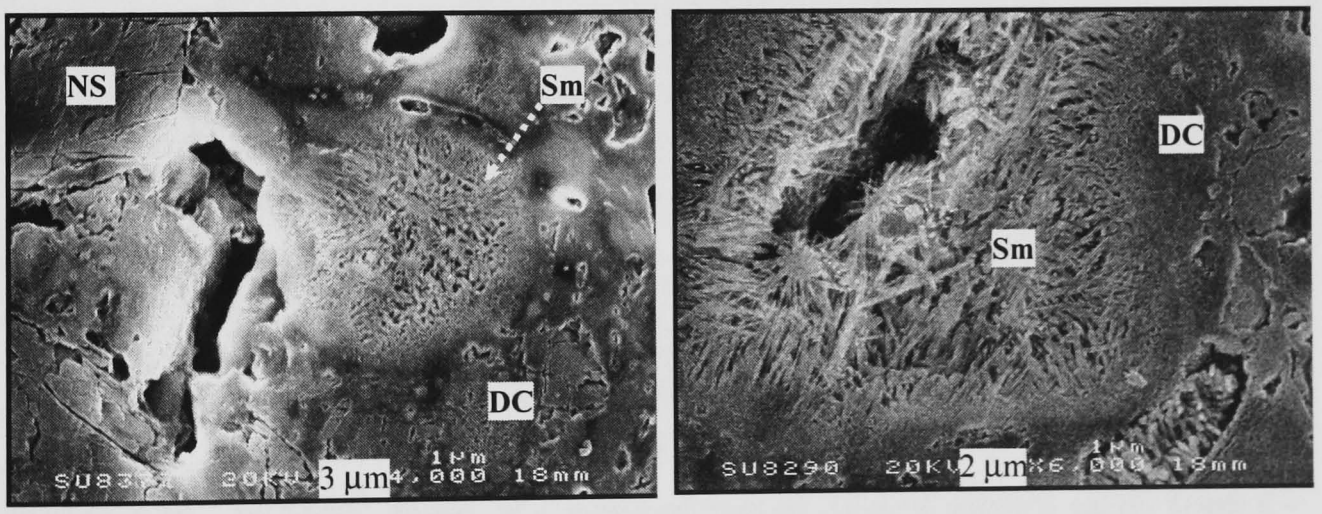

Figure 5.29 - SEM/SE image of a cross-sectioned, etched sample made from C-NS pellets fired 3h at 1000°C (a) and (b). (DC = decomposed clay, NS = nepheline syenite, Sm = secondary mullite)

After firing at 1200°C, samples from C-NS show a microstructure with well developed primary mullite and secondary mullite (Figure 5.30 and 5.31). Elongated (~3-7 μm long and <0.5 μm wide) secondary mullite crystals are evident in Figure 5.30 in the area once originally occupied by a feldspar particle. EDS of elongated secondary mullite and of decomposed clay and glass detected on a corresponding area in the matrix are shown in Figure 5.30(b) to (d).

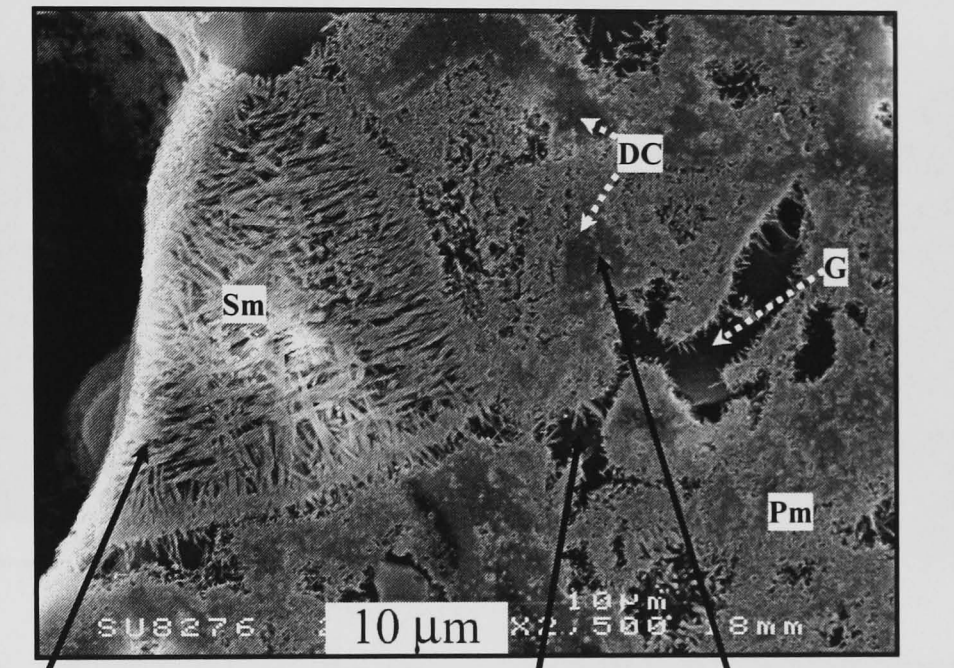

Figure 5.30 - SEM/SE image of a cross-sectioned, etched sample made from C-NS pellets fired 3h at 1200°C showing mullite crystals surrounded by decomposed clay (a). EDS traces of mullite particles, glassy phase and decomposed clay from corresponding areas are shown in (b)-(d). (DC = decomposed clay, G = glassy phase, Pm = primary mullite, Sm = secondary mullite)

Needle-like (≥2 μm long) secondary mullite crystals are evident in Figure 5.31(a) and (b). They grew in the liquid from the interface of clay relicts towards the centre of a molten feldspar relict, whereas aggregates of small (≤0.5 μm) primary mullite formed from solely decomposed clay relicts. The increased mullite crystal size from pure clay relicts to the liquid feldspar matrix is due to increasing K^+ content making the liquid more fluid, facilitating mass transport and enhancing crystal growth (Lee and Iqbal, 2001).

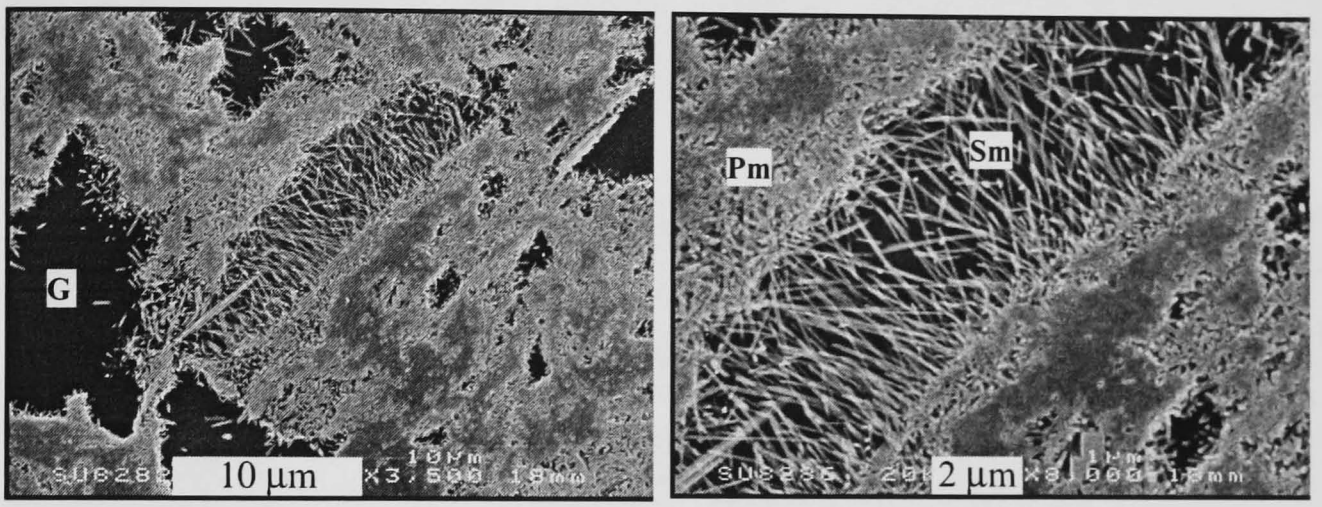

(a) **(b)**

Figure 5.31 - SEM/SE image of a cross-sectioned, etched sample made from C-NS pellets fired 3h at 1200°C (a) and of selected area in high magnification (b) showing small primary mullite crystals and needle-like mullite crystals. (G = glassy phase, Pm = primary mullite, Sm = secondary mullite)

5.4.3 - Kaolin clay and SLS glass mixtures (C-SLS)

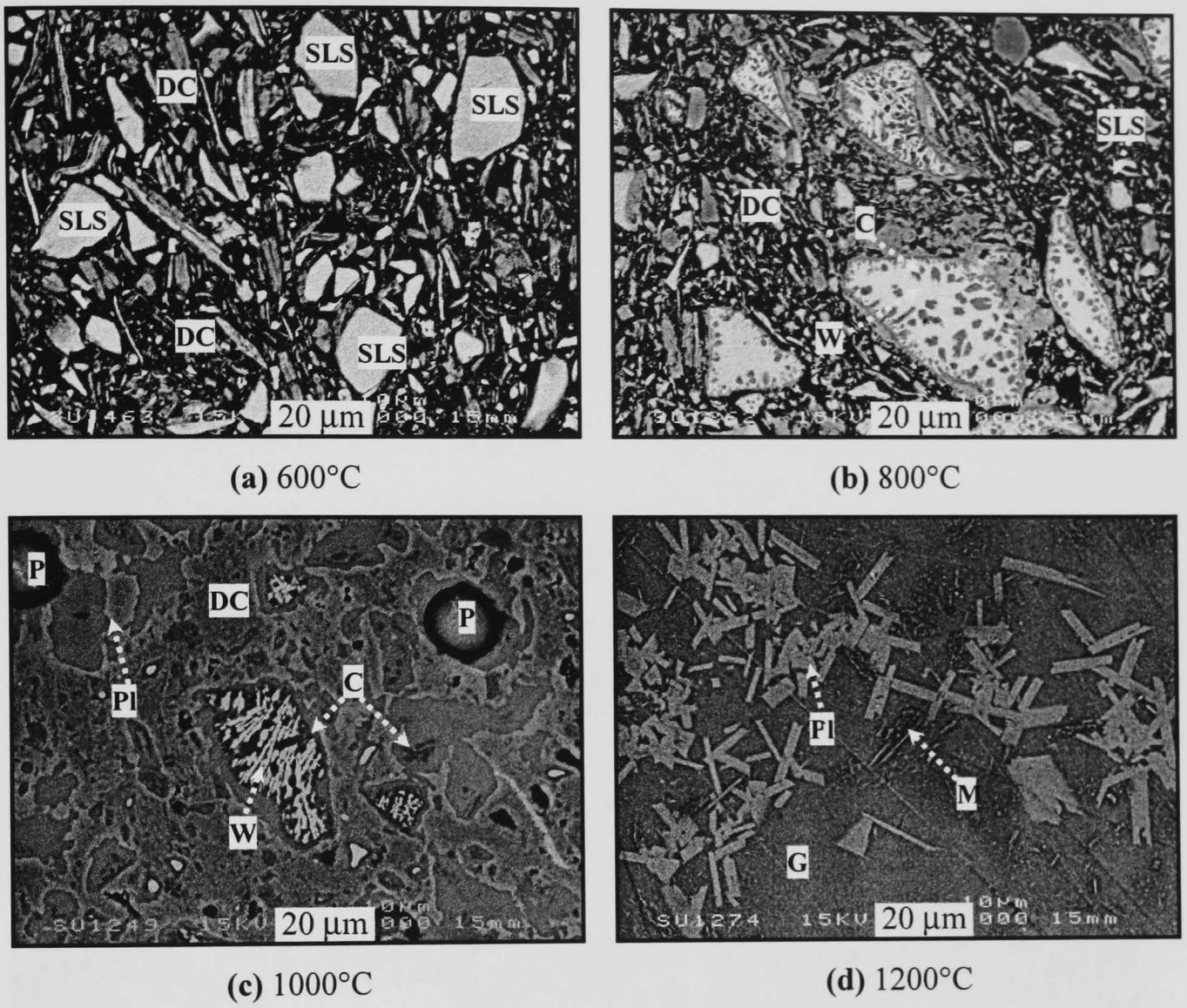

Figure 5.32 - SEM/BS images of cross-sectioned, polished C-SLS pellets fired 3h at 600°C (a), 800°C (b), 1000°C (c), and 1200°C (d). (C = cristobalite, DC= decomposed clay, G = glassy phase, M = mullite, P = pore, Pl = plagioclase, SLS = soda-lime-silica glass, W = wollastonite)

The microstructural evolution of C-SLS mixtures fired between 600-1200°C is shown in Figure 5.32. The microstructure is still open after firing for 3h at 600°C (Figure 5.32(a)), with no evidence of molten SLS glass or liquid formation, only angular SLS particles surrounded by metakaolin. After firing at 800°C, SLS particles are partially melted and bonded to decomposed clay (Figure 5.32(b)). Crystallization occurs in some of SLS particles as seen from the particles with bright contrast in Figure 5.32(b). However, the microstructure is still coarse. A "smoother" microstructure appears after firing at 1000°C (Figure 5.32(c)), as SLS glass particles melted, accelerating the dissolution of the decomposed clay and leading to more

liquid formation. Isolated and rounded pores (P) (≤25 μm diameter) are also observed in Figure 5.32(c). Complete melting of the SLS glass with formation of liquid led to the coalescence of pores into large pores (≥300 μm) after firing at 1200°C. It is also worth noting that the glass formed after firing at 1200°C appears to be more homogeneous and has spread more completely than that formed at 1000°C. Small elongated (≤30 μm) crystals (Pl) are evident in the microstructure shown in Figure 5.32(d). The early formation of liquid in the mixture containing SLS glass (C-SLS) and consequently formation of glass in the fired microstructure is visible when comparing C-SLS (Figure 5.32(c)) with C-Q (Figure 5.19(a)) and C-NS (Figure 5.26(a)) fired at 1000°C.

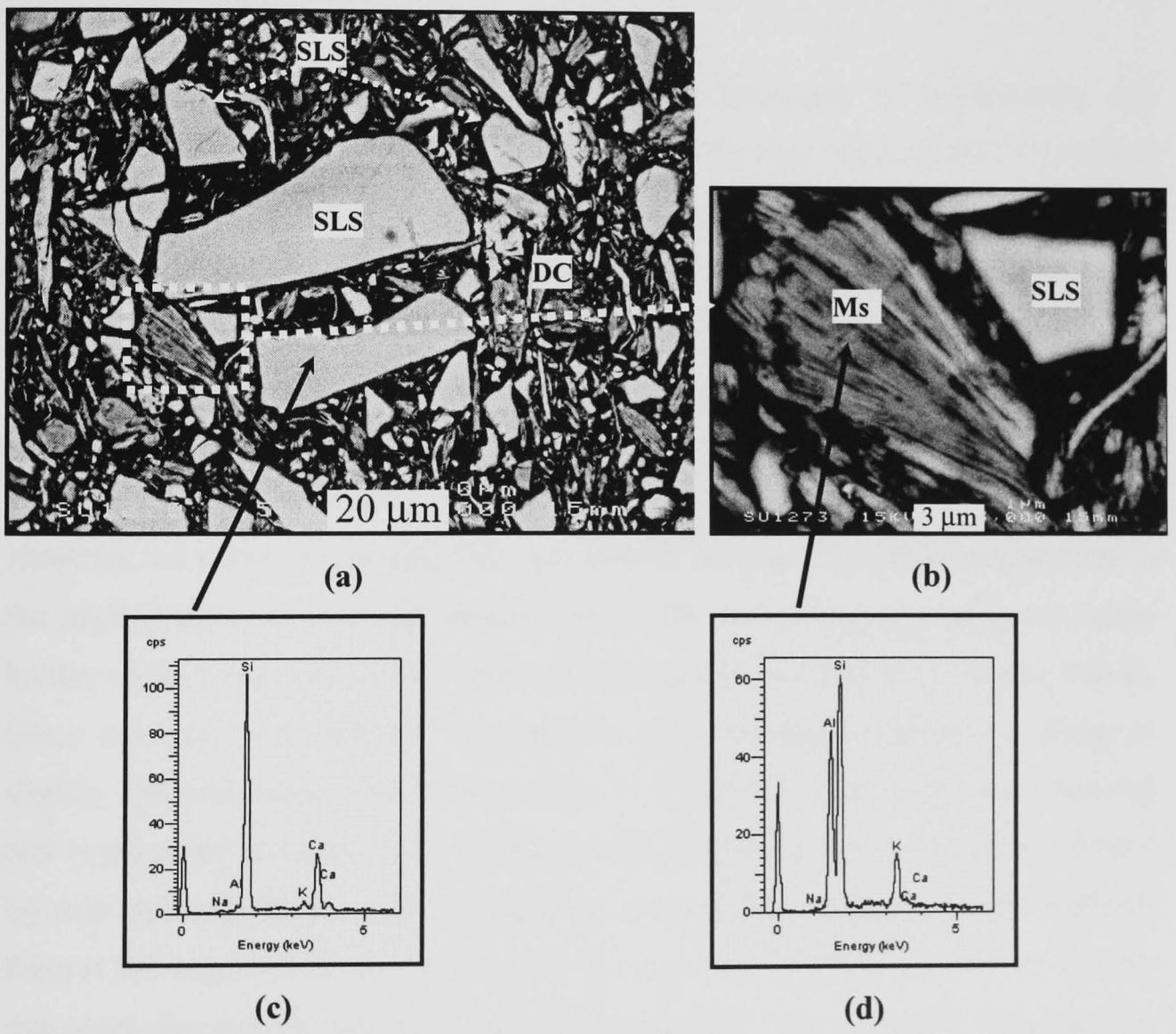

Figure 5.33 - SEM/BS images of a cross-sectioned, polished sample made from C-SLS fired 3h at 600°C (a), and of muscovite relict present in this sample (b). (c) is an EDS trace for the irregular SLS crystals shown in (a), and (d) is an EDS trace for the muscovite crystal in (b). (DC = decomposed clay, Ms = muscovite, SLS = soda-lime-silica glass)

A higher magnification SEM/BS image of C-SLS fired 3h at 600°C (Figure 5.33(a)) shows angular SLS particles with various sizes (~10-60 μm), many of them having broken during mixing/milling operations. EDS from SLS particles (Figure 5.33(c)) reveals Si and Ca peaks, as expected from the chemical composition of SLS glass (Table 4.1), although the Na peak was absent due to the beryllium window protecting the EDS detector which blocks the signal coming from light elements. No crystallization was observed in SLS particles at this temperature. There is also no evidence of liquid formation or interaction between the two components. Muscovite, which was an impurity present in the raw kaolin clay used, was observed (Figure 5.33(b)) with a layer-like morphology similar to kaolinite, but it is chemically close to $KAl_2(Si_3Al)O_{10}(OH)_2$, as revealed by EDS (Figure 5.33(d)).

Devitrification of the SLS glass leads to the formation of wollastonite and cristobalite as observed by XRD of SLS (Figure 4.16) and C-SLS (Figure 5.12) fired 3h at 800°C. However, from the microstructure of C-SLS fired at 800°C (Figure 5.32(b)) it can be seen that some of the particles have clear signs of transformation (as in Figure 5.34(a)), whereas others seem to have a delayed transformation (as in Figure 5.34(b)). This difference could be associated with the size of SLS particles or the local environment surrounding them or could be related to the heat conduction mechanisms which may cause temperature gradients during the heating operation. However, no pattern explaining this was obvious although a possible explanation is the slightly different chemical compositions of the various recycled colourless glass bottles which comprised the SLS glass powder used as a raw material (section 4.6.4). Glass particles with different compositions will undergo reactions on firing at slightly different firing temperatures/times. A sequence of reactions was observed and is presented in Figure 5.35, showing particles progressively reacted as revealed by their microstructures under BS imaging. First, small regions of Si-rich material form at the edges of the SLS glass particles as a result of phase separation. The Si-rich areas then grow toward the centre of the particles, leaving behind elongated Ca-rich areas which EDS suggests are wollastonite. XRD (Figure 5.12) revealed that the Si-rich areas were cristobalite, and confirmed the presence of wollastonite crystals. It also worth noting that the crystallisation of SLS glass occurs from the surface of the particles towards the centre. This so-called surface crystallisation is common in commercial SLS glass (Swift, 1947; Kirby, 2000; Prado and Zanotto, 2002).

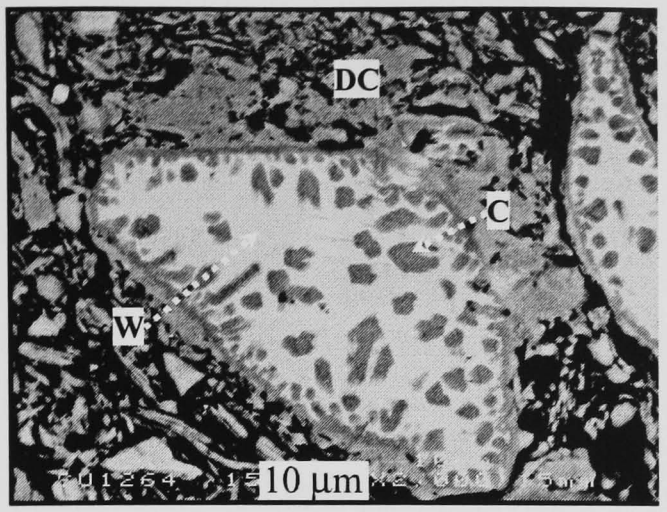

(a)

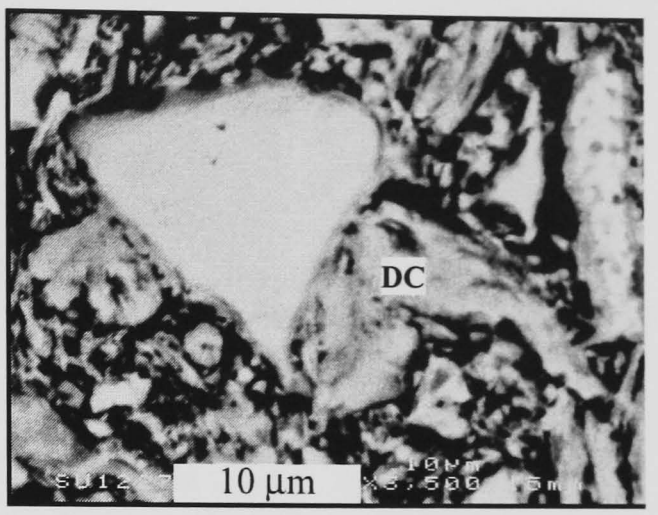

(b)

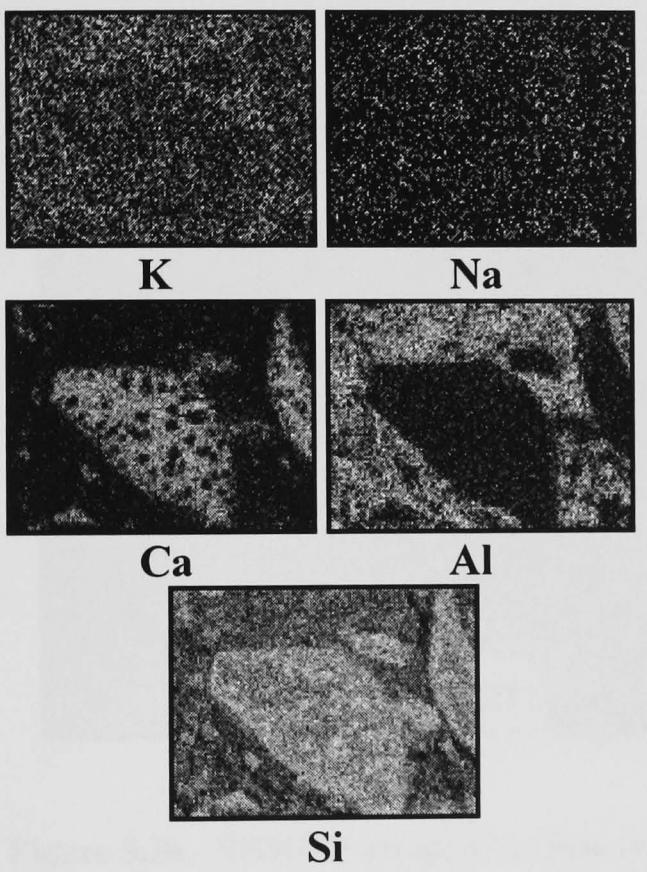

(c)

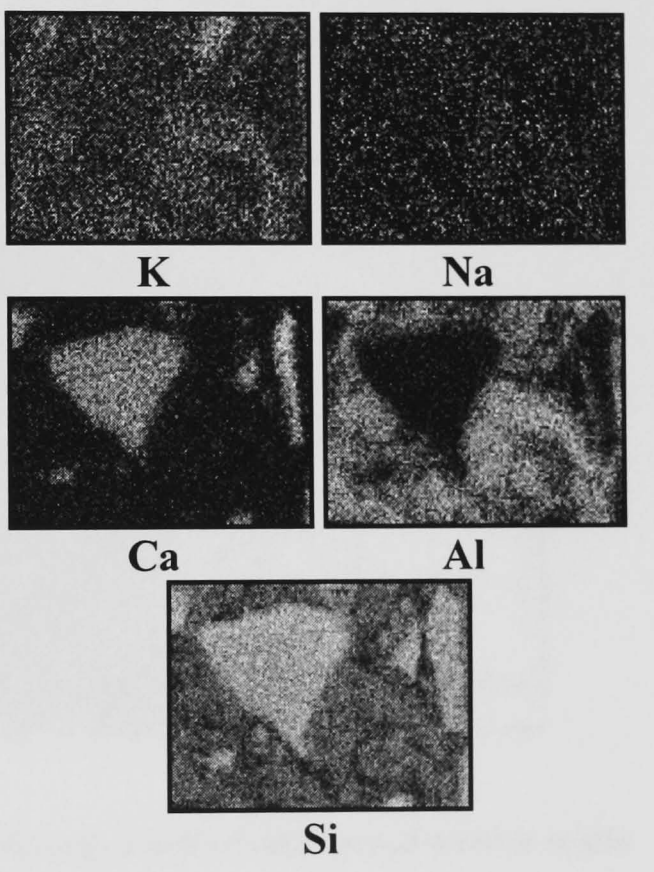

(d)

Figure 5.34 - SEM/BS images of cross-sectioned, polished pellets made from C-SLS fired 3h at 800°C showing changes occurring in the SLS (a) and (b). X-ray dot mapping of features (a) and (b) is shown in (c) and (d), respectively. (C = cristobalite, DC = decomposed clay, W = wollastonite)

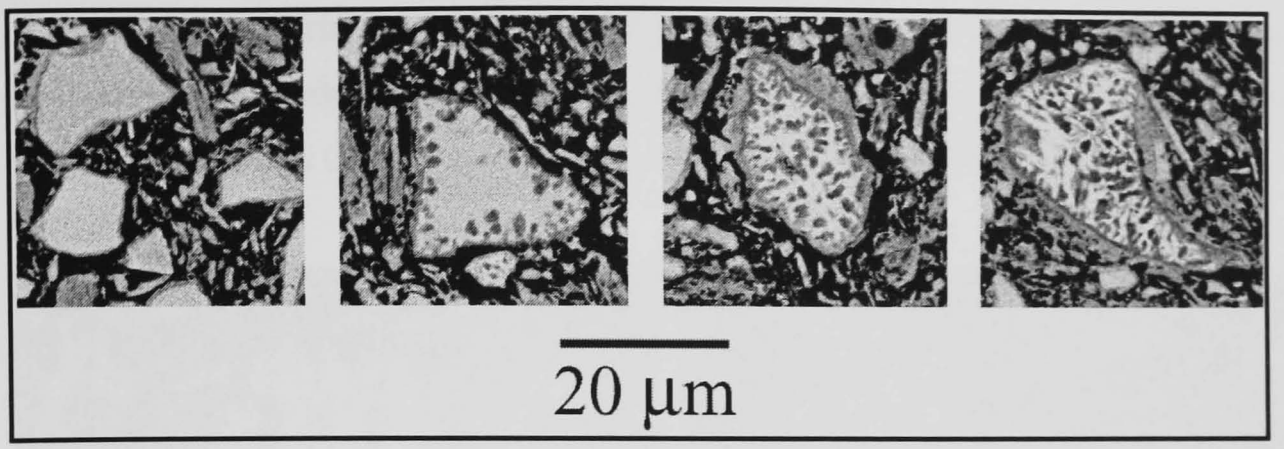

Figure 5.35 - SEM/BS images showing, from left to right, the transformation sequence of SLS glass devitrification in a sample of C-SLS fired at 800°C for 3h.

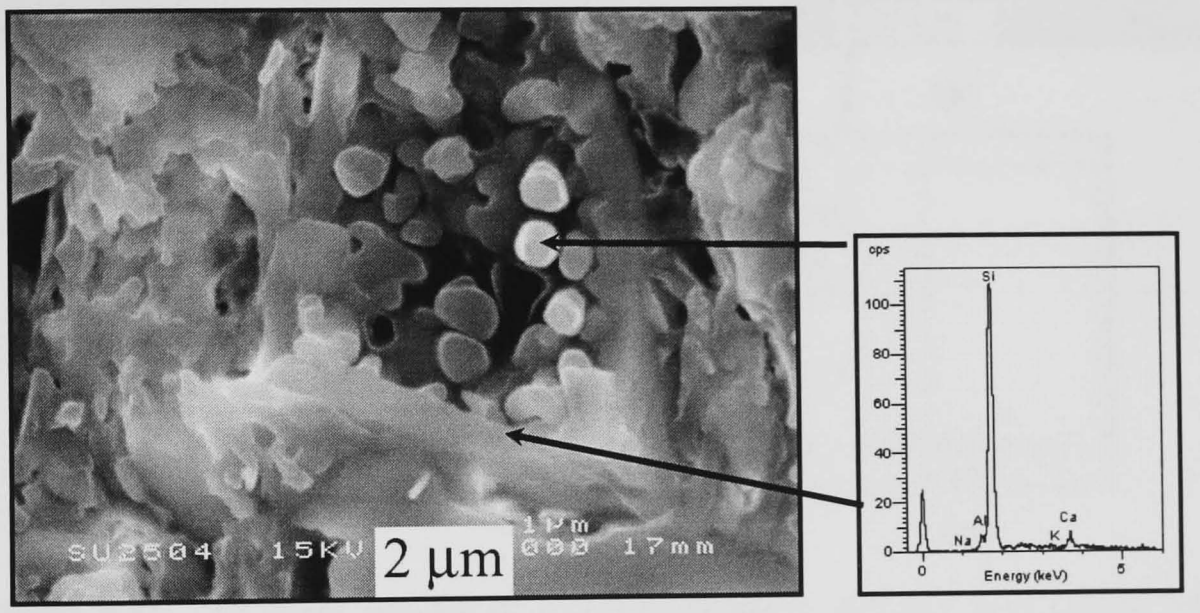

(a) **(b)**

Figure 5.36 - SEM/SE image of a cross-sectioned, polished and etched sample made from C-SLS fired 3h at 800°C showing the presence of cristobalite and absence of wollastonite after etching (a). EDS trace of cristobalite and edge of a glass particle is shown in (b).

SEM of C-SLS fired at 800°C (Figure 5.36(a)) shows the presence of rounded cristobalite particles and the absence of wollastonite crystals (possibly from etching) inside a particle which is believed to be SLS. EDS (Figure 5.36(b)) confirmed that the crystal is high in Si also the edge of the reacted SLS particle (Figure 5.36(c)).

Cristobalite and wollastonite peaks can not be clearly seen in XRD of the C-SLS mixture fired at 1000°C (Figure 5.12) due to their decreasing peak intensities and

some of them overlap with plagioclase peaks. The formation of cristobalite and wollastonite as products from devitrification of SLS glass are clearly seen in the SEM/SE image of a C-SLS sample fired at 1000°C (Figure 5.37(a) and (b)).

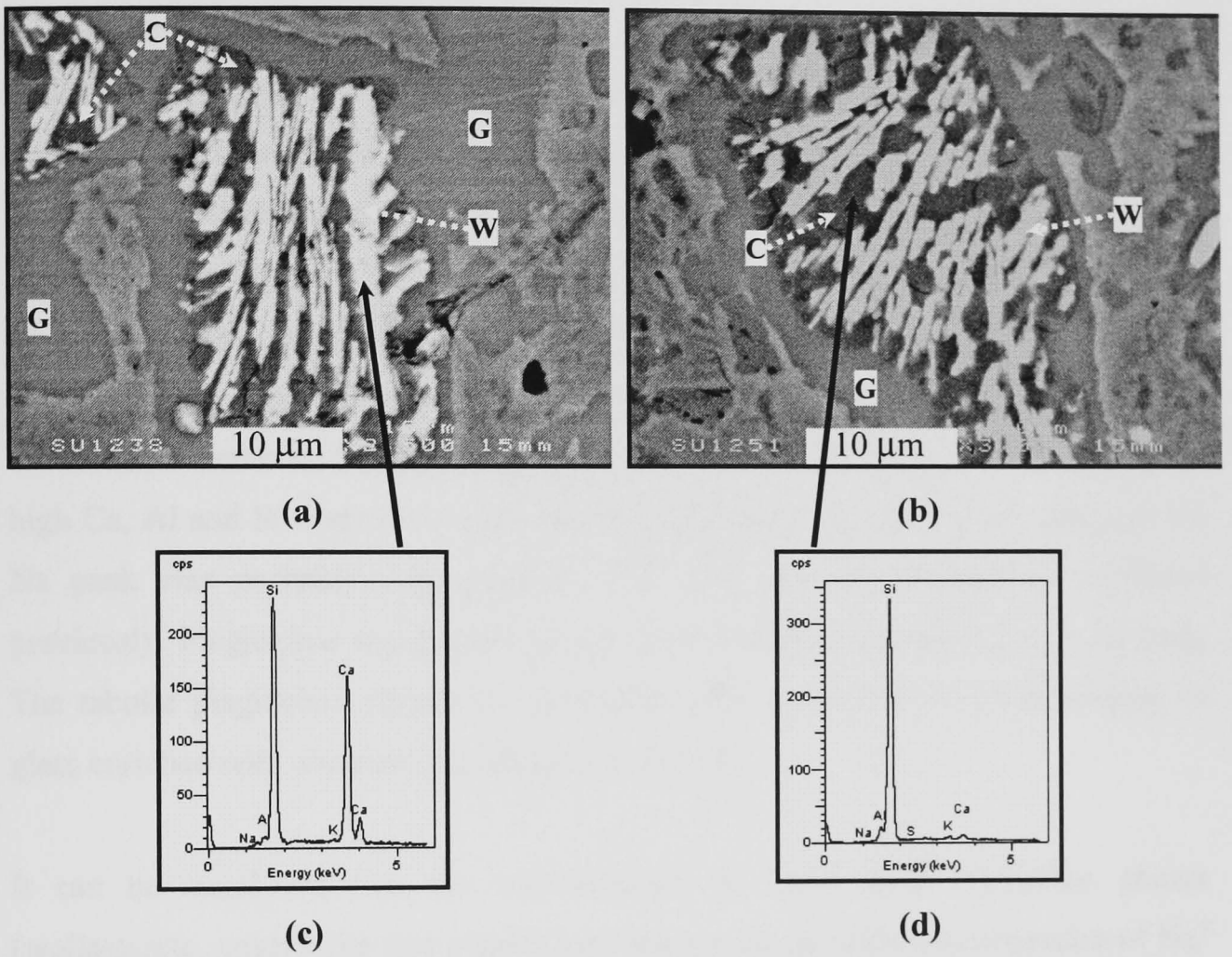

Figure 5.37 - SEM/BS images of a cross-sectioned, polished and etched sample made from C-SLS fired 3h at 1000°C showing the formation of wollastonite (bright features) and cristobalite (dark rounded particles in the background) in both (a) and (b). EDS traces of wollastonite and cristobalite are shown in (c) and (d), respectively. (C = cristobalite, G = glassy phase, W = wollastonite)

These two SEM/SE images show the crystallization of wollastonite (W) and cristobalite (C) in areas of original SLS particles. The edge of reacted SLS glass particle disappears due to progressive melting of SLS glass thus leaving remnant cristobalite and wollastonite crystals embedded in glassy phase. The lath-like crystals in both images are high in Ca and Si as confirmed by EDS (Figure 5.37(c)) whereas the darker rounded crystals are high in Si (Figure 5.37(d)). From EDS analysis, the lath-like crystals are wollastonite and the rounded crystals are cristobalite both contained in a glassy matrix (G). These results are consistent with the results of

Clark-Monks and Parker (1980) who found that wollastonite is a common devitrification product in the Na_2O-CaO-SiO_2 glass system and can occur sometimes with cristobalite because of high local concentrations of lime.

Apart from cristobalite and wollastonite, XRD of C-SLS (Figure 5.12) indicated formation of plagioclase after firing at 1000°C. The bright features at peripheral regions scattered all over the particle interiors, especially at the interfaces between glass and decomposed clay relicts in SEM/BS images of C-SLS samples fired at 1000°C (Pl in Figure 5.32(c)), is believed to be plagioclase. This was proven by SEM/BS images taken from the polished and etched sample of C-SLS fired at 1000°C (Figure 5.38(a) and (b)), showing the presence of plagioclase crystals (Pl) at the interface between clay relicts (DC) and glass (G). EDS (Figure 5.38(c)) reveals high Ca, Al and Si contents, suggesting that the feature is plagioclase, although the Na peak was probably suppressed by the EDS detection system as explained previously. Plagioclase was present in the form of tabular crystals up to 5 μm long. The tabular plagioclase should be considered to be a product of crystallization of glass enriched with alumina migrating from the clay.

It can be concluded that the crystallization of these three crystalline phases (wollastonite, cristobalite and plagioclase) starts with the diffusion/migration of Na^+ (which has higher mobility than Ca^{2+}) from molten SLS particles to their interfaces (due to the Na concentration gradient between molten SLS and its surroundings which, in this case, consists of clay relicts) leaving the reacted SLS glass particles rich in calcium and silica, providing suitable conditions for formation of wollastonite and cristobalite. Ca^{2+} ions also migrate beyond the SLS particle surfaces to the surrounding environment. The migrating Na^+ and Ca^{2+} then react with alumina and silica from the clay forming plagioclase.

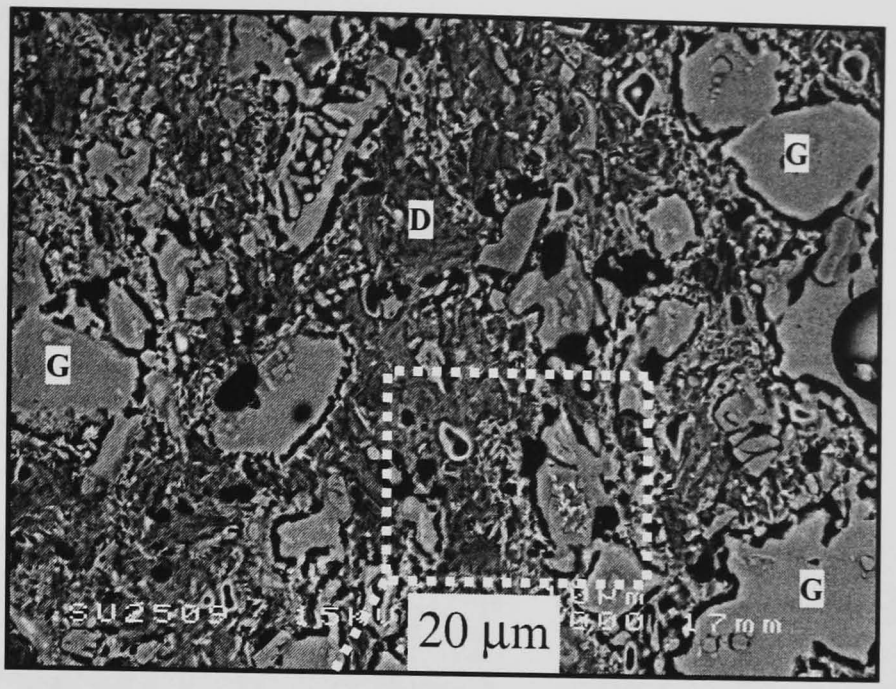

(a)

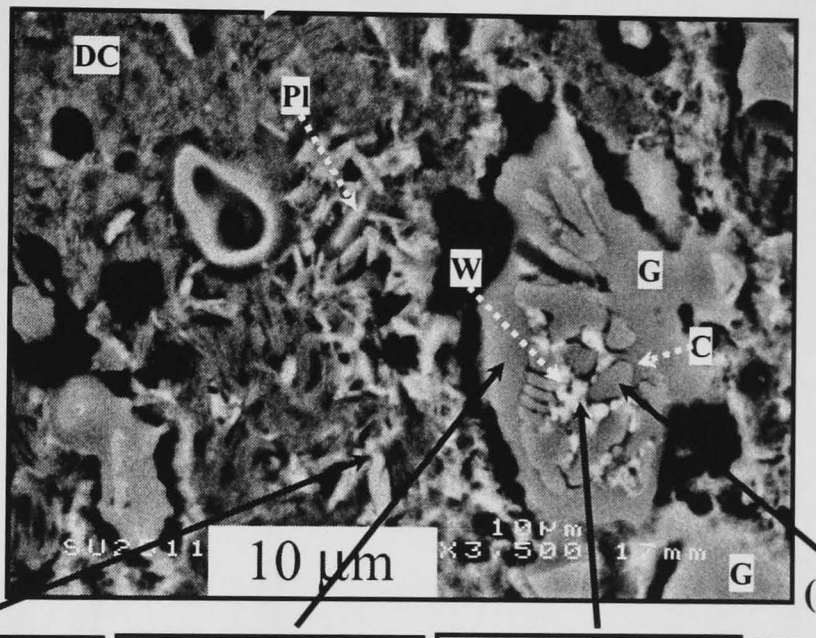

(b)

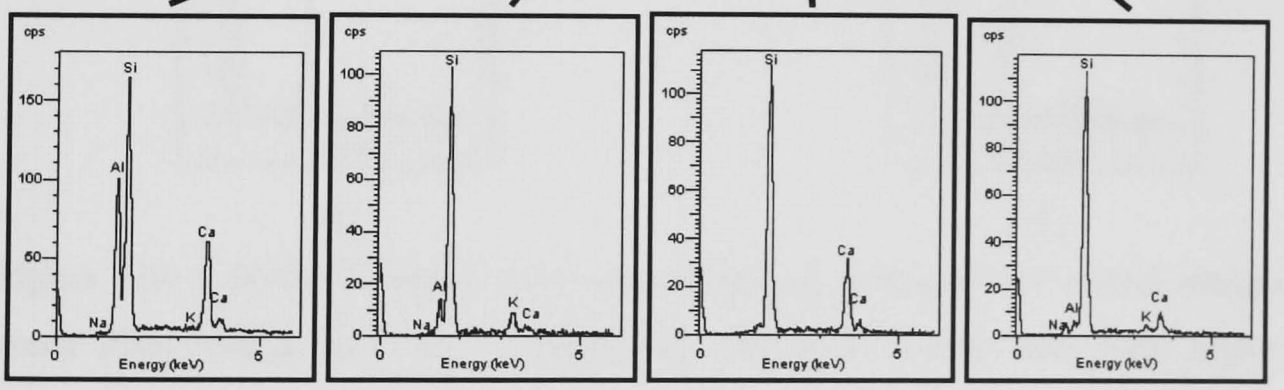

(c) (d) (e) (f)

Figure 5.38 - SEM/BS images of a cross-sectioned, polished and etched sample made from C-SLS fired 3h at 1000°C (a) and of a selected area with higher magnification (b). EDS traces from corresponding areas are shown in (c)-(f). (C = cristobalite, DC = decomposed clay, G = glassy phase, Pl = plagioclase, W = wollastonite)

Figures 5.39(a) and (b) show the morphology of mullite found in C-SLS fired at 1000°C. EDS (Figure 5.39(d)) reveals that the ≤3 μm long crystals are mullite. As the firing temperature is low for secondary mullite formation, and the EDS trace shows a high Al-content, the mullite is more likely to be primary mullite. Mullite particles are difficult to find in this mixture, this is possible due to the low amount present. The crystal high in Si present in Figure 5.39(a) may be either a partially dissolved quartz grain originating from kaolin clay impurity, or a cristobalite grain.

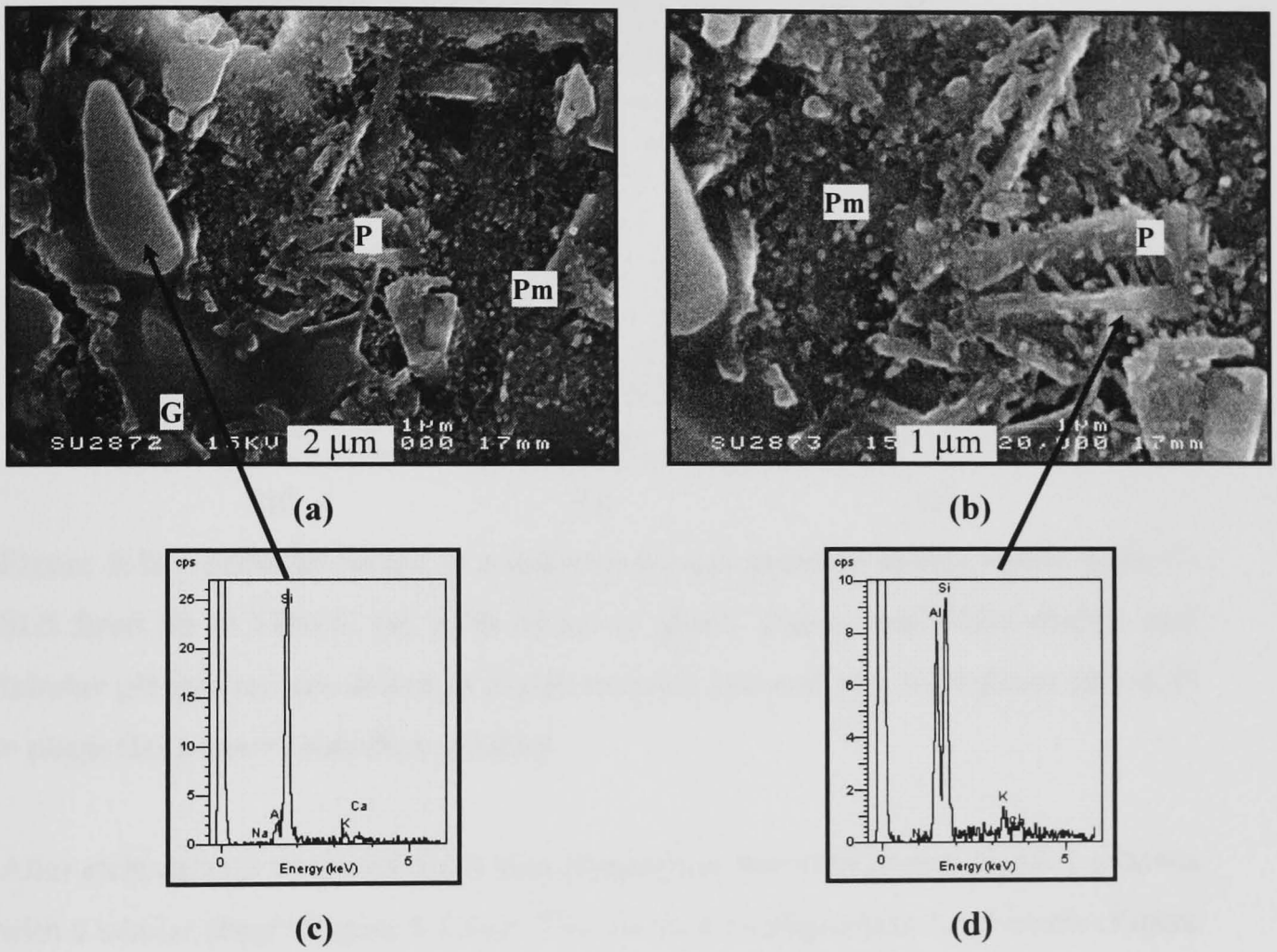

Figure 5.39 - SEM/SE images of a cross-sectioned, polished and etched sample made from C-SLS fired 3h at 1000°C (a), and of a selected area with higher magnification (b). EDS traces from corresponding areas are shown in (c) and (d). (G = glassy phase, Pm = primary mullite)

Even though XRD of C-SLS samples fired 3h at 1200°C (Figure 5.12) shows neither mullite nor plagioclase peaks, the microstructures (Figure 5.40(a)) reveal these phases which are confirmed by EDS analysis (Figure 5.40(c) and (d)).

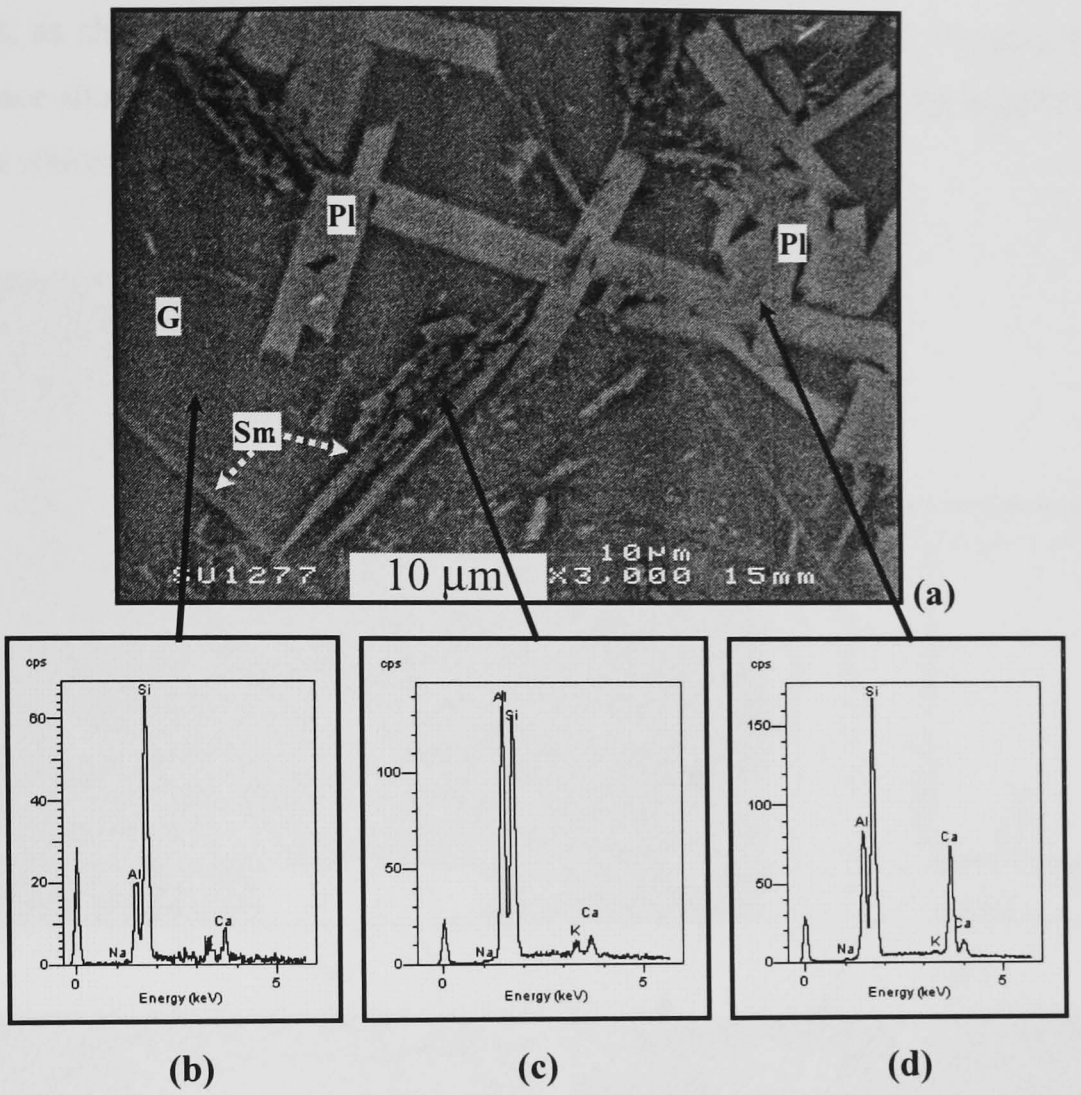

Figure 5.40 - SEM/BS image of a cross-sectioned, polished sample made from C-SLS fired 3h at 1200°C (a). EDS traces of glassy phase, needle-like mullite and tabular plagioclase are shown in (b), (c) and (d), respectively. (G = glassy phase, Pl = plagioclase, Sm = secondary mullite)

After etching with 5wt% HF for 3 min, plagioclase was etched away leaving grooves with a tabular shape (Figure 5.41(a)). The absence of plagioclase XRD peaks (Figure 5.12) and the presence of tabular shaped features with a chemical composition (EDS trace in Figure 5.40(d)) similar to that of plagioclase, suggest that its amount was below the XRD detectability (~5wt%). Needle-like mullite was also observed in C-SLS fired at 1200°C. The (≥15 µm long) mullite crystals shown in Figure 5.40(a) did not dissolve in the liquid on firing, being found as small (≤25 µm) clusters (Figure 5.41(c)) derived from the core of decomposed clay agglomerates. However, most of the mullite was dissolved in the liquid, as suggested by the absence of crystalline peaks in XRD from this sample (Figure 5.12). This XRD trace shows a very intense amorphous hump, confirming the high amount of glass formed on cooling, as well as nepheline ($K(Na,K)_3Al_4Si_4O_{16}$) peaks. Nepheline was revealed as ~1 µm rounded

crystals, as shown in Figure 5.41(d) and EDS in Figure 5.41(b). The fact that the EDS trace shows high Si and Ca peaks is likely due to overlap of the high Si and Ca glass in which the nepheline crystals are embedded.

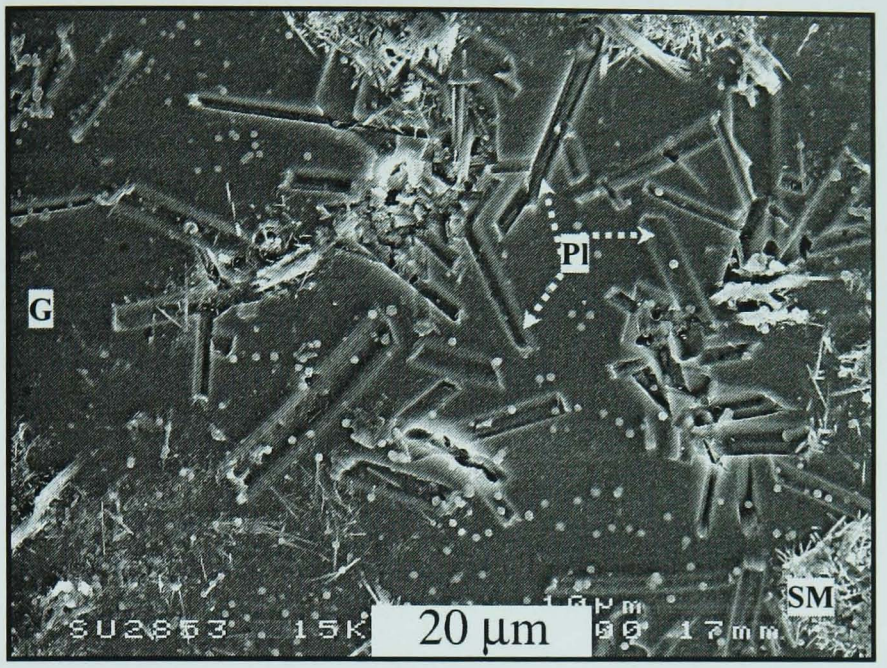

(a)

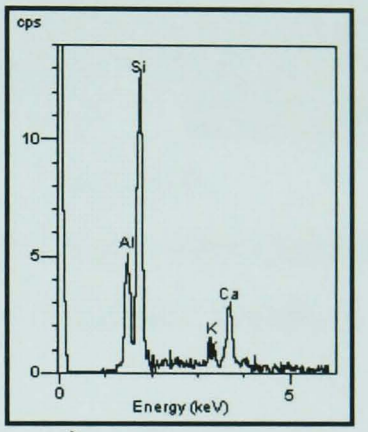

(b)

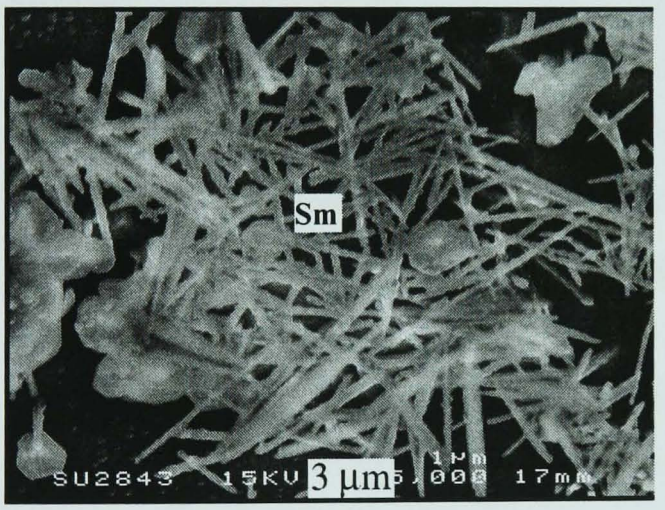

(c)

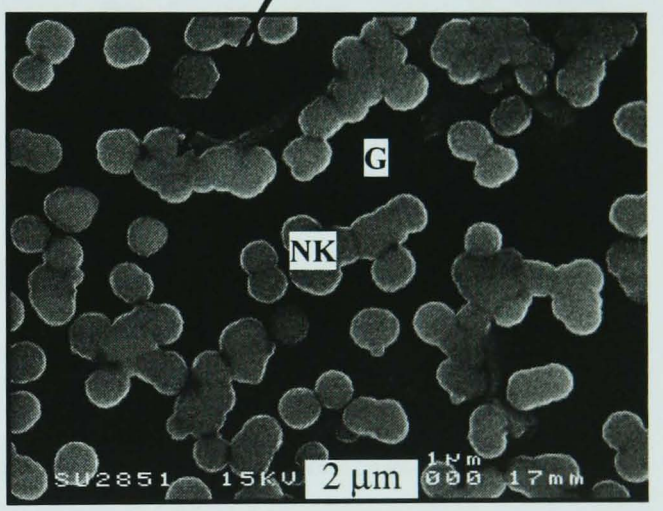

(d)

Figure 5.41 - SEM/SE image of a cross-sectioned, polished and etched sample made from C-SLS fired 3h at 1200°C (a). Aggregated acicular mullite crystals are shown in (c), and spheroidal nepheline (NK) crystals are shown in (d) with their EDS (b). (G = glassy phase, Pl = plagioclase, NK = nepheline, Sm = secondary mullite)

5.4.4 - Quartz and nepheline syenite mixtures (Q-NS)

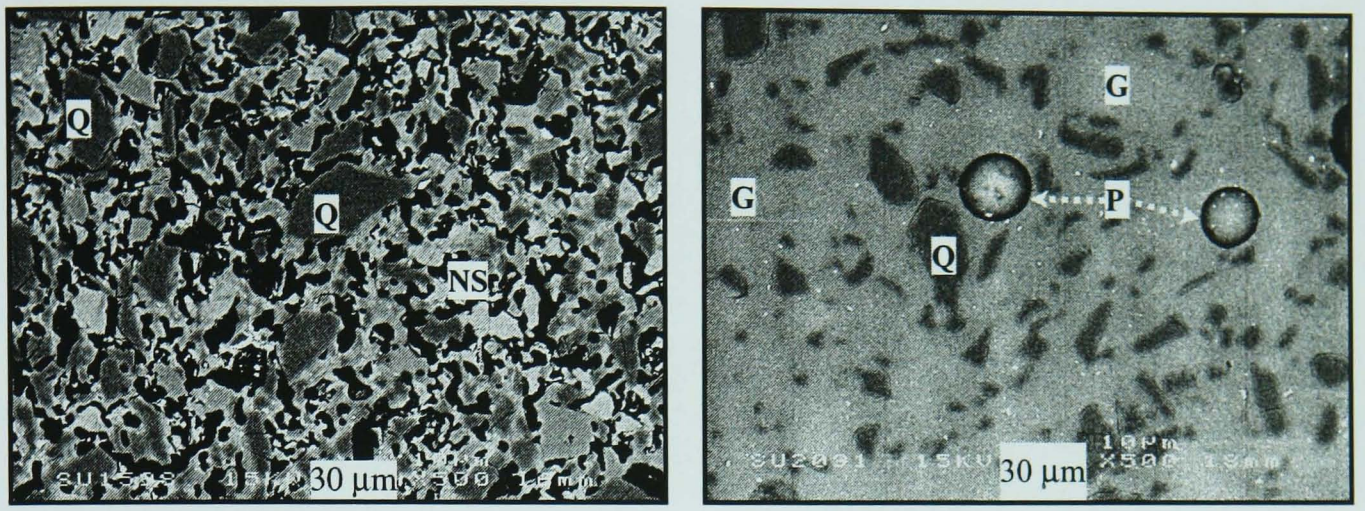

(a) 1000°C **(b)** 1200°C

Figure - 5.42 SEM/BS images of cross-sectioned, polished Q-NS pellets fired 3h at 1000°C (a), and 1200°C (b). (G = glassy phase, NS = nepheline syenite, P = pore, Q = quartz)

SEM/BS images from Q-NS (Figure 5.42(a)) revealed that after firing at 1000°C, feldspar has been partially melted, as confirmed by the decreased XRD peaks (Figure 5.14). After firing 3h at 1200°C, nepheline syenite melted entirely (no nepheline syenite XRD peaks were detected in Figure 5.14) to a liquid phase which cooled to form a glass. The presence of molten feldspar is evidenced by a dense microstructure with partially dissolved quartz grains and rounded pores. Comparing the microstructural evolution of C-Q to that of Q-NS, it can be clearly observed that the particle size of quartz in C-Q is larger than that in the Q-NS mixture fired at 1000-1200°C. This confirms dissolution of quartz by the molten feldspar.

5.4.5 - Quartz and SLS glass mixtures (Q-SLS)

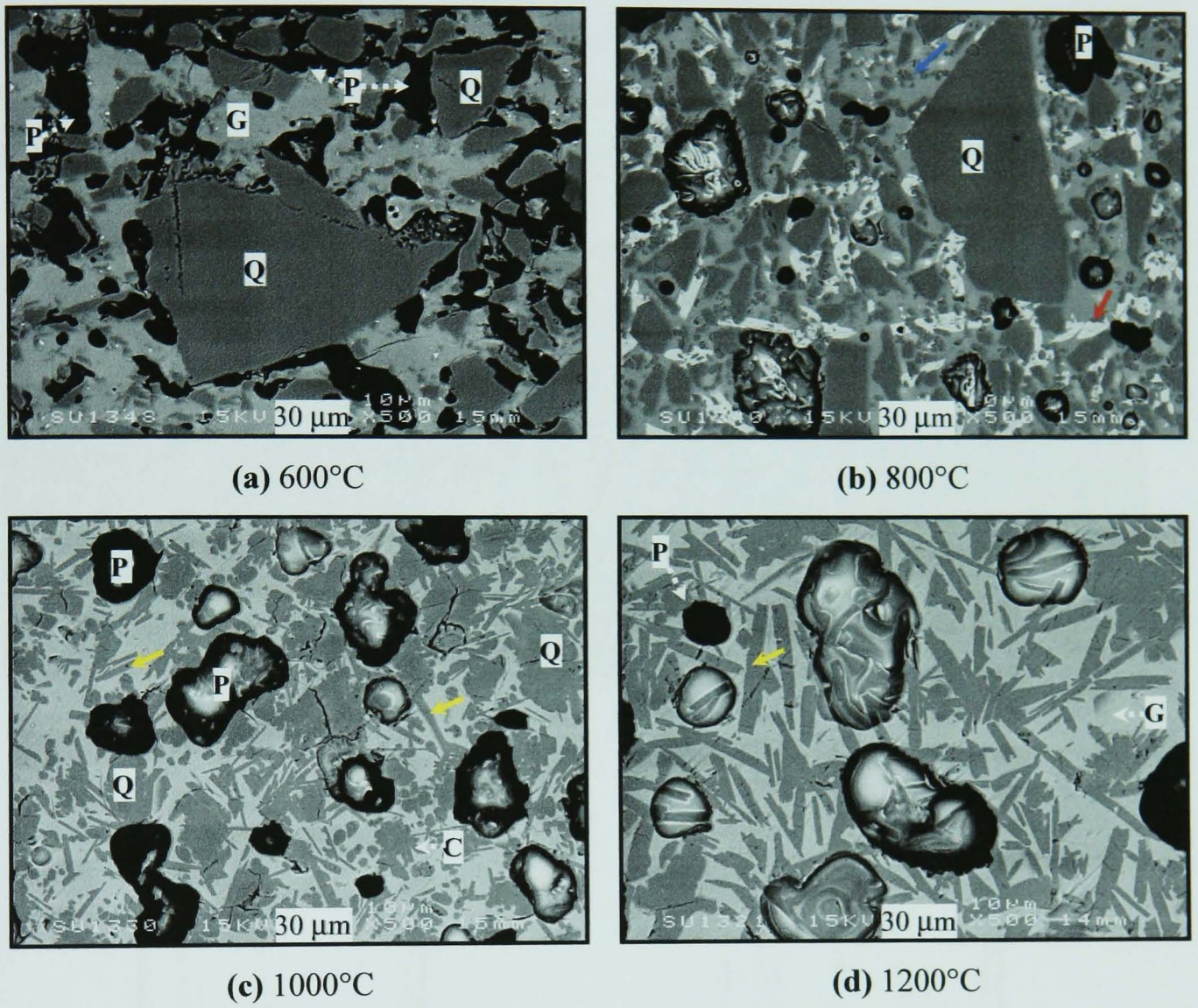

(a) 600°C **(b)** 800°C

(c) 1000°C **(d)** 1200°C

Figure 5.43 - SEM/BS images of Q-SLS fired 3h at 600°C (a), 800°C (b), 1000°C (c) and 1200°C (d). (C= cristobalite, G = glassy phase, P = pore, Q = quartz)

Microstructural evolution of fired Q-SLS samples is shown in Figure 5.43. After firing 3h at 600°C (Figure 5.43(a)), SLS glass starts to soften and sinter, although interconnected pores are still visible. Quartz (Q) does not show any evidence of reaction, apart from its α-β inversion which cannot be observed in the microstructure. After firing 3h at 800°C (Figure 5.43(b)), SLS glass melted, promoting partial dissolution of quartz, as observed by the rounded edges of the finer particles. The pores (P) become isolated and rounded, showing early densification. Crystallization was observed by the presence of bright (see red arrow in the BSI) areas and rounded fine particles (see blue arrow), which will be discussed in detail later for Figure 5.45. The bright areas are not observed after firing at 1000°C (Figure 5.43(c)), as the glass is completely reacted and transformed. Quartz particles are heavily ragged indicating

dissolution and transformation to cristobalite. The rounded pores are larger than those observed in Figure 5.43(b). Elongated particles (see yellow arrow) are observed in the glass (G) particularly surrounding quartz particles. The microstructure after firing at 1200°C (Figure 5.43(d)) comprised these elongated particles (see yellow arrow) embedded in the glass and larger pores.

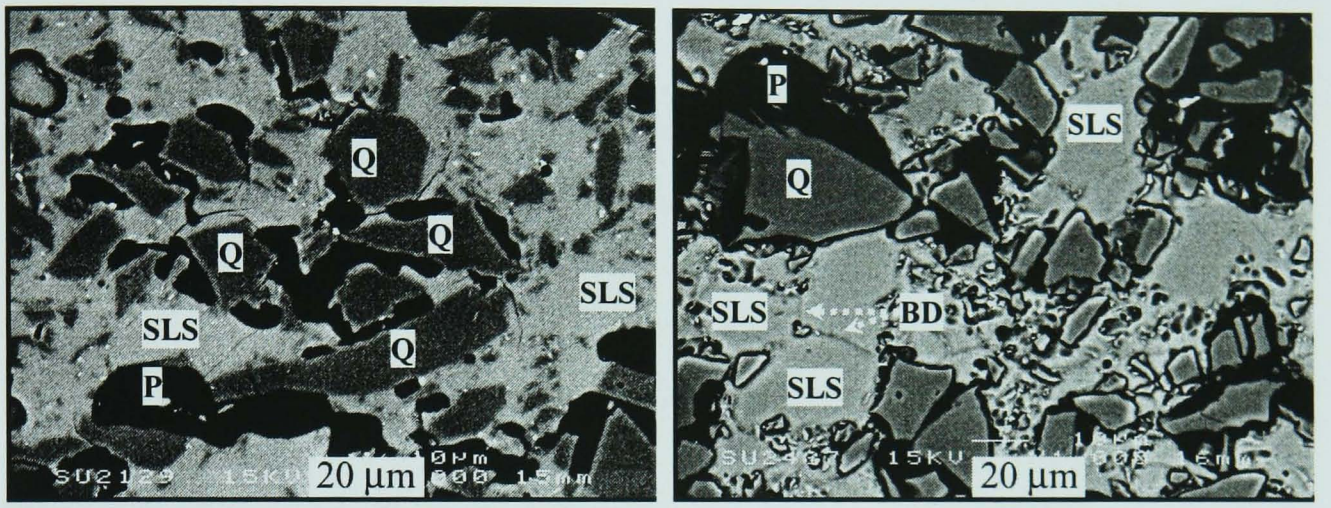

Figure 5.44 - SEM/BS image of a cross-sectioned, unetched (a) and etched samples (b) of Q-SLS fired 3h at 600°C. EDS traces of quartz and SLS glass are shown in (c) and (d). (BD = boundary between particles, P = pore, Q = quartz, SLS = soda-lime-silica glass)

Figure 5.44 shows high magnification BS images of unetched (a) and etched (b) Q-SLS after firing at 600°C. The microstructure of etched samples (Figure 5.44(b)) clearly shows sintering of SLS particles and boundaries (BD) between particles. This was not observed in the unetched sample (Figure 5.44(a)). EDS of quartz (darker regions) and SLS glass (brighter regions) are shown in Figure 5.44(c) and (d), respectively, from the unetched sample.

High magnification BS images of Q-SLS fired at 800°C (Figure 5.45(a) and (b)) show crystallization of devitrite (D) (brighter particles) and cristobalite (C, darker aggregates of small, rounded particles (≤3 μm in diameter)) as confirmed by EDS (Figure 5.45(c) and (d)) and XRD (Figure 5.16). These two crystalline phases are devitrified from softened SLS glass, as previously observed by Willems (1966). After firing at 800°C, quartz shows rounded edges indicating partial dissolution.

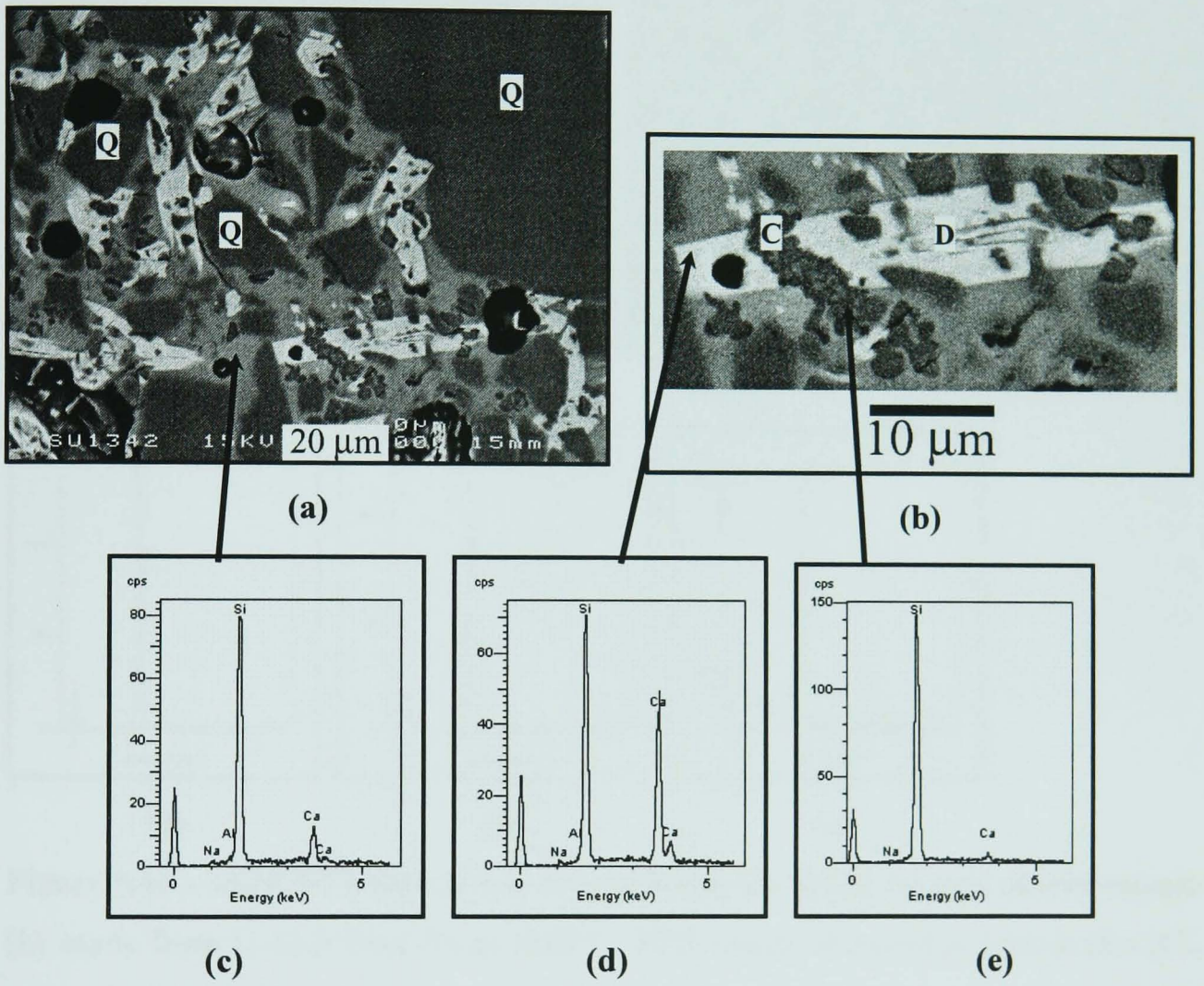

Figure 5.45 - SEM/BS image of a cross-sectioned, polished sample made from Q-SLS fired 3h at 800°C (a). Close up image of individual particles is shown in (b). EDS traces of glassy phase, devitrite particle (D) and cristobalite (C) are shown in (c), (d) and (e).

After firing at 1000°C for 3h, BS images of unetched samples (e.g. Figure 5.46(a)) and SE images of etched samples (e.g. Figure 5.46(b)) show aggregates of cristobalite crystals (C) (≤6 μm diameter) resulting from the polymorphic transformation of quartz, and some tabular (≤30 μm long) tridymite crystals (T). EDS (Figure 5.46(c)) is from agglomerates of rounded cristobalite crystals, and in Figure

5.46(d) is from tabular tridymite crystals which were not observed after firing at 600 and 800°C, and in Figure 5.46(e) is from the glassy phase. Since there is no chemical difference between these two forms of silica as observed by EDS, they can only be distinguished by their morphology and XRD analysis.

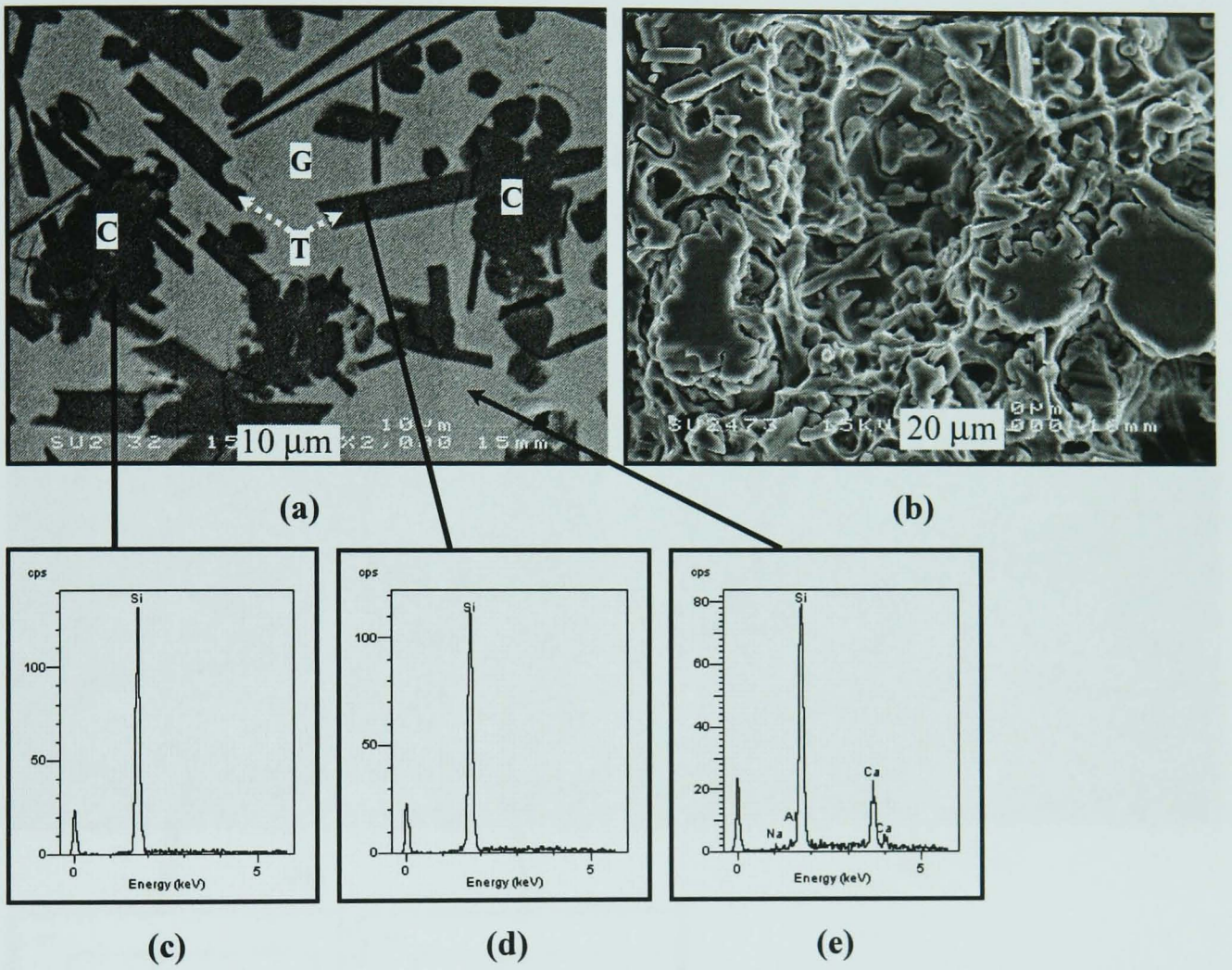

Figure 5.46 - SEM/BS image of a cross-sectioned, unetched (a) and etched sample (b) made from Q-SLS fired 3h at 1000°C. EDS traces of rounded cristobalite (C), elongated tridymite (T) and glassy phase (G) are shown in (c), (d) and (e), respectively.

XRD of Q-SLS fired at 1000°C (Figure 5.16) shows that the main silica phase is cristobalite accompanied by the main peaks of tridymite. Figure 5.16 also shows lower quartz peak intensities indicating its dissolution. The microstructure reveals that the quartz crystals lose their angular edges and are surrounded by an amorphous solution rim through reaction with melted SLS flux, and later are partially or totally replaced by groups of small rounded cristobalite crystals. Tridymite crystallizes from the Si-rich liquid in the presence of alkalis (Van Vlack, 1960; Holmquist, 1961; Stevens *et al.*, 1997; Venezia *et al.*, 2001). Monks and Parker (1980) stated that

devitrite crystals decompose at 1070°C. In the present study, devitrite disappears after firing at 1000°C probably due to the long (3h) soaking period at temperature, causing transport of alkalis to the liquid matrix.

Only tabular tridymite crystals (≤50 μm long) were observed after firing at 1200°C (Figure 5.47(a) and (b)). EDS (Figure 5.47(c)) and XRD (Figure 5.16) confirm the presence of tridymite. Cristobalite seems to have dissolved, and only small XRD peaks of this phase are seen in Figure 5.16. EDS (Figure 5.47(d)) indicates that the glass was rich in Si and Ca (Na could not be detected although its presence is expected).

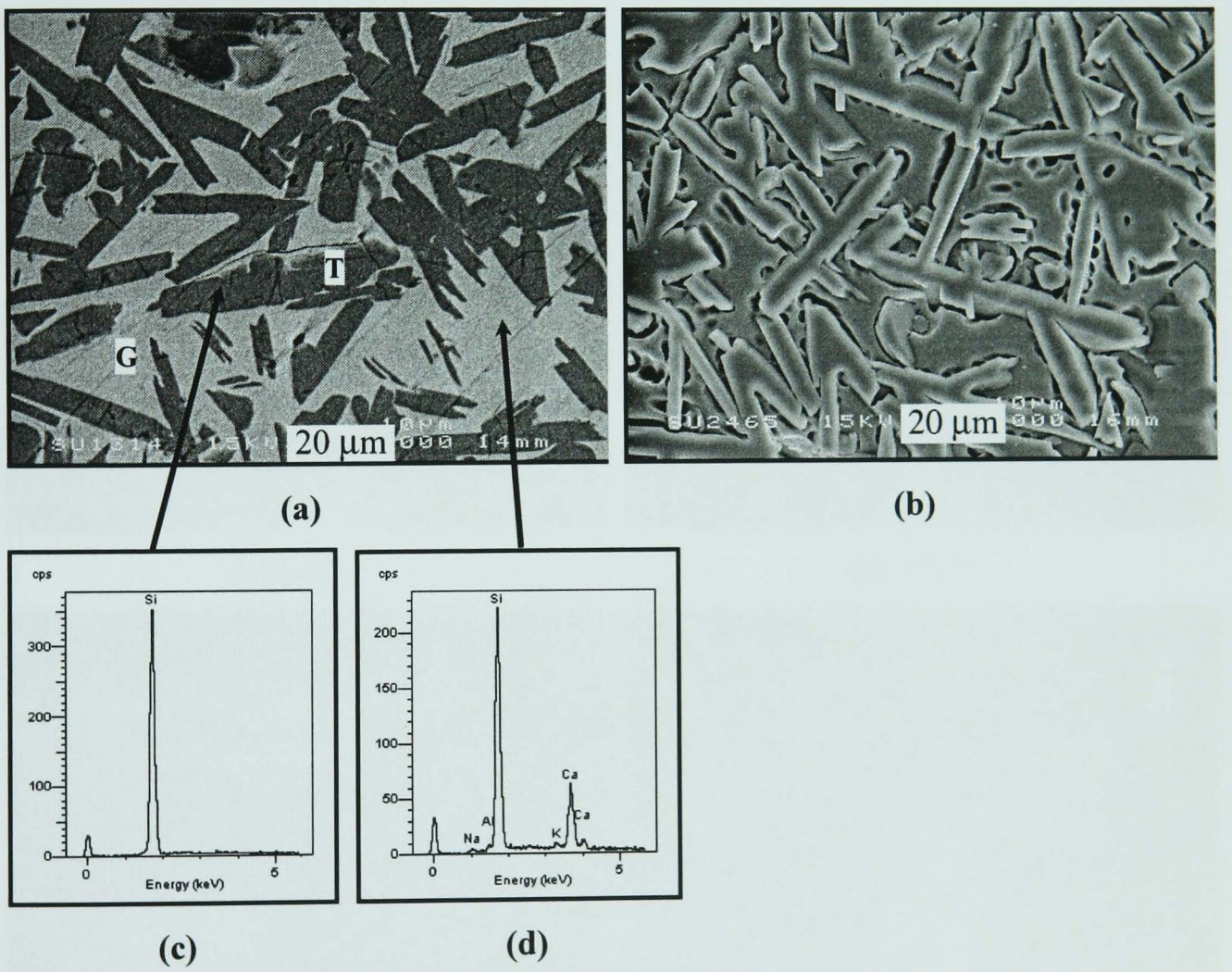

Figure 5.47 - SEM/BS image of a cross-sectioned, unetched (a) and etched sample (b) made from Q-SLS fired 3h at 1200°C. EDS traces of elongated tridymite (T) and glassy phase (G) are shown in (c) and (d), respectively.

The evolution of the quartz polymorphs in the mixture of Q-SLS on firing comprises: cristobalite crystallization from SLS glass devitrification, quartz partial dissolution and transformation to cristobalite, tridymite crystallization from the Si-rich liquid,

and cristobalite dissolution promoting further tridymite crystallization. Alternatively, it could be concluded that the microstructural evolution of these heated Q-SLS samples starts with devitrification of cristobalite and devitrite (and some wollastonite) from molten SLS glass after firing at 800°C followed by the partial dissolution of quartz and devitrite (and wollastonite), and the transformation from amorphous silica to rounded cristobalite accompanied by formation of a small amount of tabular tridymite after firing to 1000°C. At higher temperatures, 1200°C, the proportion of tabular tridymite increases and becomes the main phase whereas the proportion of rounded cristobalite decreases.

5.4.6 - Nepheline syenite and SLS glass mixtures (NS-SLS)

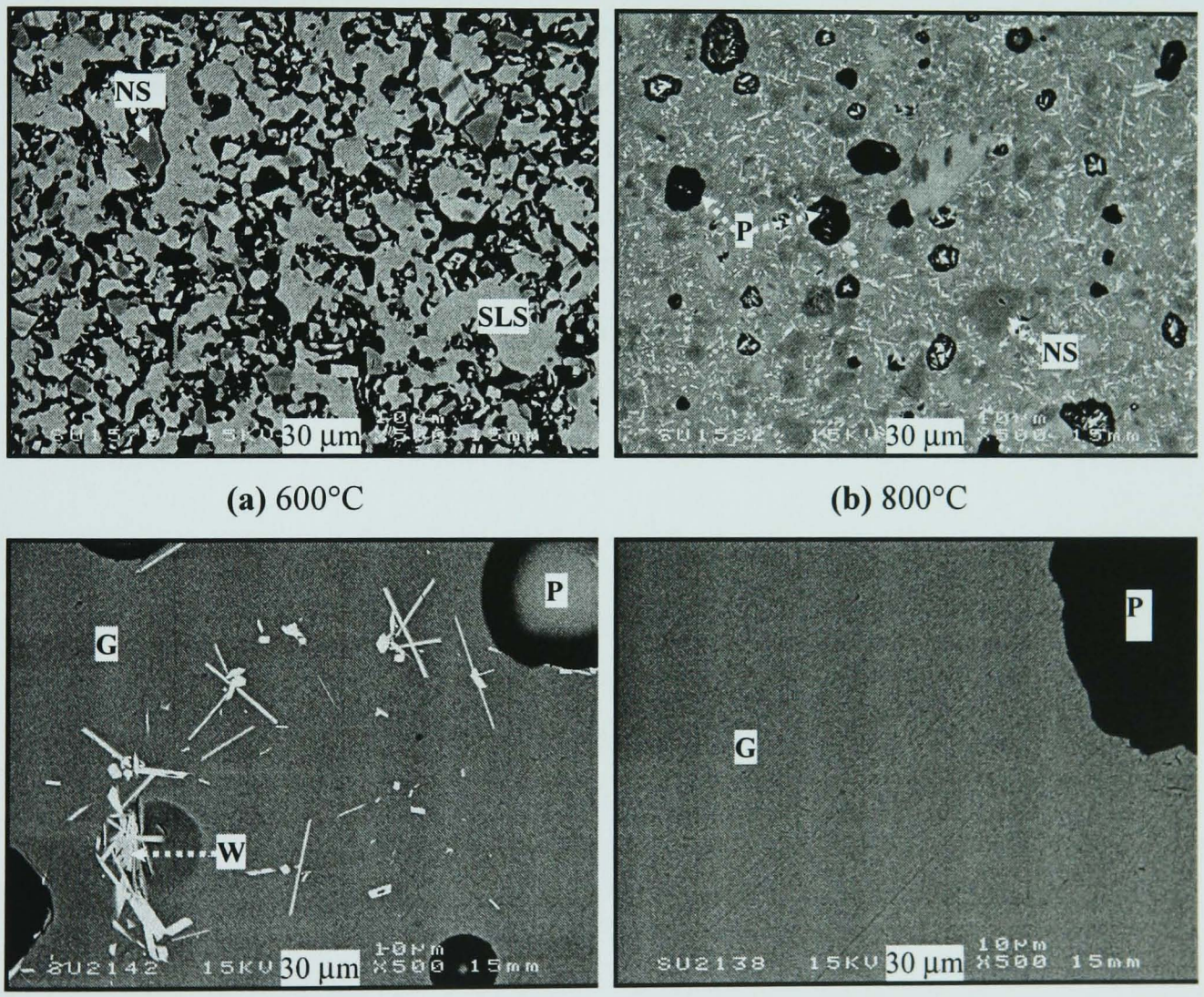

(a) 600°C **(b)** 800°C

(c) 1000°C **(d)** 1200°C

Figure 5.48 - SEM/BS images of cross-sectioned, polished NS-SLS pellets fired 3h at 600°C (a), 800°C (b), 1000°C (c) and 1200°C (d). (G = glassy phase, NS = nepheline syenite, P = pore, SLS = soda-lime-silica glass, W = wollastonite)

The microstructural evolution of NS-SLS after firing at 600, 800, 1000 and 1200°C is shown in Figure 5.48. Open porosity is still evident after firing at 600°C, and is also observed in the mixture of Q-SLS fired at 600°C (Figure 5.44). SLS glass particles in close contact were found to weld together and create continuous paths. This was not observed in the C-SLS mixture, as the proportion of SLS glass in the mixture with clay (66.67wt% clay, 33.33wt% SLS glass) was too low to allow for SLS glass inter-particle contact and also because small particles of clay were inevitably present between larger SLS particles. After firing at 800°C (Figure 5.48(b)), progressive melting of SLS glass particles promoted formation of small (≤25 μm) isolated pores (P). Small (≤10 μm), bright features indicate crystallization from the SLS glass. Those crystals are clearly observed after firing the mixture at 1000°C (Figure 5.48(c)), as they grew to ≤35 μm and the glassy phase seems to be homogeneous and contain larger (≤70 μm) isolated pores. No individual nepheline syenite and/or SLS glass particles could be observed, due to the accelerated dissolution of the feldspar contained in the nepheline syenite in the presence of melted SLS glass. Mixtures of nepheline syenite with either clay or quartz did not show such accelerated nepheline syenite dissolution. The microstructure after firing at 1200°C, from the SEM/BS image in Figure 5.48(d) does not show any trace of the previously mentioned crystals. Pores became even larger (≤100 μm) due to overfiring.

Higher magnification SEM/BS image of NS-SLS after firing at 600°C and EDS mapping (Figure 5.49) show the continuous SLS glass paths high in Ca, Si and Na (with poor signal intensity). Also shown in detail are undissolved feldspar particles from the nepheline syenite (i.e. the K, Si and Al areas correspond to microcline).

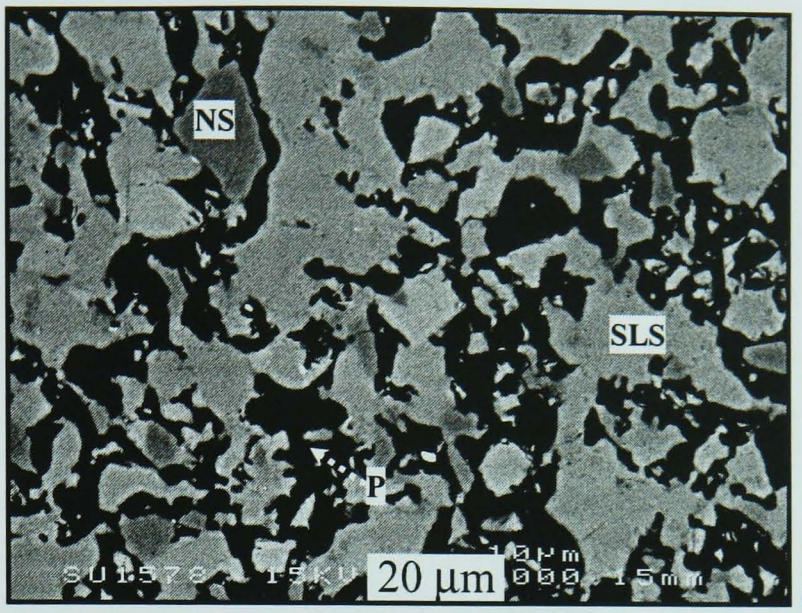

(a)

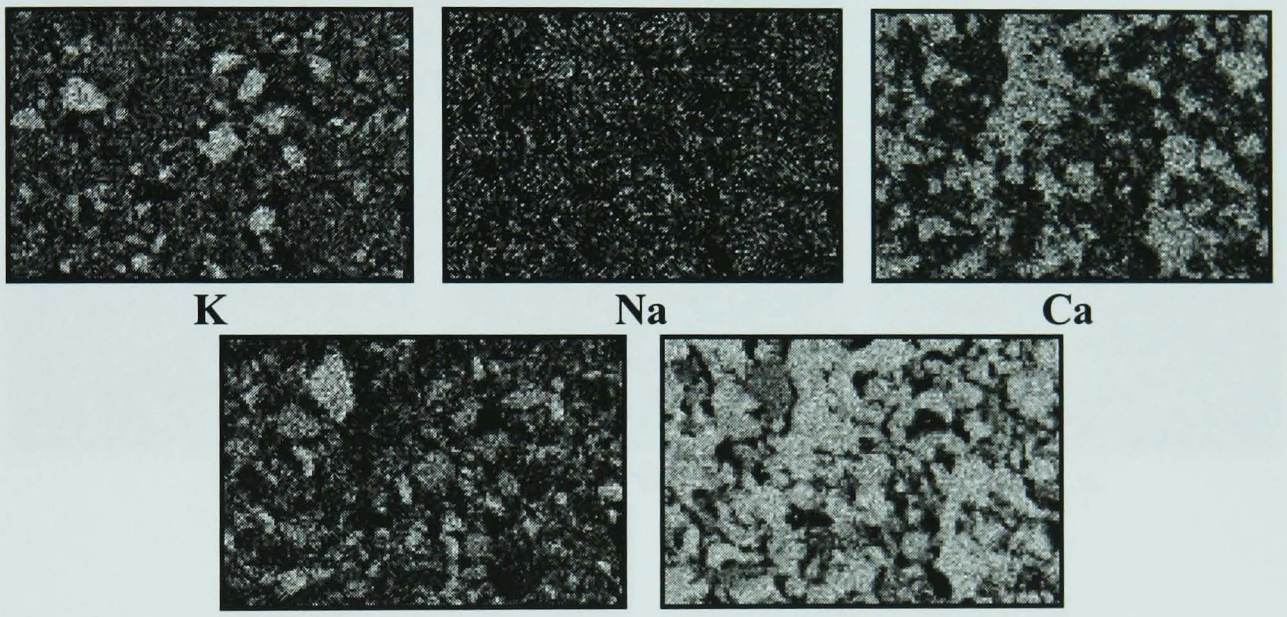

(b)

Figure 5.49 - SEM/BS image of a cross-sectioned, polished pellet made from NS-SLS fired 3h at 600°C. X-ray dot mapping is shown in (b), where the brighter regions are higher in the corresponding element.

The brighter elongated particles shown in detail in Figure 5.50(a) for NS-SLS fired at 800°C were identified by EDS (trace in Figure 5.50(c) and maps in Figure 5.50(d)) as wollastonite (W), consistent with XRD (Figure 5.18). The large (~50 µm long) particle high in K, Al and Si (Figure 5.50(b)) is probably potash feldspar (KF) which remains undissolved.

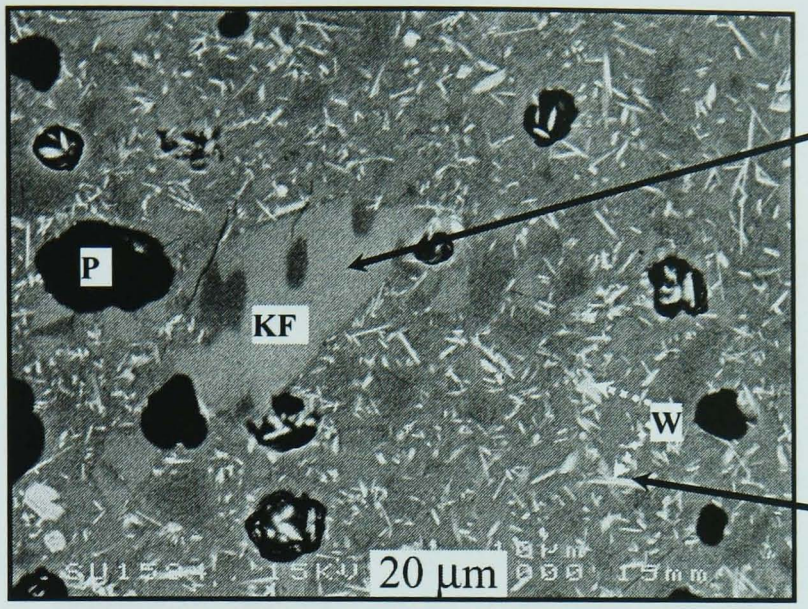

(a)

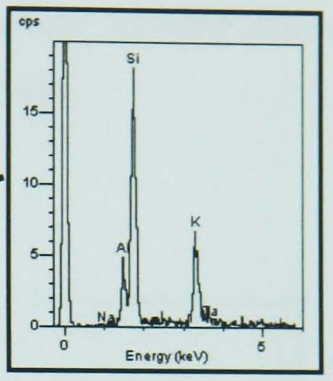

(b)

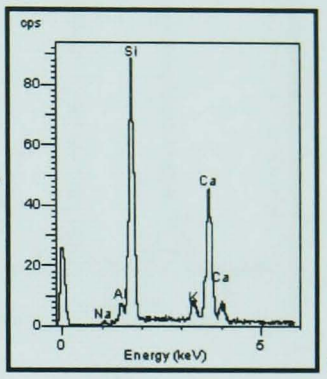

(c)

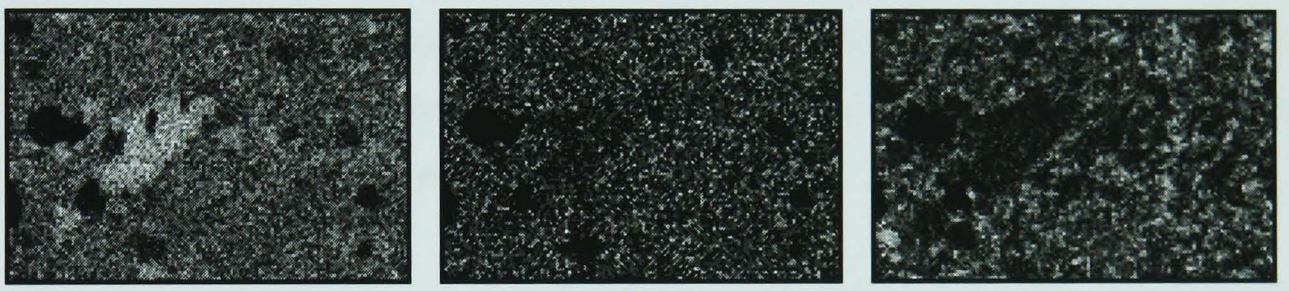

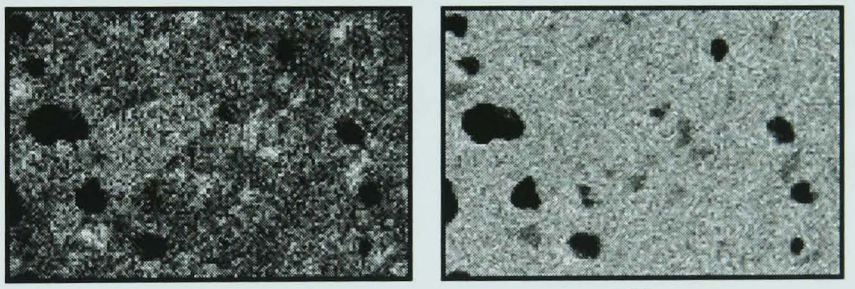

(d)

Figure 5.50 - SEM/BS image of a cross-sectioned, polished pellet made from NS-SLS fired at 800°C. (b) is an EDS trace for the irregular light grey K-feldspar crystal shown in the centre of (a). X-ray dot mapping is shown in (c), where the brighter regions are higher in the corresponding element. (KF = K-feldspar, P = pore, W = wollastonite)

The large crystals shown in detail in Figure 5.51(a) were identified as high in Ca and Si (EDS in Figure 5.51(b)), and identified by XRD (Figure 5.18) as wollastonite (W). Although no crystals were observed by SEM after firing at 1200°C, XRD (Figure

5.18) revealed small nepheline crystalline peaks, which would probably consist of nano-sized particles in the glass, not shown in the present study.

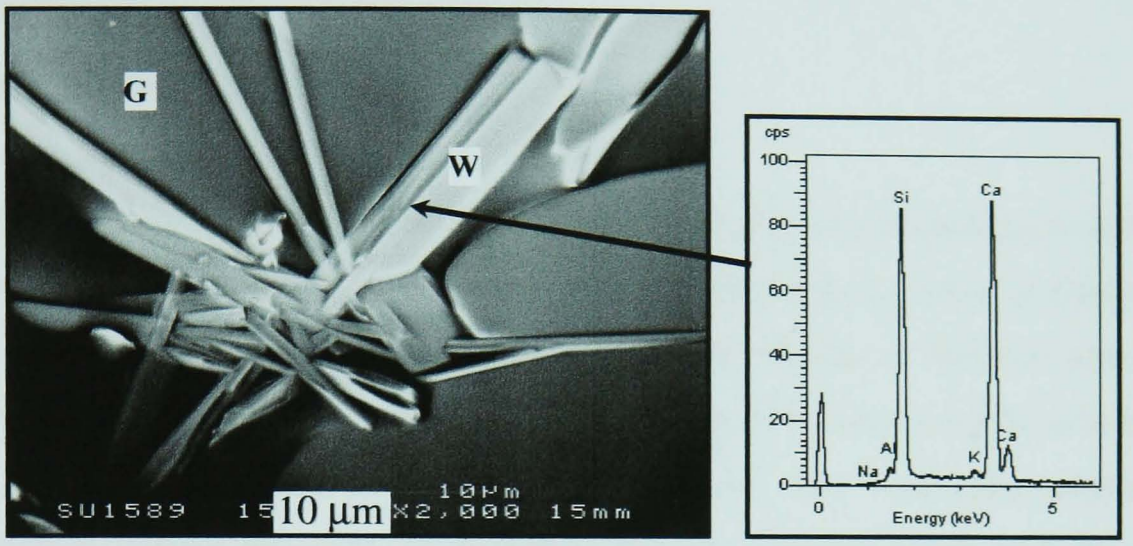

(a) (b)

Figure 5.51 - SEM/BS image of a cross-sectioned, polished sample made from NS-SLS fired 3h at 1000°C showing elongated particles (a) and its EDS trace high in Ca and Si (b). (G = glassy phase, W = wollastonite)

SEM of an NS-SLS sample polished and chemically etched with HF acid is shown in Figure 5.52. The elongated particles, probably wollastonite, were etched away leaving grooves with an elongated shape (see red arrow). This correlates well with SEM/SE images of SLS pellets fired at 800°C (Figure 4.35), which show similar grooves.

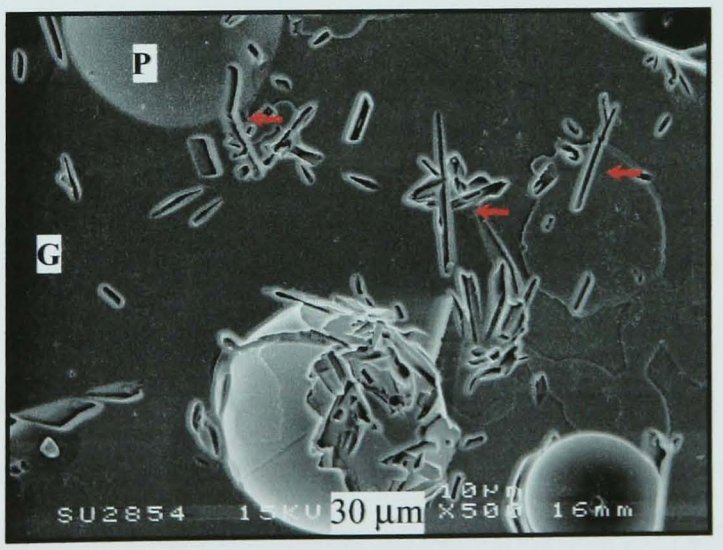

Figure 5.52 - SEM/BS image of a cross-sectioned, polished and etched sample made from NS-SLS fired 3h at 1000°C showing elongated particles. (G = glassy phase, P = pore)

CHAPTER 6 - STUDY OF THE STANDARD AND SLS-CONTAINING WHITEWARES

6.1 - INTRODUCTION

Full characterization of raw materials (kaolin clay, quartz, nepheline syenite and SLS glass) and binary mixtures between them were shown and discussed in chapters 4 and 5. In this chapter, whiteware batches (the mixtures of three or four raw materials) are presented. Standard whiteware batch composition (S0) comprising 50wt% kaolin clay, 25wt% quartz and 25wt% nepheline syenite flux was reformulated by substituting various amounts of nepheline syenite for SLS glass, and therefore creating another four whiteware batch compositions. In these new batches, nepheline syenite (NS) was partially replaced by SLS glass, as follows: 6.25wt% NS replacement (S25), 12.5wt% (S50), 18.75wt% (S75), and 25wt% (S100) containing 25wt% SLS glass as flux system and no NS. The fired samples were characterized in terms of bulk density, water absorption and linear shrinkage. DTA/TG and dilatometry are used to study the thermal behaviour on firing and cooling whiteware batches. Microstructure and the main phase transformations in the fired samples were examined by XRD, SEM/EDS and TEM/EDS.

6.2 - PHYSICAL PROPERTIES

Bulk density, water absorption and linear shrinkage of the fired pellets are reported as a function of temperature for all the batch compositions tested. Figure 6.1 shows the variation of bulk density with firing temperature for fired specimens of all batches after heating at 10°C/min to specific firing temperatures and holding for 3h before cooling at ~10°C/min. Of the samples fired at 600°C, those from batch S0 attained the lowest bulk density. This firing temperature is too low for vitrification to occur, even in those compositions containing SLS glass. Addition of SLS glass with coarser particle size distribution than nepheline syenite (Table 4.2) increased the bulk density of specimens fired at 600°C with increasing SLS up to a limit of 18.75wt% SLS glass (batch S75). Total replacement of nepheline syenite by SLS glass (S100) led to a decrease in bulk density, probably because finer nepheline syenite particles

had been filling the voids generated by the packing of coarser SLS particles (Reed, 1995) in samples S25-S75.

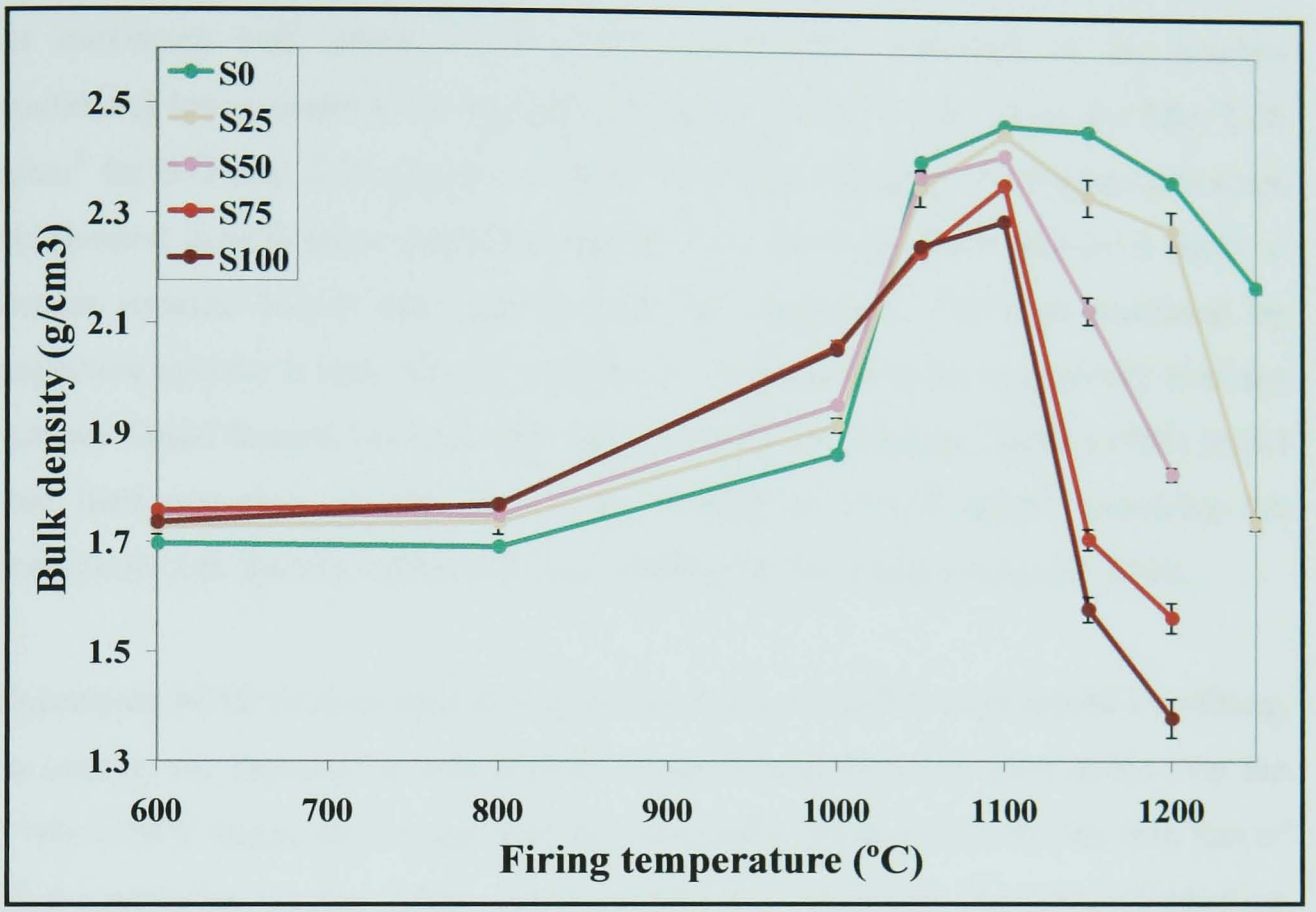

Figure 6.1 - Bulk densities of as-fired specimens from all batches. (Heating at 10°C/min, holding time 3h and cooling at 10°C/min).

Further evidence supporting the more efficient particle packing suggested when SLS glass was added to the fluxing system is that SLS glass has a density of ~2.50 g/cm^3, being lighter than nepheline syenite (density ~2.60 g/cm^3), therefore ruling out the effect of a denser component increasing the density of the mix. The same behaviour holds for samples fired at 800°C, although S100 shows an increase in bulk density, reaching that of S75. This effect can be explained by the glass transition point of the SLS glass particles at ~563°C (see DTA of SLS glass, Figure 4.4), which deform and better accommodate refractory particles, leading to accelerated densification for the batches containing the waste glass. Therefore, pellets from batches containing higher levels of SLS glass are denser between 800°C to 1000°C.

From 1000°C to 1050°C, specimens from the waste-free batch (S0) revealed a substantial increase in bulk density from 1.86 to 2.40 g/cm^3, exceeding that of

batches containing SLS glass (1.92-2.37 g/cm^3). This increase in bulk density is in line with the onset of nepheline syenite melting, giving a viscous liquid which fills the pores of the ceramic body during vitrification (Iqbal and Lee, 2000). S0 reaches its maximum bulk density (2.47 g/cm^3) at 1100°C, followed by the batches containing lower levels of SLS glass (2.45 g/cm^3 for S25, 2.41 g/cm^3 for S50, 2.36 g/cm^3 for S75 and 2.29 g/cm^3 for S100). Therefore, although SLS glass promotes accelerated densification, nepheline syenite is a more powerful flux as it leads to denser ceramic bodies after appropriate heat treatments. The melt produced by nepheline syenite is less viscous and fills in the porosity more extensively than the viscous liquid formed from the SLS glass at high temperatures. Rado (1988) found that hard porcelain usually has a bulk density of 2.3-2.5 g/cm^3, matching the maximum bulk density values from most batches in this study except for S100.

Specimens of all batches fired at temperatures above 1100°C experienced overfiring, as seen by the decrease in bulk density values. S0, however, is quite stable over the 1100-1150°C temperature range and its bulk density reduces more slowly than that of SLS-containing batches which experienced heavy bloating. The level of bloating increased with increasing SLS content. Overfiring in traditional ceramics can arise from several sources (Carty, 2002). In the present study, the most likely cause is the expansion of gases trapped from the early stages of firing. These gases are continuously released on firing, and also arise e.g. from kaolinite dehydroxylation at ~550°C (Lawrence, 1972). However, as vitrification takes place the gases have to diffuse through the liquid phase, forming bubbles inside the body and blisters and open pores on its surface. The softening of SLS glass and the early densification of batches containing this material are expected to promote gas entrapment during the early stages of densification, and therefore a compromise between SLS glass addition and the level of density attained in the fired ware should be made. Replacement of 6.25wt% SLS glass for nepheline syenite produced ceramic bodies with the same level of maximum bulk density (2.47 g/cm^3 for S0, and 2.45 g/cm^3 for S25) as waste-free whitewares. It is worth mentioning that changing the heating schedule may lesser the extent of bloating. For instance, decreasing the heating rate would allow longer time for glass softening which would give more time for gases to escape from the body and reduce gas entrapment. Also, a new heating schedule may be applied

such as holding at temperatures higher than that temperature range at which gas is released from clay dehydroxylation, but lower than the softening point of SLS glass. This may assist gas escape.

Water absorption values indicate the amount of open or interconnected porosity in the ceramic bodies (Ryan and Radford, 1987), and so reveal the opposite behaviour to the bulk density (Figure 6.1). For instance, the water absorption of hard porcelains has to be low ~0.0-0.5% (Rado, 1988). Batches containing high amounts of SLS glass as flux experience open pore closure (~0% water absorption) after firing at 1100°C, whereas S0 reaches that stage at 1200°C. Figure 6.2 also shows that S25 reaches its minimum open porosity after firing at 1150°C, and retains very low water absorption values even after firing at 1100°C and 1200°C. This is technologically beneficial, as it allows production of whitewares fired over a relatively broad range of temperatures.

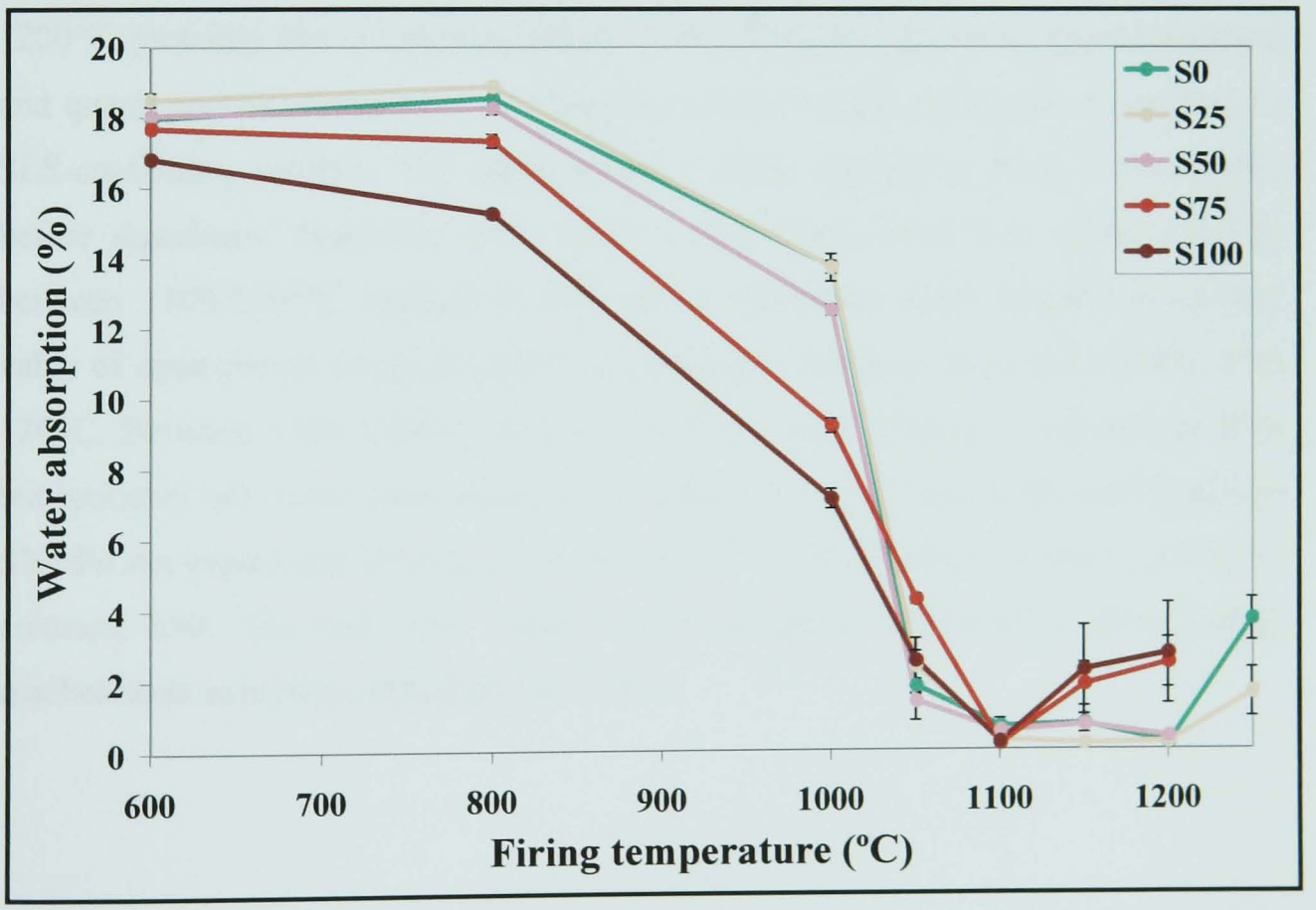

Figure 6.2 - Water absorption of as-fired specimens from all batches. (Heating at 10°C/min, holding time 3h and cooling at 10°C/min).

Using the bulk density and water absorption values from Figure 6.1 and 6.2 respectively, one can calculate the apparent porosity (Ryan and Radford, 1997) of the corresponding samples. The apparent porosity of S25 fired at 1100°C is 0.66% and that of S0 fired at the same temperature is 1.61%. This estimated result confirms that S25 has a lower porosity compared to that of the standard batch fired at 1100°C. However, S0 reaches a slightly lower apparent porosity (0.40%) after firing at 1200°C.

Linear shrinkage values confirm that the batches containing SLS glass shrink faster than the standard porcelain composition S0 (Figure 6.3). This is due to accelerated densification until 1000°C, above which melting of nepheline syenite with progressive pore closure causes increased shrinkage to a maximum at 1100°C. After firing at higher firing temperatures, specimens of S25, S50, S75 and S100 experience a significant decrease in linear shrinkage, caused by the expansion related to overfiring. Samples from S0 maintain constant shrinkage after firing from 1100-1200°C, probably due to opposing effects of densification caused by liquid formation and quartz particle dissolution, and bloating caused by gas expansion. Compared to SLS-containing batches, S25 experienced a slight expansion from 1100-1200°C before significant expansion after 1200°C. S25 experienced only slight bloating between 1100-1200°C because it attained its minimum water absorption (lowest value of open pores) firing at 1150C and retained low water absorption levels until 1200C. Between 1100-1200°C, S25 also suffered some increase in closed porosity but probably not in the same extent as in batches S50, S75 and S100, and therefore S25 did not experience bloating as severe as in S50-S100 until it reached 1200°C. In contrast, S50, S75 and S100 exhibit rapid expansion immediately after having reached their maximum shrinkage, at 1100°C.

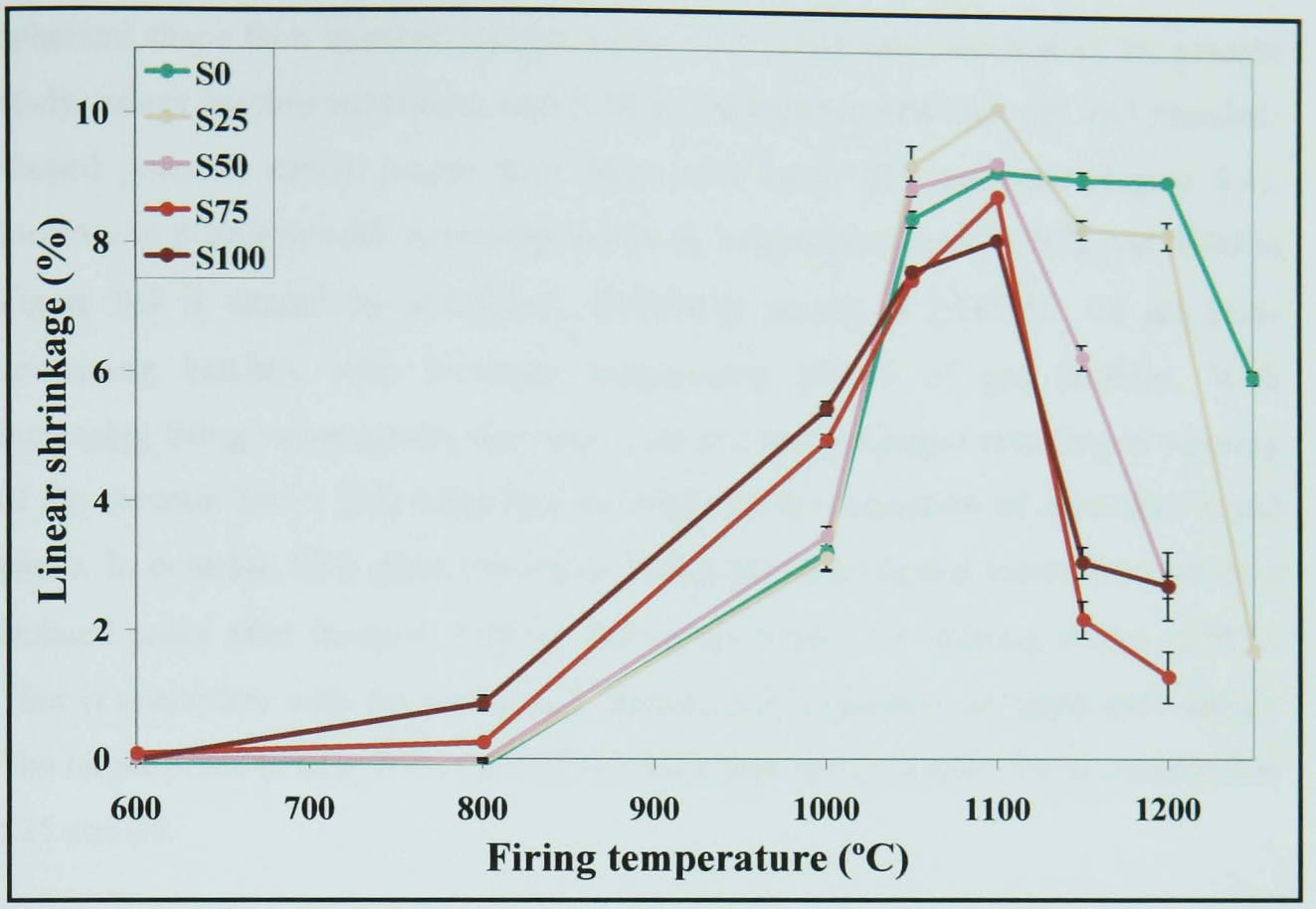

Figure 6.3 - Linear shrinkage of as-fired specimens from all batches. (Heating at 10°C/min, holding time 3h and cooling at 10°C/min).

These firing behaviours are confirmed by the low magnification SEM/SE images of fired and cross-sectioned samples (Figure 6.4 and 6.5). After firing at 1100°C, S25 exhibits a more compact microstructure in comparison to S0 (Figure 6.4), which is in good agreement with the observed water absorption and linear shrinkage values, as S25 presents lower water absorption (~0%) and higher shrinkage (~10%). Interconnected porosity is visible in S0, whereas only closed and rounded pores are present in S25. The average pore size appears to be larger in S50, S75 and S100. The firing behaviour observed could also be explained by taking into account that the higher calcium and sodium contents and lower alumina content, due to the presence of SLS glass, cause a decrease in viscosity of the liquid phase during sintering (Rambaldi, 2004). This liquid fills in the inter-particle porosity under strong capillary forces, allowing the sample to sinter at lower temperature.

Moreover, Kara *et al.* (2006) stated that pore geometry in samples exposed to the same heat treatment can indicate the relative viscosity of their melts and the degree of vitrification. In lower viscosity melts, gas bubbles can more quickly achieve their

spherical shape than in more viscous melts. This trend was observed in the present study, where batches containing higher SLS contents acquired isolated and rounded-shaped pores at earlier stages than those with lower SLS contents (Figure 6.4). Increase in pore size with increasing the firing temperature for S50, S75 and S100 in Figure 6.4 is caused by overfiring. Overfiring occurs at ≥1150°C for all SLS-containing batches, with localized exaggerated growth of gas bubbles. With increasing firing temperatures, the pores coalesce and get larger resulting in warping of the ceramic body. This behaviour is related to the formation of excessive liquid phase. In contrast, SLS glass-free batch (S0) reaches its denser microstructure with isolated pores after firing at 1200°C and shows signs of overfiring above 1250°C. This is consistent with the lower bulk density and expansion as mentioned earlier. The larger pores in S50, S75 and S100 explain their lower density when compared to S25 and S0.

Physical properties and overall microstructure of each batch revealed that addition of SLS glass in the whiteware composition increased vitrification at lower firing temperatures. Substituting 6.25wt% nepheline syenite flux for SLS glass (S25) is feasible as this new formulation had lower water absorption, slightly higher shrinkage and similar bulk density compared to standard whiteware composition (S0) fired at the same temperature (1100°C). Nevertheless, addition of higher amounts of SLS glass deteriorated whiteware physical properties after firing at temperatures higher than 1100°C due to its susceptibility to bloating. In these cases, the microstructure of the fired products became more porous, with isolated and larger pores. Changing heating schedule could have some effect on the level of bloating. Slowing the heating rate or adding a holding step at low temperatures would allow gases to escape and lesser closed porosity formation. Therefore, heating schedule is another factor that can be tailored to reach the best physical properties for each composition. Various heating rates and holding times should be studied. However, if one attempts to decrease the heating rate, it may come with the drawback of increase in firing cost and time.

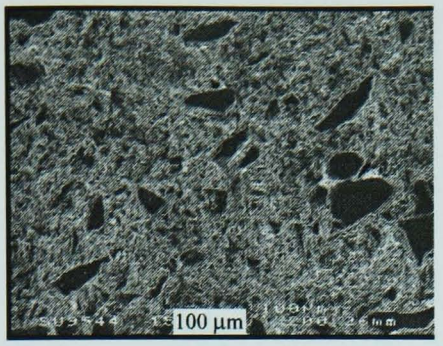

S0_1000°C

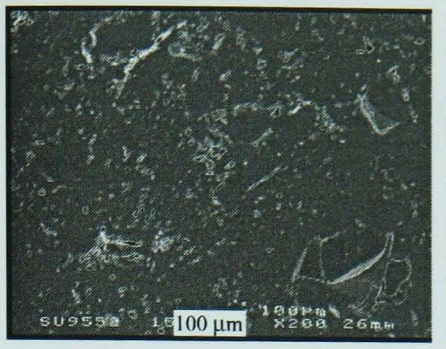

S0_1050°C

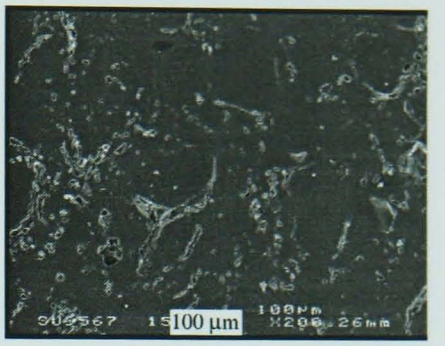

S0_1100°C

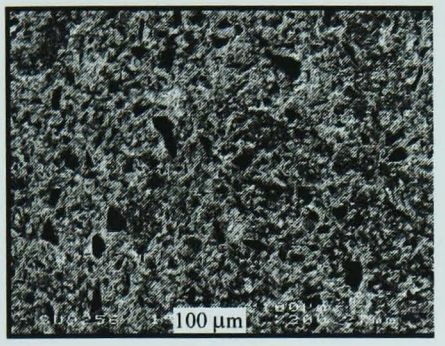

S25_1000°C

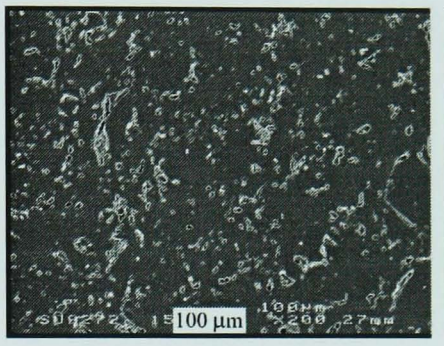

S25_1050°C

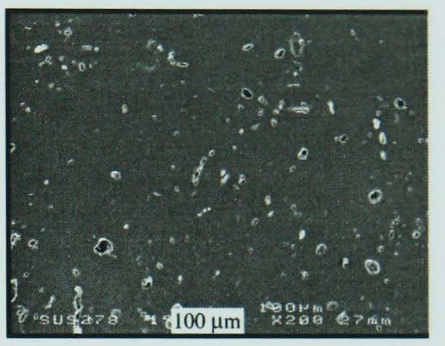

S25_1100°C

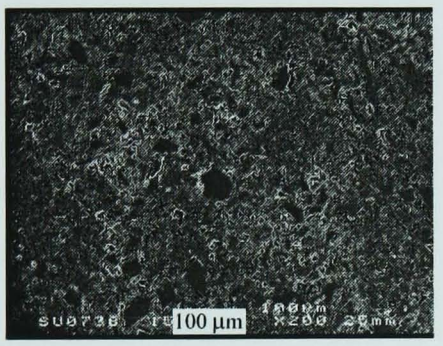

S50_1000°C

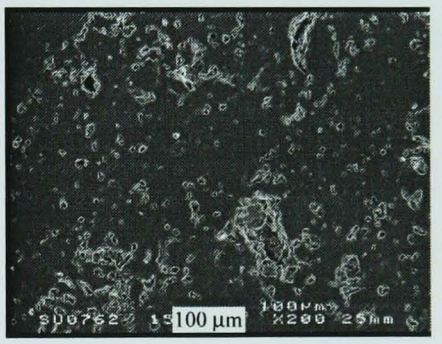

S50_1050°C

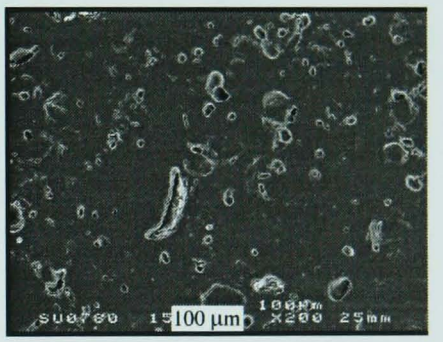

S50_1100°C

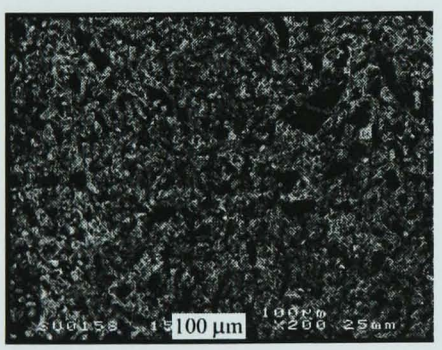

S75_1000°C

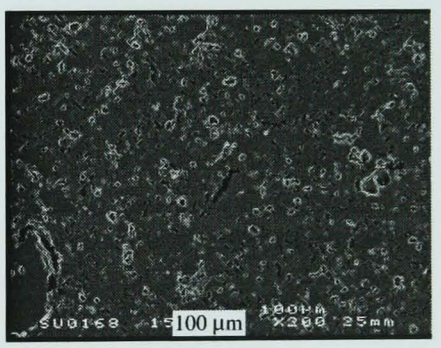

S75_1050°C

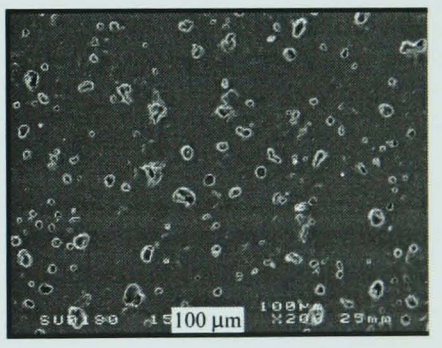

S75_1100°C

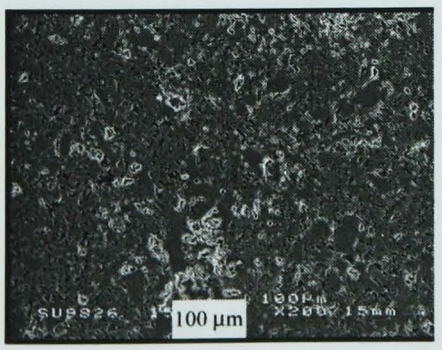

S100_1000°C

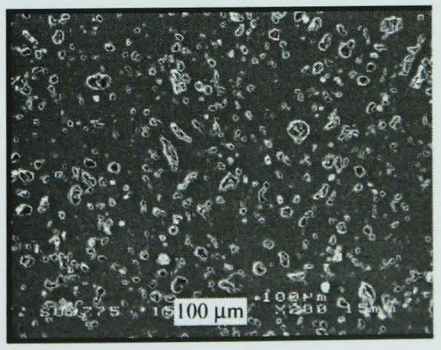

S100_1050°C

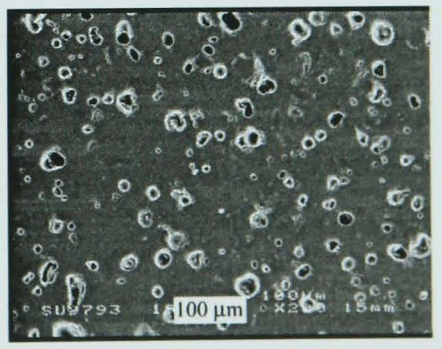

S100_1100°C

Figure 6.4 - SEM/SE images of the cross-sectioned compacts made of S0, S25, S50, S75 and S100 fired at 1000, 1050 and 1100°C.

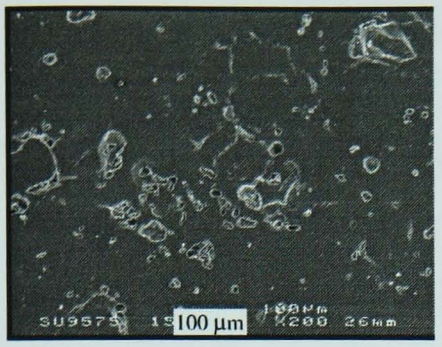

S0_1150°C

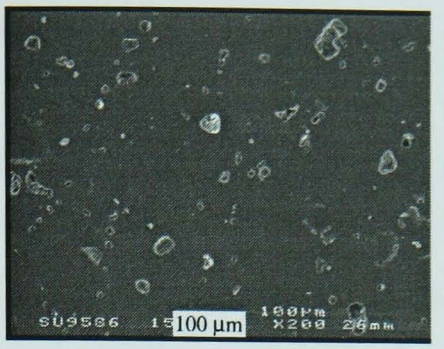

S0_1200°C

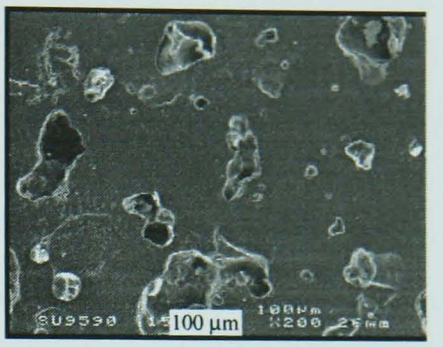

S0_1250°C

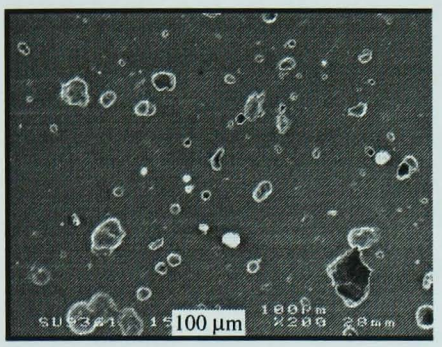

S25_1150°C

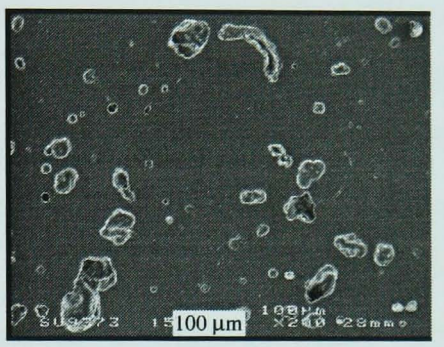

S25_1200°C

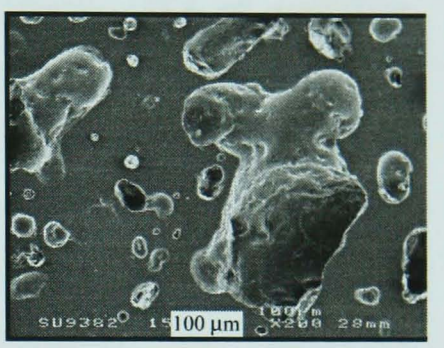

S25_1250°C

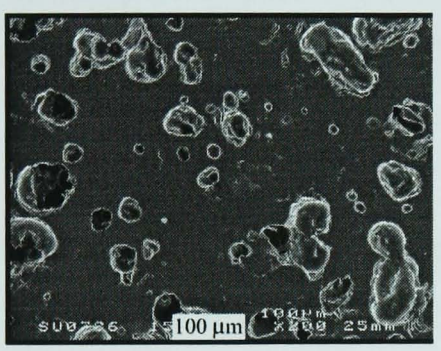

S50_1150°C

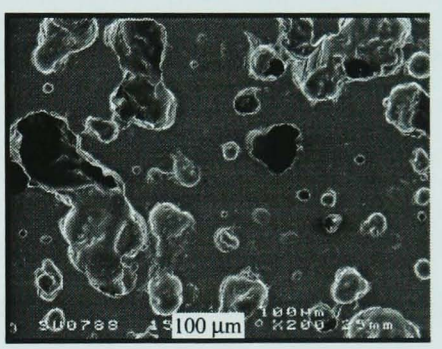

S50_1200°C

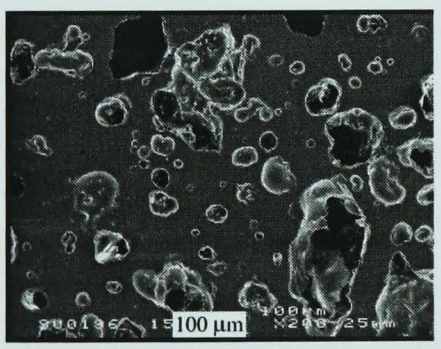

S75_1150°C

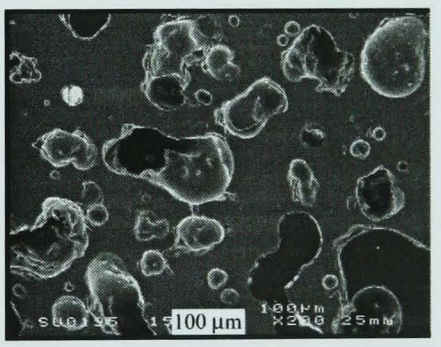

S75_1200°C

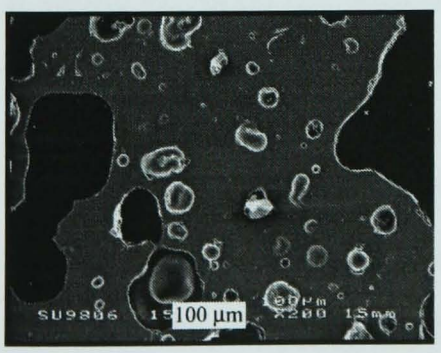

S100_1150°C

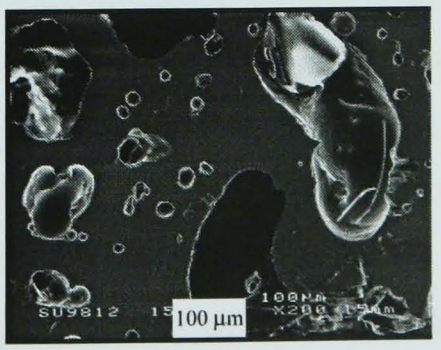

S100_1200°C

Figure 6.5 - SEM/SE images of S0 and S25 fired at 1150, 1200 and 1250°C and that of S50, S75 and S100 fired at 1150 and 1200°C.

6.3 - THERMAL BEHAVIOUR

DTA of S0, S25, S50, S75 and S100 are shown in Figure 6.6. The thermal events are similar to those observed in the DTA of C-Q (Figure 5.1(a)), since clay is the main component in each batch (50wt%). Quartz is kept constant at 25wt% in each batch, whereas the flux components (nepheline syenite and SLS glass), having thermal behaviour not obviously identifiable, are varied within 25wt%. DTA of nepheline syenite was explained earlier in chapter 4, and showed no peaks apart from a continuous endothermic drift. DTA of SLS glass on heating showed small endothermic peaks and broad exothermic peaks which cannot be seen in whiteware batches with a SLS content lower than 25wt%. The characteristic endothermic and exothermic peaks corresponding to clay reactions are clearly seen with lower intensity than those observed from DTA of clay alone (Figure 4.1(a)), or DTA of C-Q (Figure 5.1(a)), C-NS (Figure 5.2(a)) or C-SLS (Figure 5.3(a)) mixtures which have 66.67wt% clay.

The endothermic peak caused by the release of OH^- from the clay structure is present at a similar temperature (~545°C) in all batches. The exothermic peak due to the crystallization of spinel and/or primary mullite is present at ~990°C for S0, S25 and S50, and shifted to lower temperatures with increasing SLS contents: ~985°C for S75 and ~970°C for S100. This exothermic peak is smaller and broader with increasing SLS content, and is associated with the lower amount of mullite formed or the formation of another phase (plagioclase) over the same temperature range (see XRD in phase analysis section 6.4). It is noteworthy that this exothermic peak occurs at similar temperature for S100 and C-SLS mixture. Therefore SLS glass seems to have a strong effect on the temperature of mullite formation as well as the amount formed. The competition for Al between mullite and plagioclase may be retarding the kinetics of mullite formation. The second exothermic peak caused by the crystallization of secondary mullite is broader and present at ~1250°C for S0 and ~1235°C for S25. This was not observed in the DTA of S50, S75 and S100. However, DTA of S75 and S100 shows a broad exothermic peak at ~1150°C which may be related to the formation of secondary mullite. As quartz was present in the same amount in all batches, no difference on heating was observed, and the endothermic peak corresponding to the α to β quartz transformation was present at 573°C in all cases.

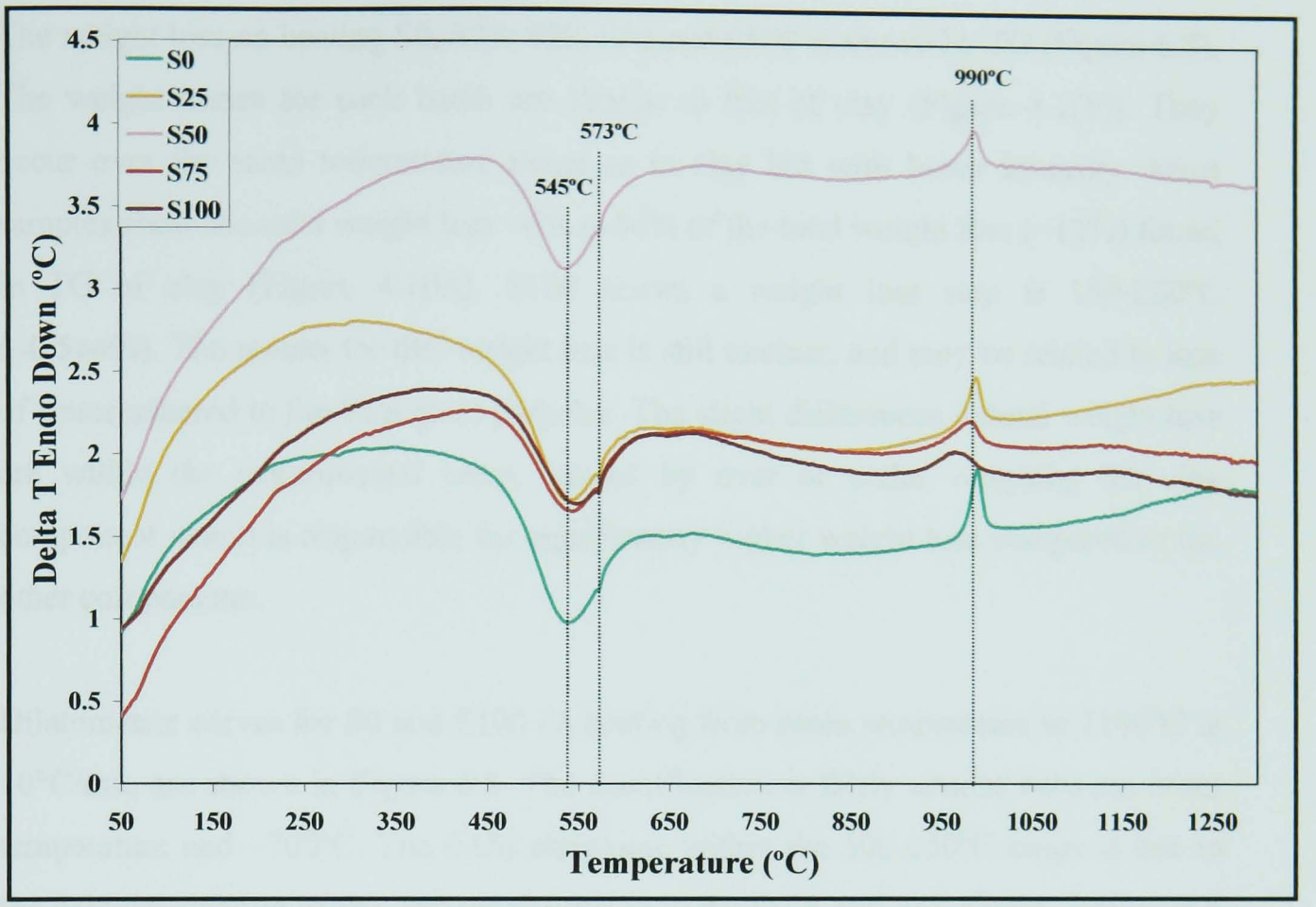

Figure 6.6 - DTA of S0, S25, S50, S75 and S100 with a heating rate of 10°C/min.

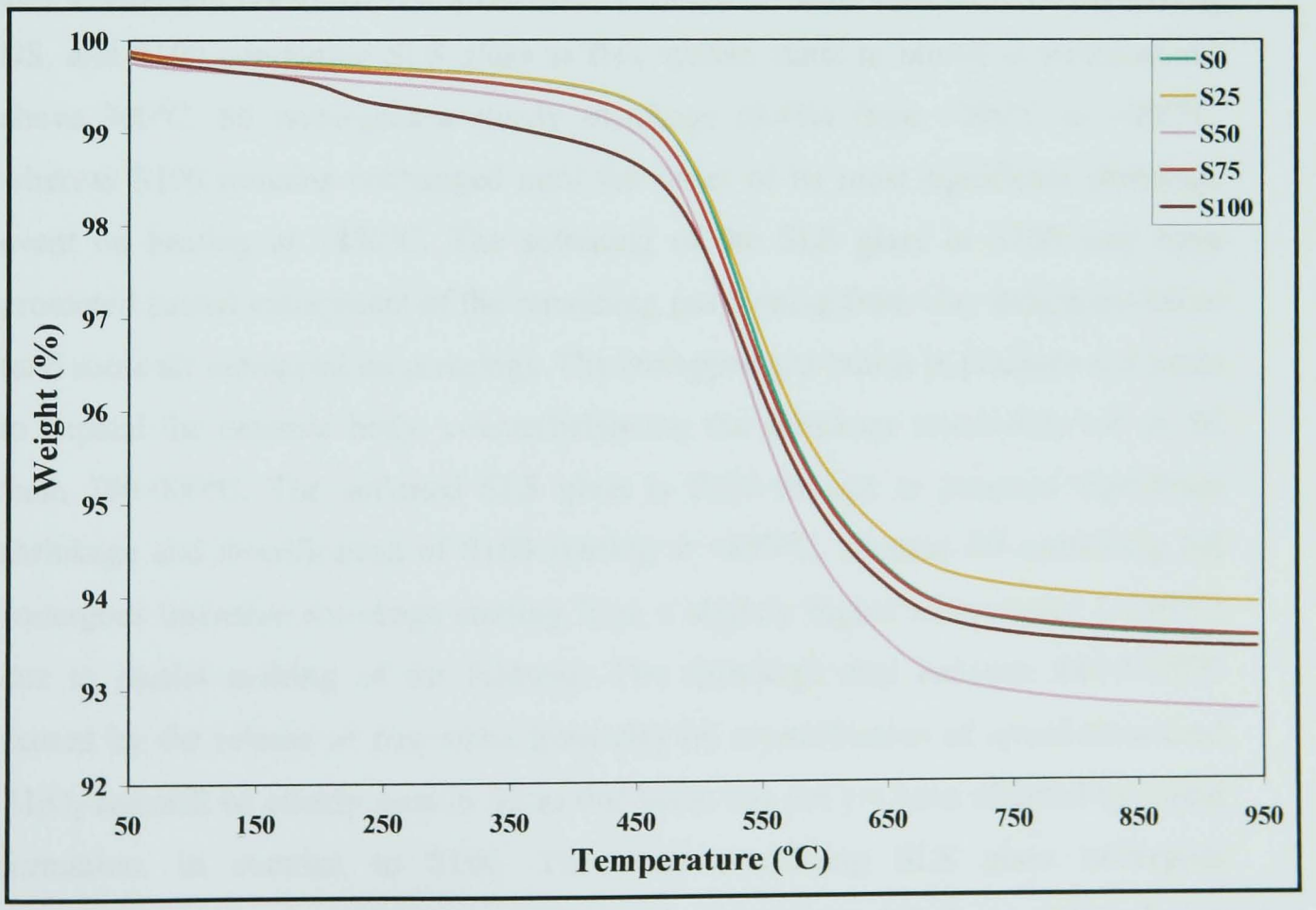

Figure 6.7 - TG traces of S0, S25, S50, S75 and S100 with a heating rate of 10°C/min.

The weight loss on heating S0, S25, S50, S75 and S100 is shown by TG (Figure 6.7). The weight losses for each batch are similar to that of clay (Figure 4.1(b)). They occur over the same temperature range as in clay but with lower intensity. Most samples show the total weight loss ~6% (~50% of the total weight loss (~12%) found in TG of clay (Figure 4.1(b)). S100 shows a weight loss step at 180-250°C (~0.5wt%). The reason for this weight loss is still unclear, and may be related to loss of water adhered to the SLS glass particles. The slight differences in total weight loss are within the experimental error, caused by over or under weighing the clay component which is responsible for significantly higher weight loss compared to the other components.

Dilatometric curves for S0 and S100 on heating from room temperature to 1100°C at 10°C/min are shown in Figure 6.8. The densification is fairly similar between room temperature and ~700°C. The 0.6% shrinkage within the 500-650°C range is due to the dehydroxylation of the clay (as suggested in the DTA and TG curves, Figures 6.6 and 6.7), which occurs equally for S0 and S100 containing the same amount of the clay component (50wt%). The differences between the densification of S0 containing NS, and S100 containing SLS glass as flux system starts to unveil at temperatures above 700°C. S0 undergoes a steady shrinkage (0.4%) from ~700°C to ~900°C, whereas S100 remains unchanged until the onset of its most significant shrinkage event on heating at ~850°C. The softening of the SLS glass in S100 may have promoted partial entrapment of the remaining gas coming from clay dehydroxylation (and some air entrapped on pressing). The entrapped gas builds in pressure and tends to expand the ceramic body, counterbalancing the shrinkage trend observed in S0 from 700-900°C. The softened SLS glass is fluid enough to promote significant shrinkage and densification of S100 starting at ~850°C, whereas S0 containing NS undergoes intensive shrinkage starting from a slightly higher temperature (~920°C) due to partial melting of the feldspar. The shrinkage step between 880-1000°C caused by the release of free silica from clay on crystallisation of spinel-structured Al_2O_3 can still be clearly seen in S0 as this batch has not yet been affected by liquid formation, in contrast to S100. The body containing SLS glass undergoes considerably higher shrinkage (~5.0%) than that containing NS flux (~2.5%) during this shrinkage stage. This corresponds to the linear shrinkage (Figure 6.3) of S100, ~5.5%, and that of S0, ~3.2% when fired to 1000°C. In this sense, it is clear that the

body containing SLS glass flux undergoes earlier densification than that containing the natural flux.

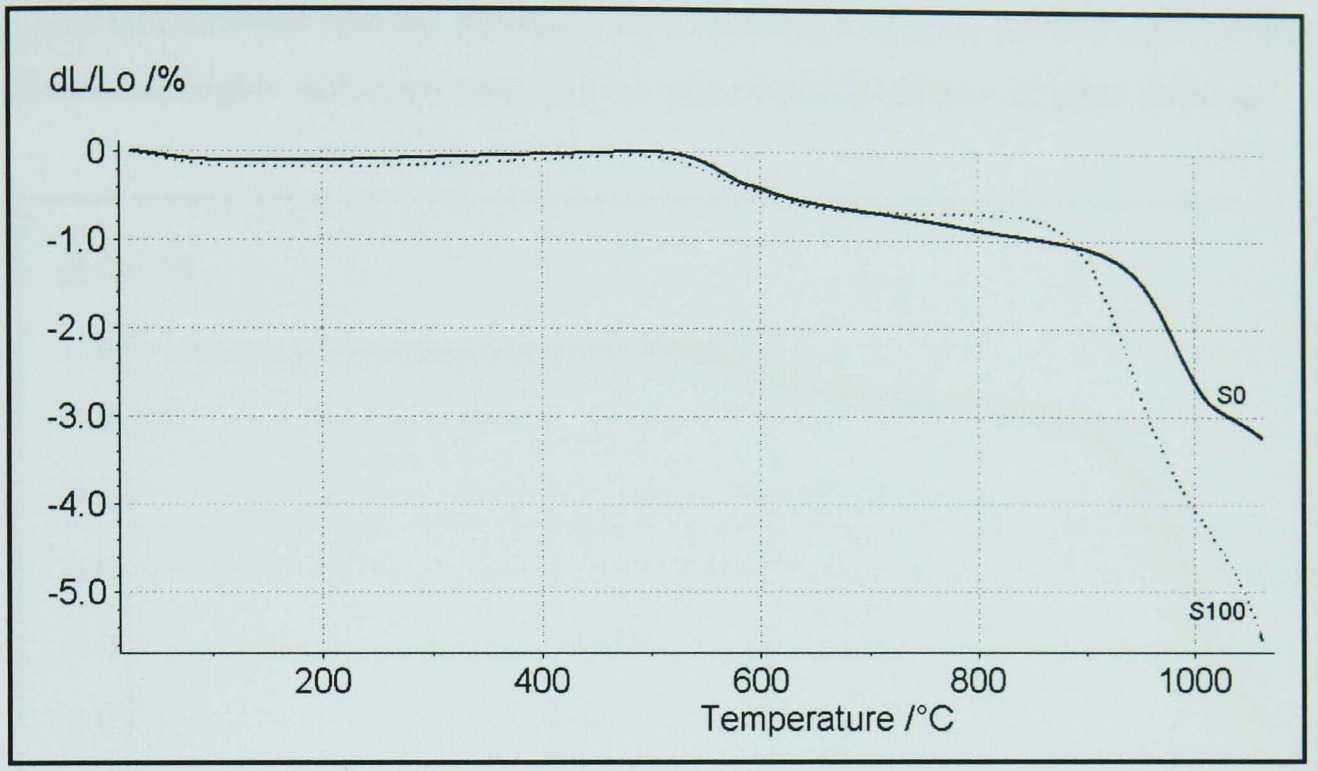

Figure 6.8 - Dilatometric curves of S0 and S100 on heating at 10°C/min from room temperature to 1100°C.

Dilatometric curves for S0, S25, S50, S75 and S100 on heating from room temperature to 1100°C at 10°C/min are shown in Figure 6.9. Starting from S0, which contains 25wt% nepheline syenite as flux (and 0wt% SLS glass), progressive additions of SLS glass flux (i.e. 6.25, 12.50, 18.75 and 25wt% for S25, S50, S75 and S100, respectively) reduce the temperature range over which the ceramic bodies undergo significant shrinkage, and increase the extent of that shrinkage, confirming the trend observed for S0 and S100 alone. S75 and S100 exhibited lower shrinkage than the other batches until ~910°C (see detailed trace in Figure 6.10), probably due to their higher SLS glass content which led to more efficient packing and gas entrapment in the very early stages of densification (e.g. during clay dehydroxylation). The entrapped gas counterbalances the tendency of the body to shrink. This is in good agreement with the higher bulk density and lower water absorption of S75 and S100. Above 910°C, specimens from S75 (18.75wt% SLS) and S100 (25.00wt% SLS) undergo more severe shrinkage than the other batches. The higher NS content in S50, which forms liquid at higher temperatures than SLS glass, may have been responsible for the intersection between the S75 and S50

curves between 1010°C and 1040°C on heating. The overall shrinkage from green to fired state of S0, S25, S50, S75 and S100 were ~3.4, 4.6, 5.2, 5.0 and 6.2%, respectively. This result was expected as SLS glass softens and forms liquid at temperatures lower than the melting point of nepheline syenite, and therefore batches containing higher SLS glass content form more liquid leading to a higher shrinkage.

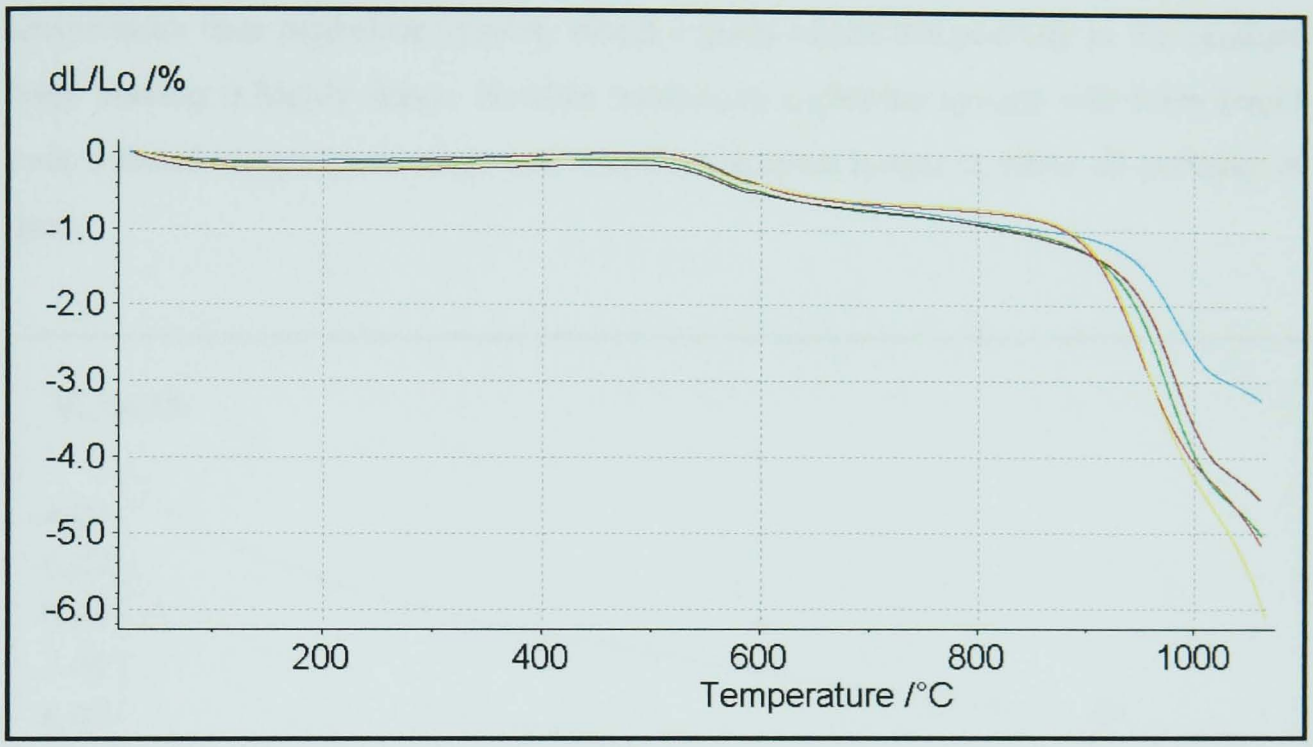

Figure 6.9 - Dilatometric curves of S0, S25, S50, S75 and S100 on heating at 10°C/min from room temperature to 1100°C.

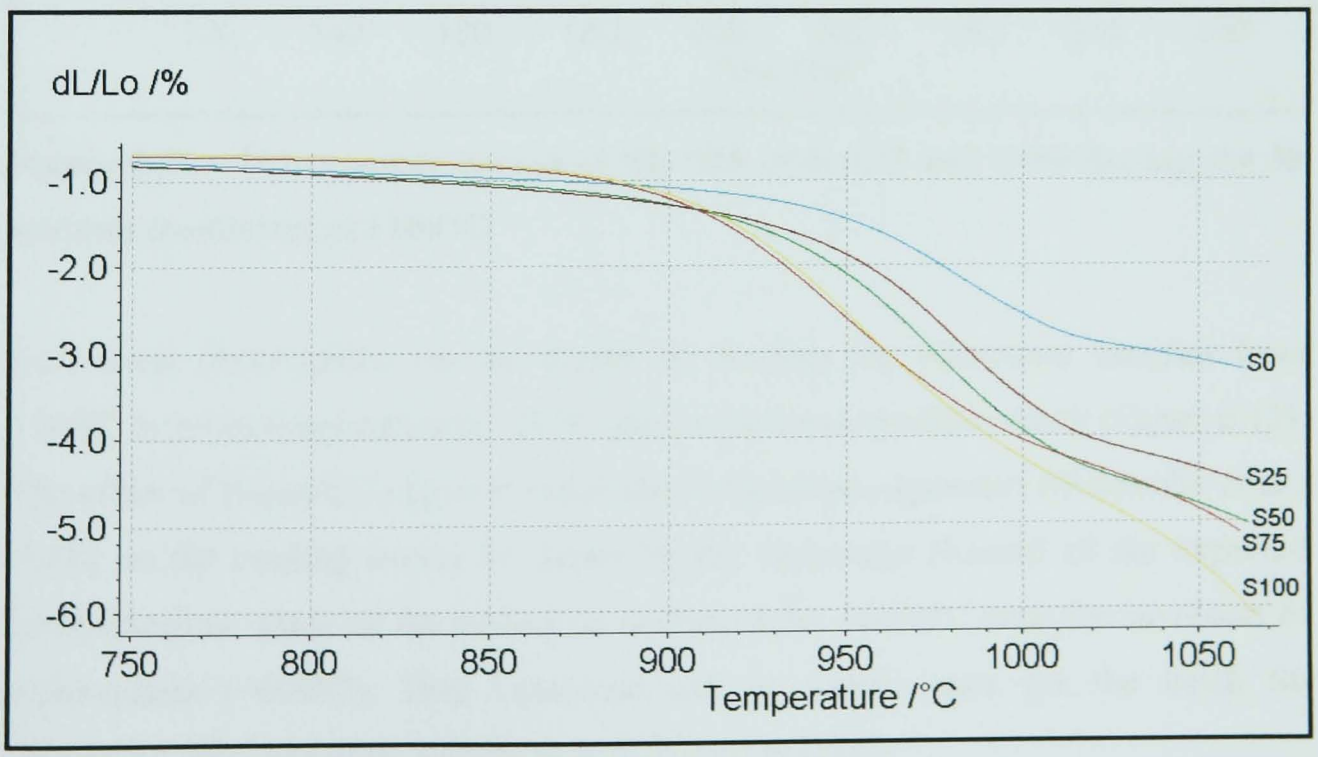

Figure 6.10 - Dilatometric curves of S0, S25, S50, S75 and S100 on heating at 10°C/min from 750 to 1100°C.

During the 180min soaking period at 1100°C, the whiteware samples experienced shrinkage which increased with the SLS glass content (Figure 6.11). Moreover, the initial rate of shrinkage decreased markedly for the samples containing SLS glass. Indeed, S100 showed no measurable shrinkage during a 100min period after the initial shrinkage within the first 60min. This remarkable dimensional stability during the soaking period for S100 can be explained by the melting of SLS glass at lower temperature than nepheline syenite, which rapidly closes the porosity in the ceramic body leaving it highly dense. Batches containing nepheline syenite will form liquid over a broad temperature range and therefore it takes longer to close all porosity in them.

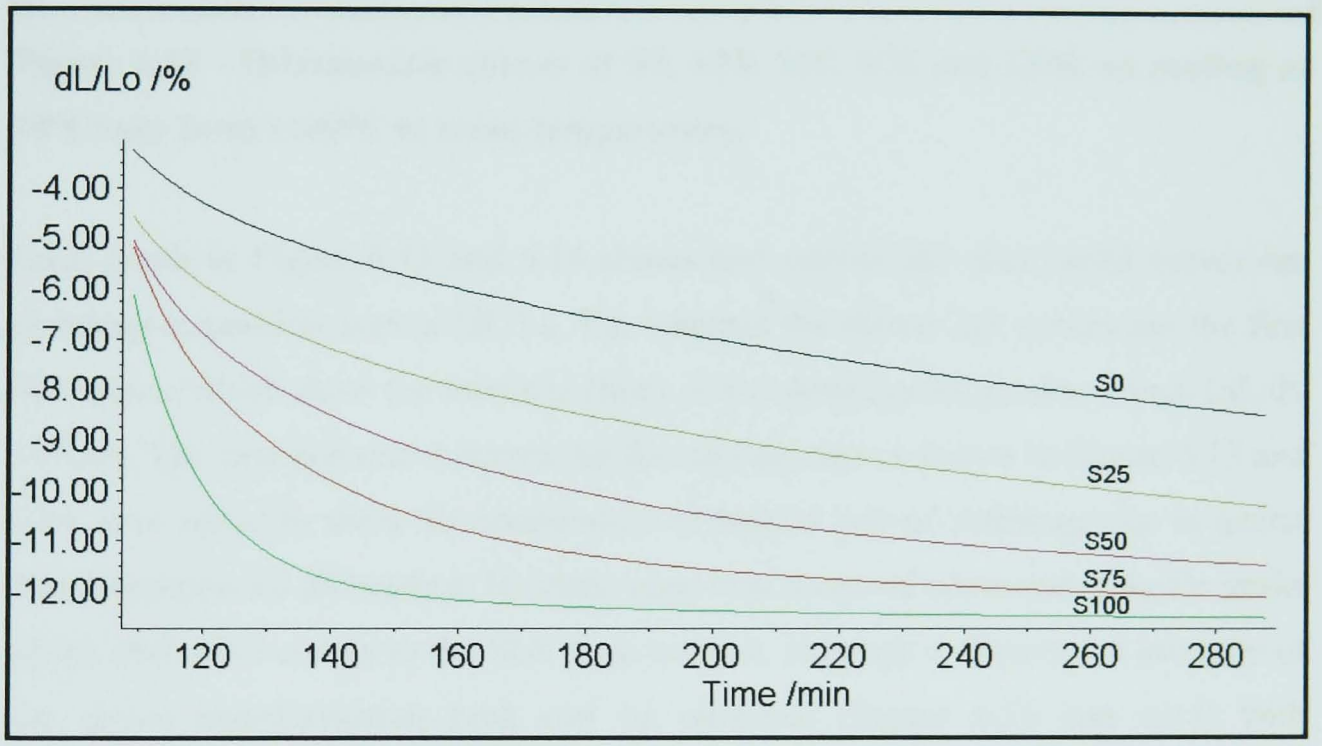

Figure 6.11 - Dilatometric curves of S0, S25, S50, S75 and S100 during the 3h soaking (isotherm) at 1100°C.

Four main observations can be drawn on cooling the whiteware samples from 1100°C to room temperature at ~10°C/min as measured by dilatometry (Figure 6.12). The effect of β-quartz's negative coefficient of thermal expansion (Goldsmith *et al.*, 1961) on the cooling curves is shown by the expansion (instead of the expected contraction) of some of the bodies on cooling from ~1050°C until the inversion to alpha-quartz (~600°C). This behaviour can be clearly seen for the batch S0 containing only nepheline syenite as flux (Figure 6.13(a)).

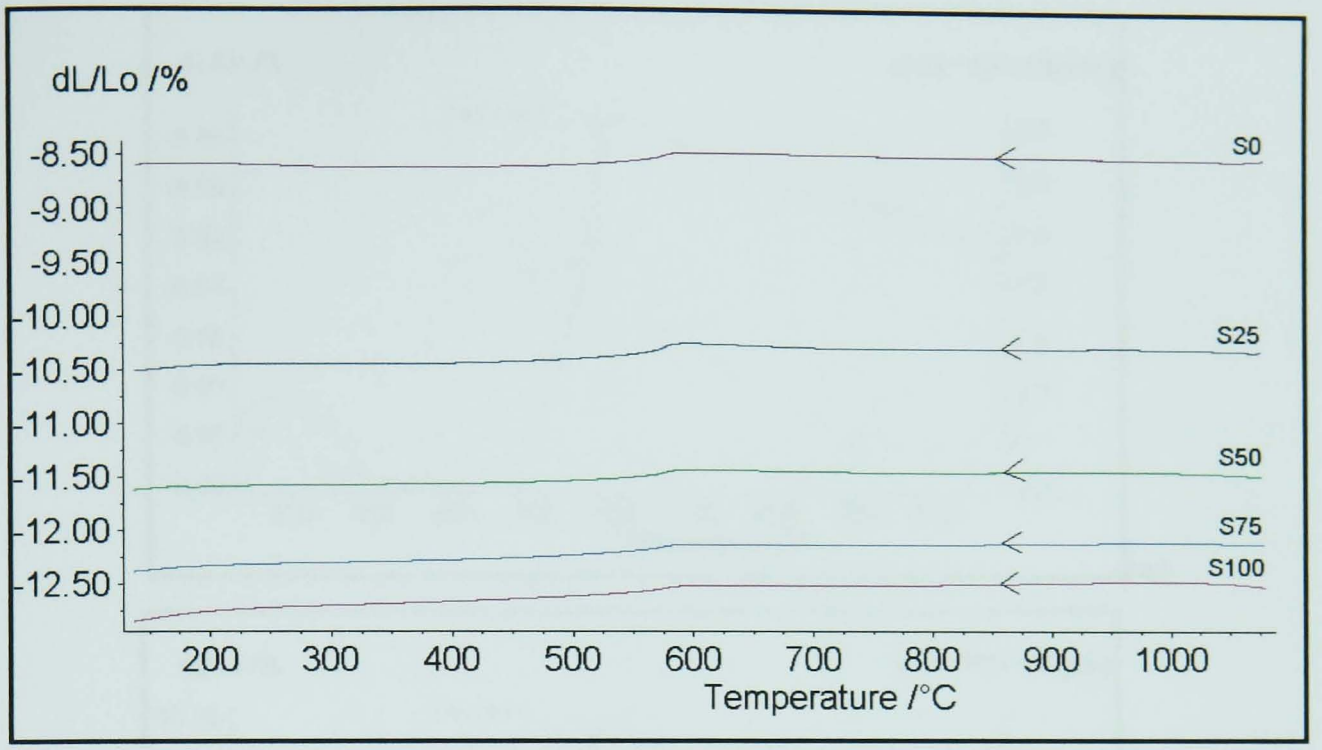

Figure 6.12 - Dilatometric curves of S0, S25, S50, S75 and S100 on cooling at 10°C/min from 1100°C to room temperature.

Each graph in Figure 6.13 and 6.14 shows two curves: the dark, solid curves are shrinkage/expansion curves (dL/L_0, %), whereas the dotted-line curves are the first derivatives which show the intensity (rate) of the shrinkage/expansion events (dL/dt, %/min). The first derivative curves for the cooling curves shown in Figure 6.13 and 6.14 were added to show the temperature of highest rate of shrinkage due to quartz transformation for all batches. No clear trend was observed when matching the peaks of the derivative curves to the SLS glass content, although a decrease in intensity of the quartz transformation peak can be observed (Figure 6.13 and 6.14) with increasing the SLS glass added. Addition of SLS glass seems to decrease the effect of β-quartz, increasingly promoting shrinkage with SLS glass addition to the whiteware composition. For 6.25wt% (Figure 6.13(b)) and 12.50wt% (Figure 6.13(c)) SLS glass added (S25 and S50, respectively), a bump is observed in the cooling curves (dL/L_0) from 1050-800°C, indicating concurrent phenomena taking place, the other being the positive coefficient of thermal expansion of the Si-rich glass formed on firing (which causes shrinkage on cooling). The cooling curves of S75 (Figure 6.14(a)) and S100 (Figure 6.14(b)), with 18.75 and 25.00wt% SLS glass flux added, respectively, show primarily the effect of the glass contracting on cooling from 1100°C to ~600°C.

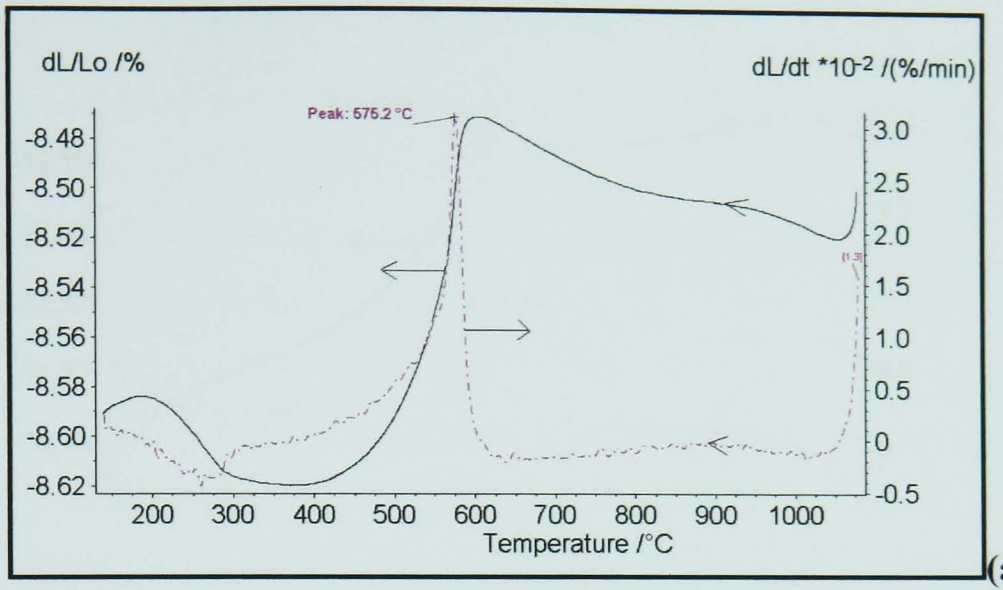

(a)

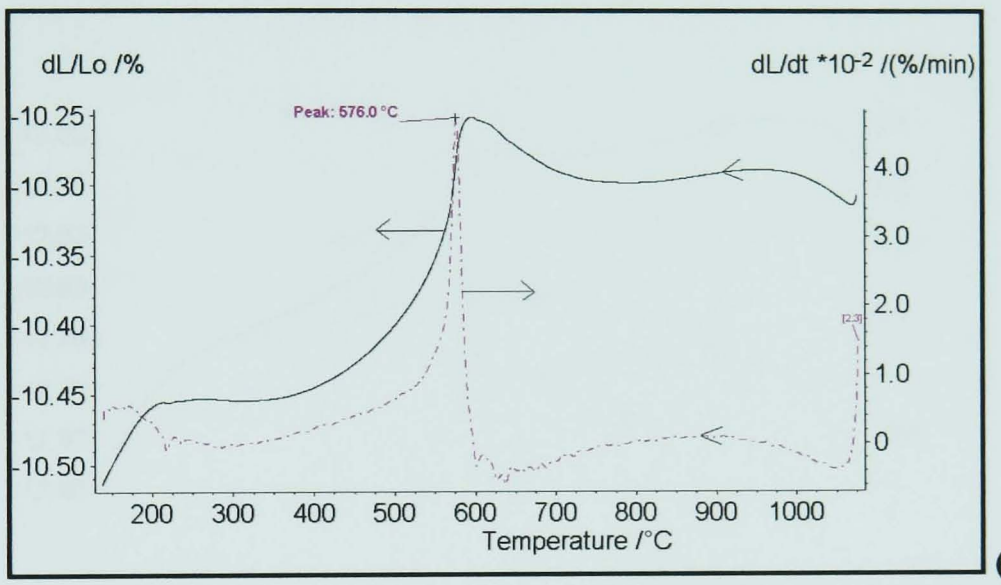

(b)

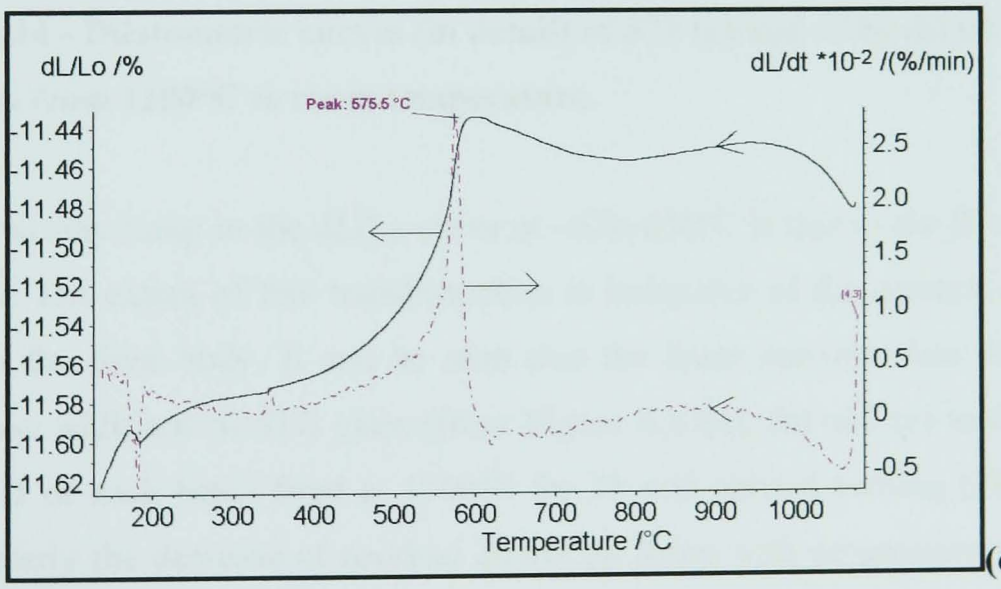

(c)

Figure 6.13 - Dilatometric curves (in detail) of S0 (a), S25 (b) and S50 (c) on cooling at 10°C/min from 1100°C to room temperature.

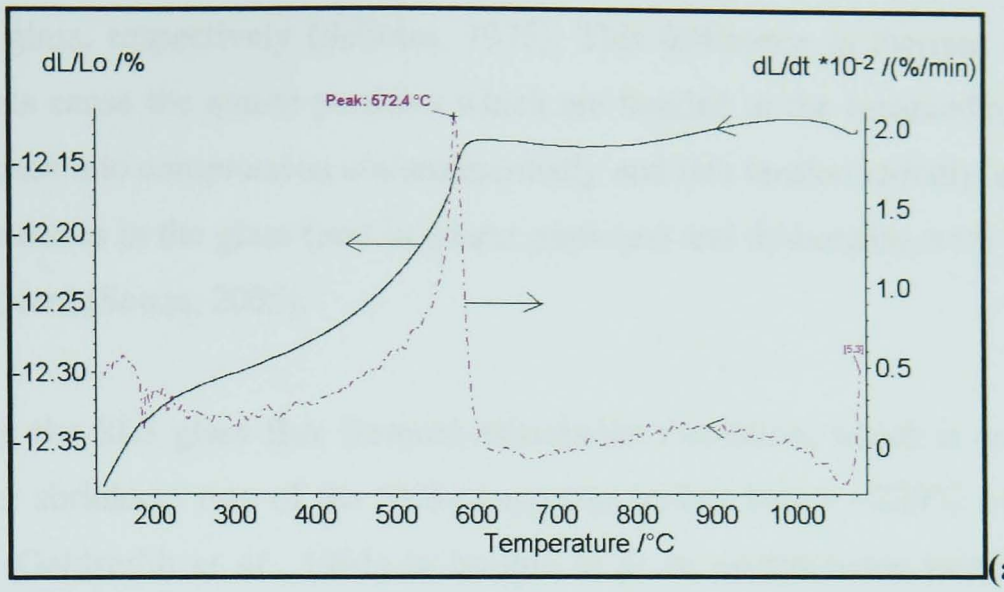

(a)

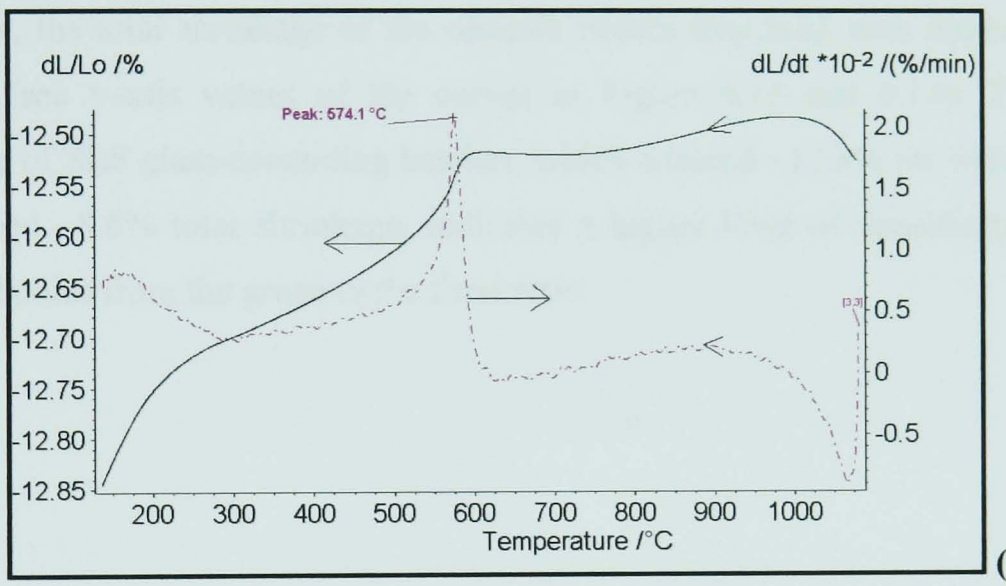

(b)

Figure 6.14 - Dilatometric curves (in detail) of S75 (a) and S100 (b) on cooling at 10°C/min from 1100°C to room temperature.

The noteworthy lump in the dL/L_0 curve at ~550-650°C is due to the β- to α-quartz inversion. The extent of this transformation is indicative of the amount of residual quartz in the fired body. It can be seen that the lump becomes less visible with progressive additions of SLS glass (from Figure 6.13(a), (b) and (c) to 6.14(a) and (b)). XRD of each batch fired at 1100°C for 3h and normal cooling (Figure 6.22) shows clearly the decrease of residual quartz on firing with progressive increase of SLS content in whiteware batches. α-quartz has a positive coefficient of thermal expansion (Goldsmith *et al.*, 1961), which is much higher than that of most Si-rich glasses. Quartz has thermal expansion coefficient of ~$23x10^{-6}$ /K (Chaudhuri, 1982; Iqbal and Lee, 2000), whereas ~$9x10^{-6}$ /K and ~$0.5x10^{-6}$ /K are the coefficient of thermal expansion for SLS glass and fused silica glass (Kingery, 1976), and ~$3.2x10^{-6}$ /K, ~$4.2x10^{-6}$ /K and ~$9x10^{-6}$ /K for borosilicate glass, aluminosilicate glass

and lead glass, respectively (Scholes, 1975). This difference in thermal expansion coefficients cause the quartz particles which are bonded to the surrounding glass to pull the glass into compression circumferentially and into tension radially, promoting residual stresses in the glass (and in quartz particles) and de-bonding with formation of quasi-pores (Souza, 2005).

Increasing the SLS glass flux fostered cristobalite formation, which is revealed by the higher shrinkage rate of the SLS-containing bodies below ~220°C on cooling, reported (Goldsmith *et al.*, 1961) to be due to β- to α-cristobalite transformation. Moreover, the total shrinkage of the ceramic bodies increased with increasing SLS addition (see y-axis values of the curves in Figure 6.13 and 6.14). The higher shrinkage of SLS glass-containing batches, which attained ~12.8% for S100 whereas S0 attained ~8.6% total shrinkage, indicates a higher level of densification of the ceramic bodies from the green to the fired state.

6.4 - PHASE EVOLUTION

Results with respect to the investigation of physical properties and thermal analysis of whiteware bodies have been discussed in previous sections. This section presents results of phase evolution on firing each batch composition, performed using XRD. Figures 6.15 - 6.19 show XRD of the five whiteware batches, from as-mixed to after firing and/or quenching from 600 - 1300°C.

XRD of as-mixed S0 and fired pellets quenched from temperatures between 600 to 1300°C are shown in Figure 6.15. The as-mixed S0 (SLS-free batch) initially contained minerals found in raw materials (i.e. kaolin clay, quartz, nepheline syenite). The minerals present in each raw material were discussed in section 4.5. Quartz is present at all firing temperatures, although its peak intensities decrease with increasing firing temperatures because of quartz's partial dissolution. Kaolinite ($Al_2Si_2O_5(OH)_4$) transformed to semi-amorphous metakaolinite between 450-550°C. Samples of S0 fired at 600°C reveal nepheline ($NaAlSiO_4$) and microcline ($KAlSi_3O_8$) derived from nepheline syenite flux, and muscovite ($KAl_2(Si_3Al)O_{10}(OH)_2$) from the kaolin clay. The breakdown of muscovite was observed in the present work for firing temperatures above 900°C, consistent with previous work on kaolinitic clays containing micaceous materials (Hajjaji *et al.*, 2002). Above this firing temperature, nepheline breaks down. Sanidine ($(K,Na)AlSi_3O_8$), crystallizes from mixed feldspars from 600°C and breaks down above 1100°C. Mullite peaks appear at firing temperatures ≥900°C, and at ~1100°C an amorphous hump indicates the formation of substantial amounts of viscous liquid, which cooled to a glassy phase. Quartz, mullite and glass are the only phases observed by XRD in S0 samples fired at higher temperatures. The phase evolution of S0 is essentially the sum of individual contributions from C-NS, C-Q and Q-NS mixtures as described in chapter 5. No new phases were detected.

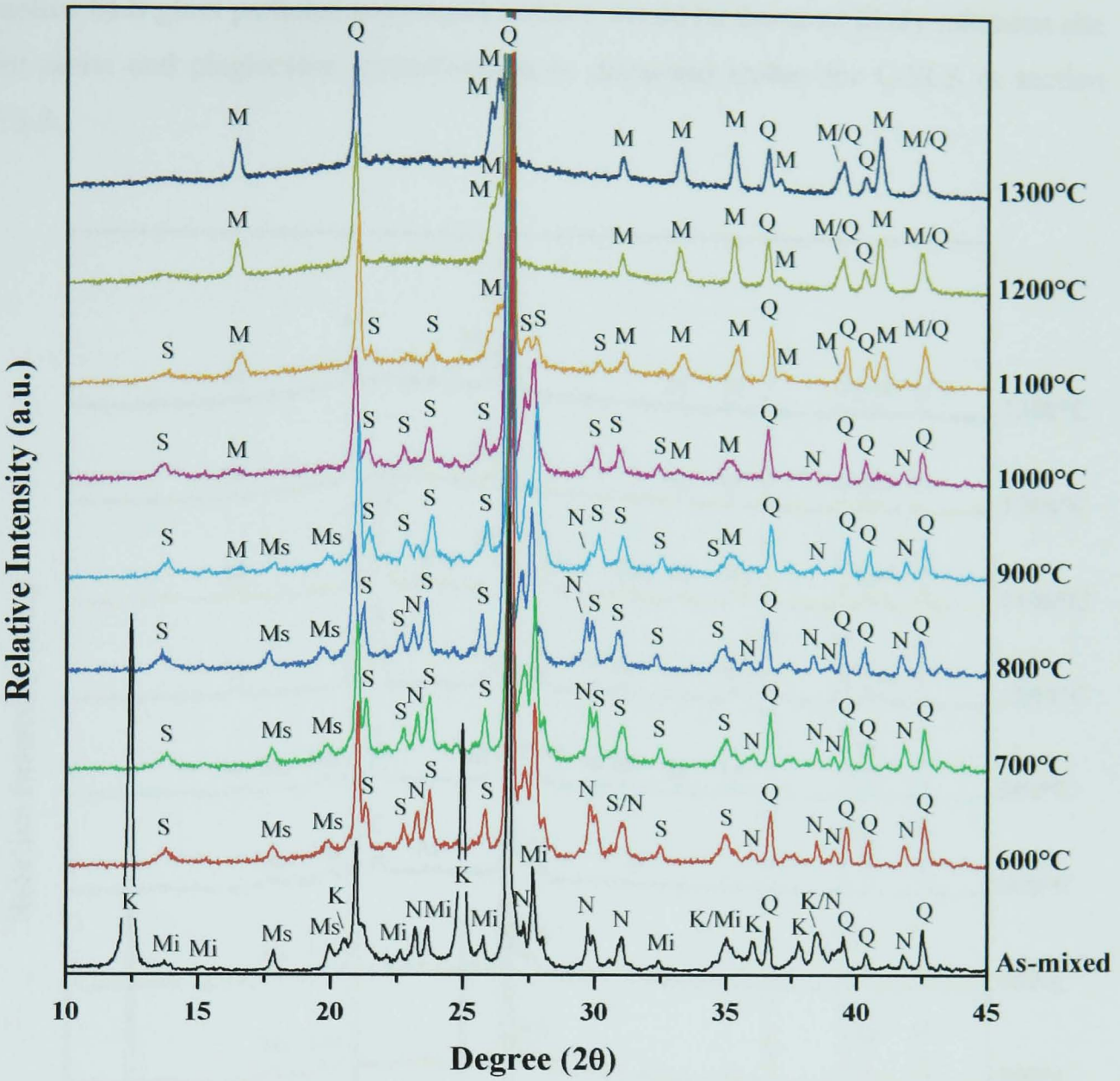

Figure 6.15 - XRD of standard porcelain (S0); as-mixed and fired pellets quenched from 600 -1300°C. (**K** – Kaolinite-1A, 14-164, **M** – Mullite, 15-776, **Mi** – Microcline, 19-926, **Ms** - Muscovite-2M#1, 6-263, **N** – Nepheline, 35-424, **Q** – α-quartz, 46-1045, **S** – Sanidine, 19-1227).

Complete substitution of nepheline syenite for SLS glass as a fluxing agent in S100 (Figure 6.16) led to formation of three new phases: cristobalite, albite (or plagioclase) and wollastonite, similar to the observations in the C-SLS mixture (Figure 5.11). Cristobalite (SiO_2) crystallised from devitrification of SLS glass at ~800°C and dissolved above 1100°C. The crystallization of albite ($NaAlSi_3O_8$) or plagioclase ($(Ca,Na)(Al,Si)_2Si_2O_8$) in S100 cannot be a direct result of the devitrification of SLS glass particles. The only source of alumina necessary to crystallize albite and plagioclase is decomposed kaolinite, as the Al_2O_3 content in the initial SLS glass is <1wt% (Table 4.1). Therefore, reactions at the interface between

molten SLS glass particles and meta-kaolinite would be the most likely initiation site for albite and plagioclase crystallisation as discussed earlier for C-SLS in section 5.3.3.

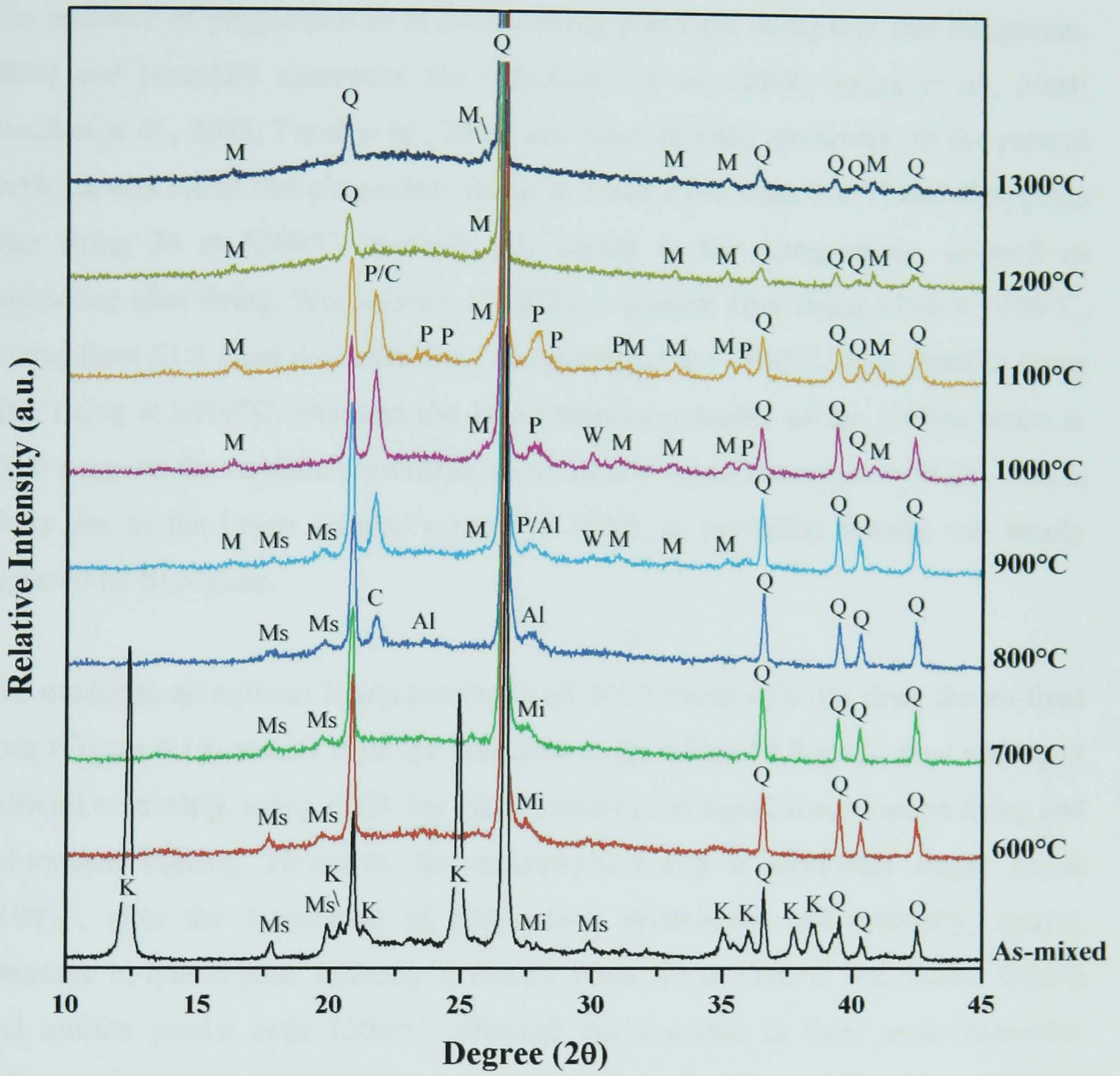

Figure 6.16 - XRD of SLS-based porcelain (S100); as-mixed and fired pellets quenched from 600-1300°C. (**Al** – Albite, 71-1153, **C** – Cristobalite, 82-512, **K** – Kaolinite-1A, 14-164, **M** – Mullite, 15-776, **Mi** – Microcline, 19-926, **Ms** – Muscovite-2M#1, 6-263, **P** – Plagioclase, 20-528, **Q** – α-quartz, 46-1045, **W** – Wollastonite-2M, 27-88).

Albite, one of the end member plagioclases, is likely to be the first product forming from the interaction of decomposed clay and molten SLS glass at ~800°C. After the softening point of SLS is reached (~590°C), alkali diffusion to its surroundings is promoted by concentration gradients. Sodium has higher mobility than calcium, thus

the former combines firstly with metakaolin to form albite. At higher temperatures, calcium ions displace some sodium ions from the albite structure giving rise to plagioclase.

The presence of plagioclase in SLS-containing porcelain (Braganca and Bergmann, 2004) and porcelain stoneware tile (Matteucci *et al.*, 2002; Souza *et al.*, 2004; Pontikes *et al.*, 2005; Tucci *et al.*, 2005) has been reported elsewhere. In the present work, its was found that plagioclase forms in batch S100 from 900°C and disappears after firing 3h at 1200°C. Nepheline is absent in this composition, as well as microcline after firing. Wollastonite ($CaSiO_3$) is present after firing S100 at 1000°C, arising from SLS glass devitrification, and dissolves at ~1100°C. Also, mullite forms after firing at ≥900°C, although the lower relative intensity of the mullite peaks in S100 suggests that mullite crystallization is modest when compared with S0. This is likely due to the lower alumina content in S100, as nepheline syenite was totally replaced by SLS glass.

The moderate amorphous hump present in all XRD traces of S100 since the un-fired state (Figure 6.16) results from the presence of the added SLS glass, thus making it difficult to identify, using XRD, the glass derived from liquid formation on firing and subsequent cooling. However, the amorphous hump is obviously larger above 1100°C, after the dissolution of plagioclase, cristobalite and (partially) quartz. Decrease in quartz peak intensity is clearly observed at 1200°C and above. Quartz and mullite persist until 1300°C, although the decrease in their peak intensities indicates dissolution as the firing temperature is increased (especially above 1100°C). It is worth noting that tridymite, which came from the transformation of cristobalite in fired Q-SLS (section 5.3.5), is not present in S100, the ternary mixture of clay, quartz and SLS glass.

Figures 6.17-6.19 show XRD of quenched S25, S50 and S75, revealing the co-existence of phases identified in quenched S0 and S100. Slight shifts in these XRD traces occurred due to error in the precise zero of the machine, and such error was not corrected. No new crystalline phases resulting from reaction between both fluxing materials (SLS glass and nepheline syenite) were observed by XRD. This same conclusion was drawn from analysis of XRD from the quenched SLS-NS

mixture (50:50 wt%) (Section 5.3.6). Phases from nepheline syenite are prominent in S25 and decrease in intensity with increasing SLS glass content (S75 and S100). In contrast, phases crystallized from SLS glass, or from its interaction with decomposed clay, are barely detected from S25 but become progressively noticeable in batches with higher SLS content.

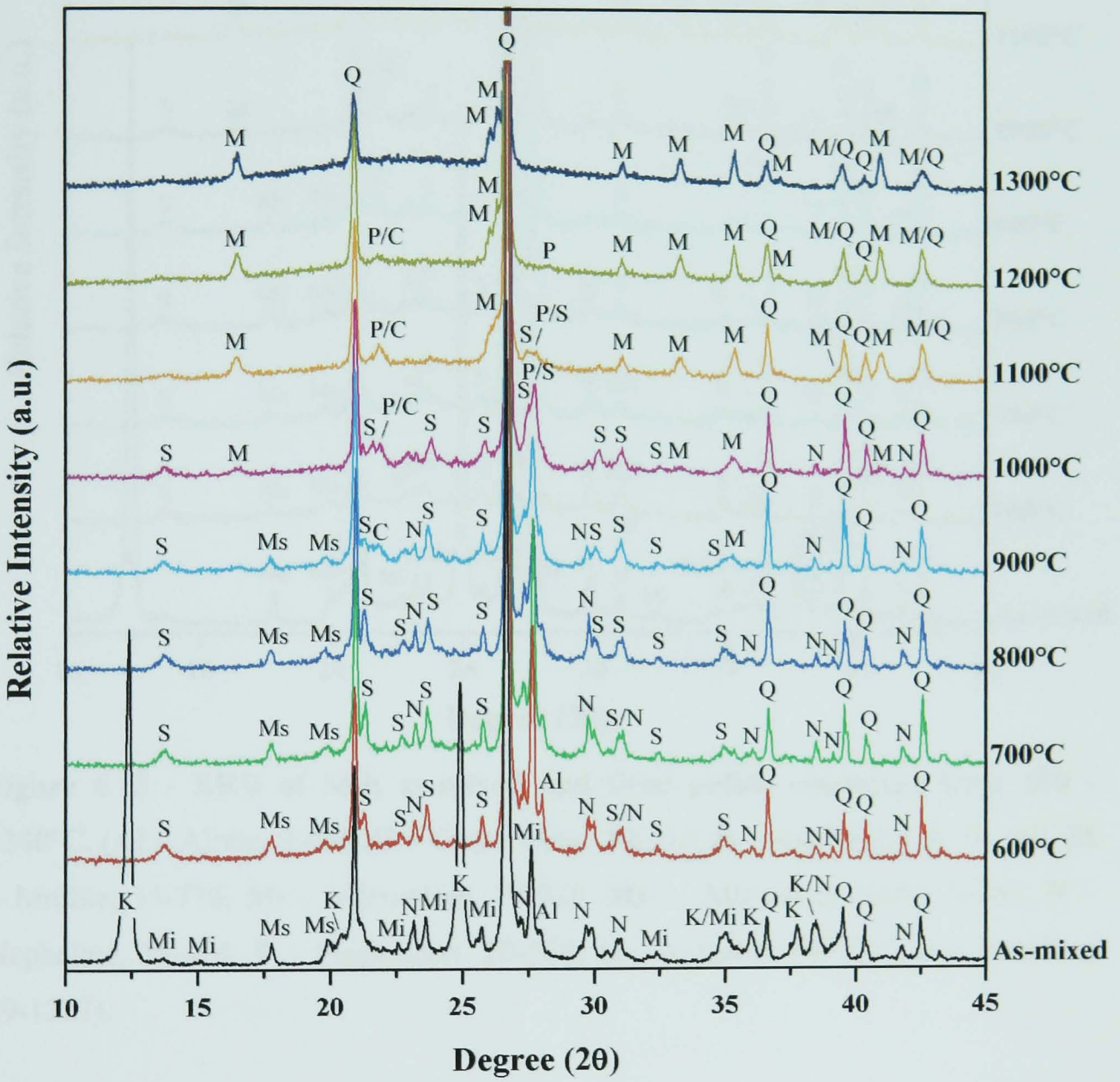

Figure 6.17 - XRD of S25; as-mixed and fired pellets quenched from 600 - 1300°C. (**Al** – Albite, 9-466, **C** – Cristobalite, 82-512, **K** – Kaolinite-1A, 14-164, **M** – Mullite, 15-776, **Mi** – Microcline, 19-926, **Ms** – Muscovite-2M#1, 6-263, **N** – Nepheline, 35-424, **P** – Plagioclase, 20-528, **Q** – α-quartz, 46-1045, **S** – Sanidine, 19-1227).

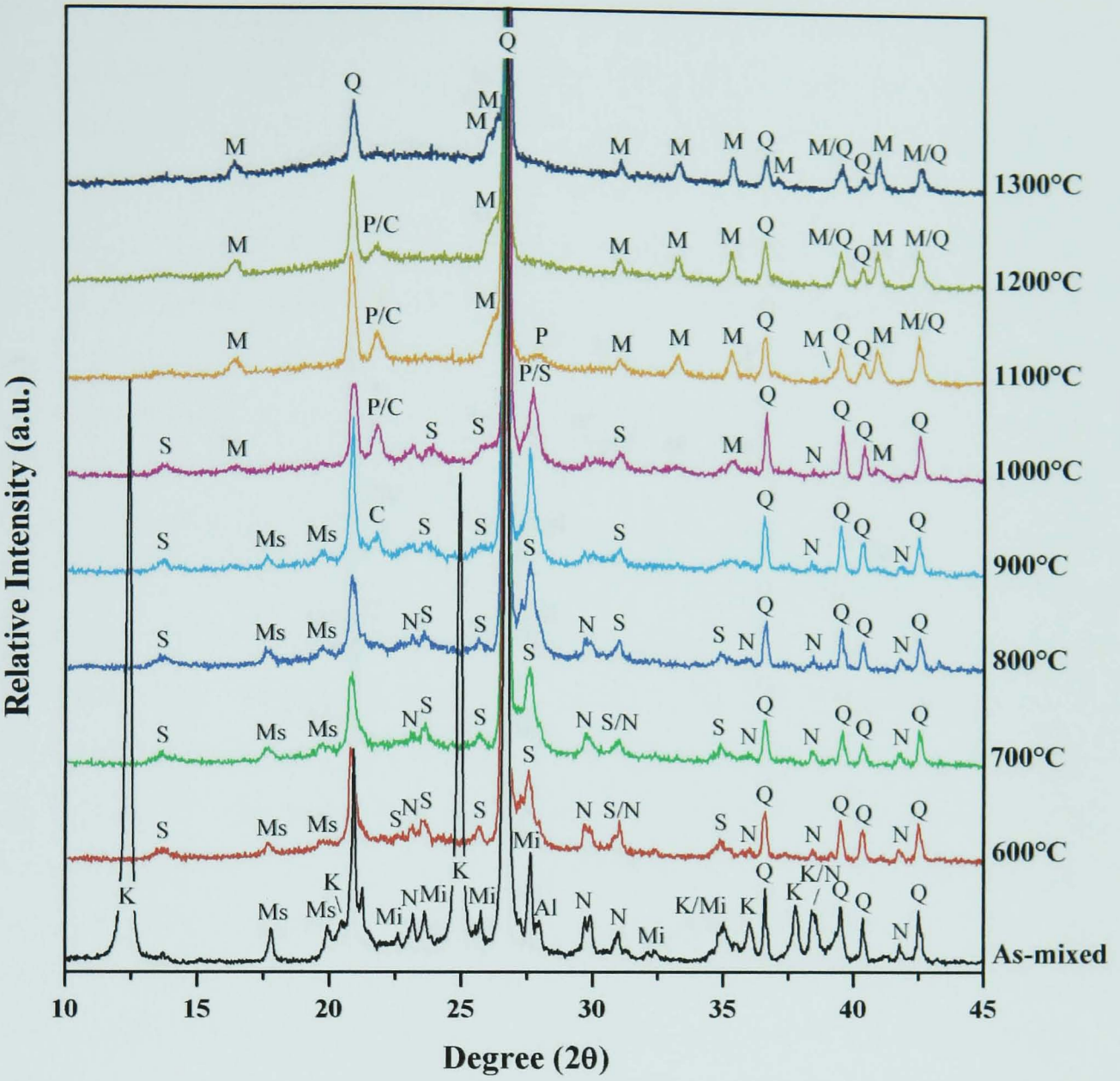

Figure 6.18 - XRD of S50; as-mixed and fired pellets quenched from 600 - 1300°C. (**Al** – Albite, 9-466, **C** – Cristobalite, 82-512, **K** – Kaolinite-1A, 14-164, **M** – Mullite, 15-776, **Mi** – Microcline, 19-926, **Ms** – Muscovite-2M#1, 6-263, **N** – Nepheline, 35-424, **P** – Plagioclase, 20-528, **Q** – α-quartz, 46-1045, **S** – Sanidine, 19-1227).

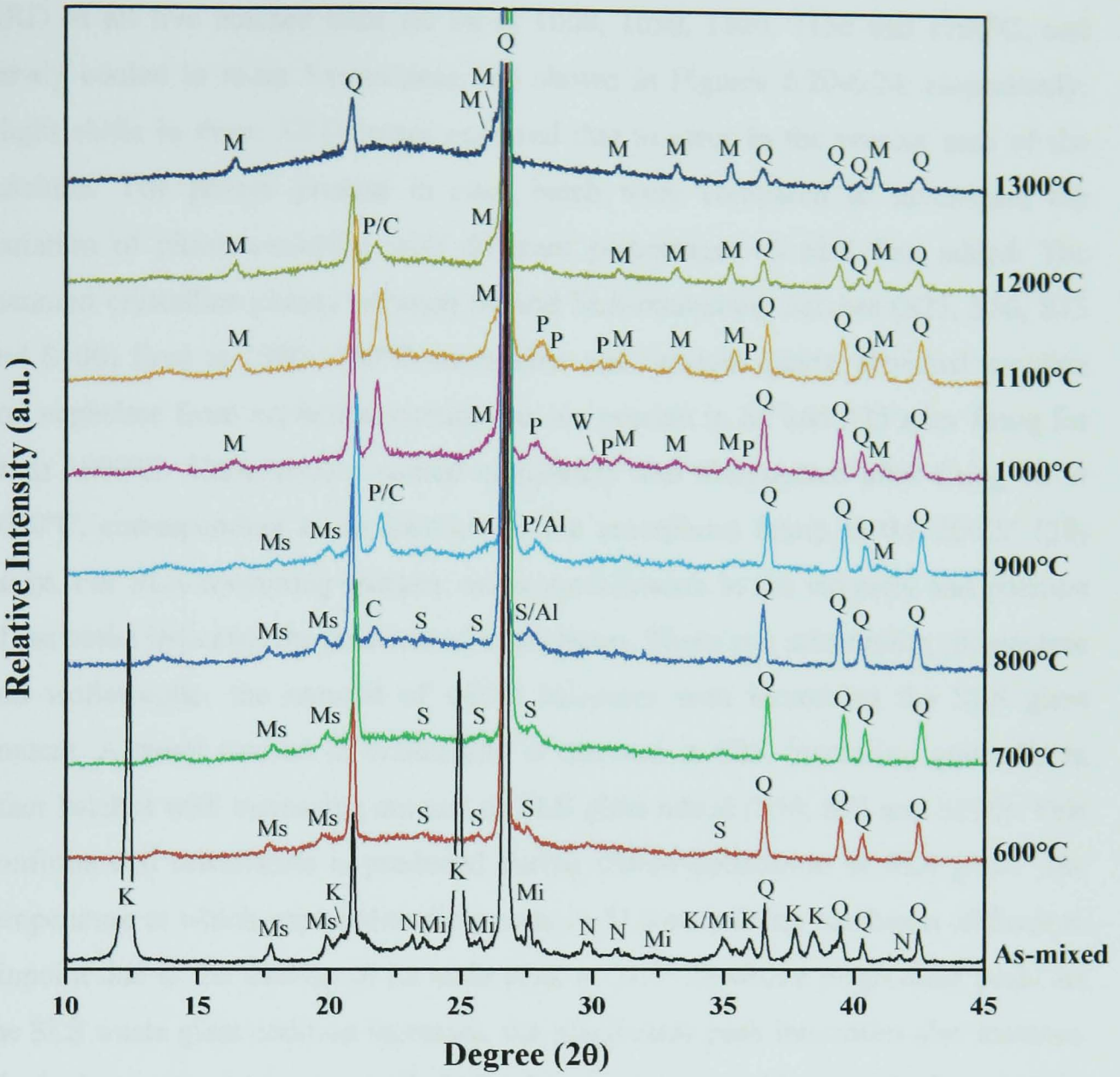

Figure 6.19 - XRD of S75; as-mixed and fired pellets quenched from 600 - 1300°C. (**Al** – Albite, 71-1153, **C** – Cristobalite, 82-512, **K** – Kaolinite-1A, 14-164, **M** – Mullite, 15-776, **Mi** – Microcline, 19-926, **Ms** – Muscovite-2M#1, 6-263, **N** – Nepheline, 35-424, **P** – Plagioclase, 20-528, **Q** – α-quartz, 46-1045, **S** – Sanidine, 19-1227, **W** – Wollastonite-2M, 27-88).

XRD of all five batches fired for 3h at 1000, 1050, 1100, 1150 and 1200°C, and slowly cooled to room temperature, are shown in Figures 6.20-6.24, respectively. Slight shifts in these XRD traces occurred due to error in the precise zero of the machine. The phases present in each batch were compared to investigate the variation of phase evolution with different percentages of SLS flux added. The common crystalline phases between S0 and SLS-containing batches (S25, S50, S75 and S100) fired at 1000-1200°C are mullite and residual quartz. Residual sanidine and nepheline from nepheline syenite flux are present in S0 and S25 after firing for 3h at 1000°C. These phases melted completely and disappeared after firing 3h at 1050°C, corresponding to an increase in the amorphous hump in the 20-25° (2θ) range. For SLS-containing batches, some modification in the intensity and position of the peaks indicated the presence of new phases. These are: cristobalite, plagioclase and wollastonite, the amount of which increases with increasing the SLS glass content. A small amount of cristobalite is detected in S25, increasing gradually in other batches with increasing amount of SLS glass added (S50, S75 and S100). This confirms that cristobalite is produced during the devitrification of SLS glass. The temperature at which cristobalite disappears in SLS-containing batches is difficult to pinpoint due to the overlap of its main peak at 21.7° 2θ with a plagioclase peak. As the SLS waste glass addition increases, the plagioclase peak intensities also increase. Plagioclase was detected in all SLS glass-containing whiteware bodies and its diffraction peaks' intensity decrease when fired above 1100°C. However, in batches with high SLS content (i.e. S75 and S100) plagioclase persists up to 1200°C. It is worth noting that soaking and/or slow cooling plays a role in plagioclase's development. In contrast, cristobalite does not seem to be affected by the soaking and cooling regimes. This can be noticed from the higher intensity of plagioclase's main peak at 27.89°(2θ) relative to cristobalite's main peak at 21.91°(2θ), detected in XRD traces of S100 in Figures 6.20-6.24, compared with XRD traces of quenched S100.

With increasing the SLS percentages in SLS-containing whiteware bodies, a progressive decrease in the intensity of mullite peaks was observed. The reason for this phenomenon was explained earlier in XRD of C-SLS (Figure 5.11) and that of S100 (Figure 6.16). It should be attributed to the decrease in alumina concentration in the glassy phase, as well as to the crystallisation of a plagioclase that consumes part of the alumina available in the system (Souza *et al.*, 2004; Pontikes *et al.*, 2005).

The formation of plagioclase occurs at lower temperatures with respect to the temperature for mullite formation. Furthermore, the lower alumina and higher silica contents in the liquid phase of the SLS fluxed system compared to the nepheline syenite fluxed system is expected to result in a more viscous liquid phase which hinders the kinetics of mullite formation. Moreover, less Na^+ would be available to decrease the viscosity of the liquid, as this ion takes part in the assemblage of high-temperature phases such as plagioclase. Although the quartz proportion is constant (25wt%) in every as-mixed batch, its peak intensity decreases with SLS glass addition and with increasing firing temperature. This effect is clearly seen at temperatures above 1050°C. This is due to the quartz dissolution and transformation to cristobalite. The dissolution of larger amounts of quartz would also contribute to the formation of a relatively viscous liquid phase. This liquid would penetrate the porosity at a lower rate, which could explain a more porous microstructure compared to SLS-free batches after firing at the same temperature (Figure 6.4 and 6.5). Fokin *et al*. (2003) also found that the nucleation and growth of sodium-enriched crystals lead to the depletion of sodium in the glass matrix of SLS-type glasses.

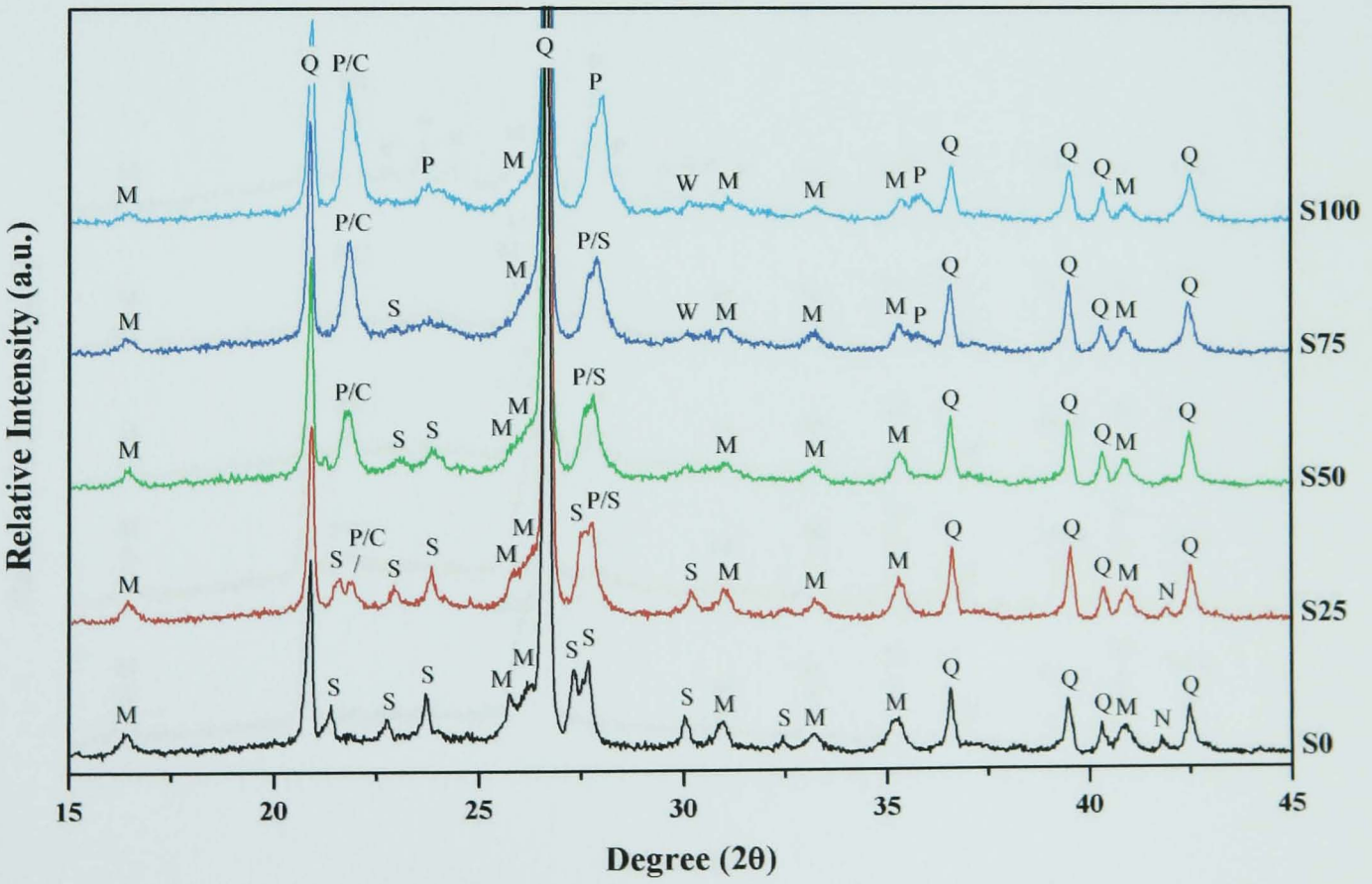

Figure 6.20 - XRD of each batch fired at 1000°C for 3h.

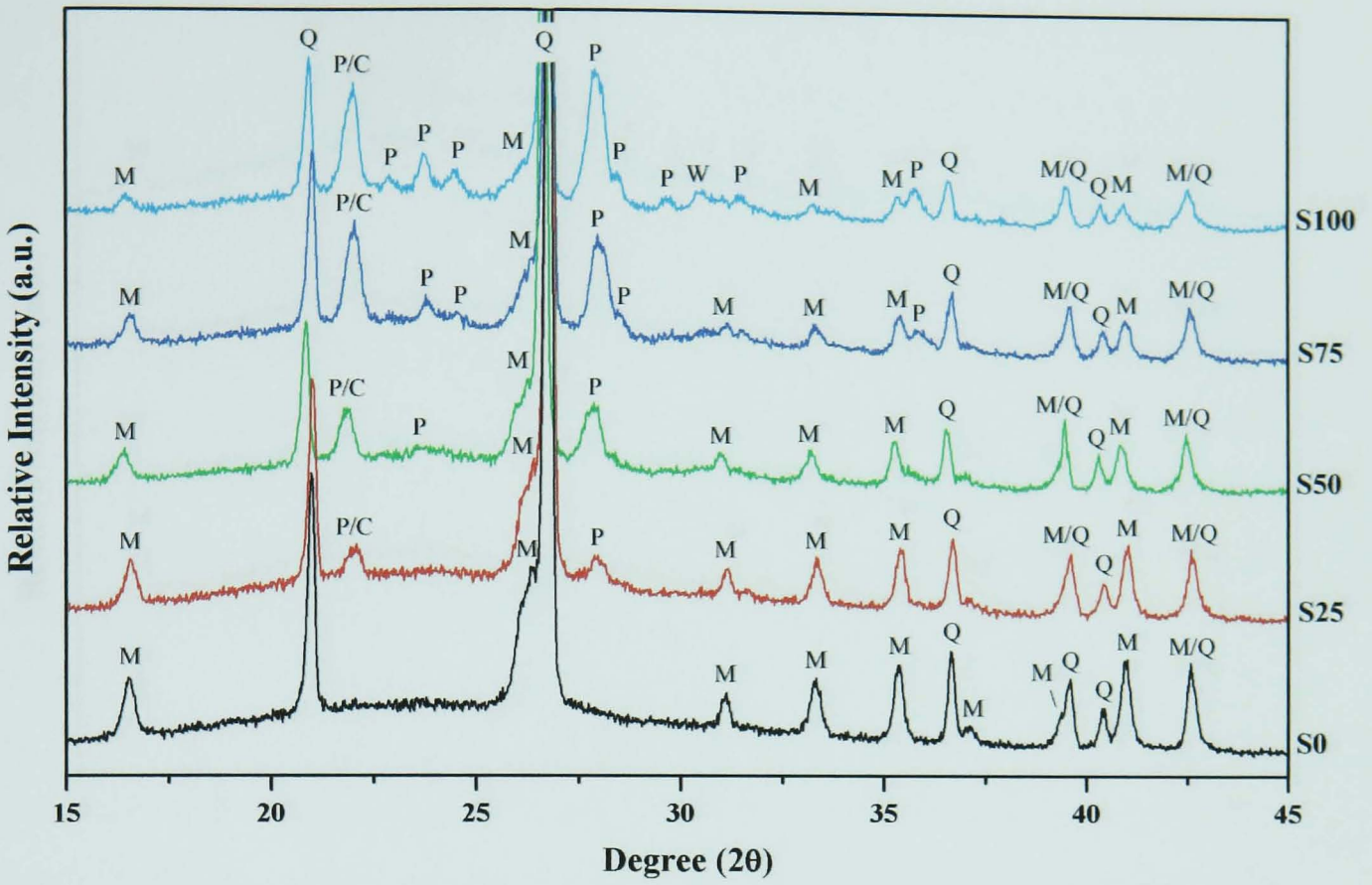

Figure 6.21 - XRD of each batch fired at 1050°C for 3h.

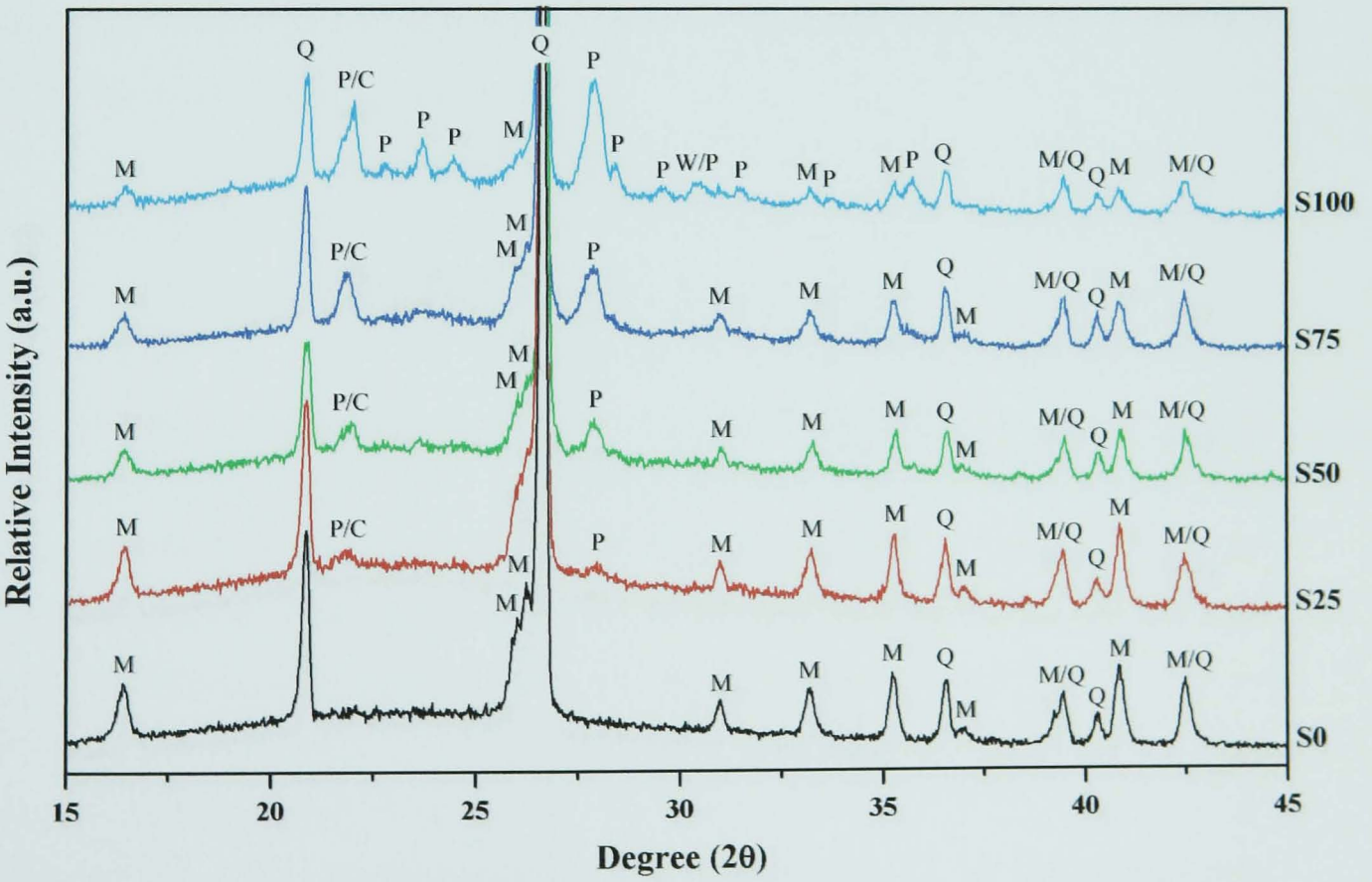

Figure 6.22 - XRD of each batch fired at 1100°C for 3h.

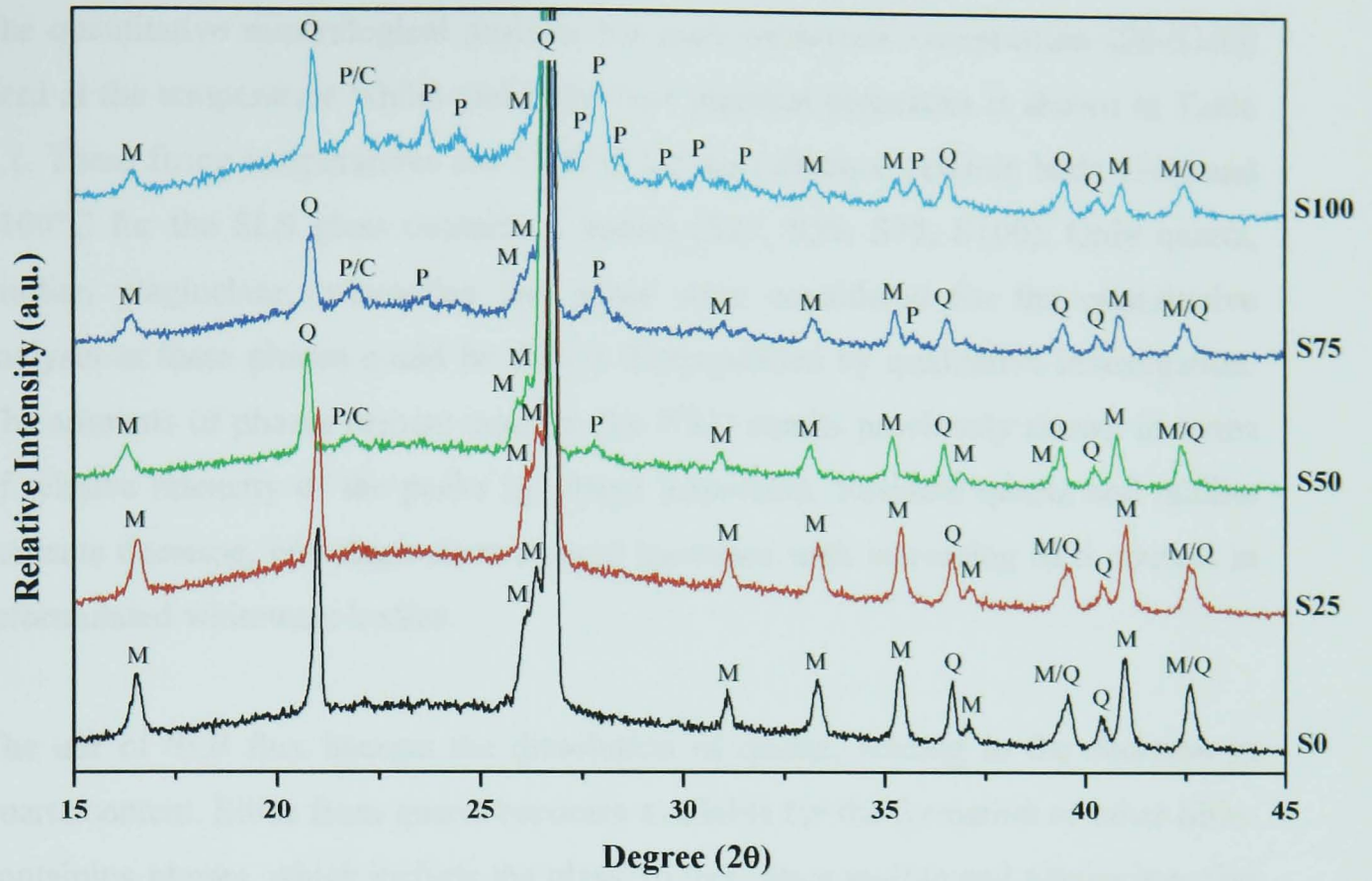

Figure 6.23 - XRD of each batch fired at 1150°C for 3h.

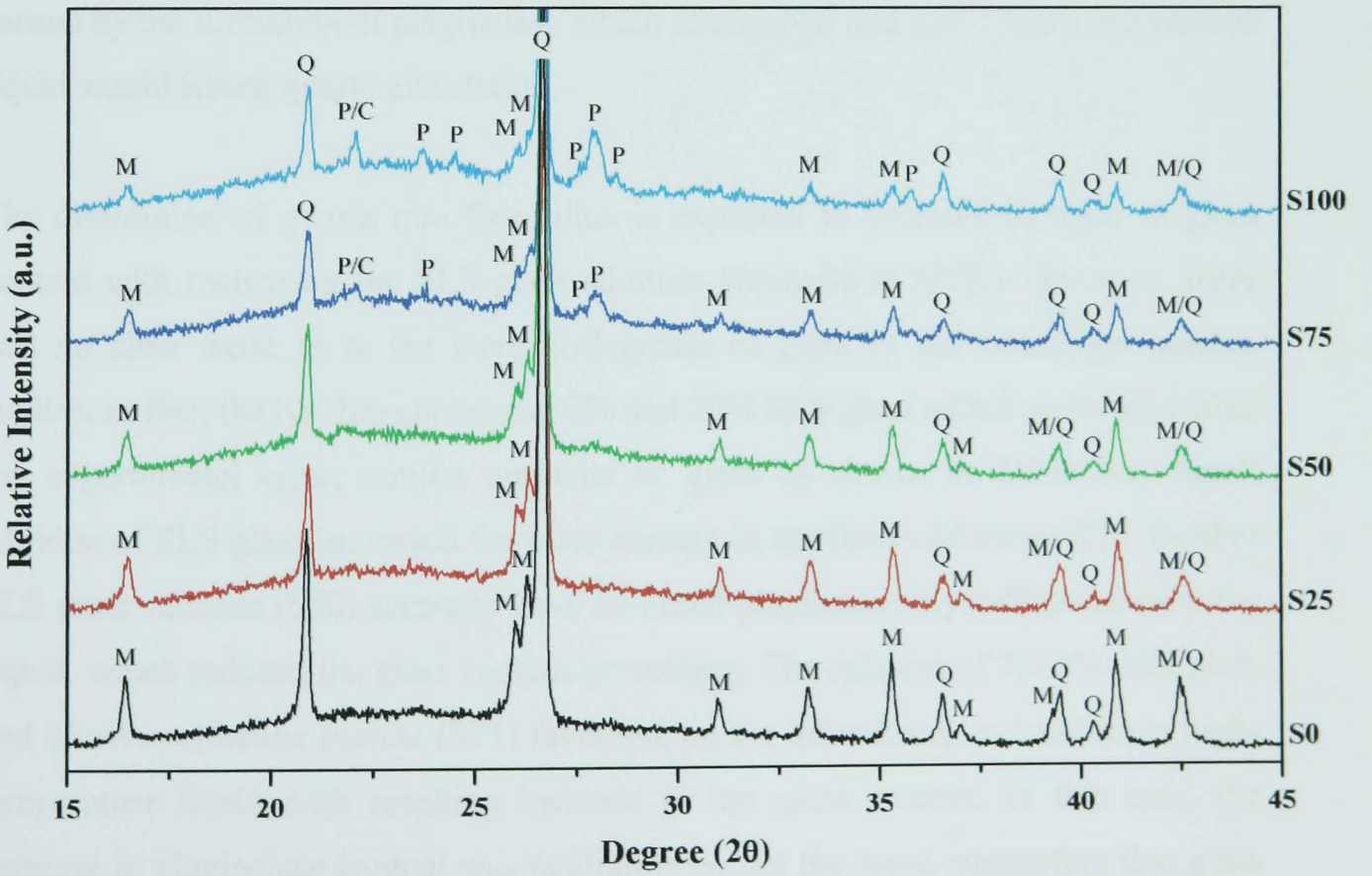

Figure 6.24 - XRD of each batch fired at 1200°C for 3h.

The quantitative mineralogical analysis for each whiteware composition (S0-S100) fired at the temperature which yields the best physical properties is shown in Table 6.1. These firing temperatures are 1200°C for the reference ceramic body (S0), and 1100°C for the SLS glass containing bodies (S25, S50, S75, S100). Only quartz, mullite, plagioclase, microcline and glass were considered for the quantitative analysis as these phases could be clearly distinguished by qualitative investigation. The amounts of phases present confirm the XRD results previously shown in terms of relative intensity of the peaks by visual inspection. Residual quartz and mullite contents decrease, but plagioclase content increases with increasing SLS content in reformulated whiteware bodies.

The use of SLS flux hastens the dissolution of quartz, leading to the decrease in quartz content. Silica from quartz becomes available for the formation of other SiO_2-containing phases, which include the glass. In fact, since mullite and plagioclase also need alumina to crystallise it is more likely that the extra silica went to the glassy phase. The percentage of quartz seems to be the same in S75 and S100 within the error. This could be the result of increased viscosity of the high-temperature liquid caused by the formation of plagioclase which retains Na^+ and Ca^{2+}. The more viscous liquid would lessen quartz dissolution.

The dissolution of quartz into free silica is expected to promote increase in glass content with increasing the SLS glass addition (from S0 to S100). However, there was no clear trend as to the increase/decrease of glass in the whiteware batches studies. In fact, the batches containing 0% and 50% SLS glass added revealed, within the experimental error, similar amounts of glass as shown in Table 6.1. Small addition of SLS glass increased the glass content in the fired whiteware S25. Further SLS glass addition (S50) seems to have favoured plagioclase crystallisation from the liquid, which reduced the glass content on cooling. The mixture of 75wt% SLS glass and 25wt% nepheline syenite (S75) favoured, on the other hand, an increase in high-temperature liquid with resulting increase in the glass content. In this case, the increase in plagioclase content was negligible within the error, suggesting that glass formation is linked somewhat with the incapacity of the system to form plagioclase. Indeed, the great contribution of SLS addition to reformulated whiteware in terms of phase composition is the formation of plagioclase crystals, as previously revealed by

XRD (Figure 6.20-6.24), and generally agreed in the literature (e.g. Souza *et al.*, 2004; Pontikes *et al.*, 2005; Tucci *et al.*, 2005).

The fluctuation in glass content observed in Table 6.1, although thought to be connected with the plagioclase crystallisation, is also due to the complexity of the system in terms of amount alkalis and also the availability of these alkalis (i.e. the viscosity of the high-temperature liquid). Additionally, surface crystallisation of SLS-glass particles on heating the system (Prado and Zanotto, 2002) may be playing a role in the reactions between the molten nepheline syenite components (not present in S100) and the decomposed clay. The crystallised surfaces of SLS glass particles form a kinetic barrier for further reactions, whereas the highly reactive liquid yielded by nepheline syenite melting is more capable of penetrating this crystallised layer.

Table 6.1 - Quantitative analysis of the mineralogical phases in S0 fired at 10°C/min and held for 3h at 1200°C, and that of S25, S50, S75 and S100 fired at 10°C/min and held for 3h at 1100°C, using the Rietveld method.

Mineralogical phase	S0		S25		S50		S75		S100	
	wt%	±Δ	wt%	±Δ	wt%	±Δ	wt%	±Δ	wt%	±Δ
Quartz	22.3	0.2	18.4	0.2	17.9	0.2	14.0	0.2	14.5	0.3
Mullite	13.0	0.4	10.8	0.4	10.0	0.4	6.7	0.5	5.0	0.4
Microcline	1.1	0.3	-	-	-	-	-	-	-	-
Plagioclase	1.8	0.4	3.6	0.6	10.6	0.5	11.2	0.6	16.3	0.6
Glass	61.8	1.8	67.2	1.5	61.5	1.4	68.0	1.6	64.2	1.7

6.5 - MICROSTRUCTURAL EVOLUTION

In this section the microstructural evolution after firing each whiteware batch composition was studied. Starting with the standard whiteware batch (S0), the microstructural investigation followed the fully SLS-fluxed whiteware batch (S100) and finally the partially SLS-fluxed whiteware batches (S25, S50 and S75).

Figure 6.25 shows SEM/SEI images of S0 samples fired at 1000°C. The overall microstructure of S0 after firing at 1000°C (Figure 6.25(a)) comprises poorly dissolved angular quartz particles (Q), decomposed clay relicts (DC) containing clay-derived material (probably primary mullite, in agreement with XRD of S0 in Figure 6.20), feldspar-penetrated clay relicts (C+F), and elongated crystals shown in more detail in Figure 6.25(b)-(c). Decomposed clay relict agglomerates (DC) could be clearly distinguished from mixed clay-feldspar (C+F) relicts because of their more contiguous microstructure (Iqbal and Lee, 2000). The Al:Si ratio from EDS analysis of the crystals shown in Figure 6.25(b) is close to 2:1. As primary mullite consists of small cuboidal crystals, the feature shown in Figure 6.25(b) might be sillimanite (Al_2SiO_5). The identification of sillimanite by XRD in the present work is complicated by the fact that its diffraction peaks overlap those of mullite, also present in samples from S0 fired at 1000°C (Figure 6.20). The elongated ($\leq$3 μm long and $\leq$0.5 μm wide) crystals in Figure 6.25(c) were identified by EDS as secondary mullite derived from feldspar particles (and clay relicts). Its aspect ratio of 3-10:1 indicates type II mullite, as previously seen from the microstructure of C-NS mixture (Figure 5.29).

The microstructure seen in Figure 6.26(a) of S0 fired at 1100°C clearly shows a denser material than that in Figure 6.25(a) because of the fact that S0 samples developed glassy phase after firing at $\geq$1050°C. BSI images of unetched S0 samples fired at 1000, 1050, 1100, 1150, 1200 and 1250°C (Figure 6.27) clearly show the presence of liquid phase at $\geq$1050°C. Pores (black in BSI) were mostly interconnected at 1000°C but became closed and isolated after firing at 1050°C. The liquid phase (light grey colour) formed permeated the microstructure and led to higher densification. The increased density of S0 fired at $\geq$1050°C (Figure 6.1) is associated with this liquid formation. Correlating with XRD of all batches fired 3h at

1050°C (Figure 6.21), no feldspar peak was observed for S0 due to the fact that it melted completely and formed glass on cooling, and an amorphous hump at ~20-30° was clearly seen at room temperature. Quartz particles are more rounded than angular, and the presence of a solution rim indicates their partial dissolution during firing. Cracks generated around and within large quartz grains were observed in all specimens fired ≥1050°C due to the rapid displacive phase transformation (β to α) of quartz on cooling. These cracks arise as a result of the thermal expansion mismatch between quartz and the surrounding glassy matrix. The cracking severity depends largely on the cooling rate (Kara *et al.*, 2006). Cracks may also be generated during specimen preparation for microscopy such as grinding and polishing, which in the case of the present study seems to be a minor issue when compared to the thermal expansion mismatch between the glassy matrix and the tightly bonded quartz. Higher magnification SE images are shown in Figures 6.26(b)-(c). The feature (indicated by an arrow) shown in Figure 6.26(b) has a chemical composition (shown by EDS) similar to that in Figure 6.25(c), suggesting that microcline or sanidine decomposed giving K and Si to the liquid, as well as providing Si and Al to form mullite. Moreover, as shown by XRD of S0 fired at 1050°C (Figure 6.21), microcline and sanidine decompose after firing at 1050°C. Figure 6.26(c) reveals cuboidal primary mullite (Type I) forming in decomposed clay relicts and needle-like secondary mullite (Type III) growing from the interface of clay relicts toward the liquid phase or molten feldspar.

SEM/SE images of S0 fired 3h at 1100°C taken using a high resolution SEM reveal particles of submicron size (Figures 6.28(a)-(d)). Secondary mullite (Type II) formed from molten feldspar particles was also detected. It has an elongated shape (≤5 μm long and ≤0.5 μm wide) and grows from the clay-feldspar interface toward the centre of the feldspar particle. A few needle-like mullite crystals (Type III) were observed near the centre of molten feldspar (Figure 6.28(b)). Primary mullite (Type I), formed from clay-rich relicts, has particle size less than 0.5 μm (length) and is clearly seen in Figure 6.28(d).

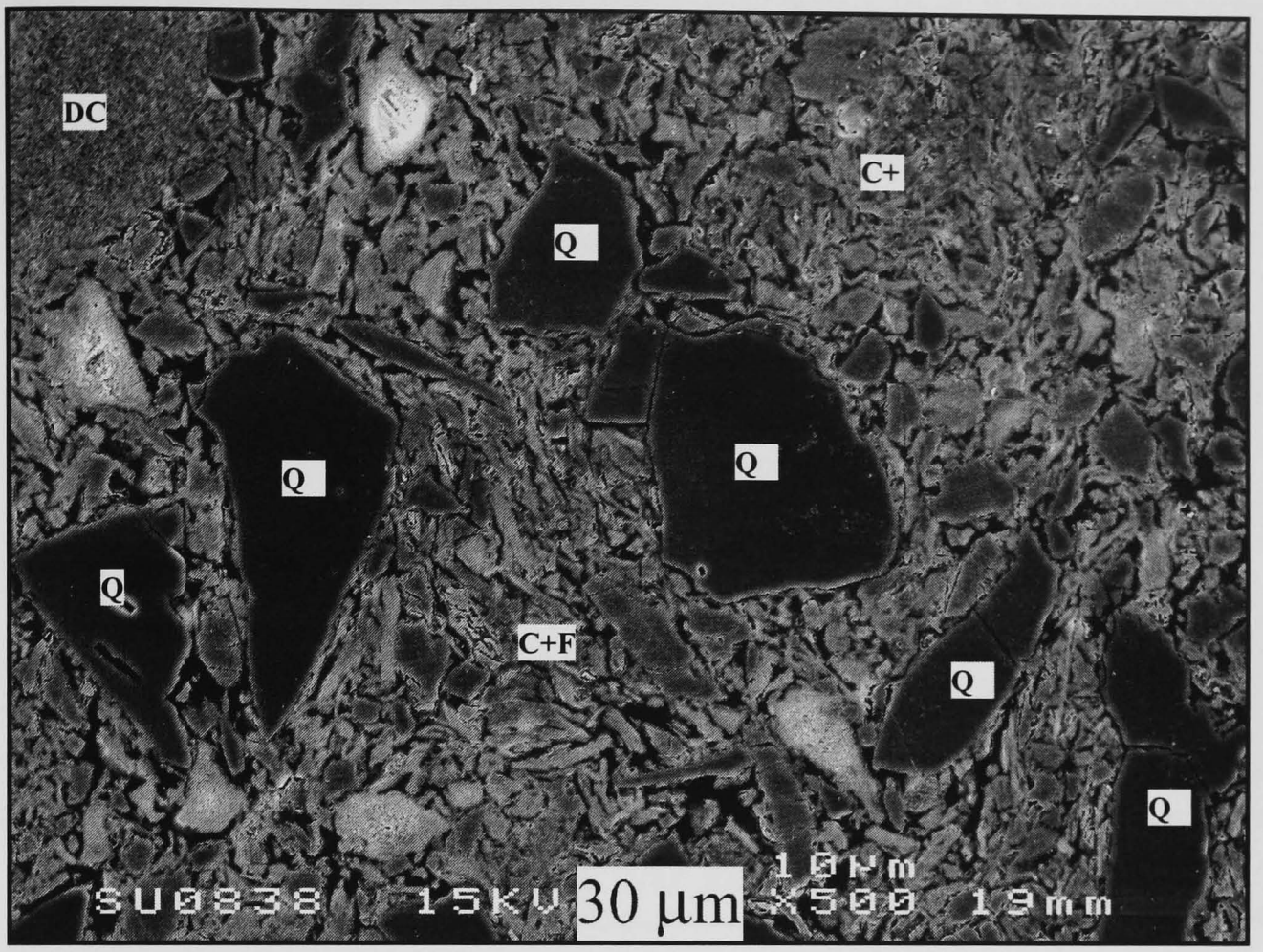

(a)

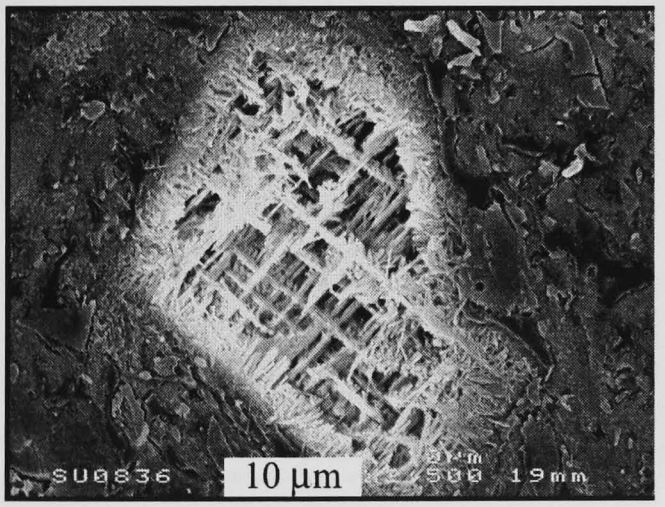

(b)

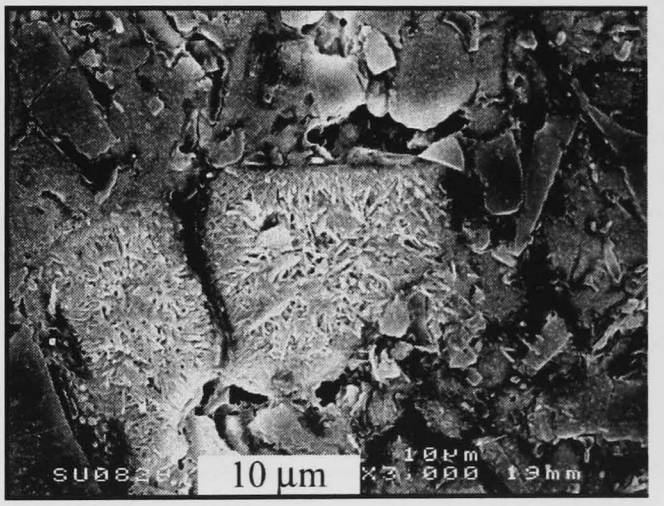

(c)

Figure 6.25 - SEM/SE images of polished and etched cross-section of standard whiteware (S0) fired at 1000°C. (a) is the overall microstructure of S0, (b) and (c) show in detail elongated crystals present in S0, which are possibly sillimanite and secondary mullite, respectively. (DC = decomposed clay, C+F = feldspar-penetrated clay relicts, Q = quartz)

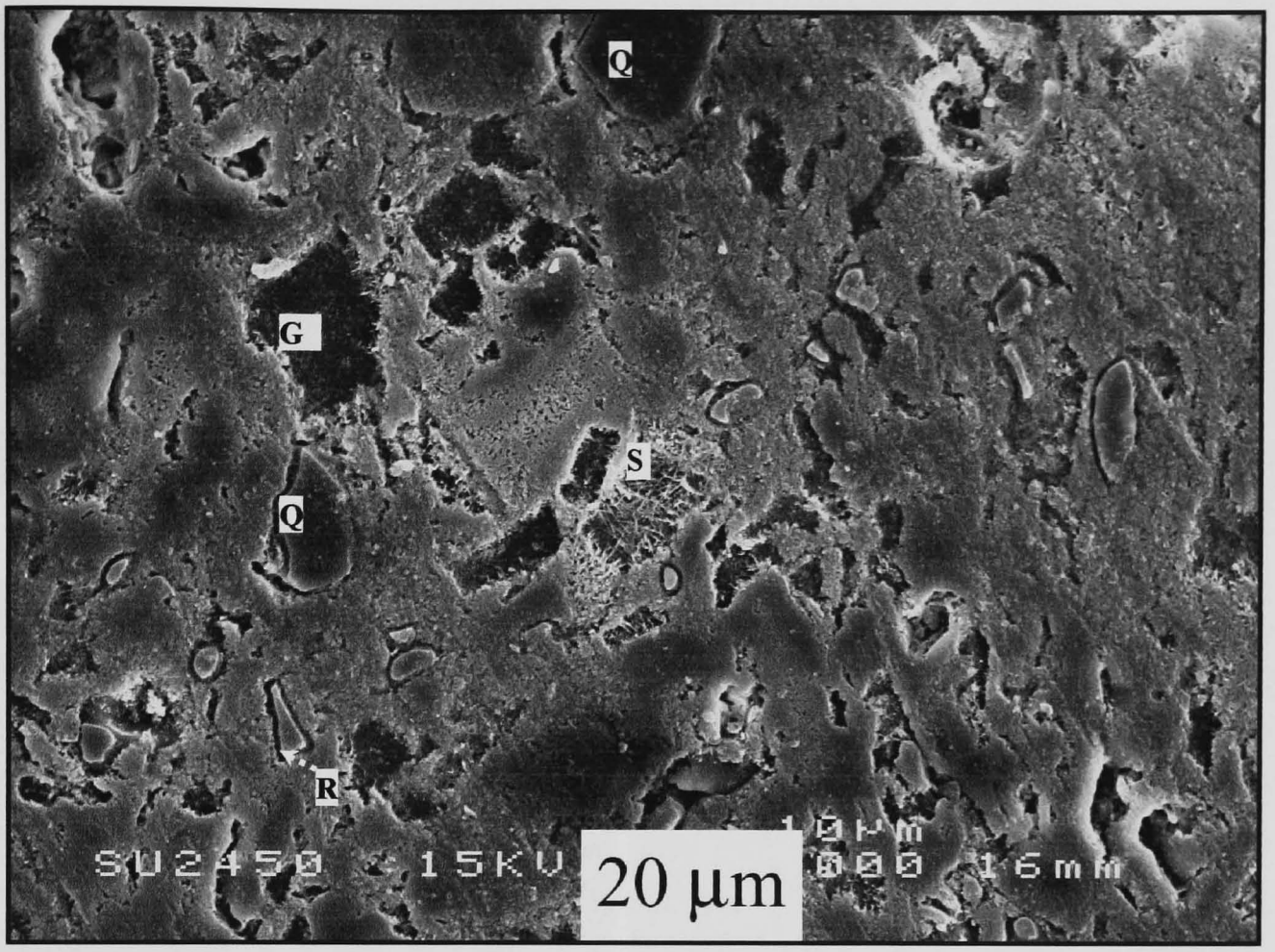

(a)

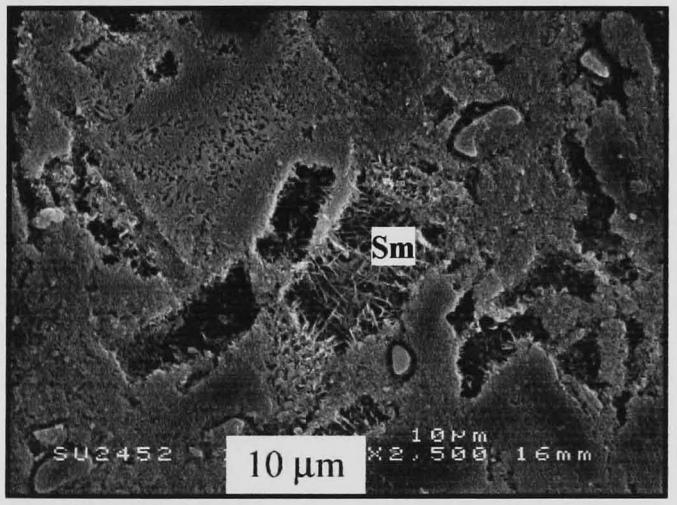

(b)

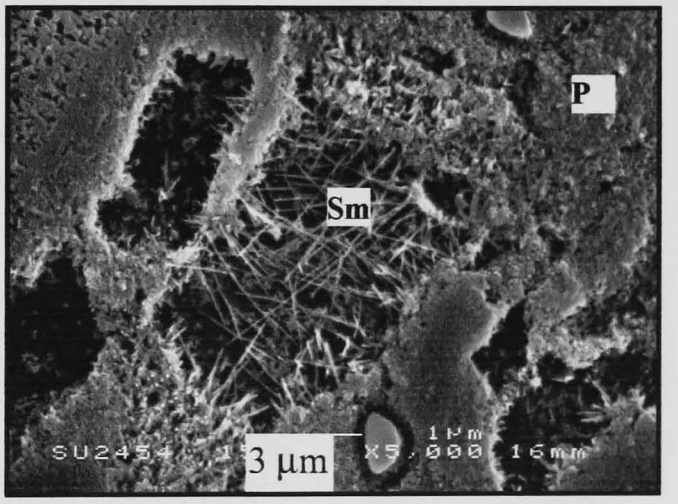

(c)

Figure 6.26 - SEM/SE images of polished and etched cross-sections of standard whiteware (S0) fired at 1100°C. (a) is the overall microstructure of S0, (b) and (c) show in detail needle-like secondary mullite and cuboidal primary mullite crystals presented in S0. (Pm = primary mullite, Sm = secondary mullite, Q = quartz, R = solution rim, G = glassy phase)

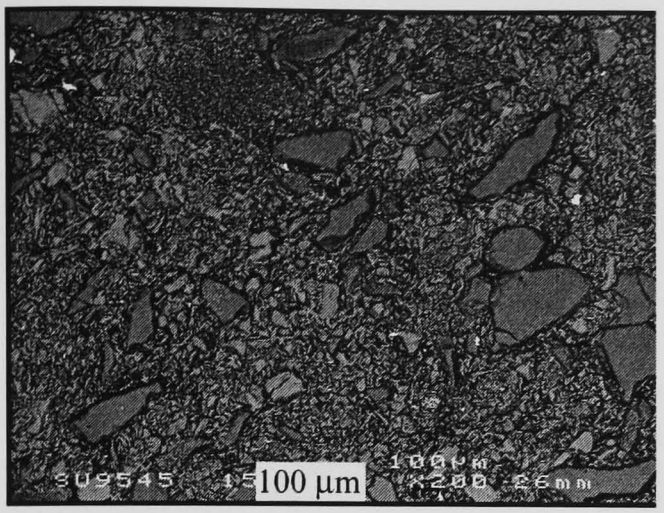

(a) 1000°C

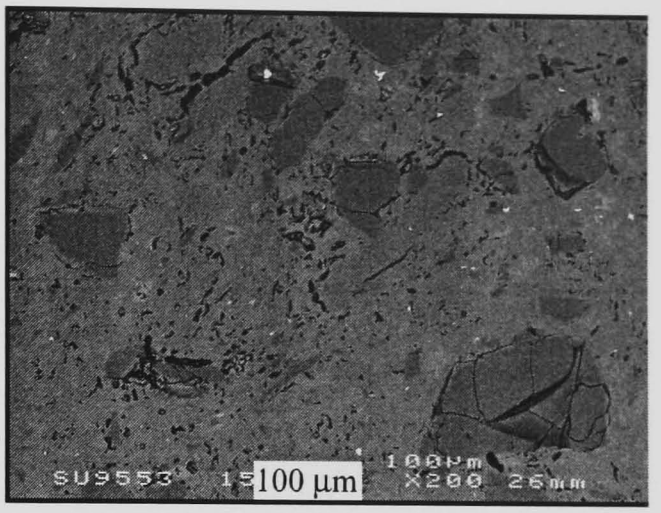

(b) 1050°C

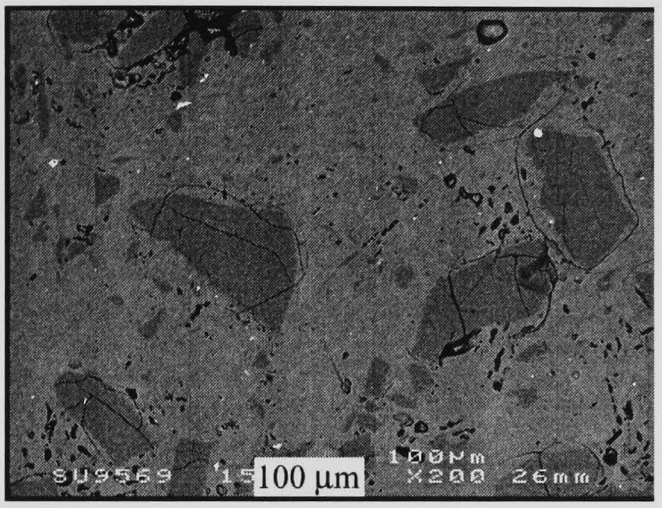

(c) 1100°C

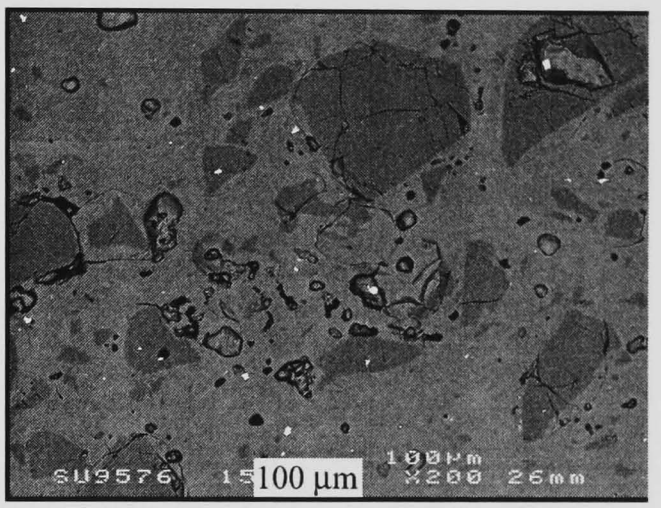

(d) 1150°C

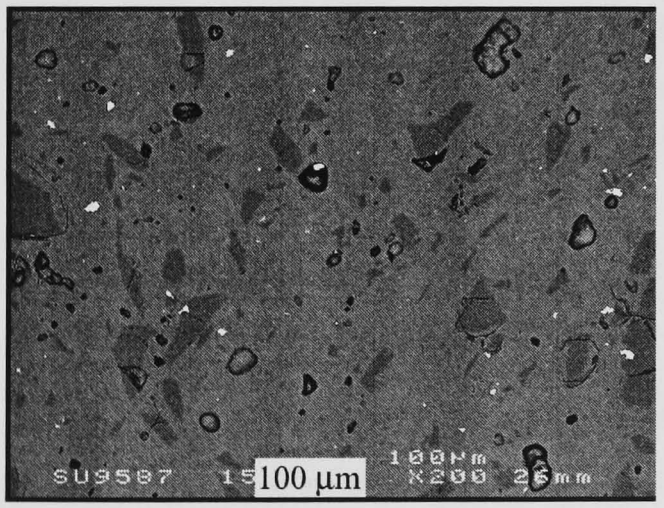

(e) 1200°C

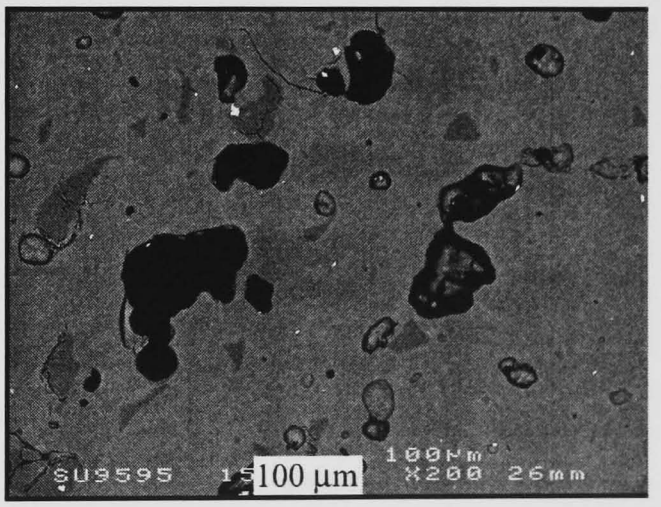

(f) 1250°C

Figure 6.27 - SEM/BS images of polished cross-sections of standard whiteware (S0) fired at 1000 - 1250°C (a)-(f).

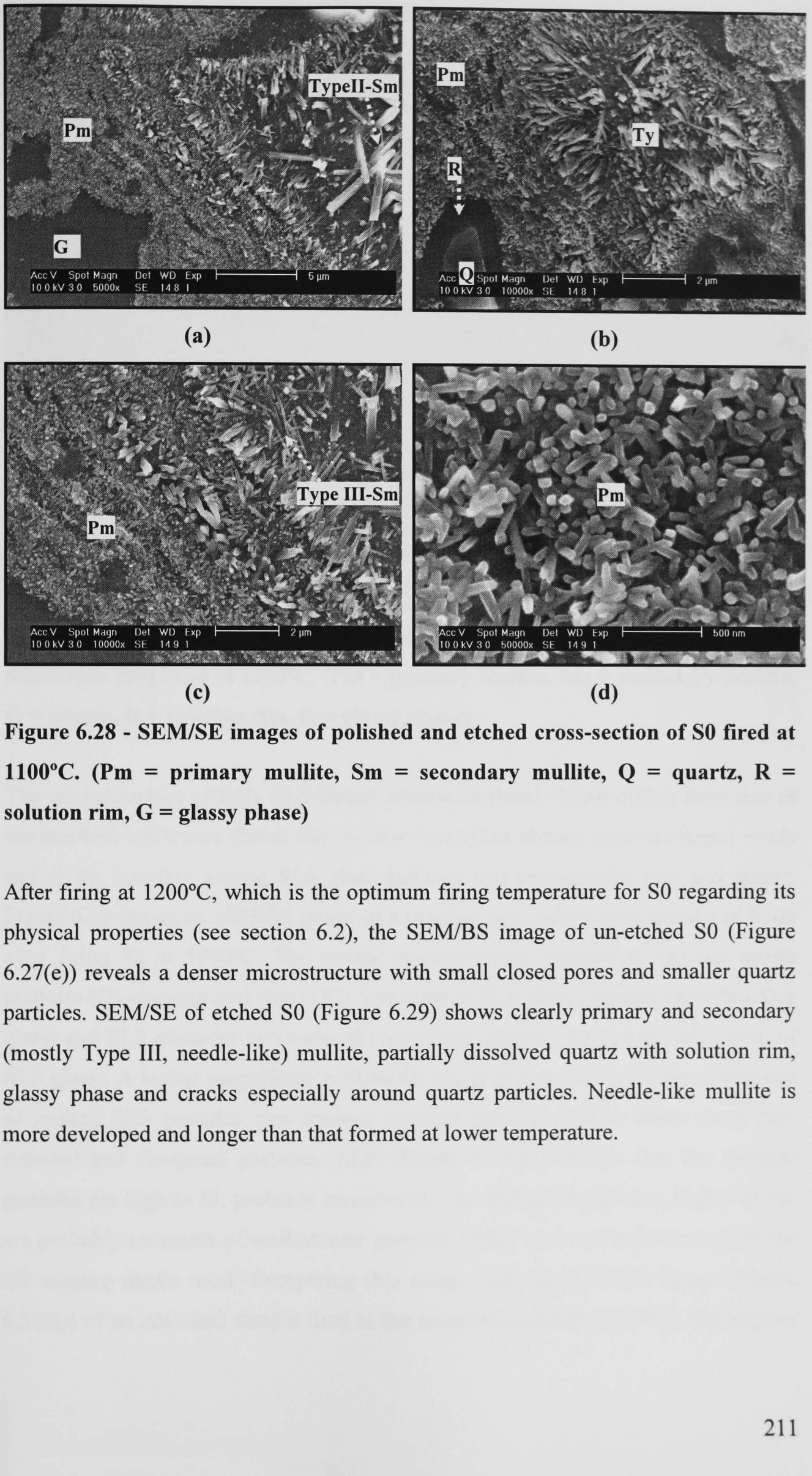

Figure 6.28 - SEM/SE images of polished and etched cross-section of S0 fired at 1100°C. (Pm = primary mullite, Sm = secondary mullite, Q = quartz, R = solution rim, G = glassy phase)

After firing at 1200°C, which is the optimum firing temperature for S0 regarding its physical properties (see section 6.2), the SEM/BS image of un-etched S0 (Figure 6.27(e)) reveals a denser microstructure with small closed pores and smaller quartz particles. SEM/SE of etched S0 (Figure 6.29) shows clearly primary and secondary (mostly Type III, needle-like) mullite, partially dissolved quartz with solution rim, glassy phase and cracks especially around quartz particles. Needle-like mullite is more developed and longer than that formed at lower temperature.

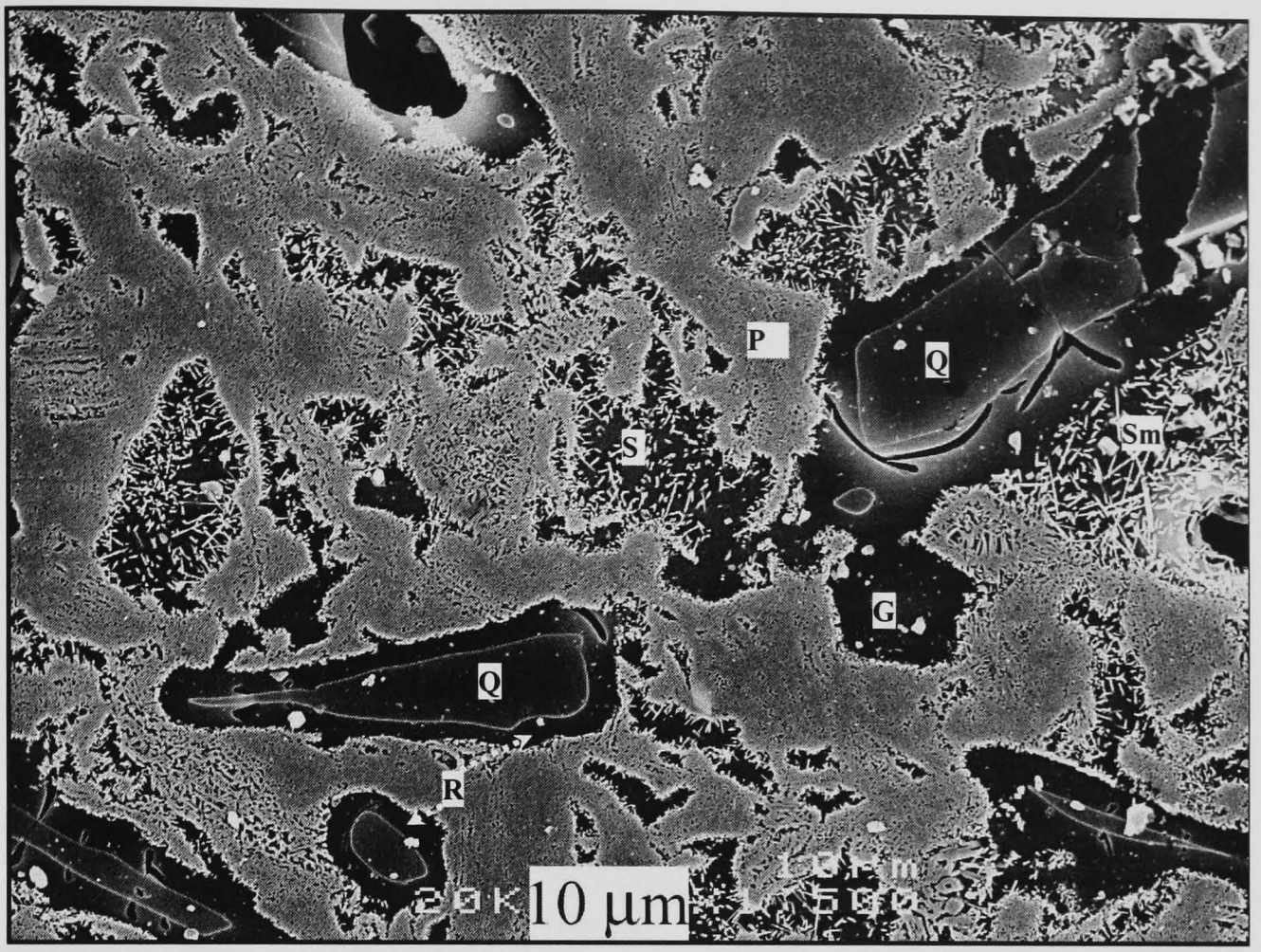

Figure 6.29 - SEM/SE image of polished and etched cross-section of standard whiteware (S0) fired at 1200°C. (Pm = primary mullite, Sm = secondary mullite, Q = quartz, R = solution rim, G = glassy phase)

The microstructure of fully SLS-fluxed whiteware (batch S100) differs from that of the standard whiteware (batch S0), as new crystalline phases were developed inside and at the interface among SLS glass particles and decomposed clay and quartz. Figure 6.30 shows an SEM/SE image of a polished and etched cross-section of S100 after firing 3h at 1000°C. The overall microstructure consists of angular quartz particles (Q), decomposed clay (DC), remnants of SLS glass (residual unmelted SLS glass) and SLS glass-derived material (crystalline phases from the devitrification of SLS glass). A higher magnification SEM/SE image (Figure 6.31(a)) shows remnants of molten SLS particles that contain rounded particles and in some cases both rounded and elongated particles. EDS (Figure 6.31(b)) reveals that the rounded particles are high in Si, probably cristobalite. The elongated particles, higher in Ca, are probably remnants of wollastonite particles which were not etched away by the HF etching media used. Comparing this image with the SEM/BS image (Figure 6.31(c)) of an unetched sample fired at the same temperature (1000°C), the brighter

areas of elongated particles are higher in Ca and Si (see EDS in Figure 6.31(d)) and the darker rounded particles are high in Si. These similar particles were also found in the C-SLS mixture fired at 1000°C (Figure 5.37) and, as discussed in earlier sections, the brighter elongated particles of calcium silicate phase within the glass grains are wollastonite and the surrounding darker rounded silica-rich particles are cristobalite. XRD of S100 fired at 1000°C (Figure 6.16 and 6.20) reveals cristobalite and wollastonite peaks, which is consistent with these findings.

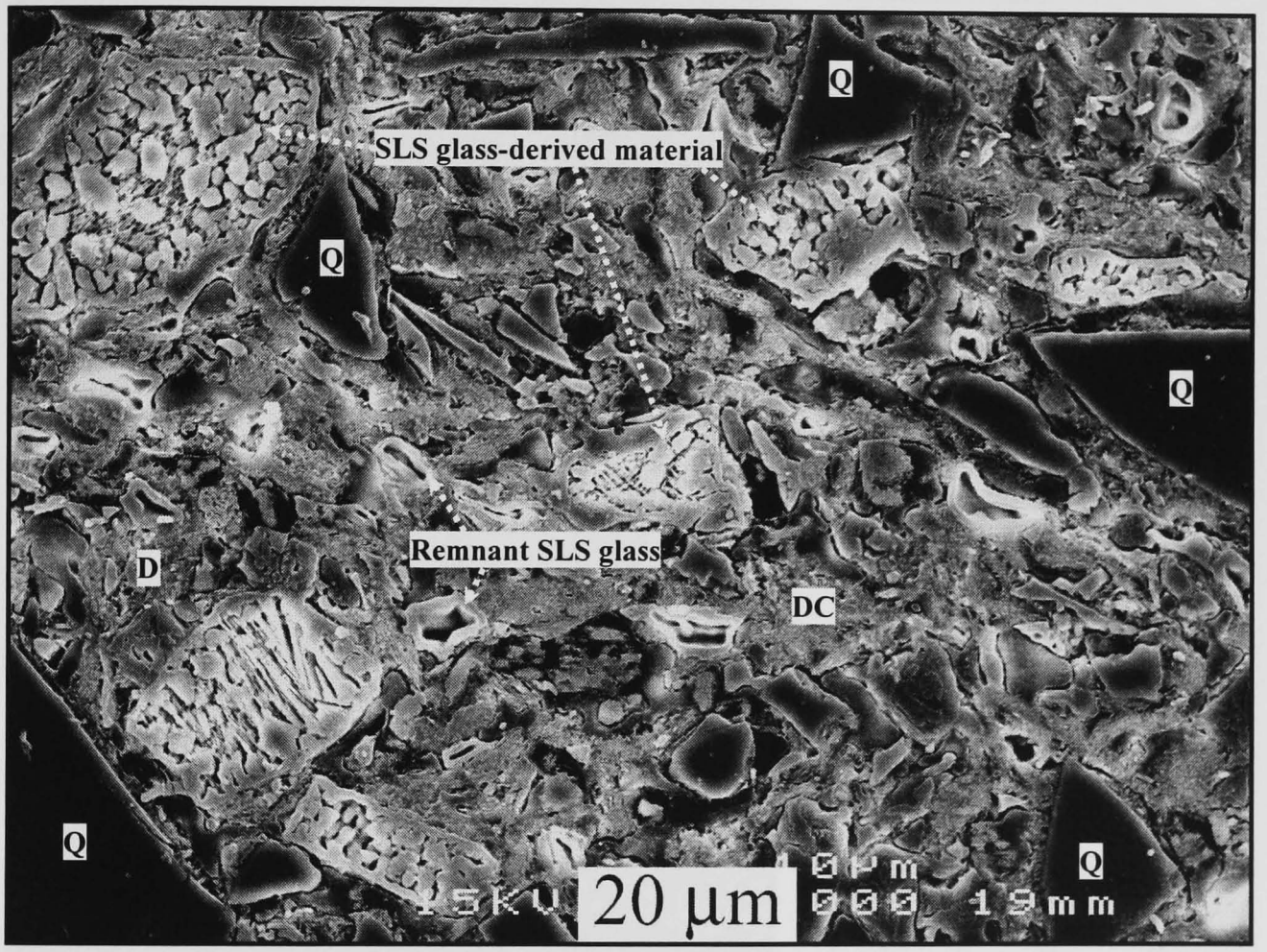

Figure 6.30 - SEM/SE image of polished and etched cross-section of SLS-fluxed whiteware (S100) fired at 1000°C. (DC = decomposed clay, Q = quartz)

Cristobalite and wollastonite both devitrified from molten SLS grains but wollastonite seems to be located mostly in the centre of molten glass grains, supposedly in areas high in Ca. After etching, most wollastonite particles seem to have been leached out leaving cristobalite particles and rims of molten glass which are still clearly distinguished. EDS revealed this zone to be richer in silica. Willems (1966) studied the devitrification of SLS glass with 73.0wt% SiO_2, 13.2wt% Na_2O and 8.3wt% CaO and found that this glass usually devitrifies to wollastonite and

cristobalite. He also concluded that wollastonite blades are usually not solid but show a core of glass, and are often accompanied by dendritic cristobalite. This statement would support the result shown in the present study which suggests that wollastonite could have been etched away by HF.

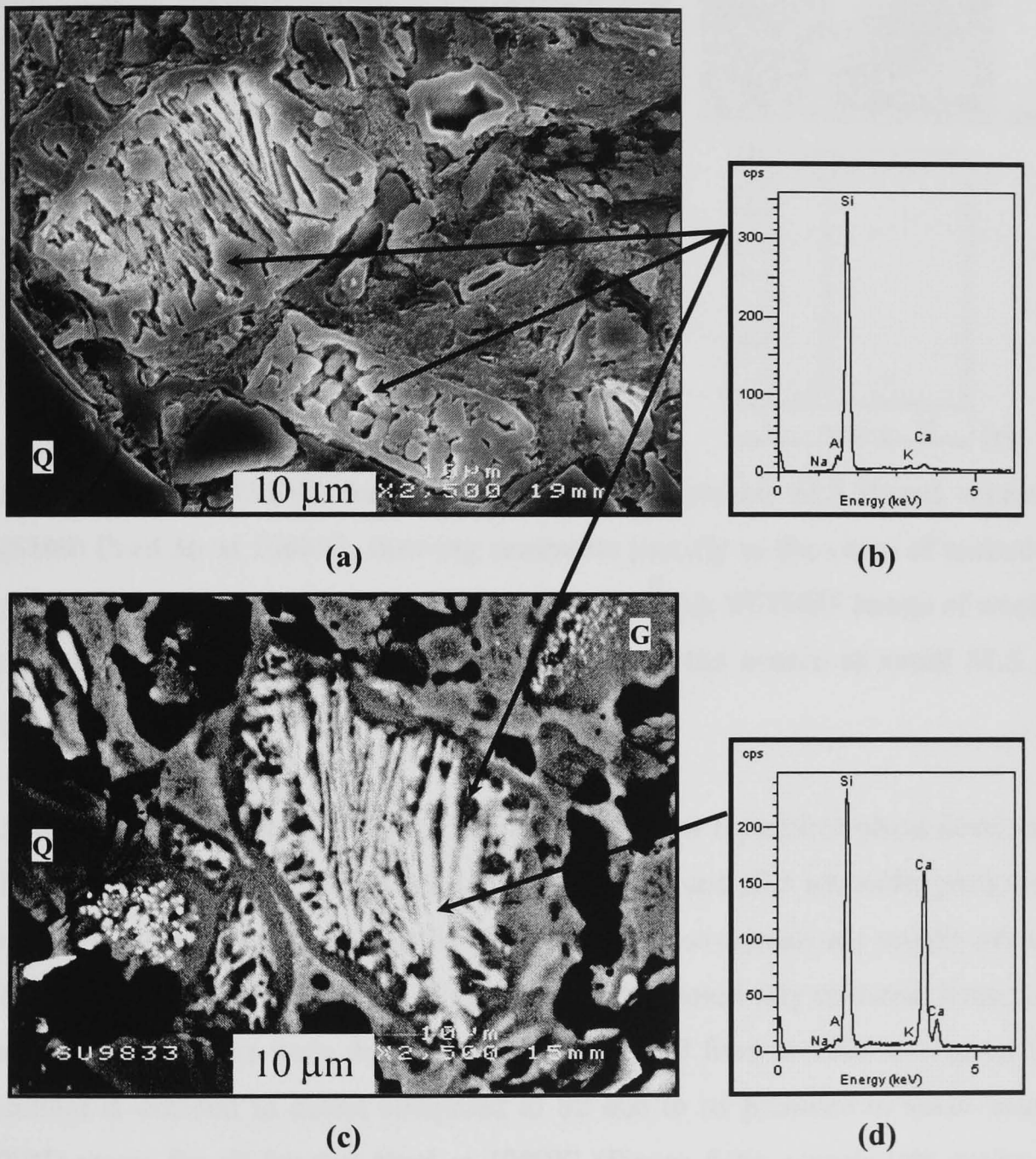

Figure 6.31 - SEM/SE image of etched sample (a) and SEM/BS image of unetched sample from SLS-fluxed whiteware (S100) fired 3h at 1000°C. EDS of the corresponding areas are shown in (b) and (c).

Another feature usually found in S100 is shown in Figure 6.32(a). These particles have a ring-shaped morphology with a hole in the centre. EDS (Figure 6.32(c)) of these particles reveal they are high in Si. These particles were also found in C-SLS

mixtures and were considered to be remnants of small SLS particles after the Ca-rich phase in the centre of the glass particles (see Figure 6.32(b)) was etched by HF.

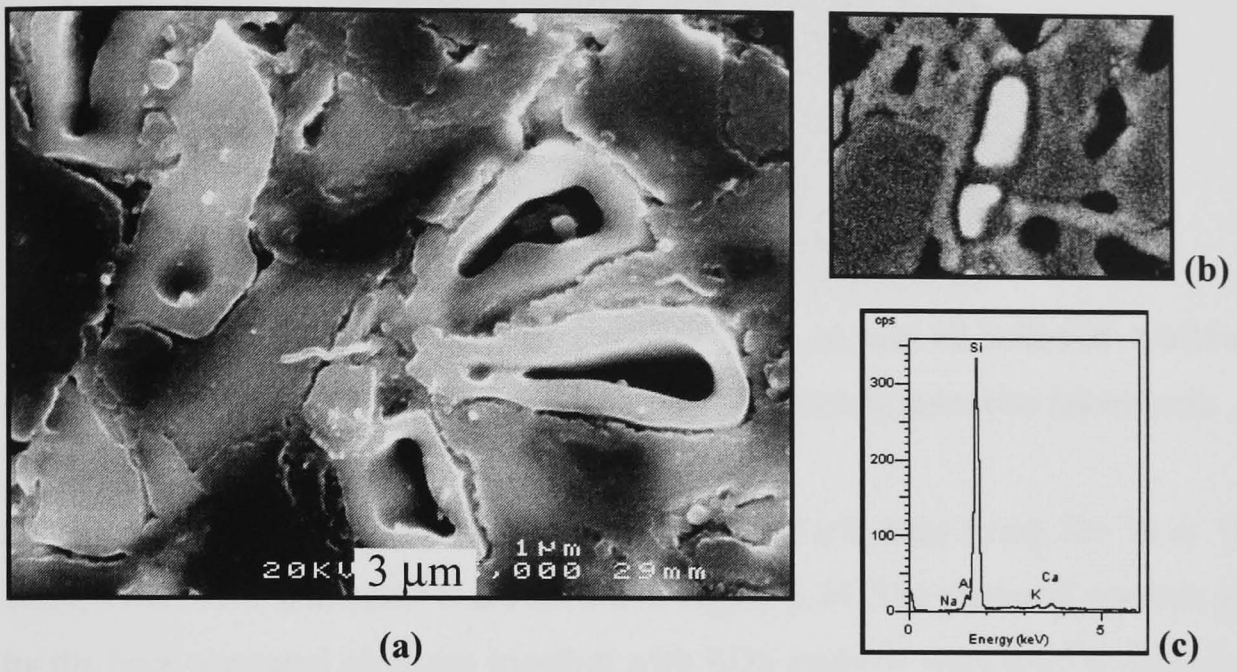

(a) (b) (c)

Figure 6.32 - SEM/SE image of polished and etched SLS-fluxed whiteware (S100) fired 3h at 1000°C, showing remnants (mostly in the rims) of melted SLS glass particles rich in Si (a) and their EDS trace (c). SEM/BS image of unetched sample (b) showing Ca-rich (brighter) areas in the centre of small SLS glass particle.

XRD (Figure 6.20) reveals plagioclase as another new crystalline phase developed in fired S100. Figure 6.33 shows lath-like (≤2 µm long and ≤0.5 µm wide) particles rich in Si, Al, Ca and Na, thought to be plagioclase. These crystals are usually present at the interface between molten SLS glass and decomposed clay material. Even though small mullite peaks were detected in XRD of S100 fired at 1000°C (Figure 6.20), mullite is difficult to detect compared to S0 due to its presence in small amounts. XRD traces for all batches fired at 1000°C (Figure 6.20) reveals less evidence of mullite because of its lower intensity peaks for S100 compared to S0, which can be correlated to the lower mullite growth in S100.

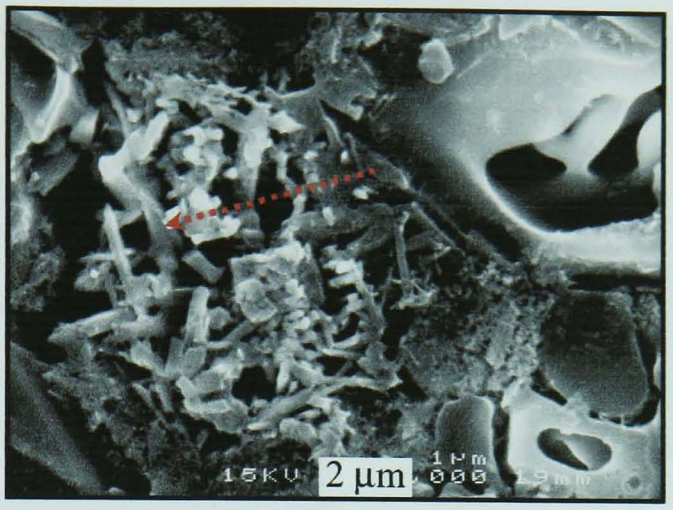

Figure 6.33 - SEM/SE image of polished and etched SLS-fluxed whiteware (S100) fired 3h at 1000°C, showing lath-like plagioclase particles (arrowed).

BS images taken from polished cross-sections of S100 after firing for 3h at 1000, 1050, 1100, 1150 and 1200°C are shown in Figure 6.34. The chemical contrast given by the back-scattered electrons together with EDS analysis were used to identify the microstructural features present. The S100 sample fired at 1000°C exhibits a large amount of porosity (both isolated and interconnected pores), represented by dark areas (black contrast) with irregular shape and variable sizes. Quartz (dark grey contrast) still showing sharp edges is surrounded by glassy phase (light grey contrast) and SLS glass-derived particles (dark-grey feature of cristobalite with white contrast of wollastonite, as seen from Figures 6.31(c) and 6.32(b)). After firing at 1050°C, the number of small pores decreases and interconnected pores become isolated and start acquiring a rounded shape. Quartz particles still retain their sharp edges with cracks clearly seen around, and within, the larger particles. The microstructure seems denser, containing more glassy phase. SLS glass derived particles were less noticeable, but "scribble" features of groups of plagioclase crystals (white-grey contrast), which will be shown in detail later, start to appear. After firing at 1100°C, the optimum firing temperature for this batch composition, a dense microstructure is observed. Quartz particles lost their sharp edges by partial dissolution. Pores are rounded and isolated, suggesting that a more fluid liquid was present and fostered densification. White-grey scribble features of plagioclase crystals are scattered all over the sample and clearly seen. These features progressively disappear at higher temperatures but can still be seen after firing at 1200°C. Bloating occurred after firing ≥1100°C, as revealed by the pore enlargement. Severe overfiring is clearly shown at 1200°C.

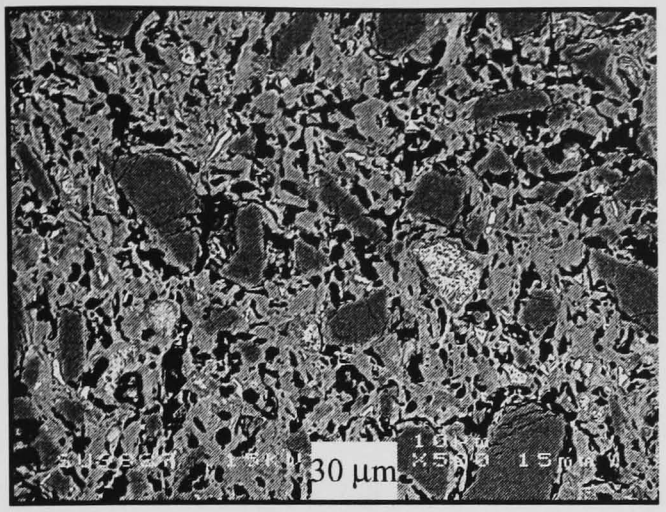

(a) 1000°C

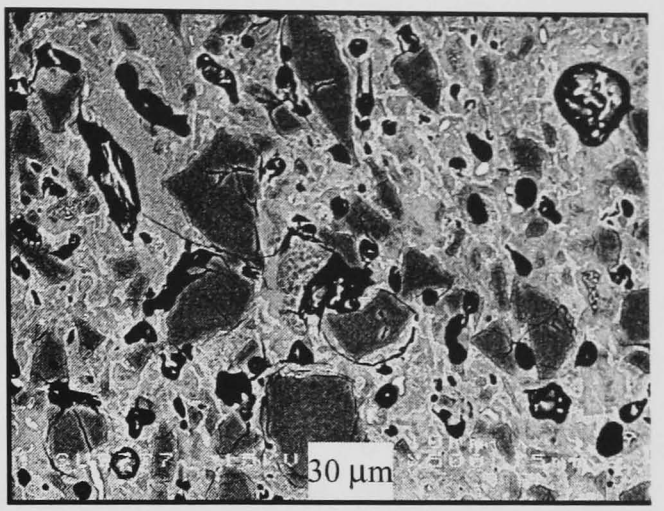

(b) 1050°C

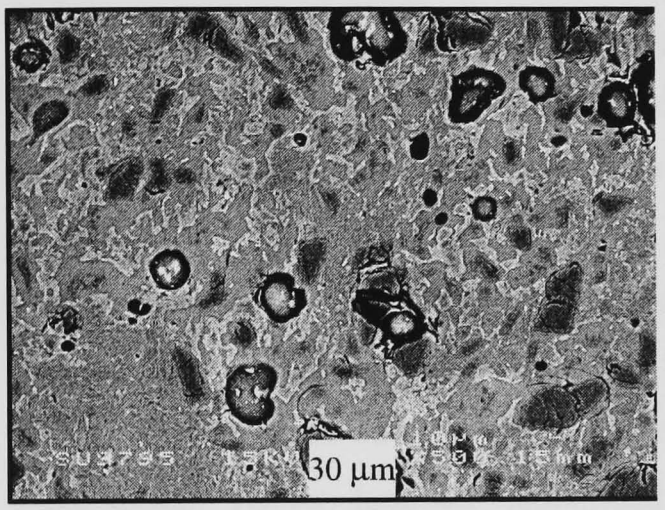

(c) 1100°C

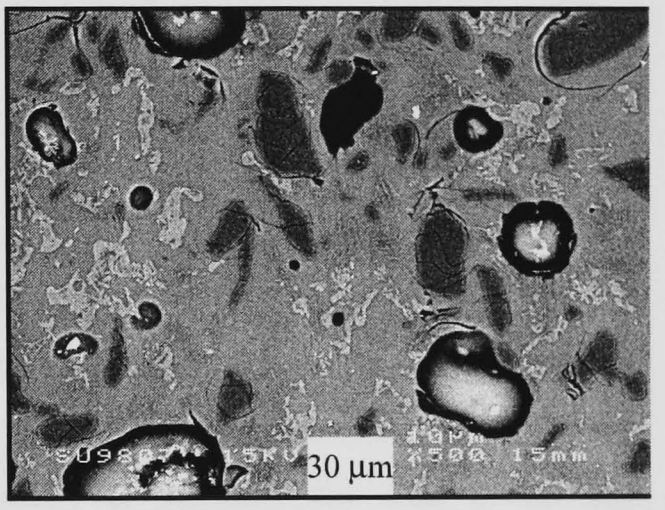

(d) 1150°C

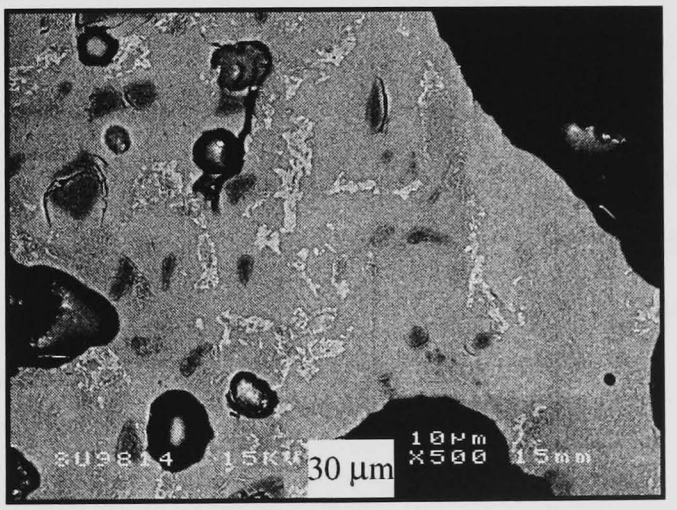

(e) 1200°C

Figure 6.34 - SEM/BS images of polished cross-sections of SLS-fluxed whiteware (S100) fired for 3h at 1000 - 1200°C ((a)-(e), respectively).

The microstructures at high magnification of polished cross-sections of S100 fired at 1000, 1050 and 1150°C are shown in Figure 6.35. Attention is given to the morphological changes occurring in SLS glass grains. At 1000°C, the white contrast of the calcium silicate phase or wollastonite is clearly seen in remnant SLS glass grains together with the dark grey contrast of cristobalite and edges of glass grains. At 1050°C, crystals are surrounded by glass and pores while edges of glass disappeared. White contrast decreases as calcium ions diffuse to the glassy phase. EDS reveals higher Ca content in the glassy phase. Rounded cristobalite is then clearly seen. White-grey scribble features can be seen at the interface between glassy phase (areas which used to be the outer edges of glass grains) and decomposed clay. EDS from these features reveals Si, Al, Ca and small traces of Na, most possibly plagioclase as suggested by XRD (Figure 6.21). This phase is likely to have been formed in the outer edges of SLS glass grains in contact with decomposed clay particles around the glass grains. As explained earlier in sections 5.4.3 and 6.4, Na ions migrate first from molten SLS grains to their surroundings, leaving molten SLS grains rich in Si and Ca which is suitable for the devitrification of cristobalite and wollastonite. Albite (sodium aluminosilicate) is possibly the first phase that crystallises from the interaction of Na ions from molten glass and Al ions from decomposed clay. Ca ions diffused later from molten glass to its surroundings, in good agreement with decreasing amount of calcium silicate phase observed. They displace Na ions in the albite structure leading to plagioclase (sodium-calcium aluminosilicate) formation. At 1100°C, the calcium silicate phase (white contrast) starts to disappear leaving rounded cristobalite embedded in glassy phase with higher Ca content. Crystal growth is enhanced for plagioclase.

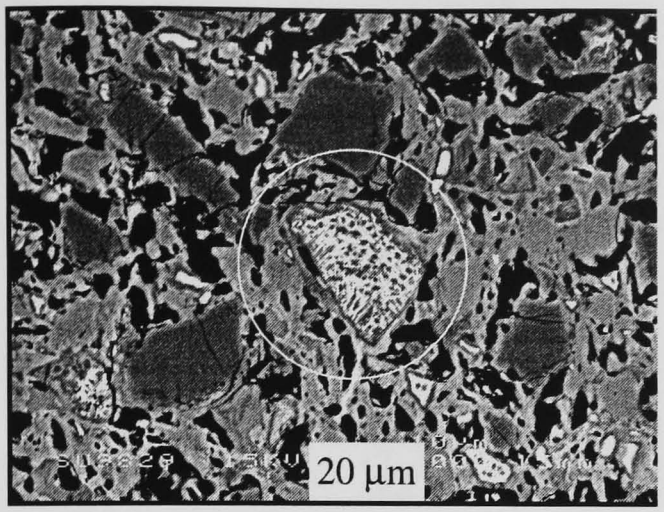

(a) 1000°C

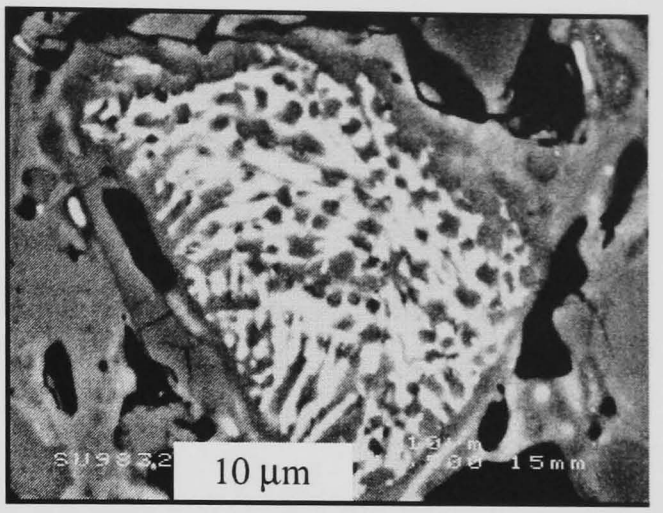

(b) 1000°C

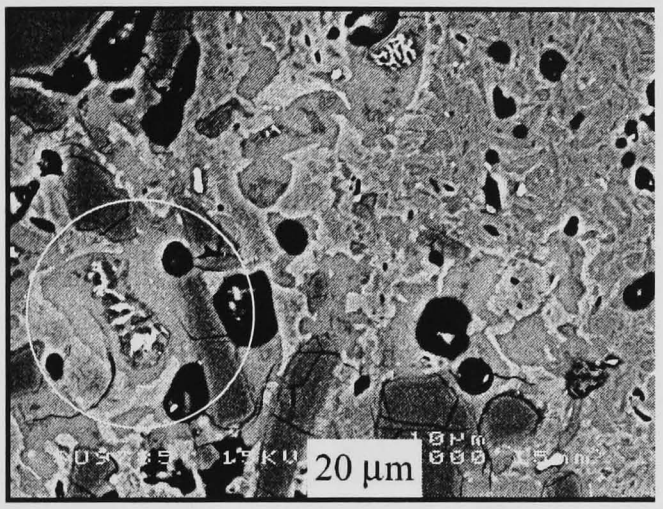

(c) 1050°C

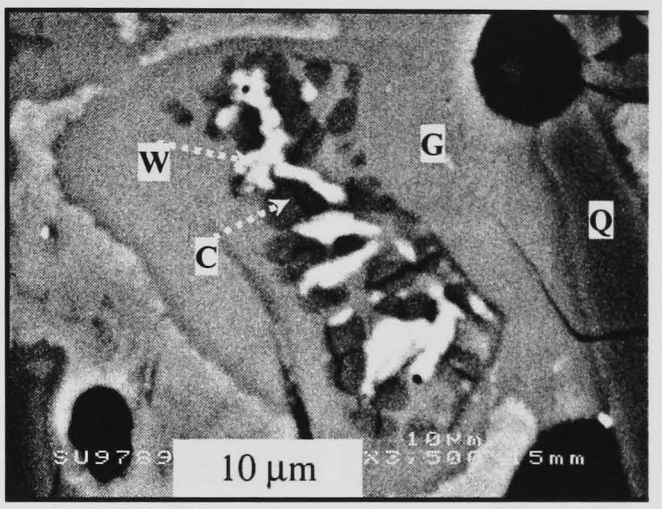

(d) 1050°C

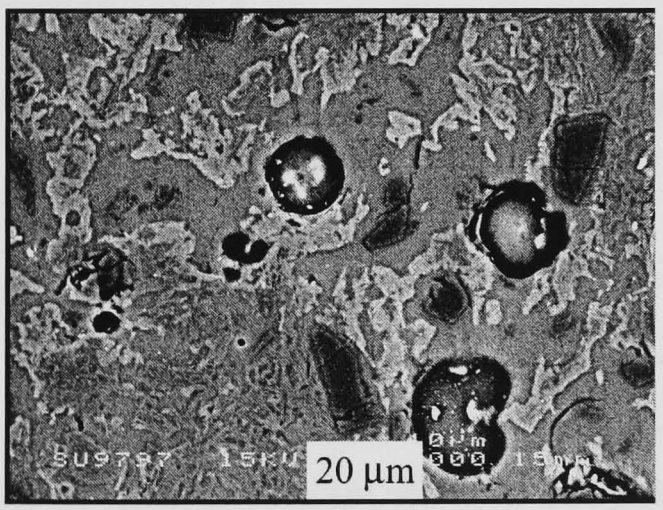

(e) 1100°C

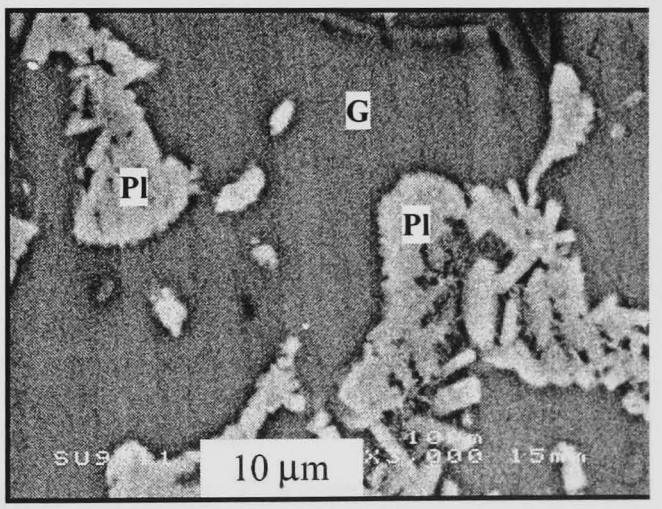

(f) 1100°C

Figure 6.35 - SEM/BS images of polished cross-sections of SLS-fluxed whiteware (S100) fired at 1000, 1050 and 1100°C. (Q = quartz, G = glass, C = cristobalite, W = wollastonite, Pl = plagioclase)

X-ray dot maps (Figure 6.36) reveal the decrease in calcium silicate (wollastonite) and the increase in Ca content in the glass and its surroundings such as in plagioclase, when firing S100 from 1000°C to 1050°C.

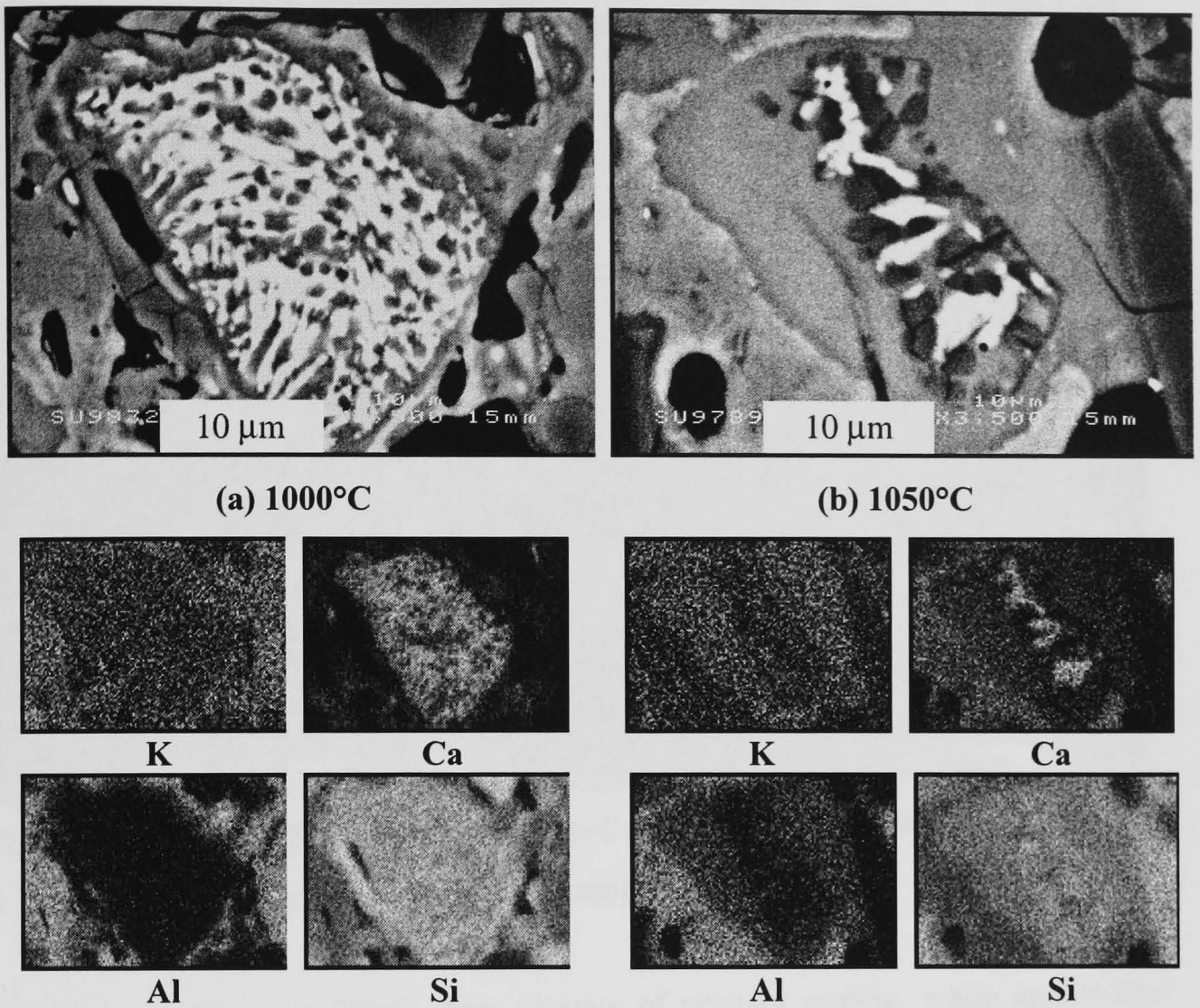

(a) 1000°C (b) 1050°C

(c) (d)

Figure 6.36 - SEM/BS images of polished cross-sections of SLS-fluxed whiteware (S100) showing the change occurring in SLS and its surroundings after firing 3h at 1000°C (a) and 1050°C (b). EDS maps of features in (a) and (b) are shown in (c) and (d) respectively.

An SEM/SE image of a polished and etched cross-section of S100 fired at 1100°C (lowest porosity as indicated in Figure 6.1) is shown in Figure 6.37. Etching exposed small crystals which are otherwise embedded in the glass. The overall microstructure of S100 fired at 1100°C contains partially dissolved quartz (as revealed by the rounding of its edges), groups of rounded cristobalite crystals embedded in glass and clusters of crystals (arrowed) containing mullite and plagioclase as will be shown in detail later.

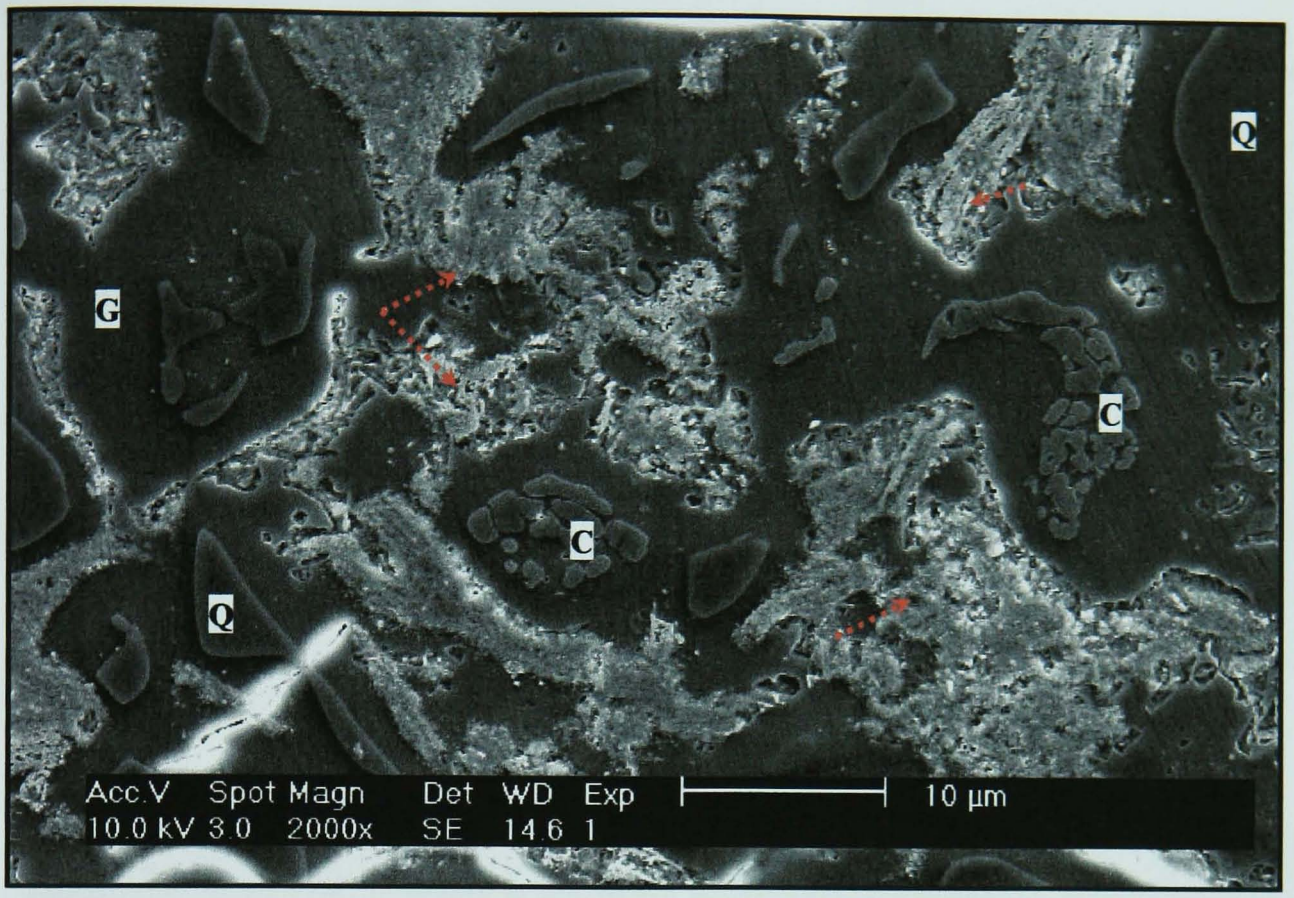

Figure 6.37 - SEM/SE image of SLS-fluxed whiteware (S100) fired at 1100°C. (Q = quartz, C = cristobalite, G = glassy phase)

SEM images (Figure 6.38(a)) show clusters of primary mullite, while needle-like secondary mullite is also present in some areas (Figure 6.38(b)). HR-SEM images (Figure 6.38(c) and 6.38(d)) show primary mullite at higher magnification. It has a rod-like morphology with an average length of ≤0.5 µm. Clusters of plagioclase are shown in Figures 6.39(a)-(d). Plagioclase generally presents a lath-like or tabular morphology with ≤5 µm long and ≤1 µm wide crystals. Plagioclase clusters are sometimes found together with those of mullite. The TEM/BF image in Figure 6.40 shows a lath-like plagioclase crystal surrounded by mullite crystals. Their EDS traces are also shown in Figure 6.40.

Cristobalite embedded in glass is clearly shown in Figure 6.41(a). The clusters of rounded (≤3 µm diameter) crystals are rich in Si. As these crystals are too small to be quartz from the raw material and are also found in the C-SLS mixture, they are probably cristobalite which grew from the Si-rich liquid from the molten SLS glass as seen in pure SLS glass after firing at ~800°C (Knapp, 1965). It is worth noting that bubbles formed in the area rich in cristobalite, as arrowed in Figure 6.41(b). Boffe *et al.* (1962) pointed out the formation of bubbles during devitrification and re-

melting of SLS glass and also observed and located bubbles occurring near cristobalite crystals. The solubility of gas in the crystalline phases is much smaller than in the vitreous liquid so that as devitrification proceeds the concentration of gas increases and when this concentration becomes higher than its solubility limit, bubbles will form near the glass/crystal interface. The authors also stated that a possible explanation for bubble formation during re-melting is the fact that the gas solubility (such as water vapour) in alkali silicate glass decreases with increasing the temperature. Small round wollastonite crystals are sometimes detected near larger rounded cristobalite particles as shown in Figure 6.41(c). The shape of pseudowollastonite crystals ranges from fibrous to granular and platy as sintering progresses (Endo *et al.*, 1994; Souza *et al.*, 2004).

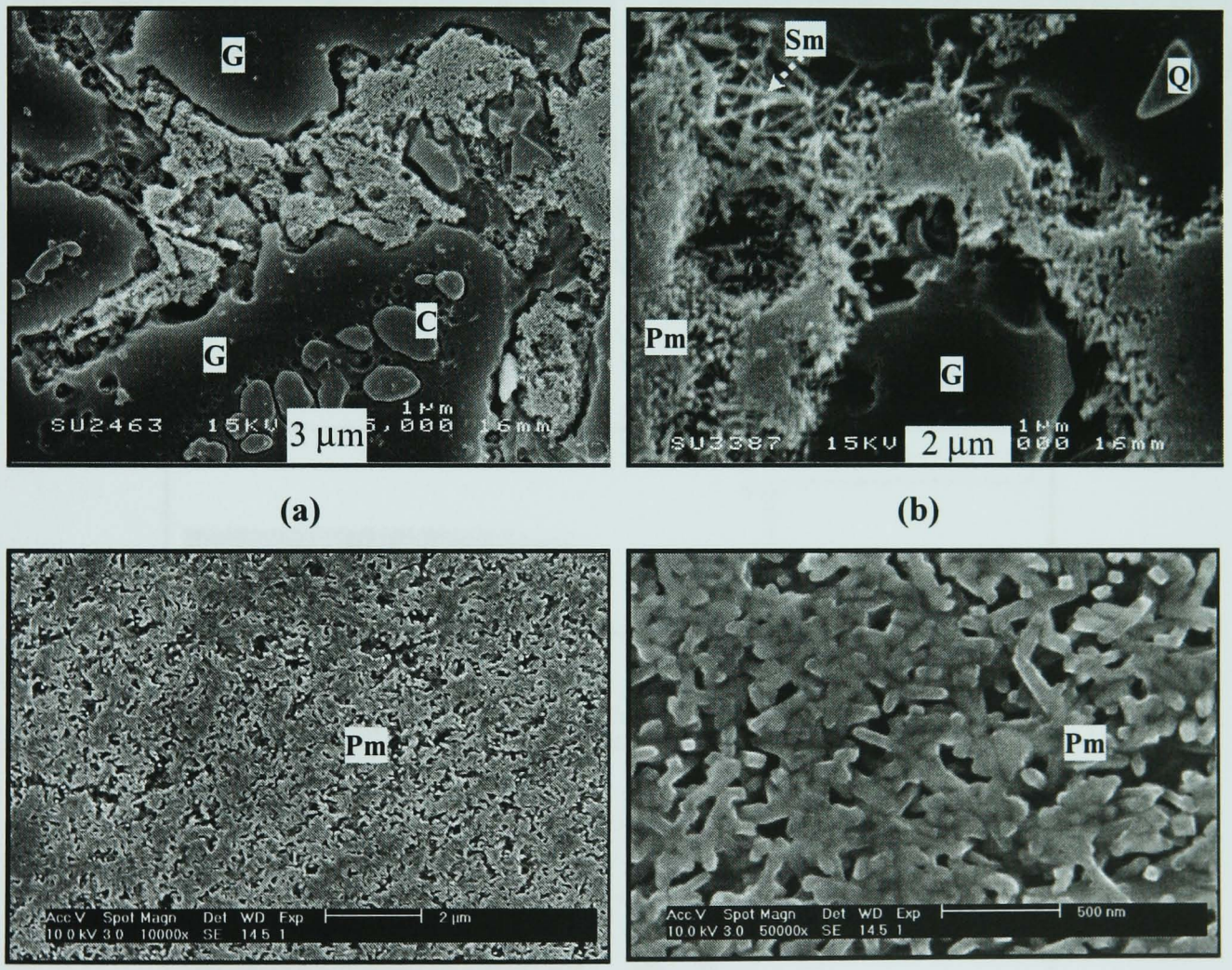

Figure 6.38 - SEM/SE images of SLS-fluxed whiteware (S100) fired at 1100°C, showing clusters of mullite. (Pm = primary mullite, Sm = secondary mullite, Q = quartz, C = cristobalite, G = glassy phase)

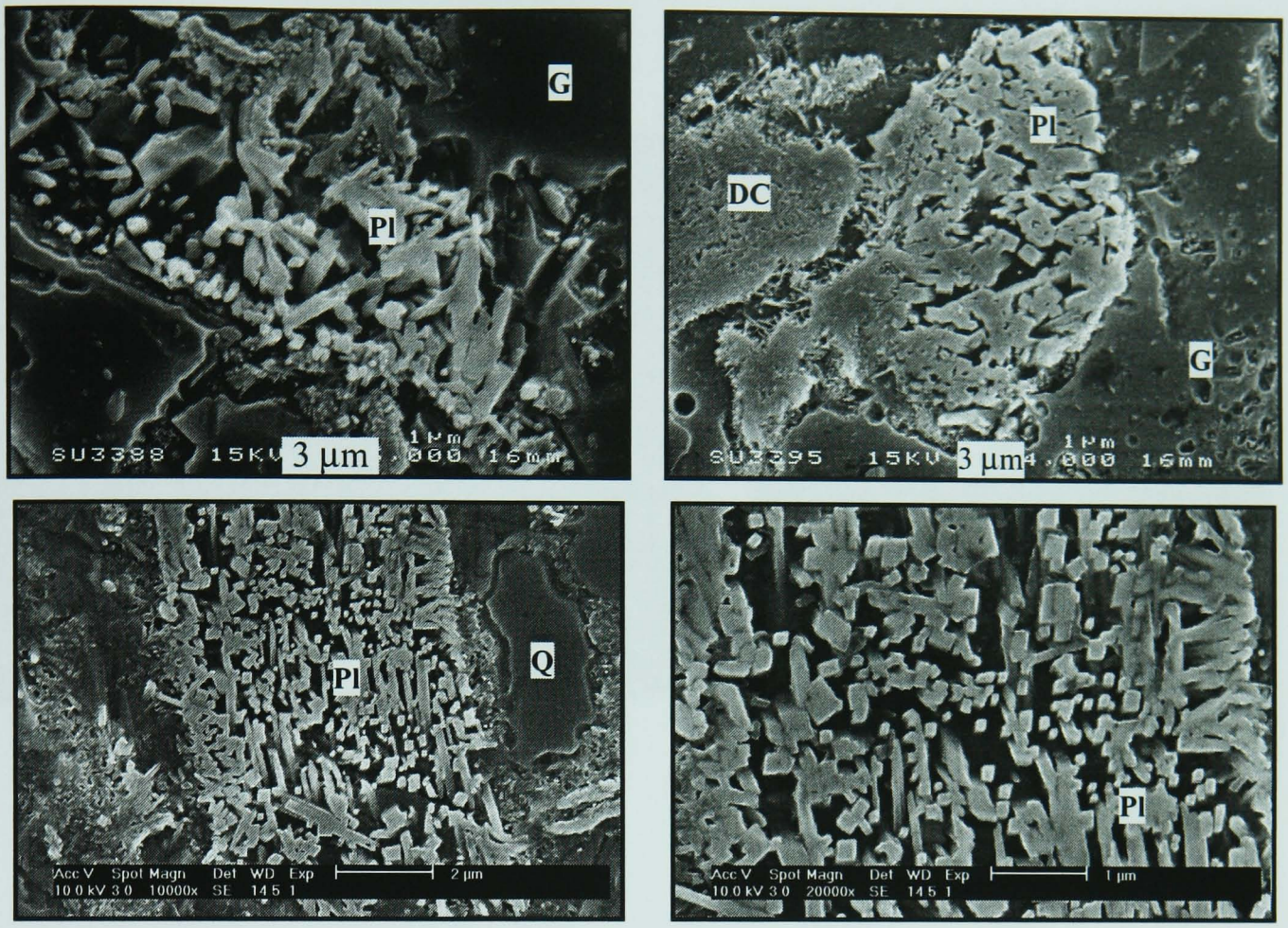

Figure 6.39 - SEM/SE images of SLS-fluxed whiteware (S100) fired at 1100°C, showing tabular plagioclase. (Pl = plagioclase, Q = quartz, G = glassy phase, DC = decomposed clay)

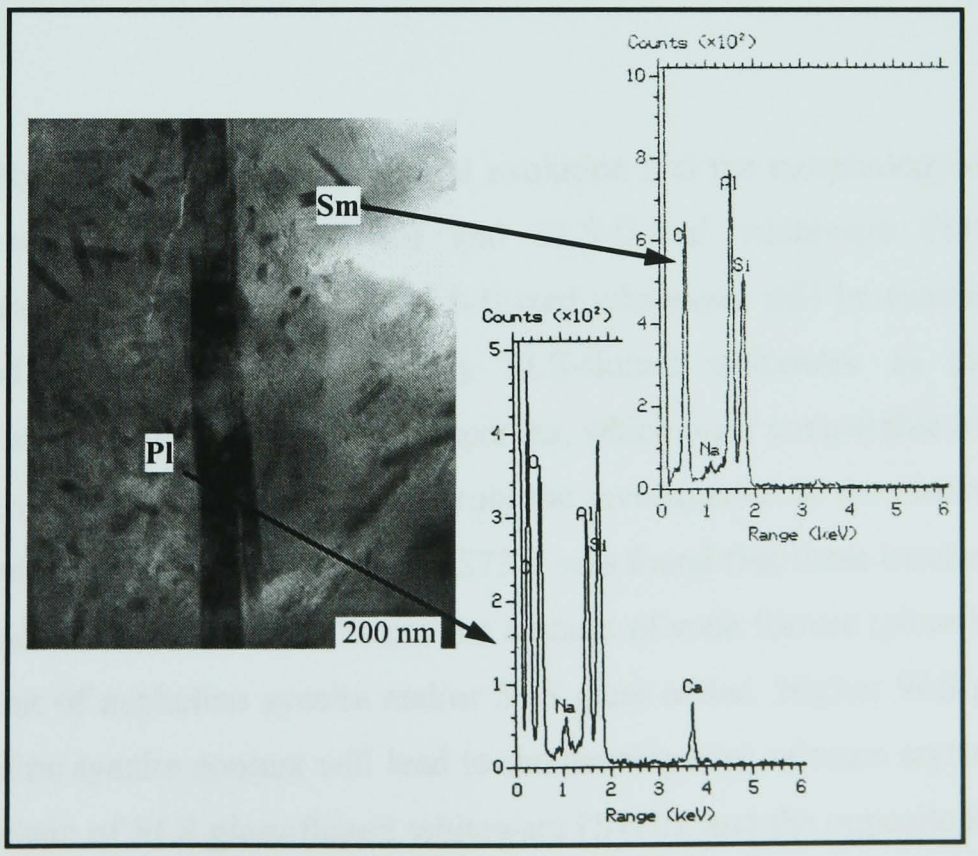

Figure 6.40 - TEM/BF image together with EDS traces from areas within the plagioclase crystal (Pl) and the secondary mullite crystal (Sm).

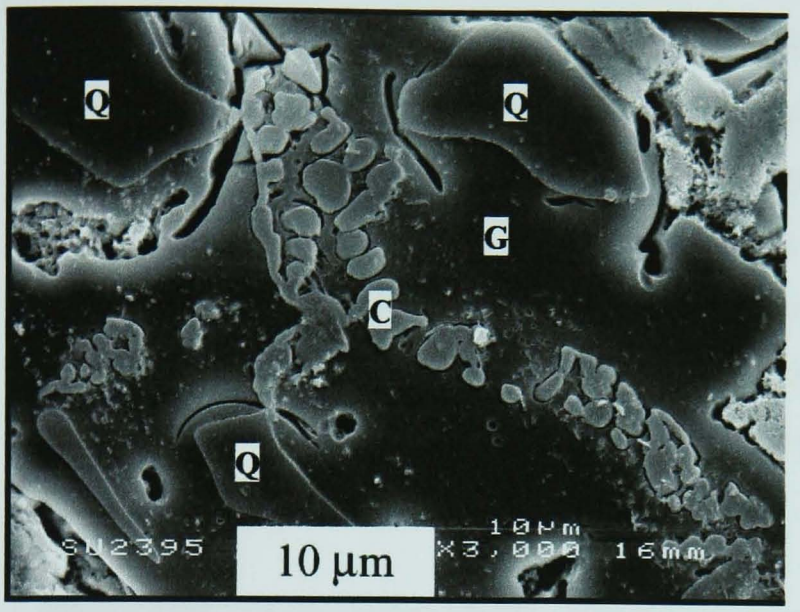

(a)

(b)

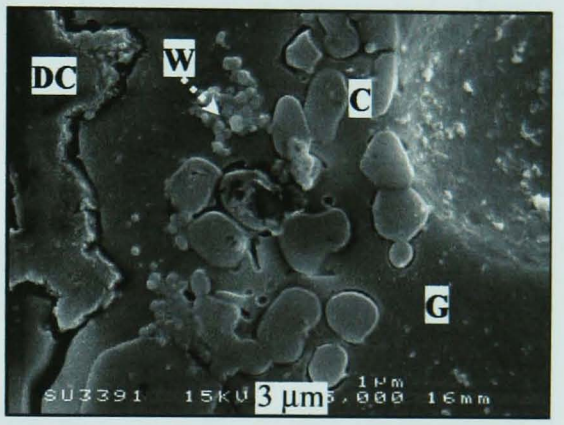

(c)

Figure 6.41 - SEM/SE images of SLS-fluxed whiteware (S100) fired at 1100°C showing cristobalite particles embedded in glassy phase. Cristobalite with bubbles and with wollastonite are shown in (b) and (c) respectively. (DC = decomposed clay, Q = quartz, C = cristobalite, W = wollastonite, G = glassy phase)

Following the study of the microstructural evolution and the morphology of phases present in standard whiteware (S0) and SLS-fluxed whiteware (S100), the microstructural evolution of partially SLS-fluxed whiteware will be examined. S25 was selected to represent the partially SLS-fluxed whiteware as this batch composition attained the best physical properties, which were comparable to those of the standard whiteware (S0). Moreover, from the investigation of the phases present and microstructural evolution of S50 and S75 it was found that these batches contain features found in both S0 and S100 and the amount of each feature (phase) depends on the amount of nepheline syenite and/or SLS glass added. Higher SLS glass and lower nepheline syenite content will lead to the development of more crystals which are characteristic of SLS glass-fluxed whiteware (S100), and the opposite for higher nepheline syenite content mixtures.

The overall microstructure of a polished and etched cross-section of S25 fired at 1000°C is shown in Figure 6.42. It contains features derived from both nepheline syenite (as in S0) and SLS glass (S100) fluxed whitewares, some of which are shown in high magnification SEM/SE images in Figure 6.43. However due to the low amount of SLS content (6.25wt%), the features derived from nepheline syenite (which contains 18.75wt% in batch composition) are more noticeable. Other features are angular quartz particles (Q), decomposed clay relicts (DC) containing primary mullite (XRD confirmed mullite present, Figure 6.20), feldspar-penetrated clay relicts (C+F) and elongated crystals of secondary mullite (Type II) (as seen in S0, Figure 6.25(c)).

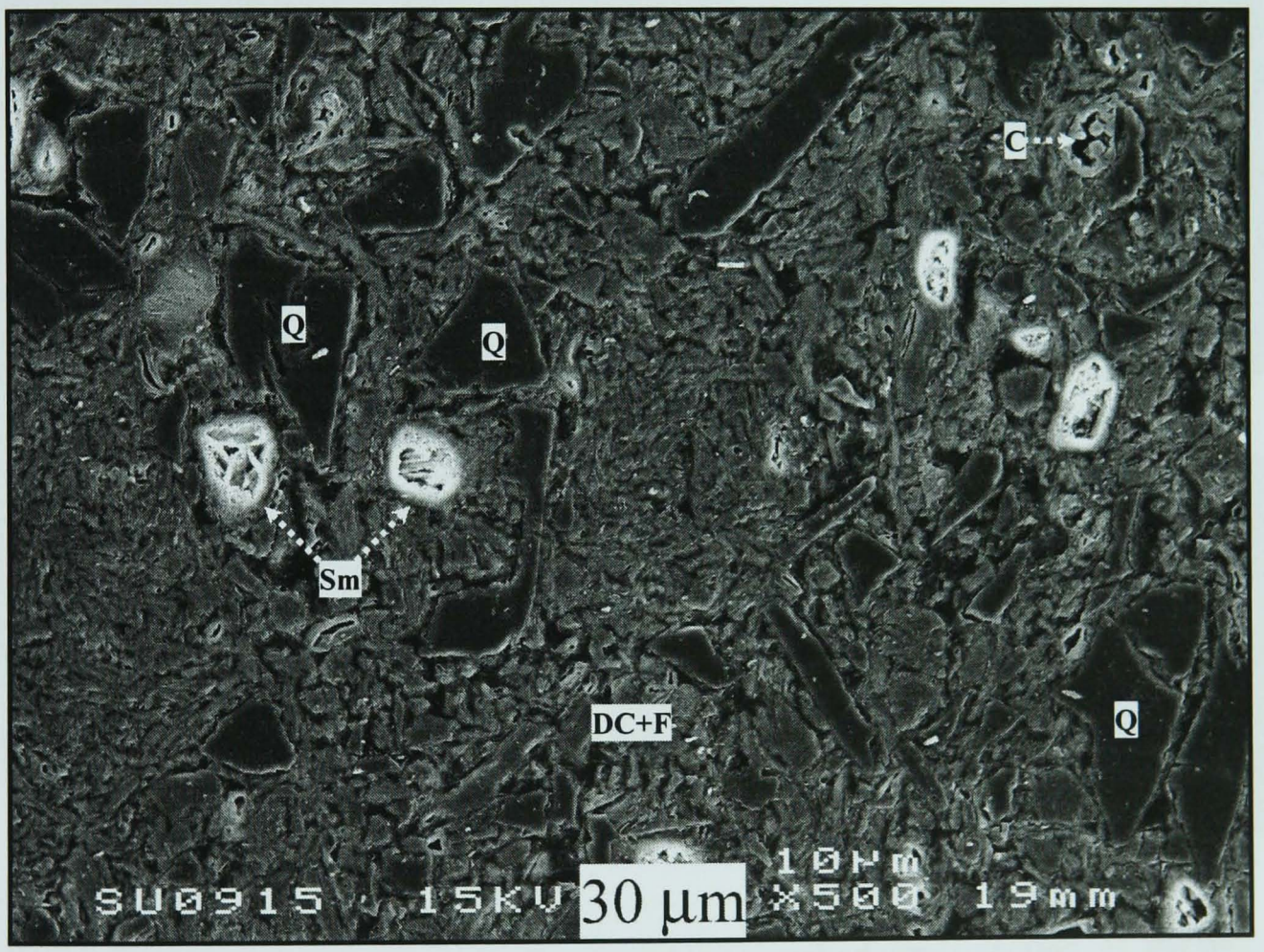

Figure 6.42 - SEM/SE images of polished cross-section of partial SLS-fluxed whiteware (S25) fired at 1000°C. (DC+F = feldspar penetrated clay relicts, Q = quartz, C = cristobalite, Sm = secondary mullite)

After firing 3h at 1000°C and etching with HF, features derived from SLS glass such as clusters of cristobalite crystals inside rims of SLS grains are revealed (Figure 6.43(a)-(c)). Ring-shaped features at the margins of small SLS grains, as present in

S100 (Figure 6.32(a)), are also occasionally present in S25 (arrowed in Figure 6.43(a)). Secondary mullite crystals (Type II) grow from the clay-feldspar interface toward the centre of molten feldspar grains. These are shown in Figure 6.43(c)-(e).

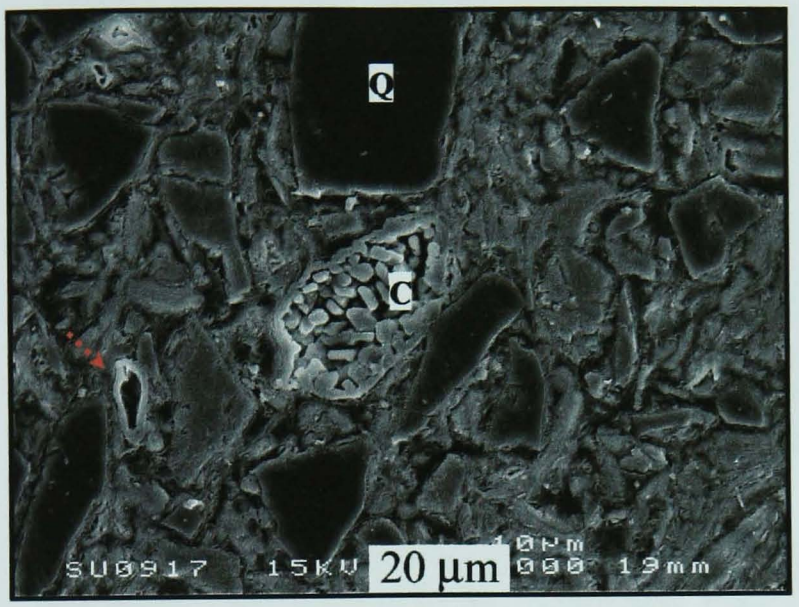

(a)

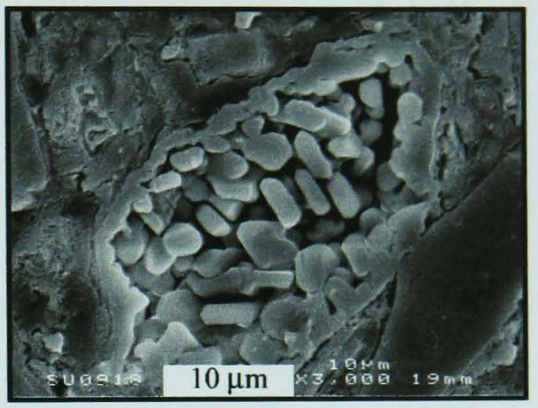

(b)

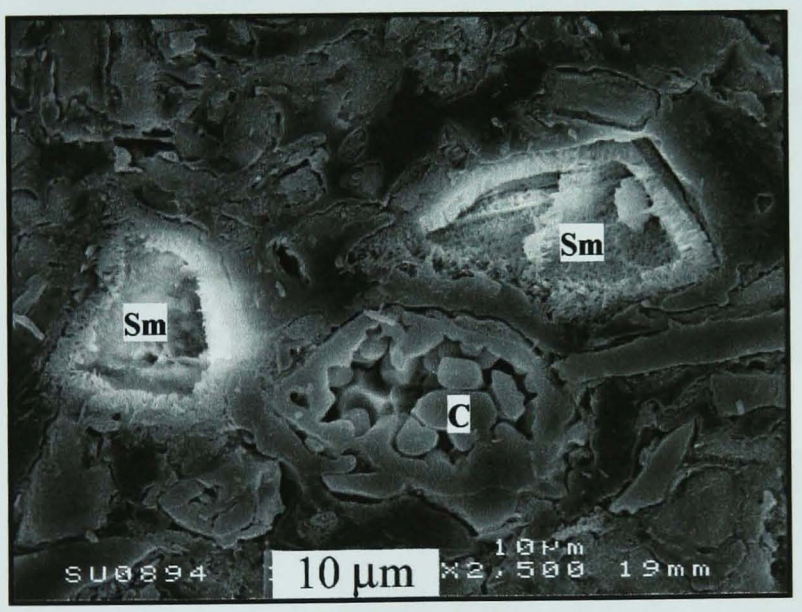

(c)

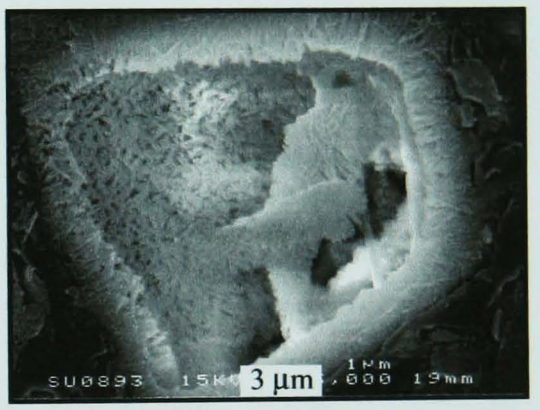

(d)

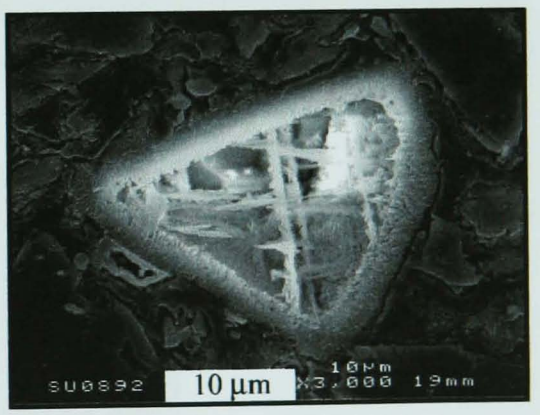

(e)

Figure 6.43 - SEM/SE images of polished and etched cross-section of partial SLS-fluxed whiteware (S25) fired at 1000°C showing cristobalite particles (C) devitrified from molten SLS glass particles (b) and elongated secondary (Type II) mullite (Sm) formed from molten feldspar particles ((d) and (e)).

SEM/BS images taken from polished cross-sections of S25 fired for 3h at 1000, 1050, 1100, 1150 and 1200°C are presented in Figure 6.44.

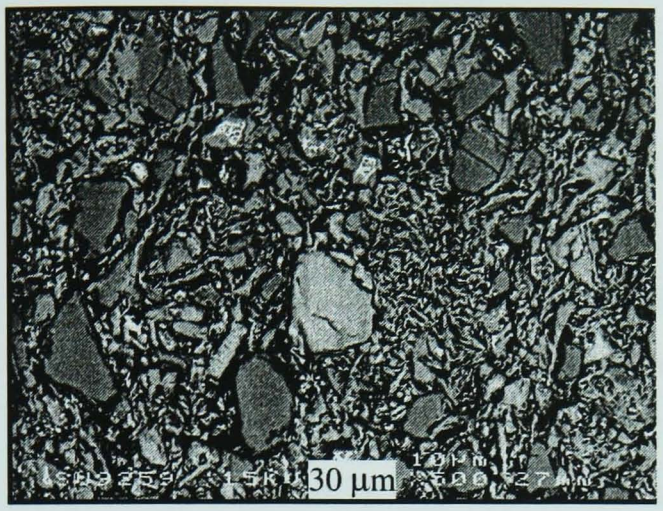

(a) 1000°C

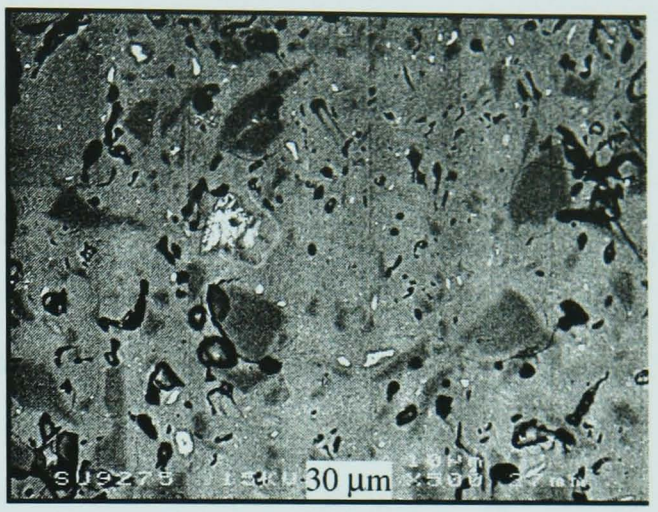

(b) 1050°C

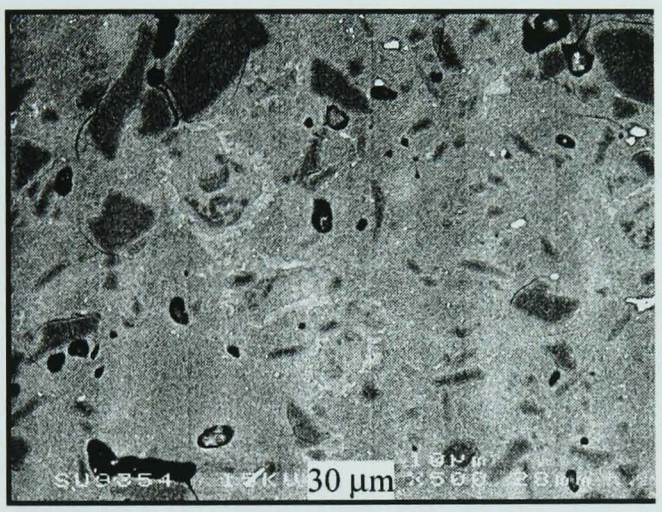

(c) 1100°C

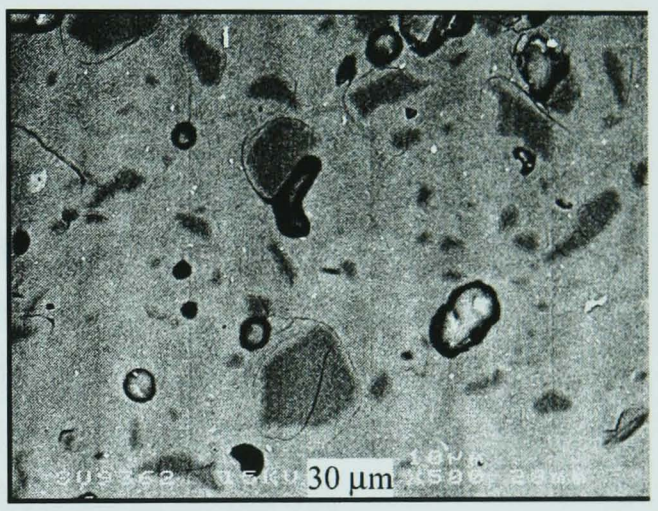

(d) 1150°C

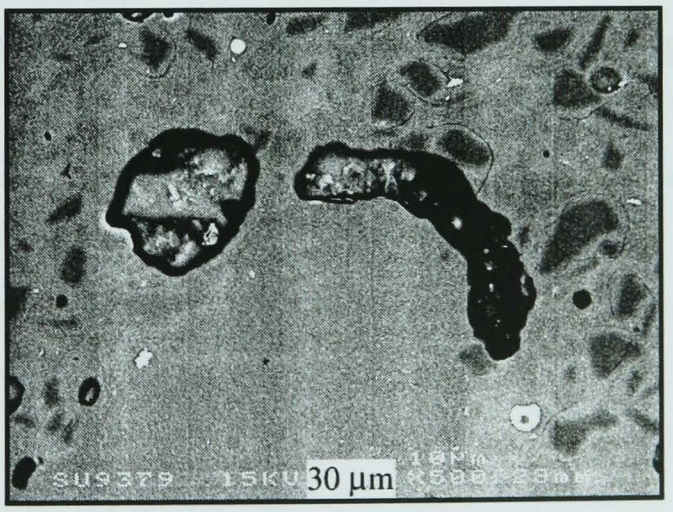

(e) 1200°C

Figure 6.44 - SEM/BS images of polished cross-sections of partially SLS-fluxed whiteware (S25) fired at 1000 - 1200°C ((a)-(e)).

Since this batch contains quite a high amount of nepheline syenite (18.75wt%) in its composition, and nepheline syenite has a melting point above 1000°C, the microstructure of S25 fired at 1000°C is still open and contains interconnected pores (dark contrast). Samples fired at 1050°C have a much denser microstructure with isolated pores due to the large amount of glassy phase present. This is consistent with XRD of S25 (Figure 6.21) which reveals complete melting of feldspar, with the presence of an amorphous hump. These results also correlate well with the steep increase in bulk density and decrease in water absorption values after firing S25 from 1000°C to 1050°C. The bright (white) contrast in these images is due to Ca enriched areas in SLS grains and SLS glass-derived particles (such as wollastonite). Dark-grey features are cristobalite and white features are wollastonite. These features can be seen in S100, present up to 1050°C before the Ca-enriched phase dissolves into the liquid phase. After firing to 1100°C, the number of pores reduces and the pores acquire a more rounded shape. This firing temperature gives the best physical properties (highest bulk density and lowest water absorption) for S25. Scribble features of plagioclase crystals (whitish grey contrast) and clusters of remaining cristobalite crystals are visible but to a lesser extent compared to those in S100. They also appear to a lesser extent with increasing the firing temperature, consistent with XRD (Figures 6.22-6.24). Pores are larger when firing S25 above 1100°C and show signs of overfiring. This was extensively discussed in section 6.2.

Attention was paid to S25 when firing at the temperature giving the lowest porosity (1100°C). SEM/BS image of S25 fired at 1100°C (Figure 6.45) and EDS analysis show the presence of groups of cristobalite and plagioclase particles (enriched in calcium), whereas these phases are completely absent from the standard batch (S0). From SEM observations on other batches containing SLS glass (S50 and S75), the amount of these phases detected increases with increasing the SLS glass content.

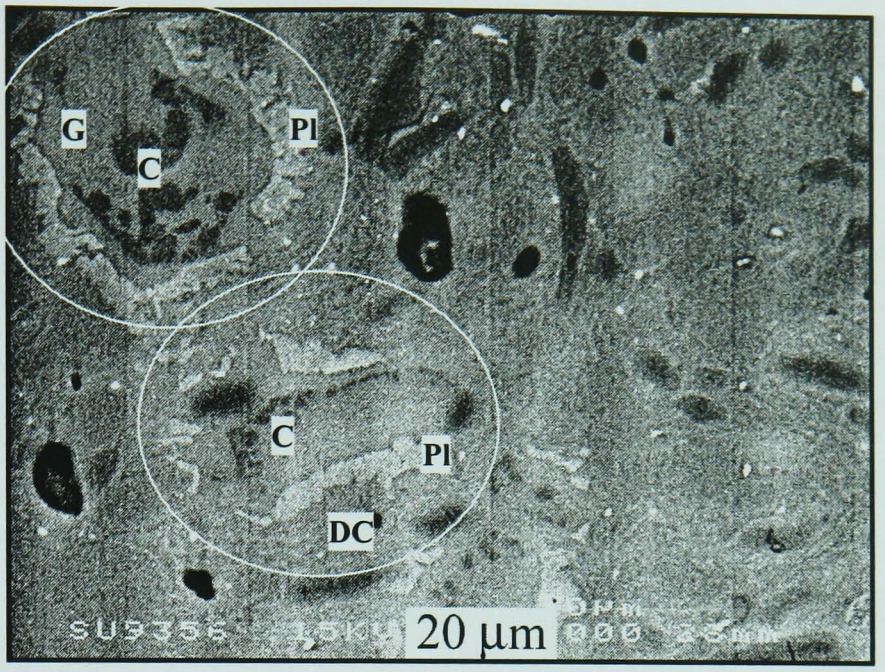

Figure 6.45 - SEM/BS images of polished cross-section of partial SLS-fluxed whiteware (S25) fired at 1100°C showing cristobalite particles (C) embedded in glass (G) which originally consisted of SLS grains, as well as plagioclase (Pl) formed at the outer edges of molten SLS glass in contact with decomposed clay (DC).

After etching, the overall microstructure of S25 fired at 1100°C, which is the partially SLS-fluxed whiteware body, is shown in Figure 6.46. This microstructure is very similar to that of the standard whiteware S0 fired at 1200°C (Figure 6.29), also containing features from the microstructural development of S100 such as cristobalite, wollastonite and plagioclase at a lesser amount. Partially dissolved quartz particles with their solution rims and needle-like secondary mullite are clearly seen (Figure 6.46).

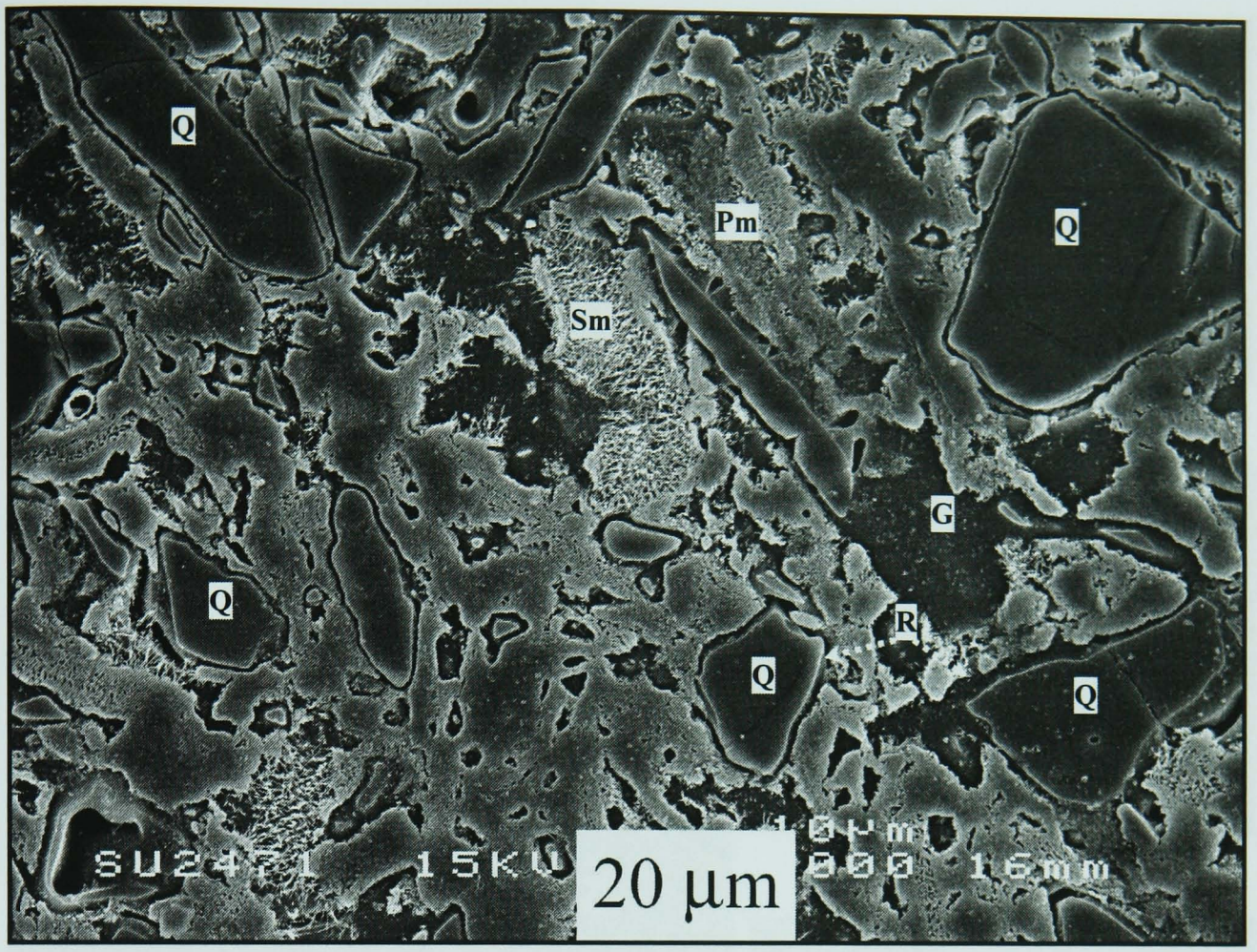

Figure 6.46 - SEM/SE image of polished and etched cross-section of partial SLS-fluxed whiteware (S25) fired at 1100°C. (Pm = primary mullite, Sm = secondary mullite, Q = quartz, G = glassy phase, R = solution rim)

Primary mullite appears together with plagioclase in Figure 6.47(a), and with elongated secondary mullite in Figure 6.47(c). Micrographs detailing lath-like plagioclase crystals, elongated secondary mullite crystals (Type II) which were derived from feldspar, and rod-like primary mullite crystals (Type I) are shown in Figures 6.47(b)-(e), respectively. Elongated secondary mullite is still evident in this batch as it was formed from feldspar. Plagioclase can be detected in some areas containing cristobalite (Figure 6.47(b)).

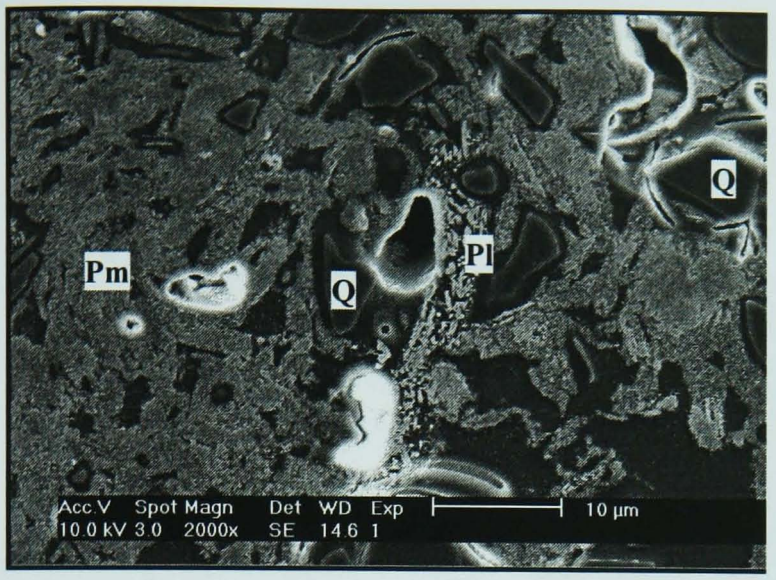

(a)

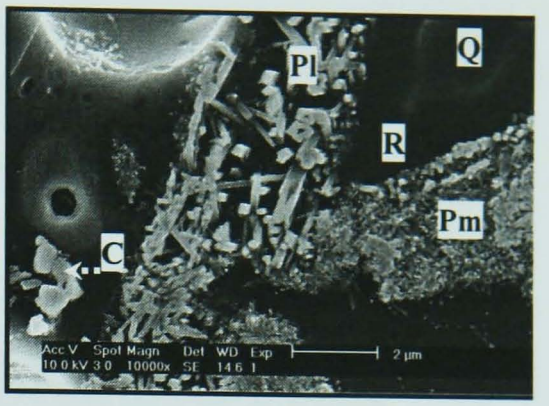

(b)

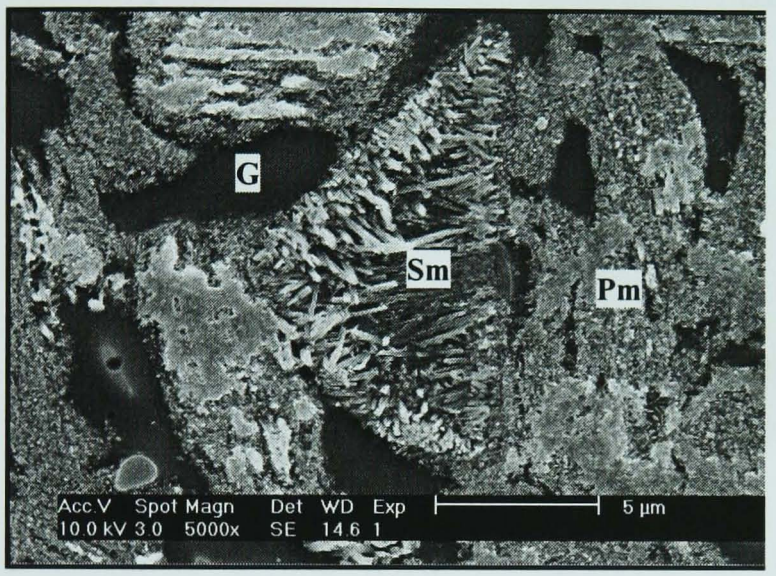

(c)

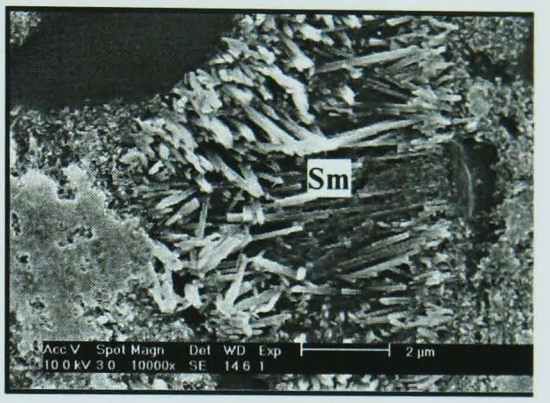

(d)

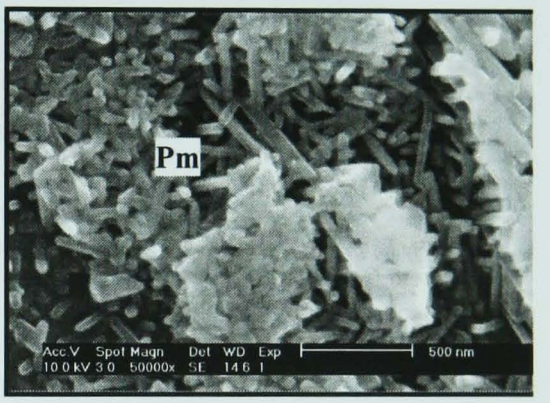

(e)

Figure 6.47 - SEM/SE images of polished and etched cross-sections of partial SLS-fluxed whiteware (S25) fired at 1100°C showing main features present. (Pm = primary mullite, Sm = secondary mullite, Q = quartz, Pl = plagioclase, C = cristobalite, G = glassy phase, R = solution rim)

For a better understanding of the possible reactions between SLS waste glass, quartz, clay and nepheline syenite, exhaustive TEM analysis was conducted. Emphasis was given to S25 samples fired at 1100°C, as this is potentially the best batch composition and firing temperature to make commercial whiteware. Figure 6.48 shows a quartz particle and its solution rim. EDS analysis of the solution rim reveals the presence of Al and K, and traces of Na and Ca, together with Si and O coming primarily from the partially dissolved quartz particles. The fact that K and Al are

present in the solution rim suggests that melted K-containing flux particles from nepheline syenite, as well as material derived from muscovite breakdown, are the major components of the viscous liquid responsible for quartz dissolution.

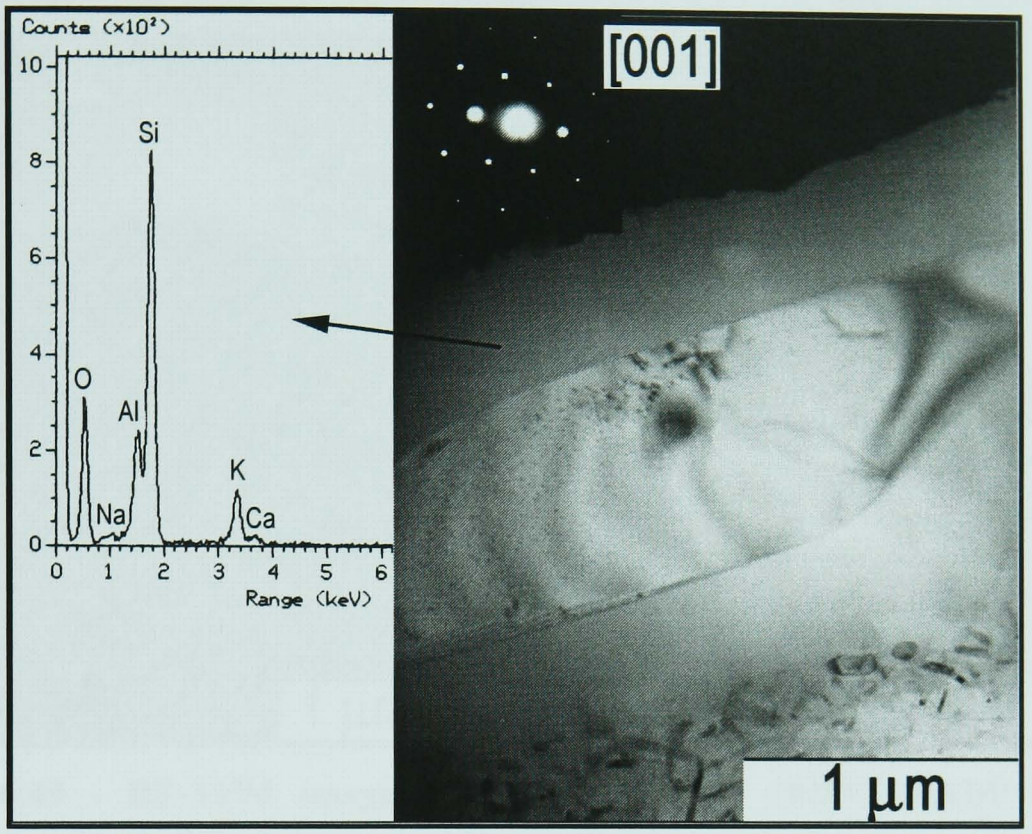

Figure 6.48 - BF-TEM image of S25 fired at 1100°C. The SADP is from the partially dissolved quartz particle and the EDS spectrum from the solution rim.

The Na_2O-CaO-SiO_2 equilibrium diagram (Knapp, 1965) shows that the dissolution of SLS glass gives Na and Ca to the viscous liquid on firing. It reveals that $CaO{\cdot}SiO_2$ (wollastonite) forms in areas high in CaO at around 1100°C, whereas $Na_2O{\cdot}2SiO_2$ (a sodium silicate) forms in areas high in Na_2O at around 800°C. Although the system studied in the present study is not in equilibrium, (≤5 µm diameter) rounded wollastonite was found in S25 fired at 1100°C, as shown in Figure 6.49, together with its diffraction pattern and EDS spectra of surrounding glass. The non-equilibrium microstructure surrounding the wollastonite particle was revealed by two different glass compositions, as shown by the EDS spectra taken from points "1" and "2", the latter being similar to the solution rim of the quartz particle shown in Figure 6.48. The fact that CaO is not present in the amorphous material "1" (Figure 6.49) indicates that wollastonite is not dissolving. Region "1", depleted in CaO, may be part of the parent glass from which wollastonite crystallised. The presence of

different glassy regions "1" and "2" is evidence of the non-equilibrium nature of the system at the sub-micron scale.

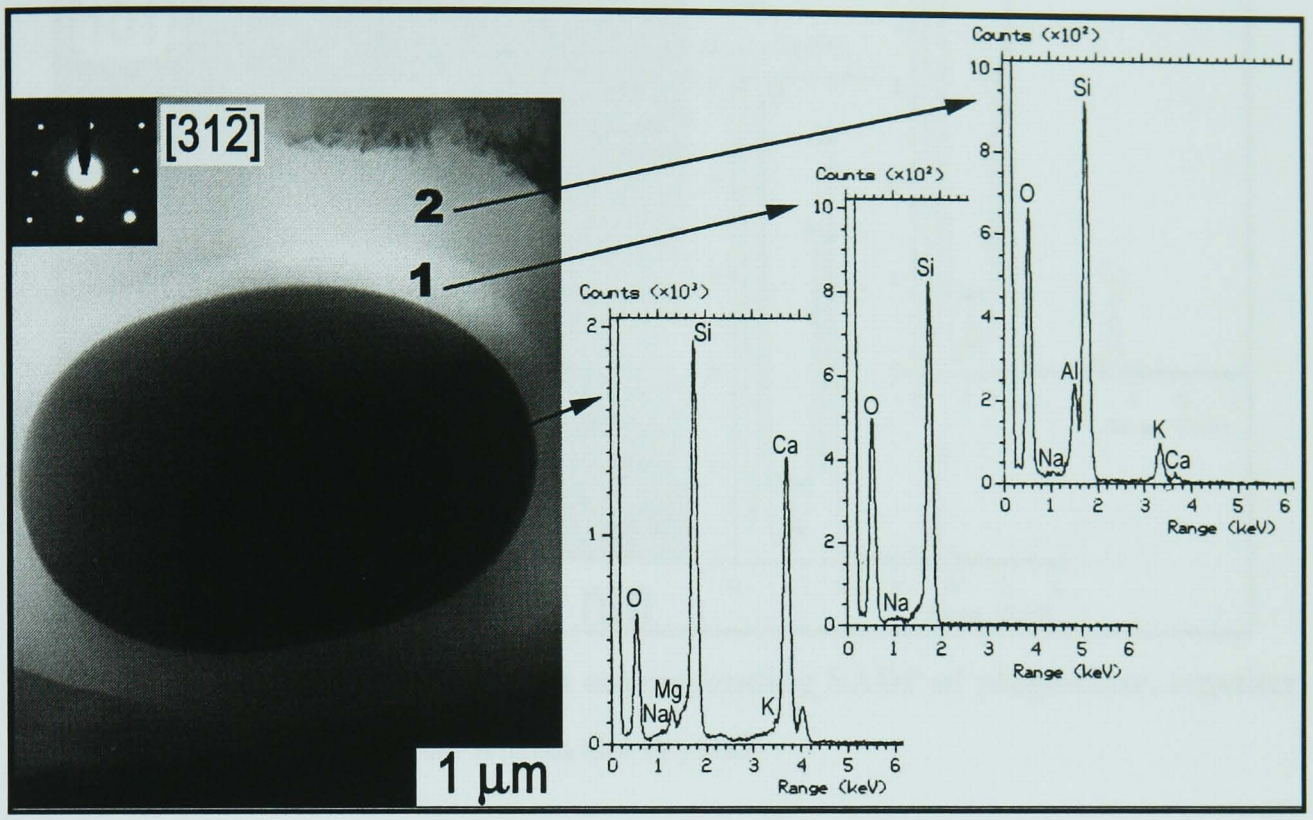

Figure 6.49 - BF-TEM image from S25 fired at 1100°C. SADP is from wollastonite, and EDS spectra are from the wollastonite particle and the surrounding glass.

The morphology of plagioclase (Figure 6.50) is similar to that observed by Souza *et al*. (2004). In the present study, EDS spectra of adjacent regions forming the planar defects are shown in Figure 6.50, confirming that these areas contain different Al:Si ratios. The crystallisation of plagioclase should involve migration of Ca^{2+} and Na^{+} cations to clay-rich areas, since the Al_2O_3 content in SLS glass is insufficient to form crystals (<1wt%).

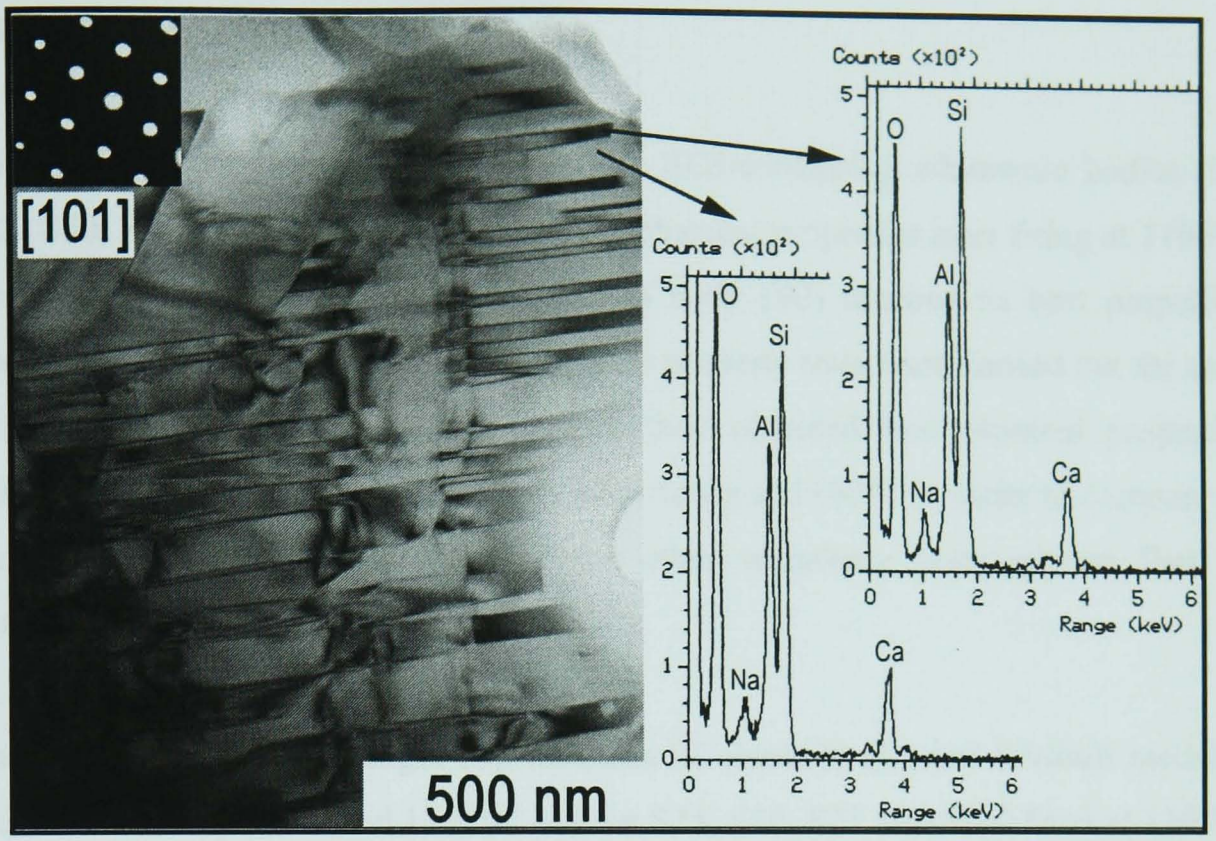

Figure 6.50 - BF TEM image and a corresponding SADP of plagioclase, together with EDS spectra of regions within the crystal.

6.6 - MECHANICAL PROPERTIES

The physical data (section 6.1) reveals that SLS-containing whiteware bodies (i.e. S25, S50, S75 and S100) attained their best physical properties after firing at 1100°C whereas the standard whiteware (SLS-free) body (S0) reached its best properties after firing at 1200°C. Therefore, mechanical property tests were carried out for each whiteware body fired at the temperature they obtained best physical properties values. Only S0 was tested additionally after firing at 1100°C in order to compare its mechanical properties with those of the other whiteware compositions fired at 1100°C.

The values of flexural strength (σ), modulus of elasticity (E) and Weibull modulus (m) for S0 fired at 1100 and 1200°C and for S25, S50, S75 and S100 fired at 1100°C are shown in Table 6.2. Fracture toughness (K_{IC}) was measured only for S0 fired at 1200°C and S25 fired at 1100°C, as their other mechanical and physical properties were similar. Samples from S50, S75 and S100 have not been tested for fracture toughness.

Table 6.2 - Mechanical properties (flexural strength (σ), modulus of elasticity (E), Weibull modulus (m) and fracture toughness (K_{IC})) of fired specimens.

Samples	Firing Temperature (°C)	σ (MPa)	E (GPa)	m	K_{IC} (MPa $\sqrt{m}$)
S0	1100	57±3	54±4	23	-
	1200	69±4	74±3	24	1.61±0.07
S25	1100	71 ±6	72±5	13	1.61±0.08
S50	1100	66±4	67±4	19	-
S75	1100	62±3	58±4	26	-
S100	1100	59±4	54±1	16	-

In general, batches containing SLS glass revealed values of flexural strength higher than those for the SLS-free batch when fired at 1100°C. The highest value of flexural strength (71±6 MPa) was attained by S25 which contains only 6.25wt% SLS glass

(and 18.75wt% nepheline syenite) fired at 1100°C. Further additions of SLS glass as in S50, S75 and S100 resulted in lower flexural strengths (66±4, 62±3 and 59±4 MPa, respectively). However, taking into consideration the standard deviation values, the flexural strength of S25, S50, S75 and S100 are not very different statistically. The flexural strength of the standard batch S0 fired at 1100°C is 57±3 MPa, and increased to 69±4 MPa after firing at 1200°C. The increase in strength is due to progressive sintering which corresponds to the increase in bulk density and decrease in water absorption from 1100 to 1200°C (Figures 6.1 and 6.2). S0 was not fully densified after firing at 1100°C. After firing S0 above 1200°C, its bulk density decreased and water absorption increased, and its flexural strength expect to decrease.

The flexural strength of S0 fired at 1200°C is higher than those of S50, S75 and S100 fired at 1100°C, but still lower than that of S25. Strength measurements generally showed considerable variation from specimen to specimen, with a standard deviation of ±5% or higher. Therefore, the difference in strength between S25 fired at 1100°C and S0 fired at 1200°C lies within the experimental error of the measurement, and therefore is not very noteworthy. The significance of this result is that SLS glass can be used as a fluxing agent in whitewares by replacing nepheline syenite up to 6.25wt% without decreasing the strength of the whiteware. Previous reports (Rado, 1988; Russell, 1991) reveal the flexural strength of earthenware, vitrified hotelware, hard porcelain and bone china are within the ranges 55-72, 82-96, 39-69 and 97-111 MPa, respectively. The flexural strength of S25 fired at 1100°C is, therefore, high enough to compete with hard porcelain.

Strength values are lower for higher SLS glass contents in the whiteware compositions. This can be explained by referring to the results from quantitative XRD analysis (Table 6.1) and physical properties (Figures 6.1-6.3). Porosity is a significant feature always present in whitewares. The pores reduce the load bearing area and also cause local stress concentration. It is therefore predictable that the strength of a whiteware would be reduced with pore volume fraction increase. Esposito *et al.* (1995) suggested that open porosity controls the mechanical properties in terms of flexural strength, Young's modulus and fracture toughness. In particular, the increase in water absorption significantly decreases all mechanical

properties. On the other hand, the best criterion to indicate the amount of porosity is bulk density (Kara *et al.*, 2006). Porosity decreases when the sample densifies, leading to higher bulk density. The denser the fired bodies, the higher the flexural strength. It is also expected that the firing temperatures that gave the highest values of bulk density for each batch provide the maximum flexural strength values. From Figure 6.1, maximum bulk density values of samples fired at 1100°C decrease with increasing SLS content from S25 to S100, which means porosity increased with SLS content. This is consistent with the decreasing flexural strength values from S25 to S100.

Apart from the effect of degree of densification on flexural strength, it is also important to consider the effect of type, morphology and amount of crystalline phases and liquid phase formed during firing. For instance, mullite content and its morphology have been shown to affect the mechanical properties of whitewares. It has been reported that increase in whitewares strength can be explained partially by an increase in secondary mullite content and randomly interlocked high aspect ratio mullite needles in the glassy matrix. This is the mullite hypothesis, in which the strength of fired whiteware body depends on the feltlike interlocking of fine mullite needles and also on the mullite content (Carty and Senapati, 1998). Coarsening of mullite needles at higher temperatures, leading to a smaller number of larger needles, do not interlock as efficiently as the smaller ones, resulting in decreased strength. Thus for the mullite hyphthesis, the choice of firing temperature for generating the properly sized mullite needles is vital in achieving the desired strength. The effect of quartz on the strength of a whiteware body is the subject of debate. Some authors believe in the pre-stress theory (Marzhal, 1955; Mattyasovsky-Zolsnay, 1957) in which stresses introduced to the fired body during cooling are said to increase the strength. When the quartz particles cool, they contract more than the glass surrounding them because quartz has a higher coefficient of thermal expansion than the glassy matrix of whiteware bodies, and therefore the glass is under compression tangentially. Radial tensile stresses also develop in the glass, and these are more severe for larger quartz grains. An increase in the quartz content causes greater compression of the glass (tangentially) and hence greater pre-stressing and increased strength. Other authors believe that the reduction in the quartz particle size is beneficial for the whiteware body as its presence in larger sizes causes severe

cracking of the ceramic body (Davidge and Green, 1968; Dinsdale, 1986; Monshi, 1990). These cracks appear in the glass near the interface between quartz and glass (circumferential cracking). In either case, the thermal mismatch between quartz and the glassy matrix results in the presence of stresses that may produce cracking and a decrease in mechanical strength of the ceramic body if these stresses are too high. Little attention has been paid to the role of other crystalline phases, such as anorthite, in strengthening whiteware bodies although three dimensional dispersions of anorthite crystals in an aluminosilicate matrix has been shown to be beneficial to the overall mechanical strength (Traore *et al.*, 2003). Apart from crystalline phases, the glassy phase also affects the strength of a whiteware body. Triaxial whiteware bodies such as hard porcelain formulated with 50wt% clay and equal amounts of feldspar and quartz are composed mainly of glass (greater than 70wt%) with some crystalline phases after firing at 1300-1500°C. High glass contents reduce the strength. Glass is weaker than most crystals thus the crystal/glass ratio should be as high as possible for maximum strength. (Rado, 1988; Monshi, 1990; Mohd Noor, 1995)

From Table 6.1, increasing the SLS content resulted in: decreased residual quartz, decreased mullite formed on heating, and increased amount of plagioclase. The decrease in strength from S25 to S100 to some extent can be attributed to the decrease in mullite content. On the other hand, thermal mismatch caused by quartz on cooling should have been lessened with decreasing residual quartz content from S25 to S100, and should result in an increase in strength. However, this was probably counterbalanced by the sharp decrease in the content of mullite needles (see SEM image of S25 fired at 1100°C (Figure 6.46) and that of S100 (Figure 6.37)), and it seems that the development of interlocking fine mullite needles in the microstructure had a stronger effect and was the key factor controlling strength in these whiteware bodies. Increasing the amount of plagioclase could have led to increase in strength, but it seems to have had only a minor influence. S0 (fired at 1200°C) has a higher mullite and lower glass content than those of S25, but possibly due to higher quartz content it has lower strength than S25. Even though S25 has a higher glassy phase content, and also a lower crystal/glass ratio than seen in S0, S50 and S100, it still showed the highest strength. This may be related to the different composition of the glassy phase present.

However definitive reasons for the decrease in flexural strength values of batches containing high % SLS glass are still uncertain as the fracture origins have not been identified.

Modulus of elasticity is a measure of the capacity of a material to withstand stress without permanent deformation. Ceramic bodies, being brittle, deform very little and can withstand relatively high stress levels without deforming and therefore have a high modulus of elasticity. Ceramics usually do not distort to relieve stress but simply crack. From Table 6.2, the presence of SLS glass in whiteware batches results in decreased Young's moduli E, as reported (Tucci, *et al.*, 2003; Pontikes *et al.*, 2005). Porosity has a deleterious influence on both the elastic properties and strength. As explained above, the bulk density decreases with SLS content when firing the whitewares at 1100°C. Therefore, an increase in SLS content results in a decrease modulus of elasticity. Moreover, SLS glass itself has a flexural strength value 69 MPa and modulus of elasticity of 69 GPa while mullite has flexural strength of ~185 MPa and E ~145 GPa (Richerson, 1992). As a result, whiteware bodies containing higher amounts of mullite are expectedly stronger. The highest E of SLS-containing whiteware bodies was attained from S25 (6.25wt% SLS content), 72±5 GPa, which is comparable to that of the standard whiteware body S0 (74±3 GPa). From the literature (Rado, 1988; Russell, 1991), E for unglazed earthenware, stoneware, vitrified hotelware, hard porcelain and bone china are 55, 69, 82, 69-79 and 96 GPa, respectively. The E value of S25 is still within the range of hard porcelains.

The average mechanical strength value is insufficient to fully characterize the mechanical properties of ceramics. It is necessary to take into account the scattering of results. Weibull modulus (m) indicates the degree of variability in strength. The higher the value of m the less the variation in strength. The scattering in the mechanical strength data decreases with increasing m. The Weibull modulus "m" has also become a criterion for the variability of ceramic materials quality. Values between 5-20 are common for ceramics. The calculated variability for the data in this work may be attributed to compositional variations, firing temperatures and homogeneity of the samples tested. Fractography have not been studied in this work therefore the discussion on the effect of parameters such as chemical composition on

Weibull modulus is rather speculative. Also, it is worth mentioning that grinding and polishing of the sample's surface prior to strength measurements may remove surface microcracks which could lead to decreased strength values upon testing. In the present study, the samples were not ground and/or polished before the mechanical tests. S25 has the lowest value of m (Table 6.2), probably because S25 contains various crystalline phases and they are inhomogeneously distributed in the intricate microstructure. However, 13 is still an acceptable value for ceramic materials.

Fracture toughness is a measure of a material's resistance to crack propagation. Unlike strength, toughness is independent of fracture-initiating flaws (microcracks), although it is a strong function (Lee and Rainforth, 1994; Esposito *et al.*, 1995) of the microstructure of the material. The fracture toughness for S0 fired at 1250°C was 1.61±0.07 MPa$\sqrt{m}$, and that for S25 fired at 1150°C was 1.61±0.08 MPa$\sqrt{m}$. These are acceptable values for porcelains. These materials usually have K_{IC} values between 1.0 and 2.5 MPa$\sqrt{m}$. Fracture toughness depends on the relative amounts of crystalline phases, glassy phase and pore fraction. Glasses have low toughness values, typically about one half to one third of those measured for whitewares such as porcelain (Batista, 2001). Increasing the proportion of crystals in the glass should increase the value of K_{IC} as it is expected that cracks will have more difficulty in propagating through the crystals dispersed in the glass. S25 has a crystal/glass ratio of 0.49 which is lower than the 0.62 seen in S0. The reason why S25 has the same fracture toughness as S0 is unclear. It has been reported that an increase in porosity reduces fracture toughness because it also reduces the load bearing area, which reduces Young's modulus, and the fracture surface area to be formed as moving cracks are attracted to pores (Batista, 2001). The porosity present in S25 could be a reason for this low fracture toughness value.

In conclusion, 6.25wt% of SLS glass could be used as a flux in whiteware bodies without deterioration in mechanical properties. This environmentally friendly whiteware composition attained higher flexural strength, similar E and K_{IC} values as a standard triaxial whiteware body (S0). It is worth noting that this remarkable achievement was observed firing S25 100°C below the firing temperature of the standard whiteware body.

CHAPTER 7 - FURTHER DISCUSSION

The characterisation of raw materials (kaolin clay, quartz sand, nepheline syenite and colourless SLS waste glass), binary mixtures of raw materials (clay-quartz, clay-nepheline syenite, clay-SLS glass, quartz-nepheline syenite, quartz-SLS glass and nepheline syenite-SLS glass), and whiteware bodies of 50wt% kaolin clay and 25wt% quartz sand with various amounts of SLS glass replacing nepheline syenite flux, have been presented in chapters 4, 5 and 6. In this chapter, those results are summarised and compared from a different perspective with schematic diagrams representing the microstructural evolution on heating the compositions quoted above, as well as their sequence of reactions on firing by XRD. Attention will be paid to phase development and microstructural evolution, as these are key to understanding the properties of whitewares when new formulations are developed.

Phase development revealed by XRD of raw materials fired for 3h at various temperatures is summarised in Table 7.1 which also shows the phases present in the raw materials in their unfired state. The kaolin clay used in this work contained impurities such as muscovite and microcline which had an influence on its phase development on firing. These impurities acted as fluxes which hastened formation of mullite and liquid phase upon firing. The quartz sand is quite pure and contains only α-quartz therefore no phase change occurred at low temperatures. Inversion from quartz to cristobalite was observed after firing for 3h at temperatures ≥1300°C. Nepheline syenite contains mainly microcline, nepheline and small amounts of albite. Sanidine formed from the mixture of these alkali feldspars after firing ≥600°C and later leucite was detected at ~1000°C. These feldspars started to decompose at temperatures above 1000°C and melted completely by 1200°C. Colourless SLS glass was used in this study to substitute for the natural flux component in whiteware compositions. Because SLS glass has a T_g at ~560°C, the main idea was to use it (due to its low viscosity) to fill gaps between other more refractory raw materials leading to densification. The phase development upon firing SLS glass is therefore important as it affects significantly the microstructure, densification behaviour and mechanical properties of fired bodies containing it.

XRD shows the development of cristobalite, wollastonite and devitrite on firing SLS glass. These phases are the product of devitrification of SLS glass when reheating SLS glass powder. The whiteware processing procedure means that SLS glass needs to be crushed into a fine powder before it can be mixed with the other raw materials. Powdered SLS glass has a high tendency to devitrify when reheating due to this high surface area and impurities that enhance its surface crystallisation (Kirby, 2000). When crystallisation occurs, the viscosity of the glass increases and the rate of softened glass flow decreases, inhibiting further densification. However, the devitrified (crystalline) phases were found to dissolve and become liquid after firing to 1000°C. All SLS glass becomes liquid phase at temperature ~200°C lower than in nepheline syenite flux. Consequently, using SLS glass as a flux component brings whiteware bodies to a dense state at lower firing temperatures than using nepheline syenite.

Table 7.1 - Constituents of raw materials held 3h at various temperatures.

Temperature (°C)	Kaolin clay	Quartz sand	Nepheline syenite	SLS glass
unfired	kaolinite (α-quartz) (muscovite) (microcline)	α-quartz	microcline nepheline albite	glass
600°C	(α-quartz) (muscovite) (microcline) (microcline)	α-quartz	microcline nepheline albite sanidine	glass cristobalite
800°C	(α-quartz) (muscovite) (microcline) spinel	α-quartz	microcline nepheline albite sanidine	glass cristobalite wollastonite devitrite
1000°C	(α-quartz) mullite (glass)	α-quartz	nepheline sanidine leucite	glass
1200°C	(α-quartz) mullite (glass)	α-quartz	glass	glass
1300°C	(α-quartz) mullite (glass)	α-quartz cristobalite	glass	glass

Note: phases in brackets are present in small amount.

For a better understanding of the sequence of reactions that occurred on heating SLS glass, a box diagram of phase evolution on firing SLS glass pellets, based on the XRD study, is shown in Figure 7.1. A schematic of the microstructural evolution of

SLS glass on firing, based on SEM studies conducted in the present research work, is shown in Figure 7.2. According to Shelby (2005), the glass transition temperature (T_g) of commercial SLS glasses lies within the range 550-580°C. The recycled SLS glass used in this study has a T_g ~563°C (see DTA of SLS glass, Figure 4.4(a)), thus above this temperature SLS glass particles start to soften. At higher temperatures, the viscosity of the glass decreases and the glass can flow to the surrounding areas and stick to other glass particles which have not completely flowed. Interconnected pores are filled with liquid from softened glass leading to a denser microstructure (Figure 7.2) where closed pores are clearly visible.

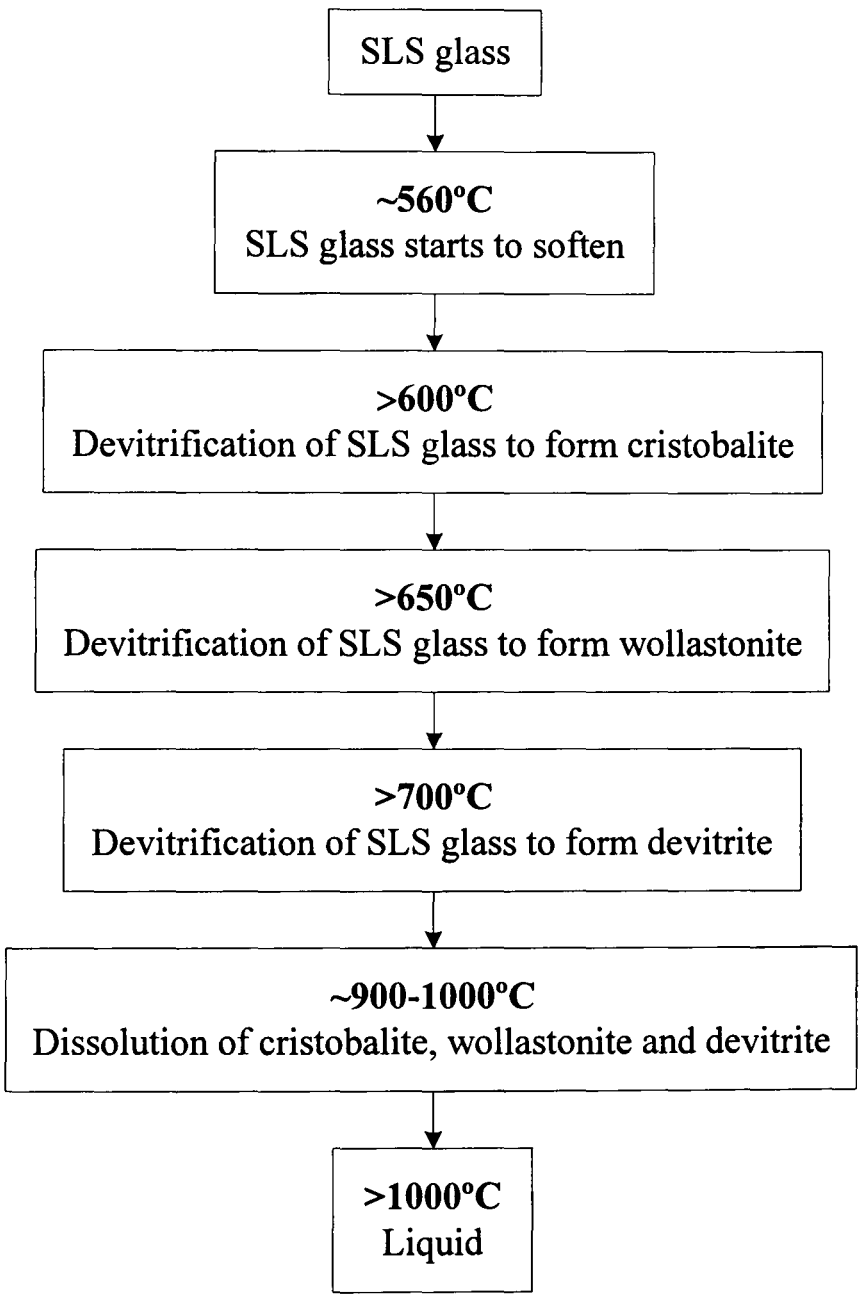

Figure 7.1 - Box diagram of phase evolution on firing SLS glass at 10°C/min.

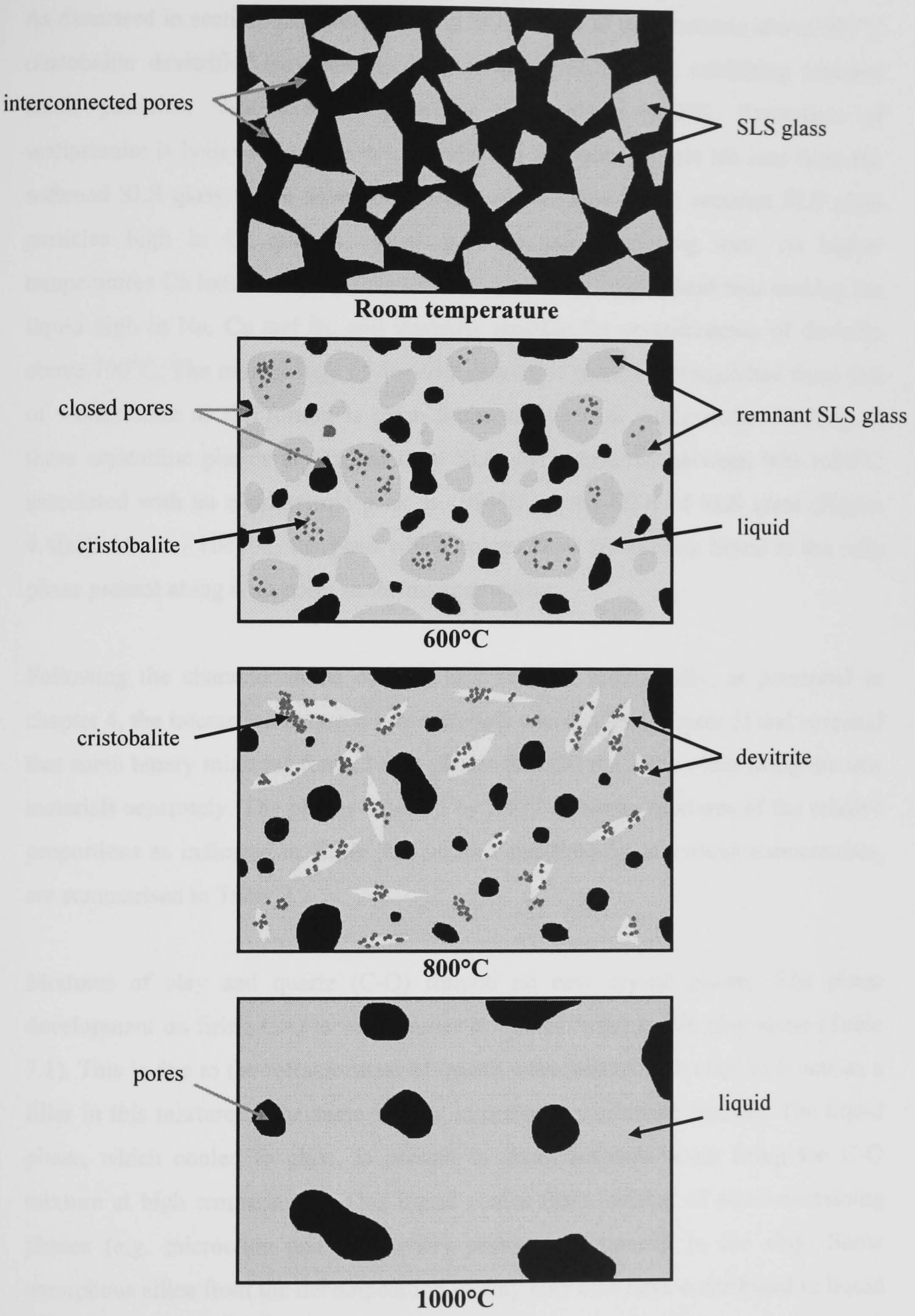

Figure7.2 - Schematic diagram of the microstructural evolution in SLS glass for firing at 10°C/min.

As discussed in section 4.5.4, after heating SLS pellets to temperatures above 600°C cristobalite devitrifies (crystallises) from softened SLS glass, exhibiting rounded small particles. Wollastonite crystallises only above 650°C. Formation of wollastonite is believed to arise due to diffusion of highly mobile Na ions from the softened SLS glass to the developing liquid phase. This leaves remnant SLS glass particles high in Ca and Si, which are the slower moving ions. At higher temperatures Ca ions start to diffuse to the surrounding liquid phase thus making the liquid high in Na, Ca and Si, and therefore suitable for crystallisation of devitrite above 700°C. The morphology of devitrite cannot be readily distinguished from that of wollastonite as the former is often found mixed with wollastonite. Melting of these crystalline phases devitrified from SLS glass occurred between 900-1000°C associated with an endothermic peak at ~990°C on the DTA of SLS glass (Figure 4.4(a)). Above ≥1000°C, the glass which comes from the cooling liquid is the only phase present along with pores in the microstructure.

Following the characterisation of each raw material individually, as presented in chapter 4, the interaction between raw materials was studied (chapter 5) and revealed that some binary mixtures formed new phases that did not form when firing the raw materials separately. The phases detected by XRD of binary mixtures of the relative proportions as indicated in Table 3.1, unfired and fired 3h at various temperatures, are summarised in Table 7.2.

Mixtures of clay and quartz (C-Q) formed no new crystal phases. The phase development on firing C-Q is very similar to that of firing kaolin clay alone (Table 7.1). This is due to the refractoriness of quartz when mixed with clay, as it acts as a filler in this mixture in the same way as in ordinary whiteware batches. The liquid phase, which cooled to glass, is present in small amounts when firing the C-Q mixture at high temperatures. This liquid comes from melting of alkali-containing phases (e.g. microcline and muscovite) present as impurity in the clay. Some amorphous silica from the decomposition of clay may also have contributed to liquid formation on firing.

Mixtures of clay and nepheline syenite (C-NS) also formed no new phases on firing. The phases present are simple mixtures of those phases present when clay and

nepheline syenite are fired individually. Leucite, however, was not found in this C-NS mixture. Nepheline, albite and sanidine began to melt at ~1000°C, and these feldspars acted as fluxes helping to form liquid leading to denser ceramic bodies than those made out of clay alone or C-Q. This liquid also hastened the formation of secondary mullite in the C-NS mixture.

Table 7.2 - Constituents of two-component mixtures held 3h at various temperatures.

Temperature (°C)	C-Q	C-NS	C-SLS	Q-NS	Q-SLS	NS-SLS
unfired	kaolinite α-quartz (muscovite) (microcline)	kaolinite (α-quartz) (muscovite) microcline nepheline albite	kaolinite (α-quartz) (muscovite) (microcline) glass	α-quartz microcline nepheline albite	α-quartz glass	microcline nepheline albite glass
600°C	α-quartz (muscovite) (microcline) (microcline)	(α-quartz) (muscovite) microcline nepheline albite sanidine	(α-quartz) (muscovite) (microcline) glass	α-quartz microcline nepheline albite sanidine	α-quartz glass	microcline nepheline albite sanidine glass
800°C	α-quartz (muscovite) (microcline) spinel	(α-quartz) (muscovite) microcline nepheline albite sanidine spinel	(α-quartz) (muscovite) (microcline) cristobalite wollastonite albite spinel mullite glass	α-quartz microcline nepheline albite sanidine	α-quartz cristobalite devitrite glass	microcline nepheline sanidine cristobalite wollastonite glass
1000°C	α-quartz mullite (glass)	sanidine mullite glass	cristobalite wollastonite plagioclase mullite glass	α-quartz microcline nepheline albite sanidine	α-quartz cristobalite tridymite glass	wollastonite glass
1200°C	α-quartz mullite (glass)	mullite glass	glass	α-quartz cristobalite glass	cristobalite tridymite glass	glass

Note: phases in blanckets are present in small amount.

It has been found that the mixture between clay and SLS glass (C-SLS) formed a new phase which was not produced by firing each component separately. That phase is plagioclase. Other phases developed in this mixture are the phases that were formed when firing clay and SLS glass separately. A box diagram of the phase evolution and the sequence of reactions occurring on firing C-SLS glass, based on the XRD studies, is shown in Figure 7.3. A schematic of the microstructural evolution of C-SLS on firing is shown in Figure 7.4.

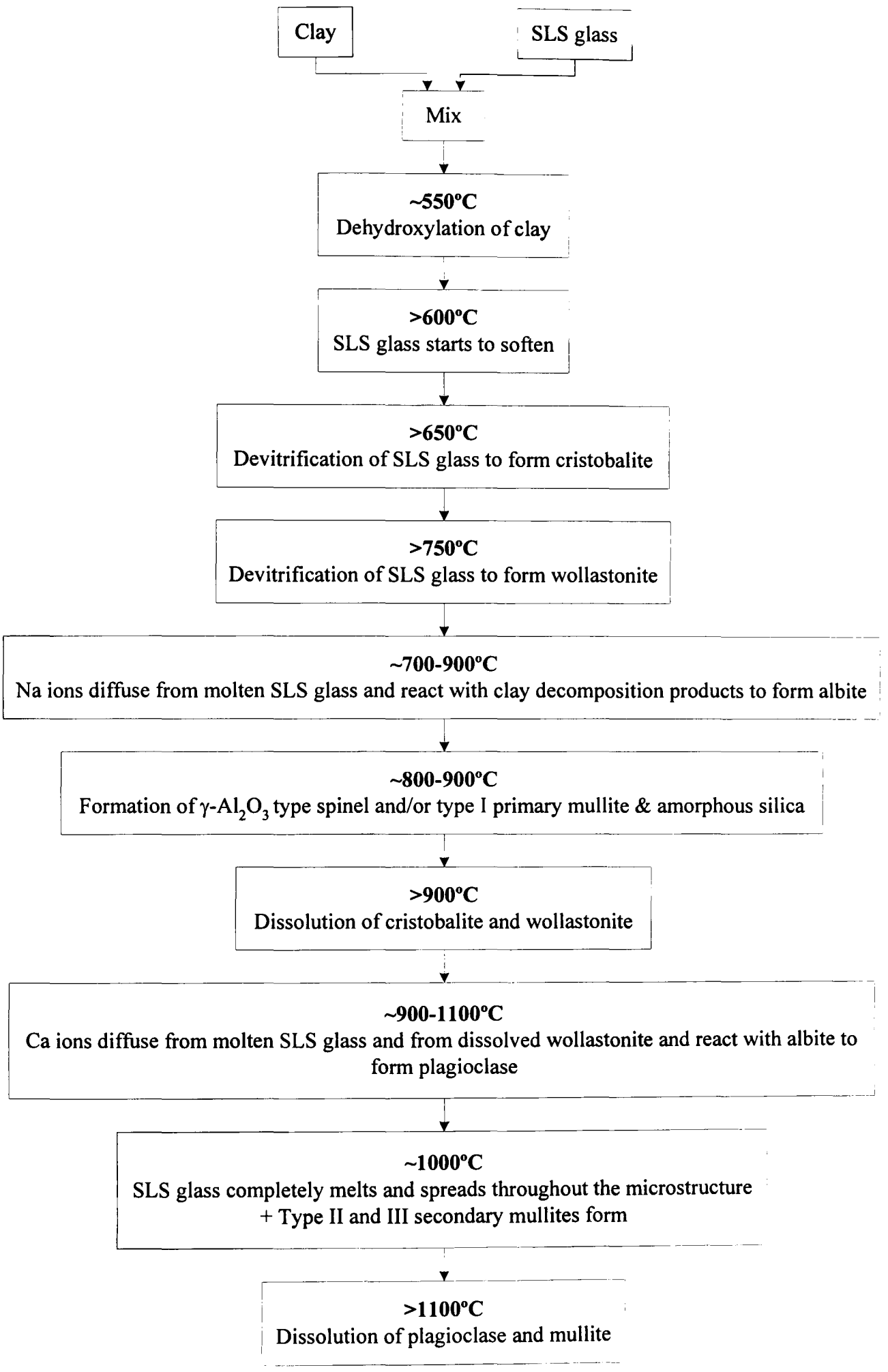

Figure 7.3 - Box diagram of phase evolution in the kaolin clay-SLS glass mixture for firing at 10°C/min.

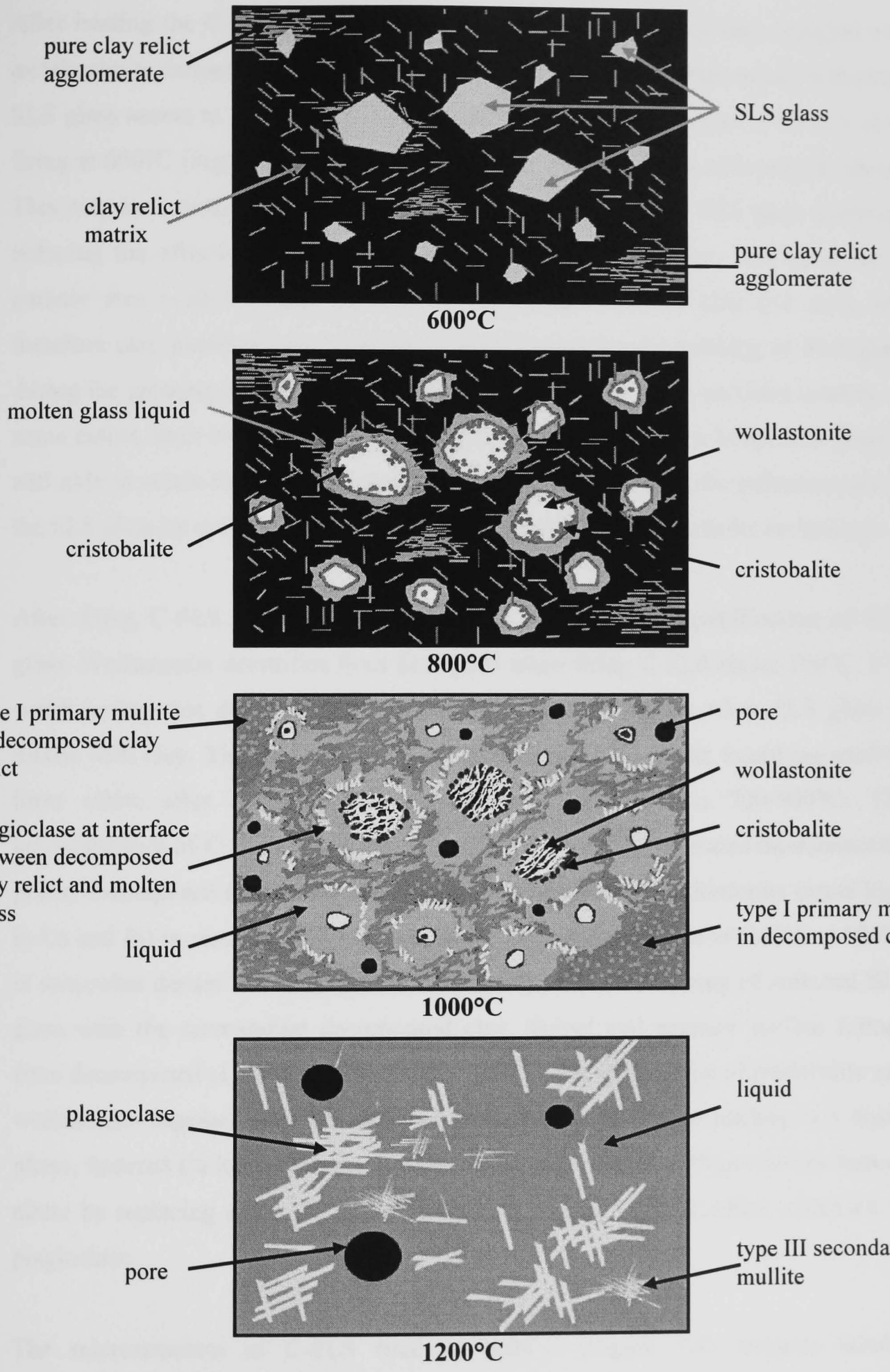

Figure 7.4 - Schematic diagram of microstructural evolution on firing the kaolin clay-SLS glass mixture at 10 °C/min.

After heating the C-SLS mixture to ~550°C, dehydroxylation of clay occurred and metakaolinite formed. SLS glass alone has a T_g at ~560°C but when mixed with clay, SLS glass seems to shift its T_g to above 600°C. The microstructure of C-SLS after firing at 600°C (Figure 7.4) still showed the SLS glass particles with angular shape. This may be a result of the presence of clay plates in between SLS glass particles, reducing the effective contact area between SLS glass particles. SLS glass has a particle size (~10-100 μm) significantly larger than that of clay (<1 μm), and therefore clay platelets can fit in the cavities formed by the packing of SLS glass during the pressing of the pellets. Limited contact between glass particles hinders, to some extent, their welding and the consequential shrinkage of the body. SLS glass is still able to retain its original shape. Hence, the clay increases the refractoriness of the SLS glass by reducing the contact area between SLS glass particles on heating.

After firing C-SLS above 650°C, cristobalite formed from devitrification of SLS glass. Wollastonite devitrifies from SLS glass when firing C-SLS above 750°C. It is worth noting that devitrite does not devitrify from SLS glass when SLS glass is mixed with clay. This is likely to be because the Na ions in the liquid are used to form albite after reacting with decomposed clay between 700-900°C. The microstructure of C-SLS pellets fired at 800°C (Figure 7.4) contains interconnected pores, decomposed clay relicts and rounded cristobalite and wollastonite (areas high in Ca and Si) in remnant SLS glass particles. The microstructure of C-SLS at 800°C is somewhat denser than that at 600°C, as some areas show fusing of softened SLS glass with the surrounding decomposed clay. Spinel and primary mullite formed from decomposed clay relicts between 800-900°C. The dissolution of cristobalite and wollastonite together with the enhanced softening of SLS glass leading to a liquid phase, fostered Ca ions diffusion into the liquid and reaction with previously formed albite by replacing some Na ions and forming a solid solution which stabilised as plagioclase.

The microstructure of C-SLS fired at 1000°C (Figure 7.4) contains tabular plagioclase at the interface between decomposed clay and decomposed SLS glass (a viscous liquid). Elongated wollastonite and rounded cristobalite can also be found in these regions. Cuboidal primary mullite (type I, Iqbal and Lee (1999)) can be seen in decomposed clay relict agglomerates. Molten glass liquid spreads throughout the

microstructure leading to open pore closure. The liquid formed allows mullite to grow longer. Elongated mullite can be found with longer tabular plagioclase particles after firing at 1200°C. Wollastonite and cristobalite are completely melted at this temperature while plagioclase and mullite are still observed by SEM, although they cannot be detected by XRD due to being present in small amounts.

Phase development on firing the mixture of quartz and nepheline syenite (Q-NS) is a blend of the phase development on firing nepheline syenite and quartz individually (see Table 7.2). Sanidine formed from the mixed alkali feldspars present in nepheline syenite after firing ≥600°C, and the system completely melted at 1100°C. The phase development of the quartz component is similar to that which occurred on firing quartz, which comprised the inversion from α to β quartz at 573°C and the conversion of some quartz to cristobalite, but in this mixture this conversion occurred when firing 3h at a lower temperature (1200°C) due to the nepheline syenite flux present in the system. Cristobalite formed on firing quartz solely at 1300°C.

The mixture of quartz and SLS glass (Q-SLS) developed tridymite on firing, a new phase that was not observed when firing quartz or SLS glass separately. A summary of the phase development on firing Q-SLS is shown in Table 7.2. Attention has been paid to this mixture as this study has not, to the author's knowledge, been reported previously. A box diagram of phase development and the sequence of reactions taking place on firing Q-SLS glass is presented in Figure 7.5. A schematic of the microstructural evolution of Q-SLS on firing, is shown in Figure 7.6.

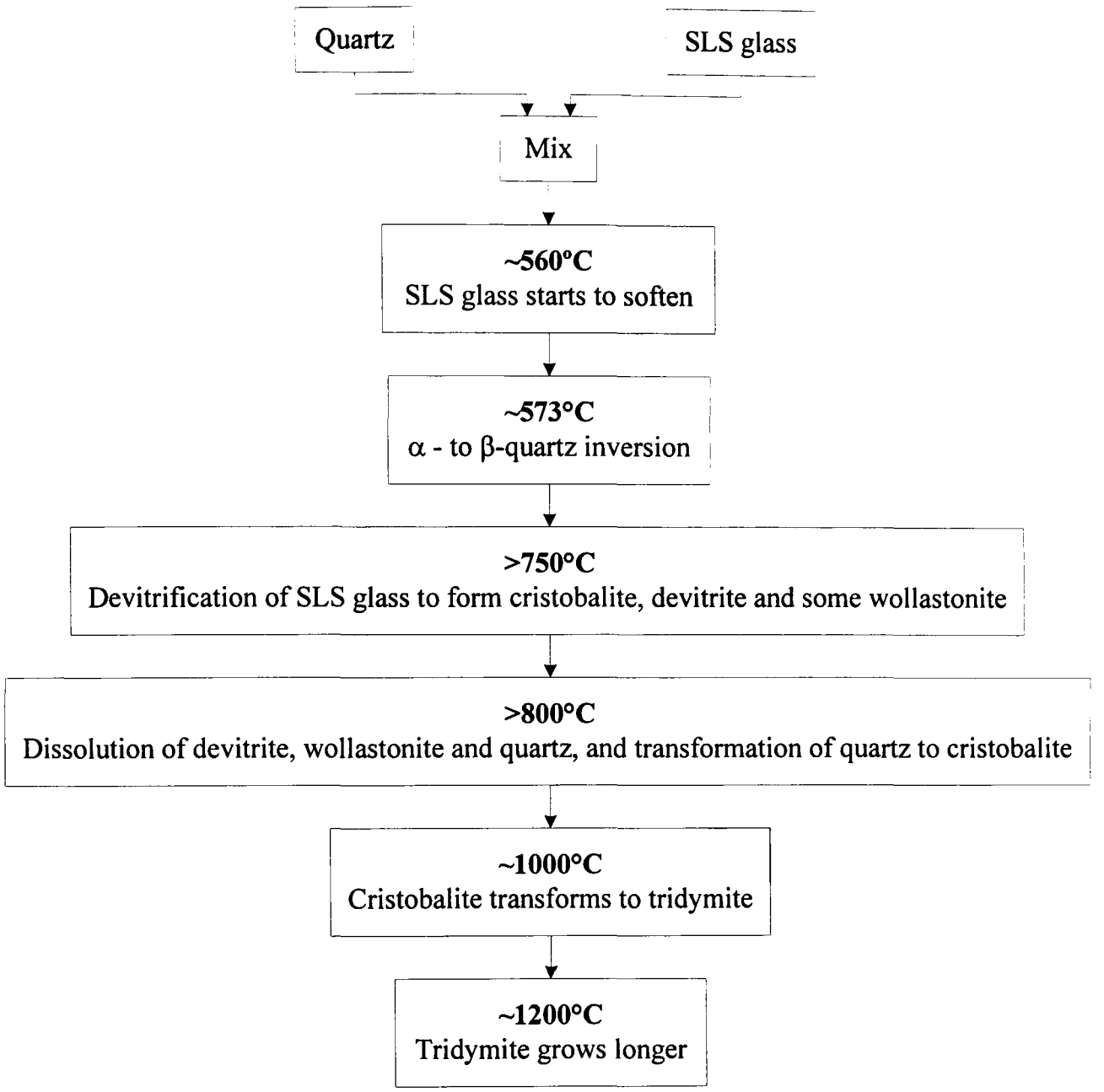

Figure 7.5 - Box diagram of phase evolution on firing the quartz-SLS glass mixture at 10°C/min.

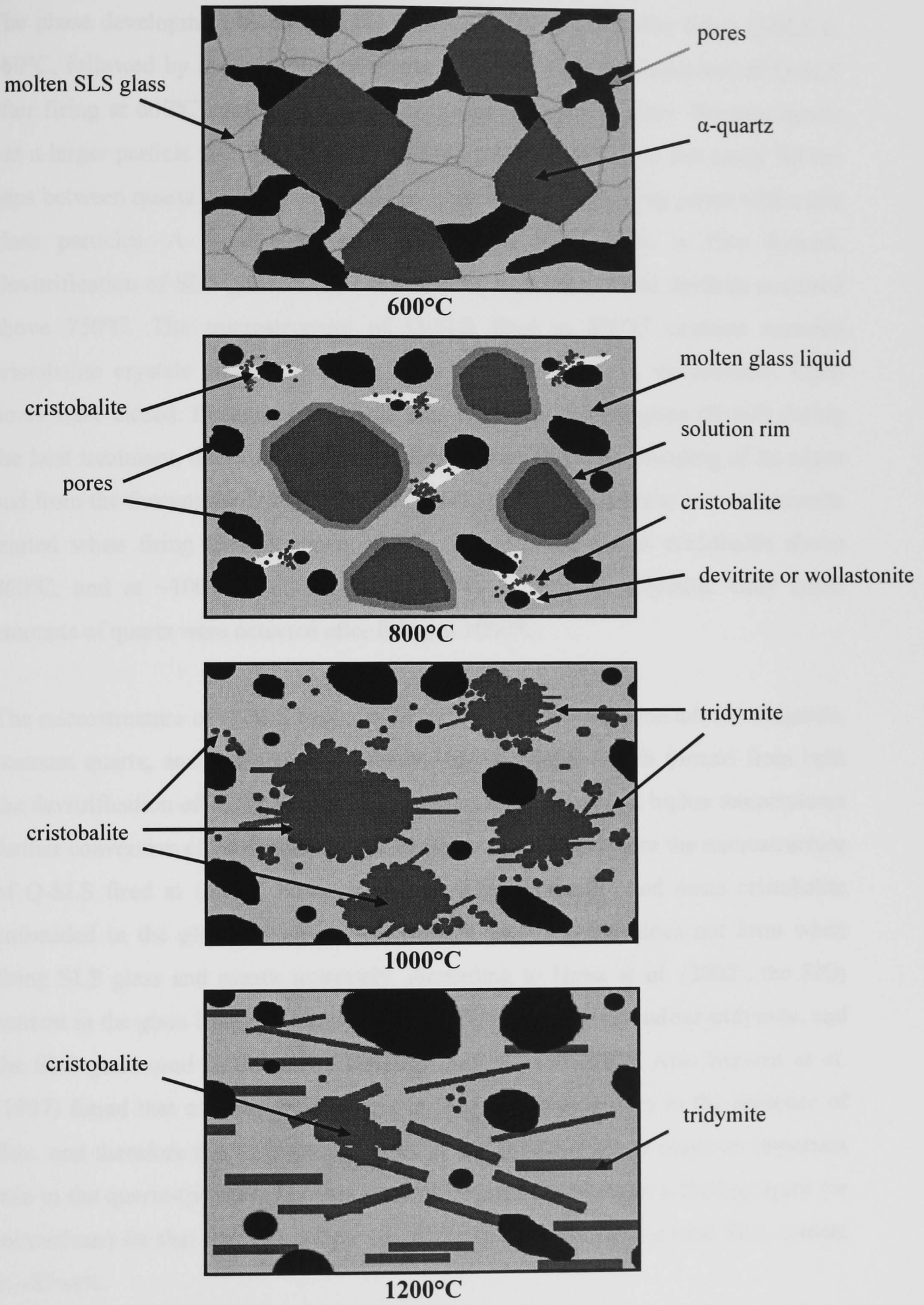

Figure 7.6 - Schematic diagram of the microstructural evolution on firing the quartz-SLS glass mixture at 10°C/min.

The phase development starts with the softening of SLS glass after firing Q-SLS to 560°C, followed by the inversion of quartz at 573°C. The microstructure of Q-SLS after firing at 600°C contains angular quartz and fusing SLS glass. Because quartz has a larger particle size distribution than the SLS glass, the latter can easily fill the gaps between quartz particles and establish a network of contacting points with other glass particles. A large area of interconnected fused glass is then formed. Devitrification of SLS glass to form cristobalite, wollastonite and devitrite occurred above 750°C. The microstructure of Q-SLS fired at 800°C contains rounded cristobalite crystals embedded in the glass near devitrite and wollastonite. Open pores were closed. Because quartz was surrounded by molten glass (liquid) during the heat treatment, dissolution of quartz can be seen from the rounding of its edges and from the formation of solution rims. The dissolution of devitrite and wollastonite started when firing Q-SLS above 800°C. Quartz converted to cristobalite above 800°C, and at ~1000°C cristobalite started to convert to tridymite. Only small amounts of quartz were detected after firing at 1000°C.

The microstructure of Q-SLS fired for 3h at 1000°C contains some tabular tridymite, remnant quartz, and agglomerates of rounded cristobalite which formed from both the devitrification of SLS glass and the conversion of quartz. At higher temperatures further conversion of cristobalite to tridymite occurs and therefore the microstructure of Q-SLS fired at 1200°C contains mostly longer tridymite and some cristobalite embedded in the glassy phase. It was noticed that tridymite does not form when firing SLS glass and quartz separately. According to Hrma *et al.* (2002), the SiO_2 content in the glass has to be higher than 75wt% in order to crystallise tridymite, and the SLS glass used in this study contains only ~73wt% SiO_2. Also Stevens *et al.* (1997) found that conversion of quartz to tridymite only occurs in the presence of flux, and therefore the SLS glass present in the Q-SLS mixture plays an important role in the quartz-tridymite conversion as SLS glass functions as a fluxing agent (or mineraliser) for that reaction. Moreover, in the Q-SLS mixture the total SiO_2 content is ~87wt%.

When mixing nepheline syenite and SLS glass (NS-SLS), the phase development on firing follows rigorously that occurring when firing nepheline syenite and SLS separately. The formation of sanidine after firing nepheline syenite above 600°C is

followed by the melting of the feldspars when firing above 1000°C. Cristobalite and wollastonite form at ~800°C as devitrification products of SLS glass. No new phase forms from the reaction between nepheline syenite and SLS glass. However it was noticed that feldspar melted faster in the NS-SLS mixture than in NS alone. This is likely to be due to the fact that both components contain high alkali contents (Ca, Na, K) thus making it easier to form liquid in the mixture on firing. SLS glass itself starts to soften and form a viscous liquid at above 560°C, whereas nepheline syenite is a well known flux component in whitewares.

The phase and microstructural evolution on firing raw materials and binary mixtures of raw materials were discussed above. The following summarises the phase development and microstructural evolution on firing whiteware bodies which comprised three or four raw materials each, as the amount of nepheline syenite flux replacement by SLS glass was systematically varied. Each whiteware body in this study consisted of 50wt% kaolin clay, 25wt% quartz and 25wt% flux (nepheline syenite and/or SLS glass). A box diagram of the sequence of reactions and phase evolution occurring on firing S0 (no SLS glass added) is shown in Figure 7.7, and a schematic of the morphologies and distribution of phases observed after firing at various temperatures is shown in Figure 7.8. When the as-mixed body is heated, kaolinite in the clay undergoes dehydroxylation at ~550°C and amorphous metakaolin is formed, similar to when firing clay alone or in binary mixtures. Inversion of quartz occurs ~573°C and was followed by sanidine formation at ≥600°C. The microstructure of S0 fired 3h at 600°C can be simply sketched as quartz and feldspar grains surrounded by clay relicts (Figure 7.8). At about 900°C, γ-Al_2O_3 spinel, cuboidal primary mullite and amorphous silica are formed. Feldspars start to melt at ~1000°C and elongated (type II) secondary mullite is initially crystallised out of the molten feldspar (in contact with clay). Primary mullite in clay relict agglomerates and secondary mullite in molten feldspar particles are seen after firing S0 at 1000°C (Figure 7.8).

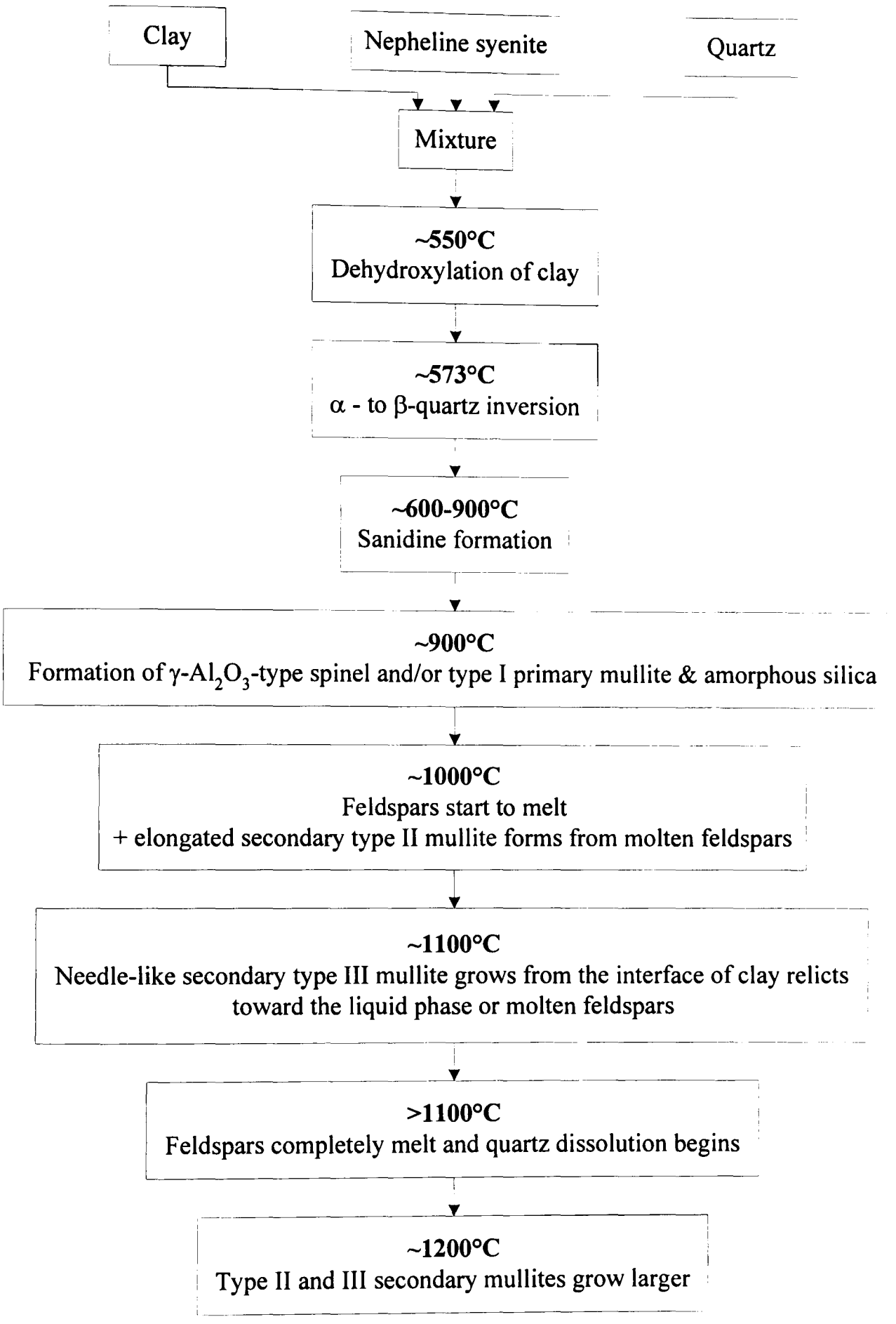

Figure 7.7 - Box diagram of phase evolution on firing standard (nepheline syenite-fluxed) whiteware at 10°C/min.

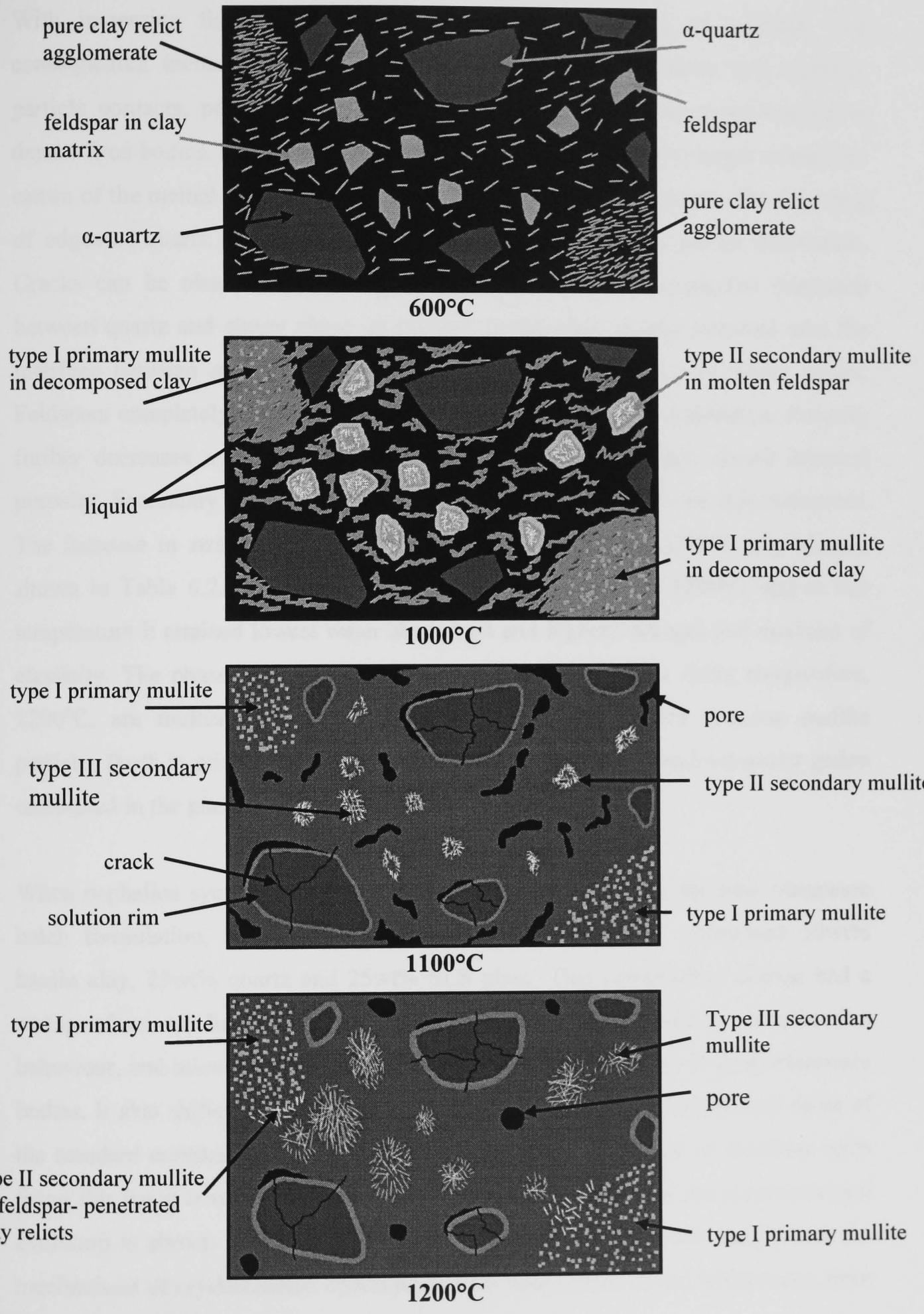

Figure 7.8 - Schematic diagram of the microstructural evolution on firing standard (nepheline syenite-fluxed) whiteware at 10°C/min.

With increasing firing temperature, the progressive melting of feldspars and consequential increase in liquid content caused the melt to move into capillary particle contacts, penetrate into gaps between particles and fill pores leading to denser fired bodies. Needle-like mullite (type III) forms and grows larger toward the centre of the melted regions. The feldspar melt dissolves more quartz. The rounding of edges of quartz particles with solution rims indicated their partial dissolution. Cracks can be observed due to the coefficient of thermal expansion mismatch between quartz and glassy phase on cooling. In the glass, cracks occurred near the interface between quartz and glass. Cracking was also noticed in quartz grains. Feldspars completely melt above 1100°C increasing the quartz dissolution. Porosity further decreases and gas trapped by flow of liquid forms into closed rounded porosity. Secondary mullite grows larger and further reinforces the microstructure. The increase in strength of fired S0 bodies from 1100°C to 1200°C was already shown in Table 6.2. S0 reaches its maximum densification at 1200°C, and at this temperature it attained lowest water absorption and highest strength and modulus of elasticity. The phases present in S0 after firing at its optimum firing temperature, 1200°C, are mullite, quartz and glass and the microstructure contains mullite particles (both in primary and secondary forms) and partially dissolved quartz grains embedded in the glass.

When nepheline syenite flux was replaced totally by SLS glass, the new whiteware batch formulation, so called 'SLS-fluxed whiteware (S100)' comprised 50wt% kaolin clay, 25wt% quartz and 25wt% SLS glass. This composition change had a strong effect on fired properties (both physical and mechanical), densification behaviour, and mineralogical and microstructural transformations of fired whiteware bodies. It also shifted the optimum firing temperature to lower values than those of the standard composition. A box diagram showing the sequence of reactions upon firing this batch is summarised in Figure 7.9, and a schematic of the microstructural evolution is shown in Figure 7.10. These figures provide a quick insight into the mechanisms of crystallisation operating in SLS waste glass-fluxed whitewares, from mineralogical and microstructural standpoints.

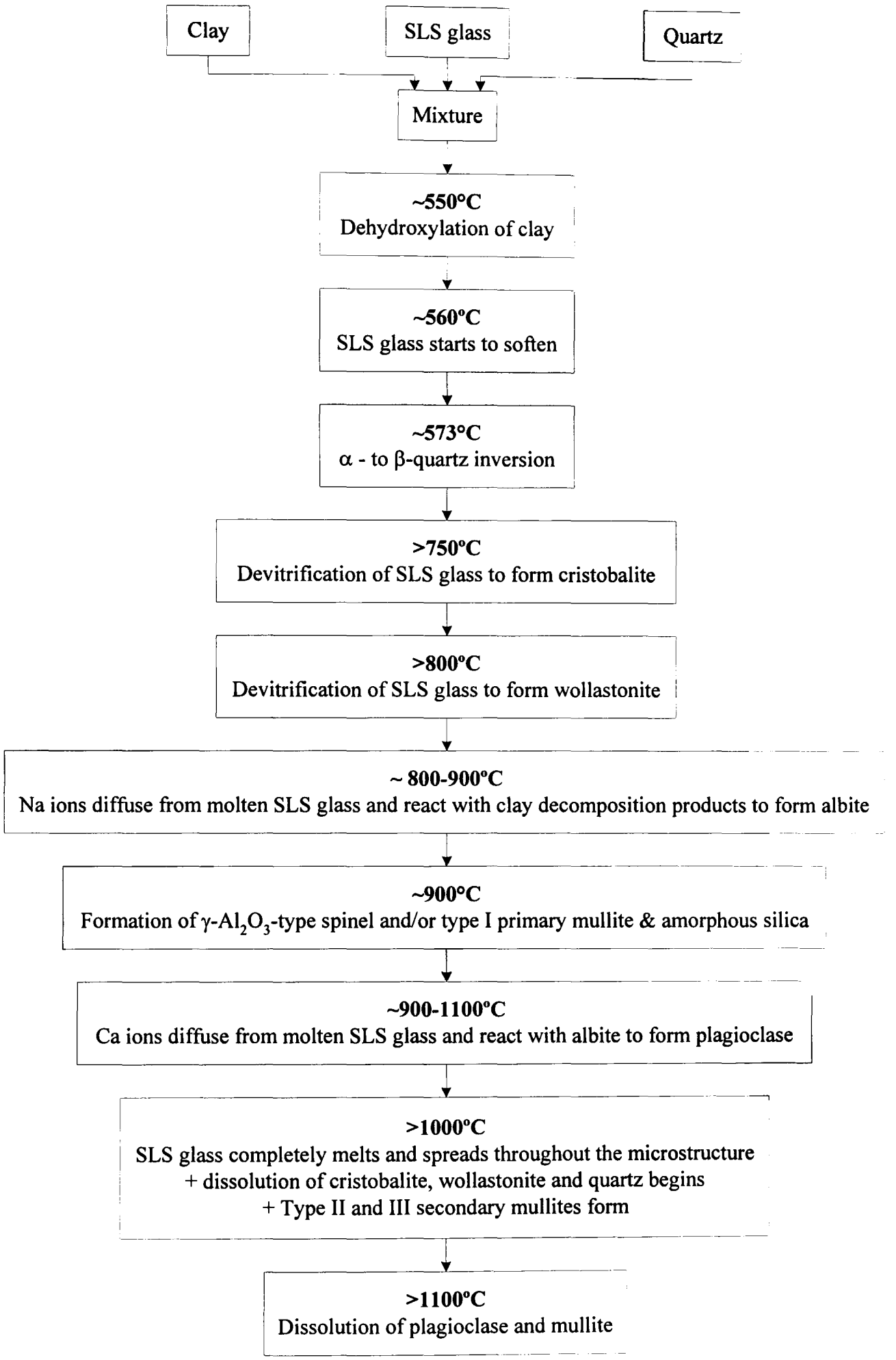

Figure 7.9 - Box diagram of phase evolution on firing SLS-fluxed whiteware at 10°C/min.

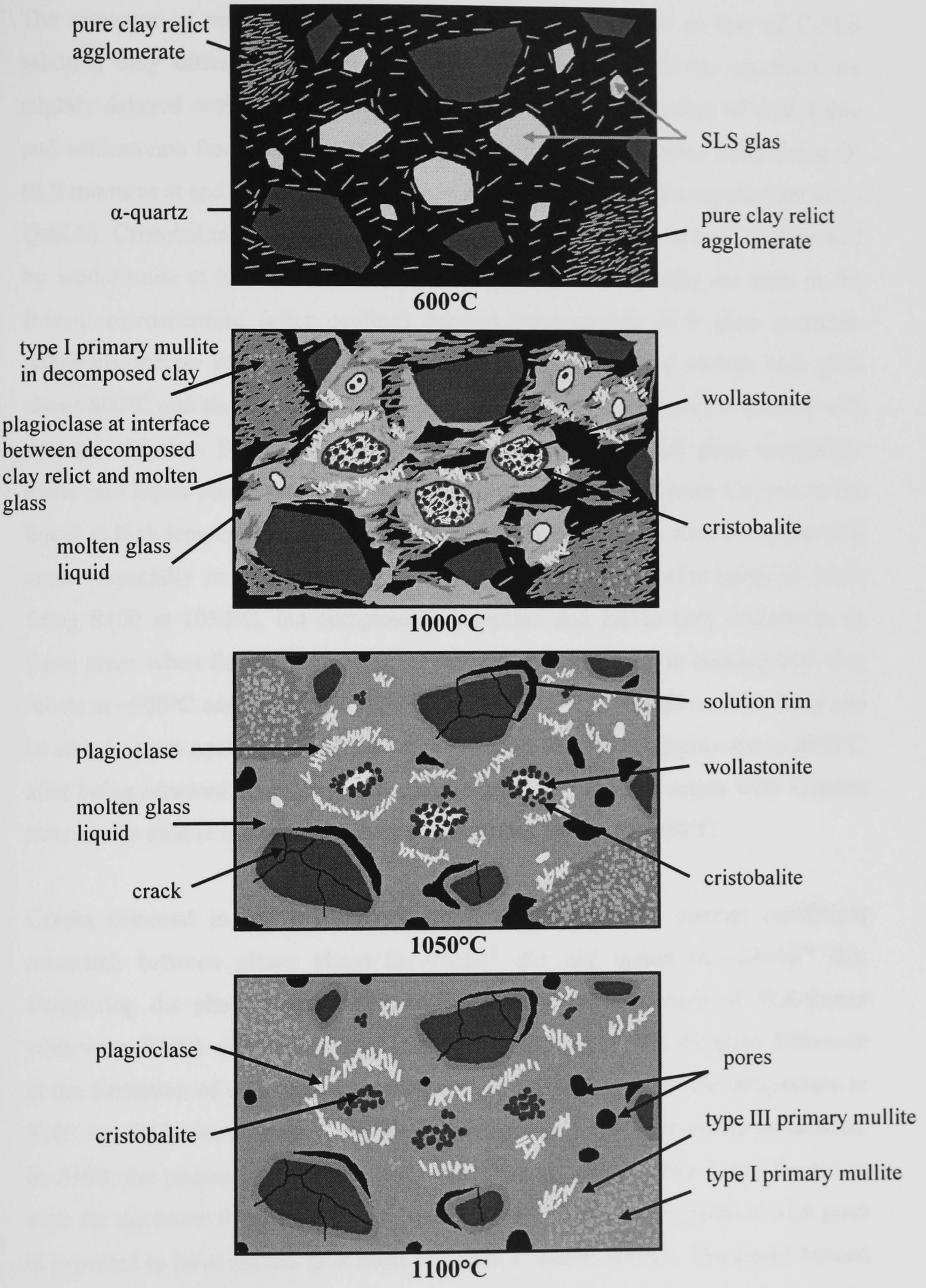

Figure 7.10 - Schematic diagram of the microstructural evolution on firing SLS-fluxed whiteware at 10°C/min.

The sequence of reactions of SLS-fluxed whiteware is similar to that of C-SLS mixture, only differing in terms of added quartz reactions. Some reactions are slightly delayed compared to C-SLS, for instance the crystallisation of cristobalite and wollastonite from devitrification of SLS glass. Tridymite forms upon firing Q-SLS mixtures at and above 1000°C but was not found in S100 (ternary mixture of C-Q-SLS). Cristobalite forms at ≥750°C (whereas it is at >650°C in C-SLS) followed by wollastonite at ≥800°C (>750°C in C-SLS). These two phases are seen in the frozen microstructure (after cooling) derived from molten SLS glass particles. Albite/plagioclase forms from the interaction between clay and molten SLS glass above 800°C and can be seen at the interface of molten SLS particles in contact with decomposed clay. Plagioclase particle size increases when SLS glass completely melts into liquid phase and when wollastonite dissolves and releases Ca ions to the liquid at high temperatures (≥1000°C). Wollastonite can still be seen in molten SLS areas (especially in the centre) together with rounded cristobalite particles when firing S100 at 1050°C, but completely disappears and leaves only cristobalite in those areas when firing up to 1100°C. Primary mullite forms in decomposed clay relicts at ~900°C and secondary mullite forms at ~1100°C and above. The latter can be seen in areas near the molten SLS glass. Quartz dissolution begins above 1000°C after being attacked by molten SLS glass. Rounding of quartz edges with solution rims can be seen in the microstructure of S100 after firing at ≥1050°C.

Cracks occurred in and around quartz particles, caused by thermal coefficient mismatch between glassy phase (α ~$3x10^{-6}$ /K) and quartz (α ~$23x10^{-6}$ /K). Comparing the phase development and microstructural evolution of SLS-fluxed whiteware (S100) with nepheline syenite-fluxed whiteware (S0), the main difference is the formation of new phases such as cristobalite, wollastonite and plagioclase in S100 and the lower amount of mullite formation and progressive quartz dissolution. In S100, the presence of 25wt% SLS glass resulted in extensive liquid formation even for the lower firing temperature applied (1000°C, at this temperature SLS glass is expected to have melted as it starts to soften at above 560°C). The liquid formed filled the porosity at an early stage of firing, causing the gases coming from the processing or evolved on firing (i.e. carbon dioxide from decomposition of organic matter, and water vapour from clay dehydroxylation) to be trapped, and resulting in severe bloating at firing temperatures higher than 1100°C.

Formation of crystalline phases such as cristobalite and wollastonite from low temperatures (below 900°C) is also likely to increase the viscosity of molten SLS glass due to its lower alkali content (i.e. Ca) which is being used to crystallise wollastonite. The higher viscosity of the liquid hinders its flow and also the diffusion of gases. An increase in closed porosity in S100 comparing to S0 was observed (Figure 6.4), and can be correlated to the lower bulk density (from 2.47 g/cm^3 in S0 to 2.29 g/cm^3 in S100) and lower shrinkage (from 9.17% in S0 to 8.11% in S100) after firing at the same temperature, 1100°C. An increase in closed porosity was also found by Matteucci *et al.* (2002), who used SLS glass as a flux in porcelain stoneware tiles. S0 has not reached its optimum firing temperature until firing to 1200°C whereas S100 reached its optimum firing temperature at 1100°C. Even though SLS accelerated the densification process making S100 reach its optimum firing temperature ~100°C lower than S0, this accelerated densification brought about formation of greater volumes of closed pores, and a subsequent lower bulk density and lower mechanical performance. The lower mechanical performance in S100 was also connected to the phase changes such as decreased mullite content. Partial substitution of nepheline syenite flux with 6.25wt% SLS glass was reported in previous chapters to be the best new formulation due to the lower optimum firing temperature, yet attaining comparable physical and mechanical properties to those of the nepheline syenite-fluxed whiteware (S0).

When 6.25wt% of nepheline syenite was partially replaced by SLS glass in the whiteware body composition, this new whiteware body (S25) comprised 50wt% kaolin clay, 25wt% quartz, 18.25wt% nepheline syenite and 6.25wt% SLS glass. A box diagram of the phase development and the sequence of reactions occurring upon firing S25 is shown in Figure 7.11, and a schematic of the microstructural evolution is shown in Figure 7.12. The reactions occurring upon firing this batch are, as expected, the combination of reactions occurring in S0 and S100. No new phase was observed. However, due to the low SLS content (6.25wt%) in this whiteware batch composition, products of devitrification of SLS glass such as cristobalite and wollastonite and products of the interaction of SLS glass and decomposed clay such as plagioclase, are formed in lesser amounts compared to S100. Less competition to use alumina for the formation of plagioclase allows more formation of mullite.

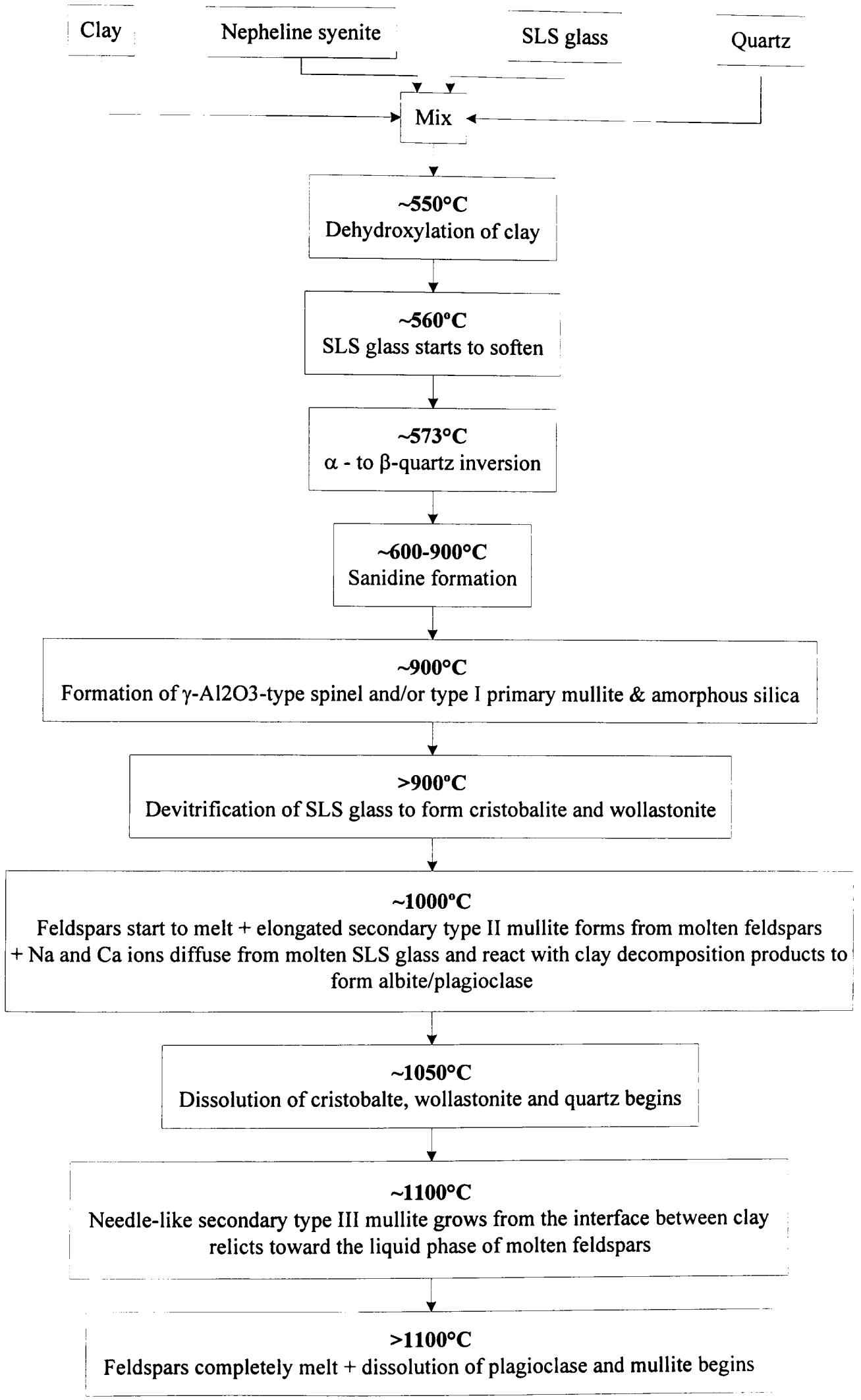

Figure 7.11 - Box diagram of phase evolution on firing partially SLS-fluxed (18.25wt% nepheline syenite and 6.75wt% SLS glass) whiteware at 10°C/min.

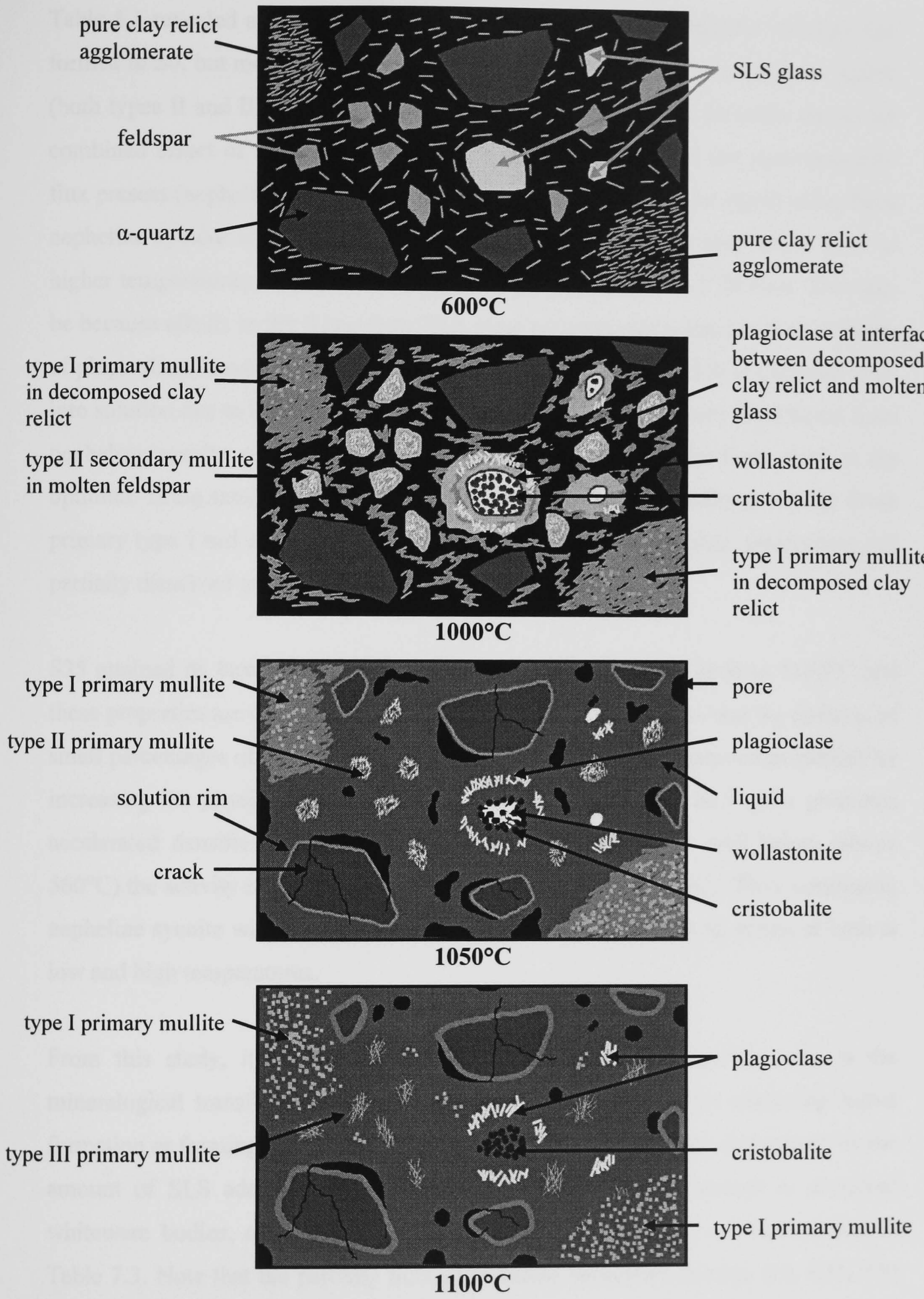

Figure 7.12 - Schematic diagram of the microstructural evolution on firing partially SLS-fluxed (18.25wt% nepheline syenite and 6.75wt% SLS glass) whiteware at 10°C/min.

Table 6.1 revealed a higher amount of mullite formed in S25 (slightly less than that formed in S0, but more than twice that in S100). The formation of secondary mullite (both types II and III) is more pronounced in S25 than in S100, probably due to the combined effect of higher alumina content in the mixture, and the more powerful flux present (nepheline syenite) when it melts. The viscosity of the liquid phase from nepheline syenite is believed to be lower than that from SLS glass when fired to higher temperatures. The viscosity for SLS glass at 1100°C is ~3.58 Pa-s. This may be because alkalis in the liquid from SLS glass are extensively used in the formation of plagioclase, leaving the liquid high in Si. Moreover, additional Si is expected to go into solution due to the larger extent of quartz dissolution. The more fluid liquid from nepheline syenite enhances the growth kinetics of mullite. The body fired at the optimum firing temperature (1100°C) has a microstructure containing mullite (both primary type I and secondary types II and III), remnant cristobalite, plagioclase and partially dissolved quartz embedded in the glassy phase.

S25 attained its best physical and mechanical properties when fired to 1100°C and these properties are comparable with S0 fired at 1200°C. It seems that the addition of small percentages of SLS glass to nepheline syenite flux has improved properties by increasing the physico-chemical activity at low temperatures. SLS glass promotes accelerated densification as it starts to soften at temperatures well below (above 560°C) the activity range of nepheline syenite flux (above 1000°C). Thus, combining nepheline syenite with SLS glass can accelerate the overall fluxing action at both at low and high temperatures.

From this study, it was found that SLS glass plays an important role in the mineralogical transformations on firing whiteware bodies, either enhancing liquid formation or forming new phases. The extent of these transformations depends on the amount of SLS added to the whiteware batch. The phases present in as-mixed whiteware bodies, and those fired 3h at various temperatures are summarised in Table 7.3. Note that the partially SLS glass-fluxed whiteware batches (i.e. S25, S50 and S75) revealed a similar phase evolution from a qualitative standpoint, but differing quantitatively according to the amount of SLS waste glass added. Semi-quantitative XRD of these batches (Figures 6.20-6.24) was discussed at length in previous section (section. 6.4).

Table 7.3 - Constituents of whiteware bodies held 3h at various temperatures.

Temperature (°C)	S0	S25	S50	S75	S100
unfired	kaolinite α-quartz muscovite microcline nepheline albite	kaolinite α-quartz muscovite microcline nepheline albite glass	kaolinite α-quartz muscovite microcline nepheline albite glass	kaolinite α-quartz muscovite microcline nepheline albite glass	kaolinite α-quartz muscovite microcline glass
600	α-quartz muscovite microcline nepheline albite	α-quartz muscovite microcline nepheline albite glass	α-quartz muscovite microcline nepheline albite glass	α-quartz muscovite microcline nepheline albite glass	α-quartz muscovite microcline glass
800	α-quartz muscovite microcline nepheline albite sanidine	α-quartz muscovite microcline nepheline albite sanidine glass	α-quartz muscovite microcline nepheline albite sanidine glass	α-quartz muscovite microcline nepheline albite sanidine glass	α-quartz muscovite microcline cristobalite albite glass
1000	α-quartz microcline nepheline sanidine mullite	α-quartz microcline nepheline sanidine cristobalite plagioclase mullite glass	α-quartz microcline nepheline sanidine cristobalite plagioclase mullite glass	α-quartz sanidine cristobalite wollastonite plagioclase mullite glass	α-quartz cristobalite wollastonite plagioclase mullite glass
1050	α-quartz mullite glass	α-quartz cristobalite plagioclase mullite glass	α-quartz cristobalite plagioclase mullite glass	α-quartz cristobalite plagioclase mullite glass	α-quartz cristobalite wollastonite plagioclase mullite glass
1100	α-quartz mullite glass	α-quartz cristobalite plagioclase mullite glass	α-quartz cristobalite plagioclase mullite glass	α-quartz cristobalite plagioclase mullite glass	α-quartz cristobalite wollastonite plagioclase mullite glass
1150	α-quartz mullite glass	α-quartz cristobalite plagioclase mullite glass	α-quartz cristobalite plagioclase mullite glass	α-quartz cristobalite plagioclase mullite glass	α-quartz cristobalite plagioclase mullite glass
1200	α-quartz mullite glass	α-quartz cristobalite plagioclase mullite glass	α-quartz cristobalite plagioclase mullite glass	α-quartz cristobalite plagioclase mullite glass	α-quartz cristobalite plagioclase mullite glass

CONCLUSIONS

The replacement of nepheline syenite with colourless SLS waste glass in whiteware bodies changed their chemical composition, as well as the extent of the availability of the fluxing agents. The amount of potassium and alumina decreased, and the amount of sodium, calcium and silica increased. The change in composition and the nature of the raw materials affected both physical and mechanical properties and also the phase and microstructural evolution of the whiteware on firing. Considering the physical properties, SLS glass seems to accelerate the densification process due to earlier vitrification. Whiteware bodies densified faster due to the formation of a highly-fluid liquid rich in sodium and calcium that filled the pores and prevented escape of trapped gas causing severe bloating, strongly limiting the actual amount of SLS glass used. Nepheline syenite-fluxed whiteware undergoes vitrification only above 1000°C. From the results of physical properties, the replacement of 6.25wt% nepheline syenite by SLS glass is by far the best composition. This batch attained the best physical properties after firing at 1100°C. It produced fired bodies with almost 0% water absorption, and slightly higher (~1%) linear shrinkage and 0.08 g/cm^3 higher bulk density than those of the best physical properties of the standard composition body fired at 1200°C. On the basis of these comparable properties, it is suggested that this combination of composition/firing temperature may allow production of whitewares from cheaper raw materials and at lower temperatures thus saving energy. The lower firing temperature required for the firing of the 6.25wt% SLS-containing whiteware batch has been estimated to save ~4.64% in the energy consumption comparing to the firing of the standard whiteware batch. The energy consumption for firing the standard whiteware is ~30.8 kWh per piece whereas that for the 6.25wt% SLS-containing whiteware is ~29.35 kWh. Assuming a current standard electricity price of £0.1614 per kWh, the energy cost for firing the standard batch would be £4.96 per piece, and £4.73 per piece for the 6.25wt% SLS-containing whiteware. Therefore, an industry producing 1 million pieces of whiteware per year could expect to achieve energy savings on firing of £230,000 per year for the use of 6.25wt% SLS glass.

Standard composition whiteware body made of 50wt% clay, 25wt% quartz and 25wt% nepheline syenite after firing at 1200°C has a microstructure comprised of primary and secondary mullites and partially dissolved quartz embedded in glassy phase. The microstructures of fired specimens from batches containing SLS glass (6.25-25wt%) comprised partially dissolved quartz, primary and secondary mullites, cristobalite, wollastonite and plagioclase, as well as glassy phases with variable composition depending on the local environment. The amount of cristobalite, wollastonite and plagioclase increased with increasing SLS content as cristobalite and wollastonite are direct products of SLS glass devitrification, and plagioclase is formed from the interaction between SLS glass and decomposed clay. The formation of plagioclase in SLS glass containing whiteware batches depends strongly on the migration of Ca^{2+} and Na^{+} to regions containing clay decomposition products. The standard whiteware body, having insufficient CaO and Na_2O (which are more abundant in SLS glass) to form plagioclase, develops a microstructure of larger mullite crystals, and quartz at variable stages of dissolution depending on the firing temperature. Quartz solution rims contain Al and K (as well as Si and O), consistent with the melting of nepheline syenite flux which ultimately attacks the quartz. Mullite and quartz contents decreased with increasing SLS content in SLS-containing whiteware batches. The decrease in mullite formation is due to the lower alumina content in the liquid because of the substitution of nepheline syenite for SLS glass which is very nearly alumina-free, and also due to the fact that alumina was consumed in the plagioclase. Ca^{2+} and Na^{+} are highly reactive and can react with decomposed clay and form plagioclase faster than mullite. No new phase formed by the interaction of nepheline syenite and SLS glass. The study of mixtures between raw materials revealed formation of tridymite on heating Q-SLS, however this phase was not clearly identified in the whiteware batches. Decreased quartz content in SLS-containing batches results from accelerated dissolution of quartz in the presence of decomposed SLS glass. This also increases the amount of liquid which deforms the ceramic body especially in batches with higher SLS content.

Fired samples made from SLS-containing batches fired at 1100°C have higher flexural strength and modulus of elasticity than those of the standard batch fired at the same temperature. Similarly to physical properties, mechanical properties were found to worsen with higher additions of SLS glass, and the best mechanical

properties were seen in the batch containing 6.25wt% SLS glass. It's worth noting that the strength results were statistically very similar, although pointing to a decrease in its values with increasing the SLS glass content above 6.25wt%. Mullite seems to be the strongest factor for strength of whiteware bodies in this study, as higher SLS contents result in decreased mullite and decreased strength. Whiteware bodies containing 6.25wt% SLS glass and 18.75wt% nepheline syenite as flux components fired at 1100°C have higher flexural strength (~71 MPa), slightly lower modulus of elasticity (~72 GPa) and similar fracture toughness (1.61 MPa$\sqrt{m}$) to those of the standard whiteware body fired at 1200°C. The lower Weibull modulus of the batch containing SLS glass was probably due to the more heterogeneous microstructure.

It is feasible to produce whitewares using ~6.25wt% recycled SLS waste glass as it shows comparable physical and mechanical properties to a standard whiteware body even firing at 100°C lower. The values of most properties actually match those of commercial porcelains, thus there is a real potential to produce porcelains using SLS glass as partial flux. Using SLS glass as the sole flux in the whiteware body narrows the firing temperature range and increases bloating that would lead to severe difficulties in production. The waste glass may be best used in combination with natural fluxes to overcome those difficulties.

SUGGESTIONS FOR FUTURE WORK

The microstructural evolution of SLS-containing whitewares could also be investigated by TEM analysis of quenched samples. Morphology of sub-micron crystalline phases and glassy phase local composition could be revealed at each step of firing.

In this study, the densification behaviour, mechanical behaviour and microstructural evolution were limited to samples subjected to traditional firing schedules. In modern whiteware industry, fast firing is also used and therefore full investigation of the densification behaviour and microstructures of fast-fired bodies should be carried out to compare with those of slowly fired bodies.

Complex shaped products are formed by slip casting. Viscosity of the slip after using SLS glass as a flux in whitewares should be measured in order to produce complex shapes such as tableware and sanitary ware. The solubility of the SLS glass in the slurry is an important factor as large amounts of sodium ions are leached out of the glass and might interfere with fluidity and thixotropy of the slips. Also the replacement of feldspar with SLS waste glass affects the viscosity of the liquid formed on firing, which is related to the capability of the liquid to wet and react with crystalline phases and fill the inter-particle voids during densification. This can cause dense or porous products, thus the viscosity of the high-temperature liquid should be measured.

The potential for extending the use of recycled coloured SLS glass in whitewares with opaque glaze and in other vitreous ceramic systems, to avoid the need to separate different colour waste glasses should be examined. Red-clay based ceramics such as structural bricks and roof tiles would certainly accommodate such recycled coloured glasses in their composition.

Devitrification of SLS glass is more likely in fine particles. If devitrification occurs, the viscosity of glass will increase and make it more difficult for further densification and also for gases trapped to be released (highly viscous glass obstructs

the elimination of gases out of the body). It would be interesting to study the use of coarser SLS particles in whitewares, and also different particle size distributions to look at their effects on both green and fired density, as well as on the overall crystallisation of the ceramic body. Waste glass is relatively easy to break into a coarse powder and therefore industrial milling should not be a limiting factor.

REFERENCES

Altamirano-Juarez, D. C., Carrera-Figueiras, C., Garnica-Romo, M. G., Mendoza-Lopez, M. L., Ortuno-Lopez, M. B. and Perez-Romos, M. E., "Effects of Metals on the Structure of Heat-Treated Sol-Gel SiO_2 glasses", J. Phys. Chem. Sol., **62**, 1911-1917, 2001.

Amigo, J. M., Clausell, J. V., Esteve, V., Delgado, J. M., Reventos, M. M., Orchando, L. E., Debaerdemaeker, T. and Marti, F., "X-Ray Powder Diffraction Phase Analysis and Thermomechanical Properties of Silica and Alumina Porcelains", J. Euro. Ceram. Soc., **24**, 75-81, 2004.

Arkhipov, I. I., Nemchenok, Z. O. and Rempel, A. P., "Using Waste for the Production of Ceramic Tiles", Glass and Ceram, **36**[10], 588-589, 1979.

Artir, R. and Yilmaz, E., "Utilization of Waste Window Glasses in the Porcelain of Traditional Ceramics" in 11th International Metallurgy and Materials Congress, Istanbul, Turkey, 2002.

ASTM, "Standard Definition of Terms Related to Ceramic Whitewares and Related Products" ASTM Designaion C242 in *Annual Book of ASTM Standard*, 15.02 American Society for Testing and Materials, Philadelphia, PA, 1996.

Barlow, S. G. and Manning, D. A. C., "Influence of Time and Temperature on Reactions and Transformations of Muscovite Mica", Brit. Ceram. Trans., **98**[3], 122-126, 1999.

Barth, T. F. W., *Feldspars*, Pitman Press, Bath, UK, 1969.

Batista S. A. F., *Design and Processing of High-Strength Anorthite/mullite Porcelains*, PhD Thesis, University of Sheffield, 2001.

Baumgart, W., Dunham, A. C. and Amstutz, G. C., *Process Mineralogy of Ceramic Materials*, Elsevier Science Publishing Co., Inc., New York, USA, 1984.

Boccaccini, A. R., Schawohl, J., Kern, H., Schunck, B., Rincon, J.M. and Romero, M., "Sintered Glass Ceramics from Municipal Incinerator Fly Ash", Glass Technol., **41**, 99-105, 2000.

Boccaccini, A. R., Stumpfe, W., Rtaplin, D. M. and Ponton, C. M., "Densification and Crystallization of Glass Powder Compacts During Constant Heating Rate Sintering", Mat. Sci. & Eng., **A219**, 26-31, 1996.

Boffe, M., Pecriaux, G. and Plumat, E., "Formation of Bubbles During Devitrification and Remelting of Crystals in Glass", in *Symposium on Nucleation and Crystallization in Glasses and Melts*, American Ceramic Society, Ohio, USA, 1962.

Boss, C. A. and Fredeen, K. J., *Concepts, Instrumentation, and Techniques in Inductively Coupled Plasma Optical Emission Spectrometry*, Perkin-Elmer Corporation, Wellesley, Massachusetts, USA, 1997.

Braganca, S. R. and Bergmann, C. P., "A View of Whitewares Mechanical Strength and Microstructure", Ceram. Int., **29**, 801-806, 2003.

Braganca, S. R. and Bergmann, C. P., "Traditional and Glass Powder Porcelain: Technical and Microstructure", J. Eur. Ceram. Soc., **24**, 2383-2388, 2004.

Braganca, S. R. and Bergmann, C. P., "Waste Glass in Porcelain", Mat. Res., **8**[1], 39-44, 2005.

Brown, G., "Crystal Structures of Clay Minerals and Related Phyllosilicates" in *Clay Minerals: Their Structure, Behaviour and Use*, The Royal Society, London, 1984.

Brown, I. W. M. and Mackenzie, K. J. D., "Process Design for the Production of a Ceramic-like Body from Recycled Waste Glass", J. Mater. Sci., **17**, 2164-2193, 1982.

Butler, J. and Hooper, P., "Dilemmas in Optimising the Environmental Benefit from Recycling: a Case Study of Glass Container Waste Management in the UK", Resources, Conservation and Recycling, **45**, 331-355, 2005.

Cameron, W. E., "Mullite: a Substituted Alumina", Am. Mineral., **62**, 747-755, 1977.

Carty, W. M., "Observation on the Glass Phase Composition in Porcelains", Chem. Eng. Sci. Proc., 23(2), 79-94, 2002.

Carty, W. M. and Senapati, U., "Porcelain – Raw Materials, Processing, Phase Evolution, and Mechanical Behavior", J. Am. Ceram. Soc., **81**[1], 3-20, 1998.

Champness, P. E., *Electron Diffraction in the Transmission Electron Microscope*, BIOS Scientific Publishers Ltd., Oxford, UK, 2001.

Chaudhuri, S. P., "Crystallization of Glass of the System $K_2O(Na_2O)$-Al_2O_3-SiO_2", Ceram. Int., **8**[1], 27-33, 1982.

Chen, Y. F., Wang, M. C. and Hon, M. H., "Phase transformation and growth of mullite in kaolin ceramics", J. Euro. Ceram. Soc., **24**[8], 2389-2397, 2004.

Clark-Monks, C. and Parker, J. M., *Stone and Cord in Glass*, H Charlesworth & Co. Ltd., Huddersfield, UK, 1980.

Cole, S. S., "The Conversion of Quartz into Cristobalite Below 1000°C, and Some Properties of the Cristobalite Formed", J. Am. Ceram. Soc., **18**[5], 149-154, 1935.

Cullity, B. D., *Elements of X-ray Diffraction*, Addison-Wesley, London, UK, 1978.

Davidge, R. W., *Mechanical Behaviour of Ceramics*, Cambridge University Press, Oxford, UK, 1980.

Davidge, R.W. and Green, T.J., "The Strength of Two-Phase Ceramic/Glass Materials", J. Mater. Sci., **3**, 629-634, 1968.

Deer, W. A., Howie, R. A. and Zussman, J., *An Introduction to the Rock-Forming Minerals*, Longman Scientific and Technical, London, UK, 1992.

Dinsdale, A., *Pottery Science Materials, Process, and Products*, Ellis Horwood Ltd., West Sussex, UK, 1986.

Echlin, C., "Evolution of a Commercial Ball Clay Deposit", Bull. Am. Ceram. Soc., **81**[8] 69-71, 2002.

Esposito, L., Timellini, G. and Tucci, A., "Fracture Toughness of Traditional Ceramic Materials: a First Approach", Proc. 4th Eur. Ceram. Soc. Conf., **11**, 221-230, 1995.

Esposito, L., Salem, A., Tucci, A., Gualtieri, A. and Jazayeri, S. H., "The Use of Nepheline-Syenite in a Body Mix for Porcelain Stoneware Tiles", Ceram. Int., **31**, 233-240, 2005.

Fenner, C. N., "Stability Relations of the Silica Minerals", Am. J. Sci., **36**[214], 331-384, 1913.

Ferreira, J.M.F., Torrres P.M.C., Silva, M.S. and Labrincha, J.A., "Recycling of Granite Sludges in Brick-Type and Floor Tile-Type Ceramic Formulations", Euroceram News, **14**, 1-5, 2003.

Fitzjohn, W. H. and Worrall, W. E., "Mineralogical Analysis of Unfired Brick Clays", Trans. J. Brit. Ceram. Soc., **79**, 67-73, 1980.

Flörke, O. W., "Structural Anomalies of Tridymite and Cristobalite", Ber. Deut. Keram. Ges., **32**[12], 369-381, 1955.

Fokin, V. M., Potapov, O. V., Zanotto, E. D., Spiandorello, F. M., Ugolkov, V. L. and Pevzner, B. Z., "Mutant Crystals in Na2O·2CaO·3SiO2 Glasses", J. Non-Cryst. Solids, **331**, 240-253, 2003.

Ford, W. F., *The Effect of Heat on Ceramics*, Maclaren and sons Ltd., London, UK, 1967.

Freiman, S. W., "Fracture Mechanics: Applications for Whitewares" in *Science of Whitewares*, Westerville, Ohio, 1996.

Goldsmith, A., Waterman, T. E., Hirshhorn, H. J., *Handbook of Thermophysical Properties of Solid Materials – Volume III: Ceramics*, Pergamon Press, London, 1961.

Green, D. J., *An Introduction to the Mechanical Properties of Ceramics*, Cambridge University Press, Cambridge, UK, 1998.

Grimshaw, R. W., *The Chemistry and Physics of Clays and Allied Ceramic Materials*, Ernest Benn Limited, London, UK, 1971.

Haber, R. A. and Smith, P. A., "Overview of Traditional Ceramics" in *Engineered Materials Handbook Volume 4: Ceramics and Glasses*, ASM International, Ohio, USA, 1991.

Haines, P. J., *Thermal Methods of Analysis*, Chapman & Hall, Glasgow, UK, 1995.

Hajjaji, M., Kacim, S. and Boulmane, M., "Mineralogy and Firing Characteristics of a Clay from the Valley of Ourika (Morocco)", Appl. Clay. Sci., **21**, 203-212, 2002.

Hand, R. J., Stevens, S. J. and Sharp, J. H., "Characterisation of Fired Silicas", Therm. Act., **318**, 115-123, 1998.

Hlavac J., *The Technology of Glass and Ceramics*, Elsevier Science Publishing Company, New York, USA, 1983.

Holmstrom, N. G., "Fast Firing of Triaxial Porcelain", Bull. Am. Ceram. Soc., **60**[4], 470-473, 1981.

Holmquist, S. B., "Conversion of Quartz to Tridymite'', J. Am. Ceram. Soc., **44**, 82-86, 1961.

Hren, J. J., Goldstein, J. I. and Joy, D. C., *Introduction to Analytical Electron Microscopy*, Plenum Press, London, UK, 1979.

Huan, M. J., "Ceramic Products Made from Waste Glass, Raw Batch Formulations, and Method", U.S. Patent No. 6,340,650, 2002.

Iqbal, Y. and Lee, W.E., "Fired Porcelain Microstructure Revisited", J. Am. Ceram. Soc., **82**[12], 3584-3590, 1999.

Iqbal, Y. and Lee, W.E., "Microstructural Evolution in Triaxial Porcelain", J. Am. Ceram. Soc., **83**[12], 3121-3127, 2000.

Iqbal, Y., Messer, P. F. and Lee, W. E., "Non-Equilibrium Microstructure of Bone China", Brit. Ceram. Tran., **99**[3], 2000.

Kara, A., Özer, F., Kayaci, K. and Özer, P., "Development of a Multipurpose Tile Body: Phase and Microstructural Development", J. Euro. Ceram. Soc., **26**[16], 3769-3782, 2006.

Kingery, W. D., *Introduction to Ceramics*, Wiley, Newyork, USA, 1976.

Kirby, R. J., *Densification, Crystallization and Sticking Behaviour of Crushed Waste Glass Sintered in Refractory Molds with Release Agents*, Clean Washington Centre-pacific NorthWest Economic Region, Seattle, USA, 2000.

Kirby, R. J., *An Investigation of the Performance of Paving Units Made from Recycled Glass with a Mineral Additive*, Chelsea Centre for Recycling and Economic Development, University of Massachusetts Lowell, 2001.

Knapp, O., *Devitrification of Silicate Glasses*, Akadémiai Kiadó, Budapest, 1965.

Koenig, C. J., "Use of Nepheline Syenite in Sanitary Porcelain", J. Am. Ceram. Soc., **22**[2], 38-46, 1939.

Koenig, C. J., "Nepheline Syenite in Whiteware and Structural Clay Products", Ceram. Inter., **2**, 100-101, 1964.

Larson, A. W. and Von Dreele, R. B., "General Structure Analysis System Manual", Los Alamos Natl. Lab. Rep. LA-UR-86-748, 1994.

Lawrence, H. V. V, "Microstructure of Silica in the Presence of Iron Oxide", J. Am. Ceram. Soc., **43**[3], 140-145, 1960.

Lawrence, W. G., *Ceramic Science for the Potter*, Chilton Book Company, New York, USA, 1972.

Lee, S., Kim, Y. J. and Moon, H. S., "Phase Transformation Sequence from Kaolinite to Mullite Investigated by an Energy-Filtering Transmission Electron Microscope", J. Am. Ceram. Soc., **82**[10], 2841-2848, 1999.

Lee, W. E. and Igbal, Y., "Influence of Mixing on Mullite Formation in Porcelain", J. Euro. Ceram. Soc., **21**[14], 2583-2586, 2001.

Lima, M. M. and Monteiro, R., "Characterization and Thermal Behaviour of a Borosilicate Glass", Thermochimica Acta, **373**, 69-74, 2001.

Lingart, Y., "Imitation Natural Material Tiling Using Waste Glass", Glass Technol., 39(2), 42-43, 1998.

Liu, W., Li, S., and Zhang, Z., "Sintered Mosaic Glass from Ground Waste Glass", Glass Technol., **32**[1], 24-27, 1991.

Lundin, S. T., "Electron Microscopy of Whiteware Bodies", in *Transactions of The IVth International Ceramics Congress*, Florence, Italy, 1954.

Lundin, S.T., "Microstructure of Porcelain", in *Microstructure of ceramic materials*, Proceedings of the American Ceramic Society Symposium, National Bureau of Standards Miscellaneous Publications No. 257. National Bureau of Standards, Gaithersburg, MD, 1964.

Marotta, A., Buri, A. and Branda, F., "Surface and Bulk Crystallisation in Non-Isothermal Devitrification of Glasses",

Marzhal, H., "Influence of Quartz on the Strength of Porcelain", Ber. Deut. Keram. Ges., **32**, 203-211, 1955.

Matteucci, F., Dondi, M., and Guarini, G., "Effect of Glass Waste Addition on Technological Properties of Porcelain Stoneware Tiles", Key. Eng. Mat., **206-213**, 851-854, 2002.

Matteucci, F., Dondi, M., and Guarini, G., "Effect of Soda-Lime-Glass on Sintering and Technological Properties of Porcelain Stoneware Tiles", Ceram. Int., **28**, 873-880, 2002.

Mattyasovsky-Zolsnay, L., "Mechanical Strength of Porcelain", J. Am. Ceram. Soc., **40**, 299-306, 1957.

McConville, C. J., Lee, W. E. and Sharp, J. H., "Microstructural Evolution in Fired Kaolinite", Brit. Ceram. Tran., **97**[4], 162-168, 1998.

Mohd Noor, A. F. B., *Reformation of Vitrified Quartz-Containing Whitewares*, PhD Thesis, University of Sheffield, 1995.

Monshi, A., *Fracture Toughness and Characterisation of some Whitewares Containing Quartz*, PhD Thesis, University of Sheffield, 1990.

Neely J. E. and Ernsberger, F. M., "Absence of Devtrification at Bubble Surfaces in Soda-Lime Glasses", J. Am. Ceram. Soc., **49**[7], 396-397, 1966.

Newcomb, R., *Ceramic Whitewares*, Pitman Publishing Corporation, New York, USA, 1947.

Newton, J.M., *The Tensile Strength and Fracture Toughness of Heavy Clay Bodies*, PhD Thesis, University of Sheffield, 1995.

Norton, C. L., "The Influence of Time on Maturing temperature of Whiteware bodies: II", J. Am. Ceram. Soc., **14**, 192-206, 1962.

Norton, F. H., *Fine Ceramics Technology and Applications*, McGraw-Hill Inc., New York, USA, 1970.

Oberschmidt, L. E., "The Use of Nepheline Syenite in Electrical Porcelain Bodies'', Bull. Am. Ceram. Soc., **36**[12], 464-465, 1957.

Papargyris, A. D. and Cooke, R. D., "Structure and Mechanical Properties of Kaolin Based Ceramics", Brit. Ceram. Trans., **95**[3], 107-120, 1996.

Pontikes, Y., Christogerou, A., Angelopoulos, G. N., Rambaldi, E., Esposito, L. and Tucci, A., "Use of Scrap Soda-Lime-Silica Glass in Traditional Ceramics", Glass Tech., **46**[2], 200-206, 2005.

Prado, M. O., Ferreira, E. B. and Zanotto, E. D., "Sintering Kinetics of Crystallizing Glass Particles, a Review" in *Proceedings of 106th Annual Meeting of the ACerS - Symposium # 26 - Melt Chemistry, Relaxation, and Solidification Kinetics of Glasses*, USA, 2004.

Prado, M. O., Fredericci, C. and Zanotto, E. D., "Isothermal Sintering and Concurrent Crystallization of Soda-Lime-Silica Glass Beads", J. Non-Cryst. Solids, **331**[1-3], 145-56, 2003.

Prado, M. O. and Zanotto, E. D., "Glass Sintering with Concurrent Crystallization", C. R. Chimie, **5**, 773-786, 2002.

Prado, M. O., Zanotto, E. D and Fredericci, C., "Sintering Polydispersed Spherical Glass Particles", J. Mater. Res., **18**[6], 1-8, 2003.

Rado, P., *An Introduction to the Technology of Pottery*, Pergamon Press, Oxford, UK, 1988.

Rambaldi, E., Tucci, A. and Esposito, L., "Glass Recycling in Porcelain Stoneware Tiles: Firing Behaviour", cfi/Ber. DKG., **81**, E1-E4, 2004.

Reed, J. S., *Principles of Ceramic Processing*, Wiley & Sons, New York, 1995.

Rice, P. M., *Pottery Analysis*, The University of Chicago Presss, Chicago, USA, 1987.

Roy, S. B., and Som. S. K., "Use of Nepheline Syenite in Ceramic Industry'', Glass and Ceram. Bull., **17**, 31-37, 1970.

Russell, K., "Ceramic Whiteware", in *Engineered Materials Handbook Volume 4: Ceramics and Glasses*, ASM International, Ohio, USA, 1991.

Ryan, W. and Radford, C., *Whitewares: Production, Testing and Quality Control*, The Institute of Materials, London, UK, 1997.

Sane, S. C. and Cook, R. L., "Effect of Grinding and Firing Treatment on the Crystalline and Glass Content and the Physical Properties of Whiteware Bodies", J. Am. Ceram. Soc., **34**[5], 145-151, 1951.

Santos, H. S., Campos, T. W., Santos, P. S. and Kiyohara, P. K., "Thermal Phase Sequences in Gibbsite/Kaolinite Clay: Electron Microscopy Studies", Ceram. Int., **31**[8], 1077-1084, 2005.

Scholes, S. R., *Modern Glass Practice*, Cahners Publishing Company, Inc., Massachusetts, USA, 1975.

Schuller, S., "Reactions between Mullite and Glassy Phase in Porcelains", Tran. Brit. Ceram. Soc., **63**[2], 103-117, 1964.

Shelby, J. E., *Introduction to Glass Science and Technology*, the Royal Society of Chemistry, Cambridge, UK, 2005.

Smykatz-Kloss, W., *Differential Thermal Analysis: Application and Results in Mineralogy*, Springer-Verlag Berlin, Heidelberg, Germany, 1974.

Sosman, R. B., *Phase of Silica*, Rutgers University Press, New Brunswick, New Jersey, USA, 1965.

Souza, G. P., *Densification Behaviour and Microstructural Evolution of a Red Clay-Based Stoneware*, PhD Thesis, University of Sheffield, 2005.

Souza, G. P., Rambaldi, E., Tucci, A., Esposito, L. and Lee, W. E., "Microstructural Variations in Porcelain Stoneware Tiles as a Function of Flux System", J. Am. Ceram. Soc., **87**[10], 1959-66, 2004.

Srinivara, R., Raghavan, H. J. W. and Saad, A. K, "Rheology of Silica Dispersions in Organic Liquids: New Evidence for Solvation Forces Dictated by Hydrogen Bonding", Langmuir, **16**, 7920-7930, 2000.

Stevens, S. J., Hand, R. J. and Sharp, J. H., "Polymorphism of Silica", J. Mater. Sci., **32**, 2929-2935, 1997.

Swift, H. R., "Some Experiments of Crystal Growth and Solution in Glasses", J. Am. Ceram. Soc., **30**[6], 165-169, 1947.

Toya, T, Kameshima Y., Yasumoru, A. and Okada, K, "Preparation and Properties of Glass-Ceramics from Waste (Kira) of Silica Sand and Kaolin Clay Refining", J. Eu. Ceram. Soc., **24**, 2367-2372, 2004.

Traore, K., Kabre, T. S. and Blanchart, P., "Gehlenite and Anorthite Crystallisation from Kaoinite and Calcite Mix", Ceram. Int., **29**[4], 377-383, 2003.

Tucci, A., Rambaldi, E. and Esposito, L., "Use of Scrap Glass as Raw Material for Porcelain Stoneware Tiles", Adv. App. Ceram., **104**[6], 1-6, 2005.

Tucci, A., Esposito, L., Ratelli, E., Palmonari, C., and Rambaldi, E., "Use of Soda-Lime-Scrap Glass as a Fluxing Agent in a Porcelain Stoneware Tile Mix", J. Euro. Ceram. Soc., **24**, 83-92, 2004.

Vangordon, D. V., "Recovered Soda-Lime Glass as a Ceramic Body Flux", Ceram. Eng. Sci. Proc., **4**[11/12], 1056-1066, 1983.

Van Vlack, L. H., "Microstructure of Silica in the Presence of Iron oxide", J. Am. Ceram. Soc., **43**[3], 140-145, 1960.

Venezia, A. M., Parola, V. A., Longo, A. and Martorana, A., "Effect of Alkali Ions on the Amorphous to Crystalline Phase Transition of Silica", J. Sol. State. Chem., **161**, 373-378, 2001.

Watanabe, O. and Kato, S., "Vitrification Behavior for the Body Composed of Recycled Glass Bottle, Feldspar and Clay", in *Environmental Issues and Waste Management Technologies in the Ceramic and Nuclear Industries VI*, American Ceramic Society, Ohio, USA, 2001.

West, R. R., "High Temperature Reactions in Domestic Ceramic Clays". Bull. Amer. Ceram. Soc., **37**[6], 1958.

Willems, H. W. V., "Primary Phase of Clear Sheet Glass", Glass Ind., **47**[5], 257-261, 1966.

Worrall, W. E., *Ceramic Raw Materials*, Pergamon Press, Oxford, UK, 1982.

Yang, J. J. and Wang, E. G., "Water Adsorption on Hydroxylated Alpha-Quartz (0001) Surfaces: from Monomer to Flat Bilayer", Physical Review B **73**[3]: Art. No. 035406, 2006.

Youssef, N. F., Abadir, M. F., and Shater, M. A. O., "Utilization of Soda Glass (Cullet) in the Manufacture of Wall and Floor Tiles", J. Euro. Ceram. Soc., **18**, 1721-1727, 1998.